Syntheses and Properties of π-Extended Indenofluorene Derivatives

Doctoral Thesis

by

Himanshu

2019CYZ0021

DEPARTMENT OF CHEMISTRY

INDIAN INSTITUTE OF TECHNOLOGY ROPAR

December, 2024

Syntheses and Properties of π-Extended Indenofluorene Derivatives

A Thesis Submitted

In Partial Fulfillment of the Requirements

for the Degree of

DOCTOR OF PHILOSOPHY

by

Himanshu

2019CYZ0021

DEPARTMENT OF CHEMISTRY

INDIAN INSTITUTE OF TECHNOLOGY ROPAR

December, 2024

Himanshu: *Syntheses and Properties of π-Extended Indenofluorene Derivatives*
Copyright © 2024, Indian Institute of Technology Ropar
All Rights Reserved

DEDICATED

TO

MY PARENTS,

AND TO EVERYONE WHO BELIEVES IN ME

Declaration of Originality

I hereby declare that the work which is being presented in the thesis entitled **Syntheses and Properties of π-Extended Indenofluorene Derivatives** has been solely authored by me. It presents the result of my own independent investigation/research conducted during the time period from December 2019 to December 2024 under the supervision of Dr Soumyajit Das, Assistant Professor, IIT Ropar. To the best of my knowledge, it is an original work, both in terms of research content and narrative, and has not been submitted or accepted elsewhere, in part or in full, for the award of any degree, diploma, fellowship, associateship, or similar title of any university or institution. Further, due credit has been attributed to the relevant state-of-the-art and collaborations with appropriate citations and acknowledgments, in line with established ethical norms and practices. I also declare that any idea/data/fact/source stated in my thesis has not been fabricated/ falsified/ misrepresented. All the principles of academic honesty and integrity have been followed. I fully understand that if the thesis is found to be unoriginal, fabricated, or plagiarized, the Institute reserves the right to withdraw the thesis from its archive and revoke the associated Degree conferred. Additionally, the Institute also reserves the right to appraise all concerned sections of society of the matter for their information and necessary action (if any). If accepted, I hereby consent for my thesis to be available online in the Institute's Open Access repository, inter-library loan, and the title & abstract to be made available to outside organizations.

Signature 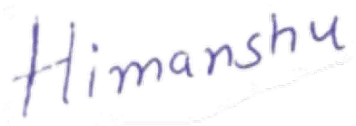

Name: Himanshu
Entry Number: 2019CYZ0021
Program: PhD
Department: Chemistry
Indian Institute of Technology Ropar
Rupnagar, Punjab 140001

Date: 13/2/2025

Acknowledgments

I would like to take this opportunity to acknowledge some very special people who have been integral parts of my journey so far.

First and foremost, I would like to express my deepest gratitude to my supervisor, **Prof. Soumyajit Das**, for his constant support, guidance, inspiration, and encouragement throughout this journey. His enthusiasm, expertise, patience, depth of knowledge, and scientific curiosity have been truly inspiring.

Besides my supervisor, I am also thankful to my doctoral committee members: **Prof. T. J. Dhilip Kumar**, **Prof. Avijit Goswami (MSc Advisor)**, **Prof. Prabal Banerjee**, and **Prof. Santanu Sarkar**, for their insightful feedback, valuable time, and useful suggestions that have significantly contributed to the refinement of this thesis.

It is my privilege to thank the present director of IIT Ropar, **Prof. Rajeev Ahuja**, and the former director of IIT Ropar, **Prof. Sarit K. Das**, for providing world-class research infrastructure.

I also express my gratitude to **Prof. Upendra Kumar Pandey**, **Prof. Subhajit Bandyopadhyay**, **Prof. Dibyendu Mallick, Ms. Ankita, Dr. Palash Jana** for their excellent collaboration. It was a great experience to work with them.

I acknowledge the central research facilities (CRF) of IIT Ropar. I want to thank the convenor of the NMR facility, **Prof. Manoj Kumar Pandey**, for his cooperation. I sincerely thank the HRMS facility committee members, **Prof. Avijit Goswami** and **Prof. Anupam Bandyopadhyay**. I am grateful to the current head of the department, **Prof. Debaprasad Mandal**, the former head of the department, **Prof. T. J. Dhilip Kumar**, for facilitating the use of various departmental instruments and their valuable suggestions.

I express my heartfelt thanks to all the **faculty members** of the Chemistry department who have been an integral part of my academic journey during my MSc and PhD studies. Their invaluable knowledge, guidance, and mentorship have been pivotal in shaping my research and my academic growth.

I acknowledge the help and support provided by the technical staff, especially *Mr. Manish Kumar*, *Mr. Kamlesh Satpute*, *Mr. Nazre*, *Dr. Nilotpal*, *Mr. Surya Kumar* and *Mrs. Hanspreet* for their timely help with NMR, Single-crystal and HRMS data, and the non-teaching staff, *Mrs. Samita*, *Mr. Sushil*, *Mrs. Poonam*, *Mr. Nagendra*, *Mr. Tanveer* and of the *Department of Chemistry*.

My extraordinary lab mates deserve special thanks for their friendly cooperation and invaluable help whenever required. I cannot express in words how fortunate I am to have talented former and current lab members: *Dr. Priyank Kumar Sharma*, *Hemonta Kumar Saha*,

Sakshi Sahewal, Neha Maurya, Rashmi Ranjan Behera, Pooja Bhardwaj, Rakesh Sheoran, Nikhil Bhardwaj, Vishal Mittal, Akanksha Babbar, Annapurna Karmakar, Vishvajeet Kumar, and *Suman Sharma*. Their support in maintaining a healthy environment and engaging in useful discussions in the lab has greatly aided my learning and understanding of various aspects of research. I will always cherish these memories and wish them great success in every aspect of their lives. I am grateful to my co-authors for their contributions to my work. I also thank all the summer trainees and project students who worked on short-term projects in our lab.

I am deeply thankful to my seniors from IIT Ropar, *Dr. Suchitra, Dr. Divya Bhatt, Dr. Pratibha (MSc mentor), Dr. Chandresh Kumari, Dr. Prasoon Raj, Dr. Pankaj Gautam, Dr. Debarshi Saha, Dr. Suman Pradhan, Dr. Gaje Singh, Dr. Gautam Kumar, Dr. Sourav Roy, Dr. Rajesh Das, Dr. Avinash Srivastava, Dr. Atal, Dr. Raghunath Dey, Dr. Manisha Lamba, Dr. Maajid, Dr. Amanpreet Singh, Dr. Manish Kumar, Dr. Ganga Singh, Dr. Sandeep Patel, Dr. Rakesh Kumar, Dr. Anoop Chahal, Deepak Sharma, Abhimanyu Rao, Narender Nain, Rajesh Bura,* for their continuous encouragement, for sharing their experiences, and for offering practical insights that helped me overcome challenges in my research. They have always been generous with their time, whether it was to discuss ideas, provide feedback on my work, or offer words of wisdom during tough times.

I owe a special debt of gratitude to my dear friends including *Braj Gopal, Naveen Yadav, Naresh Kumar, Krishna Nand, Sangay Moktan, Krishn Kumar, Rajat, Shruti Rajput, Mohit Pannu, Deepu Chandran, Pramod Godara, Vikash Kumar, Chandrabhan, Anujit Punia, Raghav, Shubham Garg, Shubham Gumber, Tanuj Pahuja, Krishan Kumar, Pankaj Patwal, Rahul, Amit, Prince Gautam, Aman Dhiman, Amandeep, Arjun, Beekesh, Apurv, Amit Nagar, Rajat Rajput, Milender Kumar, Narendra prasad, Ashish Redhu, Pruthviraj Bundel, Ketan Rohilla, Vivek Yadav, Utkarsh, Harshvardhan Singh, Rakesh Chaudhary, Abhishek Shah, Gursimar Singh, Deepak Soni, Kartik Yadav, Deepanshu Sharma, Sayak Ghosh, Parag Mistry, Surajit Das, Arijit, Rik Patra, Shubhendu Hazra, Dhanjeet, Along, Abhilash Peddada, Rajat, Divyanshu Saini, Rahul Shukla, Nakshatra Banerjee, Biprajit Paul, Akshay Kumar, Dr. Ravinder, Adarsh, Junaid, Dinesh Rajput,* for their unwavering support, encouragement, and belief in me which have been a constant source of motivation throughout this doctoral journey. I consider myself fortunate to have such wonderful friends who have not only supported me in my academic pursuits but have also made this journey more enjoyable and memorable. Their presence in my life has been a true blessing.

Finally, I would like to express my heartfelt gratitude to my parents, *Mr. Raghbir Sharma,* and *Mrs. Usha Devi,* for their eternal blessings, unconditional love, unwavering

support, and encouragement in accomplishing my dream. They have always shown me the best path to follow, and they truly mean the world to me. Thank you all for being such important parts of my life. Any words of appreciation will fall short for them. I am also deeply grateful to *Nupoor Sharma* (my brother), and *Khushansh Sharma* **(**my nephew) for their love, and support, throughout this journey.

Lastly, I would like to extend my thanks to *everyone* who may have been inadvertently omitted from this list. Your contributions, support, and encouragement have been invaluable to me, and I deeply appreciate all that you have done.

Certificate

This is to certify that the thesis entitled **Syntheses and Properties of π-Extended Indenofluorene Derivatives**, submitted by **Himanshu (2019CYZ0021)** for the award of the degree of **Doctor of Philosophy** of Indian Institute of Technology Ropar, is a record of bonafide research work carried out under my guidance and supervision. To the best of my knowledge and belief, the work presented in this thesis is original and has not been submitted, either in part or full, for the award of any other degree, diploma, fellowship, associateship or similar title of any university or institution.

In my opinion, the thesis has reached the standard fulfilling the requirements of the regulations relating to the Degree.

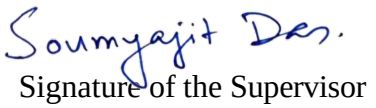

Signature of the Supervisor

Dr. Soumyajit Das

Department of Chemistry

Indian Institute of Technology Ropar

Rupnagar, Punjab 140001

Date: 13/2/2025

Lay Summary

Understanding aromaticity is essential for comprehending the stability and physical properties of π-conjugated molecules. Likewise, grasping the concept of antiaromaticity is equally important in various fields. In biological research, scientists have recently elucidated how the instability of DNA arises from the release of antiaromaticity. In materials science, Breslow demonstrated that antiaromatic π-systems could lead to high carrier mobility, as they do not suffer from the stability concerns seen in aromatic systems like benzene. Pro-aromaticity, a more recent concept, suggests that the formation of diradicals occurs through the aromaticity gained by successive non-aromatic rings. This process minimizes net energy, potentially exceeding the energy required to break a double bond and resulting in diradical formation.

In my thesis, I explored the design and synthesis of fully conjugated antiaromatic π-extended indenofluorenes derivatives with interesting optoelectronic properties for organic electronics applications. While in Chapter 1, the synthesis of five antiaromatic IF derivatives, including π-extended variants, IF oligomers/polymers, and their applications in organic electronics, is presented, the following chapters contain the syntheses and properties of symmetrical, unsymmetrical, and π-extended indenofluorenes that were invented during my doctoral research work. These new molecules were fully characterized using various spectroscopic techniques in order to investigate the ground-state photophysical and electronic properties. Furthermore, density functional theory calculations were performed to give a clear conclusion on the actual ground state electronic configurations of the new molecules, in order to support the experimental findings.

Abstract

Chemistry of alternant acenes have attracted tremendous interest due to their challenging synthesis and interesting optoelectronic properties. Pentacene derivatives had received more attention in this regard, but unfortunately, they are prone to oxidative degradation. This led to the development of five non-alternant antiaromatic indenofluorene (IF) isomers as alternative pentacene-like structures. Chapter 1 covers the synthesis of five antiaromatic IF derivatives, including π-extended variants, IF oligomers/polymers, and their applications in organic electronics. These fully conjugated IFs, along with their core-extended counterparts, have garnered significant interest because of their synthesis related challenges, (anti)aromaticity, diradicaloid properties, and optoelectronic applications. Among the five IF isomers, two *para*-quinodimethane embedded IFs, namely indeno[1,2-*b*]fluorene and indeno[2,1-*c*]fluorene have found applications in charge-transport and solar cell devices. In contrast, the application of indeno[2,1-*a*]fluorene is limited due to its instability. The traditional synthesis of IFs requires harsh conditions and doesn't allow for introduction of unsymmetrical disubstituents to the apical carbons of the five-membered rings. In Chapter 2A, I report a mild synthetic approach to make mesityl disubstituted [2,1-*c*]IF, and further extended this approach to synthesize unsymmetrically disubstituted [2,1-*c*]IFs (Chapter 2B), as well as a (4n+2)π tetraradicaloid *s*-indacenodifluorene (*s*-IDF) (Chapter 2C) that exhibit small HOMO-LUMO and singlet-triplet energy gaps. Adopting a similar synthetic approach while utilizing the steric crowding of bulky aryl substituent, a steric promoted synthesis of symmetrical and unsymmetrical [1,2-*b*]IFs including benzo-extended [1,2-*b*]IFs were reported in Chapter 3. Notably, use of less bulky pentafluorophenyl group as one of the substituent afforded a mixture of IF regioisomers ([1,2-*b*]IF and [2,1-*a*]IF) which could be purified by column chromatography in air. Since the syntheses and properties of IF dimers remain largely unexplored, while their alternant analogue pentacene dimers are well-studied for optoelectronic applications, we directed our efforts towards the design and syntheses of three mesityl substituted IF dimers, presented as biindenofluorene (BIF) derivatives in Chapter 4. These dimers were formed by dimerizing formally antiaromatic IF units through the 2,2'- and 3,3'-carbons of [2,1-*c*]IF and [1,2-*b*]IF units, respectively. This design modulated the optoelectronic properties by significantly reducing the HOMO-LUMO energy gaps, in comparison to previously reported IF-based polymers. Both experimental and theoretical studies confirmed that all three dimers, in Chapter 4, exhibit a closed-shell configuration. In the quest for open-shell BIF, Chapter 5 explores the design of a [1,2-*b*]IF-based dimer, which was synthesized by linking [1,2-*b*]IF units through their 6,6'-carbons, and it displayed an open-shell singlet ground state with 26.8% diradical character.

List of Publications from Thesis

Journals

1. **H. Sharma**, P. K. Sharma and S. Das, *Chem. Commun.* 2020, **56**, 11319.
2. **H. Sharma**, N. Bhardwaj and S. Das, *Org. Biomol. Chem.*, 2022, **20**, 8071.
3. **H. Sharma**, Ankita, P. Bhardwaj, U. K. Pandey and S. Das, *Organic Materials* 2023, **5**, 72.
4. **H. Sharma**, Ankita, V. Mittal, U. K. Pandey and S. Das, *Org. Lett.* 2024, **26**, 2617.
5. **H. Sharma**, P. Jana, D. Mallick, S. Bandyopadhyay and S. Das, *Chem. Sci.*, 2024, **15**, 20215.

Table of Contents

Declaration v

Acknowledgment vi

Certificate ix

Lay Summary x

Abstract xi

List of Publications xii

List of Figures xvii

List of Schemes xxi

List of Tables xxii

Notations and Abbreviations xxiv

Chapter 1: Introduction

1.1 Introduction 2

1.1.1 Acenes 2

1.1.2 Indenofluorenes 5

1.1.3 π-Extended indenofluorenes 14

1.1.4 Helical indenofluorenes 22

1.1.5 Indenofluorene-based oligomers and polymers 26

1.1.6 Applications of indenofluorenes 28

1.2 Thesis outline 30

1.3 References 32

Chapter 2A: A new synthetic approach to indeno[2,1-*c*]fluorene

2A.1 Abstract 44

2A.2 Introduction 44

2A.3 Results and Discussion 45

2A.3.1 Synthesis 45

2A.4 Conclusions 46

2A.5 Experimental section 46

2A.5.1 General information 46

2A.5.2 Synthesis 46

2A.6 References 49

2A.7 Appendix 51

Chapter 2B: Exploration of indeno[2,1-*c*]fluorene derivatives with unsymmetrical disubstitution and balanced ambipolar charge-transport properties

2B.1 Abstract 57

2B.2 Introduction 57

2B.3 Results and Discussion 59

2B.3.1 Synthesis 59

2B.3.2 Single crystal analysis 62

2B.3.3 Optical and electrochemical properties 65

2B.3.4 Space charge limiting current (SCLC) studies 74

2B.4 Conclusions 77

2B.5 Experimental section 77

2B.5.1 General information 78

2B.5.2 Synthesis 78

2B.5.3 Single crystal data 86

2B.5.4 DFT calculations 88

2B.5.5 Possible reason for the yield of 10 90

2B.5.6 SCLC Device 91

2B.6 References 93

2B.7 Appendix 96

Chapter 2C: Exploration of fully conjugated *s*-indaceno[2,1-*c*:6,5-*c′*]difluorene

2C.1 Abstract 117

2C.2 Introduction 117

2C.3 Results and Discussion 119

2C.3.1 Synthesis 119

2C.3.2 Single crystal, ground state, and (anti)aromaticity analysis 120

2C.3.3 Optical and electrochemical properties 123

2C.4 Conclusions 126

2C.5 Experimental section 126

2C.5.1 General information 126

2C.5.2 Synthesis 127

2C.5.3 Single crystal data 129

2C.5.4 DFT calculations 131

2C.6 References 133

2C.6 Appendix 136

Chapter 3: Revisiting indeno[1,2-*b*]fluorene by steric promoted synthesis while isolating the second stable 4nπ indeno[2,1-*a*]fluorene

3.1 Abstract 143

3.2 Introduction 143

3.3 Results and Discussion 145

3.3.1 Synthesis 145

3.3.2 Single crystal, ground state, and (anti)aromaticity analysis 147

3.3.3 Optical and electrochemical properties 150

3.4 Conclusions 157

3.5 Experimental section 158

3.5.1 General information 158

3.5.2 Synthesis 158

3.5.3 Single crystal data 166

3.5.4 DFT calculations 168

3.6 References 176

3.7 Appendix 181

Chapter 4: Syntheses and properties of hole-transporting biindenofluorenes

4.1 Abstract 196

4.2 Introduction 196

4.3 Results and Discussion 198

4.3.1 Synthesis 198

4.3.2 Single crystal and ground state analysis 199

4.3.3 Optical and electrochemical properties 200

4.3.4 SCLC studies 205

4.4 Conclusions 207

4.5 Experimental section 208

4.5.1 General information 208

4.5.2 Synthesis 209

4.5.3 Single crystal data 215

4.5.4 DFT calculations 217

4.5.5 Electrochemistry 222

4.5.6 SCLC Mobility Data for compounds 1, 2, and 3 223

4.6 References 224

4.7 Appendix 226

Chapter 5: 6,6'-Biindeno[1,2-*b*]fluorene: an open-shell indenofluorene dimer

5.1 Abstract 242

5.2 Introduction 242

5.3 Results and Discussion 245

5.3.1 DFT studies 245

5.3.2 Synthesis 247

5.3.3 Single crystal, ESR, ground state and (anti)aromaticity analysis 248

5.3.4 Optical and electrochemical properties 252

5.4 Conclusions 255

5.5 Experimental section 255

5.5.1 General information 255

5.5.2 Synthesis 256

5.5.3 Single crystal data 258

5.5.4 DFT calculations 261

5.5.5 ESR measurement and Bleaney-Bowers plot 263

5.5.6 Explanation of four-stage redox amphotericity 264

5.6 References 265

5.7 Appendix 270

Chapter 6: Conclusion

List of Figures

S. No.	Figure Caption	Page No.
1.1	Structure of acenes **4-12**.	3
1.2	Structure of twistacenes **13-15**.	4
1.3	Nomenclature, numbering and structures for fully conjugated indenofluorene isomers.	7
1.4	Structure of 6,12-disubstituted [1,2-*b*]IF derivatives.	10
1.5	Naphthalene fused π-extended IF derivatives **66-70** (naphthalene modification of core benzenoid ring).	15
1.6	Anthracene/Phenanthrene fused π-extended IF derivatives **71-73**.	16
1.7	Kekulé structure of bis(phenalenyl)-based diradicaloids **74-76**.	17
1.8	Structure of TCPTP **77** with its resonance structure.	17
1.9	Structure of ladder shaped π-extended IF derivatives **78-79**.	18
1.10	Fused [1,2-*b*]IF derivatives **80-84** (modification at outer core).	20
1.11	Benzo extended [2,1-*c*]IF derivatives **85-87** and [2,1-*a*]IF derivative **88**.	21
1.12	Structures of helical π-extended IFs **89-95**.	23
1.13	Examples of IF oligomers/polymers (solution syntheses).	26
1.14	Examples of covalently linked IF polymers (synthesized on-surface)	27
1.15	Example of fully fused IF polymer synthesized on-surface.	27
1.16	IF derivatives with device applications.	29
1.17	Structures of targeted compounds reported in this thesis.	31
2A.1	Structure of symmetrically disubstituted [2,1-*c*]IF derivatives **1-3**.	44
2B.1	(a) *p*-QDM embedded indeno[1,2-*b*]fluorene. (b) *p*-QDM embedded isomeric [2,1-*c*]IF derivatives **1-6**. (c) Frontier molecular orbital profiles of **1**. (d) Target unsymmetrical [2,1-*c*]IFs **7-10** and the unknown symmetrical **17**.	58
2B.2	ORTEP drawing of (a) **7**, (b) **17**, and (c) **9** (left: *P*-isomer; right: *M*-isomer) at 30% probability level (hydrogen omitted), with the C=C bond distances (in Å) of *p*-quinodimethane unit are shown. The packing motifs for (d) **7** and (e) **17** showing the intermolecular F···H-C_{sp^2} hydrogen bonds (in Å) and its ($\angle C_{sp^2}$–H···F) angles.	63
2B.3	(a) Short intermolecular contacts for **7** and (b) its herringbone-like packing motif.	64
2B.4	Bifurcated C-F…C_π (3.082 Å) and F···H-C($_{sp^2}$) (2.595 Å) interactions of **17**, including interplanar distance between two cofacially stacked IFs that imply π-π interaction.	65
2B.5	UV-Vis-NIR absorption plots of the new [2,1-*c*]IFs in $CHCl_3$.	69
2B.6	UV-vis spectra for **10** as solution in solvents with different polarity.	70
2B.7	UV-vis spectra for **8** as solution in solvents with different polarity.	71
2B.8	Cyclic voltammogram of the new [2,1-*c*]IF derivatives in CH_2Cl_2.	71
2B.9	(a) Differential pulse voltammograms (DPV) of the [2,1-*c*]IFs in dichloromethane. (b) CVs of **7**, **8**, **9** and **17** up to their first oxidation and reduction potentials, showing absence of any peaks/bumps which were observed in Figure 2B.8 on their return for both anodic and cathodic sweeps when oxidized or reduced to their second oxidation and reduction potentials.	72
2B.10	*J-V* characteristics in semi-log plot used for extracting (a) hole and	76

	(b) electron mobilities using modified Mott Gurney SCLC equation for compounds **1**, **7**, **8**, and **17**.	
2B.11	Optimized *P*- (left) and *M*- (right) isomers of **9** (by replacing apical substituents with H) with carbons highlighted for measuring the dihedral angle, and the intermediate TS (middle).	88
2B.12	Possible reason for the low yield of **10**.	91
2C.1	(a) Wu's *s*-indaceno[1,2-*b*:5,6-*b*']difluorene **1**. (b) Müllen's [2,1-*a*]IF-based polymer **2**. (c) 5,8-dimesitylindeno[2,1-*c*]fluorene **3**. (d) Target scaffolds: 5,8,14,17-tetramesityl-*s*-indaceno[2,1-*c*:6,5-*c*']difluorene **4**. (e) Plausible canonical structures for parent **4**.	117
2C.2	Known indacenodifluorene (IDF) isomers with 34π-electrons delocalized along the conjugated backbone.	118
2C.3	(a) X-ray crystallographic structure of **4** with the ellipsoids drawn at 30% probability level, and the hydrogens are omitted for clarity. (b) Side view of crystal structure **4** with hydrogens shown in pink colour. (c) Experimental bond lengths (Å), calculated NICS(1)zz (purple) and HOMA (green) values for each ring in **4**. (d) Packing diagram for **4**.	121
2C.4	The terminal phenyl ring is deviated from central (core) phenyl ring by 11.93° due to steric congestion in the cove-like region between two hydrogens in close proximity.	121
2C.5	(a) The shortest interplanar C-C contact in **4** was found as 3.454 Å (left image), and (b) the intermolecular [C-H$\cdots\pi$] interactions in **4** (2.831/2.785 Å) (right image).	122
2C.6	Variable temperature ^{1}H NMR spectrum of **4** (in $C_2D_2Cl_4$, 400 MHz).	123
2C.7	(a) UV-vis-NIR spectrum and (b) CV for **4**.	124
2C.8	Experimental absorption spectrum of **4**, against the simulated stick diagram showing oscillator strength at B3LYP/6-31G(d,p) level of theory.	124
2C.9	Frontier molecular orbital profiles for **4**.	125
2C.10	Crystal structure of **4** with labels.	130
2C.11	Experimental absorption spectrum of **4**, against the simulated stick diagram showing oscillator strength at CAM-B3LYP/6-31G(d,p) level of theory.	132
3.1	Target molecules: *p*-QDM embedded [1,2-*b*]IFs **1**-**5**, and *o*-QDM embedded [2,1-*a*]IF **6**	144
3.2	X-ray crystallographic structures of (a) **5** and (b) **6** with ellipsoids drawn at 30% probability level, and the C_{sp^2}-C_{sp^2} bond distances for *p*-QDM unit (in Å) of **5** (mean bond lengths of two crystallographically independent molecules) and *o*-QDM unit of **6** are shown (hydrogens omitted). The HOMA (red) and NICS(1)$_{zz}$ (blue) indices for the rings A-E are shown for the optimized ground state structure.	148
3.3	NPA charges of parent indacenes and the corresponding IF derivatives **5** and **6**. Ar = mesityl and Ar^1 = pentafluorophenyl.	149
3.4	UV-vis absorption profiles for [1,2-*b*]IFs **1**, **4**, **5** (expansion in inset), recorded in dichloromethane.	151
3.5	UV-vis absorption profiles for [1,2-*b*]IFs **2** and **3** recorded in dichloromethane.	152
3.6	UV-vis absorption profile for [2,1-*a*]IF **6**, recorded in dichloromethane.	153

3.7	(a) Cyclic voltammograms and (b) Differential pulse voltammogram of new IFs **2**-**6** in dichloromethane.	154
3.8	Supporting figure that may explain the electron-withdrawing effect on **4** *vs* **5**. Stronger the electron-withdrawing ability of the apical substituent, easier is the one-electron reduction considering **[1,2-*b*]IF-ZW2** substructure (Electron-donating power of mesityl group is not so strong).	155
3.9	Herringbone packing arrangement for **6** with two IF molecules forming T-shaped interaction in one-dimensional stack.	156
3.10	Herringbone packing arrangement for **5** with two IF molecules cofacially stacked at an interplanar distance of 3.367 Å, implying strong π-π interaction.	157
3.11	ORTEP drawing of **5** with thermal ellipsoids at 30% probability level, showing the bond lengths with e.s.d values for the two crystallographically independent molecules.	167
3.12	ORTEP drawing of **6** showing with thermal ellipsoids at 30% probability level showing the bond lengths with e.s.d values.	167
3.13	Optimized closed-shell structure of **5**.	169
3.14	Optimized closed-shell structure of **6**.	171
3.15	NPA charges of parent *as*-Indacene.	173
4.1	(a) Parent indeno[1,2-*b*]fluorene and its HOMO & LUMO profiles, including some substituted indeno[1,2-*b*]fluorenes. (b) Benzo-indaceno-thiophene (BIT) dimer and the on-surface synthesized indenofluorene polymer. (c) Targeted biindenofluorene derivatives **1**-**3**.	197
4.2	ORTEP drawing of **1** with ellipsoids at the 30% probability level (hydrogens omitted).	199
4.3	UV-vis-NIR spectra of **1**-**3** in chloroform, with inset showing expansion from 640 to 850 nm region.	201
4.4	CVs of **1**-**3** showing the reversible two-electron oxidations.	204
4.5	Highly delocalized radical cation and dication structures explaining the excellent reversibility of first and second oxidation waves. Parent **1** is drawn as representative example, and the same logic applies for **2** and **3**.	204
4.6	The non-covalent [C–H$\cdots\pi$] (2.854 Å) and [C–H$\cdots$H] (2.375/2.371 Å) interactions observed for **1** in the herringbone-type packing motif.	205
4.7	*J*–*V* characteristics in the semi-log plot used for extracting hole mobility using modified the Mott–Gurney SCLC equation for BIFs **1**, **2** and **3**. V_{bi} = 0 V, as both injecting electrode as well as counter electrodes are same (ITO/Ag/MoO_3).	207
4.8	ORTEP drawing of **1** with thermal ellipsoids at 30% probability level, showing the bond lengths with e.s.d values.	215
4.9	2D Herringbone-type packing in **1**.	216
4.10	Optimized closed shell structure for **1**.	218
4.11	Optimized closed shell structure for **2**.	218
4.12	Optimized closed shell structure for **3**.	219
4.13	Optimized closed shell structure for **1a** (E_g^{DFT} = 2.40 eV).	219
4.14	Optimized closed shell structure for **2a** (E_g^{DFT} = 2.16 eV).	220
4.15	Optimized closed shell structure for **3a** (E_g^{DFT} = 2.20 eV).	220
4.16	IUPAC representation of (a) cyclic voltammograms (asterisk (*) denotes half-wave redox potentials) and (b) differential pulse	222

	voltammograms of BIFs **1-3** (0.001 M) taken at 298 K, in dry and degassed dichloromethane with 0.1 M Bu_4NPF_6 under nitrogen atmosphere. All data were collected using Pt-disk electrode as a working electrode, Pt wire as a counter electrode and Ag wire as a pseudo-reference electrode. Starting point was 0 V (*vs* Ag wire), which is now plotted as –0.42 V (*vs* Fc/Fc^+) after referencing against ferrocene/ferrocenium. Scan direction (toward negative potential first, and then going to positive potential) is shown using arrow.	
5.1	(a) Antiaromatic indeno[1,2-*b*]fluorene derivatives **1-M**, **1-MF** and **2**. (b) Zimmerman and Stępień's tetrafluorenofulvalene (TFF) **3**. (c) Our reported 3,3′-biindeno[1,2-*b*]fluorene derivative **4**. (d) Closed-shell structure of targeted mesityl disubstituted 6,6′-biindeno[1,2-*b*]fluorene **5** and its representative open-shell (OS) diradicaloid bifluorenylidene-type structure **5-OS1** and tetraradicaloid biindenofluorene-type structure **5-OS2**.	243
5.2	(a) Spin density map of **5**. Isovalue for surfaces: MO = 0.02, density = 0.005. frontier molecular orbital profiles for the (b) α-spin and (c) β-spin of **5**.	246
5.3	(a) X-ray crystallographic structure of **5** with the ellipsoids drawn at 30% probability level (hydrogens omitted), including $NICS(1)_{zz}$ (blue) and HOMA (green) indices. (b) Side-view of **5.** (c) EPR spectra of **5** recorded at variable temperatures for powder form.	249
5.4	Variable temperature ^1H NMR spectrum of **5** (in $C_2D_2Cl_4$, 400 MHz).	250
5.5	Current–density vectors are plotted onto the ACID isosurface of 0.02 for the π system of **5**.	252
5.6	(a) UV-vis-NIR spectrum of **5** in chloroform. (b) CV and DPV of **5**.	253
5.7	(a) Absorption spectral changes under ambient light conditions for compound **5** in toluene (0 days to 25 days). (b) Fitting with first-order kinetics.	254
5.8	Full crystallographic bond length analyses of **5** with e.s.d values.	260
5.9	X-ray crystallographic C-C bond lengths of **4** (for comparison with **5**)	260
5.10	X-ray crystallographic C-C bond lengths of **5**	261
5.11	Optimized structure of **5** in the open-shell ground state.	262
5.12	Theoretical absorption of **5** at CAM-B3LYP/6-31G(d,p) level of theory.	262
5.13	ACID plots of **5** at isosurface values of 0.0353 (left) and 0.055 (right). The critical isosurface value (CIV) for central benzenoid ring C is found to be 0.0353. The CIV for outer benzene rings A as well as E is 0.055.	263
5.14	DFT-optimized C-C bond lengths of ground state open-shell structure **5**	263
5.15	Bleaney-Bowers plot for **5**.	264
5.16	Plausible reason for four-stage redox amphotericity of **5**.	264

List of Schemes

S. No.	Scheme Caption	Page No.
1.1	A general synthetic route to acenes.	2
1.2	Pentacene degradation in presence of oxygen.	5
1.3	Synthetic route to TIPSE substituted indeno[1,2-*b*]fluorenes.	9
1.4	Synthetic route to 2,8-disubstituted indeno[1,2-*b*]fluorenes.	9
1.5	Synthetic route to mesityl substituted indeno[2,1-*a*]fluorene **36**.	10
1.6	Synthetic route to indeno[2,1-*b*]fluorene **42**.	11
1.7	Synthetic route to indeno[2,1-*c*]fluorene derivatives **52-54**.	12
1.8	Synthetic route to methoxy substituted indeno[2,1-*c*]fluorene **60**.	13
1.9	Synthetic route to indeno[1,2-*a*]fluorene **65**.	13
2A.1	Synthetic route to symmetrically disubstituted [2,1-*c*]IF derivative **1.**	45
2B.1	Synthesis of new symmetrically disubstituted [2,1-*c*]IF **17**.	60
2B.2	Syntheses of the unsymmetrically disubstituted [2,1-*c*]IFs **7**, **8**, **9**.	61
2B.3	Synthesis of a push-pull disubstituted [2,1-*c*]IF **10**.	62
2C.1	Synthesis of S-shaped π-conjugated system **4**.	120
3.1	Synthesis route to [1,2-*b*]IF **1** and its benzo-extended derivatives **2** and **3**.	146
3.2	Synthesis route to [1,2-*b*]IF **4**, **5** and [2,1-*a*]IF **6** from aldehyde **15**.	147
4.1	A general synthetic route to BIFs **1**, **2** and **3**.	199
5.1	Synthesis of BIF **5**.	247

List of Tables

S. No.	Table Caption	Page No.
2B.1	TDDFT electronic transitions for **7** at B3LYP/6-31G(d,p) level of theory.	66
2B.2	TDDFT electronic transitions for **8** at B3LYP/6-31G(d,p) level of theory.	66
2B.3	TDDFT electronic transitions for **9** at B3LYP/6-31G(d,p) level of theory.	67
2B.4	TDDFT electronic transitions for **10** at B3LYP/6-31G(d,p) level of theory.	67
2B.5	TDDFT electronic transitions for **17** at B3LYP/6-31G(d,p) level of theory.	68
2B.6	Summary of photophysical and electrochemical data for **7**, **8**, **9**, **10** and **17**.	73
2B.7	Summary of SCLC hole and electron mobilities.	75
2B.8	Crystal data and structure refinement for **7**, **9** and **17**.	86
2B.9	Frontier Molecular Orbital profiles for the optimized structures.	89
2B.10	Hole Mobility in $cm^2\ V^{-1}\ s^{-1}$ for best 5 devices for compounds **1**, **7**, **8** and **17**.	92
2B.11	Electron Mobility in $cm^2\ V^{-1}\ s^{-1}$ for best 5 devices for compounds **1**, **7**, **8** and **17**.	92
2C.1	TD-DFT transitions at B3LYP/6-31G(d,p) level.	124
2C.2	Summary of experimental and theoretical HOMO-LUMO energy levels.	126
2C.3	Crystal data and structure refinement for **4**.	130
2C.4	Relative energies of optimized geometries for **4** at B3LYP/6-31G(d,p) level.	131
2C.5	Relative energies of optimized geometries, and radical character index for **4** at CAM-B3LYP/6-31G(d,p) level.	131
2C.6	$NICS(1)_{zz}$ and HOMA values of each ring for the mesityl-substituted **3** and **4**.	132
2C.7	TD-DFT transitions at CAM-B3LYP/6-31G(d,p) level.	132
3.1	Photophysical and electrochemical data of **2**–**6**.	151
3.2	Summary of TDDFT calculations of compound **6**.	152
3.3	Crystal data and structure refinement for **5** and **6.**	167
3.4	Relative energies for the optimized structure **5** at B3LYP/6-31G(d) level.	169
3.5	Relative energies for the optimized structure **6** at B3LYP/6-31G(d) level.	169
3.6	Natural Population of **5**.	170
3.7	Natural Population of **6**.	172
3.8	Frontier molecular orbital profiles.	173
3.9	Summary of TDDFT calculations of compound **5**.	174
3.10	Summary of photophysical and electrochemical data for **2**-**6**.	175
4.1	Summary of TDDFT calculations of compound **1**.	201
4.2	Summary of TDDFT calculations of compound **2**.	202
4.3	Summary of TDDFT calculations of compound **3**.	202
4.4	Photophysical and electrochemical data of BIFs **1**–**3**.	203
4.5	Measured SCLC mobility ($cm^2 \cdot V^{-1} \cdot s^{-1}$) of BIFs **1**–**3**.	206

4.6	Crystal data and structure refinement for **1**.	216
4.7	Relative energies for the optimized structure **1** at B3LYP/6-31G(d,p) level.	217
4.8	Relative energies for the optimized structure **2** at B3LYP/6-31G(d,p) level.	217
4.9	Relative energies for the optimized structure **3** at B3LYP/6-31G(d,p) level.	217
4.10	Frontier molecular orbital profiles of **1**-**3**.	221
4.11	Comparison of theoretical C_{sp}^2-C_{sp}^2 bond-length connecting the IF monomer units, as estimated by DFT calculations.	221
4.12	Statistics of 5 best hole mobilities in $cm^2 V^{-1} s^{-1}$ for best 5 devices for BIFs **1**, **2** and **3**.	223
5.1	Relative energies for the optimized structure **5** at CAM-B3LYP/6-31G(d,p) level of theory.	246
5.2	Comparison of mean C-C bond lengths (Å) for **5**, **1-MF**, and **1-M**.	250
5.3	Summary of TDDFT calculation for **5**.	253
5.4	Crystal data and structure refinement for **5**.	259
5.5	$NICS(1)_{zz}$ values of each ring for **5**.	261

Notations and Abbreviations

ACID	anisotropy of the induced current density
2,6-AQDM	2,6-anthraquinodimethane
Å	Angstroms
B.O.	bond order
BIF	Biindenofluorene
BP	bipentacene
BHJ	bulk heterojunction
BLA	bond length alternation
Bu_4NPF_6	tetra-*n*-butylammonium hexafluorophosphate
BIT	benzo-indaceno-thiophene
BF	bifluorenylidene
1,2-DCE	1,2-dichloroethane
CS	closed-shell
CCDC	Cambridge Crystallographic Data Centre
CV	cyclic voltammetry
C_{60}	carbon allotrope fullerene
CPH	conjugated polycyclic hydrocarbon
DCM	dichloromethane
DDQ	2,3-dichloro-5,6-dicyano-1,4-benzoquinone
DFT	density functional theory
DH-IFs	dihydro-indenofluorenes
ESR	electron spin resonance
ESI	electron spray ionization
ECD	electronic circular dichroism
FC	Friedel–Crafts
FF	Fluorenofluorene
FMO	frontier molecular orbital
g_{abs}	dissymmetry factor
HRMS	high resolution mass spectra
HOMA	harmonic oscillator model of aromaticity
HOMO	highest occupied molecular orbital
IFDs	indenofluorene dimers
IDF	indacenodifluorene
ICT	intramolecular charge transfer
IF	indenofluorene
LUMO	lowest unoccupied molecular orbital
MesMgBr	mesitylmagnesium bromide

NBS	*N*-bromosuccinimide
NICS	nucleus independent chemical shift
NIR	near-infrared
NMR	nuclear magnetic resonance
NPA	natural population analyses
NOON	natural orbital occupancy number
OLED	organic light-emitting diode
OFET	organic field-effect transistor
OPV	organic photovoltaic
ORTEP	oak ridge thermal ellipsoid plot
OS	open-shell
PH	polycyclic hydrocarbons
PIF	Polyindenofluorene
PCBM	[6,6]-phenyl-C_{61}-butyric acid methyl ester
PCE	power conversion efficiency
QDM	quinodimethane
s-IDN	*s*-indacenodinaphthalene
S-T	singlet-triplet energy gap
SCXRD	single-crystal X-ray diffractometry
SCLC	space charge limited current
SOMO	singly occupied molecular orbital
SF	singlet fission
TDDFT	time-dependent density functional theory
THF	tetrahydrofuran
TIPSE	Triisopropylsilylethynyl
TIPSELi	[(triisopropylsilyl)ethynyl]lithium
TLC	thin layer chromatography
TFF	Tetrafluorenofulvalene
UV-vis	ultraviolet-visible
μ_e	electron mobility
μ_h	hole mobility

Chapter 1

Introduction

"*Aromaticity is all great, but anti-aromaticity is the real fun*" – **Prof. M. M. Haley**[1]

"From a chemical point of view, aromatic molecules are boring, they are too stable, they're happy with themselves, but antiaromatic molecules – which will do whatever they can to escape this unstable state – are anything but dull, antiaromatic molecules are anxious, reactive, always ready to surprise you." – **Prof. Igor Alabugin**[1]

1.1 Introduction

Polycyclic hydrocarbons (PHs) have captivated researchers for over 150 years, playing a pivotal role in shaping the field of organic chemistry throughout the 19th and 20th centuries.[2] PHs were first identified in fossil fuel resins but have since been detected in various environments, ranging from natural mineral deposits to meteorites.[3] The extraction of PH-rich tars and ashes has not only propelled modern purification and separation methods but also brought forth key concepts like aromaticity, which remains a widely discussed and debated topic in scientific research.[4] Moreover, attempts to understand the reactivity of PHs have resulted in the revelation of various novel reaction mechanisms and catalytic pathways, which form the basis of contemporary physical organic chemistry. Over the past 25-30 years, research on PHs has seen a significant resurgence, driven by improved compound accessibility and characterization made possible through modern synthetic methods and instrumentation.[5] A major driving force behind the renewed interest in PHs is their unique optoelectronic properties, which stem from their extensive π-conjugation/delocalization. These properties make PHs highly valuable for a range of materials applications.[6]

1.1.1 Acenes

This impetus has driven the advancement and broadening of various PH classes, including acenes,[7] which consist of linearly fused benzene rings and can be viewed as nanoscale segments of graphene.[8] As illustrated in Scheme 1.1, acenoquinones **1** are widely employed as precursors for synthesizing acenes **3**. This is achieved by treating acenoquinones with nucleophilic organometallic reagents (such as alkynyl/aryl lithium or Grignard reagents), and then reducing the resulting dihydroxylated intermediates **2**.[9]

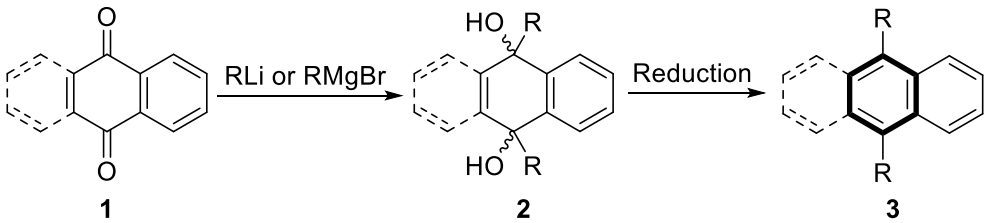

Scheme 1.1 A general synthetic route to acenes.

Acenes display unique features, including a narrow Highest Occupied Molecular Orbital–Lowest Unoccupied Molecular Orbital energy gap, reduced optical gaps, low-energy triplet states, small ionization potentials, and large electron affinities[10]—that stem from the topology of their ring fusion, where only one aromatic Clar sextet is shared across all the linearly-fused 6-membered rings.[11] These distinctive properties

make certain members of the acene family valuable for various applications.[5,12] For instance, 9,10-di(naphthalen-2-yl)anthracene **4** (Figure 1.1) holds potential as a luminescent component for full-color organic electroluminescent devices, emitting bright and stable blue light.[13] Furthermore, single crystals of 5,6,11,12-tetraphenyl-substituted tetracene **5** (Figure 1.1) have been shown to achieve hole mobility up to 40 $cm^2\ V^{-1}\ s^{-1}$.[14]

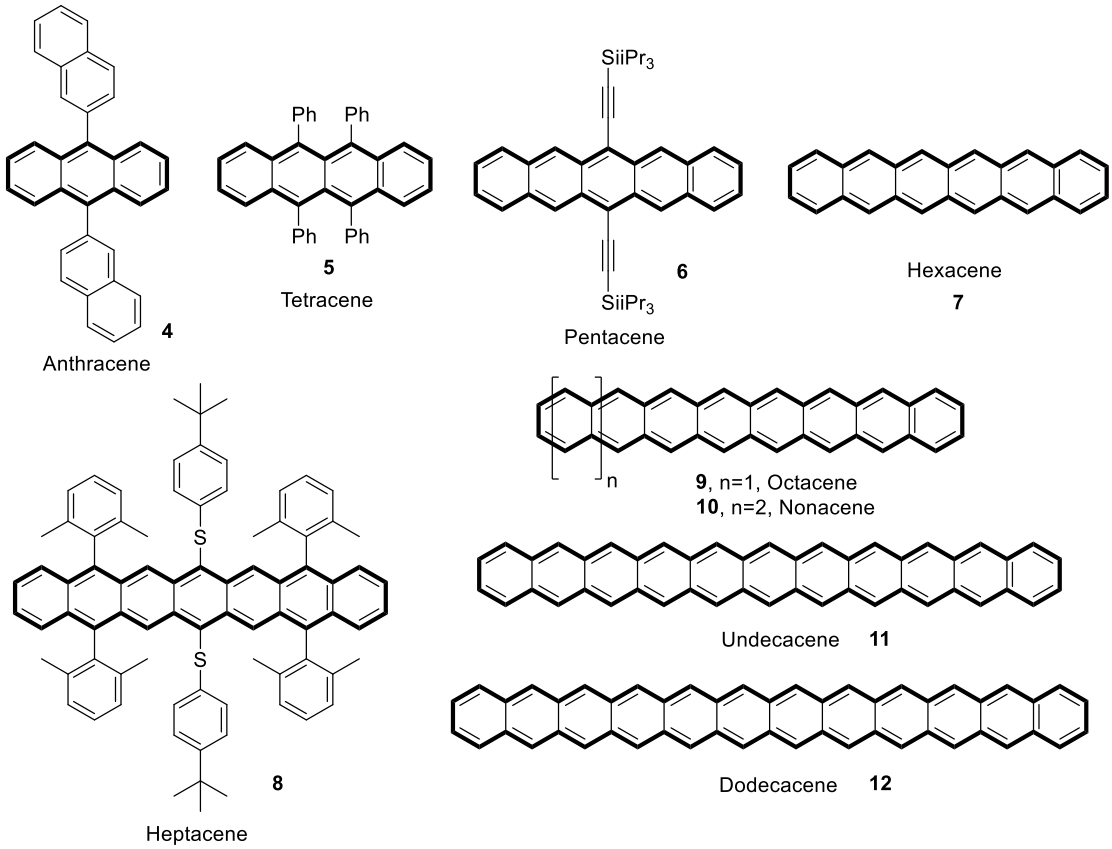

Figure 1.1 Structure of acenes **4-12**.

On the other hand, the electronic structural features that give linear acenes their unique properties also contribute to their high reactivity. Since acenes contain a single Clar sextet,[11,15] they exhibit the highest reactivity among PHs of similar size. Their kinetic stability diminishes with the addition of more rings, resulting in a greater tendency to dimerize (or potentially polymerize) and to react more readily with oxygen, particularly in the solution phase.[16] This high reactivity has posed challenges in the discovery of larger acenes.[17] To tackle these challenges, various strategies have been suggested and implemented. One approach is to introduce bulky or electron-withdrawing substituents (silyl ethynyl, fluorine, or phenylthio), at reactive sites on acene backbones to enhance stability.[12,18] Another strategy involves twisting the acene backbones or extending the π-system by introducing strong steric shielding or

benzannulated units (like pyrene, phenyl, and triphenylene), resulting in altered acenes (known as twisted acenes or π-extended acene derivatives) that deviate somewhat from the traditional definition of acenes (Figure 1.2).[19] Furthermore, larger acenes can be generated directly within a polymer matrix using specific UV light or on a gold surface through thermal treatment under ultra-high vacuum conditions.[20]

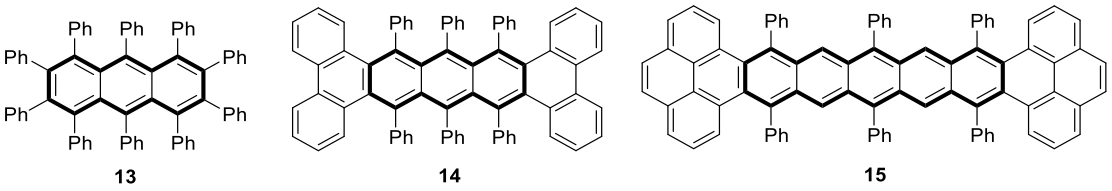

Figure 1.2 Structure of twistacenes **13-15**.

For instance, the benchmark pentacene shows very limited solubility in common organic solvents and is highly susceptible to oxidative degradation. However, its derivative, 6,13-bis(triisopropylsilylethynyl)pentacene **6**,[21] can be prepared from solution and functions as an excellent hole-transporting (i.e., *p*-channel) semiconductor, making it highly relevant in field-effect transistors. Moreover, its excited-state configuration, with $E(S_1) > 2E(T_1)$, has made it a significant focus in singlet fission research.[22] The largest acene that was synthesized in the 20th century using traditional organic chemistry methods was hexacene **7**.[23] Although it could be structurally analysed using single crystal analysis,[23h] ^{1}H NMR spectroscopy was not conducted, highlighting another challenge in acene chemistry: the low solubility of larger acenes. This poor solubility results from the strong C-H$\cdots\pi$ intermolecular interactions between neighbouring molecules within the herringbone type crystal structure. Recently, a physical vapor-transport method was introduced to produce platelet-shaped crystals of hexacene through the thermal decomposition of its ketone precursor. The hexacene formed using this method was revealed to be notably stable at room temperature when kept in the dark.[23h]

Substituted heptacenes **8** have been successfully characterized both spectroscopically and structurally, and they exhibit significant persistence in solution.[24] Preliminary findings revealed that trialkylsilylethynyl groups, with a diameter roughly 35–50% of the length of heptacene, provide enough steric shielding to greatly enhance the stability of the molecule.[24] This discovery had a significant impact on development of stable larger acenes, reaching up to nonacene. Bettinger's research group later reported the synthesis and spectroscopic characterization of unsubstituted octacene **9** and nonacene **10** using a matrix isolation method.[25] This method employs a protecting-

group strategy that relies on the photochemical bisdecarbonylation of bridged ketones. By eliminating the ketone bridges in precursors through UV irradiation under matrix-isolation conditions, unsubstituted octacene and nonacene can be generated and detected using UV–vis–NIR spectroscopy.

Miller and co-workers were the first to report a fully characterized "persistent" nonacene derivative. Although it has a narrow HOMO–LUMO gap of 1.12 eV—the smallest energy gap experimentally measured for any acene. The compound was thoroughly detected using a range of analytical techniques.[18a] The UV-vis and fluorescence spectra reported for this derivative indicate a weak S_0–S_1 transition and an unusually short-wavelength fluorescence, which may result from the formation of a decomposition product, specifically an endoperoxide. In contrast, Anthony and co-workers prepared novel nonacene derivatives featuring trialkylsilylethynyl and bis(trifluoromethyl)phenyl groups at alternating edges, as well as fluorine atoms on the peripheral phenyl rings.[18b] The spectroscopic properties of these derivatives differ considerably from those of previously reported purported nonacene. They exhibit a strong S_0–S_1 transition around 1000 nm, lack fluorescence in the visible region, and feature a small HOMO–LUMO gap of 1.2 eV. All these nonacene derivatives from Anthony's research group were clearly characterized using single crystal X-ray diffraction (SCXRD) analysis, which showed one-dimensional slipped stack packing arrangement. Notably, the lack of an NMR signal alongside the detection of an Electron Spin Resonance (ESR) signal for the nonacene sample suggest an open-shell (OS) nature, although this has not been definitively confirmed. Today, undecacene **11** is most extensive acene that has been experimentally analyzed under matrix isolation conditions[26] and through on-surface.[27] The generation of acenes on surface, accompanied by advanced microscopy techniques, has observed major advancements in last several years, culminating within investigation of acenes up to dodecacene **12**, the longest acene observed to date.[28]

1.1.2 Indenofluorenes

Pentacene serves as a crucial key constituent in organic electronics, known for its high charge-carrier mobility and its role in singlet fission (SF) studies.[22b,c,29] However, it is highly susceptible to photo- and air-oxidation[30] (Scheme 1.2), which has driven the search for alternative topologies similar to pentacene.

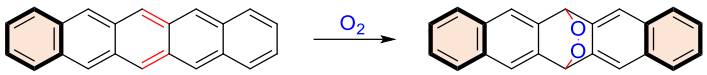

Scheme 1.2 Pentacene degradation in presence of oxygen.

In addition to modifying the peripheral substituents (6,13-position) on the conjugated backbone of alternant acenes (like pentacene), another approach involves incorporating non-benzenoid rings into unstable acenes. This has facilitated the introduction of a new class of stable non-alternant PHs known as fully conjugated indenofluorenes (IFs).[31] IFs feature fully conjugated 6-5-6-5-6 rings with sp^2-methine bridges in the 5-membered rings (Figure 1.3). IFs have two fewer carbons and π-electrons compared to pentacene, making them formally antiaromatic (containing 20π-electrons, as per Hückel's rule). These IFs are typically derived from the parent dihydro-IFs (DH-IFs), which feature sp^3-methine bridges within the 5-membered rings. DH-IFs have shown effective and stable light-emitting properties in electroluminescent devices, especially within the blue wavelength range,[32] and are also utilized as electron-transporting materials.[33]

IFs display one of the most intriguing topologies among conjugated PHs, featuring a quinoidal bonding structure in their central tricyclic component, referred to as indacenes. Indacenes are fully conjugated PHs composed of interconnected 5-6-5 membered rings. They can be generated by formally inserting a benzenoid ring into the central C-C bond of a bicyclic non-alternant PH pentalene[34] **16** (a process referred to as benzene interposition, as coined by Peters[35]), which is a fundamental molecule in the series of non-alternant PHs.[36] 12πe-Indacene exists in two possible isomeric forms: the symmetric *s*-indacene (**17**, Figure 1.3) and the asymmetric *as*-indacene (**18**). Parent *s*-indacene **17** remained unisolated because of its strong reactivity with oxygen,[36c] although its ^{1}H NMR spectrum has been recorded for *in situ* generated **17**. Extensive research by various pioneers has led to the synthesis and characterization of symmetrical *s*-indacene.[37] The asymmetrical isomer, *as*-indacene **18**, is difficult to isolate even after several trials.[38] The parent *s*-indacene (without substituents) is excessively unstable for isolation, but modification with arene groups enabled the generation of various derivatives, allowing further exploration of this motif. In addition to using bulky alkyl groups for steric protection in early *s*-indacene syntheses, another effective strategy for stabilizing antiaromatic systems, such as cyclobutadiene and pentalene, has been benzene annulation.[39]

In a similar vein, the stability of the indacenes can be improved by benzannelating both terminals of the π-conjugated framework. For 5-6-5 fused ring system, *s*-indacene **17** can make either indeno[1,2-*b*]fluorene **19** or indeno[2,1-*b*]fluorene **20**, based on the orientation of benzannelation. In contrast, *as*-indacene **17** can lead to the formation of indeno[2,1-*a*]fluorene **21**, indeno[2,1-*c*]fluorene **22**, or indeno[1,2-*a*]fluorene **23**, as depicted in Figure 1.3. Thus, the arrangement of benzene fusion mode to the five-membered ring may influence the stability of the indacene cores, resulting in five distinct structural isomers of dibenzo-fused indacenes **19-23**.

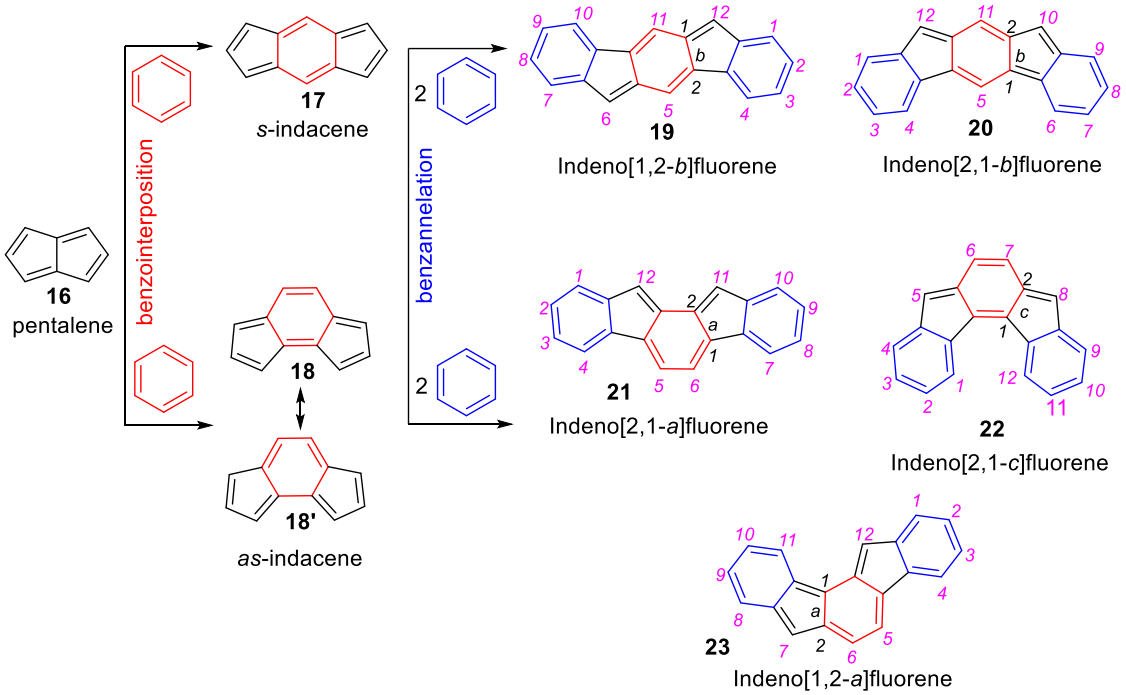

Figure 1.3 Nomenclature, numbering and structures for fully conjugated indenofluorene isomers.

The IF family consists of five structural isomers, which can be challenging to distinguish due to the various naming and numbering methods, and graphical depictions used during the last century to depict their shapes and structures (Figure 1.3). The present nomenclature employs a bracketed combination of numbers and a letter to distinguish each isomer. The numbers specify the orientation of the indene group in relation to the fluorene, whereas the letter represents the terminus where the indene and fluorene rings are fused. The 1,2-isomers **19** and **23** feature an *anti*-relation between the methylene bridges of 5-membered rings, whereas the 2,1-isomers **20-22** display a *syn*-relation. These IF scaffolds have different symmetries: the [1,2-*b*]IF isomer has centre of symmetry, and the [2,1-*a*]IF, [2,1-*b*]IF, and [2,1-*c*]IF isomers exhibit a mirror plane of symmetry.[40] These structural isomers can be identified by three distinct types of

quinodimethane (QDM) units present within their hydrocarbon framework: *para*-QDM, *ortho*-QDM, or *meta*-QDM. The non-Kekulé open-shell resonance structures of these units suggest a diradical ground state.[41] Specifically, compounds **19** and **22** feature *para*-QDM substructures, **20** and **23** have *meta*-QDM substructures, and **21** contains an *ortho*-QDM substructure. Consequently, the IF isomers exhibit varying electronic and optical properties. The computed diradical character (y_0) values for these isomers range widely, from $y_0 = 0.25$ for **22** to $y_0 = 0.80$ for **23**,[42] but different values were also reported earlier depending on the basis set used.[43] These variations can be understood by analyzing the number of Clar sextets acquired during the transition from the open-shell to the CS structure. IFs that have two Clar sextets in their CS structure and three in their open-shell (OS) structure exhibit only a slight enhancement in stability due to the addition of one extra Clar sextet, resulting in lower diradical character (e.g. **19**, **21**, and **22**). In contrast, isomers **20** and **23** gain two additional Clar sextets in the OS form, leading to greater resonance stabilization and thus a larger diradical character. The resonance between CS form and OS diradical form indicates that these compounds could behave as diradicaloids.[44] Each isomer, due to its specific ring topology, displays unique structural and electronic characteristics.

IF derivatives were initially synthesized in the 19th century by Gabriel.[45] For about seventy years,[46] research on IFs was sporadic until the 1950s when Deuschel[47] and Chardonnens[48] developed a general synthesis strategy. During that period, advanced spectroscopic and structural detection techniques were limited, so IFs were primarily characterized by their basic elemental analysis and melting points. After their preliminary synthesis, IF advancement stagnated for another forty years. However, interest in the IF scaffold was revived about a ten years ago with recognition of cyclopenta-fused PHs as usable organic materials. Prior to mid-1990s,[49,50] synthetic approaches to IFs were extremely limited. The only known synthesis before this period was by Le Berre *et al.*[51] in 1957, who developed a [2,1-*a*]IF compound which exhibited a strong tendency to react with oxygen. In 1994, Swager and co-workers[49] synthesized a purple solid [1,2-*b*]IF through a transannular cyclization reaction of a macrocyclic diacetylene compound with I_2 in benzene, achieving yields of 50–70%. Although this compound showed relatively good chemical stability in the solid state, but it was highly susceptible to ambient conditions in solution, leading to oxidation and the formation of IF-dione with yields ranging from 60% to 95%. Two years later, Scherf *et al.*[50] reported another [1,2-*b*]IF molecule as a model compound containing quinoidial conjugation to

explain the low band gap of their polyindenofluorene (PIF) system. Remarkably, following these early studies, no additional IF systems were synthesized until 2011.

In 2011, Haley et al. prepared and characterized [1,2-*b*]IF[52] **28** (Scheme 1.3). This work was inspired by earlier research from the Swager group, which involved the preparation of the unstable compound **25**.[49] The fully conjugated, formally antiaromatic [1,2-*b*]IF was analyzed by SCXRD, exhibiting notable bond alternation in its 5-6-5 tricyclic core, similar to a *p*-QDM structure. In a subsequent study, Haley and research group extended the variety of fully conjugated [1,2-*b*]IFs (Scheme 1.4).[53] They synthesized diones **25a**, **25b**, and **29** through a three-step synthesis process. The next step involved reacting with (triisopropylsilyl)ethynyllithium (TIPSE), and after an acidic work-up, the corresponding diols were obtained which were reduced with $SnCl_2$ in toluene to produce the fully conjugated derivatives **28** and **30**. Notably, the synthetic procedure reported is similar to that used for making pentacene derivatives.[9]

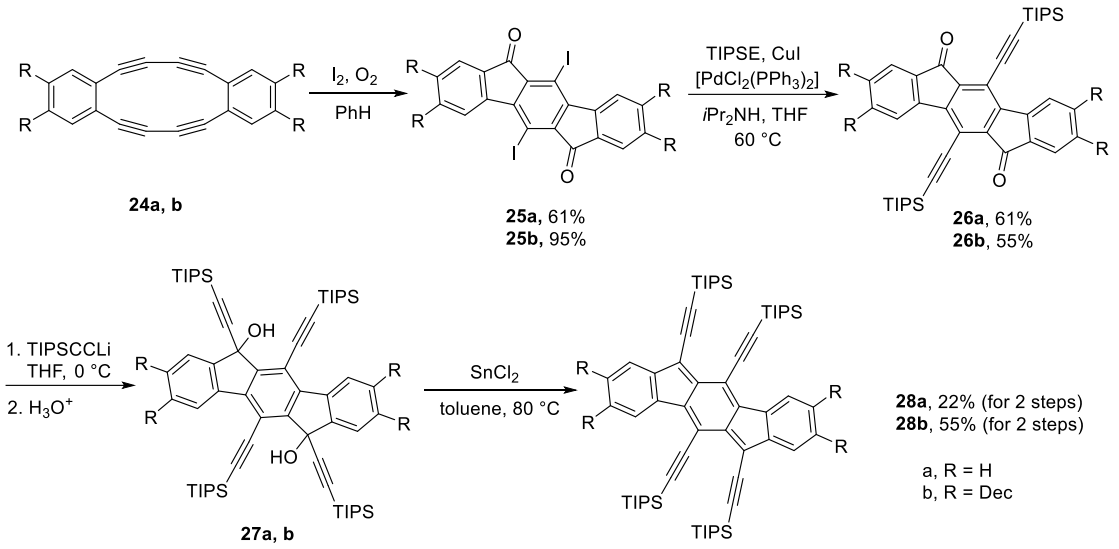

Scheme 1.3 Synthetic route to TIPSE substituted indeno[1,2-*b*]fluorenes.

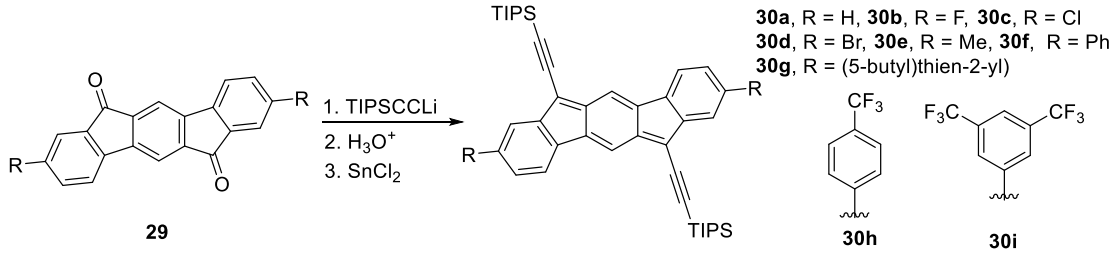

Scheme 1.4 Synthetic route to 2,8-disubstituted indeno[1,2-*b*]fluorenes.

The compounds exhibited reversible electron-acceptance with potentials of approximately −0.6 and −1.1 V, which are comparable to those of the well-established electron acceptor material [6,6]-phenyl-C_{61}-butyric acid methyl ester (PCBM).[54] This

behavior was ascribed to the conversion of a neutral 20π-electron antiaromatic system into a 22π-electron aromatic species. Recognizing this electron-accepting capability, Haley, Nuckolls, and co-workers proceeded to synthesize a series of 6,12-disubstituted [1,2-*b*]IFs **31a-31j** (Figure 1.4) and explored mesityl derivative in fabricating an ambipolar organic field-effect transistor (OFET).[55]

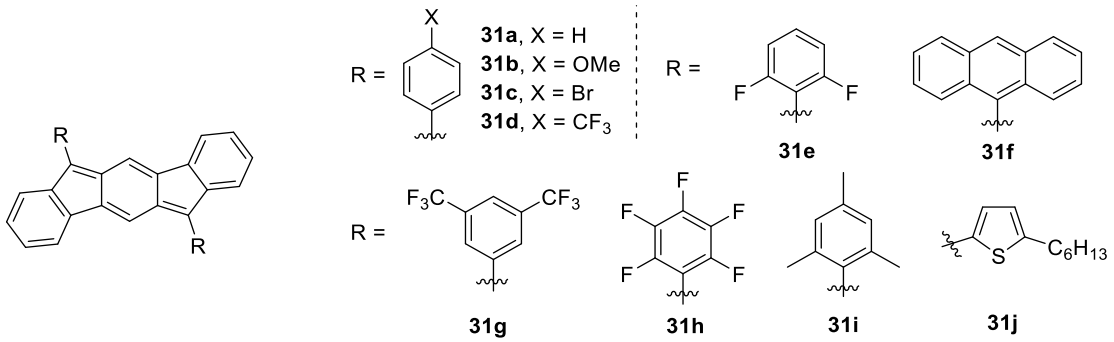

Figure 1.4 Structure of 6,12-disubstituted [1,2-*b*]IF derivatives.

The diphenyl derivative **31a**, first introduced by Scherf in 90s, lacked complete characterization during that period.[50] Recent research has addressed this gap by synthesizing and analyzing the series of derivatives **31a-31j** using electrochemistry and absorption spectroscopy. The study revealed patterns correlating the electronic properties of aryl groups with low-energy absorption (λ_{max}) and redox potentials (E_{red}/E_{ox}). Electron-rich aryl groups (**31b**) were found to elevate HOMO and LUMO energy levels, whereas electron-deficient aryl groups (**31d, g, h**) reduced these levels. The [1,2-*b*]IFs with fluorinated aryl groups (**31d**, **g**, **h**) exhibited irreversible oxidations but reversible reductions. The investigation into the amphoteric redox properties was expanded to include device fabrication. Additionally, a parallel investigation by the Yamashita group employed a similar method to synthesize and analyze 6,12-disubstituted [1,2-*b*]IFs **31a**, **31e–f**.[56] OFETs made from thin films of the **31a** demonstrated hole transport properties. In comparison, the 2,6-difluorophenyl derivative **31e** and 9-anthracenyl derivative **31f**, which featured lower LUMO energy levels, exhibited ambipolar charge transport. Additional information is available in the application section.

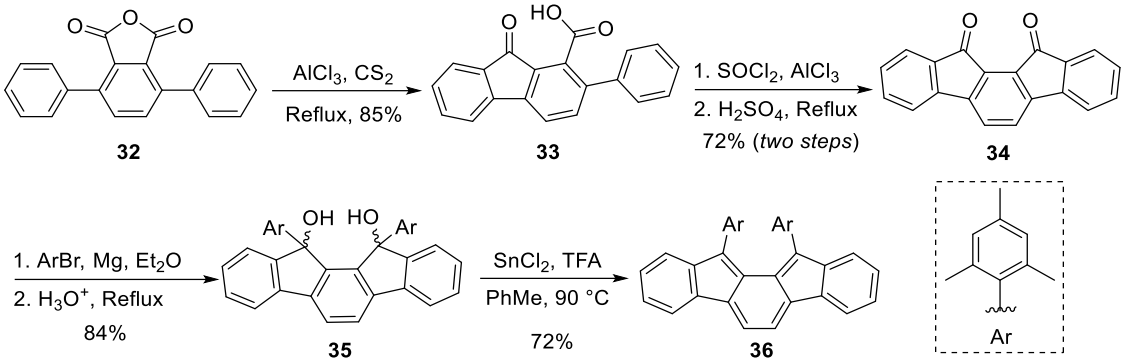

Scheme 1.5 Synthetic route to mesityl substituted indeno[2,1-*a*]fluorene **36**.

In 2011, Tobe and co-workers introduced the subsequent isomer in the series of fully conjugated IFs (Scheme 1.5).[57] They prepared 11,12-dimesitylindeno[2,1-*a*]fluorene **36** in 40% yield through a two-step process, starting with a previously known dione precursor **34**, which had been synthesized from compound **32** in two steps. Examination of the crystal structure of **36** showed bond length alternation within the core, confirming the structural characterization. Although the compound contains a reactive *o*-QDM group, it was found stable when exposed to dienophiles and oxygen. The contribution of singlet diradical form to the ground state of **36** was supported by elongated methylidyne $C_{sp}{}^2$–$C_{sp}{}^2$ bond and high HOMO/LUMO orbital coefficients observed at the apical (non-bridgehead carbon of five-membered ring) positions.

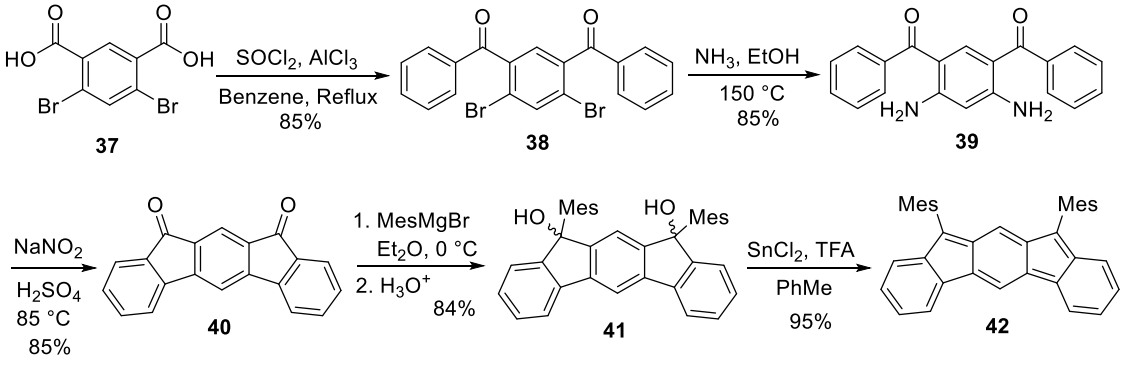

Scheme 1.6 Synthetic route to indeno[2,1-*b*]fluorene **42**.

Two years later, the same group succeeded in synthesizing a moderately stable *meta*-QDM-containing [2,1-*b*]IF **42** (Scheme 1.6).[58] The compound was synthesized with a 59% yield over two steps, commencing with a dione precursor **40**, which itself was prepared in three steps from compound **37**. Characterization through SCXRD analysis showed that the six-membered rings are slightly delocalized and connected by $C_{sp}{}^2$–$C_{sp}{}^2$ bonds with a length of approximately 1.43 Å. The absence of ^{1}H NMR signals at room temperature indicated that compound **42** exhibits a significant singlet diradical contribution to its ground state. The loss of the ESR signal and the appearance of NMR

signals upon cooling provided confirmation for the presence of a triplet biradical. The energy gap between the singlet and triplet states was calculated to be −4.20 kcal/mol using temperature-based magnetic susceptibility measurements. Compound **42** exhibited very low energy absorption extending to 2000 nm (0.62 eV), with the lowest energy peak at 1700 nm corresponding to the S_0–S_1 transition, as determined by Time-Dependent Density Functional Theory (TD-DFT) calculations. These findings indicate that derivatives of **42** may be promising candidates for applications involving low-energy light absorption.[59]

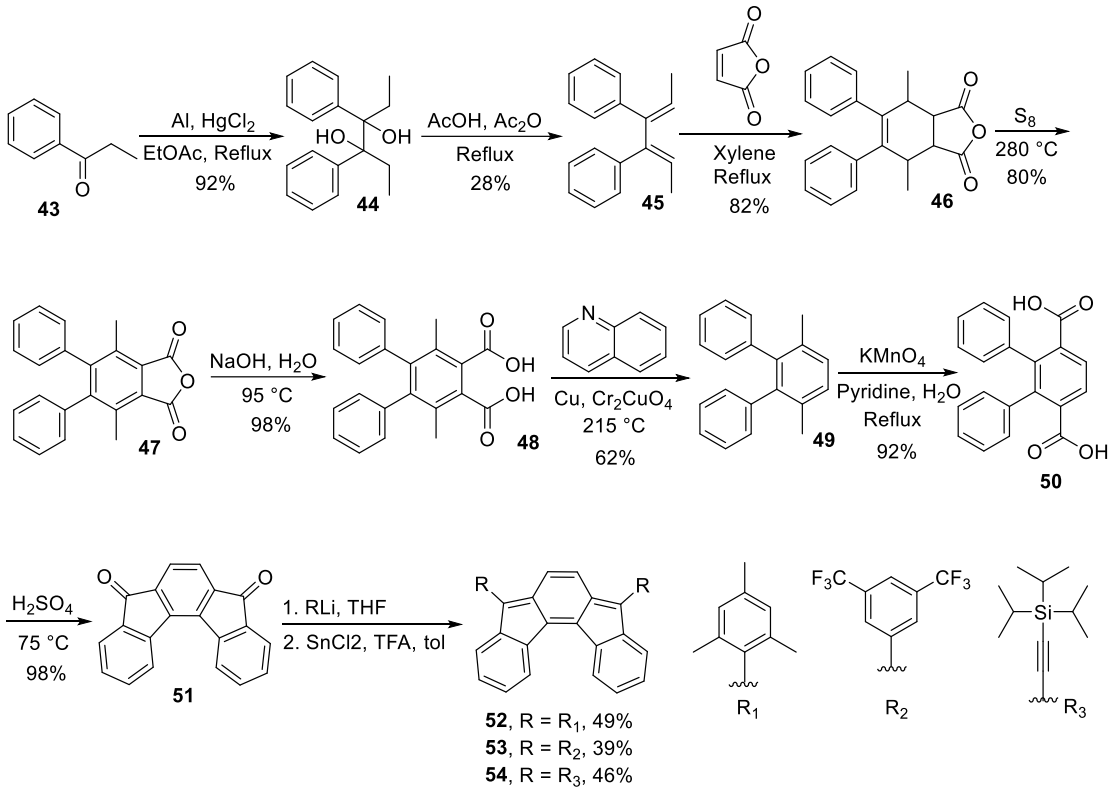

Scheme 1.7 Synthetic route to indeno[2,1-*c*]fluorene derivatives **52-54**.

Haley's research group advanced the family of fully conjugated IFs by synthesizing the [2,1-*c*]IF derivatives[60] **52-54** as shown in Scheme 1.7. These compounds feature a fragment of the carbon allotrope fullerene (C_{60}) and incorporate the rarely investigated *as*-indacene moiety. This series of compounds demonstrated greater effectiveness as electron acceptors than their [1,2-*b*]IF counterparts, with the electrochemically determined HOMO–LUMO energy gap decreased by 0.14 eV. The inclusion of the electron-deficient aryl group in **53** and TIPSE in **54** was intended to achieve lower LUMO energy levels and improve solid-state ordering, respectively. Interestingly, these compounds also displayed a low-energy S_0–S_1 transition reaching up to 850 nm, a transition that is generally forbidden in centrosymmetric systems.

Ostroverkhova et al.[54] investigated how different electron acceptors influence charge photogeneration in bulk heterojunctions. Their findings revealed that incorporating **52** or TIPSE-octafluoropentacene as electron acceptors impacted device performance by disturbing the crystallinity of the donor material. For comparative purposes, they used the commonly employed C_{60} derivative PCBM.

In 2022, Podlech and co-workers reported the design and synthesis of a methoxy-disubstituted [2,1-*c*]IF **60** as part of their work on helicenes of this class.[61] Their synthesis began with commercially available **55**, which underwent bromination using *N*-bromosuccinimide (NBS) followed by a Sandmeyer reaction, leading to compound **56** (Scheme 1.8). A double Suzuki coupling with **57** and a subsequent double intramolecular Friedel–Crafts (FC)-type cyclization produced the diketone **59**. The addition of mesityl lithium to this intermediate, followed by reduction with tin(II)chloride in trifluoroacetic acid, resulted in the formation of [2,1-*c*]IF **60**.

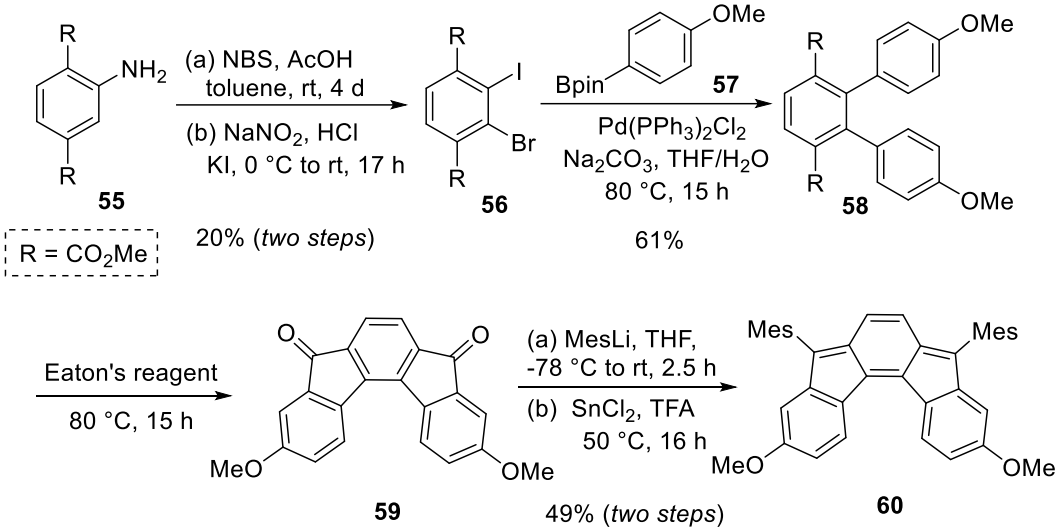

Scheme 1.8 Synthetic route to methoxy substituted indeno[2,1-*c*]fluorene **60**.

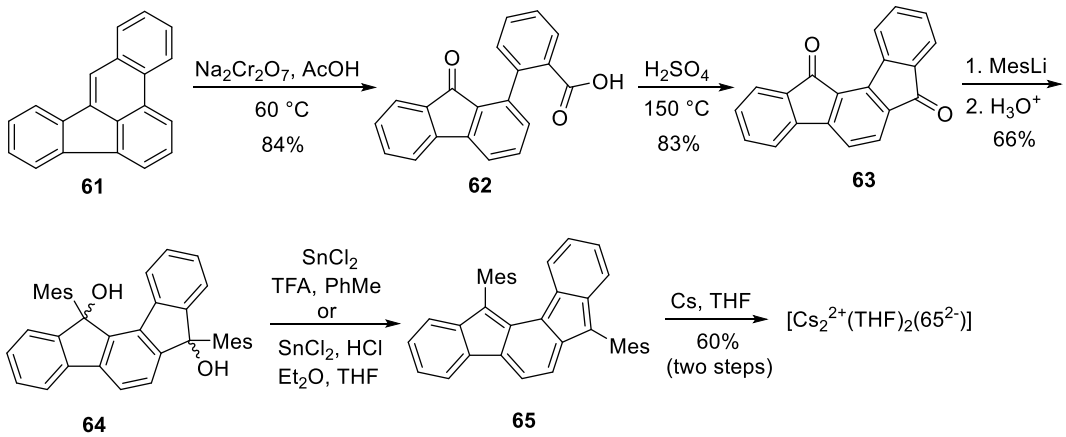

Scheme 1.9 Synthetic route to indeno[1,2-*a*]fluorene **65**.

The last antiaromatic IF isomer, [1,2-*a*]IF, was theoretically estimated to exhibit the highest diradical character (y_0 = 0.80) and possess a triplet ground state, setting it apart from other isomers. The formation of the mesityl derivative **65** (Scheme 1.9) was confirmed experimentally by Haley's group.[42] However, it could not be fully characterized by Nuclear Magnetic or Electron Spin Resonance because of its high sensitivity to air. The characteristic absorption band in the UV–vis–NIR spectrum and the redox potentials obtained from cyclic voltammetry (CV) correspond with the anticipated values for **65**. Furthermore, compound **65** was reduced with cesium to produce its dianion, which was subsequently isolated and thoroughly characterized through spectroscopy and single crystal analysis, offering additional proof of the presence of **65**. Notably, Nucleus Independent Chemical Shift (NICS(1)) values show that the outer benzene ring exhibits a strong diatropic effect, while the inner *as*-indacene component shows a weaker diatropic character. Additionally, Anisotropy of Induced Current Density (ACID) calculations confirm the presence of a diatropic ring current. These results imply that **65** may be classified as a Baird aromatic system, owing to its 20π-electron conjugation and triplet ground state. Recently, Pena and Gross[62] reported generation of unsubstituted parent [1,2-*a*]IF on surface by cleaving C–H bonds in dihydro-[1,2-*a*]IF using voltage pulses delivered through the tip of a combined atomic force and scanning tunneling microscope.

1.1.3 π-Extended indenofluorenes

IFs hold a unique place where diradical character and antiaromaticity intersect. Modifications to the IF scaffold generally involve two strategies: core π-extension and outer π-extension. π-Extending the quinoidal IF core from a single benzenoid ring (indacene) to three benzenoid rings substantially boosts the diradical character.[63] In contrast, alterations to the outer π-system of these IFs generally maintain a greater degree of antiaromaticity in the core, which typically retains an indacene core and does not exhibit strong diradical character. This discussion will first cover core-extended IF systems, followed by examples of outer-extended IF structures.

In core-extended systems, two effective strategies are commonly used to induce open-shell structures and adjust key factors like y_0 and singlet (S)-triplet (T) energy gap. First strategy involves modifying the overall π-conjugation to restore Clar sextets, either by extending the quinoidal conjugation or by changing the locations of radical centers. Second strategy involves introducing heteroatoms into the quinoidal or antiaromatic

skeletons to alter the electronic structures. Utilizing these two approaches, a variety of open-shell carbocyclic systems and their heterocyclic derivatives have been investigated, including various IFs and their topological derivatives.[64] This section focuses on molecules that employ the first strategy.

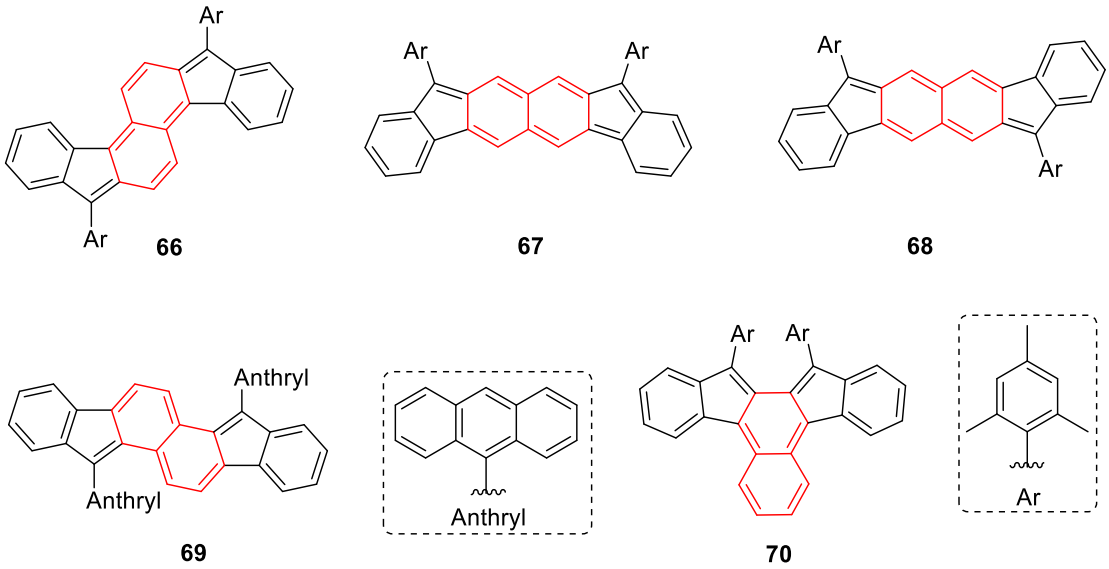

Figure 1.5 Naphthalene fused π-extended IF derivatives **66-70** (naphthalene modification of core benzenoid ring).

Among the various systems, modifying the central arene core can lead to either CS or OS structures, each exhibiting different diradical characters. These variations are influenced by the structure of the central π-system and ring fusion patterns. Considering the predominantly CS nature of *p*-QDM, expanding the central six-membered ring in **19** effectively increases diradical character while maintaining the similar fused peripheral rings. Extending the quinoidal core in IFs results in a series of fluorenofluorene (FF) derivatives (Figure 1.5). The [4,3-*c*]FF **66**, initially reported by Haley and co-workers,[65] exhibits aromaticity in outer six-membered rings, while the central fused 5-6-6-5 ring structure includes a bond-localized 2,6-naphthaquionodimethane moiety. Both experimental and computational studies of compound **66** indicate a CS ground state. In comparison to extended IFs that integrate a *p*-QDM-type unit, [2,3-*b*]FF[66] **67**, an *m*-QDM-type analog reported by Tobe's group, exhibits a stronger OS character and a narrower S-T gap compared to its smaller counterpart **42**. A significant characteristic of **67** is its higher excitation energy, which reaches a maximum at 1293 nm and is blue-shifted compared to **42**. [3,2-*b*]FF[67] **68**, documented by Haley group, was extensively analyzed for its diradical character and antiaromatic properties. The quinoidal extension in **67** leads to a moderate diradical character, with the primary driving force being the

recovery of Clar sextets in the central naphthalene core as reported by Casado and co-workers.[68] Frantz and Casado synthesized [2,1-*a*]FF **69**, which incorporates fused *o*-QDM units within a 1,5-naphthoquinodimethane core.[69] The presence of this core leads to a moderate diradical character, indicating that *ortho* fusion serves as a balanced approach in the design of organic diradicaloids.

In contrast to lateral expansion, vertical expansion of the QDM core can also significantly affect the electronic ground state properties of PHs. As previously noted, [2,1-*a*]IF **36**, which contains *o*-QDM, exhibits CS ground state. However, compound **70**, which results from the vertical expansion of the *o*-QDM core, is anticipated to show a greater diradical character compared to **36**. In 2016, Tobe *et al.* successfully prepared this vertically expanded scaffold[70] **70**, with its structure corroborated by single crystal X-ray analysis. DFT studies indicated that **70** possesses large OS character (y_0 = 0.63) and smaller S-T energy gap (–7.45 Kcal/mol) as compared with **36** (–12.88 Kcal/mol). Compound **70** exhibited significantly higher reactivity than **36** due to its enhanced biradical character. However, integrating the 2,3-naphthoquinodimethane unit into IF framework, along with effective steric protection from mesityl groups, provided kinetic stabilization. This allowed for a detailed investigation of its distinctive physical and chemical properties.

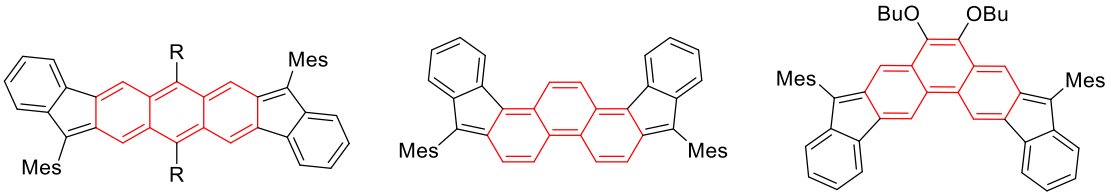

71, R = CCSi*i*-Pr$_3$ **72** **73**

Figure 1.6 Anthracene/Phenanthrene fused π-extended IF derivatives **71-73**.

Fusing indene moieties onto large acenes to create extended IFs is an effective strategy for achieving both stability and diradical character. A prominent example is molecule **71**[63] (Figure 1.5), which exhibits a singlet diradical ground state and a triplet excited state that can be accessed thermally. The narrow S-T gap (–4.18 kcal/mol) indicates that compound **71** can switch its magnetic response by undergoing a reversible heating and cooling process. Two more examples are molecules **72** and **73**, as documented by M. Stępień and co-workers, which display notable diradical character and have comparable experimental S-T energy gaps of approximately −1.2 kcal/mol.[71] Compound **72** remains stable under ambient conditions, while compound **73**, although

manageable in air, deteriorates within a few days. In addition, compound **73** was employed as a component within OS macrocyclic coronoids.

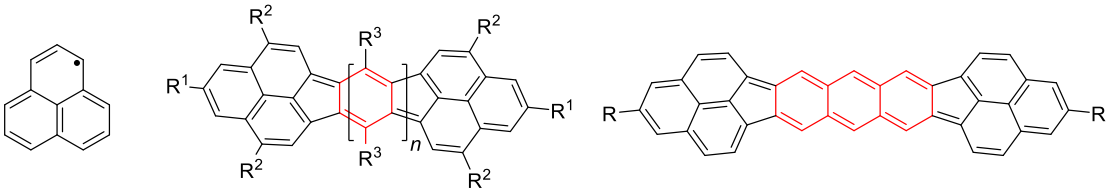

Phenalene

74a, n = 1, R^1 = R^2 = R^3 = H
74b, n = 1, R^1 = R^2 = H, R^3 = ^{i}Pr
74c, n = 1, R^1 = R^3 = H, R^2 = ^{t}Bu
74d, n = 1, R^1 = R^2 = H, R^3 = Ph
74e, n = 1, R^1 = Me, R^2 = H, R^3 = Ph
75a, n = 2, R^1 = ^{t}Bu, R^2 = H, R^3 = Ph
75b, n = 2, R^1 = R^2 = H, R^3 = Ph

76a, R = H
76b, R = ^{t}Bu

Figure 1.7 Kekulé structure of bis(phenalenyl)-based diradicaloids **74-76**.

Nakasuji and Kubo also developed similar open-shell systems by connecting two phenalenyl units with an aromatic bridge (Figure 1.7), which have attracted significant interest in both fundamental and materials science.[72] Two key factors contribute to the stabilization of these systems: first, the inherent delocalization within the phenalenyl moiety, and second, aromatic stabilization through the formation of an additional aromatic sextet as the system shifts from the quinoidal to the diradical resonance form. They synthesized compound **74a**, which includes a central fused benzene ring, and introduced various substituents to enhance solubility.[73]. The broadening of the ^{1}H NMR spectra at higher temperatures, along with the appearance of sharp peaks at lower temperatures and the presence of ESR peaks, provided clear evidence of a singlet ground state in these systems. The diradical character was further increased when the central benzene ring in **74** (y_0 = 0.30) was expanded to naphthalene in compound **75a** (y_0 = 0.50)[74] and to anthracene in compound **76** (y_0 = 0.68).[75] The higher diradical contribution of **76** was further confirmed by single-crystal analysis and was attributed to the strong aromatic stabilization energy provided by the anthracene linker.

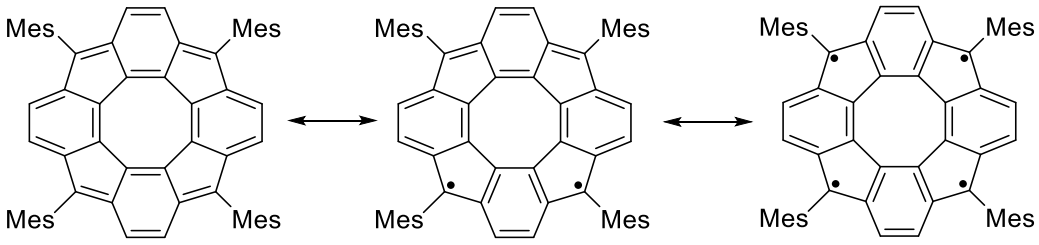

D_{2h} **77-A** C_{2v} **77-B** D_{4h} **77-C**

Figure 1.8 Structure of TCPTP **77** with its resonance structure.

The previously discussed examples of IF congeners and their isomers feature only two five-membered rings, where the two diradicaloid components are either paired or unpaired. In contrast, the examples shown in Figure 1.8 involve IF congeners with more than two five-membered rings, potentially exhibiting multiple radical characters. In 2015, Tobe et al. reported the tetraradicaloid molecule tetracyclopenta[*def*,*jkl*,*pqr*,*vwx*]tetraphenylene[76] **77** (Figure 1.8). This compound was synthesized by introducing four sterically hindered mesityl groups through a dehydrogenation reaction from its precursor. DFT calculations revealed that the closed-shell D_{2h} form of **77** had y_0 and tetraradical character (y_1) values of 0.095 and 0.032, respectively. SCXRD analysis confirmed a structure very close to this D_{2h} model, with y_0 measured at 0.258 and y_1 at 0.085. Conversely, the open-shell D_{4h} form, which was less energetically favorable, showed a y_0 of 1.000 and y_1 of 0.166. The bond lengths obtained from SCXRD were consistent with the theoretical predictions for the D_{2h} geometry. In the ^{1}H NMR spectrum of **77** at room temperature, a single peak was observed at 2.85 ppm for the core aromatic proton, likely due to the paramagnetic shielding effect of the 20π-electron system. NICS calculations indicated that the six-membered rings had nonaromatic or weakly antiaromatic characteristics, whereas the five- and eight-membered rings exhibited significant antiaromaticity. At 50 °C, the NMR signals for **77** began to broaden, suggesting the presence of a thermally accessible triplet state, despite the relatively large calculated S-T value (–16.49 Kcal/mol). Additionally, **77** showed a pronounced UV-vis absorption at 475 nm and a broad band located around 909 nm.

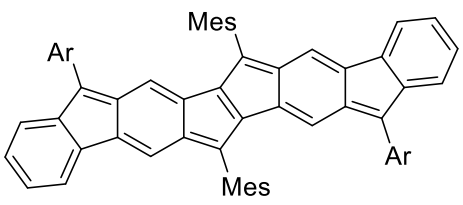

78a, Ar = mesityl
78b, Ar = 9-anthryl

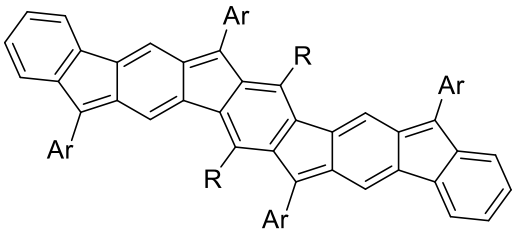

79a, R = OC_6H_{13}, Ar = mesityl
79b, R = OC_6H_{13}, Ar = 3,5-$(CF_3)_2C_6H_3$

Figure 1.9 Structure of ladder shaped π-extended IF derivatives **78-79**.

In 2015, Itami and Haley reported the synthesis of ladder-shaped conjugated systems,[77] **78** (Figure 1.9). These compounds, consisting of eight fused rings including both five- and six-membered rings, were constructed *via* Palladium-catalysed C–H/C–H annulation. SCXRD analysis and ESR spectroscopy confirmed their OS nature, attributed to their extended conjugation. The near-IR absorption features and narrow

redox potentials identified by CV suggest that these fused ring systems possess small optical and fundamental energy gaps. To further investigate how fusion modes affect diradical/tetraradical characters and chemical reactivity, Wu and co-workers reported linear tetraradicaloids[78] **79** in the form of indenofluorene dimers (IFDs) with four cyclopenta rings, featuring mesityl and 3,5-bis(trifluoromethyl)phenyl substituents for improved solubility (Figure 1.9). The pronounced bond length alternation observed highlighted a major contribution of the CS resonance form to the ground state. Theoretical calculations estimated that the parent IFD core has a very low OS character (y_0 = 0.038) and a large S-T energy gap (−8.4 kcal/mol). In accordance with this, compound **79** displayed sharp ^{1}H NMR spectrum in solution and no ESR signal in either solution or powdered form, indicating that it is more appropriately classified as a CS compound.

The five isomers of IF have 4nπ-electrons. The symmetry in the fusion of peripheral arenes or core expansion preserves the 4nπ electron configuration in IFs and their derivatives, making them formally antiaromatic. However, like observed in the series of dicyclopentafused-acenes,[79] core-expanded IFs exhibit less pronounced antiaromaticity compared to those with an *s*-indacene core.[80] Consequently, efforts to modulate antiaromaticity have largely focused on altering the outer arenes. While aromaticity and antiaromaticity cannot be directly quantified, several methods have been developed to evaluate these properties. According to Hückel's rule, cyclic, planar, and fully conjugated systems with (4n+2)π-electrons exhibit aromaticity, while those with 4nπ-electrons are considered antiaromatic. Though this rule applies effectively to monocyclic systems, it fails in addressing the complexities of polycyclic systems. However, the overall π-electron count is frequently employed as a preliminary measure to evaluate a molecule's degree of aromaticity or antiaromaticity. To identify the antiaromatic character or paratropic ring current in *s*-indacene within IF scaffolds, a common method involves examining the ^{1}H NMR chemical shifts of two indacene protons and assessing antiaromaticity through DFT analyses, such as NICS and ACID plots. Early efforts to modulate the antiaromaticity of the IF scaffold were made by Haley and co-workers, who incorporated thiophene and benzothiophene into the *s*-indacene core.[81] While their objective was not specifically to enhance the antiaromaticity compared to the parent [1,2-*b*]IF, their NICS calculations revealed that these heterocycles restored the antiaromatic character of *s*-indacene core to levels comparable to those of the parent *s*-indacene.

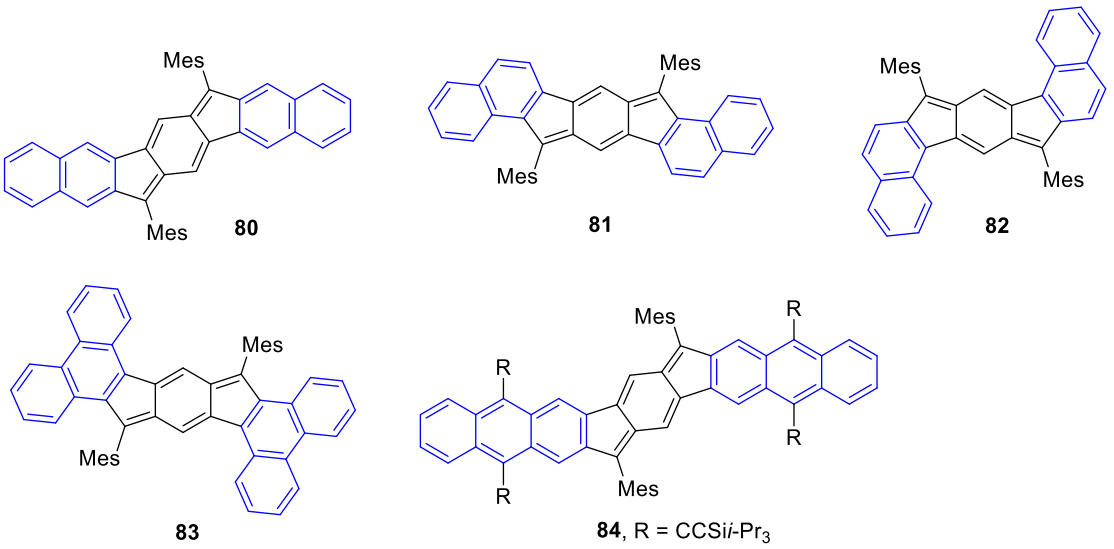

Figure 1.10 Fused [1,2-*b*]IF derivatives **80-84** (modification at outer core).

Further modifications to antiaromaticity of the *s*-indacene core were achieved by combining pure hydrocarbons such as naphthalene and phenanthrene. This led to the creation of molecules **80-84** (Figure 1.10), which displayed antiaromatic properties that were between those observed in [1,2-*b*]IFs and thiophene/benzothiophene derivatives.[82] These findings showed that bonds fused with greater double bond character contributed to the increased antiaromaticity observed in the *s*-indacene core. For example, molecule **84** was obtained by fusing *s*-indacene with anthracene at the 2,3-position, where the bond order (B.O.) is 1.25. This compound shows weak antiaromatic character in indacene core, as confirmed by the significantly downfield-shifted *s*-indacene protons of **84** compared to those in compound **31i** and **80**, both of which share same fusion pattern at 2,3-position. Among the indacenodinaphthalene isomers, the antiaromatic character is most pronounced when *s*-indacene is fused with naphthalene at the 1,2-position, where the bond order (B.O.) is 1.66. In this case, the indacene core protons are significantly upfield shifted, for two regioisomers **81** (6.62 ppm) and **82** (6.68 ppm). These results indicate that a higher π-bond contribution (reflected in a higher B.O.) to the *s*-indacene unit leads to stronger antiaromatic character. Further evidence supporting this idea is the preparation of **84**, which remains the only fluorescent derivative identified so far. The fusion of 2,3-anthracene[83] in **84** markedly reduces the core's antiaromatic character, which results in an increased energy gap between S_0 and S_1. This change effectively deactivates the low-barrier conical intersection found in other *s*-indacene derivatives.[84]

Following the observation of increased antiaromaticity in *s*-indacenes fused with thiophene and benzothiophene compared to [1,2-*b*]IF, Haley and co-workers also investigated the effects of heterocycle fusion in three directions: oxidizing the thiophene fused *s*-indacenes into sulfones,[85] extending the π-system of peripheral arenes from thiophenes and benzene fused thiophenes to naphthalene fused thiophenes,[86] and substituting sulfur with oxygen[69] in the heterocycles. Recently, Das and co-workers have investigated the antiaromatic characteristics of *s*-indacenes fused with dibenzoheterole.[87] They tuned the paratropic ring-current strength of *s*-indacene by inserting a benzene ring between *s*-indacene and the heterole unit. Unlike previous studies, where the larger double-bond character of five-membered heteroles was commonly exploited through annealing with the *s*-indacene unit to increase its paratropic ring-current strength, their design approach for the target scaffolds was distinct. Berger and Feng[88] reported two pyrene-fused *s*-indacenes that showed a significant bathochromic shift compared to the parent IF **19**. They also investigated the antiaromaticity of the internal *s*-indacene core using NICS calculations. The positive NICS values at the five-membered and central six-membered rings confirmed the antiaromatic nature of the *s*-indacene unit. At the same time, the negative NICS values for the outer pyrene units supported the proposed structure and the electronic properties of the pyrene-fused *s*-indacene.

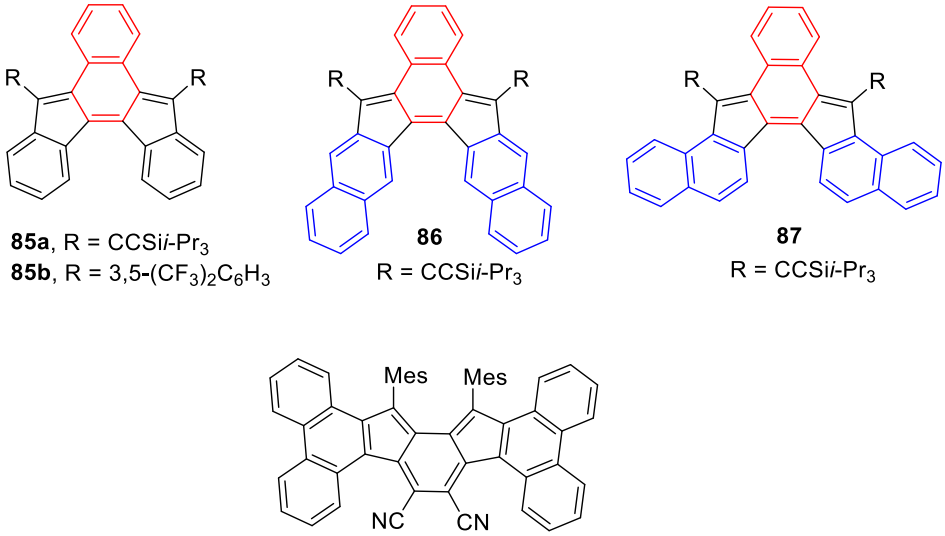

Figure 1.11 Benzo extended [2,1-*c*]IF derivatives **85-87** and [2,1-*a*]IF derivative **88**.

While the majority of research has focused on modifying antiaromaticity in *s*-indacene based scaffolds, Haley group made a pioneering contribution in 2013 with their work on the [2,1-*c*]IF scaffold, which incorporates an *as*-indacene core. To assess the

effects of benzo-fusion on the aromaticity and antiaromaticity of *as*-indacene derivatives, they investigated benzo-fused [2,1-*c*]IF structures **85-87**.[89] Their findings revealed that *as*-indacene exhibits lower antiaromaticity compared to *s*-indacene, especially within the central six-membered ring. NICS calculations revealed that all IF isomers shown in Figure 1.11 exhibit moderate to weak antiaromatic character in the indacene core and moderate to strong aromatic character in the outer benzene rings. Fusing an arene at the benz[*a*]-position of [2,1-*c*]IFs in compounds **85** further reduces the antiaromaticity of the indacene core while slightly enhancing the aromaticity of the peripheral benzene rings. Similar to [1,2-*b*]IF derivatives, the naphthalene fused derivatives display a similar pattern within the indacene core: those with a lower bond order of ring fusion (**86**, B.O. = 1.33) exhibit decreased antiaromaticity, whereas those with a higher bond order of ring fusion (**87**, B.O. = 1.66) show increased antiaromaticity relative to **85** (B.O. = 1.5).

The *as*-indacene-containing molecules discussed above, when extended both inward and outward, were found to be closed-shell systems. In contrast, Liu and Feng reported pyrene-fused dicyclopenta[*a*,*f*]naphthalenes,[90] where ortho-fusion of pyrene moieties to different bonds of dicyclopentanaphthalene led to OS configurations, with y_0 ranging from 0.44 to 0.48. Furthermore, a solution-processed field-effect transistor based on the 2,6-NQDM-embedded molecule demonstrated potential for organic electronics. Recently Das and co-workers[91] reported the unusual synthesis of a formally antiaromatic diphenanthro-*as*-indacene derivative **88** with a small HOMO–LUMO gap (0.85 eV). NMR/ESR studies revealed its open-shell diradical nature, supported by DFT calculations, which showed a 30% diradical character and a small S–T gap of −2.52 kcal/mol. This compound is an example of a rare diradicaloid with a small y_0, despite its small S–T gap. The bond length alternation in the *as*-indacene unit of **88** is significantly larger than in **36**, suggesting greater antiaromaticity compared to **36** in addition to diradical property in ground state.

1.1.4 Helical indenofluorenes

Helicenes represent a fascinating class of compounds characterized by *ortho*-fused rings and polyaromatic systems.[92] Their twisted three-dimensional conformations, resulting from steric constraints, impart unique inherent chirality to these molecules, leading to distinctive physical properties. Typically, these systems consist solely of aromatic benzene or heterocyclic rings, which exhibit local aromatic characteristics. However,

integrating quinoidal conjugated units into helicene structures is anticipated to introduce novel properties, such as magnetic activity. This is because quinoidal polycyclic hydrocarbons have a natural propensity to form open-shell diradicals, which can restore the aromaticity of the quinoidal unit. The combination of chiral optical properties and magnetic activity may pave the way for the development of magneto-optical materials and magnetic chiral dichroism.[93] The structural versatility and intriguing properties of quinoidal units embedded in IFs also encourage the study of helical chirality. Among the five isomers, the C-shaped [2,1-*c*]IF **52** bears resemblance to a [5]helicene. In this context, significant structural modifications have been made to develop chiral forms of **52** (Figure 1.12).

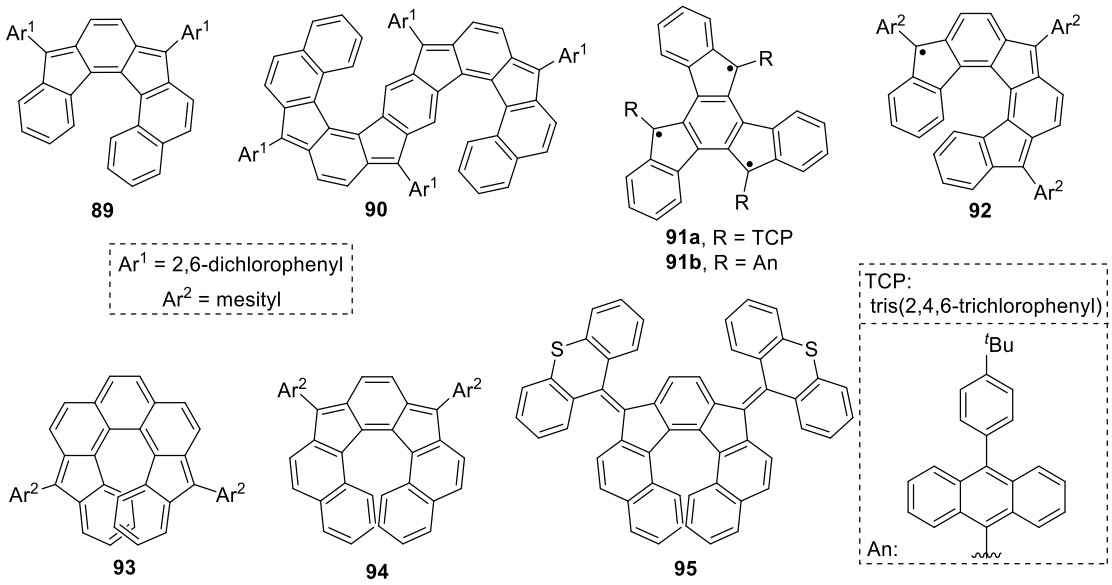

Figure 1.12 Structures of helical π-extended IFs **89-95**.

In 2020, Chi and co-workers synthesized a π-extended helical [2,1-*c*]IF **89**. This compound serves as an isoelectronic analog to the dianionic form of [6]helicene and was used as a model for comparing ground state and optoelectronic properties with the S-shaped double [6]helicene **90** during its synthesis.[94] Both experimental and theoretical studies of compound **89** showed that it adopts a closed-shell ground state, with a *P*/*M* racemization barrier of 15.29 kcal/mol. This barrier is similar to that of compound **90** (14.27 kcal/mol), but is higher than that of compound **52** and lower than that of [6]helicene. In contrast to **89**, double [6]helicene **90** features an open-shell singlet ground state with weak diradical character and a small singlet–triplet energy gap. Single-crystal analysis of **90** revealed a double-helical geometry, with the two terminal [6]helicene units bent in opposite directions. The reduced racemization barriers in both **89** and **90** are attributed to the presence of five-membered rings, which result in a smaller

turning angle, making it difficult to resolve the two enantiomers at room temperature. Additionally, the authors performed NICS and ACID calculations on **89** and **90** to further explore their antiaromatic properties. In **90**, the terminal naphthalene rings exhibit more negative NICS values compared to those in **89**, while the three rings in the *as*-indacene unit have higher positive NICS values than those in **89**. The central benzenoid ring in **90** shows a small positive NICS, consistent with the ACID calculations.

In 2020, Zhao and co-workers[95] aimed to synthesize air-stable polyradical species, focusing on triradical molecules **91** based on the [1,2-*a*]IF framework with a truxene-triyl core (Figure 1.12). Attempts to stabilize the targeted truxene triradical **91** using common bulky substituents, such as 2,4,6-trichlorophenyl and 9-anthracenyl, proved unsuccessful, as these groups could not adequately stabilize the triradical, making it challenging to isolate and fully characterize. However, single-crystal structures of adducts formed by related radicals were obtained, providing strong evidence for the transient existence of the designed triradicals. Electrochemical studies further supported the triradical structure by revealing three oxidation/reduction steps, while ESR experiments confirmed the paramagnetic nature of molecule **91**.

In 2022, Podlech and co-workers introduced a chiral helicene **92**,[61] a structural isomer of **91**, which also features three five-membered rings. This helicene was synthesized through cyclization reactions of a suitably *ortho*, *ortho*'-substituted terphenyl, followed by re-establishing conjugation. Both experimental and theoretical analyses revealed that the radical centre of **92** is located in the outer five-membered rings, which preserves the maximum number of intact benzene rings. The compound **92** exhibited negligible triradical character. NICS and HOMA calculations indicated that the five-membered rings in **92** displays significant antiaromaticity, with the central ring showing the highest level of this property. Additionally, the most prominent feature in the Electronic Circular Dichroism (ECD) spectrum of **92** was a dominant transition at 812 nm, which was identified as the most significant band.

In 2023, Stępień and co-workers developed a configurationally stable molecule **93**,[96] which is an analogue of [7]helicene. This molecule was synthesized using a combination of phenanthrene annulation and FC cyclization, resulting in a significant inversion barrier of 47 kcal/mol. The geometry, configurational dynamics, and electronic structure of **93** were thoroughly examined through crystal structure analysis, spectroscopy, and theoretical calculations. Their studies revealed that **93** possesses an

open-shell singlet ground state with a thermally accessible triplet state, characterized by y_0 of 0.69 and an experimental S-T gap of −3.5 kcal/mol. The molecule exhibits a narrow optical gap of 1.02 eV, which leads to strong absorption in NIR region and demonstrates reversible redox chemistry. NICS calculations were employed to explore the antiaromatic properties of **93** in both singlet and triplet states. In the singlet state, **93** showed pronounced paratropicity in the five-membered rings, while the terminal benzene rings were notably diatropic. However, the diatropicity of the inner phenanthrene fragment was reduced, suggesting significant quinoidal contribution to its electronic structure. In the triplet state, the aromaticity of the inner π-system was enhanced, as indicated by the decreased NICS values.

Parent [2,1-*c*]IF **52** is known to be configurationally unstable due to its small *P*/*M* inversion barrier.[60] To address this, Cruz and Millán recently improved the configurational stability by synthesizing molecule **94**,[97] and explored its optoelectronic, magnetic, and chiroptical properties. Compared to **52**, molecule **94** demonstrated enhanced performance with absorption extending up to 1000 nm and a smaller HOMO–LUMO energy gap of 1.75 eV. It largely retained a closed-shell structure with a minimal y_0 and a smaller S–T gap of −9.36 kcal/mol, which is lower than that of **52**. The increased configurational stability of **94**, evidenced by an inversion barrier of 24.64 kcal/mol, allowed for the measurement of its ECD spectra for each enantiomer. The dissymmetry factor (g_{abs}) achieved for **94** was 1.2×10^{-3}.

At the same time, Feringa and co-workers developed a similar helical system **95**, featuring two redox-active thioxanthylidene units attached to both five-membered rings of the [2,1-*c*]IF backbone *via* congested double bonds.[98] This differs from the mesityl groups used in previous studies. Their objective was to alter the antiaromatic properties of the [2,1-*c*]IF core through two-electron redox process. In crystal structure, the thioxanthylidene units in **95** adopt an anti-folded configuration. Upon oxidation, these units shift to singly bonded, contorted conformations. This transformation leads to significant changes in (chir)optical properties including the formation of a fully conjugated, formally antiaromatic *as*-indacene motif within the helical core. Notably, this process occurs without generating radical cation intermediates, allowing for highly reversible switching in absorbance, chiral properties, molecular geometry, absorbance, under normal conditions. VT NMR studies revealed that the [2,1-*c*]IF motif displayed a small diradical character. To investigate the (anti)aromaticity of the helical core, NICS calculations were performed on both the neutral and dicationic forms. For the neutral

form, diamagnetic ring currents were observed in the six-membered rings, indicating aromaticity, while the five-membered rings showed negligible ring currents, suggesting non-aromaticity. In contrast, the dicationic form exhibited strong paratropic ring currents in the *as*-indacene core, indicating antiaromaticity. These findings match well with previous studies on [2,1-*c*]IF derivatives **85-87**.[89]

1.1.5 Indenofluorene-based oligomers and polymers

The main appeal of IFs lies in their potential applications for IF oligomers and polymers, where extended chains are formed by covalently linking monomeric IF units. Such materials are difficult to synthesize due to issues with solubility, processability, and chemical stability of large macromolecules. Despite these challenges, significant progress was made in 1991 by Scherf and Müllen,[99] who successfully synthesized ladder-shaped polymers using polymer-based cyclization after establishing appropriate polyphenylene backbones. These innovative studies laid the foundation for the advancement of additional ladder-like polymers.[100] These materials have been identified as suitable candidates for electroluminescent applications, especially for blue-light emission. Additionally, polymers with a step ladder-type structure were explored, which were created through Yamamoto-based polymerization and connect IF units with carbon-carbon single bonds.[101] Polymers with repeating units linked at 5-membered rings of the IF scaffold have been also studied, and their nonlinear optical properties have been analyzed.[50,102]

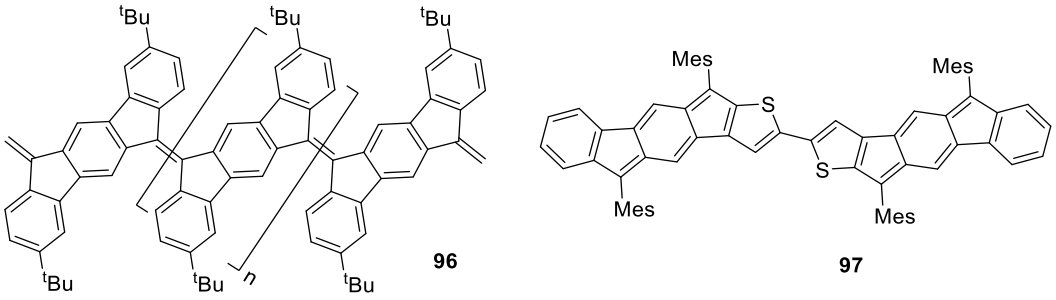

Figure 1.13 Examples of IF oligomers/polymers (solution syntheses).

An example in this category is polymer **96**,[50] which showed small band gap of 1.55 eV and had a quinoidal ground state (Figure 1.13). A quinoidal [1,2-*b*]IF core serves as a key chromophore for **96**, as predicted by theory, although the synthetic details of the quinoidal core was not revealed that time. In 2016, Haley and colleagues reported an unexpected low-yield synthesis of a benzo-indaceno-thiophene dimer (BIT dimer) **97**,[103] which represents a heterocyclic IF dimer (Figure 1.13).

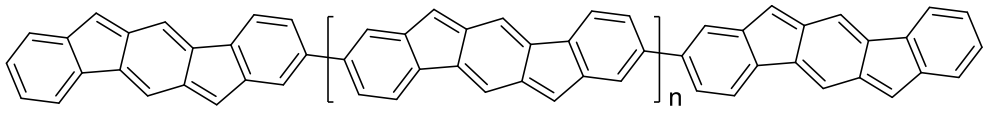

98

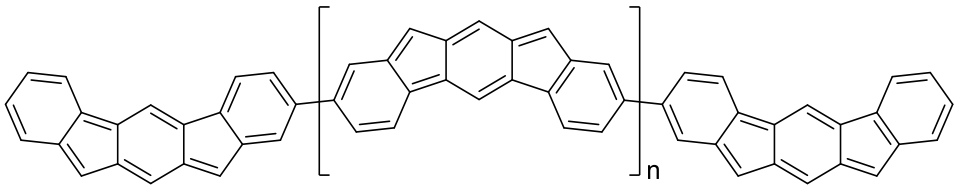

99

Figure 1.14 Examples of covalently linked IF polymers (synthesized on-surface)

Recently, unprotected IF polymers, which lack substituents on the indacene subunit, have been successfully synthesized using an on-surface strategy on gold substrates.[104] In 2018, Müllen and Fasel developed a synthetic method using methyl groups to form five-membered rings at targeted positions within a fully conjugated polymer. The IF polymer **98**[104b] (Figure 1.14) is predominantly comprised of [1,2-*b*]IF repeating units. The polymer exhibited a band gap of 2.3 eV and demonstrated a closed-shell electron configuration when characterized on gold surface. In next year, the same group revealed the synthesis of polymer **99**, featuring unprotected [2,1-*b*]IF subunits (Figure 1.14). This polymer **99**,[104a] that exhibited a band gap of just 0.4 eV. Theoretical calculations of a free-standing model oligomer revealed a notable diradical character with spin densities concentrated at the apical carbons of five-membered rings, in accordance with Clar sextet concept. The study also showed that the poly-IF maintains both the radical character and antiaromatic properties of individual IF unit. The existence of many spins in IF polymers suggest their suitability for carbon-based spintronic applications.[105]

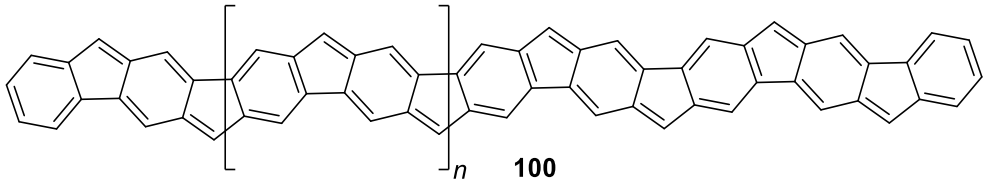

100

Figure 1.15 Example of fully fused IF polymer synthesized on-surface.

The IF polymers previously described are stepladder-type structures, with the doubly stranded IF units forming the ladder's crossbars, and single C-C bonds acting as the connecting steps. Preparation of ladder polymers, which involve connecting rings such that adjacent rings share two or more atoms,[106] offer several advantages but also present significant challenges. The lack of torsional movement around single bonds in ladder polymers contributes to their rigidity and coplanarity, leading to improved

mechanical and thermal stability and greater charge distribution.[107] These conjugated polymers could show promises for high charge transport properties,[108] longer exciton diffusion lengths,[109] and small energy gaps.[110] Müllen and Fasel reported the synthesis of fused polymer **100**[111] on a gold surface, achieved by stepwise aryl–aryl coupling of a terphenyl-type precursor followed by cyclization of the methyl groups. Electronic characterizations and theoretical calculations provided detailed insights, revealing its small band gap (0.8 eV) and anti-ferromagnetic character (Figure 1.15).

1.1.6 Applications of indenofluorenes

Fully conjugated π-IFs feature a unique π-topology among PHs, characterized by a quinoidal structure in the central indacene core. These antiaromatic molecules, featuring 20π-electrons, exhibit excellent electron-accepting properties. Due to their narrow HOMO–LUMO energy gap, IFs are particularly valuable as ambipolar semiconductors. Additionally, their performance in photovoltaic applications has also been investigated.

As previously mentioned, Haley's group enhanced the structural versatility of IFs by introducing various aryl groups at carbons 6 and 12 of [1,2-*b*]IF unit.[55] Unlike substitutions at carbons 2 and 8 in **30a-i**, the 6,12-functionalization in **31a-j** significantly influenced the low energy absorption, redox potentials, and HOMO–LUMO energies due to presence of larger orbital density at these non-bridgehead carbon atoms. The range of HOMO-LUMO energy gaps for IFs **31a-j** was between 1.82 and 2.17 eV. The value of LUMO energies for these compounds ranged from −3.56 eV to −4.00 eV, similar to the values commonly observed in high-performance *n*-type semiconductors used in field-effect transistors and electron acceptors in solar cells. In this work, micro-scale single crystals of **31h** were directly grown on a silicon wafer with surface treatment to create OFETs. As shown in Figure 1.16, the hole mobility for these scaffolds was 7×10^{-4} cm^2 V^{-1} s^{-1}, while the electron mobility was 3×10^{-3} cm^2 V^{-1} s^{-1}. This study showcased the first IF semiconductor active in OFETs and represents one of the few examples of an ambipolar OFET employing a single crystal.[112]

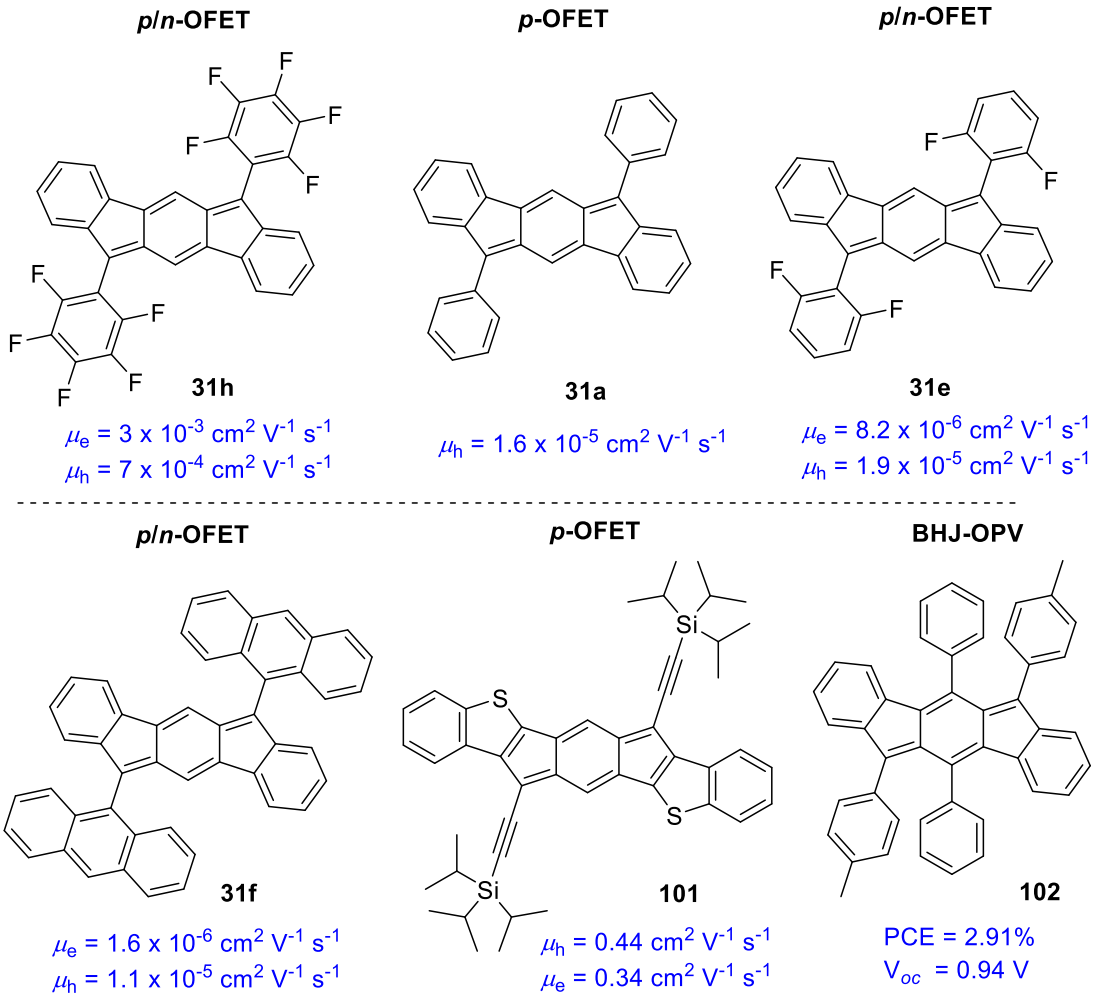

Figure 1.16 IF derivatives with device applications.

In the same year, Yamashita *et al.*[56] synthesized structurally similar [1,2-*b*]IFs (**31a**, **30e-f**), with various aryl substituents at the 6,12-carbon positions. DFT calculations and experimental results indicated that incorporating difluorophenyl or anthryl groups at these positions enhanced π-delocalization, resulting in narrower HOMO–LUMO energy gaps. Following the fabrication of the OFETs, devices **31e** and **31f** exhibited ambipolar semiconducting behavior, with electron/hole mobilities of 8.2 × 10^{-6} / 1.9 × 10^{-5} cm² V^{-1} s^{-1} and 1.6 × 10^{-6} / 1.1 × 10^{-5} cm² V^{-1} s^{-1}, respectively (Figure 1.16). In contrast, devices based on **31a** displayed exclusively *p*-type transport character, attaining a hole mobility of 1.6 × 10^{-5} cm² V^{-1} s^{-1} (Figure 1.16). The non-crystalline nature of the film microstructure may be responsible for the lower charge transport mobilities observed in these molecules.

In 2016, an efficient IF semiconductor **101** was reported by extending the [1,2-*b*]IF scaffold by introducing additional thiophene rings between indacene and outer benzenes along the long molecular axis (Figure 1.16).[113] The crystal structure of **101**

disclosed that it was arranged into slipped 1D stacking with π–π distances of 3.36 Å and significant molecular interaction. Following the fabrication of OFETs, **101** showed the highest hole mobility (0.44 $cm^2\ V^{-1}\ s^{-1}$) under standard conditions.[113a] Notably, in a report by Zhu and co-workers, charge carrier mobilities of up to 0.64 $cm^2\ V^{-1}\ s^{-1}$ for holes and 0.34 $cm^2\ V^{-1}\ s^{-1}$ for electrons were achieved for **101** under ambient conditions.[113b] In 2019, Haley and co-workers investigated the charge-transport properties of π-extended IFs and discovered that even subtle variations in the indacene framework resulted in significant changes in molecular packing, which in turn influenced the electrical properties. As a result, they achieved the highest charge-carrier mobilities, exceeding 7 $cm^2\ V^{-1}\ s^{-1}$.[114]

An example of a bulk heterojunction organic photovoltaic (BHJ-OPV) utilizing an indacene framework is [1,2-*b*]IF derivative **102**[115] (Figure 1.16). SCXRD analysis revealed that the peripheral aryl substitutions in **102** adopt highly twisted conformations relative to the IF core. This twisting disrupts the conjugation between the IF backbone and the terminal aryl groups, resulting in a blue shift in absorption relative to molecule **102**. The film of **102** showed a low ionization potential and a wide absorption range extending up to 700 nm, suggesting its suitability as an electron donor in solar cell applications. Moreover, this molecular design ensures strong photostability, but due to the limited solubility of molecule **102**, bulk heterojunctions devices were fabricated using vacuum deposition with $PC_{71}BM$ as the acceptor and these devices demonstrated a power conversion efficiency (PCE) of 2.91% and open-circuit voltage of 0.94 V. Similar [1,2-*b*]IF based structures have also been used in small molecule BHJs by Ostroverkhova and co-workers to quantify the properties of charge transfer states and their impact on photoconductive performance.[116]

These IF systems show great potential as *n*-type electron acceptors for field effect transistors and photovoltaics because of their low lying LUMO level, 20π-electron backbone, and the ease with which they can be functionalized. Although *p*-type organic semiconductors are readily accessible, advancing the development of *n*-type stable materials remains a major aim in organic electronics[117], since *n*-type organic semiconductors continue to pose challenges due to the inherent tendency of many materials to trap electrons, particularly at the semiconductor-dielectric interface.[118] Besides, core-expanded IFs are expected to exhibit energy levels that are well-suited for SF studies,[119] and the small HOMO/LUMO energy gap and diradical properties of some

IF scaffolds could make them ideal candidates for NIR absorption and applications in single-molecule conductance[120] and molecular spintronics.[121]

1.2 Thesis outline

This thesis is divided into five chapters: **Chapter 1** presents an introduction to five antiaromatic IF derivatives (non-alternant analogues of pentacenes), detailing their synthetic approach as well as π-extended derivatives with modifications to both the core and outer regions. In addition to the synthesis related challenges, (anti)aromaticity, diradical, and optoelectronic properties, this chapter explores the synthesis of IF oligomers/polymers, whether in solution or on-surfaces, and concludes with a discussion on the applications of IFs in organic electronics. In **Chapter 2** (Figure 1.17), which is divided in three sub-chapters (2A, 2B and 2C), I reported a mild synthetic approach to make [2,1-*c*]IF, the syntheses and properties of unsymmetrically disubstituted [2,1-*c*]IFs, and the synthesis and properties of curved *s*-indacenodifluorene (*s*-IDF) that absorbed in the near-IR region. In **Chapter 3** (Figure 1.17), a steric promoted synthesis approach was presented to make some symmetric and unsymmetric π-extended [1,2-*b*]IFs, including the only unsymmetrical [2,1-*a*]derivative known to date. **Chapter 4** (Figure 1.17) deals with the syntheses and properties of IF dimers, that showed smaller bandgaps when compared to Müllen's π-IF based polymer. Finally, in **Chapter 5** (Figure 1.17), the first synthesis and ground state electronic properties of an open-shell IF dimer will be discussed.

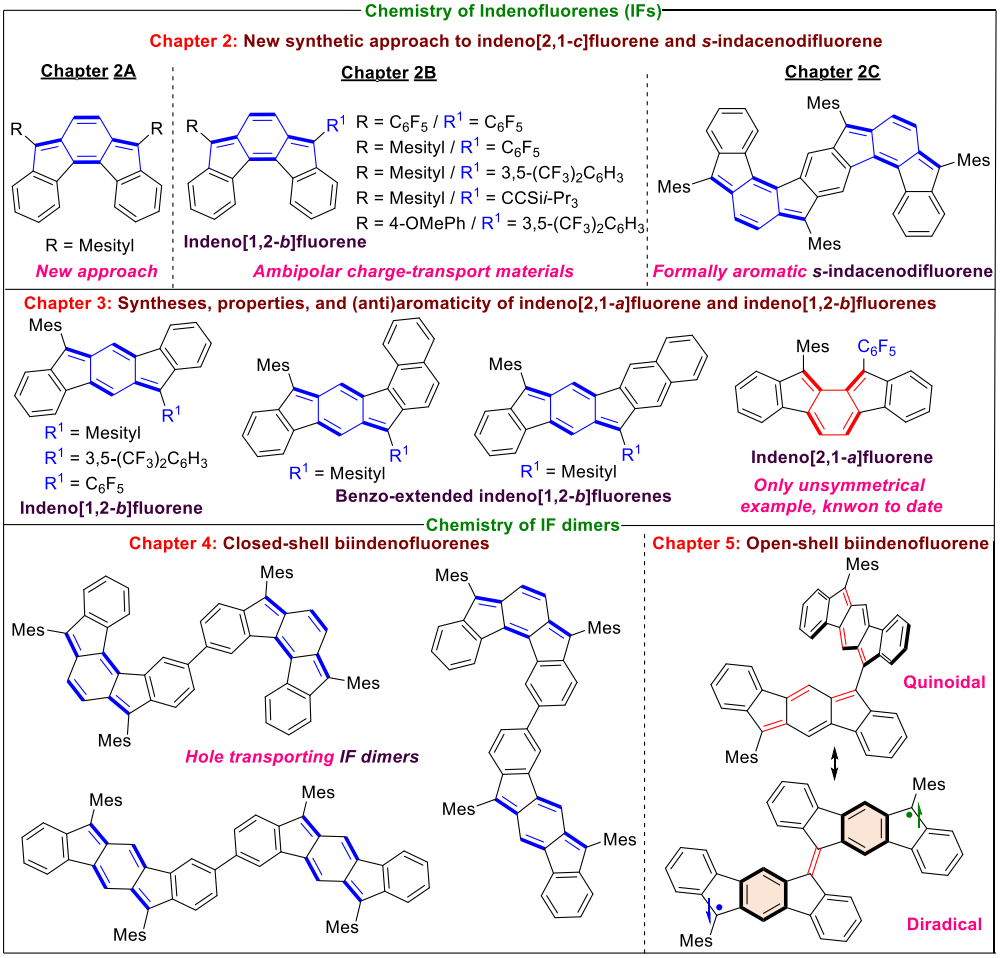

Figure 1.17 Structures of targeted compounds reported in this thesis.

The objective of this study is to synthesize and comprehensively investigate the effect of structural modifications on the electronic ground state properties of newer arrays of π-extended IFs using computational and various analytical approaches. All reported molecules exhibit interesting optoelectronic properties, making them potential candidates for application in organic optoelectronics.

1.3 References

1. A. McMahon, *Illuminating antiaromaticity*. Chemistry World. https://www.chemistryworld.com/features/illuminating-antiaromaticity/4019362.article (accessed on: November 10, 2024).

2. (*a*) R. G. Harvey, *Polycyclic Aromatic Hydrocarbons*, Wiley-VCH: New York, 1997; (*b*) E. Clar, *Polycyclic Hydrocarbons*, Academic Press: London, 1964.

3. S. A. Wise, R. M. Campbell, W. R. West, M. L. Lee and K. D. Bartle, *Chem. Commun.*, 1986, **54**, 339–351.

4. A. Stanger, *Chem. Commun.*, 2009, 1939–1947.

5. (*a*) T. J. J. Müller and U. H. F. Bunz, *Functional Organic Materials*, Wiley-VCH: Weinheim, 2007; (*b*) K. Müllen and U. Scherf, *Organic Light Emitting Devices: Synthesis, Properties, and Applications*, Wiley-VCH: Weinheim, 2006; (*c*) M. M. Haley and R. R. Tykwinski, *Carbon-Rich Compounds: From Molecules to Materials*, Wiley-VCH: Weinheim, 2006; (*d*) Q. Miao, *Polycyclic Arenes and Heteroarenes: Synthesis, Properties, and Applications*, John Wiley & Sons, 2015; (*e*) Y. Tobe and T. Kubo, *Physical Organic Chemistry of Quinodimethanes*, Springer, 2018; (*f*) J. Wu, *Diradicaloids*, Jenny Stanford Publishing, New York, 2022.

6. (*a*) J. E. Anthony, A. Facchetti, M. Heeney, S. R. Marder and X. Zhan, *Adv. Mater.*, 2010, **22**, 3876–3891; (*b*) M. Bendikov, F. Wudl and D. F. Perepichka, *Chem. Rev.*, 2004, **104**, 4891–4946; (*c*) H. Jiang and W. Hu, *Angew. Chem., Int. Ed.*, 2020, **59**, 1408–1428; (*d*) H. Dong, X. Fu, J. Liu, Z. Wang and W. Hu, *Adv. Mater.*, 2013, **25**, 6158–6183; (*e*) G. Hong, X. Gan, C. Leonhardt, Z. Zhang, J. Seibert, J. M. Busch and S. Brase, *Adv. Mater.*, 2021, **33**, e2005630; (*f*) Z. G. Zhang and Y. Li, *Angew. Chem., Int. Ed.*, 2021, **60**, 4422–4433; (*g*) C. Wang, H. Dong, W. Hu, Y. Liu and D. Zhu, *Chem. Rev.*, 2012, **112**, 2208–2267;(*h*) Q. Li, Y. Zhang, Z. Xie, Y. Zhen, W. Hud and H. Dong, *J. Mater. Chem. C*, 2022, **10**, 2411-2430.

7. (*a*) J. E. Anthony, *Chem. Rev.*, 2006, **106**, 5028–5048; (*b*) J. E. Anthony, *Angew. Chem. Int. Ed.*, 2008, **47**, 452–456; (*c*) C. Tönshoff and H. F. Bettinger, *Chem. Eur. J.* 2021, **27**, 3193; (*d*) W. Chen, F. Yu, Q. Xu, G. Zhou and Q. Zhang, *Adv. Sci.* 2020, **7**, 1903766.

8. W. Zeng and J. Wu, *Chem*, 2021, **7**, 358–386.

9. J. L. Marshall, D. Lehnherr, B. D. Lindner and R. R. Tykwinski, *ChemPlusChem*, 2017, **82**, 967.

10. (*a*) R. Pino-Rios, R. Báez-Grez and Miquel Solà, *Phys. Chem. Chem. Phys.*, 2021, **23**, 13574–13582; (*b*) M. Bendikov, H. M. Duong, K. Starkey, K. N. Houk, E. A. Carter and F. Wudl, *J. Am. Chem. Soc.* 2004, **126**, 7416–7417; (*c*) C. Tçnshoff and H. F. Bettinger, *Chem. Eur. J.* 2021, **27**, 3193–3212; (*d*) W. Chen, F. Yu, Q. Xu, G. Zhou and Q. Zhang, *Adv. Sci.* 2020, **7**, 1903766; (*e*) Y. Guo, C. Chen and X.-Y. Wang, *Chin. J. Chem.* 2023, **41**, 1355–1373.

11. (*a*) D. Bhattacharya, A. Panda, A. Misra, D. J. Klein, *J. Phys. Chem. A*, 2014, **118**, 4325; (*b*) M. Solà, *Front. Chem.*, 2013, **1**, 1.

12. (*a*) M. Bendikov, F. Wudl and D. F. Perepichka, *Chem. Rev.*, 2004, **104**, 4891–4946; (*b*) K. J. Thorley and J. E. Anthony, *Isr. J. Chem.*, 2014, **54**, 642–655; (*c*) F. Ortmann,

K. S. Radke, A. Genther, D. Kasemann, K. Leo and G. Cuniberti, *Adv. Funct. Mater.*, 2015, **25**, 1933–1940.

13. J. Shi and C. W. Tang, *Appl. Phys. Lett.*, 2002, **80**, 3201–3203.

14. J. Takeya, M. Yamagishi, Y. Tominari, R. Hirahara, Y. Nakazawa, T. Nishikawa, T. Kawase, T. Shimoda and S. Ogawa, *Appl. Phys. Lett.*, 2007, **90**, 102120.

15. (*a*) E. Clar, *Polycyclic Hydrocarbons*, Academic Press, London, 1964; (*b*) R. G. Harvey, *Polycyclic Aromatic Hydrocarbons*, Wiley-VCH, New York, 1997; (*c*) Z. Sun, S. Lee, K. H. Park, X. Zhu, W. Zhang, B. Zheng, P. Hu, Z. Zeng, S. Das, Y. Li, C. Chi, R. Li, K. Huang, J. Ding, D. Kim and J. Wu, *J. Am. Chem. Soc.*, 2013, **135**, 18229–18236.

16. (*a*) W. Fudickar and T. Linker, *J. Am. Chem. Soc.*, 2012, **134**, 15071–15074; (*b*) R. Mondal, R. M. Adhikari, B. K. Shah and D. C. Neckers, *Org. Lett.*, 2007, **9**, 2505–2508.

17. M. M. Payne, S. R. Parkin and J. E. Anthony, *J. Am. Chem. Soc.*, 2005, **127**, 8028–8029.

18. (*a*) I. Kaur, M. Jazdzyk, N. N. Stein, P. Prusevich and G. P. Miller, *J. Am. Chem. Soc.*, 2010, **132**, 1261–1271; (*b*) B. Purushothaman, M. Bruzek, S. R. Parkin, A. F. Miller and J. E. Anthony, *Angew. Chem., Int. Ed.*, 2011, **50**, 7013–7017.

19. (*a*) Y. Xiao, J. T. Mague, R. H. Schmehl, F. M. Haque and R. A. Pascal, Jr., *Angew. Chem., Int. Ed.*, 2019, **58**, 2831–2835; (*b*) J. Xiao, H. M. Duong, Y. Liu, W. Shi, L. Ji, G. Li, S. Li, X. W. Liu, J. Ma, F. Wudl and Q. Zhang, *Angew. Chem., Int. Ed.*, 2012, **51**, 6094–6098; (*c*) M. Müller, S. Maier, O. Tverskoy, F. Rominger, J. Freudenberg and U. H. F. Bunz, *Angew. Chem., Int. Ed.*, 2020, **59**, 1966–1970; (*d*) M. Müller, L. Ahrens, V. Brosius, J. Freudenberg and U. H. F. Bunz, *J. Mater. Chem. C*, 2019, **7**, 14011–14020.

20. (*a*) R. Mondal, B. K. Shah and D. C. Neckers, *J. Am. Chem. Soc.*, 2006, **128**, 9612–9618; (*b*) J. Kruger, F. Garcia, F. Eisenhut, D. Skidin, J. M. Alonso, E. Guitian, D. Perez, G. Cuniberti, F. Moresco and D. Pena, *Angew. Chem., Int. Ed.*, 2017, **56**, 11945–11949.

21. (*a*) G. P. Miller, J. Mack and J. Briggs, *Org. Lett.*, 2000, **2**, 3983–3986; (*b*) J. E. Anthony, J. S. Brooks, D. L. Eaton and S. R. Parkin, *J. Am. Chem. Soc.*, 2001, **123**, 9482–9489.

22. (*a*) N. V. Korovina, N. F. Pompetti and J. C. Johnson, *J. Chem. Phys.*, 2020, **152**, 040904; (*b*) C. Hetzer, D. M. Guldi and R. R. Tykwinski, *Chem. Eur. J.*, 2018, **24**, 8245–8254; (*c*) R. R. Tykwinski, *Acc. Chem. Res.*, 2019, **52**, 2056–2067.

23. (*a*) R. Mondal, R. M. Adhikari, B. K. Shah and D. C. Neckers, *Org. Lett.*, 2007, **9**, 2505–2508; (*b*) E. Clar, *Ber. Dtsch. Chem. Ges.*, 1939, **72B**, 1817–1821; (*c*) C.

Marschalk, *Bull. Soc. Chim. Fr.*, 1939, **6**, 1112–1118; (*d*) E. Clar, *Ber. Dtsch. Chem. Ges.* B, 1942, **75B**, 1283–1288; (*e*) W. J. Bailey and C.-W. Liao, *J. Am. Chem. Soc.*, 1955, **77**, 992–996; (*f*) K. F. Lang and M. Zander, *Chem. Ber.*, 1963, **96**, 707–714; (*g*) M. P. Satchell and B. E. Stacey, *J. Chem. Soc. C*, 1971, 468–472; (*h*) M. Watanabe, Y. J. Chang, S.-W. Liu, T.-H. Chao, K. Goto, M. Minarul Islam, C.-H. Yuan, Y.-T. Tao, T. Shinmyozu and T. J. Chow, *Nat. Chem.*, 2012, **4**, 574–580.

24. (*a*) I. Kaur, N. N. Stein, R. P. Kopreski and G. P. Miller *J. Am. Chem. Soc.*, 2009, **131**, 3424-3425; (*b*) S. S. Zade and M. Bendikov, *Angew. Chem., Int. Ed.*, 2010, **49**, 4012–4015.

25. C. Tönshoff and H. F. Bettinger, *Angew. Chem., Int. Ed.*, 2010, **49**, 4125–4128.

26. B. Shen, J. Tatchen, E. Sanchez-Garcia and H. F. Bettinger, *Angew. Chem., Int. Ed.*, 2018, **57**, 10506–10509; *Angew. Chem.*, 2018, **130**, 10666–10669.

27. R. Zuzak, R. Dorel, M. Kolmer, M. Szymonski, S. Godlewski and A. M. Echavarren, *Angew. Chem., Int. Ed.*, 2018, **57**, 10500–10504; *Angew. Chem.*, 2018, **130**, 10660–10664.

28. F. Eisenhut, T. Kehne, F. Garcia, S. Fernández, E. Guitián, D. Pérez, G. Trinquier, G. Cuniberti, C. Joachim, D. Peña and F. Moresco, *ACS Nano*, 2020, **14**, 1011–1020.

29. (*a*) O. D. Jurchescu, J. Baas and T. T. M. Palstra, *Appl. Phys. Lett.*, 2004, **84**, 3061–3063; (*b*) S. K. Park, T. N. Jackson, J. E. Anthony and D. A. Mourey, *Appl. Phys. Lett.*, 2007, **91**, 063514; (*c*) M. B. Smith and J. Michl, *Chem. Rev.*, 2010, **110**, 6891–6936.

30. S. S. Zade and M. Bendikov, *J. Phys. Org. Chem.*, 2012, **25**, 452–461.

31. (*a*) Y. Tobe, *Chem. Rec.* 2015, **15**, 86; (*b*) G. E. Rudebusch and M. M. Haley, *Polycyclic arenes and heteroarenes: synthesis, properties, and applications.* Wiley-VCH, 2015, 37; (*c*) C. K. Frederickson, B. D. Rose and M. M. Haley, *Acc. Chem. Res.* 2017, **50**, 977.

32. (*a*) D. Marsitzky, J. C. Scott, J.-P. Chen, V. Y. Lee, R. D. Miller, S. Setayesh and K. Müllen, *Adv. Mater.*, 2001, **13**, 1096–1099; (*b*) A. C. Grimsdale, P. Leclère, R. Lazzaroni, J. D. MacKenzie, C. Murphy, S. Setayesh, C. Silva, R. H. Friend and K. Müllen, *Adv. Funct. Mater.*, 2002, **12**, 729–733; (*c*) J. Jacob, J. Zhang, A. C. Grimsdale, K. Müllen, M. Gaal and E. J.-W. List, *Macromolecules*, 2003, **36**, 8240–8245; (*d*) C. Poriel and J. Rault-Berthelot, *Acc. Chem. Res.* 2018, **51**, 1818; (*e*) S. Bebiche, P. A. Cisneros-Perez, T. Mohammed-Brahim, M. Harnois, J. Rault-Berthelot, C. Poriel and E. Jacques, *Mater. Chem. Front.*, 2018, **2**, 1631; (*f*) M. Romain, M. Chevrier, S. Bebiche, T. Mohammed-Brahim, J. Rault-Berthelot, E.

Jacques and C. Poriel, *J. Mater. Chem. C,* 2015, **3**, 5742. (*g*) M. Romain, C. Quinton, D. Tondelier, B. Geffroy, O. Jeannin, J. Rault-Berthelot and C. Poriel, *J. Mater. Chem. C,* 2016, **4**, 1692; (*h*) M. Romain, D. Tondelier, B. Geffroy, O. Jeannin, E. Jacques, J. Rault-Berthelot and C. Poriel, *Chem. Eur. J.* 2015, **21**, 9426; (*i*) D. Thirion, M. Romain, J. Rault-Berthelot and C. Poriel, *Mater. Adv.,* 2021, **2**, 1271.

33. Y. Ie, Y. Umemoto, M. Nitani and Y. Aso, *Appl. Chem.*, 2008, **80**, 589–597.

34. (*a*) K. Hafner and H. U. Süss, *Angew. Chem., Int. Ed.*, 1973, **12**, 575–576; (*b*) T. Bally, S. Chai, M. Neuenschwander and Z. Zhu, *J. Am. Chem. Soc.*, 1997, **119**, 1869–1870.

35. (a) D. Peters, *J. Chem. Soc.*, 1958, 1028–1030; (*b*) D. Peters, *J. Chem. Soc.*, 1958, 1039–1043.

36. (*a*) D. Ginsburg, *Non-Benzenoid Aromatic Compounds*; Interscience Publishers: New York, 1959; (*b*) D. Lloyd, *Non-Benzenoid Conjugated Carbocyclic Compounds*; Elsevier: Amsterdam, 1984; (*c*) K. Hafner, K. H. Häfner, C. König, M. Kreuder, G. Ploss, G. Schulz, E. Sturm and K. H. Vöpel, *Angew. Chem., Int. Ed.*, 1963, **2**, 123–126; (*d*) K. Hafner, *Angew. Chem., Int. Ed.*, 1964, **3**, 165–166; (*e*) K. Hafner, *Pure Appl. Chem.*, 1971, **28**, 153–168; (*f*) T. Nozoe, *Topics in Nonbenzenoid Aromatic Chemistry*, **Vols. 1 and 2**; Wiley: 1974. (*g*) Y. Tobe, *Top. Curr. Chem. (Z)*, 2018, **376**, 12.

37. (*a*) K. Hafner, B. Stowasser, H. P. Krimmer, S. Fischer, M. C. Böhm and H. J. Lindner, *Angew. Chem., Int. Ed.*, 1986, **25**, 630–632; (*b*) J. D. Dunitz, C. Krüger, H. Irngartinger, E. F. Maverick, Y. Wang and M. Nixdorf, *Angew. Chem., Int. Ed.*, 1988, **27**, 387–389.

38. H. Prinzbach and L. Knothe, *Pure Appl. Chem.*, 1986, **58**, 25–37.

39. (*a*) K. Brand, *Ber. Dtsch. Chem. Ges.*, 1912, **45**, 3071–3077; (*b*) C. T. Blood, and R. P. Linstead, *J. Chem. Soc.*, 1952, 2263–2270; (*c*) W. C. Lothrop, *J. Am. Chem. Soc.*, 1941, **63**, 1187–1191.

40. A. G. Fix, *Synthesis and Properties of Indenofluorene and Diindenothiophene Derivatives for Use as Semiconducting Materials in Organic Electronic Devices*, PhD Thesis, University of Oregon, 2013.

41. (*a*) Z. Zeng, X. Shi, C. Chi, J. T. L. Navarrete, J. Casado and J. Wu, *Chem. Soc. Rev.*, 2015, **44**, 6578–6596; (*b*) T. Krygowski, M. Cyranski, Z. Czarnocki, G. Häfelinger and A. R. Katritzky, *Tetrahedron*, 2000, **56**, 1783–1796; (*c*) M. Randić, *Chem. Rev.*, 2003, **103**, 3449–3606; (*d*) Z. Sun and J. Wu, *J. Mater. Chem.*, 2012, **22**, 4151–4160; (*e*) Z.

Sun, Q. Ye, C. Chi and J. Wu, *Chem. Soc. Rev.*, 2012, **41**, 7857–7889; (*f*) T. Y. Gopalakrishna, W. Zeng, X. Lu and J. Wu, *Chem. Commun.*, 2018, **54**, 2186–2199; (*g*) X. Hu, W. Wang, D. Wang and Y. Zheng, *J. Mater. Chem. C*, 2018, **6**, 11232–11242; (*h*) Z. Sun, Z. Zeng and J. Wu, *Chem. Asian J.*, 2013, **8**, 2894–2904; (*i*) Q. Ye and C. Chi, *Chem. Mater.*, 2014, **26**, 4046–4056; (*j*) Z. Sun, Z. Zeng and J. Wu, *Acc. Chem. Res.*, 2014, **47**, 2582–2591; (*k*) P. Hu and J. Wu, *Can. J. Chem.*, 2017, **95**, 223–233; (*l*) J. Liu and X. Feng, *Angew. Chem. Int. Ed.*, 2020, **59**, 23386–23401; (*m*) J. Su, M. Telychko, S. Song and J. Lu, *Angew. Chem. Int. Ed.*, 2020, **59**, 7658–7668; (*n*) Y.-T. Wu and J. S. Siegel, *Chem. Rev.*, 2006, **106**, 4843–4867; (*o*) V. M. Tsefrikas and L. T. Scott, *Chem. Rev.*, 2006, **106**, 4868–4884; (*p*) Y. Tobe, T. Kubo, Eds. *Physical Organic Chemistry of Quinodimethanes*; Springer: 2018.

42. J. J. Dressler, Z. Zhou, J. L. Marshall, R. Kishi, S. Takamuku, Z. Wei, S. N. Spisak, M. Nakano, M. A. Petrukhina and M. M. Haley, *Angew. Chem. Int. Ed.*, 2017, **56**, 15363.

43. K. Fukuda, T. Nagami, J. Fujiyoshi and M. Nakano, *J. Phys. Chem. A*, 2015, **119**, 10620–10627.

44. G. George, A. J. Stasyuk and M. Solà, *Chem. Sci.* 2024, **15**, 13676–13687.

45. S. Gabriel, *Ber. Dtsch. Chem. Ges.*, 1884, **17**, 1389–1393.

46. (*a*) G. Errera, *Gazz. Chim. Ital.*, 1907, **37** (II), 624–630; (*b*) G. Errera, *Gazz. Chim. Ital.*, 1908, **38**, 588–594; (*c*) G. Errera and G. Vaccarino, *Gazz. Chim. Ital.*, 1909, **39**, 1–10; (*d*) D. Marotta, *Gazz. Chim. Ital.*, 1911, **41**, 59–65; (*e*) D. Radulescu and V. Georgescu, *Bull. Soc. Chim. Fr.*, 1925, **37**, 1187–1190; (*f*) F. Strauss, R. Kühnel and R. Hansel, *Ber. Dtsch. Chem. Ges.*, 1933, **66**, 1847–1854; (*g*) C. Weizmann, E. Bergmann and L. Haskelberg, *J. Chem. Soc.*, 1939, 391–395; (*h*) D. Radulescu and M. Alexa, *Chem. Zentralbl.*, 1943, **I**, 622–624.

47. (*a*) W. Deuschel, *Helv. Chim. Acta*, 1951, **35**, 168–174; (b) W. Deuschel, *Helv. Chim. Acta*, 1951, **35**, 2403–2410.

48. L. Chardonnens and R. Ritter, *Helv. Chim. Acta*, 1955, **38**, 393–396.

49. Q. Zhou, P. J. Carroll and T. M. Swager, *J. Org. Chem.*, 1994, **59**, 1294–1301

50. H. Reisch, U. Wiesler, U. Scherf and N. Tuytuylkov, *Macromolecules*, 1996, **29**, 8204–8210.

51. A. Le Berre, *Ann. Chim.*, 1957, **13**, 371–379.

52. D. T. Chase, B. D. Rose, S. P. McClintock, L. N. Zakharov and M. M. Haley, *Angew. Chem., Int. Ed.*, 2011, **50**, 1127–1130.

53. D. T. Chase, A. G. Fix, B. D. Rose, C. D. Weber, S. Nobusue, C. E. Stockwell, L. N. Zakharov, M. C. Lonergan and M. M. Haley, *Angew. Chem., Int. Ed.*, 2011, **50**, 11103–11106.

54. K. Paudel, B. Johnson, M. Thieme, M. M. Haley, M. M. Payne, M. Marcia, J. E. Anthony and O. Ostroverkhova, *Appl. Phys. Lett.*, 2014, **105**, 043301.

55. D. T. Chase, A. G. Fix, S. J. Kang, B. D. Rose, C. D. Weber, Y. Zhong, L. N. Zakharov, M. C. Lonergan, C. Nuckolls and M. M. Haley, *J. Am. Chem. Soc.*, 2012, **134**, 10349–10352.

56. J.-I. Nishida, S. Tsukaguchi and Y. Yamashita, *Chem. Eur. J.*, 2012, **18**, 8964–8970.

57. A. Shimizu and Y. Tobe, *Angew. Chem., Int. Ed.*, 2011, **50**, 6906–6910.

58. A. Shimizu, R. Kishi, M. Nakano, D. Shiomi, K. Sato, T. Takui, I. Hisaki, M. Miyata and Y. Tobe, *Angew. Chem., Int. Ed.*, 2013, **52**, 6076–6079.

59. (*a*) J. Fabian, H. Nakazumi and M. Matsuoka, *Chem. Rev.*, 1992, **92**, 1197–1226; (*b*) V. J. Pansare, S. Hejazi, W. J. Faenza and R. K. Prud'homme, *Chem. Mater.*, 2012, **24**, 812–827.

60. A. G. Fix, P. E. Deal, C. L. Vonnegut, B. D. Rose, L. N. Zakharov and M. M. Haley, *Org. Lett.*, 2013, **15**, 1362–1365.

61. S. Herzog, A. Hinz, F. Breher and J. Podlech, *Org. Biomol. Chem.*, 2022, **20**, 2873–2880.

62. S. Mishra, M. Vilas-Varela, L.-A. Lieske, R. Ortiz, S. Fatayer, I. Rončević, F. Albrecht, T. Frederiksen, D. Peña and L. Gross, *Nature Chem.*, 2024, **16**, 755-761.

63. G. E. Rudebusch, J. L. Zafra, K. Jorner, K. Fukuda, J. L. Marshall, I. Arrechea-Marcos, G. L. Espejo, R. Ponce Ortiz, C. J. Gómez-García, L. N. Zakharov, M. Nakano, H. Ottosson, J. Casado and M. M. Haley, *Nat. Chem.*, 2016, **8**, 753–759.

64. (*a*) J. J. Dressler and M. M. Haley, *J. Phys. Org. Chem.*, 2020, **33**, e4114; (*b*) W. Zeng and J. Wu, *Chem.*, 2021, **7**, 358; (*c*) Y. Tobe, *Top. Curr. Chem.*, 2018, **376**, 12.

65. B. D. Rose, C. L. Vonnegut, L. N. Zakharov and M. M. Haley, *Org. Lett.*, 2012, **14**, 2426–2429.

66. H. Miyoshi, M. Miki, S. Hirano, A. Shimizu, R. Kishi, K. Fukuda, D. Shiomi, K. Sato, T. Takui, I. Hisaki, M. Nakano and Y. Tobe, *J. Org. Chem.*, 2017, **82**, 1380.

67. J. E. Barker, C. K. Frederickson, M. H. Jones, L. N. Zakharov and M. M. Haley, *Org. Lett.*, 2017, **19**, 5312.

68. H. Hayashi, J. E. Barker, A. C. Valdivia, R. Kishi, S. N. MacMillan, C. J. Gómez-García, H. Miyauchi, Y. Nakamura, M. Nakano, S. Kato, M. M. Haley and J. Casado, *J. Am. Chem. Soc.*, 2020, **142**, 20444–20455.

69. A. S. Hacker, M. Pavano, J. E. Wood, H. Hashimoto, K. M. D'Ambrosio, C. K. Frederickson, J. L. Zafra, C. J. Gómez-García, V. Postils, A. Ringer McDonald, D. Casanova, D. K. Frantz and J. Casado, *Chem. Commun.*, 2019, **55**, 14186.

70. H. Miyoshi, S. Nobusue, A. Shimizu, I. Hisaki, M. Miyata and Y. Tobe, *Chem. Sci.*, 2014, **5**, 163–168.

71. (*a*) M. A. Majewski, P. J. Chmielewski, A. Chien, Y. Hong, T. Lis, M. Witwicki, D. Kim, P. M. Zimmerman and M. Stępień, *Chem. Sci.*, 2019, **10**, 3413; (*b*) B. Prajapati, D. Dang, P. J. Chmielewski, M. A. Majewski, T. Lis, C. J. Gómez-García, P. M. Zimmerman and M. Stępień, *Angew. Chem., Int. Ed.*, 2021, **60**, 22496.

72. K. Nakasuji and T. Kubo, *Bull. Chem. Soc. Jpn.*, 2004, **77**, 1791–1801.

73. (*a*) I. Murata, S. Sasaki, K. U. Klabunde, J. Toyoda and K. Nakasuji, *Angew. Chem., Int. Ed. Engl.*, 1991, **30**, 172–173; (*b*) K. Ohashi, T. Kubo, T. Masui, K. Yamamoto, K. Nakasuji, T. Takui, Y. Kai and I. Murata, *J. Am. Chem. Soc.*, 1998, **120**, 2018–2027.

74. T. Kubo, A. Shimizu, M. Uruichi, K. Yakushi, M. Nakano, D. Shiomi, K. Sato, T. Takui, Y. Morita and K. Nakasuji, *Org. Lett.*, 2007, **9**, 81–84.

75. A. Shimizu, Y. Hirao, K. Matsumoto, H. Kurata, T. Kubo, M. Uruichi and K. Yakushi, *Chem. Commun.*, 2012, **48**, 5629.

76. S. Nobusue, H. Miyoshi, A. Shimizu, I. Hisaki, K. Fukuda, M. Nakano and Y. Tobe, *Angew. Chem., Int. Ed.*, 2015, **54**, 2090–2094.

77. T. Maekawa, H. Ueno, Y. Segawa, M. M. Haley and K. Itami, *Chem. Sci.*, 2016, **7**, 650-654.

78. P. Hu, S. Lee, T. S. Herng, N. Aratani, T. P. Gonçalves, Q. Qi, X. Shi, H. Yamada, K.-W. Huang, J. Ding, D. Kim and J. Wu, *J. Am. Chem. Soc.*, 2016, **138**, 1065-1077.

79. (*a*) R. W. A. Havenith, J. J. Engelberts, P. W. Fowler, E. Steiner, J. H. Van Lenthe and P. Lazzeretti, *Phys. Chem. Chem. Phys.*, 2004, **6**, 289–294; (*b*) I. García Cuesta, S. Coriani, P. Lazzeretti and A. M. Sánchez De Merás, *J. ChemPhysChem*, 2006, **7**, 240–244; (*c*) M. Makino and J. Aihara, *Phys. Chem. Chem. Phys.*, 2008, **10**, 591–599; (*d*) S. Motomura, M. Nakano, H. Fukui, K. Yoneda, T. Kubo, R. Carion and B. Champagne, *Phys. Chem. Chem. Phys.*, 2011, **13**, 20575; (*e*) T. Nagami, J. Fujiyoshi, T. Tonami, K. Watanabe, M. Yamane, K. Okada, R. Kishi, M. Nakano, B. Champagne and V. Liégeois, *Chem. Eur. J.*, 2018, **24**, 13457–13466.

80. J. E. Barker, T. W. Price, L. J. Karas, R. Kishi, S. N. MacMillan, L. N. Zakharov, C. J. Gómez-García, J. I. Wu, M. Nakano and M. M. Haley, *Angew. Chem. Int. Ed.*, 2021, **60**, 22385–22392.

81. (*a*) B. S. Young, D. T. Chase, J. L. Marshall, C. L. risko, L. N. Zakharov and M. M. Haley, *Chem. Sci.*, 2014, **5**, 1008–1014; (*b*) J. L. Marshall, G. E. Rudebusch, C. L. Vonnegut, L. N. Zakharov and M. M. Haley, *Tetrahedron Lett.*, 2015, **56**, 3235–3239; (*c*) J. L. Marshall, K. Uchida, C. K. Frederickson, C. Schütt, A. M. Zeidell, K. P. Goetz, T. W. Finn, K. Jarolimek, L. N. Zakharov, C. Risko, R. Herges, O. D. Jurchescu and M. M. Haley, *Chem. Sci.*, 2016, **7**, 5547–5558.

82. C. K. Frederickson, L. N. Zakharov and M. M. Haley, *J. Am. Chem. Soc.*, 2016, **138**, 16827–16838.

83. C. Frederickson, J. Barker, J. Dressler, Z. Zhou, E. Hanks, J. Bard, L. Zakharov, M. Petrukhina and M. M. Haley, *Synlett*, 2018, **29**, 2562–2566.

84. B. D. Rose, L. E. Shoer, M. R. Wasielewski and M. M. Haley, *Chem. Phys. Lett.*, 2014, **616**–**617**, 137–141.

85. J. J. Dressler, J. E. Barker, L. J. Karas, H. E. Hashimoto, R. Kishi, L. N. Zakharov, S. N. MacMillan, C. J. Gómez-García, M. Nakano, J. I. Wu and M. M. Haley, *J. Org. Chem.*, 2020, **85**, 10846–10857.

86. (*a*) G. I. Warren, J. E. Barker, L. N. Zakharov and M. M. Haley, *Org. Lett.*, 2021, **23**, 5012–5017; (*b*) G. I. Warren, L. J. Zocchi, L. N. Zakharov and M. M. Haley, *Chem. Eur. J.*, 2023, e202301153.

87. (*a*) H. K. Saha, D. Mallick and S. Das, *J. Org. Chem.*, 2023, **88**, 16248–16258; (*b*) H. K. Saha, D. Mallick and S. Das, *Chem. Commun.*, 2022, **58**, 8492–8495.

88. J. Melidonie, J. Liu, Y. Fu, J. J. Weigand, R. Berger and X. Feng, *J. Org. Chem.* 2018, **83**, 6633–6639.

89. T. Jousselin-Oba, P. E. Deal, A. G. Fix, C. K. Frederickson, C. L. Vonnegut, A. Yassar, L. N. Zakharov, M. Frigoli and M. M. Haley, *Chem. Asian J.*, 2019, **14**, 1737.

90. J. Melidonie, E. Dmitrieva, K. Zhang, Y. Fu, A. A. Popov, W. Pisula, R. Berger, J. Liu and X. Feng, *J. Org. Chem.* 2020, **85**, 215–223.

91. P. K. Sharma, P. Jana, S. Bandyopadhyay and S. Das, *Chem. Commun.*, 2024, **60**, 7319–7322.

92. (*a*) Y. Shen and C.-F. Chen, *Chem. Rev.*, 2012, **112**, 1463–1535; (*b*) M. Gingras, *Chem. Soc. Rev.*, 2013, **42**, 968–1006; (*c*) M. Gingras, G. Félix and R. Peresutti, *Chem.*

Soc. Rev., 2013, **42**, 1007–1050; (*d*) M. Gingras, *Chem. Soc. Rev.*, 2013, **42**, 1051–1095; (*e*) M. Rickhaus, M. Mayor and M. Juríček, *Chem. Soc. Rev.*, 2016, **45**, 1542–1556.

93. (*a*) C.-K. Lim, M. J. Cho, A. Singh, Q. Li, W. J. Kim, H. S. Jee, K. L. Fillman, S. H. Carpenter, M. L. Neidig, A. Baev, M. T. Swihart and P. N. Prasad, *Nano Lett.*, 2016, **16**, 5451–5455; (*b*) P. Wang, I. Jeon, Z. Lin, M. D. Peeks, S. Savagatrup, S. E. Kooi, T. Van Voorhis and T. M. Swager, *J. Am. Chem. Soc.*, 2018, **140**, 6501–6508; (*c*) G. L. J. A. Rikken and E. Raupach, *Nature*,1997, **390**, 493–494; (*d*) Y. Kitagawa, H. Segawa and K. Ishii, *Angew. Chem., Int. Ed.*, 2011, **50**, 9133–9136; *Angew. Chem.*, 2011, **123**, 9299–9302.

94. Q. Jiang, Y. Han, Y. Zou, H. Phan, L. Yuan, T. S. Herng, J. Ding and C. Chi, *Chem. Eur. J.*, 2020, **26**, 15613–15622.

95. X. Yang, D. Zhang, Y. Liao and D. Zhao, *J. Org. Chem.*, 2020, **85**, 5761–5770.

96. A. Borissov, P. J. Chmielewski, C. J. Gómez García, T. Lis and M. Stępień, *Angew. Chem., Int. Ed.*, 2023, **62**, e202309238.

97. Á. Martínez-Pinel, L. Lezama, J. M. Cuerva, R. Casares, V. Blanco, C. M. Cruz and A. Millán, *Org. Lett.*, 2024, **26**, 6012–6017.

98. E. Sidler, R. Hein, D. Doellerer and B. L. Feringa, *J. Am. Chem. Soc.*, 2024, **146**, 19168–19176.

99. (*a*) U. Scherf and K. Müllen, *Makromol. Chem., Rapid Commun.*, 1991, **12**, 489; (*b*) U. Scherf and K. Müllen, *Polymer*, 1992, **33**, 2443.

100. U. Scherf, *J. Mater. Chem.*, 1999, **9**, 1853.

101. (*a*) S. Setayesh, D. Marsitzky and K. Müllen, *Macromolecules*, 2000, **33**, 2016; (*b*) J. Jacob, J. Zhang, A. C. Grimsdale, K. Müllen, M. Gaal and E. J. W. List, *Macromolecules*, 2003, **36**, 8240; (*c*) J. Jacob, S. Sax, T. Piok, E. J. W. List, A. C. Grimsdale and K. Müllen, *J. Am. Chem. Soc.*, 2004, **126**, 6987; (*d*) A. C. Grimsdale, P. Leclère, R. Lazzaroni, J. D. MacKenzie, C. Murphy, S. Setayesh, C. Silva, R. H. Friend and K. Müllen, *Adv. Funct. Mater.*, 2002, **12**, 729.

102. M. Samoc, A. Samoc, B. Luther-Davies, H. Reisch and U. Scherf, *Opt. Lett.*, 1998, **23**, 1295.

103. J. L. Marshall, N. J. O'Neal, L. N. Zakharov and M. M. Haley, *J. Org. Chem.*, 2016, 81, 3674−3680.

104. (*a*) M. Di Giovannantonio, K. Eimre, A. V. Yakutovich, Q. Chen, S. Mishra, J. I. Urgel, C. A. Pignedoli, P. Ruffieux, K. Müllen, A. Narita and R. Fasel, *J. Am. Chem. Soc.*, 2019, **141**, 12346–12354; (*b*) M. Di Giovannantonio, J. I. Urgel, U. Beser, A. V.

Yakutovich, J. Wilhelm, C. A. Pignedoli, P. Ruffieux, A. Narita, K. Müllen and R. Fasel, *J. Am. Chem. Soc.*, 2018, **140**, 3532–3536.

105. M. Di Giovannantonio and R. Fasel, *J. Polym. Sci.*, 2022, **60**, 1814.

106. ***Compendium of Polymer Terminology and Nomenclature**, 2009.*

107. (*a*) C. Zhu, A. J. Kalin and L. Fang, *Acc. Chem. Res.*, 2019, **52**, 1089; (*b*) J. Lee, A. J. Kalin, T. Yuan, M. Al-Hashimi and L. Fang, *Chem. Sci.*, 2017, **8**, 2503.

108. (*a*) P. Prins, F. C. Grozema, J. M. Schins, S. Patil, U. Scherf and L. D. A. Siebbeles, *Phys. Rev. Lett.*, 2006, **96**, 146601; (*b*) A. Babel and S. A. Jenekhe, *J. Am. Chem. Soc.*, 2003, **125**, 13656.

109. M. Samiullah, D. Moghe, U. Scherf and S. Guha, *Phys. Rev. B*, 2010, **82**, 205211.

110. (*a*) M. Kertesz and T. R. Hughbanks, *Synth. Met.*, 1995, **69**, 699; (*b*) A. Tsuda and A. Osuka, *Science*, 2001, **293**, 79.

111. M. Di Giovannantonio, Q. Chen, J. I. Urgel, P. Ruffieux, C. A. Pignedoli, K. Müllen, A. Narita and R. Fasel, *J. Am. Chem. Soc.*, 2020, **142**, 12925–12929.

112. (*a*) R. W.-I. de Boer, A. F. Stassen, M. F. Craciun, C. L. Mulder, A. Molinari, S. Rogge and A. F. Morpurgo, *Appl. Phys. Lett.*, 2005, **86**, 262109; (*b*) T. Takahashi, T. Takenobu, J. Takeya and Y. Iwasa, *Appl. Phys. Lett.*, 2006, **88**, 033505.

113. (*a*) J. L. Marshall, K. Uchida, C. K. Frederickson, C. Schütt, A. M. Zeidell, K. P. Goetz, T. W. Finn, K. Jarolimek, L. N. Zakharov, C. Risko, R. Herges, O. D. Jurchescu and M. M. Haley, *Chem. Sci.*, 2016, **7**, 5547–5558; (*b*) L. Ren, C. Liu, Z. Wang and X. Zhu, *J. Mater. Chem. C*, 2016, **4**, 5202–5206.

114. A. M. Zeidell, L. Jennings, C. K. Frederickson, Q. Ai, J. J. Dressler, L. N. Zakharov, C. Risko, M. M. Haley and O. D. Jurchescu, *Chem. Mater.*, 2019, **31**, 6962–6970.

115. Y.-C. Lo, H.-C. Ting, Y.-Z. Li, Y.-H. Li, S.-W. Liu, K.-W. Huang and K.-T. Wong, *Org. Chem. Front.*, 2017, **4**, 675–681.

116. M. J. Kendrick, A. Neunzert, M. M. Payne, B. Purushothaman, B. D. Rose, J. E. Anthony, M. M. Haley and O. Ostroverkhova, *J. Phys. Chem. C*, 2012, **116**, 18108–18116.

117. (*a*) Z. Wang, C. Kim, A. Facchetti and T. J. Marks, *J. Am. Chem. Soc.*, 2007, **129**, 13362–13363; (*b*) J. Mei, Y. Diao, A. L. Appleton, L. Fang and Z. Bao, *J. Am. Chem. Soc.*, 2013, **135**, 6724–6746; (*c*) Y. Zhao, Y. Guo and Y. Liu, *Adv. Mater.*, 2013, **25**, 5372–5391; (*d*) A. Can, I. Deneme, G. Demirel and H. Usta, *ACS Appl. Mater. Interfaces* 2023, **15**, 41666–41679; (*e*) K. Park, E. Shin, X. Jiao, C. R. McNeill, Y. Kim, S. Kwon,

and Y. Noh, *ACS Appl. Mater. Interfaces*, 2019, **11**, 35185–35192; (*f*) A. P. Dhondge, J. Chen, T. Lin, F. Yen, K. Li, H. Hsieh and M. Kuo, *Org. Lett.* 2018, **20**, 40–43.
118. (*a*) M. Li, M. Liu, F. Qi, F. R. Lin and A. K.-Y. Jen, *Chem. Rev.* 2024, **124**, 2138–2204; (*b*) L. Miozzo, A. Yassar and G. Horowitz, *J. Mater. Chem.* 2010, **20**, 2513; (*c*) M. H. Yoon, C. Kim, A. Facchetti, T. J. Marks, *J. Am. Chem. Soc.* 2006, **128**, 12851;
119. S. Ito, T. Minami and M. Nakano, *J. Phys. Chem. C*, 2012, **116**, 19729–19736.
120. (*a*) R. Casares, Á. Martínez-Pinel, S. Rodríguez-González, I. R. Márquez, L. Lezama, M. T. González, E. Leary, V. Blanco, J. G. Fallaque, C. Díaz, F. Martín, J. M. Cuerva and A. Millán, *J. Mater. Chem. C*, 2022, **10**, 11775–11782; (*b*) R. Casares, S. Rodríguez-González, Á. Martínez-Pinel, I. R. Márquez, M. T. González, C. Díaz, F. Martín, J. M. Cuerva, E. Leary and Alba Millán, *J. Am. Chem. Soc.* 2024, **146**, 29977–29986.
121. (*a*) S. Muhammad, M. Nakano, A. G. Al-Sehemi, Y. Kitagawa, A. Irfan, A. R. Chaudhry, R. Kishi, S. Ito, K. Yoneda and K. Fukuda, *Nanoscale*, 2016, **8**, 17998–18020; (*b*) M. Nakano, *Chem. Rec.*, 2017, **17**, 27–62; (*c*) M. Nakano, R. Kishi, T. Nitta, T. Kubo, K. Nakasuji, K. Kamada, K. Ohta, B. Champagne, E. Botek and K. Yamaguchi, *J. Phys. Chem. A*, 2005, **109**, 885–891; (*d*) X. Hu, W. Wang, D. Wang and Y. Zheng, *J. Mater. Chem. C*, 2018, **6**, 11232–11242.

Chapter 2

Chapter 2A

A new synthetic approach to indeno[2,1-*c*]fluorene

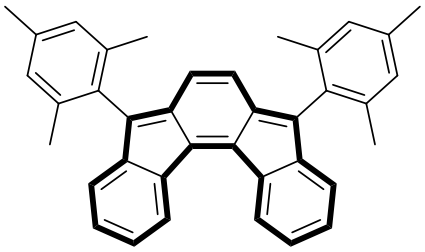

1

A fullerene-C_{60} fragment

Our mild synthetic approach

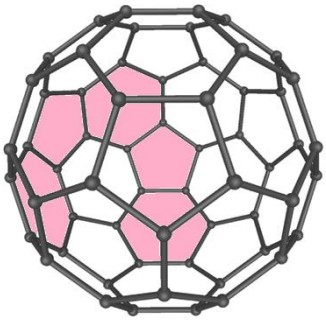

Fullerene-C_{60}

❖ This work was co-authored with Dr. Priyank Kumar Sharma, who provided synthetic support, Dr. Soumyajit Das, who provided guidance and editorial assistance. This work was originally published in ***Chemical Communications***. (Reference: *Chem. Commun.,* 2020, **56**, 11319-11322)

2A.1 Abstract

The chemistry of acenes, known for their challenging synthesis and optoelectronic properties, has spurred significant interest. While pentacene is notable for its applications in organic electronics, its derivatives are prone to oxidative degradation. This has led to the development of five non-alternant indenofluorene (IF) isomers, which are antiaromatic analogues of pentacene with promising redox, optoelectronic, and magnetic properties. Among the IF isomers, indeno[2,1-*c*]fluorene is a small isolable fullerene-C_{60} fragment that received less attention due to previous synthetic methods requiring harsh conditions. In this work, we present a mild and convenient synthetic approach to [2,1-*c*]IF **1** using inexpensive and commercially available materials.

2A.2 Introduction

As discussed in Chapter 1, non-alternant fully conjugated indenofluorene (IF) isomers, namely indeno[1,2-*b*]fluorene,[1] indeno[2,1-*a*]fluorene,[2] indeno[2,1-*b*]fluorene,[3] indeno[2,1-*c*]fluorene,[4] and indeno[1,2-*a*]fluorene[5] have gained remarkable attention because of the amphoteric redox behaviour, open shell character, and unique optical properties.[6]

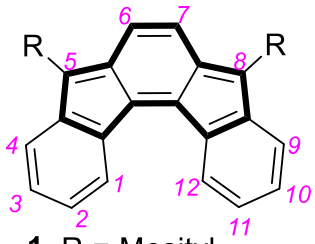

1, R = Mesityl
2, R = 3,5-$(CF_3)_2C_6H_3$
3, R = CCSi*i*-Pr_3

Figure 2A.1 Structure of symmetrically disubstituted [2,1-*c*]IF derivatives **1**-**3**.

Being a fragment of fullerene-C_{60}, [2,1-*c*]IF derivative welcomed as a new electron-accepting scaffold that showed promise in bulk-heterojunction devices.[7] In addition, its potential to show lower HOMO–LUMO energy gap[4] compared to the analogous [1,2-*b*]IF, and kinked structure favouring the formation of tetracyclopenta[*def*,*jkl*,*pqr*,*vwx*]tetraphenylene (TCPTP) make [2,1-*c*]IF a unique IF isomer.[8] Studies on [2,1-*c*]IF revealed its slightly helical backbone with a *para*-quinoidal arrangement of the *as*-indacene subunit, and negligible diradical contribution

in the singlet ground state, affording three stable symmetrically disubstituted derivatives **1**, **2**, and **3** (Figure 2A.1).[4]

The usual synthetic route to [2,1-*c*]IF scaffolds **1-3** was comprised of a nucleophilic addition of aryl/ethynyl groups[4] to the benzo-fused diketone[9] precursor in pre-final step, followed by $SnCl_2$-mediated reduction of the hydroxy groups at the final step.[10] This approach has certain drawbacks such as the final reductive dehydroxylation with mesityl substituent failed at times,[11] and the synthetic route to the benzo-fused diketone precursor required usage of harsh reaction conditions including high temperatures ranging from 220 to 280 °C.[9b]

2A.3 Results and Discussion

2A.3.1 Synthesis

Herein, we developed a mild and convenient multistep approach to synthesize the known [2,1-*c*]IF **1**, 5,8-dimesitylindeno[2,1-*c*]fluorene, from cheap and commercially available starting materials (Scheme 1).

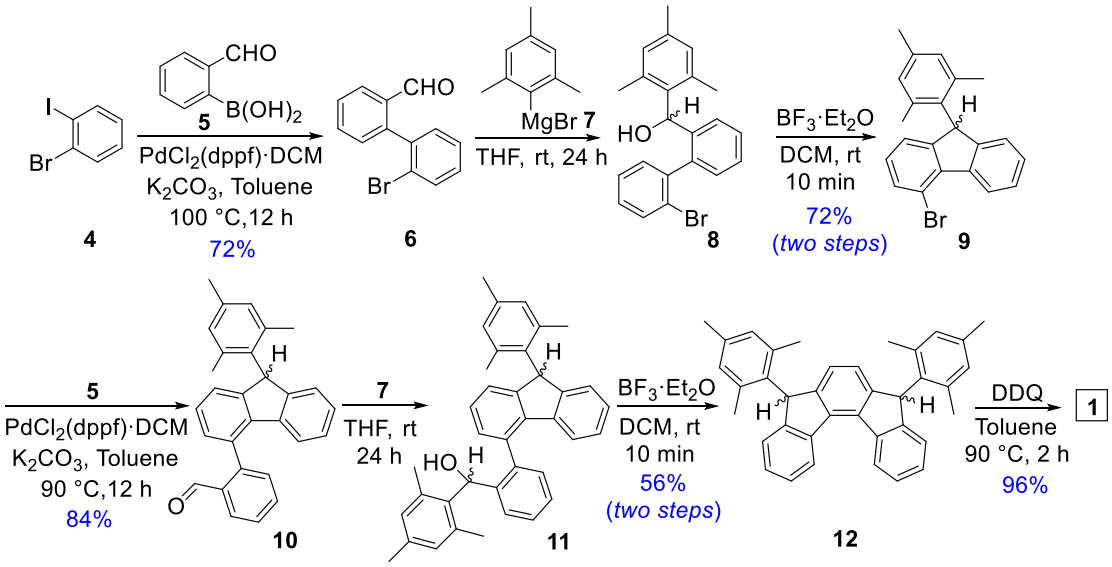

Scheme 2A.1 Synthetic route to symmetrically disubstituted [2,1-*c*]IF derivative **1**.

Selective Suzuki reaction between the 1-bromo-2-iodobenzene **4** and (2-formylphenyl)boronic acid **5** afforded **6** in 72% yield (Scheme 2A.1). Treatment of **6** with 2-mesitylmagnesium bromide **7** at ambient temperature afforded **8**, which was subsequently converted to **9** using $BF_3{\cdot}Et_2O$ mediated Friedel-Crafts alkylation approach. Pd^{II}-catalyzed Suzuki reaction of racemic **9** and **5** afforded **10** in 84% yield, which was treated with **7** to give crude alcohol **11.** Treatment of crude **11** with $BF_3{\cdot}Et_2O$ gave the dihydro precursor **12** in 56% yield (in two steps). Under inert atmosphere, a

near quantitative formation of **1** in 2 h *via* oxidative dehydrogenation of **12** using 1.3 equivalents of 2,3-dichloro-5,6-dicyano-1,4-benzoquinone (DDQ) was attained at 90 °C in dry toluene. Compound **1** was unambiguously confirmed by nuclear magnetic resonance (NMR) spectroscopy, high resolution mass spectrometry (HRMS), and melting point analysis (*vide infra*) which were consistent with the literature report.[4]

2A.4 Conclusions

In conclusion, we have successfully synthesized compound **1** using a new cost-effective approach that relies on readily available starting materials. Unlike previous synthetic routes,[4,9] this method avoids the need for harsh reaction conditions, such as elevated temperatures, which can often complicate the process. This new approach also provides the flexibility to introduce various aryl, heteroaryl, or ethynyl groups at the exo-methylene carbons of the *p*QDM subunits. This capability opens up possibilities for the development of new derivatives of compound **1**, which could exhibit improved solid-state packing and optoelectronic properties. Such derivatives could potentially broaden the scope of applications in fields such as organic electronics and materials science.

2A.5 Experimental Section

2A.5.1 General Information

All reagents and chemicals were obtained from commercial sources and used as received. Silica gel (100-200 mesh) was used for column chromatography. NMR spectra, in solution, were recorded on JEOL JNM ECS-400 spectrometer at 298 K. The following abbreviations were used to explain the multiplicities: s = singlet, d = doublet, t = triplet, m = multiplet. ^{1}H and ^{13}C chemical shifts (δ) are reported in ppm relative to the residual $CHCl_3$ (^{1}H: 7.26 ppm, ^{13}C: 77.16 ppm) reference. High resolution mass spectra (HRMS) were recorded using electron spray ionization (ESI) methods on Waters (XEVO G2-XS QTOF) mass spectrometer. Melting points were determined using BIBBY-SMP30 melting point analyzer.

2A.5.2 Synthesis

2'-bromo-[1,1'-biphenyl]-2-carbaldehyde (6). An oven-dried thick-walled glass tube was charged with **4** (1 g, 3.53 mmol), 2-formylphenylboronic acid **5** (583 mg, 3.86 mmol), anhydrous K_2CO_3 (2.44 g, 17.67 mmol), dry toluene (5 mL), and purged with nitrogen for 30 mins. The vial was sealed under nitrogen after adding $PdCl_2$(dppf)·DCM complex (144 mg, 0.18 mmol), and the mixture was warmed at 100 °C for 12 h. After

being cooled to room temperature, water was added and the resultant mixture was extracted with DCM (3 x 50 mL). The organic layer was dried over anhydrous Na_2SO_4, filtered, and evaporated under reduced pressure to afford a crude residue which was column chromatographed on silica gel (hexanes:EtOAc, 95:5) to afford the title product **6** as light yellow viscous oil (664 mg, 72% yield). R_f = 0.45 (5% EtOAc/hexanes); **^{1}H NMR** (400 MHz, $CDCl_3$): δ 9.74 (s, 1H), 7.99 (d, *J* = 7.7 Hz, 1H), 7.67–7.59 (m, 2H), 7.50 (t, *J* = 7.5 Hz, 1H), 7.37 (t, *J* = 7.4 Hz, 1H), 7.31–7.21 (m, 3H); **^{13}C{^{1}H} NMR** (100 MHz, $CDCl_3$): δ 191.7, 144.6, 138.9, 133.8, 133.7, 132.8, 131.7, 130.9, 129.9, 128.6, 127.5, 127.4, 123.9; **HRMS** (ESI) *m/z*: $[M + H]^+$ Calcd for $C_{13}H_{10}OBr$ 260.9915, found 260.9902.

4-bromo-9-mesityl-9*H*-fluorene (8). 2-Mesitylmagnesium bromide (1 M solution in THF, 4.98 mL, 4.98 mmol) was added dropwise to the 10 mL dry THF solution of compound **6** (650 mg, 2.49 mmol) under nitrogen, and the mixture was stirred at room temperature for 24 h. The reaction mixture was quenched with saturated solution of ammonium chloride (50 mL), and the volatile organics were evaporated *in vacuo*. The residue was extracted with DCM (3 x 50 mL), washed with water, and dried over sodium sulfate. The organic layer was filtered, and the filtrate was removed under reduced pressure to afford crude **8** as yellow solid (1.2 g). To the solution of crude **8** (1.2 g) in anhydrous DCM (10 mL) at room temperature, $BF_3{\cdot}Et_2O$ (0.1 mL) was added dropwise under nitrogen, and the reaction mixture was stirred for 10 min at room temperature to perform an intra-molecular ring-closure reaction. After 10 min, a saturated aqueous NH_4Cl solution was added to the reaction mixture and it was extracted with DCM (3 x 50 mL). The organic layer was dried over anhydrous Na_2SO_4, filtered, and removed under reduced pressure to afford a residue which was purified by silica gel column chromatography (hexanes) to give **9** as white solid (655 mg, 72% yield in two steps). R_f = 0.47 (hexanes); **mp**: 108-109 °C; **^{1}H NMR** (400 MHz, $CDCl_3$): δ 8.66 (d, *J* = 7.8 Hz, 1H), 7.54 (d, *J* = 7.7 Hz, 1H), 7.44 (t, *J* = 7.5 Hz, 1H), 7.31 (t, *J* = 7.4 Hz, 1H), 7.21 (d, *J* = 7.4 Hz, 1H), 7.15 (d, *J* = 7.3 Hz, 1H), 7.08 (t, *J* = 7.6 Hz, 1H), 7.02 (s, 1H), 6.66 (s, 1H) 5.48 (s, 1H), 2.65 (s, 3H), 2.28 (s, 3H), 1.08 (s, 3H); **^{13}C{^{1}H} NMR** (100 MHz, $CDCl_3$): δ 150.2, 147.7, 140.2, 139.1, 137.8, 137.8, 136.6, 133.5, 131.9, 130.7, 129.0, 128.0, 127.9, 126.7, 123.9, 123.7, 123.0, 117.2, 49.9, 29.8, 21.8, 21.0, 18.9; **HRMS** (ESI) *m/z*: $[M - H]^+$ Calcd for $C_{22}H_{18}Br$ 361.0592, found 361.0593.

2-(9-mesityl-9*H*-fluoren-4-yl)benzaldehyde (10). An oven-dried thick-walled glass tube was charged with **9** (125 mg, 0.344 mmol), **5** (103.18 mg, 0.688 mmol), anhydrous

K_2CO_3 (237.76 mg, 1.72 mmol), dry toluene (6 mL) and purged with nitrogen for 30 min. Catalyst $PdCl_2$(dppf)·DCM complex (28.09 mg, 10 mol%) was added subsequently under nitrogen, and the glass tube was sealed. The reaction mixture was then warmed at 90 °C for 12 h. After being cooled to room temperature, the mixture was washed with water and extracted with DCM (3 x 50 mL). The DCM layer was dried over anhydrous Na_2SO_4, filtered, and removed under vacuum. The crude residue was purified by silica gel column chromatography (hexanes:DCM, 52:48) to afford the desired compound **10** as white solid (112 mg, 84% yield). $\boldsymbol{R_f}$ = 0.30 (30% DCM/hexanes); **mp:** 173-174 °C; **^{1}H NMR** (400 MHz, $CDCl_3$): δ 9.88-9.79 (m, 1H), 8.15 (d, *J* = 7.7 Hz, 1H), 7.76 (t, *J* = 7.4 Hz, 1H), 7.65 (t, *J* = 7.6 Hz, 1H), 7.58–7.46 (m, 1H), 7.37–7.27 (m, 2H), 7.25–7.07 (m, 3H), 7.06–6.91 (m, 2H), 6.68 (s, 1H), 6.55 (dd, *J* = 7.7, 3.2 Hz, 1H), 5.54 (s, 1H), 2.70 (m, 3H), 2.29 (s, 3H), 1.14-1.13 (m, 3H); **^{13}C{^{1}H} NMR** (100 MHz, $CDCl_3$): δ 192.3, 192.0, 147.9, 147.9, 147.8, 144.9, 140.1, 139.1, 139.0, 137.9, 137.8, 137.7, 136.6, 136.5, 134.3, 134.2, 134.1, 133.7, 132.6, 131.0, 130.8, 130.6, 129.4, 129.2, 129.1, 129.0, 128.6, 127.4, 127.4, 127.4, 126.9, 126.8, 124.2, 124.1, 124.1, 122.4, 49.7, 29.8, 21.9, 21.0, 18.8, 18.8; **HRMS** (ESI) *m/z*: $[M + H]^+$ Calcd for $C_{29}H_{25}O$ 389.1905, found 389.1898.

5,8-dimesityl-5,8-dihydroindeno[2,1-*c*]fluorene (12). 2-Mesitylmagnesium bromide (1.0 M in THF, 0.50 mL, 0.50 mmol) was added dropwise to the dry THF solution of **10** (98 mg, 0.25 mmol) under nitrogen atmosphere. The mixture was stirred at room temperature for 24 h, and then quenched by saturated aqueous NH_4Cl solution and extracted with DCM (3 x 50 mL). The organic layer was dried over anhydrous Na_2SO_4 and the solvent was removed under reduced pressure to afford crude product **11** as yellow solid (146 mg, **HRMS** *m/z*: $[M - H^+]$ Calcd for $C_{38}H_{35}O$ 507.2688, found 507.2691). To the solution of crude **11** (141 mg, 0.277 mmol) in anhydrous DCM (10 mL) at room temperature, $BF_3·Et_2O$ (0.1 mL) was added dropwise under nitrogen, and the reaction mixture was stirred for 10 min at room temperature. Progress of the intra-molecular ring-closure reaction was monitored by TLC. As the starting material disappeared, a saturated aqueous NH_4Cl solution was added to the reaction mixture and extracted with DCM. The organic layer was dried over anhydrous Na_2SO_4, filtered, and the solvent was subsequently removed under reduced pressure. The residue was purified by silica gel column chromatography (hexanes:DCM, 92:8) to afford dihydro precursor **12** as mixture of diastereomers, as white solid (69 mg, 56% yield in two steps). $\boldsymbol{R_f}$ = 0.50 (10% DCM/hexanes); **mp:** 204-205 °C; **^{1}H NMR** (400 MHz, $CDCl_3$): δ 8.64 (dd,

J = 16.1, 7.9 Hz, 2H), 7.55–7.47 (m, 2H), 7.37–7.27 (m, 4H), 7.06 (d, *J* = 7.9 Hz, 2H), 7.02 (s, 2H), 6.64 (d, *J* = 11.4 Hz, 2H), 5.58 (d, *J* = 9.2 Hz, 2H), 2.69 (s, 3H), 2.68 (s, 3H), 2.28 (s, 3H), 2.27 (s, 3H), 1.09 (s, 3H), 1.05 (s, 3H). **^{13}C{^{1}H} NMR** (100 MHz, $CDCl_3$): δ 148.5, 148.4, 148.1, 147.5, 141.5, 141.3, 137.9, 137.8, 136.4, 136.3, 136.2, 134.6, 134.5, 130.7, 128.9, 127.1, 126.7, 124.5, 124.4, 123.9, 123.7, 122.8, 122.5, 50.0, 29.8, 21.9, 21.0, 20.9, 18.8, 18.6; **HRMS** (ESI) *m/z*: $[M + H]^+$ Calcd for $C_{38}H_{35}$ 491.2739, found 491.2710.

5,8-dimesitylindeno[2,1-*c*]fluorene (1). Precursor **12** (44 mg, 0.089 mmol) was dissolved in dry toluene (1 mL) and purged with nitrogen for 10 mins. DDQ (26.5 mg, 0.116 mmol, 1.3 equiv) as solid was added into the solution, and the reaction mixture was warmed to 90 °C for 2 h while the progress was monitored by TLC. After 2 h, the solvent was removed by vacuum and the crude residue was purified by silica gel column chromatography (hexanes) to afford the final compound **1** as green solid (42 mg, 96% yield). R_f = 0.27 (hexanes); **mp**: 182-183 °C; **^{1}H NMR** (400 MHz, $CDCl_3$): δ 8.10 (d, *J* = 7.4 Hz, 2H), 7.14 (t, *J* = 7.4 Hz, 2H), 7.07 (t, *J* = 7.4 Hz, 2H), 6.96 (s, 4H), 6.69 (d, *J* = 7.2 Hz, 2H), 6.11 (s, 2H), 2.35 (s, 6H), 2.14 (s, 12H); **^{13}C{^{1}H} NMR** (100 MHz, $CDCl_3$): δ 146.2, 143.4, 138.9, 137.5, 137.1, 136.4, 130.0, 129.2, 128.2, 126.6, 125.5, 121.8, 121.0, 21.3, 20.4; **HRMS** (ESI) *m/z*: $[M]^+$ Calcd for $C_{38}H_{32}$ 488.2504, found 488.2496.

2A.6 References

1. D.T. Chase, B.D. Rose, S.P. McClintock, L.N. Zakharov and M. M. Haley, *Angew. Chem. Int. Ed.* 2011, **50**, 1127–1130.

2. A. Shimizu and Y. Tobe, *Angew. Chem. Int. Ed.* 2011, **50**, 6906–6910.

3. A. Shimizu, R. Kishi, M. Nakano, D. Shiomi, K. Sato, T. Takui, I. Hisaki, M. Miyata and Y. Tobe, *Angew. Chem. Int. Ed.* 2013, **52**, 6076–6079.

4. A. G. Fix, P. E. Deal, C. L. Vonnegut, B. D. Rose, L. N. Zakharov and M. M. Haley, *Org. Lett.* 2013, **15**, 1362–1365.

5. J. J. Dressler, Z. Zhou, J. L. Marshall, R. Kishi, S. Takamuku, Z. Wei, S. N. Spisak, M. Nakano, M. A. Petrukhina and M. M. Haley, *Angew. Chem. Int. Ed.* 2017**, *56***, 15363–15367.

6. (*a*) Y. Tobe, *Chem. Rec.* 2015, **15**, 86–96; (*b*) G. E. Rudebusch and M. M. Haley, *Polycyclic arenes and heteroarenes: synthesis, properties, and applications.* Wiley-

VCH, 2015, 37–68; (*c*) C. K. Frederickson, B. D. Rose and M. M. Haley, *Acc. Chem. Res.* 2017, **50**, 977–987.

7. K. Paudel, B. Johnson, M. Thieme, M. M. Haley, M. M. Payne, J. E. Anthony and O. Ostroverkhova, *Appl. Phys. Lett.*, 2014, **105**, 043301.

8. S. Nobusue, H. Miyoshi, A. Shimizu, I. Hisaki, K. Fukuda, M. Nakano and Y. Tobe, *Angew. Chem. Int. Ed.* 2015, **54**, 2090–2094.

9. (*a*) Y. Altman and D. Ginsburg, *J. Chem. Soc.* 1961, 1498–1505; (*b*) L. Chardonnens and H. Chardonnens, *Helv. Chim. Acta*. 1966, **49**, 1931–1934.

10. (*a*) L. Ren, C. Liu, Z. Wang and X. Zhu. *J. Mat. Chem. C* 2016**, 4**, 5202–5206; (*b*) Y. Tobe, *Physical Organic Chemistry of Quinodimethanes. Top. Curr. Chem.* Springer, 2018, 375, 107–168.

11. T. Jousselin-Oba, P. E. Deal, A. G. Fix, C. K. Frederickson, C. L. Vonnegut, A. Yassar, L. N. Zakharov, M. Frigoli and M. M. Haley, *Chem. Asian J.* 2019, **14**, 1737–1744.

2A.7 Appendix

NMR spectra

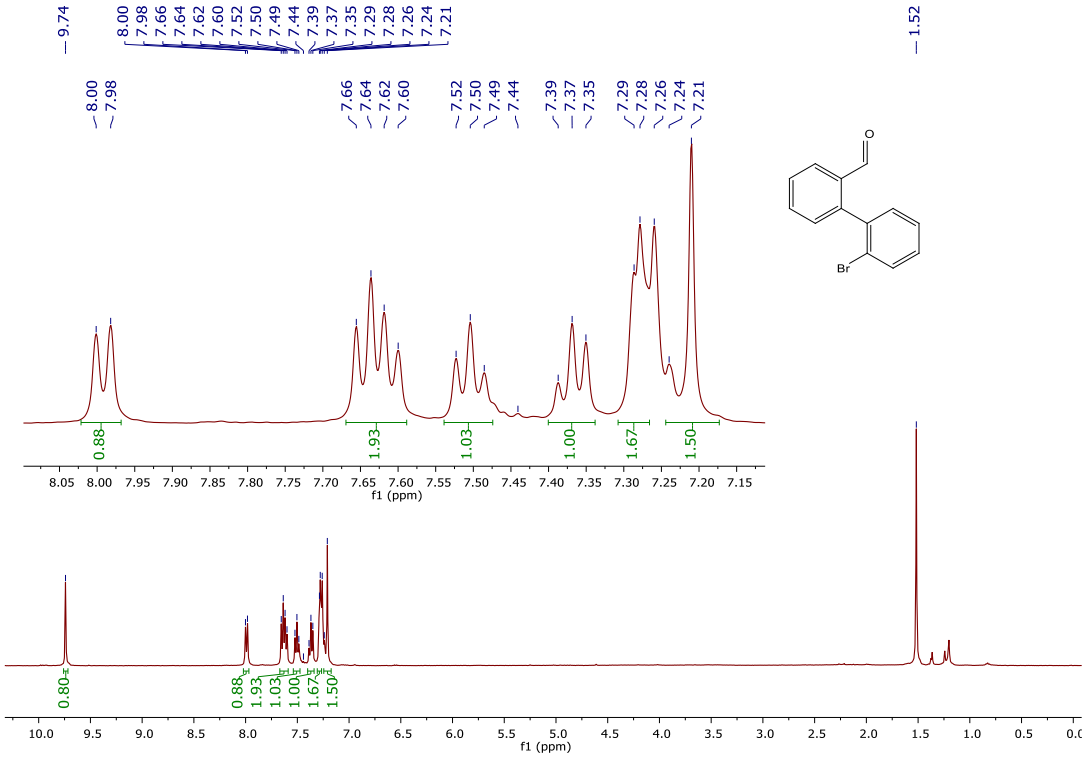

Figure 2A.2 ^{1}H NMR spectrum of **6** (in $CDCl_3$, 400 MHz).

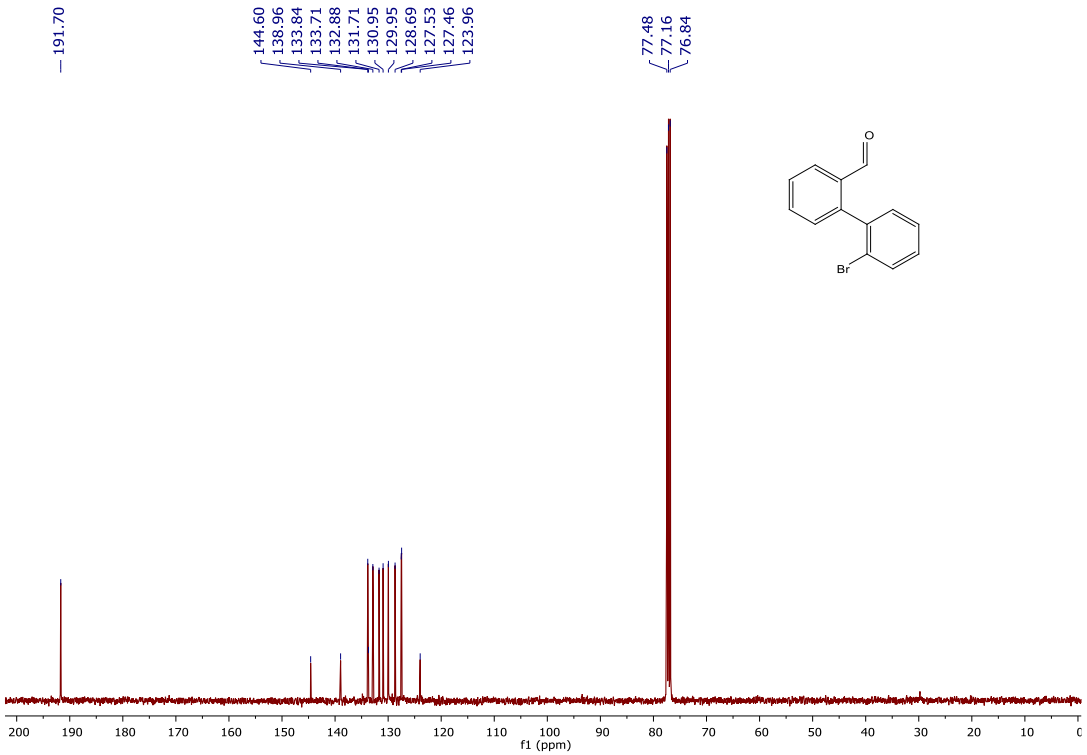

Figure 2A.3 ^{13}C NMR spectrum of **6** (in $CDCl_3$, 100 MHz).

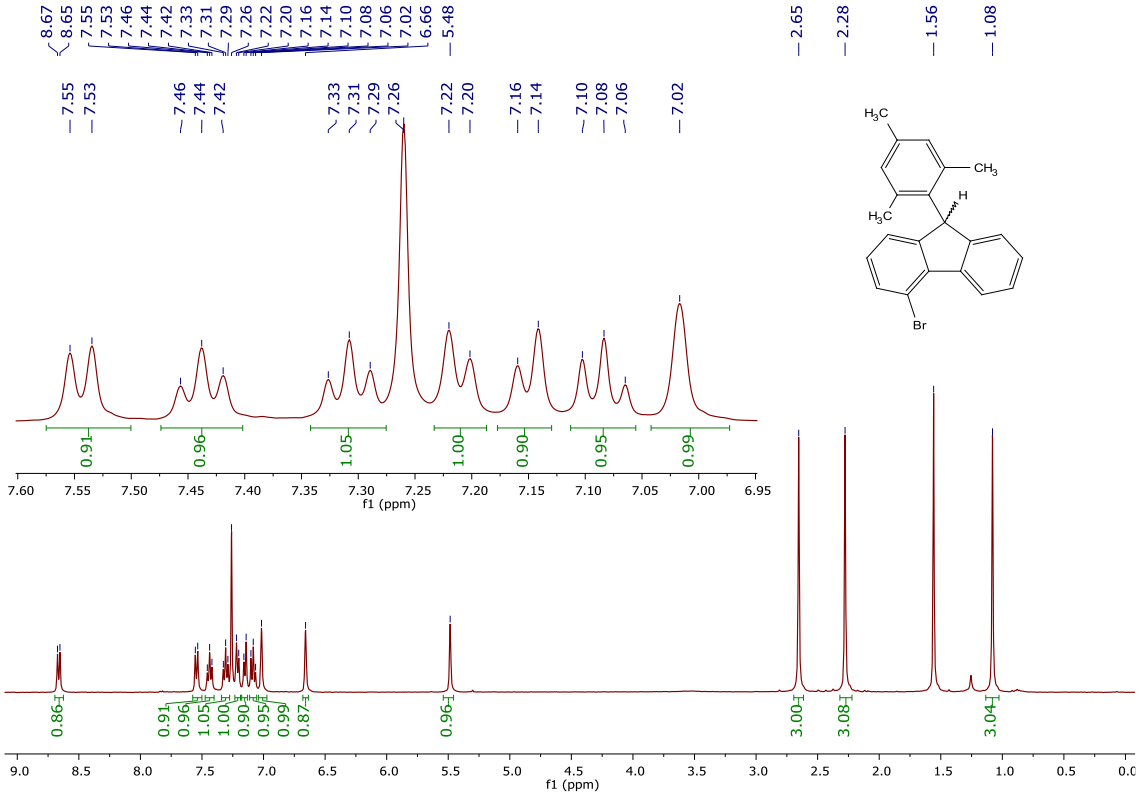

Figure 2A.4 ^{1}H NMR spectrum of **9** (in $CDCl_3$, 400 MHz).

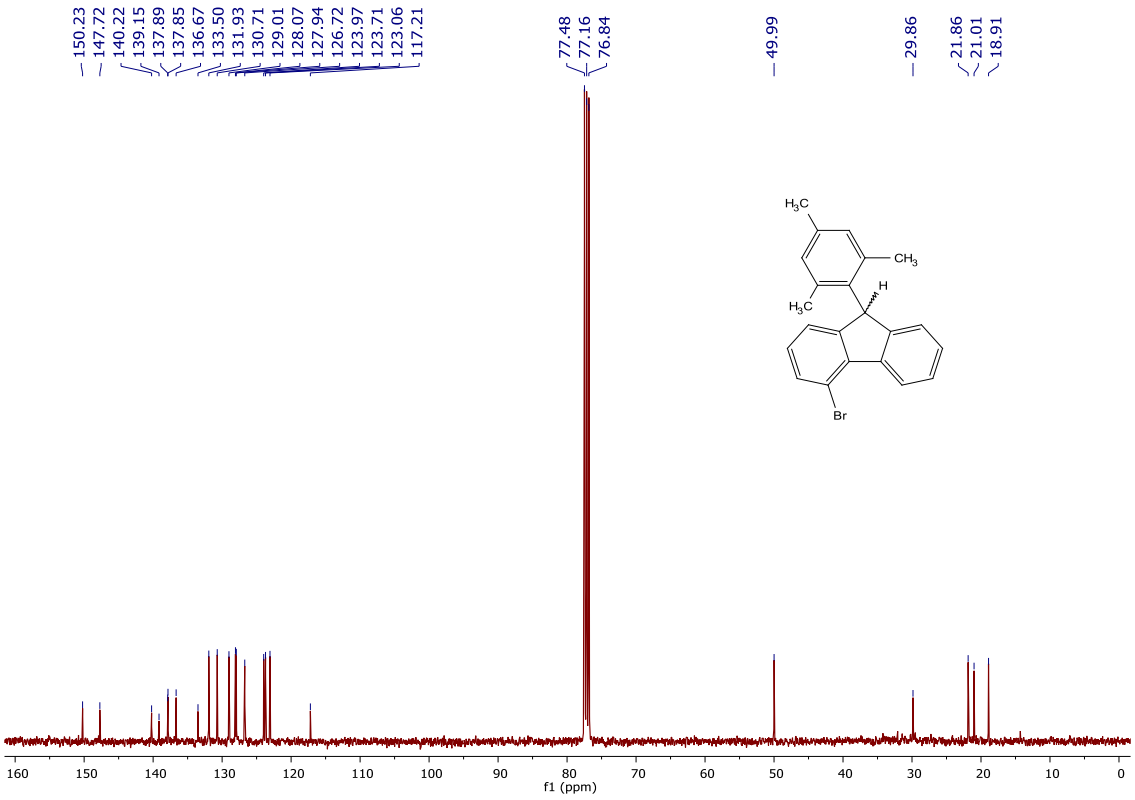

Figure 2A.5 ^{13}C NMR spectrum of **9** (in $CDCl_3$, 100 MHz).

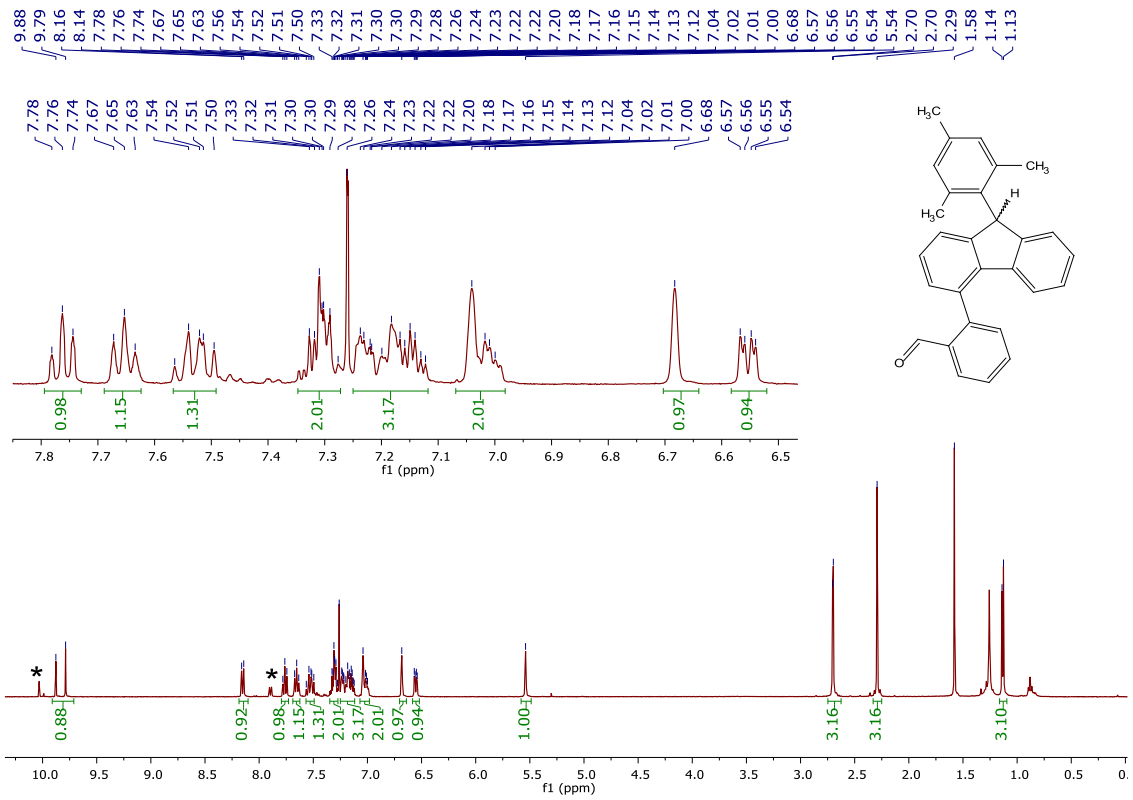

Figure 2A.6 ^{1}H NMR spectrum of **10** (in $CDCl_3$, 400 MHz). *Impurity of PhCHO by-product.

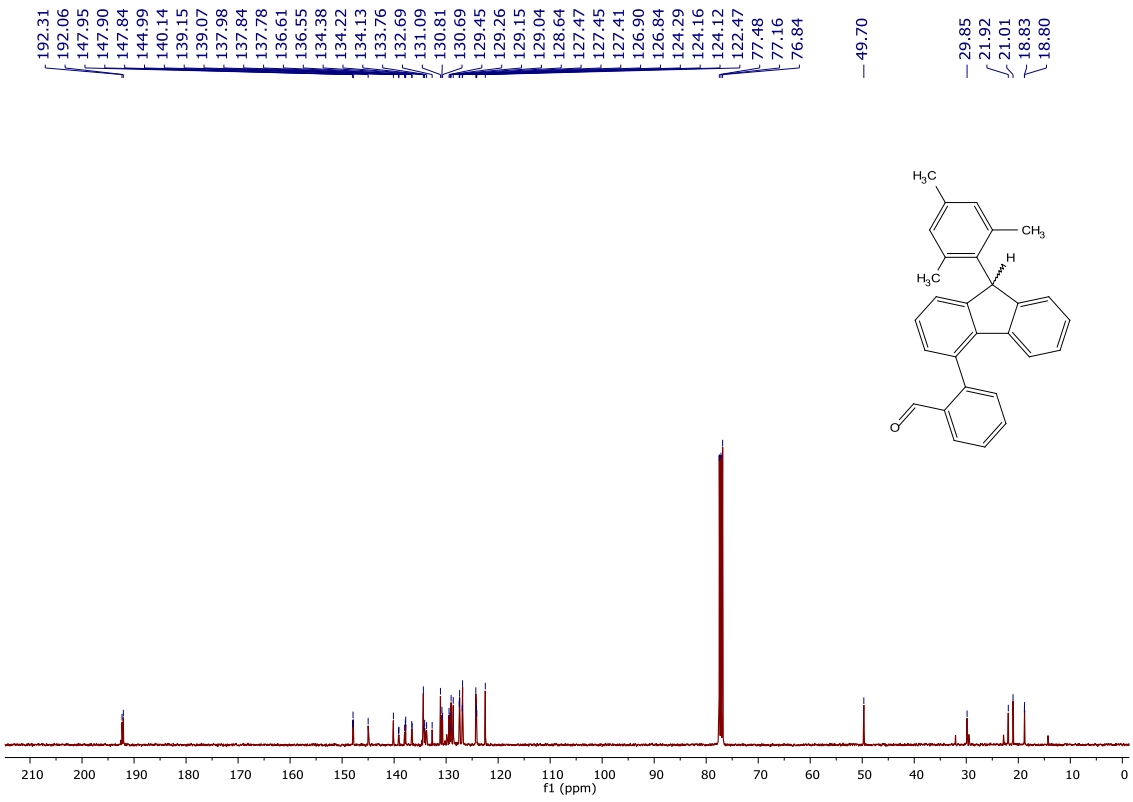

Figure 2A.7 ^{13}C NMR spectrum of **10** (in $CDCl_3$, 100 MHz).

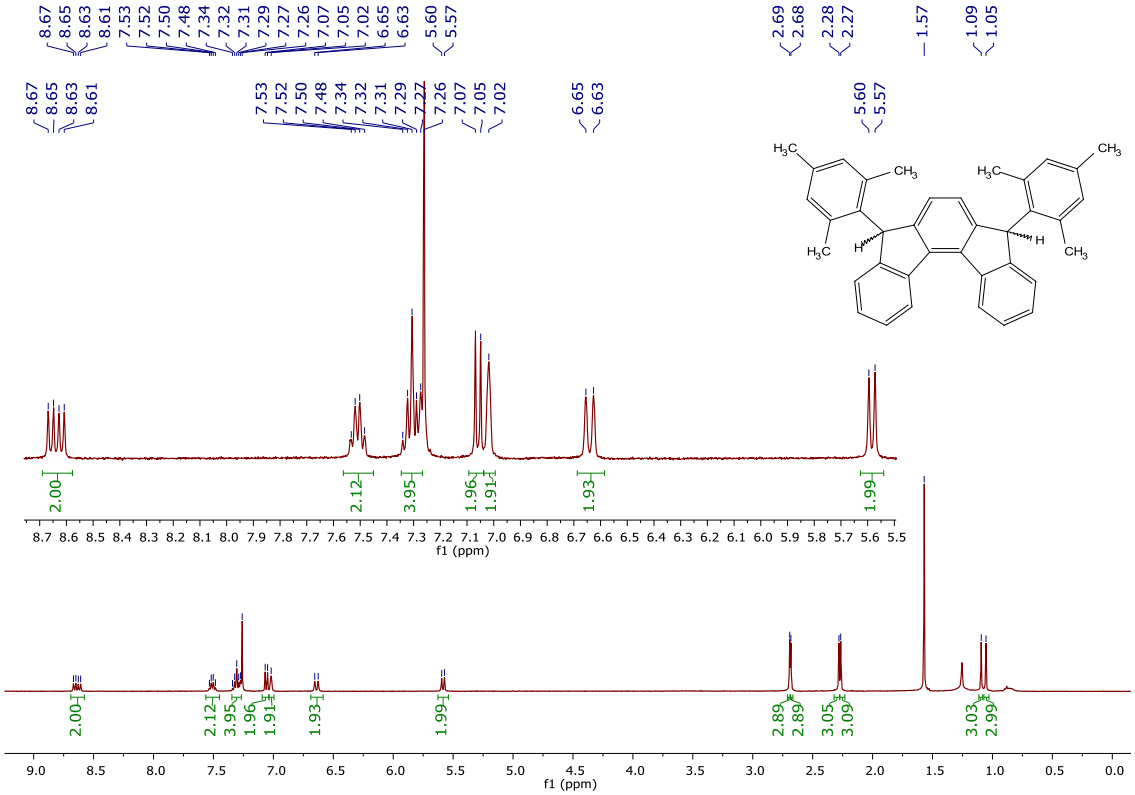

Figure 2A.8 ^{1}H NMR spectrum of **12** (in $CDCl_3$, 400 MHz).

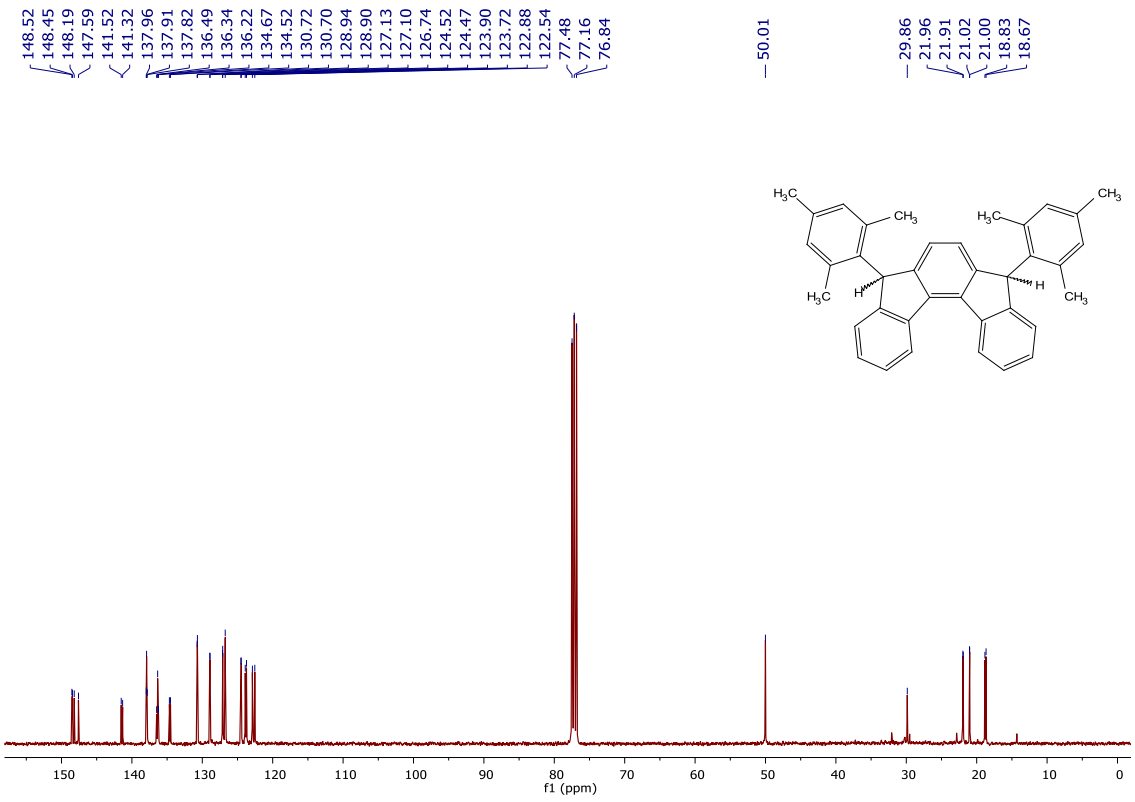

Figure 2A.9 ^{13}C NMR spectrum of **12** (in $CDCl_3$, 100 MHz).

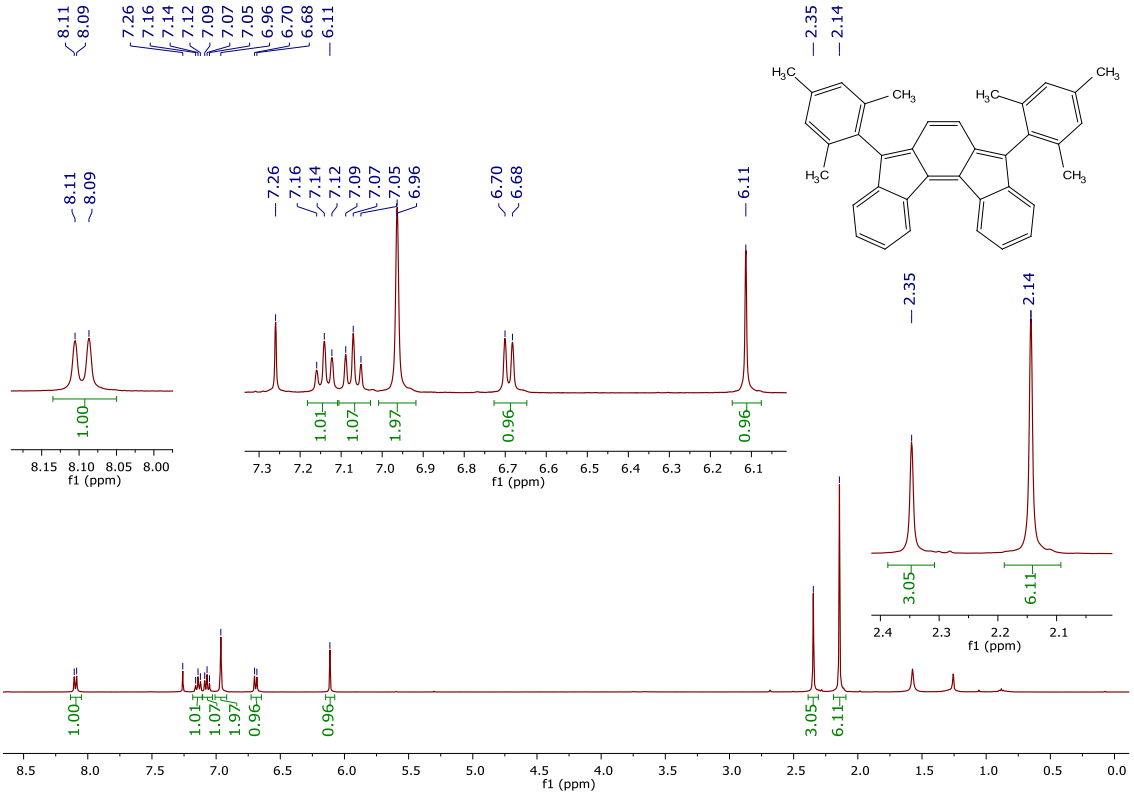

Figure 2A.10 ^{1}H NMR spectrum of **1** (in $CDCl_3$, 400 MHz).

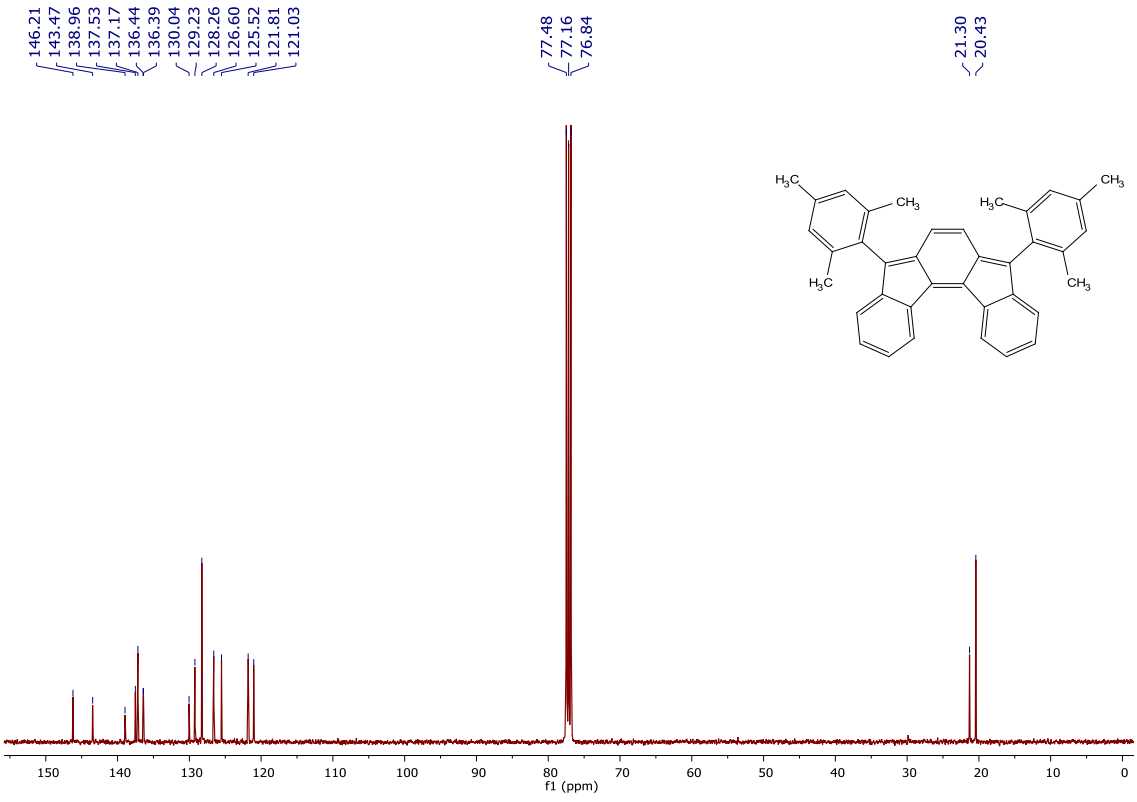

Figure 2A.11 ^{13}C NMR spectrum of **1** (in $CDCl_3$, 100 MHz).

Chapter 2

Chapter 2B

Exploration of Indeno[2,1-*c*]fluorene Derivatives With Unsymmetrical Disubstitution and Balanced Ambipolar Charge-Transport Properties

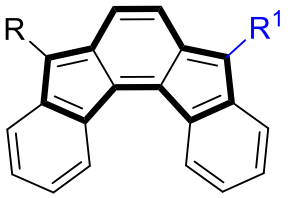

1, R = R^1 = Mesityl
Synthesis: ***Known***
Carrier mobilities
(μ_h & μ_e): ***Unknown***

Synthesis: **7**-**10**, **17**. μ_h & μ_e: **1**, **7**, **8** & **17**
7, R = Mesityl / R^1 = C_6F_5
8, R = Mesityl / R^1 = 3,5-$(CF_3)_2C_6H_3$
9, R = Mesityl / R^1 = CCSi*i*-Pr_3
10, R = 4-OMePh / R^1 = 3,5-$(CF_3)_2C_6H_3$
17, R = R^1 = C_6F_5 ***Present work***

❖ This work was co-authored with Pooja Bhardwaj who provided synthetic support, Ankita and Dr. Upendra Kumar Pandey, who performed SCLC measurements, Dr. Soumyajit Das, who provided guidance and editorial assistance. This work was originally published in ***Organic Materials***. (Reference: *Organic Materials* 2023, **5**, 72-83)

2B.1 Abstract

Unsymmetrically disubstituted antiaromatic indenofluorene (IF), in comparison to aromatic pentacene counterpart with unsymmetrical disubstitution, was rare in literature until our recent report on indeno[1,2-*b*]fluorene and indeno[2,1-*a*]fluorene. Described herein is straightforward access to unsymmetrically disubstituted indeno[2,1-*c*]fluorenes bearing mesityl at one apical carbon and C_6F_5, 3,5-$(CF_3)_2C_6H_3$, and CCSi*i*-Pr_3 at the other apical carbon, including 4-methoxyphenyl/3,5-$(CF_3)_2C_6H_3$ push/pull substitution at the apical carbons with appreciable orbital density, and a previously unknown symmetrically C_6F_5-disubstituted [2,1-*c*]IF. The electronic properties of the unsymmetrical derivatives lie halfway in between the two symmetrical counterparts, while the 4-methoxyphenyl derivative showed the smallest HOMO-LUMO energy gap and near-infrared absorption with intramolecular charge transfer character. Single-crystal analyses showed 1D-columnar stacks for the unsymmetrical motif with the C_6F_5 units co-facially π-stacked with the IF core, whereas symmetrically C_6F_5-disubstituted [2,1-*c*]IF, with a low-lying LUMO, showed intermolecular π-π stacks between the IFs that resulted in good electron mobility ($\mu_e = 8.66 \times 10^{-3}$ cm^2 V^{-1} s^{-1}) under space charge limited current measurements. Importantly, balanced ambipolar charge-transport behaviour could be extracted for an IF series with symmetrical/unsymmetrical substitutions, in comparison to its π-contracted pentalene congener.

2B.2 Introduction

Fully conjugated indeno[2,1-*c*]fluorene is a structural isomer of the five antiaromatic indenofluorene (IF) regioisomers.[1,2] Studies on [2,1-*c*]IF revealed its slightly helical backbone with a *para*-quinoidal arrangement of the *as*-indacene subunit, and negligible diradical contribution in the singlet ground state, affording three stable symmetrically disubstituted derivatives **1**, **2**, and **3** (Figure 2B.1b).[1] In comparison to the isomeric indeno[1,2-*b*]fluorene[2a] with a *para*-quinodimethane (*p*-QDM) arrangement in the *s*-indacene subunit (shown in bold, Figure 2B.1a), the *as*-indacene (shown in bold, Figure 2b.1b) embedded [2,1-*c*]IF is less documented,[2e] despite showing smaller HOMO-LUMO energy gap[1] and potential application as electron-acceptor in the bulk-heterojunctions.[3]

Majority of the studies conducted with the [2,1-*c*]IF revealed that its electronic, redox, and solid-state properties can be tuned by elongating the pentacyclic backbone by quinoidal fluorenofluorene[4] modification (*as*-indacene subunit not retained) or by

condensing benzene unit in the form of benzo-fused [2,1-*c*]IF derivatives **4**, **5** and **6**, where *as*-indacene subunit is retained.[5] However, unsymmetrical variation of both substituents at the apical carbon (the non-bridgehead carbon of five-membered ring) centers to tune the electronic and solid-state properties was never explored.[1,2e]

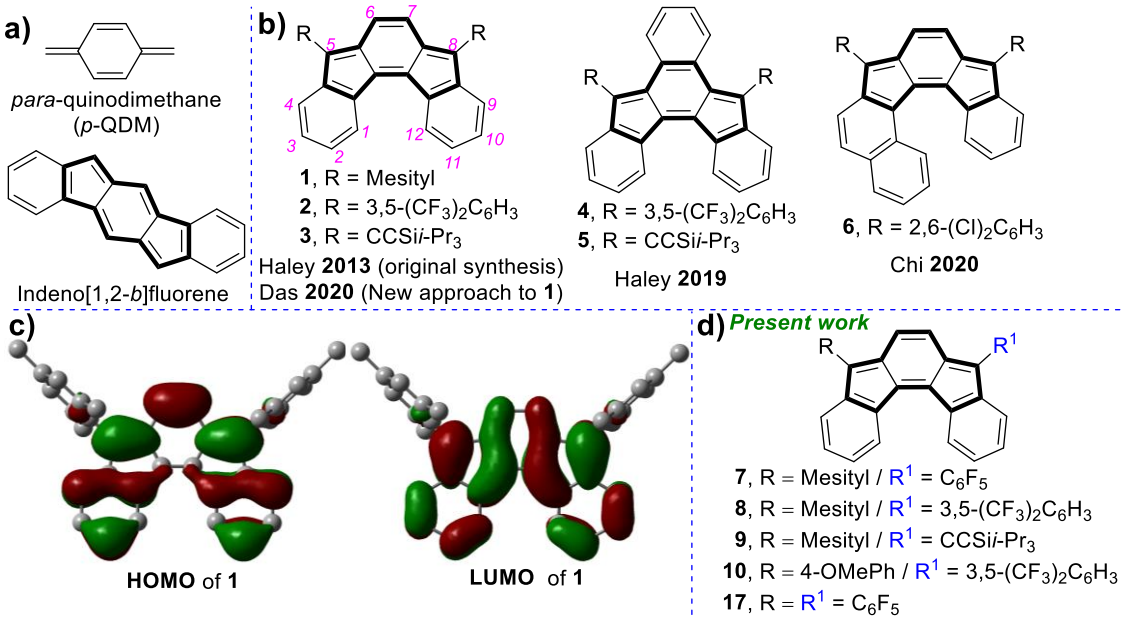

Figure 2B.1 (a) *p*-QDM embedded indeno[1,2-*b*]fluorene. (b) *p*-QDM embedded isomeric [2,1-*c*]IF derivatives **1**-**6**. (c) Frontier molecular orbital profiles of **1**. (d) Target unsymmetrical [2,1-*c*]IFs **7**-**10** and the unknown symmetrical **17**.

Lack of access to the unsymmetrically disubstituted IFs[1,2,5] is likely due to the limitation of a controlled nucleophilic addition[6] of aryl/ethynyl groups to the benzo-fused diketone precursor, which have hampered exploration of unsymmetrically disubstituted IFs. Lately, two unsymmetrically disubstituted IF regioisomers were reported by us with tuneable antiaromaticity.[7] We had reported a new synthesis approach of **1**,[8] and further to a (4n+2)π *s*-indacenodifluorene. Inspired by the general route for unsymmetrically 6,13-disubstituted pentacene molecules for various applications[9] and considering appreciable molecular orbital density at the apical carbons of **1** (Figure 2B.1c) or related *as*-indacene[10] that suggested possibility to tune the electronic properties of [2,1-*c*]IFs by apical elongation, including the non-availability of unsymmetrically 5,8-disubstituted [2,1-*c*]IFs, we envisaged to extend our synthetic approach[8] as a general route to access the yet inaccessible unsymmetrically 5,8-disubstituted [2,1-*c*]IF scaffolds **7**, **8**, **9**, **10** (Figure 2B.1d), and a previously unknown[1] symmetrically disubstituted [2,1-*c*]IF **17**.

The aryl or ethynyl groups like C_6F_5,[11] [3,5-bis(trifluoromethyl)phenyl],[12] and [(triisopropylsilyl)ethynyl][13] are chosen due to their proven ability to sterically protect the apical carbons and the electron-accepting nature.[14] It was also anticipated that replacing weakly electron-donor mesityl of **8** with 4-methoxyphenyl for **10** may offer improved push-pull character. Additionally, [2,1-*c*]IF scaffold was known[1] but its charge-carrier mobility was unknown, and it was speculated to have poor performance due to its U-shape hindering π-π stacks.[2e] Inspired by the reports of ambipolar charge-transport of [1,2-*b*]IF[2f] with symmetrical di-substitution, and use of [1,2-*b*]IF for single-molecule conductance studies,[2h] herein, we report the syntheses of four unsymmetrical [2,1-*c*]IFs **7**-**10** and one symmetrical [2,1-*c*]IF **17** including their characterization by both experimental and computational[15] approaches, and the charge-carrier mobilities of **1**, **7**, **8** and **17** were experimentally investigated by space charge limited current (SCLC) method.

2B.3 Results and Discussion

2B.3.1 Synthesis

C_6F_5-disubstitued [1,2-*b*]IF is ambipolar material,[16] that motivated us to synthesize **17** as it was not reported earlier.[1] Treating our pre-synthesized aldehyde **11**[8] with pentafluorophenylmagnesium bromide (C_6F_5MgBr) at ambient condition afforded **12** **(**Scheme 2B.1**)**, which was converted to **13** using $BF_3{\cdot}Et_2O$ mediated Friedel–Crafts (FC) alkylation. The Suzuki reaction between **13** and (2-formylphenyl)boronic acid gave aldehyde **14** which was treated further with C_6F_5MgBr to afford the carbinol **15**. Treatment of crude **15** with $BF_3{\cdot}Et_2O$ gave the dihydro precursor **16** in 62% yield over two steps. Dichloro-5,6-dicyano-1,4-benzoquinone (DDQ) mediated oxidative dehydrogenation of **16** at 100 °C in 1,2-dichloroethane afforded **17** in 94% yield.

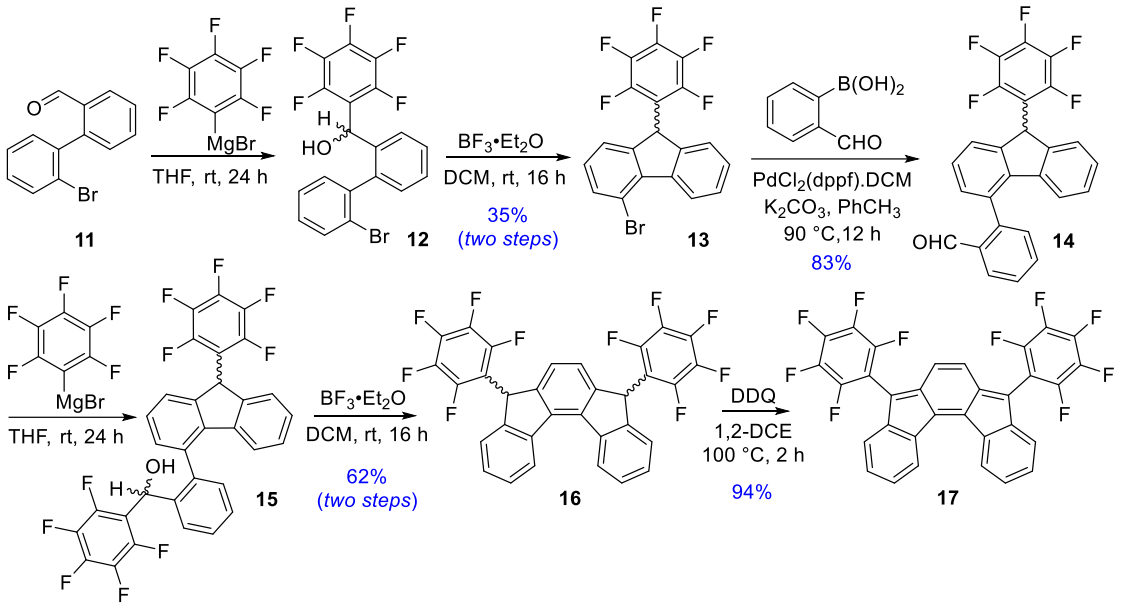

Scheme 2B.1 Synthesis of new symmetrically disubstituted [2,1-*c*]IF **17**.

We then turned our attention to make the unsymmetrically disubstituted [2,1-*c*]IF derivatives **7**, **8** and **9**. Nucleophilic addition of Grignard/ethynyllithium reagents like C_6F_5MgBr, [3,5-bis(trifluoromethyl)phenyl]magnesium bromide, and [(triisopropylsilyl)ethynyl]lithium (TIPSELi) to our pre-synthesized aldehyde **18**[8] afforded the three different carbinols **19**, **21**, and **23**, respectively (Scheme 2B.2). These carbinols were further treated with $BF_3{\cdot}Et_2O$ to afford the dihydro precursors **20**, **22**, and **24**, respectively. Conversion of **23** to **24** was accompanied with partial formation of **9**. Nevertheless, DDQ-mediated oxidative dehydrogenation of **20**, **22** and crude **24** proceeded smoothly (in different solvents) to afford **7**, **8**, and **9**, respectively, which are confirmed by NMR spectroscopy (*vide infra*), including single crystal X-ray analyses for **7**, **9**, and **17**.

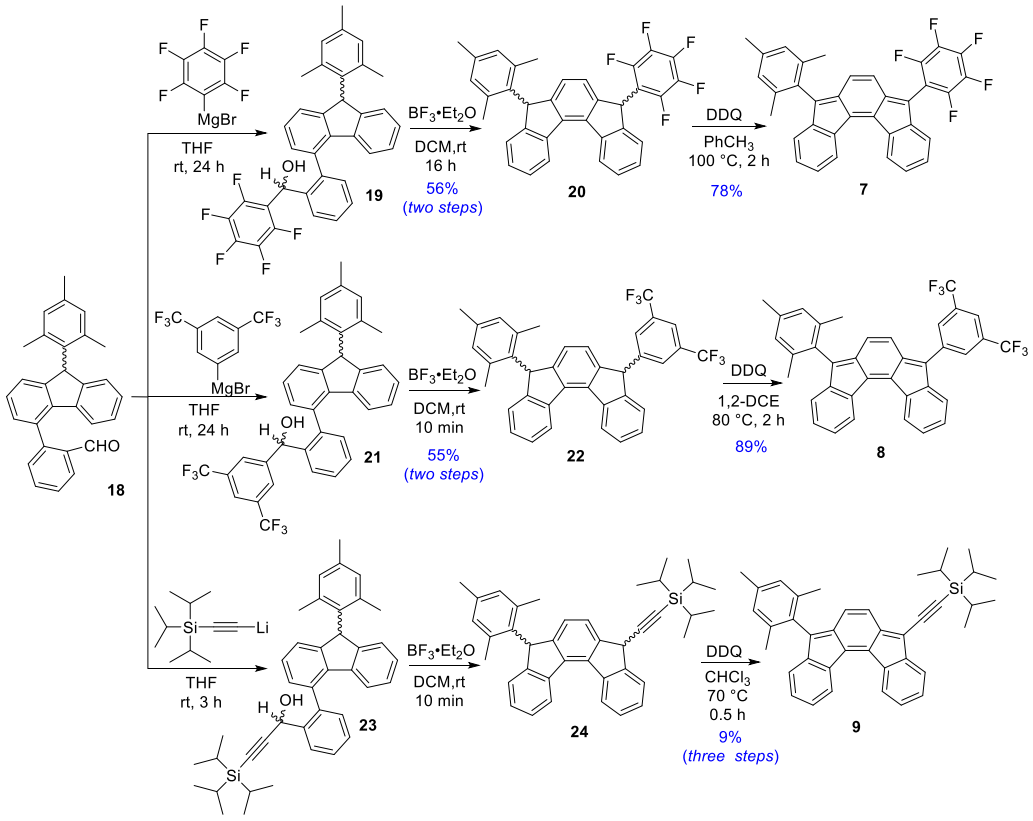

Scheme 2B.2 Syntheses of the unsymmetrically disubstituted [2,1-*c*]IFs **7**, **8**, **9.**

Unlike our steric approach to synthesize [1,2-*b*]IF that required mesityl as a bulky substituent,[7] the current approach can be used to attach less bulky donors (like: 4-methoxyphenyl) to afford push-pull dyes. Compound **10** was synthesized using the analogous synthesis approach (Scheme 2B.3) that started with a nucleophilic addition of (4-methoxyphenyl)magnesium bromide to aldehyde **11** to afford **25**. Treating **25** with triflic acid at room temperature gave **26**, which underwent Suzuki cross-coupling reaction with (2-formylphenyl)boronic acid to give **27** in 75% yield. Nucleophilic addition of 3,5-$(CF_3)_2C_6H_3$-MgBr to **27**, followed by $BF_3{\cdot}OEt_2$ treatment afforded the dihydro-precursor **29** in 61% yield over two steps. Finally, treatment of **29** with excess of DDQ in toluene afforded **10** with donor and acceptor[14] substituents in moderate yield.

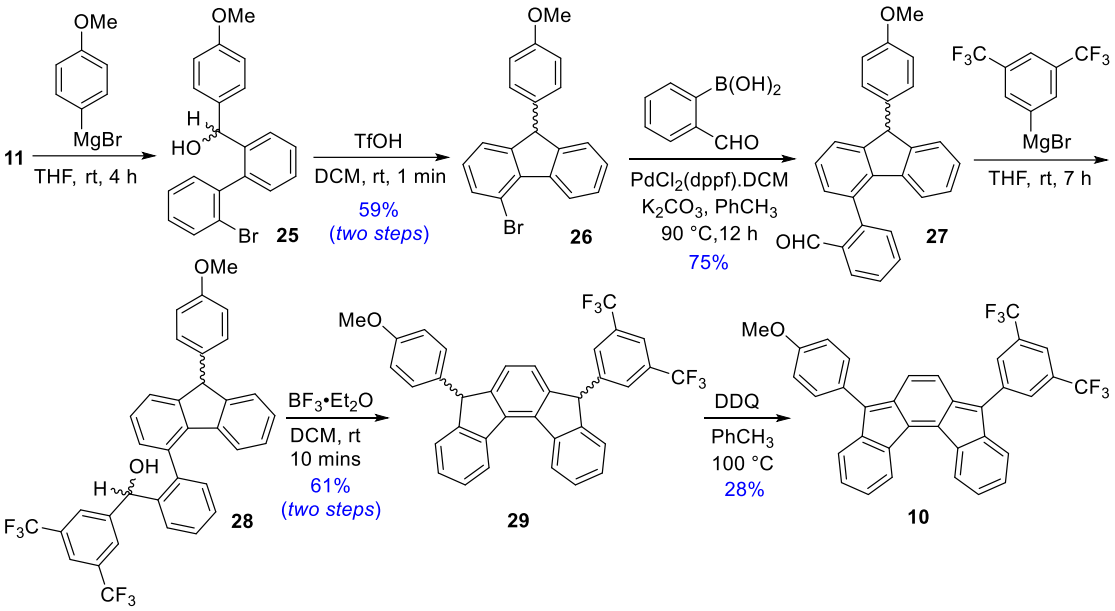

Scheme 2B.3 Synthesis of a push-pull disubstituted [2,1-*c*]IF **10**.

2B.3.2 Single crystal analysis

Single crystals for **7**, **9** and **17** were grown successfully, and analyzed. The X-ray crystallographic analysis showed a nearly planar [2,1-*c*]IF backbone for **7** (Figure 2B.2a, CCDC 2117444) with the outer benzenoid ring (near to C_6F_5) twisted by 7.0° from the average plane of cyclopenta[*c*]fluorene subunit. Compound **9** (Figure 2B.2c, CCDC 2117445) packs in two independent arrangements with 12.9° and 13.6° twist angles, suggesting subtle *P*/*M*-like helicity with a very small 0.48 kcal/mol *P*/*M*-interconversion barrier (*vide infra*).[1]

The mesityl group is found to be near orthogonally oriented to the [2,1-*c*]IF backbone (dihedral angle 86.9°-89.7° for **7** and **9**), while the other aryl/ethynyl groups suggest better π-delocalization trend on moving from C_6F_5 in **7** (a reduced dihedral angle ~ 52.6°) to TIPSE in **9** (co-planar). The bond-lengths of the [2,1-*c*]IF backbones clearly suggested a *para*-quinoidal arrangement of the *as*-indacene[1,7,8] (C=C double bond distances are shown in Figure 2B.2a, 2B.2b and 2B.2c) for all the derivatives, including homogeneous C_{sp}^2-C_{sp}^2 bond length distributions in the outer benzenoid rings for **7**, **9**, and **17**, which clearly imply benzene aromaticity for outer six-membered rings.[1,7]

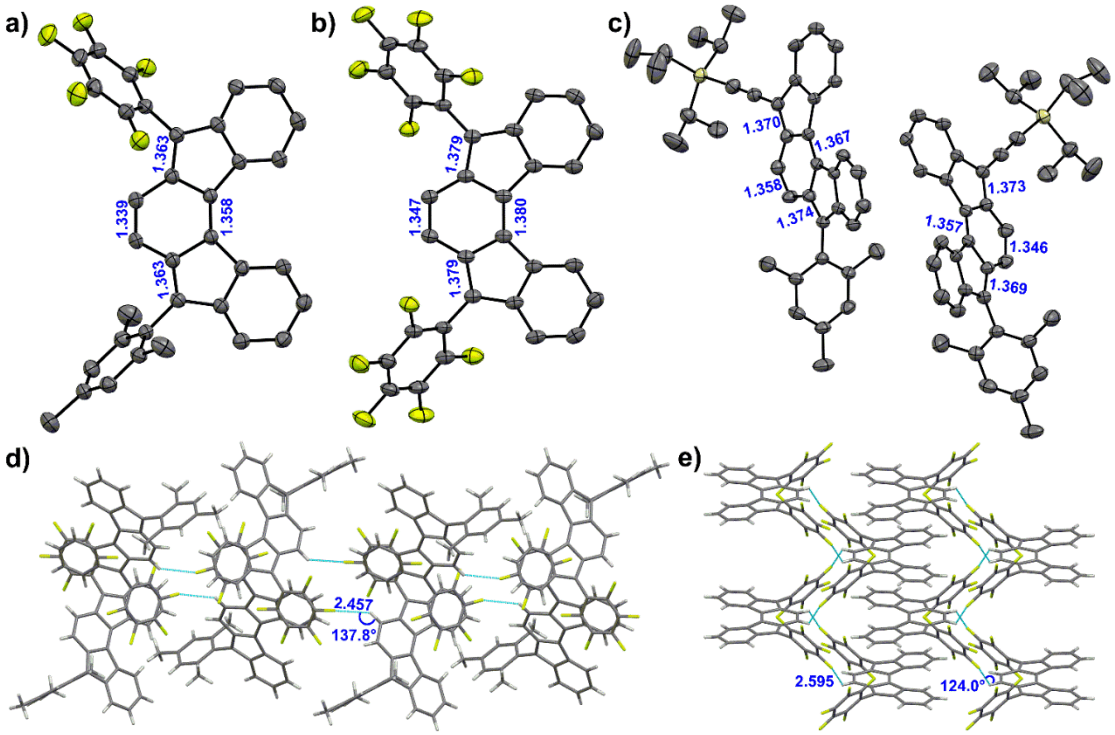

Figure 2B.2 ORTEP drawing of (a) **7**, (b) **17**, and (c) **9** (left: *P*-isomer; right: *M*-isomer) at 30% probability level (hydrogen omitted), with the C=C bond distances (in Å) of *p*-quinodimethane unit are shown. The packing motifs for (d) **7** and (e) **17** showing the intermolecular F···H-C_{sp^2} hydrogen bonds (in Å) and its (∠C_{sp^2}–H···F) angles.

X-ray crystallographic analysis of **7** has shown several close contacts in the solid-state (Figure 2B.3) with intermolecular non-covalent interactions between $C_{(9)}$-$C_{(5)}$ (3.238 Å, π-π) and $C_{(4)}$–$F_{(4)}$···$C_{(15)}$ (3.137 Å, C-F···π) centers of the C_6F_5 and [2,1-*c*]IF π-rings, including two intermolecular $C_{(20)}$–$H_{(20)}$···$C_{(18)}$ and $C_{(9)}$–$H_{(9)}$···$C_{(34)}$ C-H···π interactions (2.859 Å) between the [2,1-*c*]IF backbones and strong intermolecular C_{sp^2}-$F_{(2)}$···$H_{(34)}$-C_{sp^2} hydrogen bonding interaction measuring 2.457 Å (the value is less than the sum of the van der Waals radii of F and H = 2.67 Å)[17] with ∠C_{sp^2}–H···F = 137.8°, affording a herringbone-like packing arrangement (Figure 2B.3) with an one-dimensional columnar stack featuring the C_6F_5 unit partly, cofacially, π-stacking (3.238 Å) with the outer ring of IF (Figure 2B.2d). The hydrogen-bond distance and bond-angle meet the geometrical requirements for intermolecular hydrogen bonding interactions.[18]

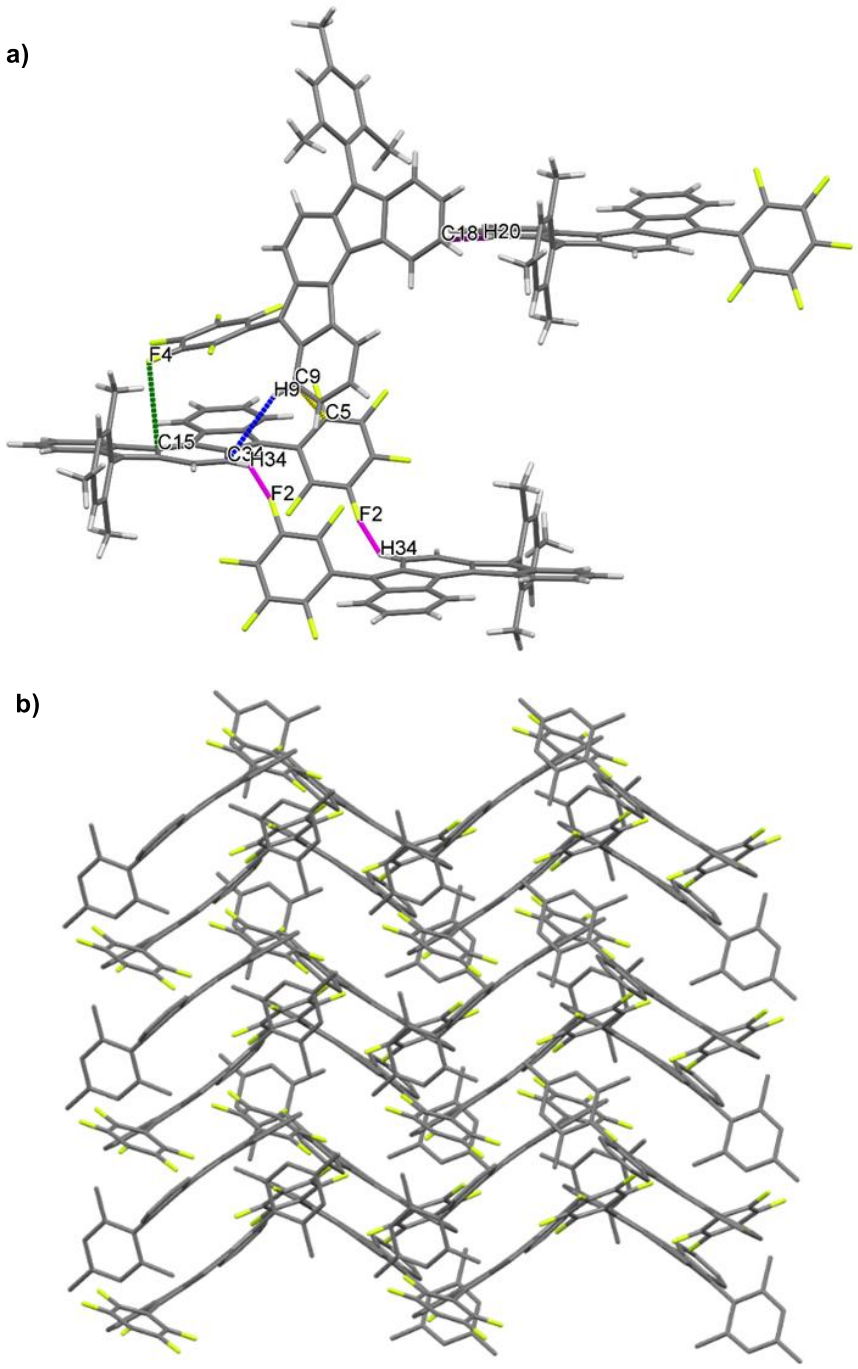

Figure 2B.3 (a) Short intermolecular contacts for **7** and (b) its herringbone-like packing motif.

The H···F-C_{sp}^2 hydrogen bond interaction is critical in formation of supramolecular assembly for calixphyrins[19] or antiaromatic isophlorins,[20] however, from the perspective of diradicaloid polycyclic hydrocarbons[11] including antiaromatic IFs,[2,16,21] H···F-C hydrogen bonding interactions received seldom attention. In comparison to **7**, symmetrical **17** (CCDC 2117446) displayed weaker intermolecular $F_{(3)}\cdots H_{(8)}$-$C_{(8)}$ (2.595 Å, $\angle C_{sp}^2$–H···F = 124.0°) hydrogen bonding interactions in an one-dimensional columnar arrangement featuring two IF backbones π-stacking at 3.574

Å, cofacially, at about a point of inversion (Figure 2B.2e), implying strong intermolecular π-π interaction (Figure 2B.4).

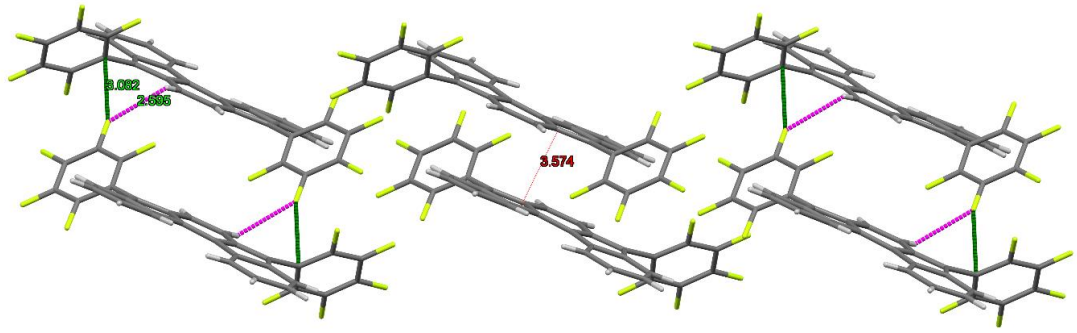

Figure 2B.4 Bifurcated C-F…C_π (3.082 Å) and F···H-C_{sp}^2 (2.595 Å) interactions of **17**, including interplanar distance between two cofacially stacked IFs that imply π-π interaction.

2B.3.3 Optical and electrochemical properties

All new [2,1-*c*]IF derivatives displayed strong absorbance in the higher energy (UV-vis) region and a broad absorption in the lower energy (visible) region extending to 800 nm (Figure 2B.5), except for **10** that has extended to 840 nm in the near-infrared region. Symmetrical diarylation/ethynylation at the 5/8 positions to tune optoelectronic properties[1] seems logical by the calculated HOMO/LUMO plots (Figure 2B.1c) which show considerable orbital density at the apical carbons. It is thus expected that unsymmetrical aryl/aryl or aryl/ethynyl di-substitution could be a realistic step to fine-tune the optoelectronic properties. The source of the broad low energy absorption band was predicted by the time dependent density functional theory (TDDFT) calculations as $\pi \rightarrow \pi^*$ electronic transitions, originating from admixture of the HOMO→LUMO and HOMO-1→LUMO transitions in the singlet closed-shell ground state (Table 2B.1-2B.5). The absorption profiles were also characteristically similar to the symmetrically 5,8-disubstituted [2,1-*c*]IF derivatives,[1] with **17** being the newest entry with λ_{max} = 616 nm (theoretical λ_{max} = 746 nm, oscillator strength (*f*) = 0.1056, Table 2B.5).

Table 2B.1 TDDFT electronic transitions for **7** at B3LYP/6-31G(d,p) level of theory.

Wavelength (nm)	Oscillator Strength	Major contributions
719.5	0.1052	H-1->LUMO (11%), HOMO->LUMO (88%)
462.9	0.0817	H-2->LUMO (69%), H-1->LUMO (25%)

457.6	0.2321	H-3->LUMO (18%), H-2->LUMO (19%), H-1->LUMO (49%)
436.9	0.0388	H-3->LUMO (78%), H-2->LUMO (10%)
419.5	0.0012	H-4->LUMO (97%)
357.2	0.0038	H-5->LUMO (96%)
351.1	0.207	H-6->LUMO (32%), HOMO->L+1 (55%)
346.9	0.362	H-6->LUMO (61%), HOMO->L+1 (28%)
332.7	0.0562	H-7->LUMO (81%)
317.0	0.0426	HOMO->L+2 (81%)
298.3	0.0024	HOMO->L+3 (97%)
294.8	0.1222	H-8->LUMO (83%)
284.0	0.0314	H-2->L+1 (15%), HOMO->L+4 (72%)
282.5	0.0379	HOMO->L+5 (89%)
278.4	0.0129	H-9->LUMO (78%)
271.9	0.3998	H-9->LUMO (10%), H-1->L+1 (75%)
265.3	0.0323	H-2->L+1 (22%), HOMO->L+6 (45%), HOMO->L+7 (16%)
263.5	0.0218	H-2->L+1 (21%), HOMO->L+6 (53%), HOMO->L+7 (14%)
260.1	0.0046	H-3->L+1 (66%), H-2->L+1 (14%)
257.9	0.0107	H-11->LUMO (92%)

Table 2B.2 TDDFT electronic transitions for **8** at B3LYP/6-31G(d,p) level of theory.

Wavelength (nm)	Osc. Strength	Major contributions
724.9	0.1197	H-1->LUMO (11%), HOMO->LUMO (88%)
462.4	0.1698	H-2->LUMO (45%), H-1->LUMO (47%)
457.5	0.1362	H-3->LUMO (24%), H-2->LUMO (35%), H-1->LUMO (28%)
438.6	0.0395	H-3->LUMO (66%), H-2->LUMO (18%)
422.3	0.0012	H-4->LUMO (91%)
372.6	0.0054	HOMO->L+1 (98%)
357.8	0.4204	HOMO->L+2 (85%)
340.1	0.09	H-5->LUMO (79%), HOMO->L+3 (10%)
335.0	0.0851	HOMO->L+3 (75%)
320.5	0.1959	H-6->LUMO (84%)
294.6	0.0019	H-7->LUMO (95%)
289.4	0.0614	H-8->LUMO (43%), HOMO->L+4 (39%)
285.8	0.0085	H-8->LUMO (38%), HOMO->L+4 (35%)
283.2	0.0385	H-1->L+1 (45%), HOMO->L+5 (47%)
282.9	0.0132	H-1->L+1 (51%), HOMO->L+5 (42%)
277.4	0.0695	H-9->LUMO (58%), H-1->L+2 (28%)
272.5	0.3234	H-9->LUMO (22%), H-1->L+2 (52%)

267.7	0.0116	H-3->L+1 (12%), H-2->L+1 (38%), H-1->L+3 (18%)
266.9	0.0097	H-3->L+1 (12%), H-2->L+1 (27%), H-1->L+3 (38%)
266.0	0.0256	H-1->L+3 (27%), HOMO->L+6 (36%), HOMO->L+7 (13%)

Table 2B.3 TDDFT electronic transitions for **9** at B3LYP/6-31G(d,p) level of theory.

Wavelength (nm)	Osc. Strength	Major contributions
742.4	0.1516	H-1->LUMO (13%), HOMO->LUMO (87%)
473.1	0.216	H-2->LUMO (33%), H-1->LUMO (48%)
464.9	0.1524	H-2->LUMO (64%), H-1->LUMO (29%)
437.7	0.0282	H-3->LUMO (91%)
419.2	0.0011	H-4->LUMO (99%)
369.6	0.0006	H-6->LUMO (90%)
359.5	0.5783	HOMO->L+1 (82%)
357.8	0.0724	H-5->LUMO (85%)
335.8	0.015	H-7->LUMO (84%)
311.4	0.0876	H-8->LUMO (87%)
298.9	0.0009	H-9->LUMO (93%)
291.5	0.0476	H-2->L+1 (11%), HOMO->L+2 (72%)
290.6	0.0145	HOMO->L+3 (97%)
285.7	0.031	H-11->LUMO (10%), H-10->LUMO (78%)
277.0	0.4924	H-1->L+1 (72%), HOMO->L+5 (10%)
272.8	0.0539	H-11->LUMO (31%), H-2->L+1 (11%), HOMO->L+4 (17%), HOMO->L+5 (22%), HOMO->L+6 (11%)
271.6	0.0072	H-11->LUMO (15%), HOMO->L+4 (72%)
269.9	0.0219	HOMO->L+7 (86%)
265.7	0.0702	H-2->L+1 (27%), HOMO->L+5 (20%), HOMO->L+6 (25%)
261.7	0.0889	H-11->LUMO (18%), HOMO->L+5 (34%)

Table 2B.4 TDDFT electronic transitions for **10** at B3LYP/6-31G(d,p) level of theory.

Wavelength (nm)	Osc. Strength	Major contributions
755.3	0.1708	H-1->LUMO (11%), HOMO->LUMO (88%)
482.5	0.3436	H-1->LUMO (79%)
460.8	0.0732	H-3->LUMO (14%), H-2->LUMO (74%)
411.3	0.0799	H-3->LUMO (79%), H-2->LUMO (11%)
383.6	0.0046	HOMO->L+1 (98%)

368.7	0.4271	HOMO->L+2 (83%)
345.4	0.084	H-5->LUMO (16%), HOMO->L+3 (72%)
341.1	0.0296	H-4->LUMO (83%)
339.4	0.0401	H-5->LUMO (70%), H-4->LUMO (10%), HOMO->L+3 (11%)
319.6	0.1508	H-6->LUMO (81%)
304.4	0.0145	HOMO->L+4 (95%)
296.2	0.0024	H-7->LUMO (95%)
294.3	0.0172	HOMO->L+5 (68%)
289.4	0.0904	H-8->LUMO (25%), HOMO->L+6 (54%)
287.3	0.0124	H-1->L+1 (86%)
287.0	0.1692	H-9->LUMO (13%), H-8->LUMO (42%), HOMO->L+6 (25%)
277.4	0.1034	H-9->LUMO (21%), H-1->L+2 (50%), HOMO->L+6 (16%)
275.4	0.0993	H-9->LUMO (38%), H-2->L+2 (12%), H-1->L+2 (16%), HOMO->L+7 (12%)
270.9	0.0389	H-9->LUMO (14%), H-1->L+3 (53%)
269.5	0.0102	H-2->L+1 (82%), H-1->L+3 (10%)

Table 2B.5. TDDFT electronic transitions for **17** at B3LYP/6-31G(d,p) level of theory.

Wavelength (nm)	Osc. Strength	Major contributions
746.8	0.1056	H-1->LUMO (13%), HOMO->LUMO (87%)
476.0	0.0249	H-2->LUMO (93%)
472.4	0.3843	H-1->LUMO (77%), HOMO->LUMO (10%)
373.9	0.002	H-3->LUMO (99%)
372.8	0.0025	H-4->LUMO (99%)
361.5	0.0862	H-5->LUMO (94%)
356.7	0.0642	H-6->LUMO (96%)
347.3	0.4938	HOMO->L+1 (88%)
335.4	0.0001	H-7->LUMO (81%), HOMO->L+2 (15%)
315.4	0.1057	H-7->LUMO (12%), HOMO->L+2 (82%)
308.1	0.044	HOMO->L+3 (85%)
296.5	0.067	H-8->LUMO (74%)
292.3	0.0027	HOMO->L+4 (96%)
291.9	0.002	HOMO->L+5 (96%)
281.2	0.0082	H-9->LUMO (70%), H-1->L+1 (14%)
280.6	0.0218	H-2->L+1 (24%), HOMO->L+6 (68%)
270.5	0.407	H-9->LUMO (11%), H-1->L+1 (75%)
263.1	0.0182	H-2->L+1 (31%), H-1->L+2 (27%), HOMO->L+7 (20%)
259.3	0.0625	H-1->L+2 (68%), HOMO->L+7 (16%)
256.3	0.0087	H-11->LUMO (96%)

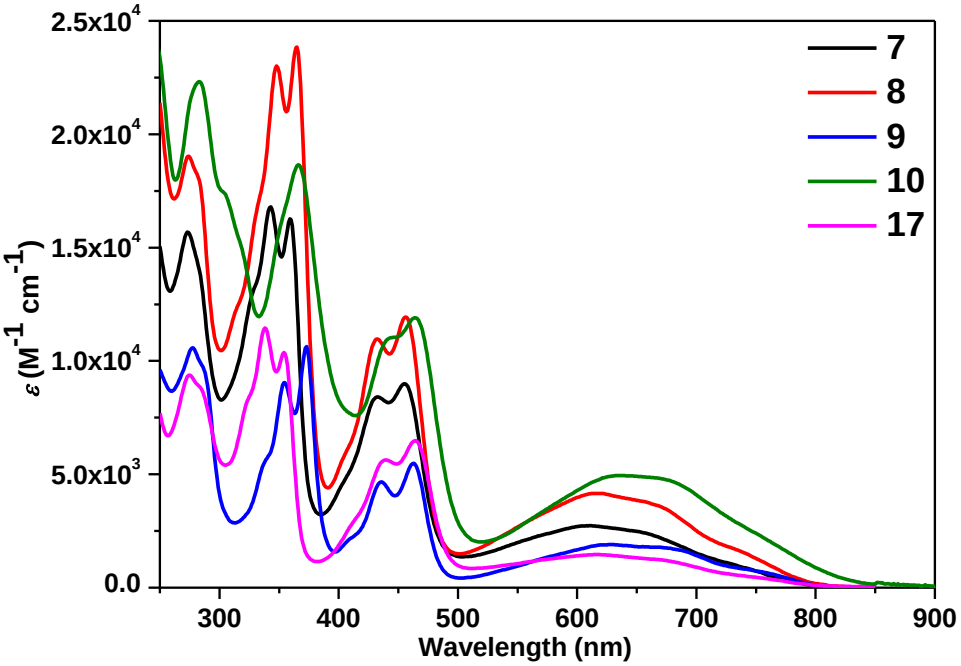

Figure 2B.5 UV-Vis-NIR absorption plots of the new [2,1-*c*]IFs in $CHCl_3$.

To our expectation, the absorption maxima for **8** are found to lie in between those of **1** and **2**, and similarly for **9** (between the **1** and **3**) as well as **7** (between the **1** and **17**). The red-shift in absorption band (λ_{max} = 610 nm, ε = 2780 M^{-1} cm^{-1}) with theoretical f = 0.1052 (719 nm, Table 2B.1) for **7** in the visible region, in comparison to **1**, can be attributed to some electronic communication between the C_6F_5 and [2,1-*c*]IF π-rings due to the decrease in dihedral angle (observed for crystals). This observation is also supported by the DFT studies with a reduced dihedral angle ca. 52-53° for **7**, in comparison to the orthogonally oriented mesityl group. The lower energy absorption maximum is further red-shifted for **8** (λ_{max} = 615 nm, ε = 4170 M^{-1} cm^{-1}; f = 0.1197 at 724 nm, Table 2B.2), suggesting a better π-delocalization between the 3,5-bis(trifluoromethyl)phenyl and [2,1-*c*]IF π-rings due to a further reduction of the dihedral angle (ca. 44-46° for **8** at B3LYP/6-31G(d,p)) including stronger electron-withdrawing effect. Further improvement in the electronic communication between the coplanar TIPSE and [2,1-*c*]IF core in **9** is reflected by the more red-shifted absorption (λ_{max} = 625 nm, ε = 1880 M^{-1} cm^{-1}; f = 0.1516 at 742 nm, Table 2B.3) and a smaller optical HOMO-LUMO energy gap of 1.52 eV than that of **7** (E_g^{opt} = 1.56 eV) or **8** (E_g^{opt} = 1.55 eV).

Compound **10** showed the smallest optical energy gap (E_g^{opt} = 1.47 eV) with a red-shifted low-energy absorption band (λ_{max} = 640 nm, ε = 4940 M^{-1} cm^{-1}; f = 0.1708

at 755 nm, Table 2B.4), with the absorption tail reaching to the near-IR region. A weak but non-negligible blue-shift (~10 nm) of the low-energy wavelength maximum for **10** was noticed by changing solvent from polar $CHCl_3$ to non-polar hexane (Figure 2B.6), which is suggesting intramolecular charge transfer (ICT) character due to a better push-pull interaction between the 4-methoxyphenyl (electron-donor) and 3,5-$(CF_3)_2C_6H_3$ (electron-acceptor)[14] substituents through *as*-indacene backbone. However, no obvious change in absorption profile was noticed by changing the solvent polarity for **8** (Figure 2B.7), indicating negligible ICT interaction due to weakly electron-donating mesityl group. Compounds **7**, **8**, **9**, **10** and **17** are found to be non-emissive, a common trait for antiaromatic [2,1-*c*]IF.[22]

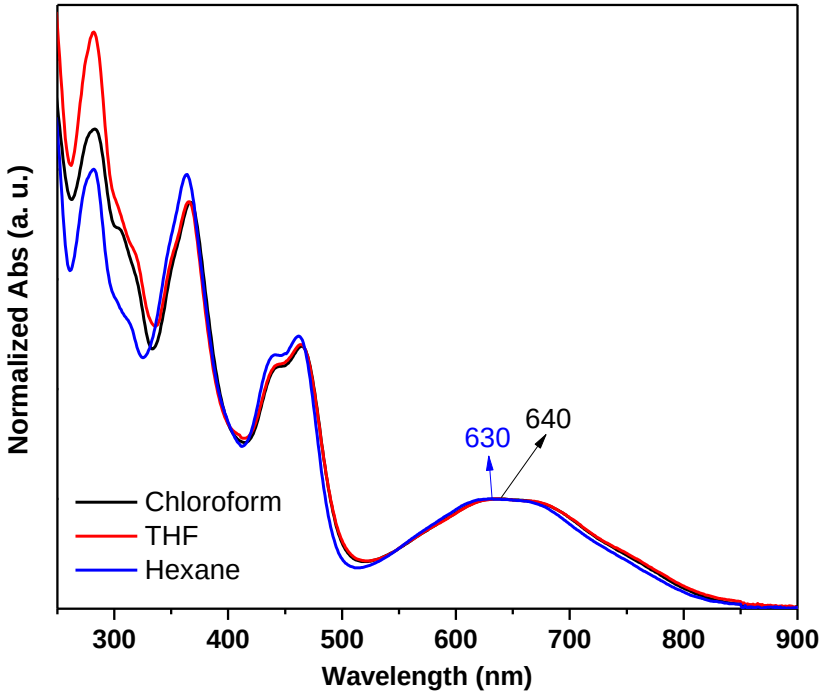

Figure 2B.6 UV-vis spectra for **10** as solution in solvents with different polarity.

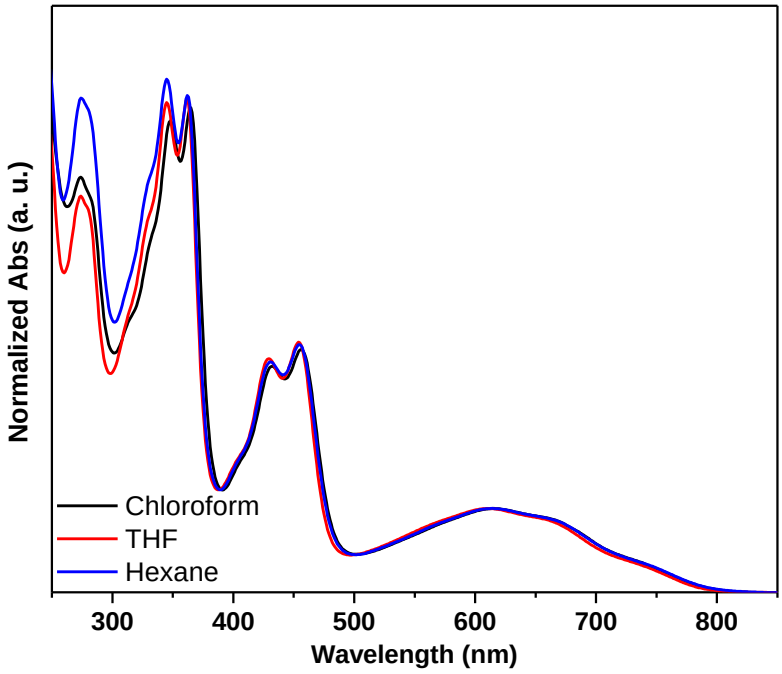

Figure 2B.7 UV-vis spectra for **8** as solution in solvents with different polarity.

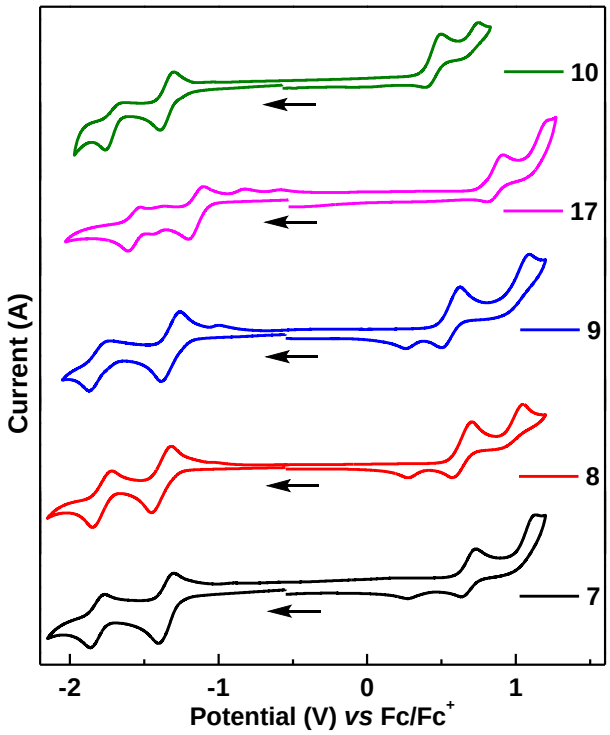

Figure 2B.8 IUPAC representation of cyclic voltammograms of new [2,1-*c*]IF derivatives (0.001 M) taken at 298 K, in dry and degassed dichloromethane with 0.1 M Bu_4NPF_6 under nitrogen atmosphere. All data were collected using Pt-disk electrode as a working electrode, Pt wire as a counter electrode and Ag/AgCl as a reference electrode. Scan direction (toward negative potential first, and then going to positive potential) is shown using arrow.

The unsymmetrical [2,1-*c*]IFs accept two electrons quasi-reversibly, and they are quasi-reversibly oxidized to a radical cation, and further, quasi-reversibly to the dications (Figure 2B.8, Table 2B.6). It was noticed that if current was swept through the second reduction for **9** and **17**, and second oxidation for **7**, **8** and **9**, new peaks (as bumps) appeared on their return during the cathodic and anodic scans. Such peaks were not observed if the current is not swept past the first reduction and oxidation potentials (Figure 2B.9b), indicating likely formation of some reactive species during second reduction and oxidation.

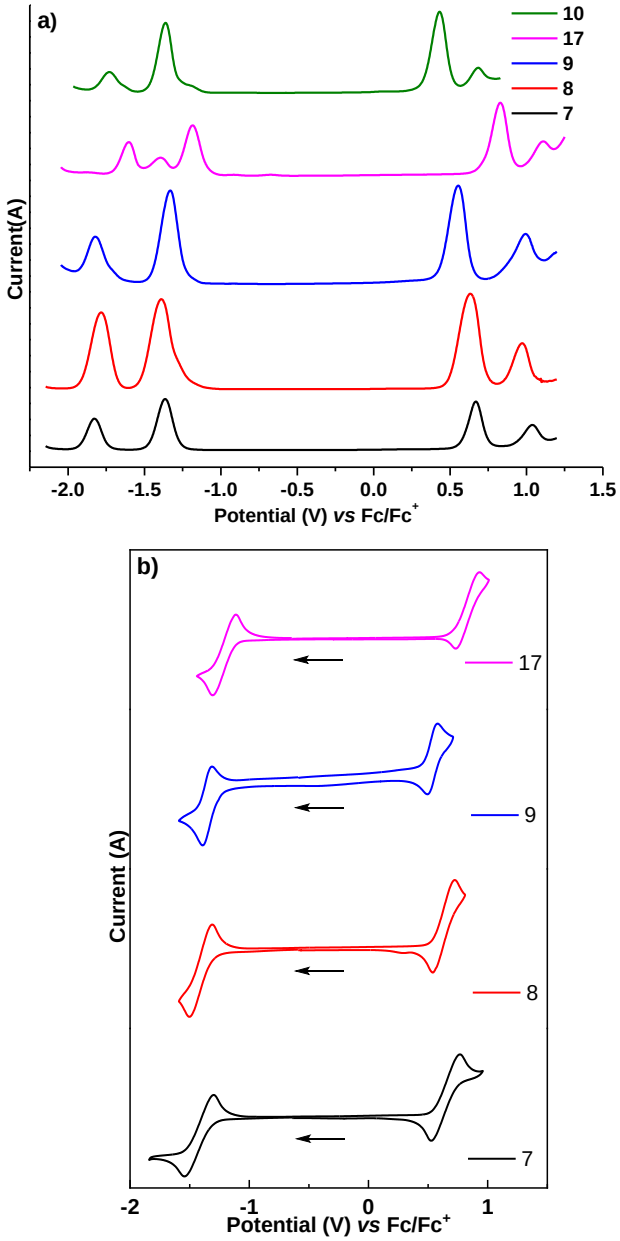

Figure 2B.9 (a) Differential pulse voltammograms (DPV) of the [2,1-*c*]IFs (0.001 M). (b) CVs of **7**, **8**, **9** and **17** (0.001 M) up to their first oxidation and reduction potentials, showing absence of any peaks/bumps which were observed in Figure 2B.8 on their return for both anodic and cathodic sweeps when oxidized or reduced to their second oxidation and reduction potentials.

All data were collected at 298 K, in dry and degassed dichloromethane with 0.1 M Bu_4NPF_6 under nitrogen atmosphere, using Pt-disk electrode as a working electrode, Pt wire as a counter electrode and Ag/AgCl as a pseudo-reference electrode. Scan direction (toward negative potential first, and then going to positive potential) is shown using arrow.

Table 2B.6 Summary of photophysical and electrochemical data for **7**, **8**, **9**, **10** and **17**.[a]

Comp	$E_{1/2}^{red}$ [V]	$E_{1/2}^{ox}$ [V]	HOMO [eV]	LUMO [eV]	E_g^{ec} [eV]	λ_{abs} [nm]	ε [M^{-1} cm^{-1}]	E_g^{opt} [eV]	E_g^{DFT} [eV]
7	–1.36 –1.83	0.66 1.04	–5.35	–3.59	1.76	610, 454, 431, 359, 342, 272	2780, 9040, 8410, 16330, 16870, 15740	1.56	2.18
8	–1.39 –1.78	0.63 0.97	–5.33	–3.58	1.75	615, 456, 432, 364, 347, 273	4170, 11930, 10960, 23880, 22990, 19000	1.55	2.15
9	–1.32 –1.82	0.55 0.99	–5.24	–3.65	1.59	625, 462, 435, 372, 354, 277	1880, 5490, 4620, 10590, 9000, 10560	1.52	2.03
10	–1.36 –1.73	0.43 0.68	–5.16	–3.62	1.54	640, 464, 445, 366, 283	4940, 11910, 11040, 18650, 22330	1.47	2.02
17	–1.16 –1.37 –1.58	0.84 1.12	–5.51	–3.80	1.71	616, 464, 439, 354, 338, 274	1450, 6470, 5640, 10390, 11450, 9350	1.53	2.11

[a]λ_{abs} = Absorption maxima; ε = Molar extinction coefficient for the corresponding absorption maximum; $E_{1/2}$ = Half-wave potentials (first and second) for oxidative and reductive waves against the Fc/Fc^+ couple; HOMO = $-(4.8+E_{ox}^{onset})$ and LUMO = $-(4.8+E_{red}^{onset})$; E_g^{ec} = Electrochemical HOMO-LUMO energy gap; E_g^{opt} = Optical HOMO-LUMO energy gap

calculated from the onset absorption wavelength; E_g^{DFT} = Theoretical HOMO-LUMO energy gap.

The first half-wave ($E_{1/2}$) oxidation potential, obtained from differential pulse voltammogram peak values (Figure 2B.9a), at $E_{1/2}^{ox1}$ = 0.66 V (*vs.* ferrocene/ferrocenium (Fc/Fc^+) for **7** is the highest among the unsymmetrical motifs, and **8** and **9** appeared at $E_{1/2}^{ox1}$ = 0.63 V and 0.55 eV, respectively, while **10** showed the smallest value at $E_{1/2}^{ox1}$ = 0.43 V. Compound **9** appears to be a comparatively better electron-acceptor with a low first half-wave reduction potential at $E_{1/2}^{red1}$ = –1.32 V, than **7** or **10** with $E_{1/2}^{red1}$ = –1.36 V and **8** with $E_{1/2}^{red1}$ = –1.39 V. The estimated electrochemical HOMO-LUMO energy gaps (E_g^{ec}) are 1.54 eV for **10**, 1.56 eV for **9**, 1.75 eV for **8**, and 1.76 eV for **7**. Symmetrical **17** could be oxidized at high potential $E_{1/2}^{ox1}$ = 0.84 V, and reduced at a much lower reduction potential $E_{1/2}^{red}$ = –1.16 V with an estimated E_g^{ec} = 1.71 eV.

2B.3.4 Space charge limiting current (SCLC) studies

The trend of optical and electrochemical energy gaps for **7**, **8**, **9**, **10** and **17** are consistent with the theoretical HOMO-LUMO energy gaps (Table 2B.6). The low-lying LUMO of **17** (–3.80 eV) and improved solid-state packing interaction suggested its potential as a good electron-transporter, however, the amphoteric redox waves[23] observed for these new IFs prompted us to investigate both hole and electron transport behavior for a [2,1-*c*]IF series **1**, **7** and **17**. Since reports suggest that possibly the device architecture in solar cells may not appropriately fit with the transistor mobility,[24] the more relevant[25] SCLC method was adopted by us to measure the charge-carrier mobility (*vide infra*), in order to find the potential for these new molecules as new semiconductors for organic electronic devices.

The charge carrier mobilities of compounds **1**, **7**, **8** and **17** were determined from the current-voltage characteristic of devices having hole (ITO/PEDOT:PSS/**1**,**7**, **8** and **17**/MoO_3/Ag) and electron only (ITO/SnO_2/**1**,**7**, **8** and **17**/Al) architecture. The charge carrier mobility is determined from fitting the *J*-*V* characteristics with semi-log plot for compounds **1**, **7**, **8** and **17** using the modified Mott-Gurney equation given by[26]:

$$J = \frac{9}{8}\mu\varepsilon_r\varepsilon_o\frac{V^2}{d^3}\exp\left(0.891.\gamma.\sqrt{V/d}\right) \qquad (1)$$

where *J* is measured as current density, ε_o is the permittivity of free space (8.86×10^{-14} F/cm), ε_r is relative dielectric constant of the material, *V* is applied voltage, *d* is the

thickness of the active layer of material, μ is mobility, γ is the fitting parameter representing the strength of the field dependence on mobility. The extracted mobilities of the compounds are summarized in Table 2B.7.

Table 2B.7 Summary of SCLC hole and electron mobilities.

Compounds	Mobility ($cm^2 \cdot V^{-1} \cdot s^{-1}$)		
	Hole (x 10^{-3})	Electron (x 10^{-3})	μ_e/μ_h
1	1.27 ± 0.23	2.20 ± 1.37	1.73
7	1.80 ± 0.82	7.26 ± 5.12	4.03
8	1.47 ± 0.30	3.82 ± 3.04	2.60
17	1.64 ± 0.50	8.66 ± 2.89	5.28

The *J-V* characteristics for compounds **1**, **7**, **8** and **17** are shown in Figure 2B.10. From the SCLC mobilities shown in Table 2B.7, it is evident that the known compound **1**, and the new compounds **7**, **8** and **17** showed ambipolarity for charge carrier transport where for both hole and electron order of the observed charge carrier mobility is same. Overall, for a device application, material having balanced electron and hole mobility is preferred.[27] In these reported compounds, the closeness order for the balanced ambipolar compound is found to be in order **17** < **7** < **8** < **1**, which seems reasonable considering appreciable intermolecular interactions observed in the solid state for **7** and **17** resulted in a better charge-transport properties. On the other hand, compound **1** with bulkier mesityl substituents lacks any appreciable intermolecular π-π interactions,[1,2e] unlike **17**, affording relatively low SCLC mobilities than those of **17** or **7**. Nonetheless, the charge-transport behavior of unsymmetrical **7** lie nearly halfway in between its symmetrical counterparts **1** and **17** (Table 2B.7). The observed higher electron mobility for compound **17** can be attributed to its favorable energy level alignment in electron only devices with aluminium and a better intermolecular π-π interaction when compared with compound **1** and **7**.

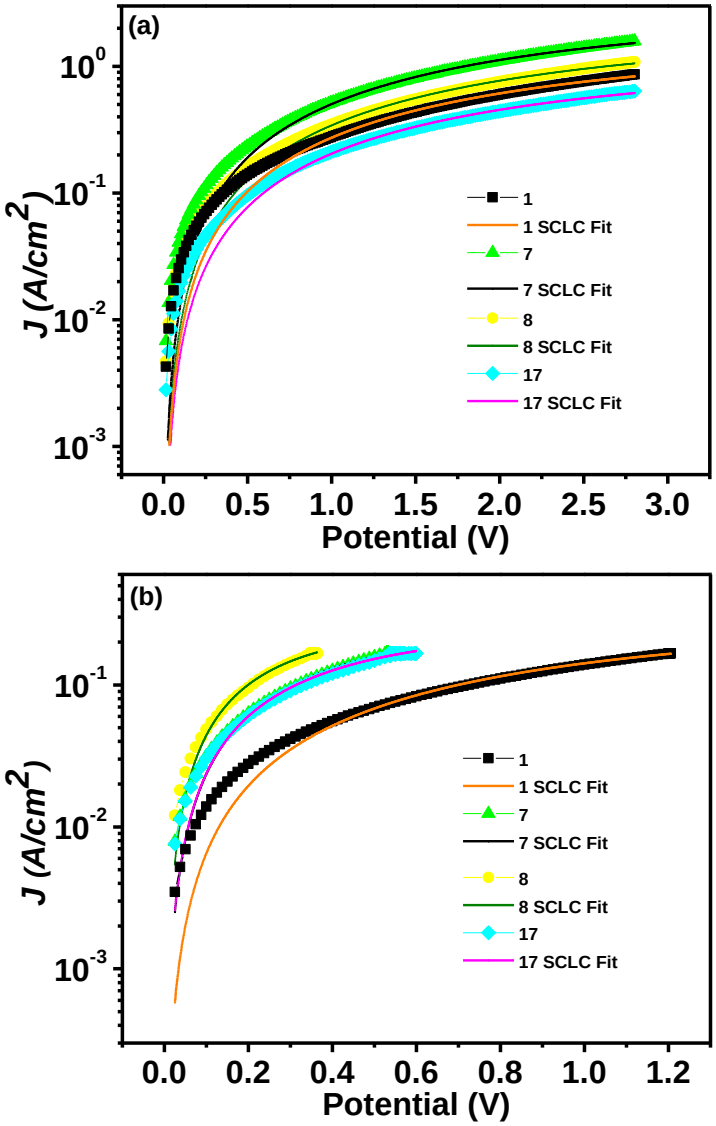

Figure 2B.10 *J-V* characteristics in semi-log plot used for extracting (a) hole and (b) electron mobilities using modified Mott Gurney SCLC equation for compounds **1**, **7**, **8**, and **17**.

It is worth noting that SCLC mobilities of organic semiconductor thin films are much lower in comparison to the field-effect mobility, usually within 10^{-6} to 10^{-4} cm^2 V^{-1} s^{-1}.[28] Although sulfur-embedded small polycyclic aromatic system was reported to show good SCLC hole mobility (8.72×10^{-2} cm^2 V^{-1} s^{-1}),[25a] hydrocarbon motifs like antiaromatic diareno-pentalene showed low hole-carrier mobility (4.37×10^{-4} cm^2 V^{-1} s^{-1}) under SCLC method.[29] Considering [2,1-*c*]IF as a benzo-interpositioned[30] pentalene system, our studies on the symmetrical or unsymmetrical [2,1-*c*]IFs **1**, **7**, **8** and **17** π-systems revealed an order of magnitude greater charge-carrier mobility for both hole and electrons. Moreover, a balanced ambipolar charge-transport behavior could be extracted for the first time. It suggests, [2,1-*c*]IF-based antiaromatic systems could be useful candidate for applications in organic optoelectronic devices, and high-

performance materials with proper structural modifications are in the scope of our future studies.

2B.4 Conclusions

In summary, unsymmetrically 5,8-disubstituted [2,1-*c*]IFs **7**, **8**, **9** and a push-pull disubstituted **10**, and a symmetrically 5,8-disubstituted [2,1-*c*]IF **17** were reported for the first time using a synthetic approach that has the potential to generate strongly polarized [2,1-*c*]IFs, as well as heteroatom-modified[31] isoelectronic [2,1-*c*]IF in near future. X-ray crystallographic analyses revealed improved solid-state properties for **7** and **17**, including shorter intermolecular F···H-C_{sp}^2 hydrogen bonding interactions in unsymmetrical **7** (2.457 Å, 137.8°) than that was observed for symmetrical **17** (2.595 Å, 124.0°), and intermolecular π-π interactions. The electronic properties of the unsymmetrical **7**, **8** and **9** lie halfway in between two symmetrically disubstituted [2,1-*c*]IF counterparts. The HOMO-LUMO energy gap of **10** was found to be the smallest due to the ICT character arising from the push-pull effect of apical substituents, implying possibilities to further lowering the energy gap by substituent modification.

Our report of convenient access to fully conjugated [2,1-*c*]IFs bearing desired substituents with balanced ambipolar charge-transport properties for **1**, **7**, **8** and **17** in the order of 10^{-3} cm^2 V^{-1} s^{-1} could open the gateway to previously inaccessible apically extended antiaromatic materials for diverse applications in organic optoelectronics devices. To the best of our knowledge, this is the first systematic study of charge-carrier mobility of antiaromatic [2,1-*c*]IFs bearing symmetrical (**1**, **17**) and unsymmetrical (**7**) disubstitution comprising two particular substituents (mesityl and C_6F_5). Our work distinctly showed the potential of [2,1-*c*]IF scaffolds as efficient charge-transporting materials, one of the fundamental requirements for efficient organic electronic devices, which is in contrast to earlier prediction.[2e] Further exploration of the [2,1-*c*]IF derivatives for optoelectronic applications with focus on transistors and solar cells alongside the unsymmetrical [1,2-b]IF[7] regioisomers is currently being explored.

2B.5 Experimental Section

2B.5.1 General Information

All reagents and chemicals were obtained from commercial sources and used as received. Silica gel (100-200 mesh) was used for column chromatography. NMR spectra, in solution, were recorded on JEOL JNM ECS-400 spectrometer at 298 K.

Chemical shifts (δ) are given in ppm relative to residual solvent (chloroform δ = 7.26 for ^{1}H, and δ = 77.16 for proton-decoupled ^{13}C NMR), and coupling constants (*J*) are expressed in hertz (Hz). Multiplicity is tabulated as s for singlet, d for doublet, dd for doublet of doublet, t for triplet, q for quartet and m for multiplet. High resolution mass spectra (HRMS) were recorded using electron spray ionization (ESI) methods on Waters (XEVO G2-XS QTOF) mass spectrometer. UV-Vis-NIR absorption spectra were recorded as solution, on a JASCO V-770 spectrophotometer. Cyclic voltammetry (CV) measurements were performed in dry dichloromethane at room temperature under nitrogen atmosphere on CHI-1110C instrument electrochemical analyzer with a three-electrode cell, using Bu_4NPF_6 as supporting electrolyte, Ag/AgCl as reference electrode, Pt disk as working electrode, and Pt wire as counter electrode at 50 mV/s scan rate. The potential was externally calibrated against the ferrocene/ferrocenium couple. Melting points were determined using BIBBY-SMP30 melting point analyzer.

2B.5.2 Synthesis

4-Bromo-9-(perfluorophenyl)-9H-fluorene (13). To a dry THF solution (10 mL) of pre-synthesized compound **11** (246 mg, 0.94 mmol), (perfluorophenyl)magnesium bromide (0.5 M solution in diethylether, 3.8 mL, 1.88 mmol) was added dropwise under nitrogen and the solution was stirred for 24 h at room temperature. The formation of product was monitored by a thin-layer chromatography (TLC), and once the conversion to **12** is complete, saturated solution of ammonium chloride (20 mL) was added to quench the reaction. The solvent was removed under reduced pressure and the residue was extracted with dichloromethane (DCM) (3 x 50 mL). The combined organic layer was dried over sodium sulfate and the solvent was removed under vacuum to afford crude **12** as brown solid (415.8 mg). Crude **12** (415.8 mg) was further dissolved in dry DCM (15 mL) and treated with 0.1 ml of boron trifluoride·diethyl etherate ($BF_3{\cdot}Et_2O$) under nitrogen to perform an intra-molecular ring-closure (Friedel-Crafts) reaction. After stirring overnight, a saturated aqueous NH_4Cl solution (20 mL) was added to the reaction mixture and extracted with dichloromethane (3 x 50 mL). The solvent was dried over sodium sulfate, and was evaporated to dryness. The crude mixture obtained was subjected to silica gel column chromatography (hexanes) to afford the title product **13** as white solid (136 mg, 35% yield over two steps). $\boldsymbol{R_f}$ = 0.4 (hexanes); **mp**: 124-125 °C; **^{1}H NMR** (400 MHz, $CDCl_3$): δ 8.66 (d, *J* = 8.0 Hz, 1H), 7.60 (d, *J* = 7.9 Hz, 1H), 7.49 (t, *J* = 7.6 Hz, 1H), 7.36 (m, 1H), 7.28 (d, *J* = 7.5 Hz, 1H), 7.23 (d, *J* = 7.5 Hz, 1H), 7.14

(t, *J* = 7.7 Hz, 1H), 5.46 (s, 1H); **$^{13}C\{^{1}H\}$ NMR** (100 MHz, $CDCl_3$): δ 146.8, 144.4, 140.4, 139.5, 133.2, 128.3, 128.3 127.9, 124.0, 123.1, 117.3, 42.8; **HRMS** (ESI) *m/z*: $[M - H]^+$ Calcd for $C_{19}H_7BrF_5$ 408.9651, found 408.9691.

2-(9-(Perfluorophenyl)-9H-fluoren-4-yl)benzaldehyde (14). A solution of **13** (122 mg, 0.29 mmol), (2-formylphenyl)boronic acid (89 mg, 0.59 mmol), anhydrous K_2CO_3 (205 mg, 1.48 mmol) and dry toluene (6 mL) was degassed by sparging with N_2 for 0.5 h in an oven-dried thick-walled glass tube. $PdCl_2$(dppf)·DCM complex (24 mg, 10 mol%) was added thereafter, and the reaction vessel was sealed. The reaction mixture was then heated under stirring at 90 °C for 12 h. After cooling to room temperature, water was added and the mixture was extracted with DCM (3 x 50 mL) and the combined organic extracts were dried over Na_2SO_4. After removal of solvent, the crude was subjected to column chromatography on silica gel (hexanes:EtOAc, 95:5) as eluent to afford **14** as white solid (108 mg, 83% yield). $\boldsymbol{R_f}$ **=** 0.47 (5% EtOAc/hexanes); **mp**: 135-136 °C; **^{1}H NMR** (400 MHz, $CDCl_3$): δ 9.82 (m, 1H), 8.15 (m, 1H), 7.77 (m, 1H), 7.66 (t, *J* = 7.3 Hz, 1H), 7.57 – 7.47 (m, 1H), 7.41 – 7.35 (m, 2H), 7.32 – 7.27 (m, 1H), 7.25 (s, 1H), 7.20 (m, 1H), 7.06 (t, *J* = 7.6 Hz, 1H), 6.55 (dd, *J* = 7.8, 3.2 Hz, 1H), 5.52 (d, *J* = 6.9 Hz, 1H); **$^{13}C\{^{1}H\}$ NMR** (100 MHz, $CDCl_3$): δ 192.0, 191.9, 144.7, 144.6, 144.3, 144.2, 140.4, 139.5, 139.3, 134.5, 134.4, 134.2, 134.1, 133.1, 133.0, 131.1, 130.8, 130.4, 128.8, 128.1, 128.0, 127.8, 127.7, 127.6, 127.5, 127.3, 127.2, 124.4, 124.3, 124.2, 122.7, 42.5; **HRMS** (ESI) *m/z*: $[M + H]^+$ Calcd for $C_{26}H_{14}OF_5$ 437.0965, found 437.0988.

5,8-Bis(perfluorophenyl)-5,8-dihydroindeno[2,1-*c*]fluorene (16). Under nitrogen atmosphere, in 10 mL dry THF solution of **14** (79 mg, 0.18 mmol), (perfluorophenyl)magnesium bromide (0.5 M solution in diethylether, 1.1 mL, 0.54 mmol) was added dropwise. The mixture was stirred at room temperature for 24 h. After removal of the solvent, the crude compound was quenched with NH_4Cl (20 mL) and extracted into DCM (3 x 40 mL), washed with brine, and dried over anhydrous sodium sulfate. The starting material **14** was consumed, so the crude **15** (131 mg, **HRMS** *m/z*: $[M - H^+]$ Calcd for $C_{32}H_{13}OF_{10}$ 603.0807, found 603.0805) was used for next step without purification. To the solution of crude brown solid **15** (125 mg, 0.206 mmol) in anhydrous DCM (10 mL) at room temperature, 0.1 mL of $BF_3{\cdot}Et_2O$ was added dropwise under nitrogen, and the reaction mixture was stirred for 16 h at room temperature. Once the reaction was complete, as monitored by thin layer chromatography (TLC), a saturated aqueous NH_4Cl (10 mL) solution was added to the reaction mixture and

extracted with DCM (3 x 30mL). The organic layer was dried over anhydrous Na_2SO_4, filtered, and concentrated under reduced pressure. Product **16** was purified from crude mixture using silica gel column (hexanes) as white solid, as mixture of stereoisomers (66 mg, 62% yield over two steps). $\boldsymbol{R_f}$ = 0.66 (hexanes); **mp**: 222-223 °C; **^{1}H NMR** (400 MHz, $CDCl_3$): δ 8.60 (d, *J* = 7.9 Hz, 2H), 7.63 – 7.51 (m, 2H), 7.46 – 7.32 (m, 4H), 7.18 (d, *J* = 4.5 Hz, 2H), 5.56 (s, 1H), 5.51 (s, 1H); **^{13}C{^{1}H} NMR** (100 MHz, $CDCl_3$): δ 145.8, 145.4, 145.2, 145.1, 141.2, 136.9, 128.0, 127.8, 127.7, 124.6, 124.2, 124.1, 123.1, 43.0; **HRMS** (ESI) *m/z*: $[M - H]^+$ Calcd for $C_{32}H_{11}F_{10}$ 585.0701, found 585.0718.

5,8-Bis(perfluorophenyl)indeno[2,1-*c*]fluorene (17). 2,3-Dichloro-5,6-dicyano-1,4-benzoquinone (18.6 mg, 0.08 mmol, 2.5 equiv) was added as solid to the degassed 1,2-dichloroethane (1 mL) solution of **16** (19.2 mg, 0.03 mmol) under nitrogen in a glass tube, and the resultant solution was heated at 100 °C under sealed condition for 2 h. The reaction mixture was cooled to room temperature, and then run through a short silica gel plug eluting with hexanes to obtain the title product. Following a pentane wash, pure compound **17** was obtained as green solid (18 mg, 94% yield). $\boldsymbol{R_f}$ = 0.63 (hexanes); **mp**: 274-275 °C; **^{1}H NMR** (400 MHz, $CDCl_3$, 25 °C) δ 8.08 – 8.00 (m, 2H), 7.22 – 7.12 (m, 4H), 6.85 (dd, *J* = 6.9, 1.9 Hz, 2H), 6.29 (s, 2H); **^{13}C{^{1}H} NMR** (100 MHz, $CDCl_3$, 25 °C): δ 144.0, 140.0, 138.9, 135.9, 129.9, 127.9, 126.1, 122.3, 122.0; **^{19}F NMR** (376 MHz, $CDCl_3$, 25 °C) δ -135.69 (s), -152.46 (d, *J* = 21.9 Hz), -160.63 (t, *J* = 22.6 Hz); **HRMS** (ESI) *m/z*: $[M + H]^+$ Calcd for $C_{32}H_{11}F_{10}$ 585.0701, found 585.0690.

5-Mesityl-8-(perfluorophenyl)-5,8-dihydroindeno[2,1-*c*]fluorene (20). To a 10 mL dry THF solution of **18** (93 mg, 0.24 mmol) under nitrogen atmosphere, dropwise addition of pentafluorophenylmagnesium bromide (0.5 M in diethylether, 2.87 mL, 1.44 mmol) was done and the mixture was stirred at room temperature for 24 h. The reaction mixture was quenched with NH_4Cl (20 mL), and extracted with DCM (3 x 40 mL) after evaporation of THF. After drying the solvent mixture over sodium sulfate, the solvents were removed to isolate crude alcohol **19** as dark brown solid (373.8 mg, **HRMS** (ESI) *m/z*: $[M - H]^+$ Calcd for $C_{35}H_{24}OF_5$ 555.1747, found 557.1757.), which (370 mg, 0.66 mmol) was further dissolved in dry DCM (10 mL) at room temperature and treated with 0.1 ml of $BF_3{\cdot}Et_2O$ and the reaction mixture was stirred for 16 h at room temperature under N_2. After complete consumption of carbinol **19**, as monitored by TLC, a saturated aqueous NH_4Cl solution (10 mL) was added to the reaction mixture and extracted with DCM (3 x 30 mL). The organic layer was dried over anhydrous Na_2SO_4, filtered, and

the solvent was subsequently removed under reduced pressure. The residue was purified by silica gel column chromatography (hexanes) to afford title product **20** (72.6 mg, 56% yield over two steps) as white solid, as mixture of stereoisomers. $\boldsymbol{R_f}$ = 0.5 (hexanes); **mp**: 70-71 °C; **^{1}H NMR** (400 MHz, $CDCl_3$): δ 8.66 – 8.59 (m, 2H), 7.59 – 7.49 (m, 2H), 7.39 – 7.27 (m, 4H), 7.16 – 7.10 (m, 2H), 7.04 –7.02 (m, 1H), 6.67 – 6.65 (m, 1H), 5.60 – 5.54 (m, 2H), 2.70 - 2.68 (m, 3H), 2.29 - 2.27 (m, 3H), 1.08 -1.06 (m, 3H); **^{13}C{^{1}H} NMR** (100 MHz, $CDCl_3$): δ 149.3, 148.9, 148.6, 148.5, 145.2, 145.1, 144.8, 144.2, 141.7, 141.0, 140.9, 138.0, 137.9, 137.8, 136.7, 136.6, 136.5, 136.4, 134.3, 130.8, 130.7, 128.9, 127.9, 127.5, 127.4, 126.8, 124.6, 124.5, 124.0, 124.1, 123.9, 123.8, 123.0, 122.9, 122.8, 122.5, 50.1, 50.0, 43.0, 21.9, 21.8, 21.0, 18.8, 18.7; **HRMS** (ESI) *m/z*: [M + H]$^+$ Calcd for $C_{35}H_{24}F_5$ 539.1798, found 539.1776.

5-(3,5-Bis(trifluoromethyl)phenyl)-8-mesityl-5,8-dihydroindeno[2,1-*c*]fluorene (22). (3,5-bis(trifluoromethyl)phenyl)magnesium bromide was firstly prepared from 1-bromo-3,5-bis(trifluoromethyl)benzene (0.6 ml, 5 equiv, 3.5 mmol), Mg (101.7 mg, 6 equiv, 4.2 mmol) and catalytic I_2 in freshly distilled THF (5 ml). Afterwards, to anhydrous 20 mL THF solution of aldehyde **18** (271 mg, 0.697 mmol)) was added to the freshly prepared (3,5-bis(trifluoromethyl)phenyl)magnesium bromide at room temperature under N_2 atmosphere, and the resulting solution was stirred at room temperature for 24 h. After addition of aqueous NH_4Cl (20 mL), the organic phase was separated, and the aqueous phase was extracted with dichloromethane (3 x 40 mL) and washed by brine solution. Upon evaporating off the solvent, the crude **21** (511.6 mg) (**HRMS** (ESI) *m/z*: [M - H]$^+$ Calcd for $C_{37}H_{27}OF_6$ 601.1966, found 601.1977) was obtained as yellow oil which was used without purification. Crude **19** (466.8 mg, 0.77 mmol) in anhydrous DCM (10 mL), at room temperature, was treated with 0.1 mL of $BF_3{\cdot}Et_2O$ and stirred for 10 mins. The reaction was quenched by 10 mL aqueous NH_4Cl solution, and extracted with DCM (3 x 30 mL). The solvent was dried over anhydrous sodium sulfate, filtered, and was removed under vacuum to afford crude **22** which was purified by column chromatography (silica, hexanes) to give white solid **22** as mixture of stereoisomers (232 mg, 55% yield over two steps). $\boldsymbol{R_f}$ = 0.55 (hexanes); **mp**: 115-116 °C; **^{1}H NMR** (400 MHz, $CDCl_3$): δ 8.66 – 8.61 (m, 2H), 7.77 – 7.75 (m, 1H), 7.58 – 7.51 (m, 4H), 7.37—7.29 (m, 4H), 7.12 – 7.02 (m, 3H), 6.67 – 6.65 (m, 1H), 5.59 (s, 1H), 5.25 – 5.23 (m, 1H), 2.70 – 2.69 (m, 3H), 2.29 – 2.27 (m, 3H), 1.09 – 1.05 (m, 3H). **^{13}C{^{1}H} NMR** (100 MHz, $CDCl_3$): δ 149.3, 148.6, 147.3, 147.1, 146.7, 146.2, 145.3, 145.2, 141.6, 141.5, 140.9, 137.9, 137.8, 136.7, 136.5, 134.2, 132.6, 132.3, 131.9, 131.6,

130.8, 130.7, 129.0, 128.9, 128.7, 128.6, 128.0, 127.6, 127.6, 127.5, 126.8, 125.5, 125.4, 124.7, 124.6, 124.1, 124.0, 123.9, 123.8, 123.7, 123.3, 123.2, 122.0, 121.2, 54.1, 53.9, 50.1, 50.0, 21.9, 21.9, 21.8, 21.0, 20.9, 18.8, 18.6; **HRMS** (ESI) *m/z*: $[M + H]^+$ Calcd for $C_{37}H_{27}F_6$ 585.2017, found 585.2070.

5-Mesityl-8-(perfluorophenyl)indeno[2,1-*c*]fluorene (7). DDQ (34 mg, 0.14 mmol, 2 equiv) was added to degassed solution of precursor **20** (40 mg, 0.07 mmol) in toluene (2 mL), and the reaction mixture was heated to 100 °C for 2 h. The progress of the reaction was monitored by TLC and stopped after 2 h, followed by purification by silica gel column chromatography (hexanes) to afford the final compound **7** as green solid (31 mg, 78 % yield). R_f = 0.50 (hexanes); **mp**: 246-247 °C; **^{1}H NMR** (400 MHz, $CDCl_3$, 25 °C): δ 8.10 (d, *J* = 6.4 Hz, 1H), 8.03 (d, *J* = 7.5 Hz, 1H), 7.17 (m, 3H), 7.06 (t, *J* = 7.4 Hz, 1H), 6.97 (s, 2H), 6.88 (d, *J* = 5.9 Hz, 1H), 6.67 (d, *J* = 7.2 Hz, 1H), 6.21 (s, 2H), 2.35 (s, 3H), 2.15 (s, 6H); **^{13}C{^{1}H} NMR** (100 MHz, $CDCl_3$, 25 °C): δ 147.2, 146.1, 144.1, 140.8, 139.3, 138.1, 137.9, 136.9, 136.7, 136.3, 135.6, 129.8, 129.4, 129.3, 128.3, 127.7, 126.9, 125.8, 125.7, 125.6, 122.9, 122.6, 121.5, 120.2, 21.3, 20.3; **^{19}F NMR** (376 MHz, $CDCl_3$, 25 °C) δ -135.99 (d, *J* = 21.9 Hz), -153.51 (d, *J* = 20.4 Hz), -161.09 (t, *J* = 23.4 Hz); **HRMS** (ESI) *m/z*: $[M + H]^+$ Calcd for $C_{35}H_{22}F_5$ 537.1642, found 537.1631.

5-(3,5-Bis(trifluoromethyl)phenyl)-8-mesitylindeno[2,1-*c*]fluorene (8). DDQ (69.8 mg, 0.30 mmol, 1.2 equiv) was added to dry 1,2-dichloroethane (1 mL) solution of precursor **22** (150 mg, 0.25 mmol) to carry out the oxidative dehydrogenation reaction. The reaction mixture was then heated to 80 °C for 2 h, and the progress was monitored by TLC. After 2 h, the solvent was removed in vacuo and the crude residue was purified on silica gel column chromatography (hexanes) to afford the pure compound **8** as green solid (133 mg, 89 % yield). R_f = 0.51 (hexanes); **mp**: 197-198 °C; **^{1}H NMR** (400 MHz, $CDCl_3$, 25 °C): δ 8.17 – 8.12 (m, 1H), 8.07 (d, *J* = 7.4 Hz, 1H), 7.96 (s, 2H), 7.90 (s, 1H), 7.25 – 7.04 (m, 5H), 6.97 (s, 2H), 6.71 (d, *J* = 7.2 Hz, 1H), 6.49 (d, *J* = 9.3 Hz, 1H), 6.27 (d, *J* = 9.4 Hz, 1H), 2.35 (s, 3H), 2.15 (s, 6H); **^{19}F NMR** (376 MHz, $CDCl_3$, 25 °C) δ -62.77 (s); **^{13}C{^{1}H} NMR** (100 MHz, $CDCl_3$, 25 °C): δ 146.4, 146.1, 144.5, 140.6, 138.4, 137.9, 137.8, 137.0, 136.9, 136.5, 136.3, 136.2, 132.4, 132.1, 129.7, 129.5, 129.4, 129.3, 128.3, 127.4, 127.2, 126.0, 125.8, 124.7, 123.0, 122.5, 122.0, 121.6, 121.0, 119.5, 21.3, 20.3; **HRMS** (ESI) *m/z*: $[M + H]^+$ Calcd for $C_{37}H_{25}F_6$ 583.1860, found 583.1824.

Triisopropyl((8-mesitylindeno[2,1-*c*]fluoren-5-yl)ethynyl)silane (9). A flame dried round-bottomed flask equipped with a stir bar was charged with TIPS-acetylene (0.52

ml, 2.32 mmol, 5.0 equiv.). Freshly distilled THF (5 mL) was then introduced into the flask and the resulting solution was cooled to 0 °C under inert atmosphere. A 1.6 M solution of *n*-butyllithium in hexanes (5.0 equiv.) was then added and reaction mixture was stirred at 0 °C. After 30 mins, the reaction was mixed with solution of **18** (180 mg, 0.46 mmol) in THF. After complete consumption of carbonyl **18**, the reaction mixture was quenched with saturated aqueous solution of ammonium chloride (20 mL) and diluted with ethyl acetate (30 mL). The layers were separated and the organic layer was washed with brine. The extracts were dried over sodium sulfate, filtered, and was concentrated in vacuo to afford crude product **23** as dark brown solid (451 mg, **HRMS** (ESI) *m/z*: $[M + H]^+$ Calcd for $C_{40}H_{47}OSi$ 571.3396, found 571.3273). To the solution of crude **23** (431 mg, 0.75 mmol) in anhydrous DCM (10 mL) at room temperature, $BF_3{\cdot}Et_2O$ (0.1 mL) was added dropwise under nitrogen, and the reaction mixture was stirred for 10 min at room temperature. Completion of the reaction was monitored by TLC (partial formation of **9** was observed in TLC, likely due to air oxidation), and the mixture was extracted with DCM/water to afford **24** (78 mg, including the partly dehydrogenated **9**), which was used directly for next step. A chloroform (10 ml) solution of the crude **24** was treated with DDQ (38 mg, 0.16 mmol, 1.2 equiv) for 0.5 h at 70 °C. The final compound **9** was obtained as green gummy solid (23 mg, 9% yield over three steps) after purification of the crude reaction residue by silica gel (hexanes) column chromatography. $\boldsymbol{R_f}$ = 0.44 (hexanes); **mp**: 104-105 °C; **^{1}H NMR** (400 MHz, $CDCl_3$, 25 °C): δ 8.00 (d, *J* = 7.3 Hz, 2H), 7.29 (d, *J* = 7.1 Hz, 1H), 7.21 (dd, *J* = 11.3, 4.1 Hz, 1H), 7.17 (dd, *J* = 7.3, 6.2 Hz, 1H), 7.11 (t, *J* = 7.2 Hz, 1H), 7.04 (t, *J* = 7.2 Hz, 1H), 6.96 (s, 2H), 6.73 (d, *J* = 9.2 Hz, 1H), 6.67 (d, *J* = 7.2 Hz, 1H), 6.25 (d, *J* = 9.2 Hz, 1H), 2.35 (s, 3H), 2.13 (s, 6H), 1.16 – 1.15 (m, 21H). **^{13}C{^{1}H} NMR** (100 MHz, $CDCl_3$, 25 °C): δ 146.1, 145.9, 145.0, 142.8, 139.6, 138.5, 137.7, 136.9, 136.8, 136.6, 135.6, 129.7, 129.4, 128.3, 127.2, 127.0, 125.6, 125.2, 123.3, 122.3, 122.0, 121.8, 121.0, 107.4, 101.6, 21.2, 20.3, 18.8, 11.4. **HRMS** (ESI) *m/z*: $[M + H]^+$ Calcd for $C_{40}H_{43}Si$ 551.3134, found 551.3112.

4-bromo-9-(4-methoxyphenyl)-9H-fluorene (26). To a dry THF solution (10 mL) of pre-synthesized compound **11** (850 mg, 3.26 mmol), was added (4-methoxyphenyl)magnesium bromide (prepared from 1-bromo-4-methoxybenzene (0.49 ml 3.91 mmol) and Magnesium turning (142 mg, 5.86 mmol) in dry THF (5 mL)) and the solution was stirred for 4 h at room temperature. Then the reaction was quenched with a saturated aqueous solution of NH_4Cl and extracted with EtOAc. The extract was

washed with brine and dried over Na_2SO_4 to afford crude **25** as brown solid (1263 mg). Crude **25** (1249 mg) was further dissolved in dry DCM (10 mL) and treated with TfOH (1 drop) under N_2 atmosphere to perform an intra-molecular ring-closure (Friedel-Crafts) reaction. After stirring for one-minute, appropriate amount of silica gel was added to the mixture, and the solvent was evaporated in vacuo. The residue was purified by column chromatography on silica gel (hexanes) to afford the title product **26** as white solid (669 mg, 59% yield in two steps). $\boldsymbol{R_f}$ = 0.3 (hexanes); **mp**: 56-57 °C; **^{1}H NMR** (400 MHz, $CDCl_3$): δ 8.64 (d, *J* = 7.8 Hz, 1H), 7.54 (d, *J* = 8.0 Hz, 1H), 7.44 (m, 1H), 7.36 – 7.29 (m, 2H), 7.24 (d, *J* = 7.5 Hz, 1H), 7.09 (t, *J* = 7.7 Hz, 1H), 6.99 (d, *J* = 8.7 Hz, 2H), 6.82 (d, *J* = 8.6 Hz, 2H), 5.01 (s, 1H), 3.78 (s, 3H); **^{13}C{^{1}H} NMR** (100 MHz, $CDCl_3$): δ 158.8, 151.2, 148.7, 140.2, 139.2, 133.1, 132.3, 129.5, 128.2, 128.0, 127.1, 125.2, 124.3, 123.5, 116.9, 114.3, 55.3, 53.9; **HRMS** (ESI) *m/z*: $[M - H]^+$ Calcd for $C_{20}H_{14}OBr$ 349.0228, found 349.0218.

2-(9-(4-methoxyphenyl)-9H-fluoren-4-yl)benzaldehyde (27). A solution of **26** (669 mg, 1.90 mmol), (2-formylphenyl)boronic acid (571 mg, 3.81 mmol), anhydrous K_2CO_3 (1.32 g, 9.52 mmol) and dry toluene (8 mL) was degassed by sparging with N_2 for 0.5 h in an oven-dried thick-walled glass tube. $PdCl_2$(dppf)·DCM complex (155 mg, 10 mol%) was added thereafter, and the reaction vessel was sealed. The reaction mixture was then heated under stirring at 90 °C for 12 h. After cooling to room temperature, water was added and the mixture was extracted with EtOAc (3 x 50 mL) and the combined organic extracts were dried over Na_2SO_4. After removal of solvent, the crude was subjected to column chromatography on silica gel (hexanes:DCM, 1:1 as eluent) to afford **27** as white solid (537 mg, 75% yield). $\boldsymbol{R_f}$ = 0.8 (50% DCM/hexanes); **mp**: 55-56 °C; **^{1}H NMR** (400 MHz, $CDCl_3$): δ 9.92 – 9.86 (m, 1H), 8.17 (m, 1H), 7.80 – 7.73 (m, 1H), 7.69 – 7.62 (m, 1H), 7.55 (m, 1H), 7.42 – 7.37 (m, 1H), 7.33 (m, 1H), 7.29 (d, *J* = 7.5 Hz, 1H), 7.23 (d, *J* = 7.3 Hz, 1H), 7.17 (m, 1H), 7.09 – 6.99 (m, 3H), 6.86 (dd, *J* = 8.8, 2.3 Hz, 2H), 6.55 (dd, *J* = 7.3, 2.1 Hz, 1H), 5.07 – 5.06 (m, 1H), 3.80 (s, 3H); **^{13}C{^{1}H} NMR** (100 MHz, $CDCl_3$): δ 192.2, 192.1, 158.7, 148.9, 148.8, 144.9, 140.1, 139.0, 134.3, 134.3, 134.2, 134.0, 133.4, 133.3, 132.4, 131.0, 131.0, 129.7, 129.5, 129.4, 128.6, 127.5, 127.4, 127.4, 127.2, 126.9, 126.9, 125.4, 125.3, 125.2, 122.3, 114.3, 114.3, 55.3, 53.6, 53.6; **HRMS** (ESI) *m/z*: $[M + H]^+$ Calcd for $C_{27}H_{21}O_2$ 377.1542, found 377.1542.

5-(3,5-bis(trifluoromethyl)phenyl)-8-(4-methoxyphenyl)-5,8-dihydroindeno[2,1-*c*]fluorene (29). Under nitrogen atmosphere, in 10 mL dry THF solution of **27** (162 mg,

0.43 mmol), (3,5-bis(trifluoromethyl)phenyl)magnesium bromide (prepared from 1-bromo-3,5-bis(trifluoromethyl)benzene (0.37 ml, 2.15 mmol) and Magnesium turning (63 mg, 2.58 mmol) in dry THF (5 mL)) was added dropwise. The mixture was stirred at room temperature for 7 h. After removal of the solvent, the crude compound was quenched with NH_4Cl (20 mL) and extracted into EtOAc (3 x 40 mL), washed with brine, and dried over anhydrous sodium sulfate. The starting material **27** was consumed, so the crude **28** (367 mg, **HRMS** *m/z*: [M – H^+] Calcd for $C_{35}H_{23}O_2F_6$ 589.1602, found 589.1603) was used for next step without purification. To the solution of crude brown solid **28** (361 mg, 0.61 mmol) in anhydrous DCM (10 mL) at room temperature, 0.2 mL of $BF_3 \cdot Et_2O$ was added dropwise under nitrogen, and the reaction mixture was stirred for 10 mins at room temperature. Once the reaction was complete, as monitored by thin layer chromatography (TLC), a saturated aqueous NH_4Cl (10 mL) solution was added to the reaction mixture and extracted with DCM (3 x 30mL). The organic layer was dried over anhydrous Na_2SO_4, filtered, and concentrated under reduced pressure. Product **29** was purified from crude mixture using silica gel column (hexanes:EtOAc, 98:2) as white solid, as mixture of stereoisomers (155 mg, 61% yield over two steps). $\boldsymbol{R_f}$ = 0.4 (5% EtOAc/hexanes); **mp**: 109-110 °C; **^{1}H NMR** (400 MHz, $CDCl_3$): δ 8.67 – 8.55 (m, 2H), 7.77 (s, 1H), 7.63 – 7.48 (m, 4H), 7.42 – 7.28 (m, 4H), 7.21 (d, *J* = 7.3 Hz, 1H), 7.10 (d, *J* = 7.5 Hz, 1H), 7.04 (dd, *J* = 8.8, 7.1 Hz, 2H), 6.82 (d, *J* = 8.6 Hz, 2H), 5.21 (s, 1H), 5.08 (s, 1H), 3.78-3.77 (m, 3H); **^{13}C{^{1}H} NMR** (100 MHz, $CDCl_3$): δ 158.7, 150.0, 149.9, 149.5, 149.4, 147.2, 147.0, 146.9, 146.7, 145.1, 144.9, 141.6, 141.4, 140.9, 140.9, 136.7, 136.6, 136.4, 136.2, 133.8, 133.6, 132.2, 131.9, 129.6, 129.5, 128.7, 128.0, 127.6, 127.6, 127.5, 127.3, 125.8, 125.5, 124.7, 124.6, 124.4, 124.0, 123.9, 123.8, 123.6, 122.0, 121.2, 114.3, 55.3, 54.0; **HRMS** (ESI) *m/z*: [M – $H]^+$ Calcd for $C_{35}H_{21}OF_6$ 571.1497, found 571.1497.

5-(3,5-bis(trifluoromethyl)phenyl)-8-(4-ethoxyphenyl)indeno[2,1-*c*]fluorene (10). To a solution of **29** (92 mg, 0.16 mmol) in toluene (10 mL) was added 2,3-dichloro-5,6-dicyano-*p*-benzoquinone (DDQ) (365 mg, 1.61 mmol, 10 equiv). The reaction mixture was heated at 100 °C under sealed condition. After 2 h, the solution was cooled to 0 °C and hydrazine monohydrate (0.5 ml) was added. The reaction mixture was purified by column chromatography on silica gel (EtOAc/hexane = 1:99), to give the product **10** as green solid (26 mg, 28%). $\boldsymbol{R_f}$ = 0.5 (hexanes:EtOAc = 95:5); **mp**: 160-161 °C; **^{1}H NMR** (400 MHz, $CDCl_3$, 25 °C): δ 8.14 (dd, *J* = 5.8, 2.9 Hz, 1H), 8.12 – 8.06 (m, 1H), 7.98

(s, 2H), 7.90 (s, 1H), 7.54 – 7.45 (m, 2H), 7.25 – 7.23 (m, 1H), 7.21 – 7.18 (m, 2H), 7.18 – 7.12 (m, 3H), 7.06 – 7.02 (m, 2H), 6.78 (d, *J* = 9.5 Hz, 1H), 6.58 (d, *J* = 9.3 Hz, 1H), 3.89 (s, 3H); **$^{13}C\{^{1}H\}$ NMR** (100 MHz, $CDCl_3$, 25 °C): δ 160.2, 145.6, 144.9, 144.4, 141.0, 138.4, 137.1, 137.0, 136.6, 136.1, 134.8, 132.7, 132.4, 132.1, 131.7, 130.8, 129.4, 129.3, 129.2, 127.5, 126.9, 126.1, 126.0, 125.8, 124.8, 123.0, 122.7, 122.1, 121.5, 120.9, 119.6, 114.4, 55.5; **^{19}F NMR** (376 MHz, $CDCl_3$, 25 °C) δ -62.79 (s); **HRMS** (ESI) *m/z*: $[M]^+$ Calcd for $C_{35}H_{20}OF_6$ 570.1418, found 570.1418. Note: Excess of DDQ in toluene was required to convert **29** to **10** at 100 °C, likely due to a competing side-reaction involving the oxidative insertion of DDQ into the Csp^3-H bond of toluene under near-refluxing condition, thus inhibiting the oxidizing capacity of DDQ.[32] A plausible reason of such low yield is further discussed (*see section 2B.5.5*).

2B.5.3 Single crystal data

Suitable single crystals of **7**, **9** and **17** were selected using paratone oil and mounted on glass fiber with the help of gum. The intensity data and geometric parameters of these crystals were garnered with the help of Bruker D8 Venture X-ray diffractometer having a micro-focus sealed X-ray tube Mo-Kα (λ = 0.71073 Å) source of X-rays along with a PHOTON 100 detector with inclining Phi and Omega (width of 0.5 for one frame) working at a scan speed of 10 s per frame. The crystal was kept at 298 K during data collection. Data acquisition as well as extraction of data was accomplished by utilizing Bruker Apex-3 and Bruker SAINT software packages using a narrow -frame algorithm.[33] By utilizing OLex2,[34] the crystal structure was solved with the help of olex2.solve[35] structure solution program by employing intrinsic Phasing methods and crystal structure refinement was done with the SHELXL[36] refinement package by putting into use Least Squares minimization. Refinement of all non-hydrogen atoms was completed with the help of anisotropic thermal parameters.

Table 2B.8 Crystal data and structure refinement for **7**, **9** and **17**.

Compounds	**7**	**9 (*P*/*M*)**	**17**
CCDC numbers	2117444	2117445	2117446
Solvents, and conditions for recrystallization	MeOH, by evaporation at rt in dark	Hexane, by evaporation at rt in dark	MeOH/$CHCl_3$, by evaporation at rt in dark
Empirical formula	$C_{35}H_{21}F_5$	$C_{80}H_{84}Si_2$	$C_{32}H_{10}F_{10}$
Formula weight	536.52	1101.65	584.40

Temperature/K	298(2)	298	298
Crystal system	Monoclinic	Orthorhombic	Monoclinic
Space group	$P2_1/c$	$P2_12_12_1$	C2/c
a/Å	17.08(2)	7.9288(6)	25.651(5)
b/Å	7.942(7)	25.461(2)	10.511(2)
c/Å	19.233(18)	32.690(3)	8.9692(15)
α/°	90	90	90
β/°	95.46(3)	90	101.225(5)
γ/°	90	90	90
Volume/Å^3	2597(5)	6599.2(9)	2371.9(7)
Z	4	4	4
ρ_{calc}g/cm^3	1.372	1.109	1.637
μ/mm^{-1}	0.104	0.097	0.150
F(000)	1104.0	2368.0	1168.0
Crystal size/mm^3	0.302 × 0.275 × 0.087	0.546 × 0.189 × 0.078	0.456 × 0.056 × 0.025
Radiation	MoKα (λ = 0.71073)	MoKα (λ = 0.71073)	MoKα (λ = 0.71073)
2θ range for data collection/°	4.68 to 54.412	4.92 to 50.942	6.014 to 50.72
Index ranges	$-21 \le h \le 21$, $-10 \le k \le 10$, $-24 \le l \le 24$	$-9 \le h \le 9$, $-30 \le k \le 30$, $-39 \le l \le 39$	$-30 \le h \le 30$, $-12 \le k \le 12$, $-10 \le l \le 10$
Reflections collected	73863	89898	8341
Independent reflections	5739 [R_{int} = 0.1235, R_{sigma} = 0.0549]	12143 [R_{int} = 0.1150, R_{sigma} = 0.0752]	2127 [R_{int} = 0.1019, R_{sigma} = 0.0872]
Data/restraints/parameters	5739/0/365	12143/0/757	2127/0/190
Goodness-of-fit on F^2	1.072	1.038	1.014
Final R indexes [I>=2σ (I)]	R_1 = 0.0489, wR_2 = 0.1134	R_1 = 0.0532, wR_2 = 0.1149	R_1 = 0.0516, wR_2 = 0.1240
Final R indexes [all data]	R_1 = 0.1229, wR_2 = 0.1603	R_1 = 0.1421, wR_2 = 0.1588	R_1 = 0.1017, wR_2 = 0.1632
Largest diff. peak/hole / e Å^{-3}	0.18/-0.16	0.17/-0.23	0.16/-0.21

2B.5.4 DFT Calculations

Density functional theory calculations were performed with Gaussian 09 package using a high performance computing cluster facility of IIT Ropar, at B3LYP/6-31G(d,p) in the gas phase.[15] Excitation energies were computed using time-dependent DFT (TDDFT)

for the singlet closed shell structure. Molecular orbital contributions were determined using GaussSum 3.0 package.[37]

2B.5.4.1 Inversion barrier to *P*/*M*-interconversion for 9: The transition state for **9** was calculated to have an imaginary frequency (–102.33) corresponding to the interconversion between optimized *P*- and *M*- isomers with the Mesityl/TIPSE groups replaced by hydrogens, using a similar approach adopted from the reported work.[1] The dihedral angle is measured as 11.07°, from the highlighted sky-blue coloured carbons (C1, C2, C3, C4) in the Figure 2B.11. A very small barrier to inversion for **9** (*P*/*M*-interconversion) is calculated, $\Delta E_{TS\text{-}P/M}$ = 0.48 kcal/mol, as shown below.

	Kcal/mol
***P*-9**	-482773.8102
***M*-9**	-482773.8102
***TS*-9**	-482773.3303

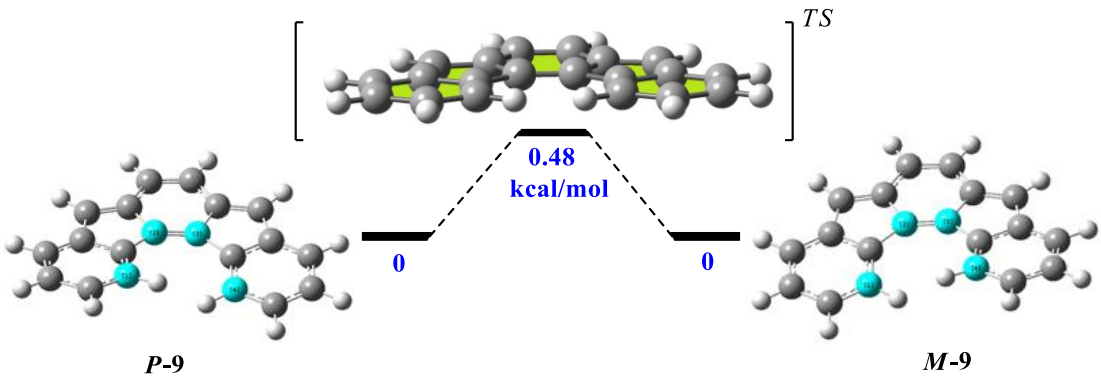

Figure 2B.11 Optimized *P*- (left) and *M*- (right) isomers of **9** (by replacing apical substituents with H) with carbons highlighted for measuring the dihedral angle, and the intermediate TS (middle).

Table 2B.9 Frontier Molecular Orbital profiles for the optimized structures.

Compd.	HOMO	LUMO
1	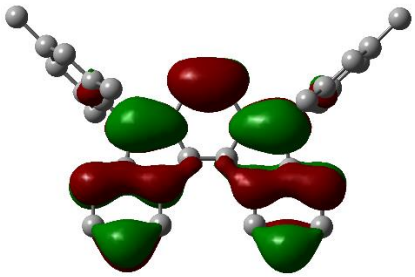 **-4.90 eV**	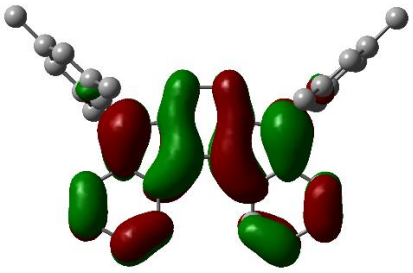 **-2.65 eV**

7	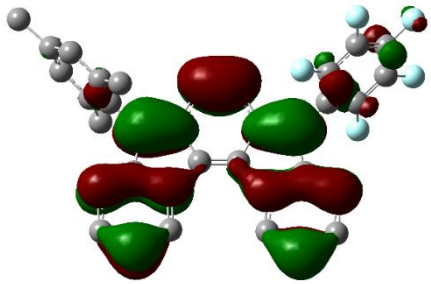 **-5.13 eV**	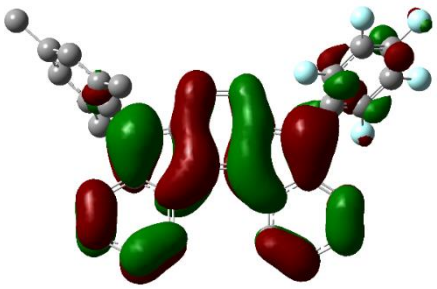 **-2.95 eV**
8	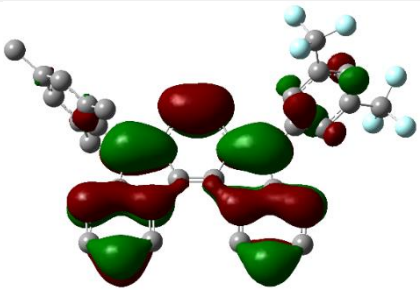 **-5.14 eV**	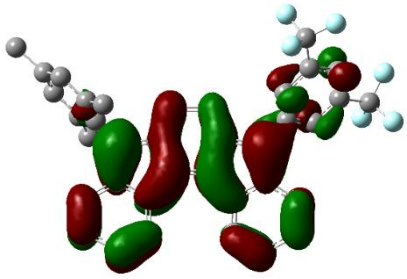 **-2.99 eV**
9	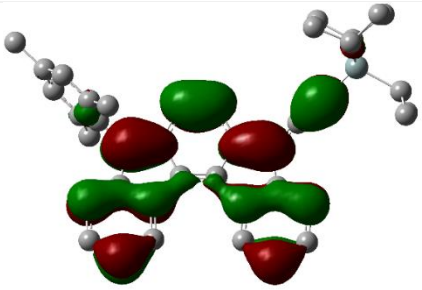 **-4.91 eV**	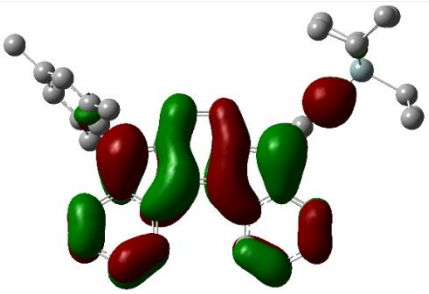 **-2.87 eV**
10	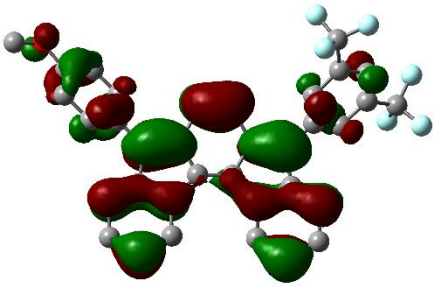 **-4.97 eV**	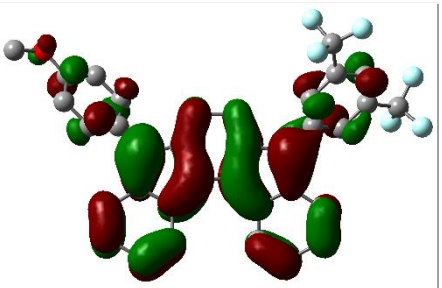 **-2.95 eV**

17	**-5.37 eV**	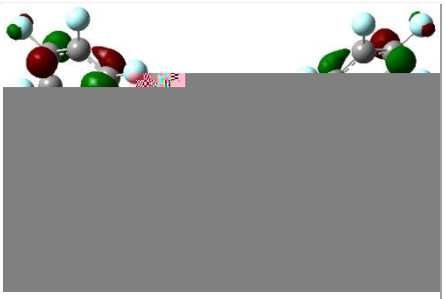 **-3.25 eV**

2B.5.5 Possible reason for the yield of 10: There could be three competing reactions when **29** is treated with DDQ, which might contribute in low yield of **10** (Figure 2B.12)**.**

1) Excess of DDQ was required in toluene at 100 °C to drive the reaction forward. A plausible reason could be that DDQ in toluene at 100 °C (near-reflux condition) may undergo a side-reaction which is known as the oxidative insertion of DDQ into the C_{sp}^3-H bond of toluene (Figure 2B.12), and thus resulted in a low yield for **10**.

   In comparison, the yield for conversion of **20** to **7** (yield = 78%) is also on a lower side under identical condition, however, due to mesityl protection, the yield is not too low as compared to that of **10** (yield = 28%). For **7**, the low yield could be attributed to the side-reaction involving oxidative insertion of DDQ into the C_{sp}^3-H bond of toluene.

2) Furthermore, DDA can convert **29** to **29B** which may avoid its antiaromaticity through resonance contribution from the 4-methoxyphenyl group to form **29A**. Intermediate **29A** may undergo deprotonation by $DDQH^-$ or hydride abstraction by DDQ to afford **10**.

3) At the same time, **29A** may also take part in forming the possible unwanted by-product **29-DDQ**, in a similar oxidative insertion fashion of DDQ into the C_{sp}^3-H bond of **29**, which could not be ignored. Further studies are in our scope of future research to identify the plausible by-products.

~ 100 nm thick films of compounds **1**, **7**, **8** and **17** were spin coated from the same solution as used for hole only devices. Lastly, 120 nm of Al was thermally evaporated at a base pressure of 3×10^{-6} mbar to complete the device. The active area of both hole and electron-only devices was 6.6 mm^2, calculated from the overlap area of patterned ITO and top contact. *J-V* characteristics were measured using a Keithley 2450 source measure unit. The dielectric constant of the compounds **1**, **7**, **8** and **17** was measured using high-frequency LCR meter ZM2376 with an applied oscillation level voltage of 1V over the frequency range 20Hz-1MHz.

2B.5.6.2 SCLC Mobility Data for compounds **1**, **7**, **8** and **17**:

Table 2B.10 Hole Mobility in $cm^2 V^{-1} s^{-1}$ for best 5 devices for compounds **1**, **7**, **8** and **17**.

	1	**7**	**8**	**17**
1	1.14E-03	1.14E-03	1.46E-03	1.50E-03
2	1.29E-03	1.26E-03	1.36E-03	2.13E-03
3	1.30E-03	2.29E-03	1.98E-03	1.24E-03
4	1.63E-03	3.02E-03	1.24E-03	1.14E-03
5	1.01E-03	1.31E-03	1.29E-03	2.21E-03
AVERAGE	1.27E-03	1.80E-03	1.47E-03	1.64E-03
STDEV	2.32E-04	8.21E-04	2.99E-04	4.99E-04

Table 2B.11 Electron Mobility in $cm^2 V^{-1} s^{-1}$ for best 5 devices for compounds **1**, **7**, **8** and **17**.

	1	**7**	**8**	**17**
1	1.92E-03	3.04E-03	7.52E-03	1.00E-02
2	1.02E-03	3.98E-03	1.11E-03	8.35E-03
3	1.01E-03	1.50E-02	2.48E-03	1.04E-02
4	2.77E-03	4.27E-03	6.66E-03	3.77E-03
5	4.28E-03	1.00E-02	1.35E-03	1.08E-02
AVERAGE	2.20E-03	7.26E-03	3.82E-03	8.66E-03
STDEV	1.37E-03	5.12E-03	3.04E-03	2.89E-03

2B.6 References

1. A. G. Fix, P. E. Deal, C. L. Vonnegut, B. D. Rose, L. N. Zakharov and M. M. Haley, *Org. Lett.*, 2013, **15**, 1362–1365.

2. (*a*) D. T. Chase, B. D. Rose, S. P. McClintock, L. N. Zakharov and M. M. Haley, *Angew. Chem. Int. Ed.*, 2011, **50**, 1127–1130; (*b*) A. Shimizu and Y. Tobe, *Angew. Chem. Int. Ed.*, 2011, **50**, 6906–6910; (*c*) A. Shimizu, R. Kishi, M. Nakano, D. Shiomi, K. Sato, T. Takui, I. Hisaki, M. Miyata and Y. Tobe, *Angew. Chem. Int. Ed.*, 2013, **52**, 6076–6079; (*d*) J. J. Dressler, Z. Zhou, J. L. Marshall, R. Kishi, S. Takamuku, Z. Wei, S. N. Spisak, M. Nakano, M. A. Petrukhina and M. M. Haley, *Angew. Chem. Int. Ed.*, 2017, **56**, 15363–15367; (*e*) Y. Tobe, *Top. Curr. Chem. (Cham)*, 2018, **376**, 12; (*f*) J. Nishida, S. Tsukaguchi and Y. Yamashita, *Chem. Eur. J.*, 2012, **18**, 8964–8970; (*g*) S. Das and J. Wu, *Phys. Sci. Rev.*, 2017, **2**, 20160109; (*h*) R. Casares, Á. Martínez-Pinel, S. Rodríguez-González, I. R. Márquez, L. Lezama, M. T. González, E. Leary, V. Blanco, J. G. Fallaque, C. Díaz, F. Martín, J. M. Cuerva and A. Millán, *J. Mater. Chem. C*, 2022, **10**, 11775–11782.

3 K. Paudel, B. Johnson, M. Thieme, M. M. Haley, M. M. Payne, M. Marcia, J. E. Anthony and O. Ostroverkhova, *Appl. Phys. Lett.*, 2014, **105**, 043301.

4. J. E. Barker, C. K. Frederickson, M. H. Jones, L. N. Zakharov and M. M. Haley, *Org. Lett.*, 2017, **19**, 5312–5315.

5. (*a*) T. Jousselin-Oba, P. E. Deal, A. G. Fix, C. K. Frederickson, C. L. Vonnegut, A. Yassar, L. N. Zakharov, M. Frigoli and M. M. Haley, *Chem. Asian J.*, 2019, **14**, 1737–1744;(*b*) Q. Jiang, Y. Han, Y. Zou, H. Phan, L. Yuan, T. S. Herng, J. Ding and C. Chi, *Chem. Eur. J.*, 2020, **26**, 15613–15622.

6. (*a*) J. L. Marshall, D. Lehnherr, B. D. Lindner and R. R. Tykwinski, *ChemPlusChem*, 2017, **82**, 967–1001; (*b*) S. Herzog, A. Hinz, F. Brehr, J. Podlech, *Org. Biomol. Chem.*, 2022, **20**, 2873–2880.

7. H. Sharma, N. Bhardwaj and S. Das, *Org. Biomol. Chem.*, 2022, **20**, 8071–8077.

8. H. Sharma, P. K. Sharma and S. Das, *Chem. Commun.*, 2020, **56**, 11319–11322.

9. (*a*) D. Lehnherr, J. Gao, F. A. Hegmann and R. R. Tykwinski, *Org. Lett.*, 2008, **10**, 4779–4782; (*b*) S. H. Etschel, A. R. Waterloo, J. T. Margraf, A. Y. Amin, F. Hampel, C. M. Jäger, T. Clark, M. Halik and R. R. Tykwinski, *Chem. Commun.*, 2013, **49**, 6725–6727; (*c*) J. Zirzlmeier, D. P. Lehnherr, B. Coto, E. T. Chernick, R. Casillas, B. S. Basel,

M. Thoss, R. R. Tykwinski and D. M. Guldi, *Proc. Natl. Acad. Sci. U. S. A.*, 2015, **112**, 5325–5330; (*d*) R. R. Tykwinski, *Acc. Chem. Res.*, 2019, **52**, 2056–2069.

10. L. Ren, C. Liu, Z. Wang and X. Zhu, *J. Mater. Chem. C*, 2016, **4**, 5202–5206.

11. P. Hu, S. Lee, T. S. Herng, N. Aratani, T. P. Gonçalves, Q. Qi, X. Shi, H. Yamada, K.-W. Huang, J. Ding, D. Kim and J. Wu, *J. Am. Chem. Soc.*, 2016, **138**, 1065–1077.

12. W. Zeng, Z. Sun, T. S. Herng, T. P. Gonçalves, T. Y. Gopalakrishna, K.-W. Huang, J. Ding and J. Wu, *Angew. Chem. Int. Ed.*, 2016, **55**, 8615–8619.

13. P. Yadav, S. Das, H. Phan, T. S. Herng, J. Ding and J. Wu, *Org. Lett.*, 2016, **18**, 2886–2889.

14. P. K. Sharma and S. Das, *J. Org. Chem.*, 2022, **87**, 5430–5436.

15. Gaussian 09, Revision B.01, M. J. Frisch, G. W. Trucks, H. B. Schlegel, G. E. Scuseria, M. A. Robb, J. R. Cheeseman, G. Scalmani, V. Barone, B. Mennucci, G. A. Petersson, H. Nakatsuji, M. Caricato, X. Li, H. P. Hratchian, A. F. Izmaylov, J. Bloino, G. Zheng, J. L. Sonnenberg, M. Hada, M. Ehara, K. Toyota, R. Fukuda, J. Hasegawa, M. Ishida, T. Nakajima, Y. Honda, O. Kitao, H. Nakai, T. Vreven, J. A. Montgomery, Jr., J. E. Peralta, F. Ogliaro, M. Bearpark, J. J. Heyd, E. Brothers, K. N. Kudin, V. N. Staroverov, T. Keith, R. Kobayashi, J. Normand, K. Raghavachari, A. Rendell, J. C. Burant, S. S. Iyengar, J. Tomasi, M. Cossi, N. Rega, J. M. Millam, M. Klene, J. E. Knox, J. B. Cross, V. Bakken, C. Adamo, J. Jaramillo, R. Gomperts, R. E. Stratmann, O. Yazyev, A. J. Austin, R. Cammi, C. Pomelli, J. W. Ochterski, R. L. Martin, K. Morokuma, V. G. Zakrzewski, G. A. Voth, P. Salvador, J. J. Dannenberg, S. Dapprich, A. D. Daniels, O. Farkas, J. B. Foresman, J. V. Ortiz, J. Cioslowski and D. J. Fox, Gaussian, Inc., Wallingford CT, 2010;

16. D. T. Chase, A. G. Fix, S. J. Kang, B. D. Rose, C. D. Weber, Y. Zhong, L. N. Zakharov, M. C. Lonergan, C. Nuckolls and M. M. Haley, *J. Am. Chem. Soc.*, 2012, **134**, 10349–10352.

17. Considering r(H) 1.1 Å, the F···H distance is still less than Σr_{vdW}. R. S. Rowland and R. Taylor, *J. Phys. Chem.*, 1996, **100**, 7384–7391.

18. (*a*) G. R. Desiraju, *Angew. Chem. Int. Ed.*, 2011, **50**, 52–59; (*b*) P. A. Champagne, J. Desroches and J. S. Paquin, *Synthesis*, 2015, **47**, 306–322.

19. G. Karthik, P. V. Krushna, A. Srinivasan and T. K. Chandrashekar, *J. Org. Chem.*, 2013, **78**, 8496–8501.

20. T. Y. Gopalakrishna, J. S. Reddy and V. G. Anand, *Angew. Chem. Int. Ed.*, 2013, **52**, 1763–1767.

21. (*a*) M. M. Haley, *Chem. Rec.*, 2015, **15**, 1140–1143; (*b*) C. K. Frederickson, B. D. Rose and M. M. Haley, *Acc. Chem. Res.*, 2017, **50**, 977–987.

22. B. D. Rose, L. E. Shoer, M. R. Wasielewski and M. M. Haley, *Chem. Phys. Lett.*, 2014, **616–617**, 137–141.

23. T. Y. Gopalakrishna, W. Zeng, X. Lu and J. Wu, *Chem. Commun.*, 2018, **54**, 2186–2199.

24. (*a*) C. Goh, R. J. Kline, M. D. McGehee, E. N. Kadnikova and J. M. J. Fréchet, *Appl. Phys. Lett.*, 2005, **86**, 122110; (*b*) B. C. Thompson, B. J. Kim, D. F. Kavulak, K. Sivula, C. Mauldin and J. M. J. Frechet, *Macromolecules*, 2007, **40**, 7425–7428.

25. (*a*) Y. Li, R. G. Clevenger, L. Jin, K. V. Kilway and Z. Peng, *J. Mater. Chem. C*, 2014, **2**, 7180–7183; (*b*) J. C. Blakesley, F. A. Castro, W. Kylberg, G. F. A. Dibb, C. Arantes, R. Valaski, M. Cremona, J. S. Kim and J.-S. Kim, *Org. Electron.*, 2014, **15**, 1263–1272.

26. P. N. Murgatroyd, *J. Phys. D. Appl. Phys.*, 1970, **3**, 151.

27. (*a*) P. W. M. Blom, V. D. Mihailetchi, L. J. A. Koster and D. E. Markov, *Adv. Mater.*, 2007, **19**, 1551–1566; (*b*) H. Yin, P. Bi, S. H. Cheung, W. L. Cheng, K. L. Chiu, C. H. Y. Ho, H. W. Li, S. W. Tsang, X. Hao and S. K. So, *Sol. RRL*, 2018, **2**, 1700239.

28. (*a*) T.-Y. Chu and O.-K. Song, *Appl. Phys. Lett.*, 2007, **90**, 203512; (*b*) L. Zhang, X. Xing, Z. Chen, L. Xiao, B. Qu and Q. Gong, *Energy Technol.*, 2013, **1**, 613–616; (*c*) C. Zhou, Z. Chen, G. Zhang, C. McDowell, P. Luo, X. Jia, M. J. Ford, M. Wang, G. C. Bazan, F. Huang and Y. Cao, *Adv. Energy Mater.*, 2018, **8**, 1701668.

29. K. Horii, A. Nogata, Y. Mizuno, H. Iwasa, M. Suzuki, K.-i. Nakayama, A. Konishi and M. Yasuda, *Chem. Lett.*, 2022, **51**, 325–329.

30. (*a*) A. Konishi and M. Yasuda, *Chem. Lett.*, 2021, **50**, 195–212; (*b*) D. Peters, *J. Chem. Soc.*, 1958, 1028–1039; (c) D. Peters, *J. Chem. Soc.*, 1958, 1039–1047.

31. J. L. Marshall, N. J. O'Neal, L. N. Zakharov and M. M. Haley, *J. Org. Chem.*, 2016, **81**, 3674–3680.

32. V. S. Batista, R. H. Crabtree, S. J. Konezny, O. R. Luca and J. M. Praetorius, *New J. Chem.*, 2012, **36**, 1141–1144.

33. Bruker, SAINT V8.38A, (Bruker AXS Inc., 2017).

34. O. V. Dolomanov, L. J. Bourhis, R. J. Gildea, J. A. Howard and H. Puschmann, *J. Appl. Crystallogr.* 2009, **42**, 339–341.

35. L. J. Bourhis, O. V. Dolomanov, R. J. Gildea, J. A. Howard and H. Puschmann, *Acta Crystallogr. A.* 2015, **71**, 59–75.

36. G. M. Sheldrick, *Acta Crystallogr. C Struct. Chem*. 2015, **71**, 3–8.

37. N. M. O'Boyle, A. L. Tenderholt and K. M. Langner, *J. Comp. Chem.* 2008, **29**, 839–845.

2B.7 Appendix

NMR Spectra

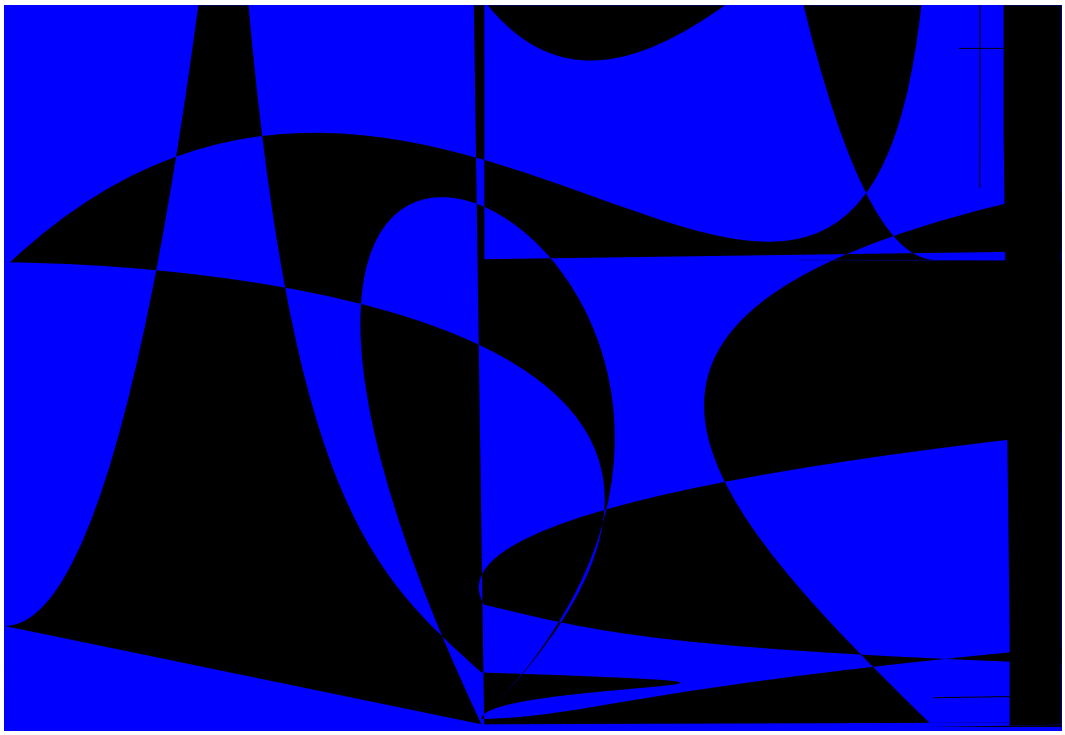

Figure 2B.13 ^{1}H NMR spectrum of **13** (in $CDCl_3$, 400 MHz).

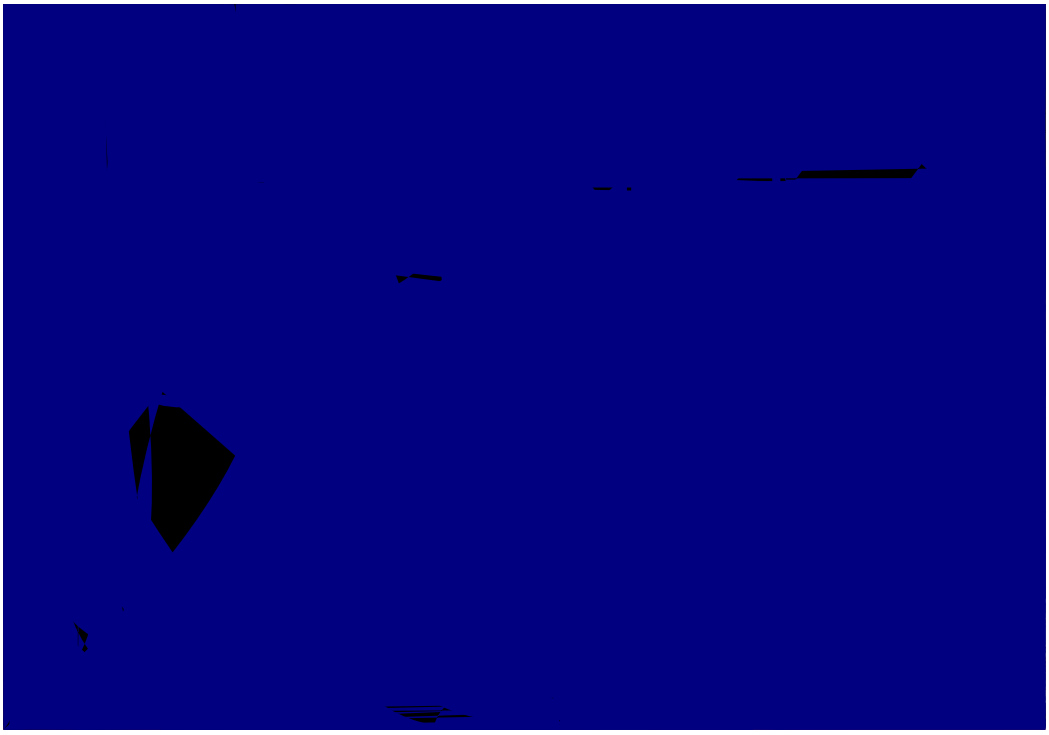

Figure 2B.14 ^{13}C NMR spectrum of **13** (in $CDCl_3$, 100 MHz).

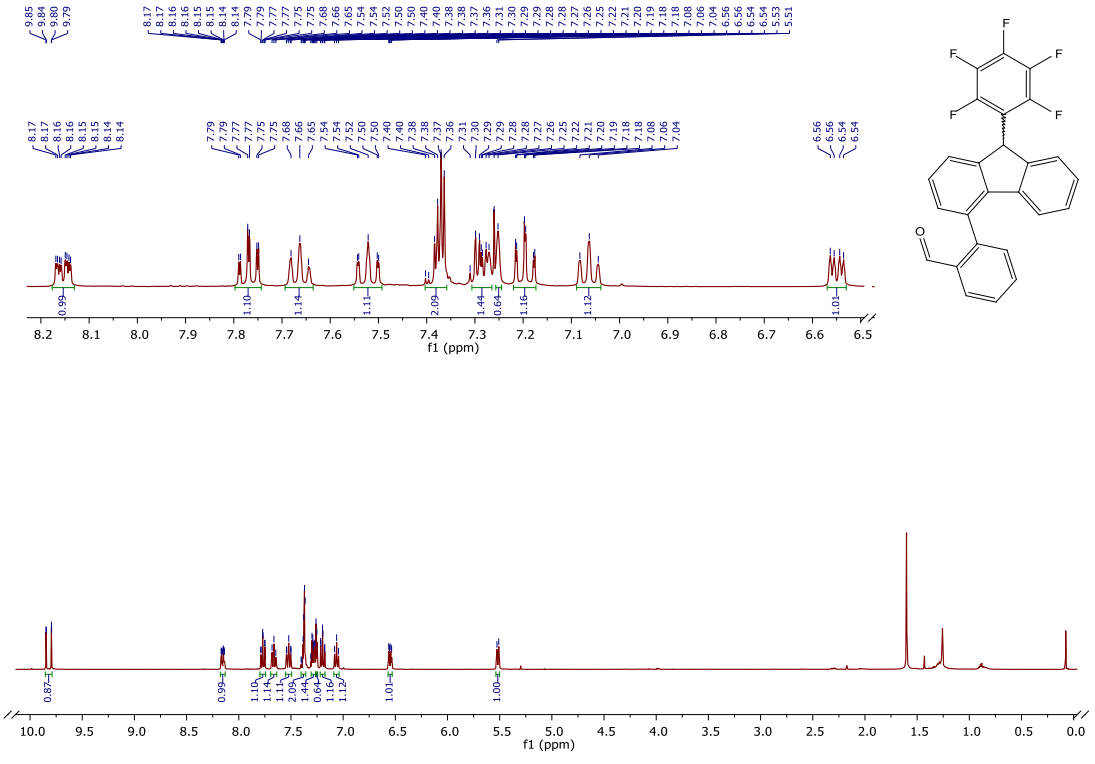

Figure 2B.15 ^{1}H NMR spectrum of **14** (in $CDCl_3$, 400 MHz).

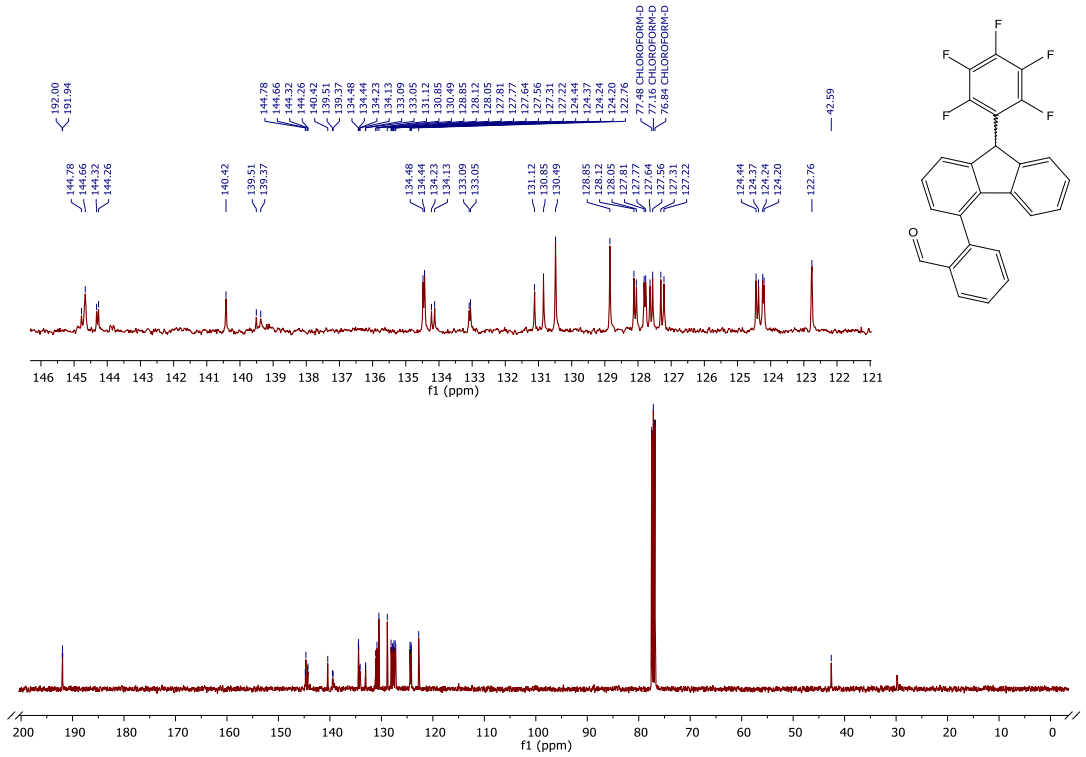

Figure 2B.16 ^{13}C NMR spectrum of **14** (in $CDCl_3$, 100 MHz).

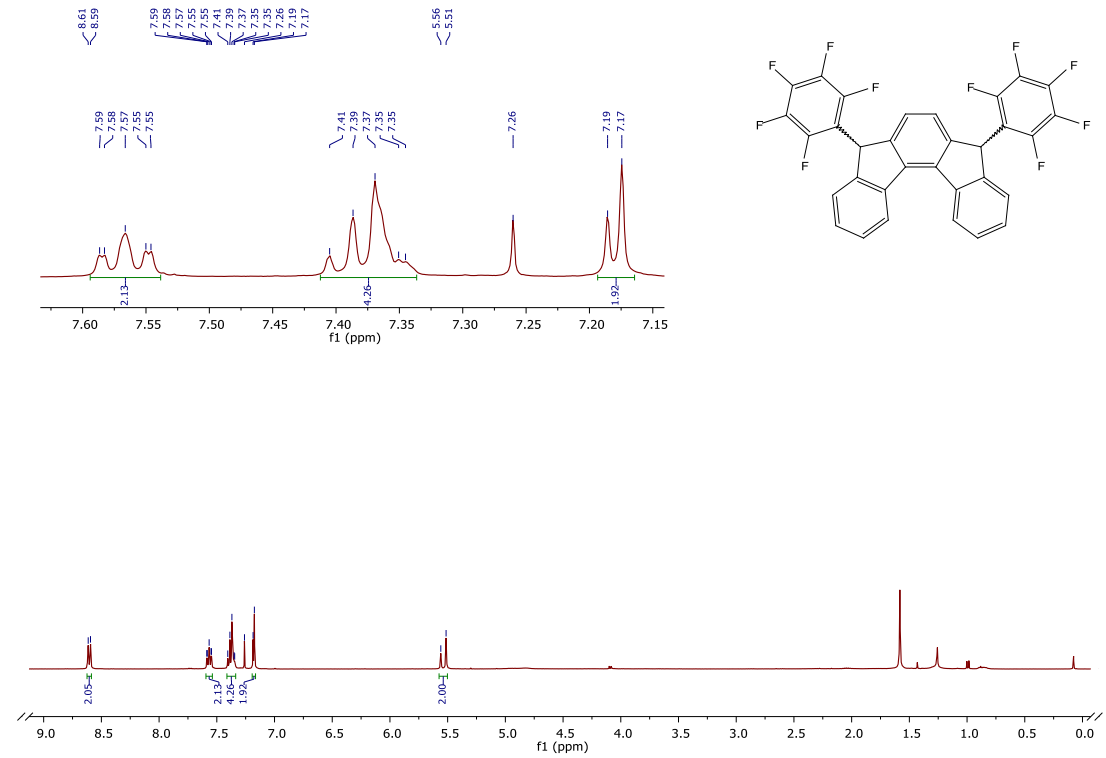

Figure 2B.17 ^{1}H NMR spectrum of **16** (in $CDCl_3$, 400 MHz).

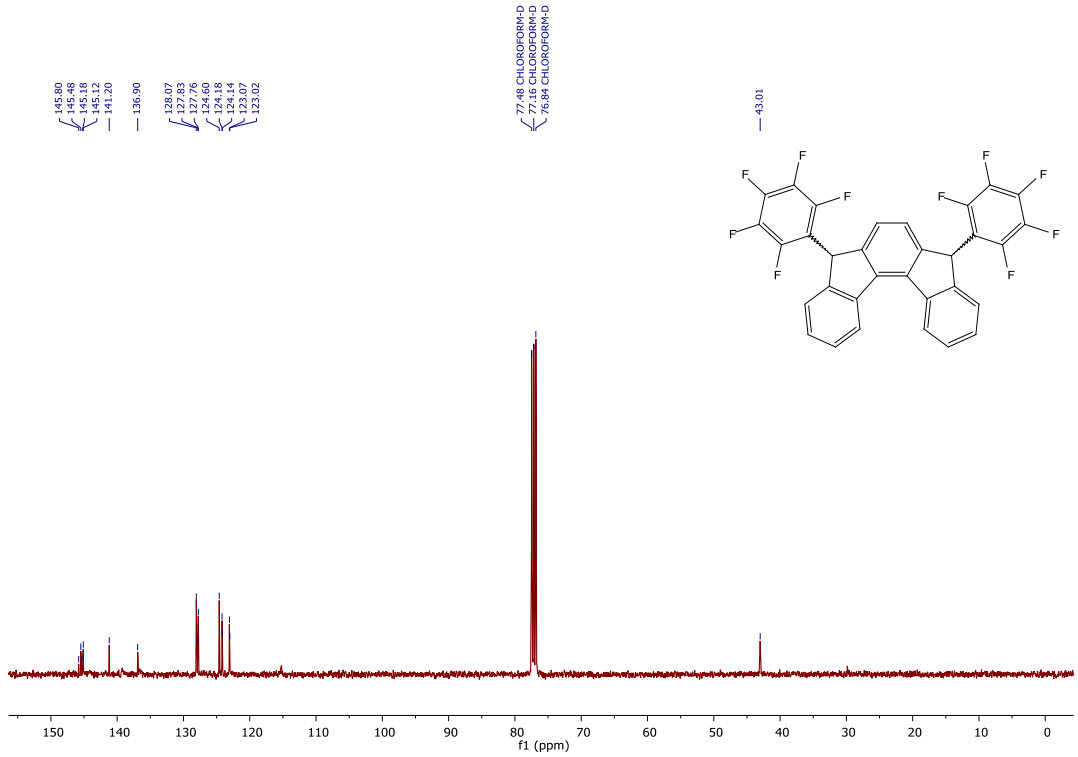

Figure 2B.18 ^{13}C NMR spectrum of **16** (in $CDCl_3$, 100 MHz).

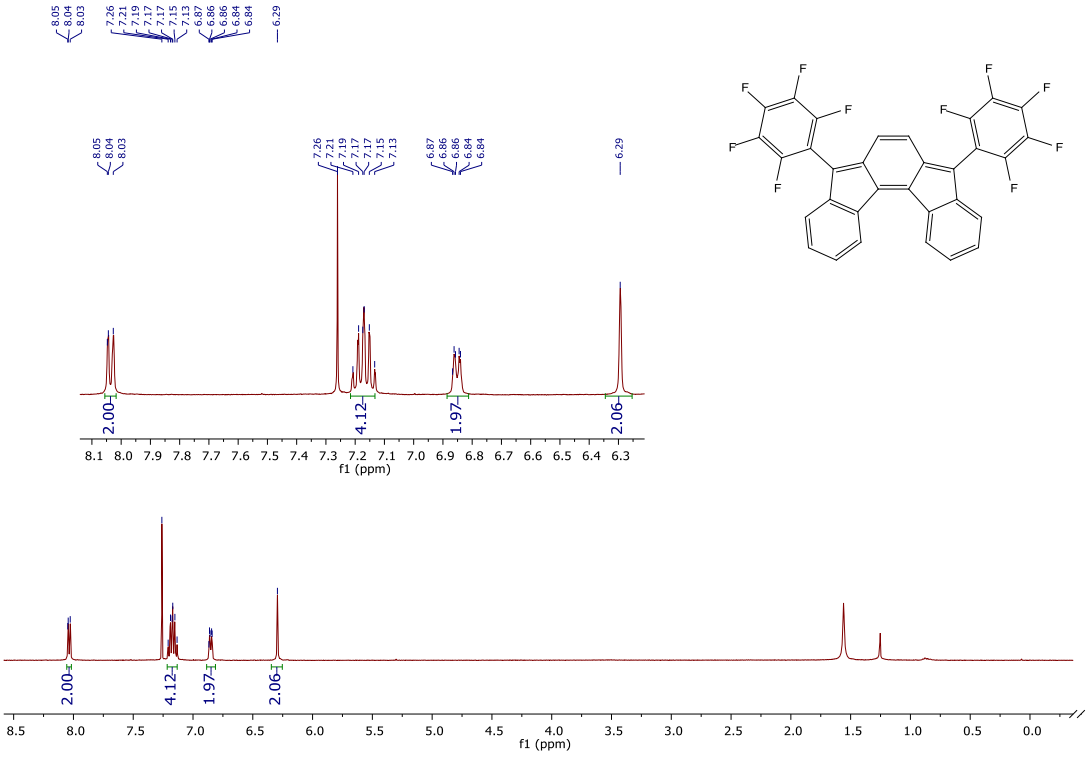

Figure 2B.19 ^{1}H NMR spectrum of **17** (in $CDCl_3$, 400 MHz).

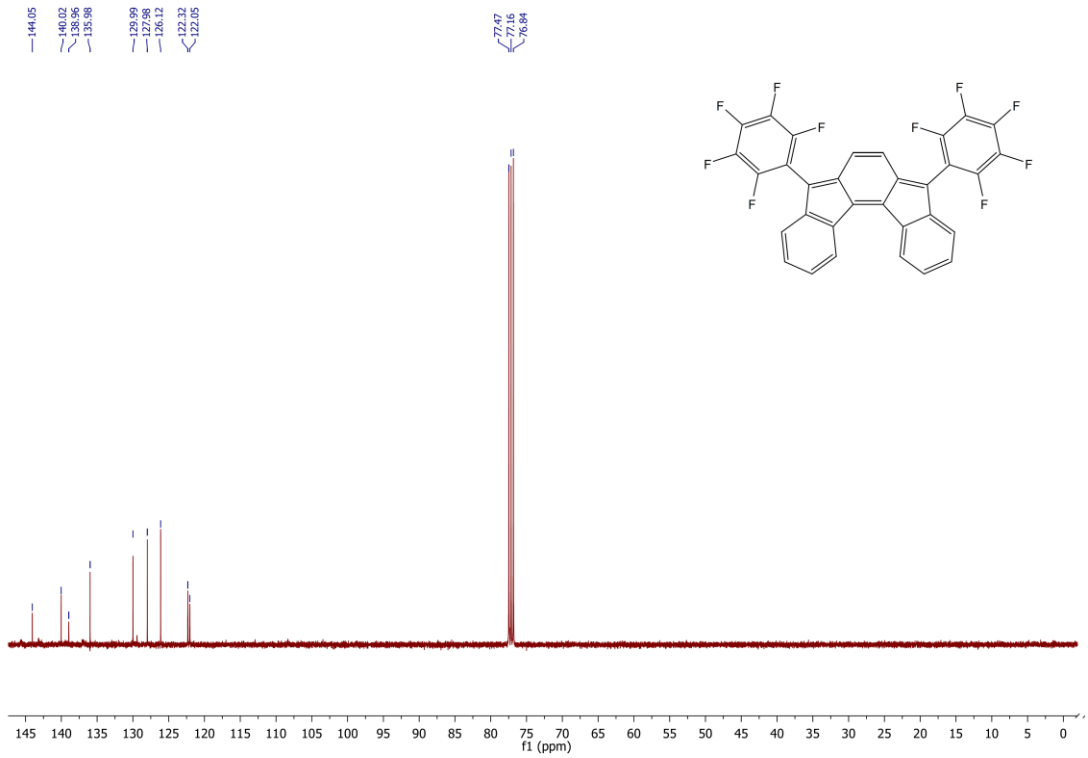

Figure 2B.20 ^{13}C NMR spectrum of **17** (in $CDCl_3$, 100 MHz).

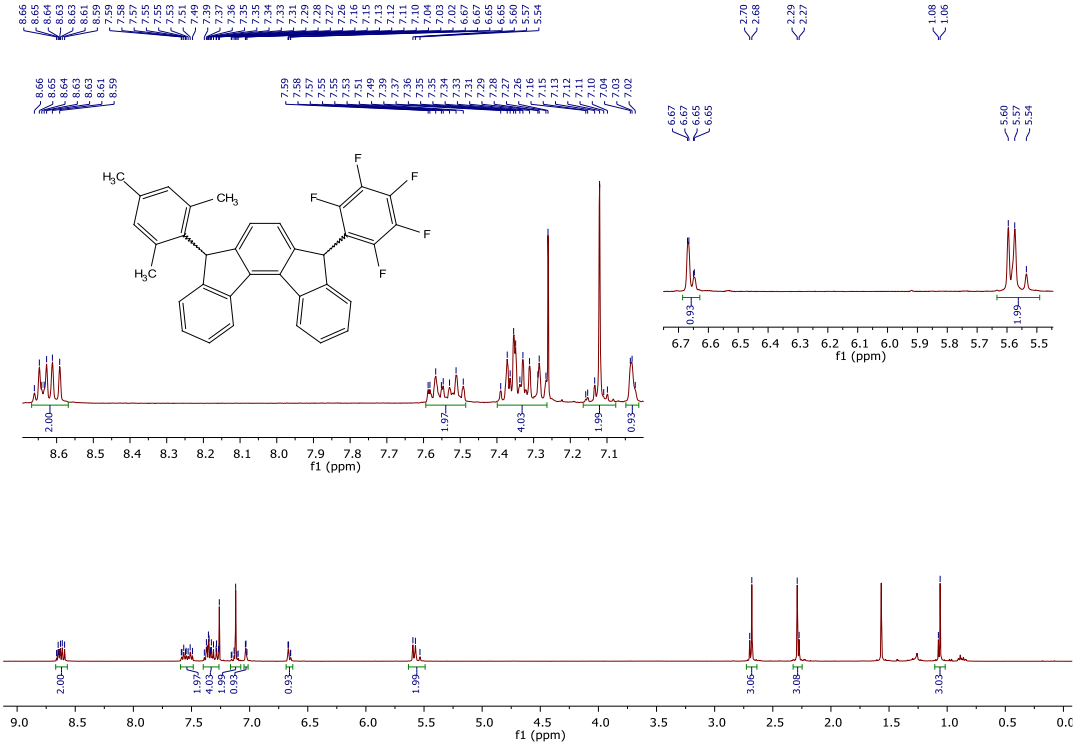

Figure 2B.21 ^{1}H NMR spectrum of **20** (in $CDCl_3$, 400 MHz).

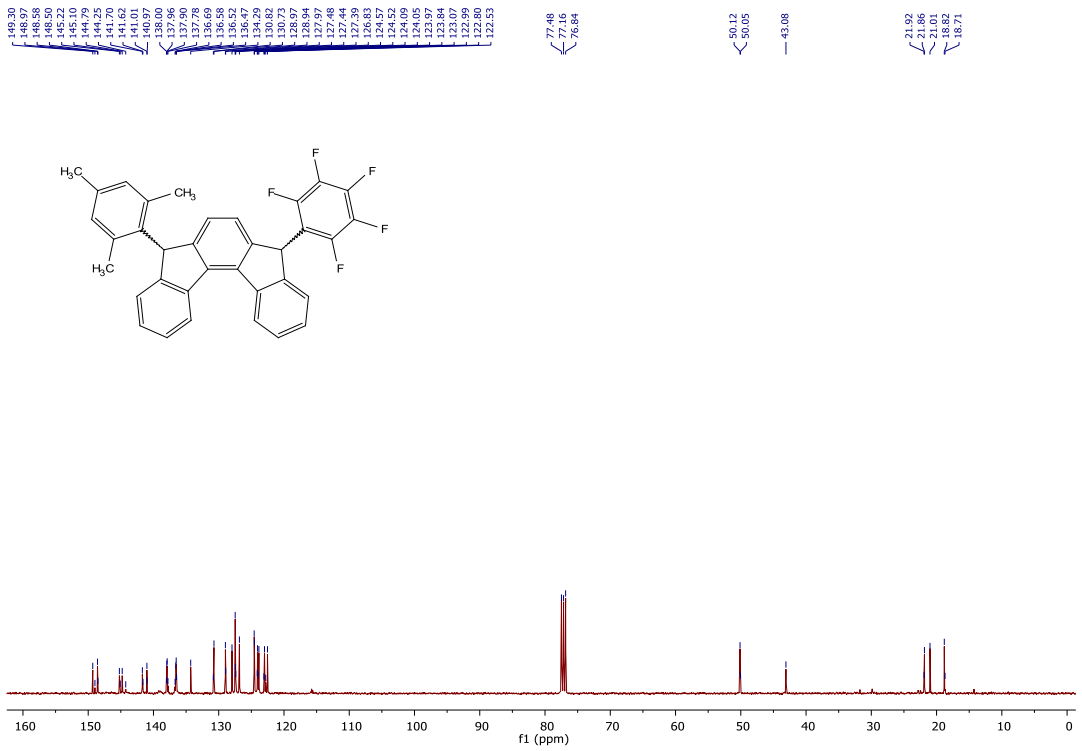

Figure 2B.22 ^{13}C NMR spectrum of **20** (in $CDCl_3$, 100 MHz).

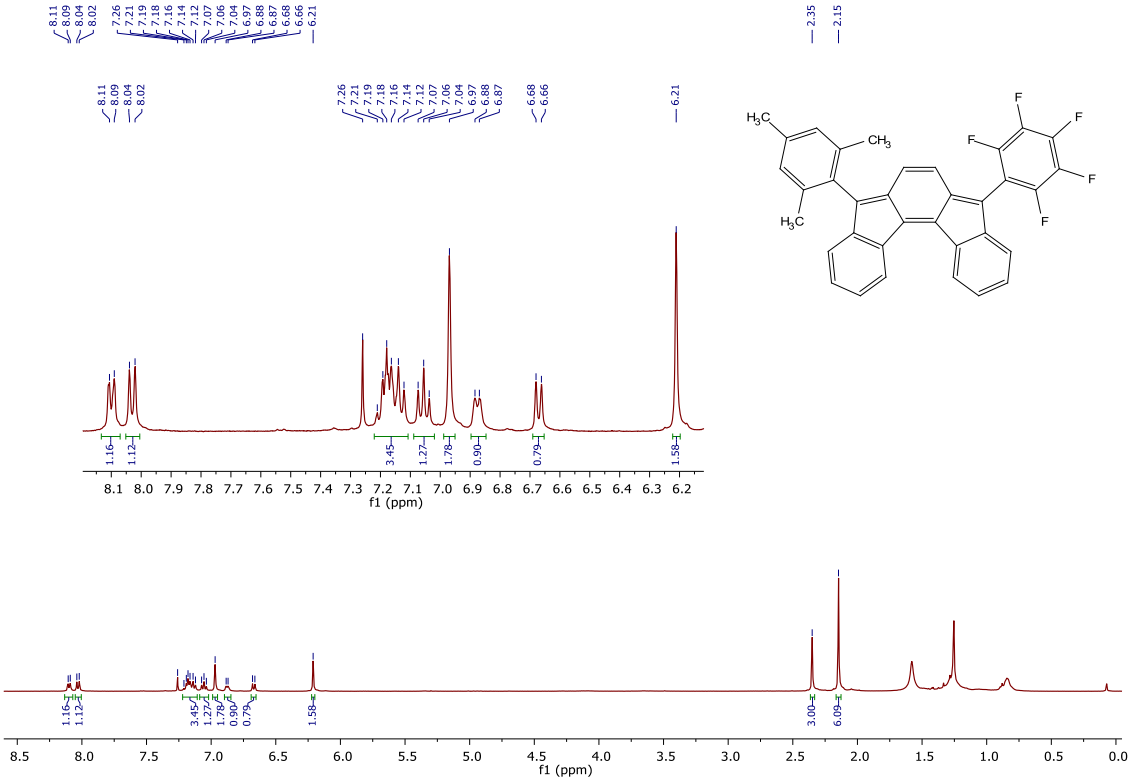

Figure 2B.23 ^{1}H NMR spectrum of **7** (in $CDCl_3$, 400 MHz).

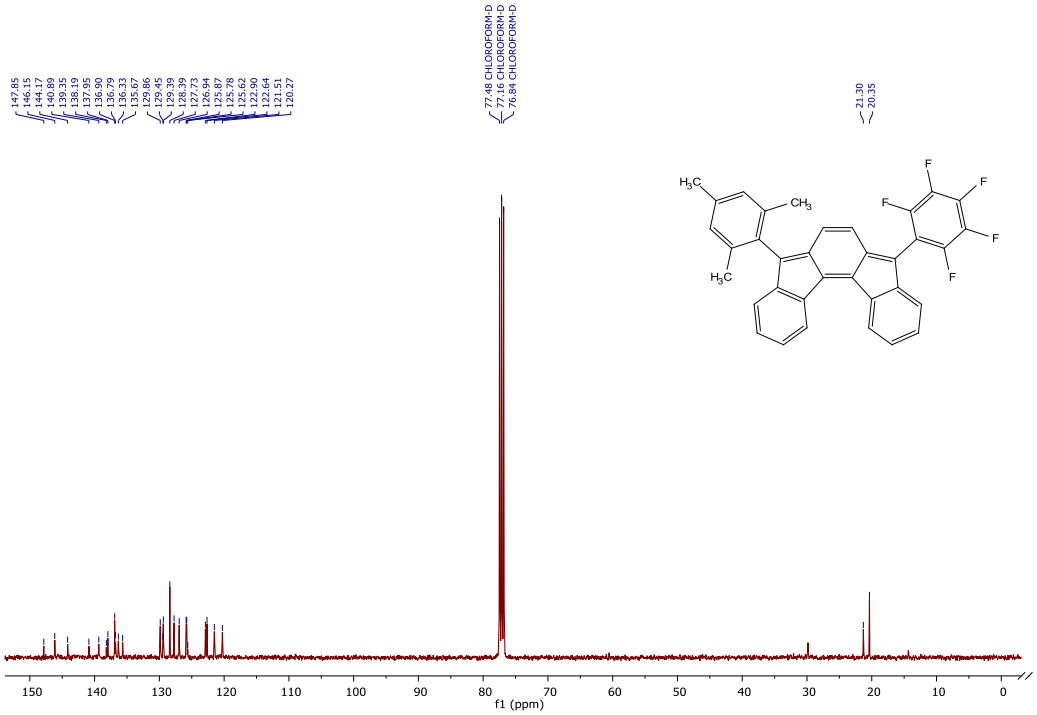

Figure 2B.24 ^{13}C NMR spectrum of **7** (in $CDCl_3$, 100 MHz).

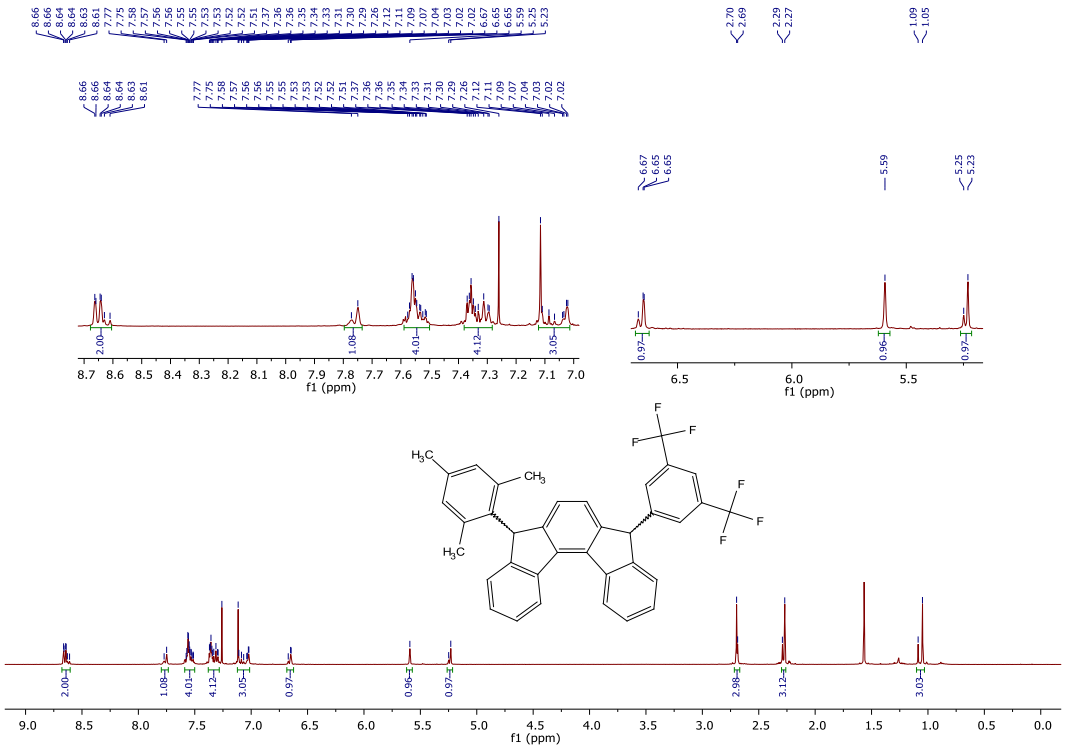

Figure 2B.25 ^{1}H NMR spectrum of **22** (in $CDCl_3$, 400 MHz).

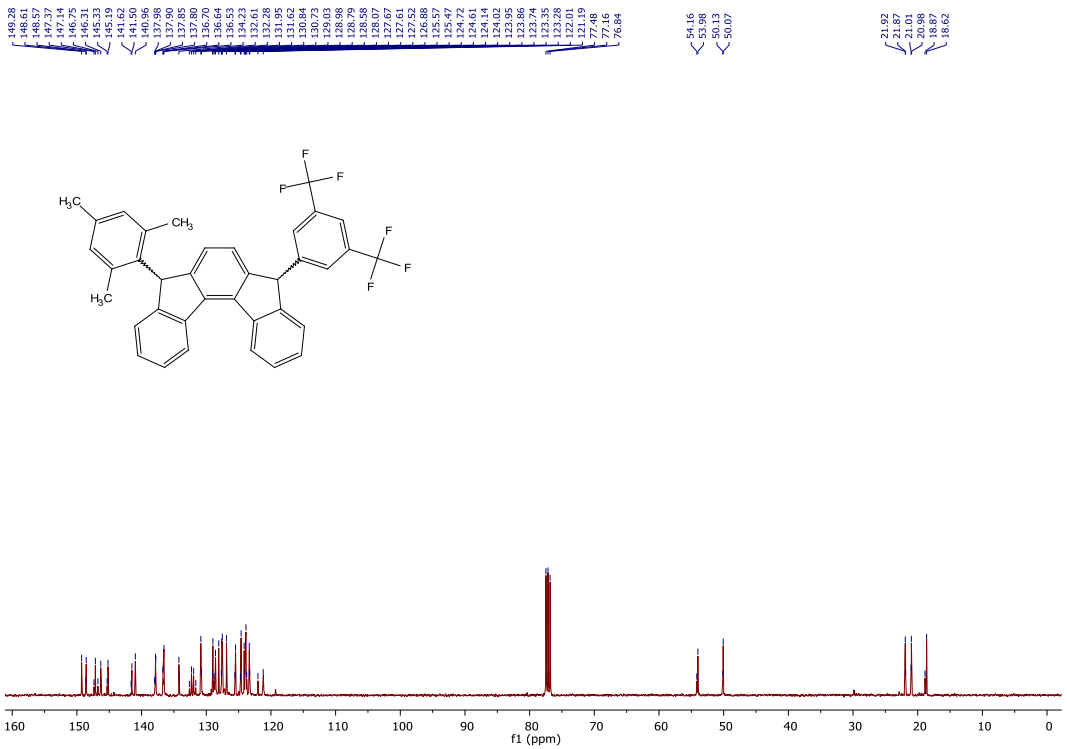

Figure 2B.26 ^{13}C NMR spectrum of **22** (in $CDCl_3$, 100 MHz).

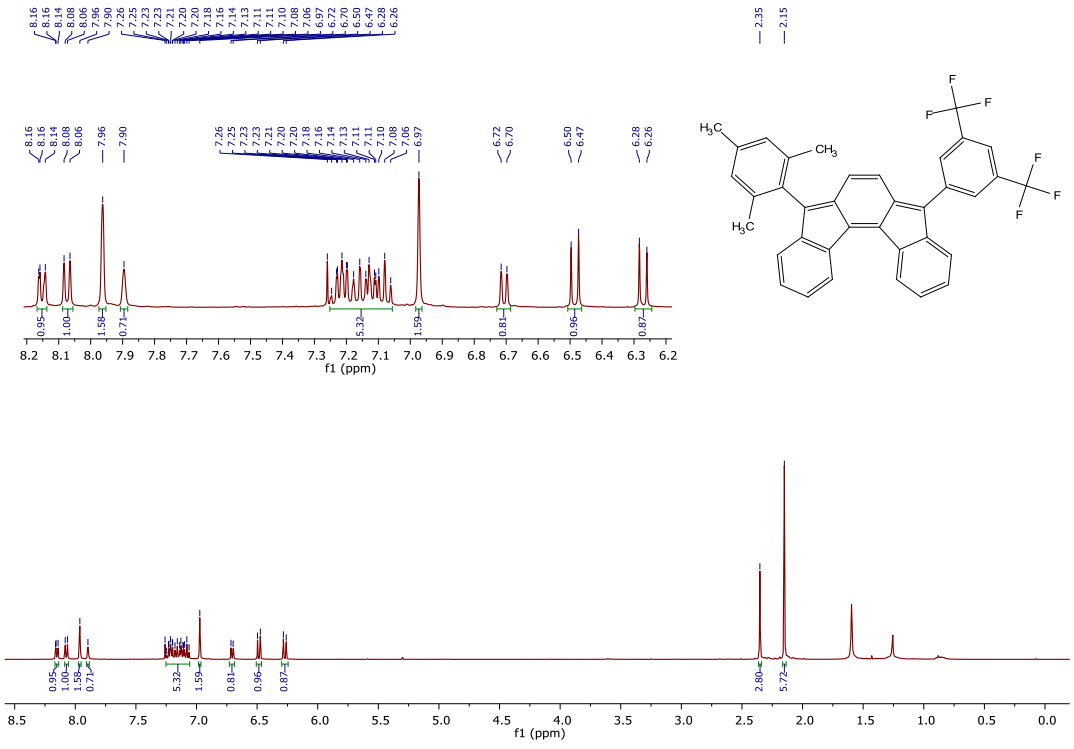

Figure 2B.27 ^{1}H NMR spectrum of **8** (in $CDCl_3$, 400 MHz).

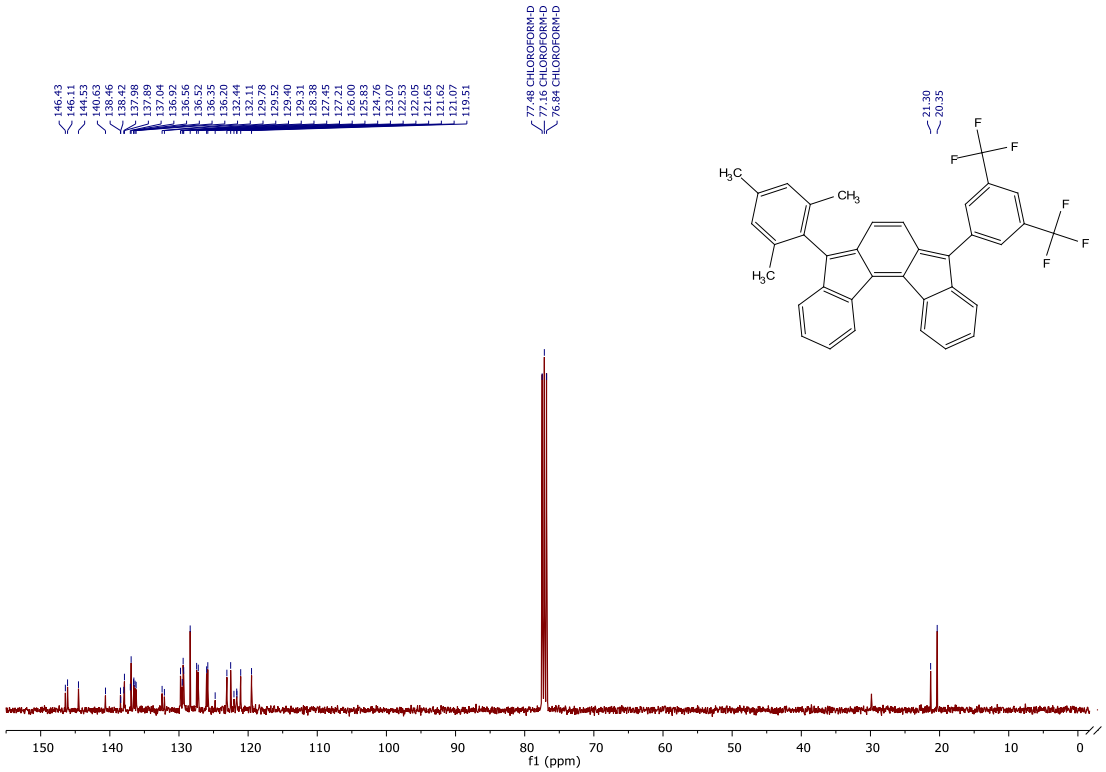

Figure 2B.28 ^{13}C NMR spectrum of **8** (in $CDCl_3$, 100 MHz).

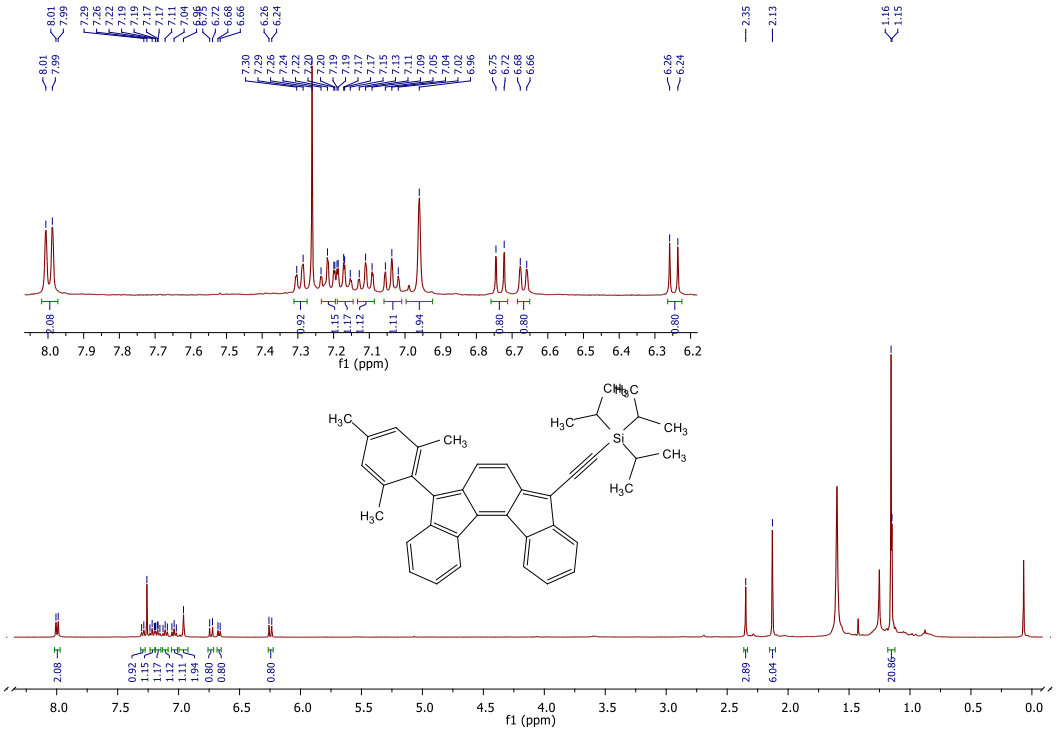

Figure 2B.29 ^{1}H NMR spectrum of **9** (in $CDCl_3$, 400 MHz).

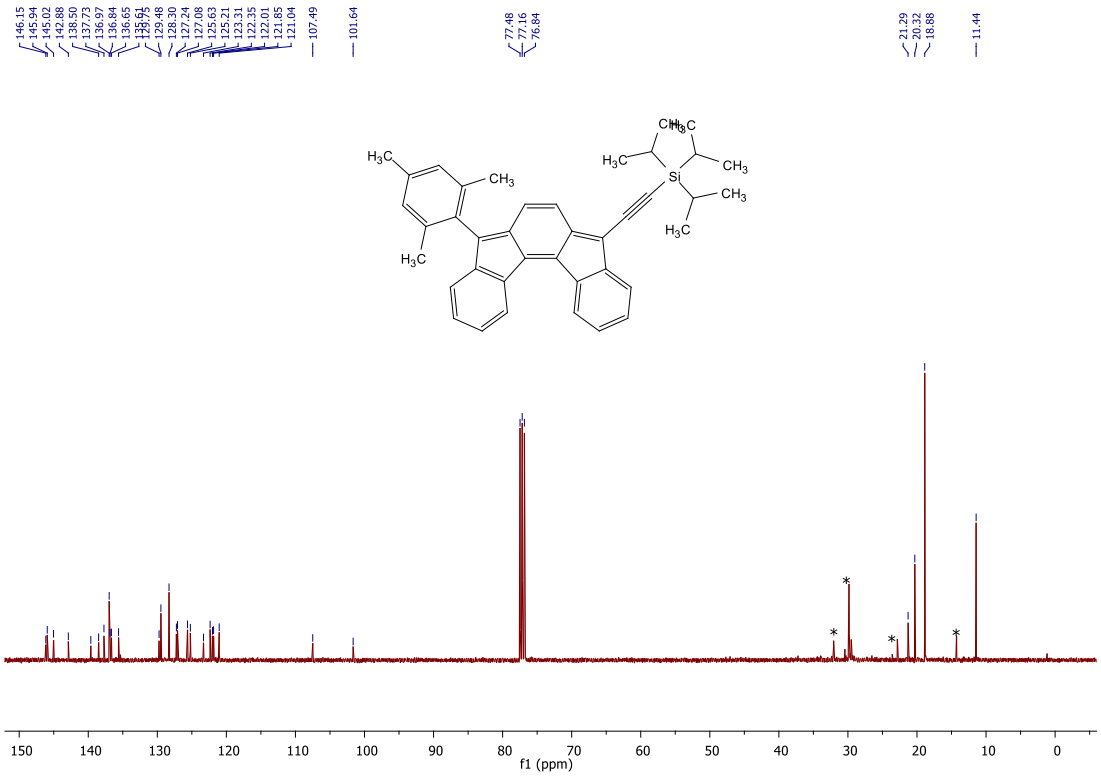

Figure 2B.30 ^{13}C NMR spectrum of **9** (in $CDCl_3$, 100 MHz). (*grease/hexanes residuals)

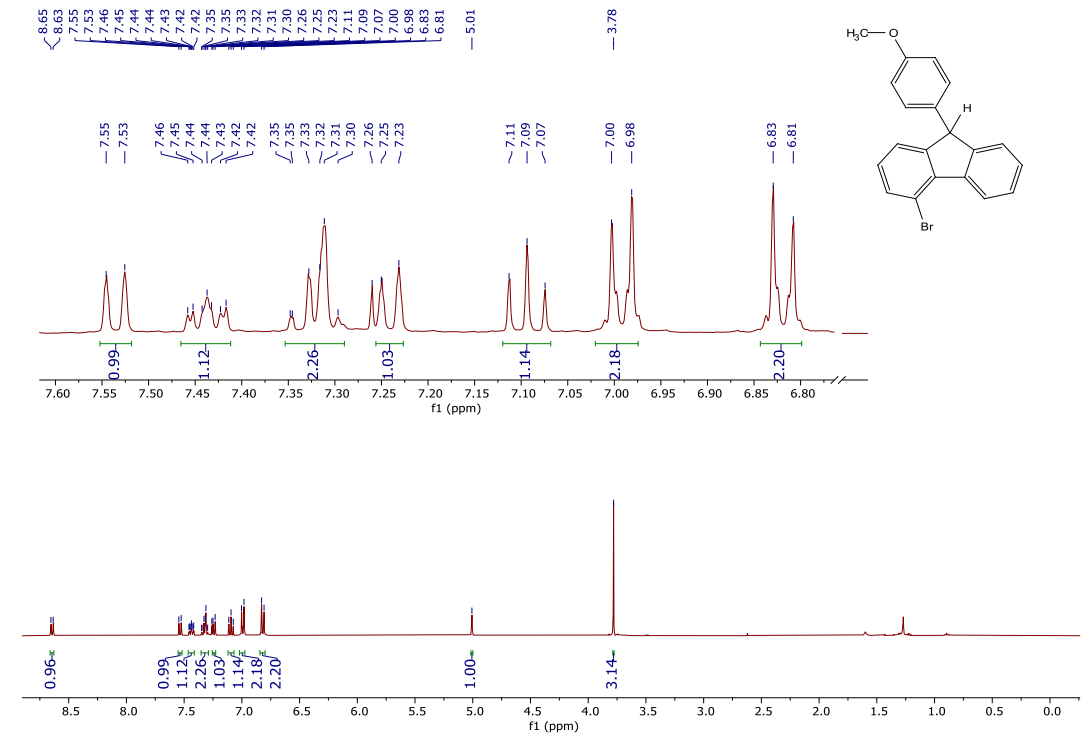

Figure 2B.31 ^{1}H NMR spectrum of **26** (in $CDCl_3$, 400 MHz).

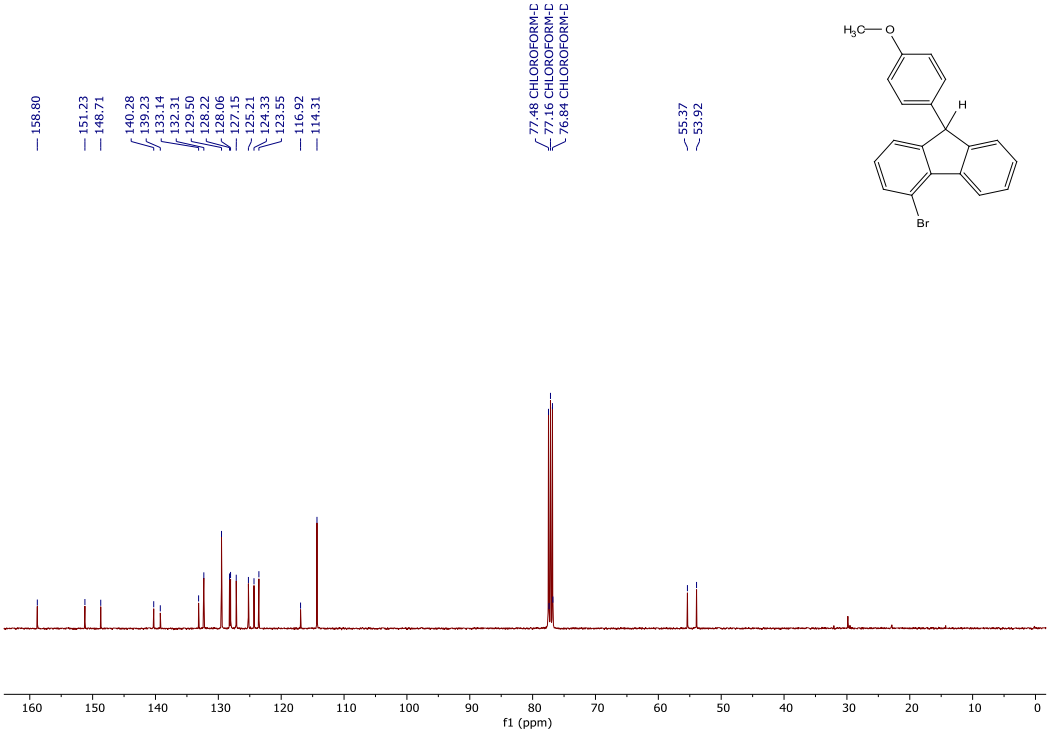

Figure 2B.32 ^{13}C NMR spectrum of **26** (in $CDCl_3$, 100 MHz).

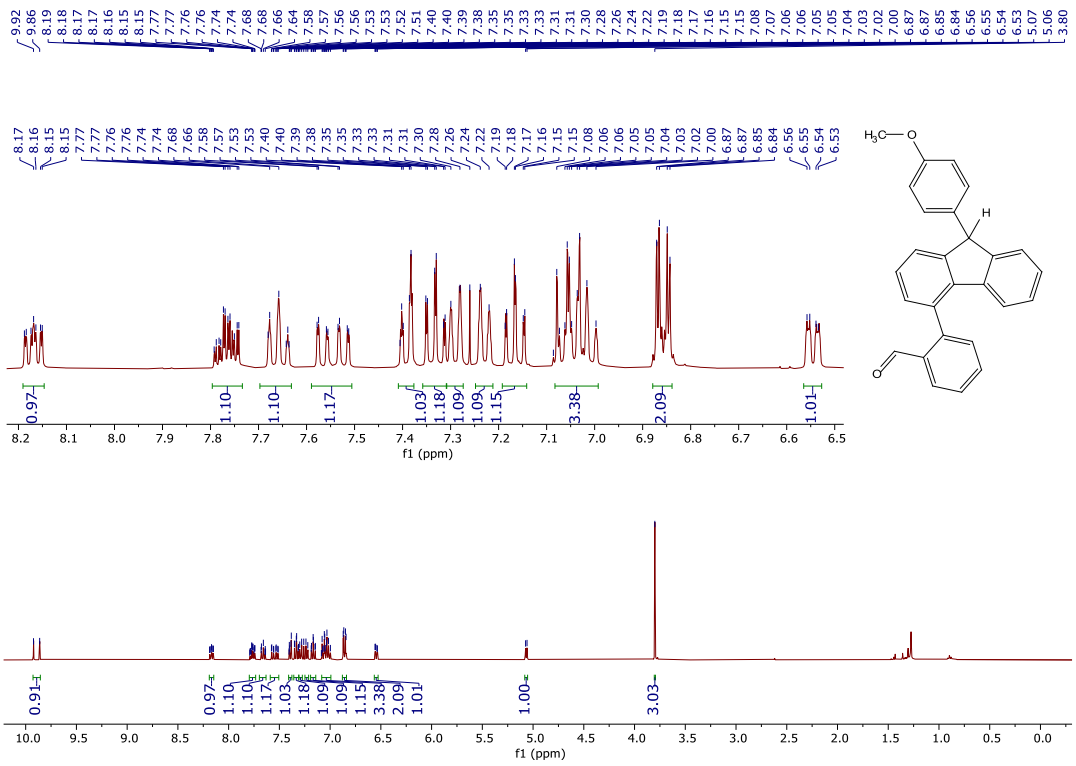

Figure 2B.33 ^{1}H NMR spectrum of **27** (in $CDCl_3$, 400 MHz).

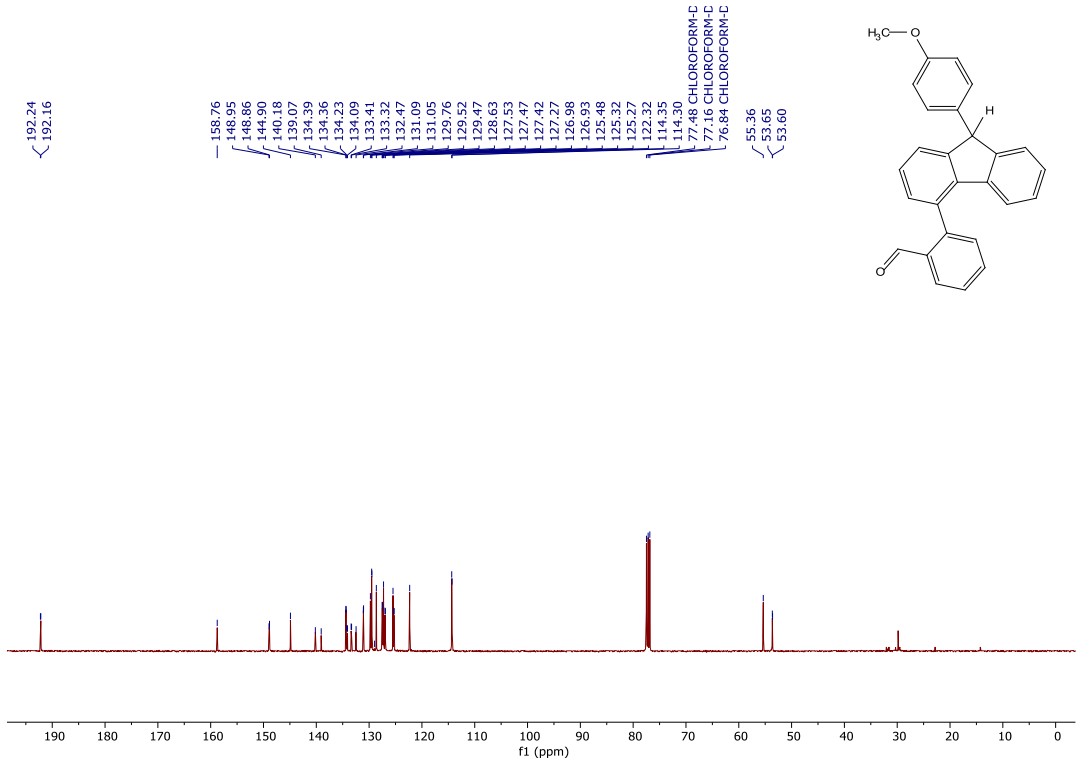

Figure 2B.34 ^{13}C NMR spectrum of **27** (in $CDCl_3$, 100 MHz).

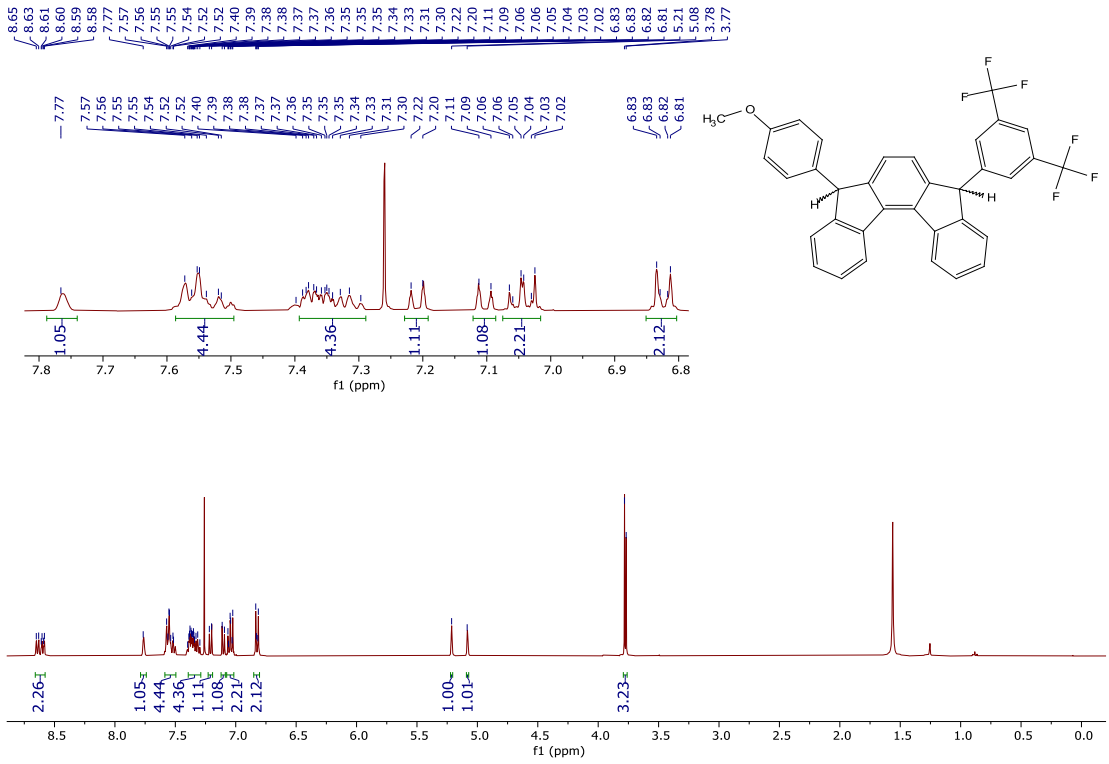

Figure 2B.35 ^{1}H NMR spectrum of **29** (in $CDCl_3$, 400 MHz).

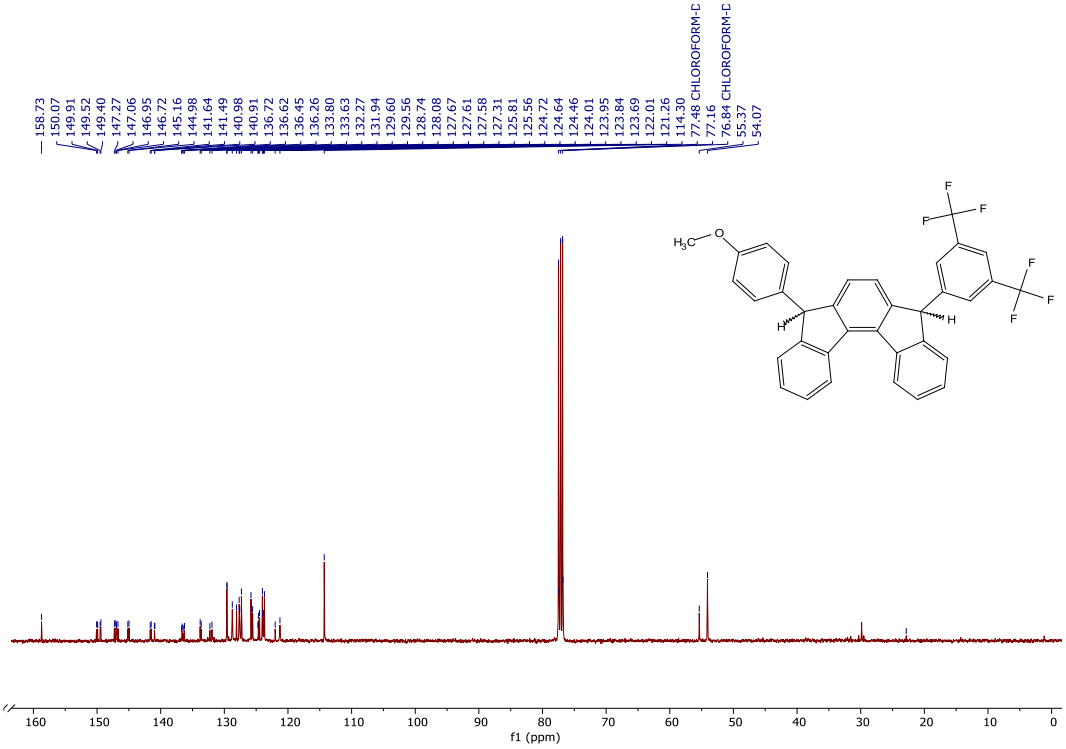

Figure 2B.36 ^{13}C NMR spectrum of **29** (in $CDCl_3$, 100 MHz).

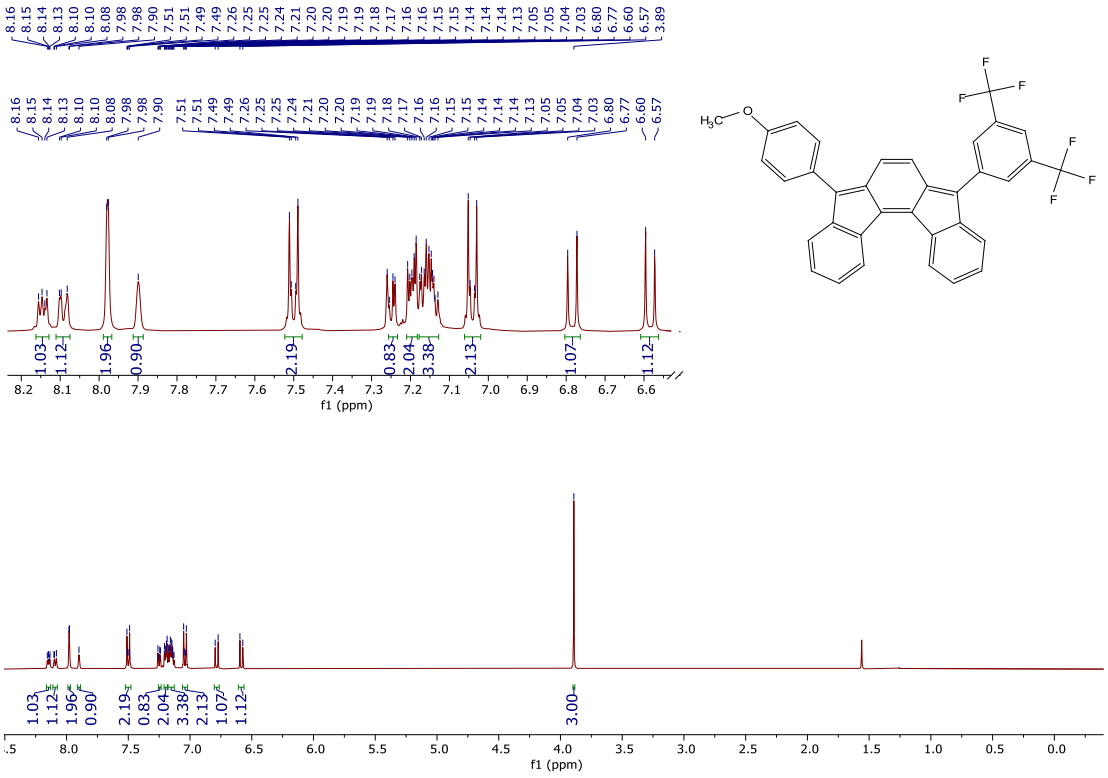

Figure 2B.37 ^{1}H NMR spectrum of **10** (in $CDCl_3$, 400 MHz).

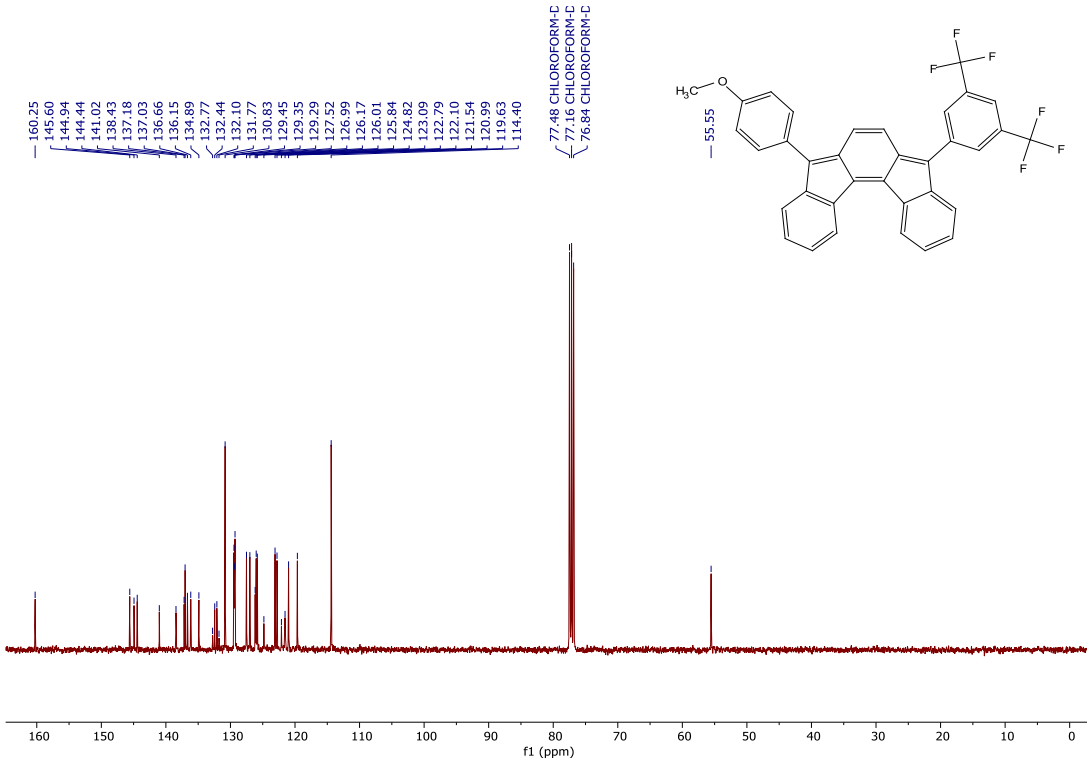

Figure 2B.38 ^{13}C NMR spectrum of **10** (in $CDCl_3$, 100 MHz).

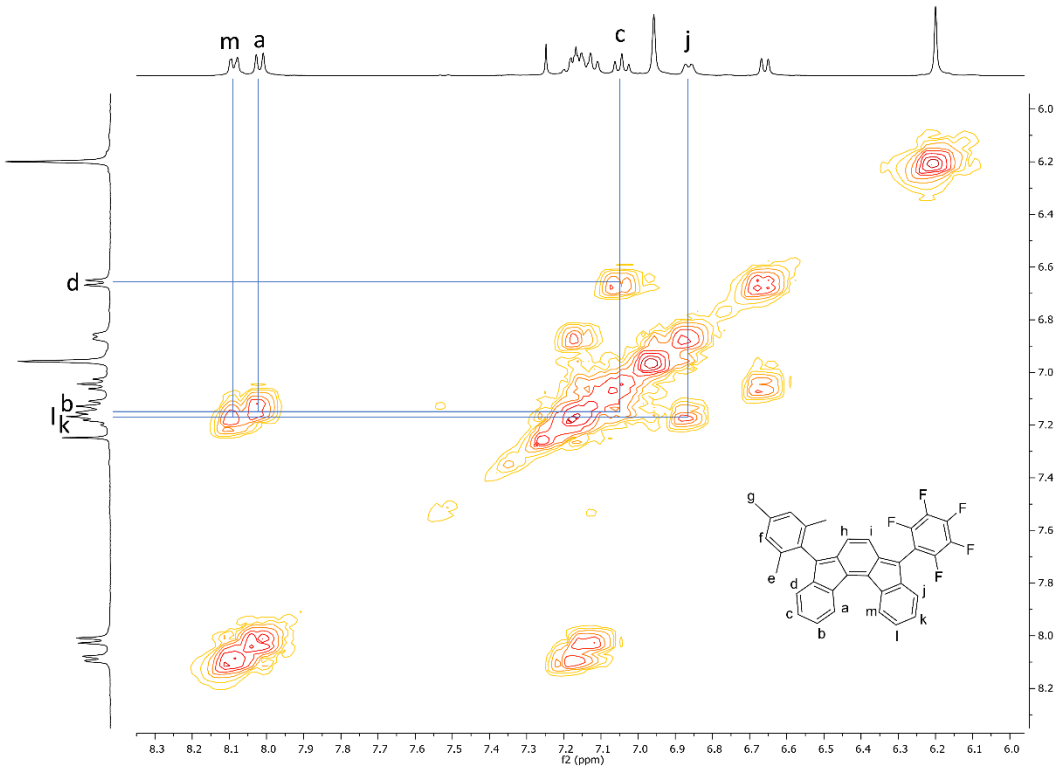

Figure 2B.39 ^{1}H-^{1}H COSY NMR of **7** (in $CDCl_3$).

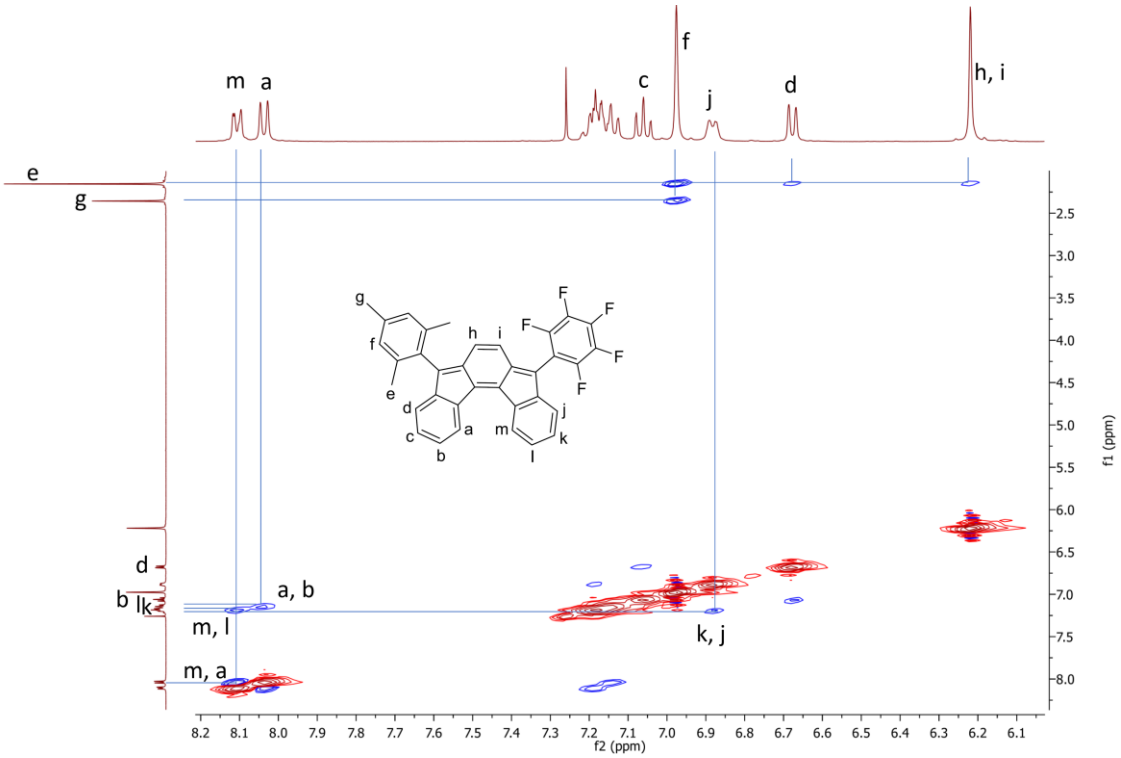

Figure 2B.40 ^{1}H-^{1}H NOESY NMR of **7** (in $CDCl_3$).

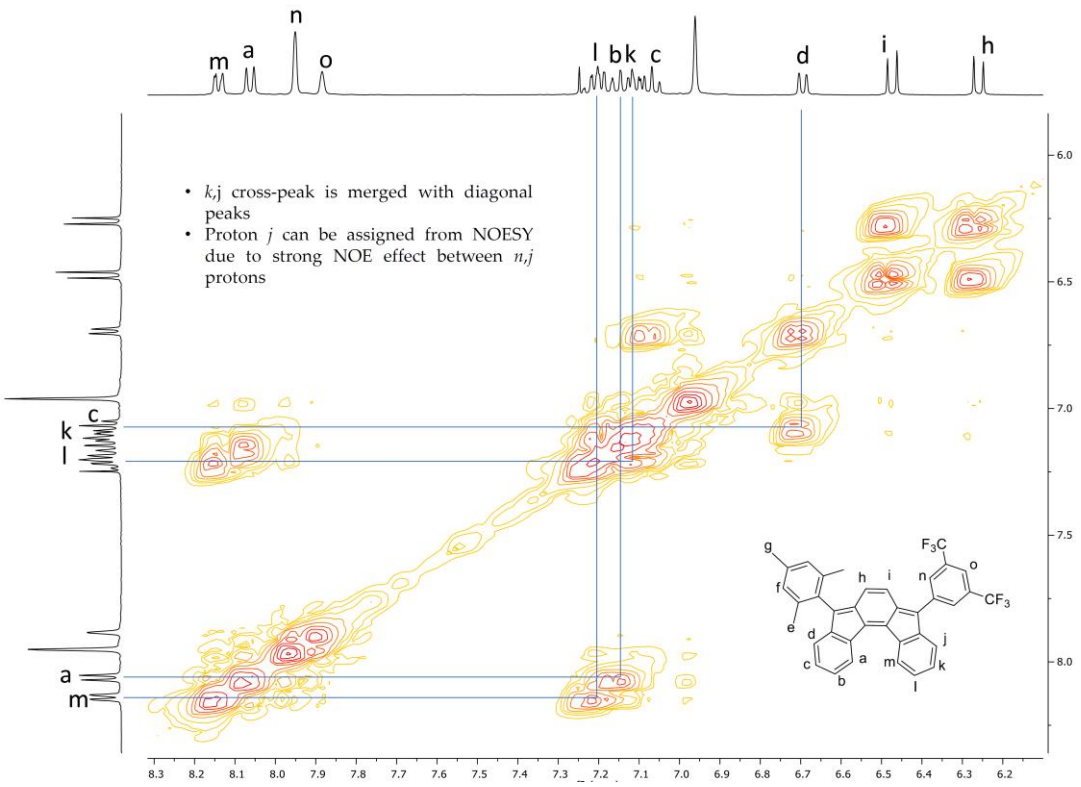

Figure 2B.41 ^{1}H-^{1}H COSY NMR of **8** (in $CDCl_3$).

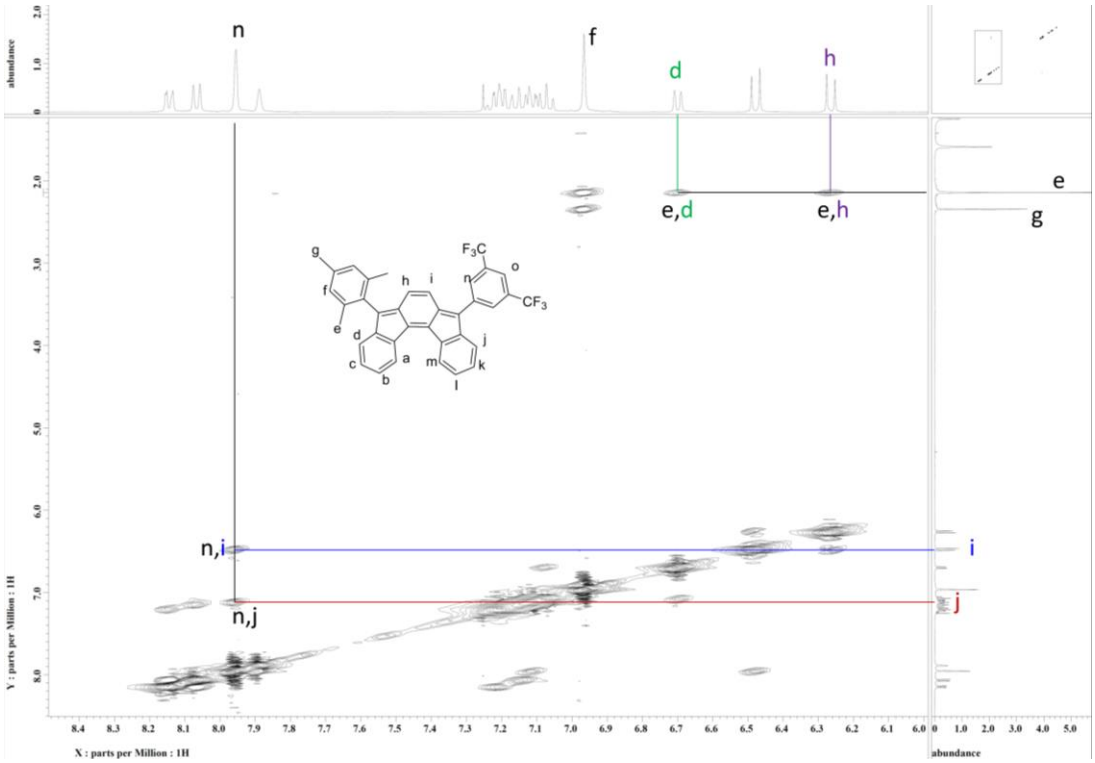

Figure 2B.42 ^{1}H-^{1}H NOESY NMR of **8** (in $CDCl_3$).

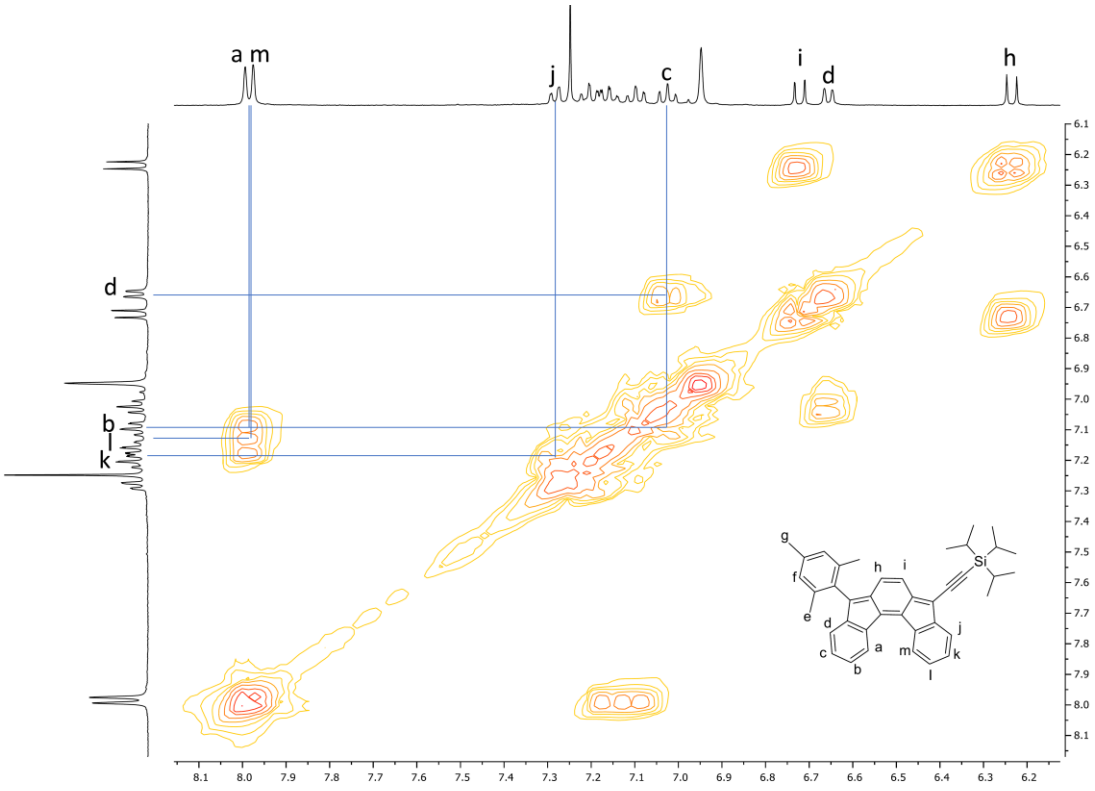

Figure 2B.43 ^{1}H-^{1}H COSY NMR of **9** (in $CDCl_3$).

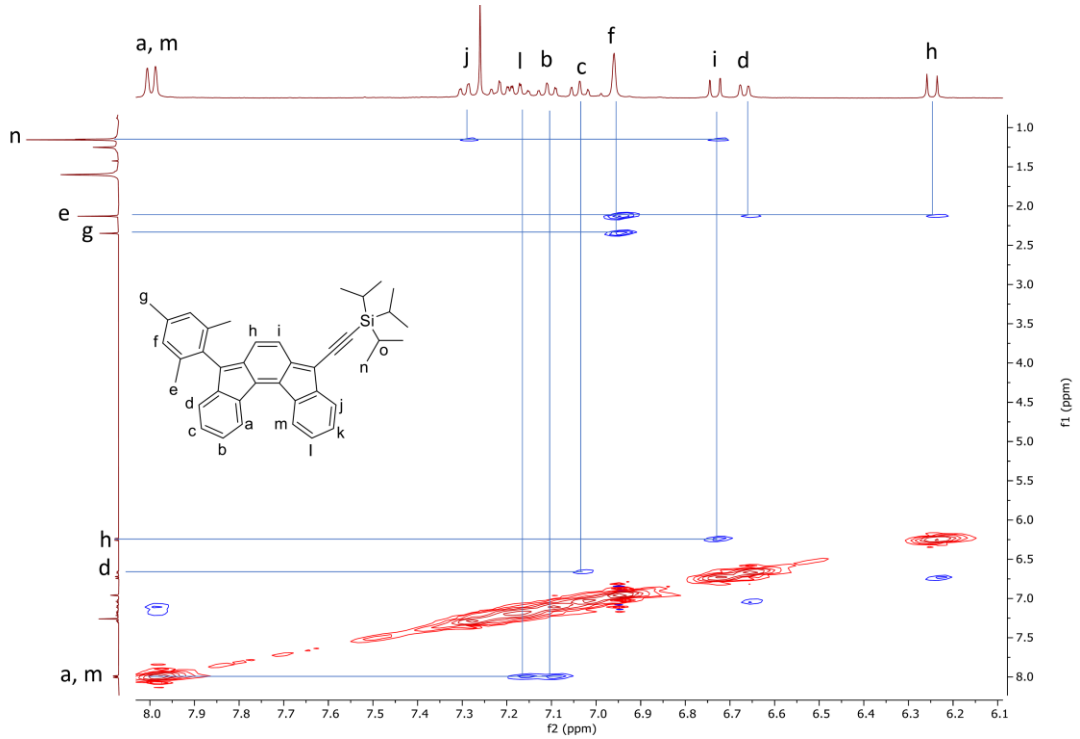

Figure 2B.44 ^{1}H-^{1}H NOESY NMR of **9** (in $CDCl_3$).

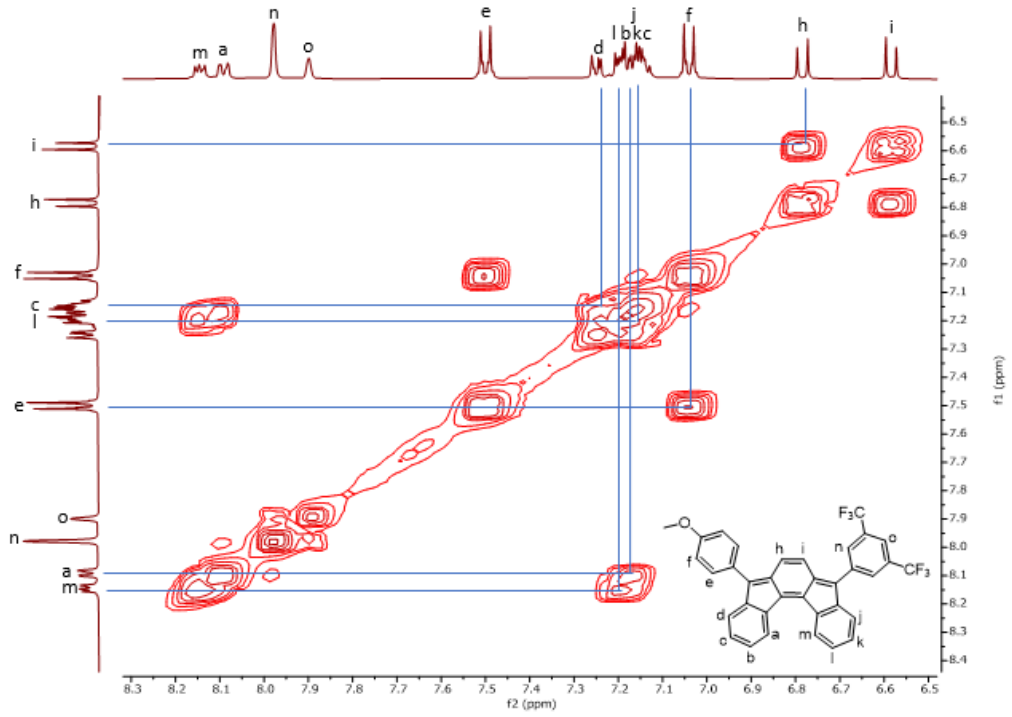

Figure 2B.45 ^{1}H-^{1}H COSY NMR of **10** (in $CDCl_3$).

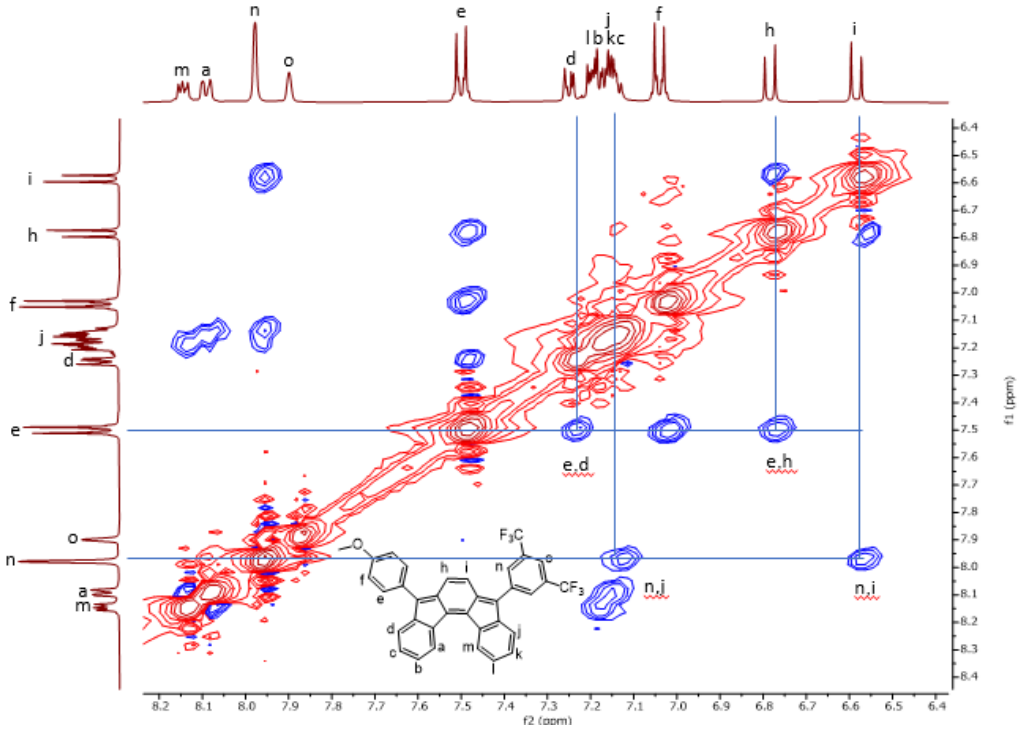

Figure 2B.46 ^{1}H-^{1}H NOESY NMR of **10** (in $CDCl_3$).

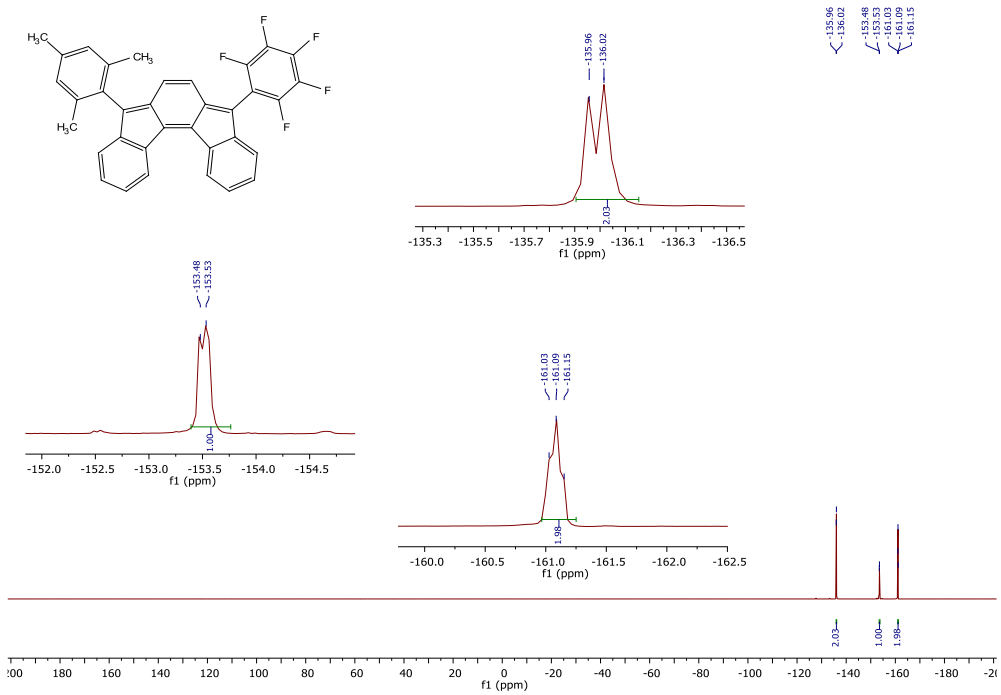

Figure 2B.47 ^{19}F NMR of **7** (in $CDCl_3$).

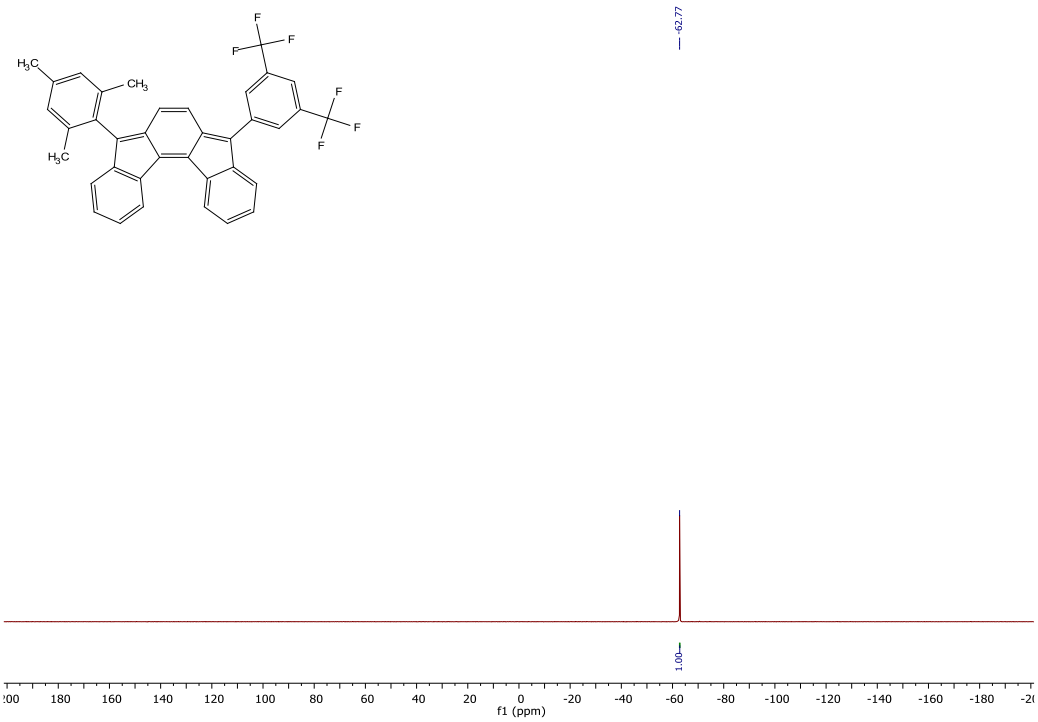

Figure 2B.48 ^{19}F NMR of **8** (in $CDCl_3$).

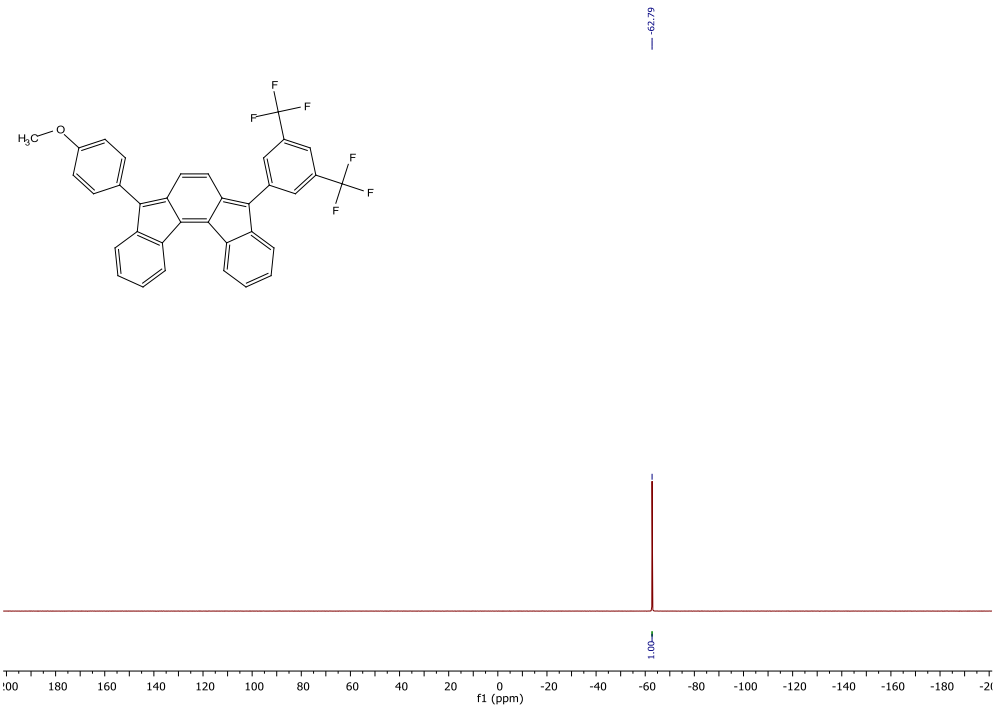

Figure 2B.49 ^{19}F NMR of **10** (in $CDCl_3$).

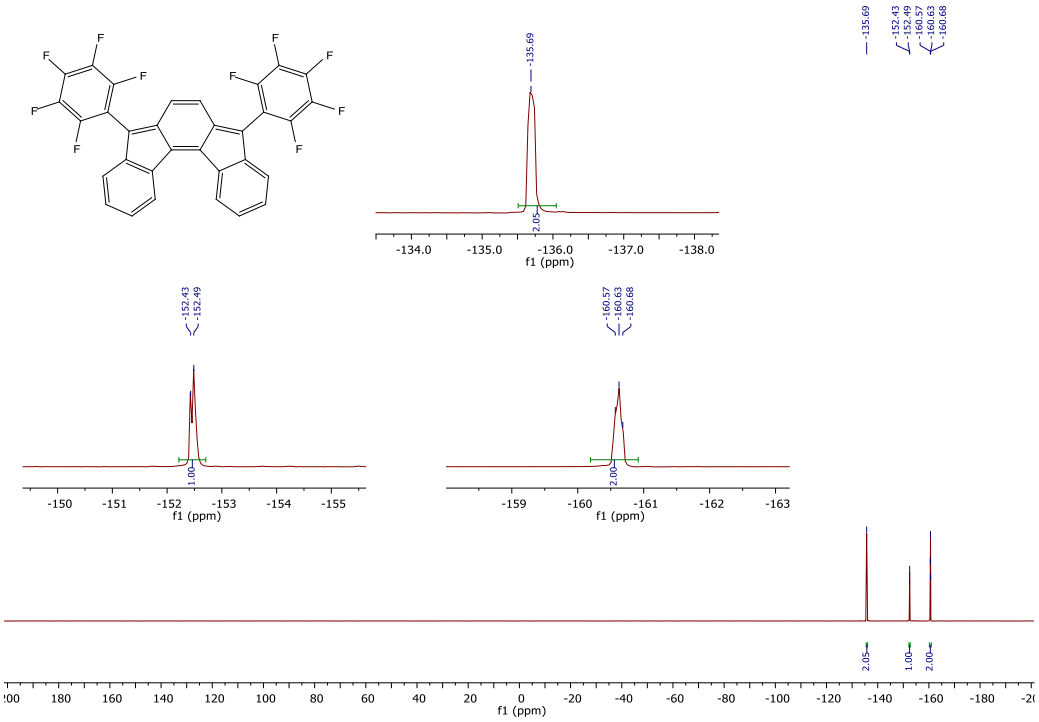

Figure 2B.50 ^{19}F NMR of **17** (in $CDCl_3$).

Chapter 2

Chapter 2C

Exploration of fully conjugated *s*-indaceno[2,1-*c*:6,5-*c*′]difluorene

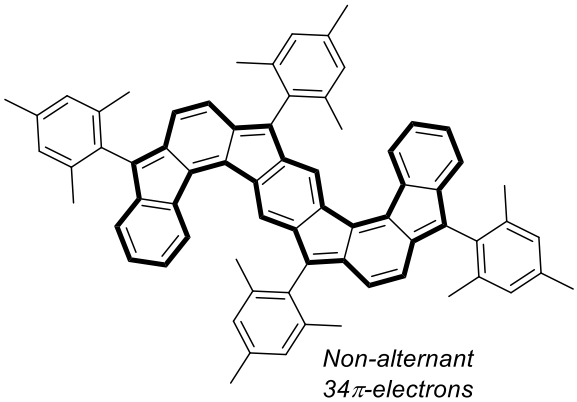

Non-alternant
34π-electrons
The first synthesis and characterization

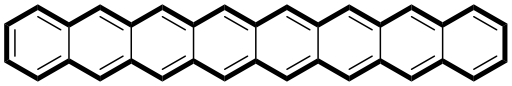

Octacene
Alternant
34π-electrons
No isolation report, Only photogenerated
Theoretically Open-shell

- This work was co-authored with Dr. Priyank Kumar Sharma, who provided synthetic support, Dr. Soumyajit Das, who provided guidance and editorial assistance. This work was originally published in ***Chemical Communications***. (Reference: *Chem. Commun.*, 2020, **56**, 11319-11322)
- This work was highlighted by Prof. T.M. Swager and H. Feng in ***Synfacts***. (Reference: *Synfacts* 2021, **17**, 32)

2C.1 Abstract

This work presents the experimental and theoretical investigations of a tetraradicaloid *s*-indaceno[2,1-*c*:6,5-*c*']difluorene, a member of rarely explored indacenodifluorene family containing 4*n*+2 monocyclic conjugated π-electrons. Expedient synthesis, broad absorption reaching 1150 nm, and small HOMO-LUMO energy gap make [2,1-*c*:6,5-*c*']*s*-IDF a promising candidate for optoelectronic applications.

2C.2 Introduction

As discussed in previous chapters, fully conjugated indenofluorene (IF) isomers,[1] have gained remarkable attention of the scientific community because of their unique properties.[2] There were significant efforts to synthesize core-extended IFs,[3] heteroatom-modified IFs,[4] and phenyl-fused IF derivatives too.[5]

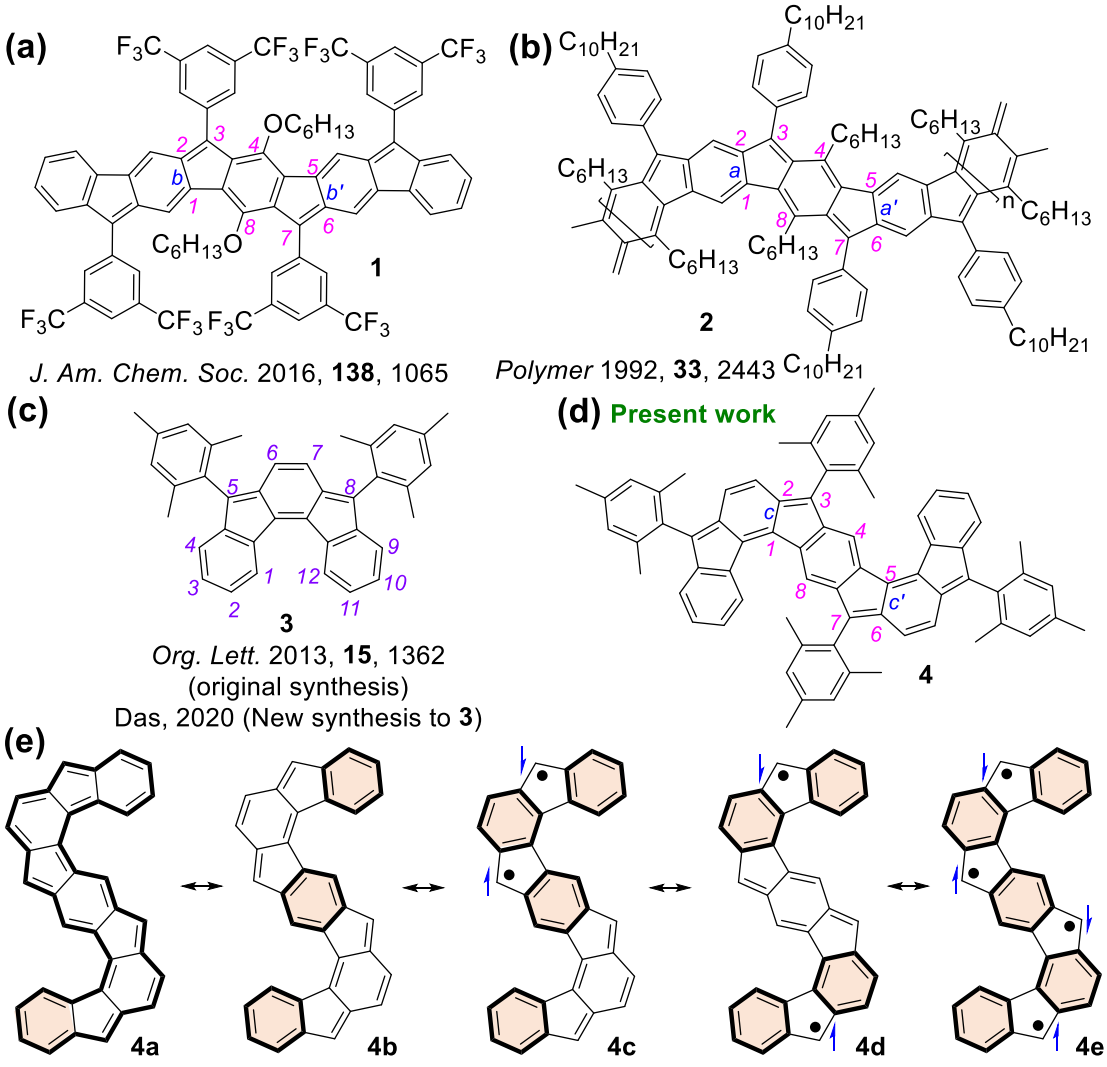

Figure 2C.1 (a) Wu's *s*-indaceno[1,2-*b*:5,6-*b*']difluorene **1**. (b) Müllen's [2,1-*a*]IF-based polymer **2**. (c) 5,8-dimesitylindeno[2,1-*c*]fluorene **3**, (d) Target scaffolds: 5,8,14,17-tetramesityl-*s*-indaceno[2,1-*c*:6,5-*c*']difluorene **4**. (e) Plausible canonical structures for parent **4**.

Now that all the IF isomers have been successfully studied, we envisaged exploring higher order fully fused π-extended IF oligomers as the non-alternant conjugated polycyclic hydrocarbon (CPH) analogues of oligoacenes. A simple approach could be the cyclopentafluorene fusion at the outer benzene ring of IF that may generate newer arrays of CPHs containing formally 34π-electrons, called indacenodifluorene (IDF) isomers. Conjugated IDFs are made of 9 alternatingly fused 6-5-6-5-6-5-6-5-6 rings, and are seldom investigated. As also discussed in Chapter 1, to our knowledge, the only conjugated IDF that exists in literature was based on the cyclopenta[*b*]fluorene fused [1,2-*b*]IF **1**, *s*-indaceno[1,2-*b*:5,6-*b'*]difluorene (Figure 2C.1).[6] IDF isomers may be further categorized into *s*-indacenodifluorenes (*s*-IDFs) and *as*-indacenodifluorenes (*as*-IDFs) (Figure 2C.2).

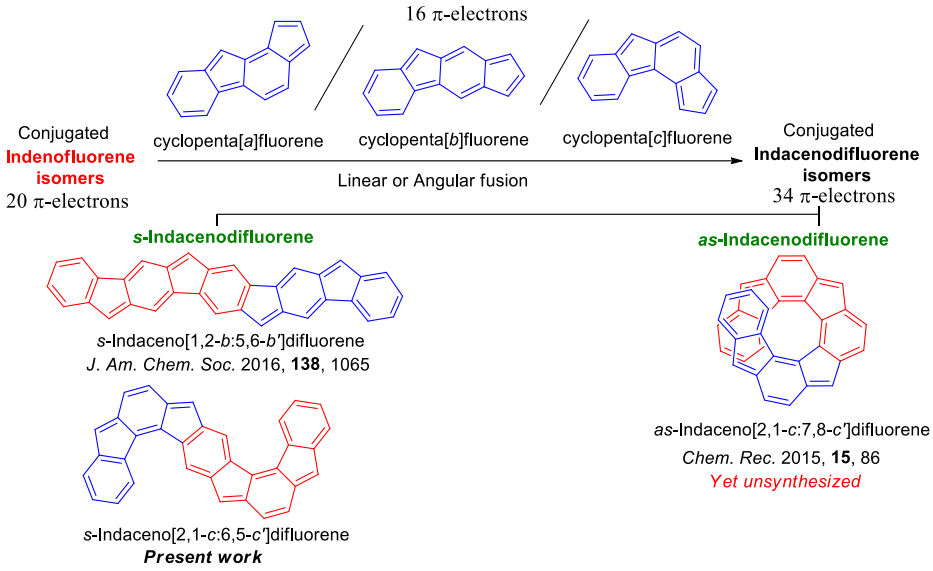

Figure 2C.2 Known indacenodifluorene (IDF) isomers with 34π-electrons delocalized along the conjugated backbone.

Tetraradicaloid **1** was the first isomer of the *s*-IDF series, and no *as*-IDF isomer was synthesized to date, likely due to the unavailability of proper synthetic strategies or suitable intermediates. Notably, an *as*-IDF isomer (*as*-indaceno[2,1-*c*:7,8-*c'*]difluorene) was mentioned in Tobe's personal account but its synthesis was undisclosed.[2a] Interestingly, IDF isomers may be regarded as the non-alternant isoelectronic (not isomeric) CPH analogues for the alternant oligoacenes like synthetically challenging octacene,[7] as well as [8]phenacene;[8] considering the bonding picture of the outer conjugated circuit as [34]annulene.

The π-extension concept through non-benzenoid repeating units was first proposed by Müllen in the form of π-extended ladder polymer **2** (Figure 2C.1) which

may be regarded as the repeating units of cyclopenta[*a*]fluorene fused [2,1-*a*]IF.[9] Polymer **2**, however, suffered incomplete unsaturation in the hydrocarbon backbone and slowly decomposed upon exposure to air/oxygen. Further theoretical studies by Kertesz on similar structural isomers of IF-based π-extended ladder polymers revealed their inherently low band gap, and more importantly the prospects of having high spin ground states.[10] A recent theoretical revisit by Nakano et al. on the IF-based π-extended oligomers demonstrated their ability to show small multiple diradical characters that may result in potentially high second-hyperpolarizability for non-linear optical materials compared to the polyacenes.[11] This novel class of fully fused CPHs, realized by the condensation of 6- and 5-membered rings in alternating fashion, thus deserve to be investigated experimentally since they may become potential low band gap (perhaps open shell too) materials for optoelectronic applications.

We designed a cyclopenta[*c*]fluorene fused [2,1-*c*]IF **4**, *s*-indaceno[2,1-*c*:6,5-*c*']difluorene, as the second unknown constitutional isomer of the barely explored *s*-IDF series (Figure 2C.1). We extended our mild and convenient approach to construct the fully conjugated *s*-IDF isomer **4**, 5,8,14,17-tetramesityl-*s*-indaceno[2,1-*c*:6,5-*c'*]difluorene, which can be regarded as a potential tetraradicaloid due to the presence of two pro-aromatic *p*-quinodimethane (*p*QDM) subunits that may recover additional Clar π-sextets in the open shell form (Figure 2C.1), similar to **1**. The ground electronic state of tetraradicaloid **4** was investigated experimentally, with the support of density functional theory (DFT) calculations at the B3LYP/6-31G(d,p) level of theory.[12]

2C.3 Results and Discussion

2C.3.1 Synthesis

Racemic **5** (see Chapter 2A) was conveniently converted to the desired pinacolboronic acid ester **6** in 77% yield by the standard Pd^{II}-catalyzed Miyaura borylation reaction (Scheme 2C.1). A Pd^0-catalyzed Suzuki reaction between the pre-synthesized **8**,[13] and 2.5 equivalents of **7** afforded **9** in 76% yield. Compound **9** was subsequently treated with an excess of **10** to afford the dicarbinol **11**. The addition of $BF_3 \cdot Et_2O$ to the solution of crude **11** in dry dichloromethane (DCM) afforded the ring-fused product **12** as mixture of stereoisomers, and confirmed by HRMS analysis. Unsurprisingly, it was difficult to interpret the structure from its complicated ^1H NMR spectrum, and hence **12** was treated with 2.1 equivalents of DDQ in dry toluene at 80 °C for 45 mins to

quantitatively afford a brown solid **4** with desired mass, as analysed by HRMS after column chromatographic purification on silica gel in air.

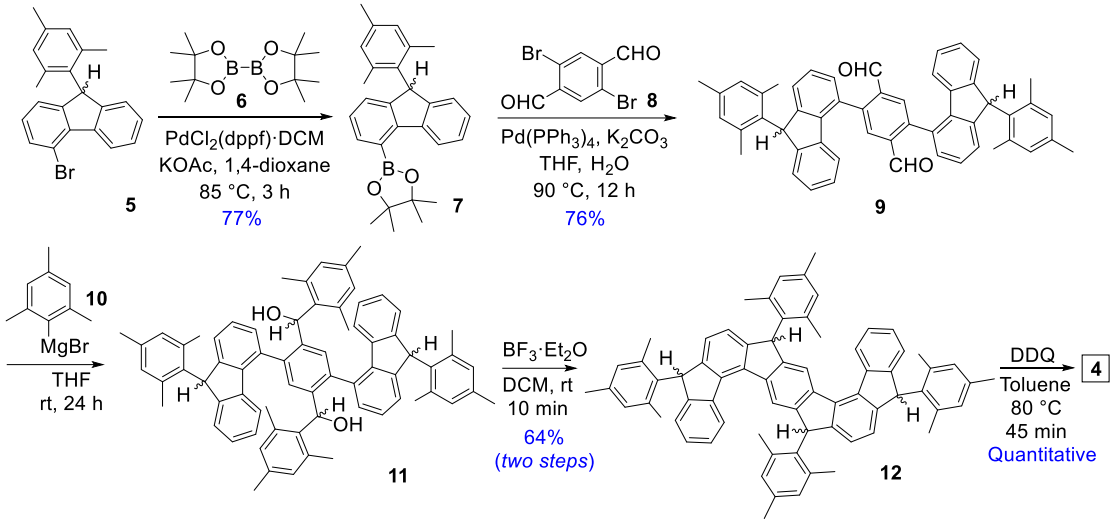

Scheme 2C.1 Synthesis of S-shaped π-conjugated system **4**.

The structure of **4** was confirmed by ^{1}H NMR, 2D-COSY, and 2D-NOESY spectroscopic analysis in benzene-d_6 (*vide infra*). ^{1}H-^{1}H NOESY correlation was found to be useful in assigning the two different kinds of mesityl substituents attached to the *exo*-methylene carbons of *p*QDM subunit. The structure of **4** was further unequivocally confirmed by the X-ray crystallographic analysis. The region-selectivity of the $BF_3{\cdot}Et_2O$ mediated Friedel-Crafts ring-closure alkylation could be attributed to the more thermodynamically favourable formation of two 5-membered rings over the 7-membered rings. Notably, the oxidative dehydrogenation to **4** took lesser time and temperature to complete, compared to that of [2,1-*c*]IF **3**[1d] which was formally antiaromatic.

2C.3.2 Single crystal, ground state, and (anti)aromaticity analysis

Single crystals of **4**, suitable for X-ray crystallographic analysis, were successfully grown by slow evaporation from chloroform/tetrahydrofuran solvent mixture for two weeks at ambient temperature (Figure 2C.3a).[14] The molecule has a rigid and essentially planar core structure with the terminal benzene rings deviated by 11.9° due to the steric congestion at the cove-like region, as measured from the average planes between the central (E) and terminal (A) 6-membered rings (Figure 2C.4).

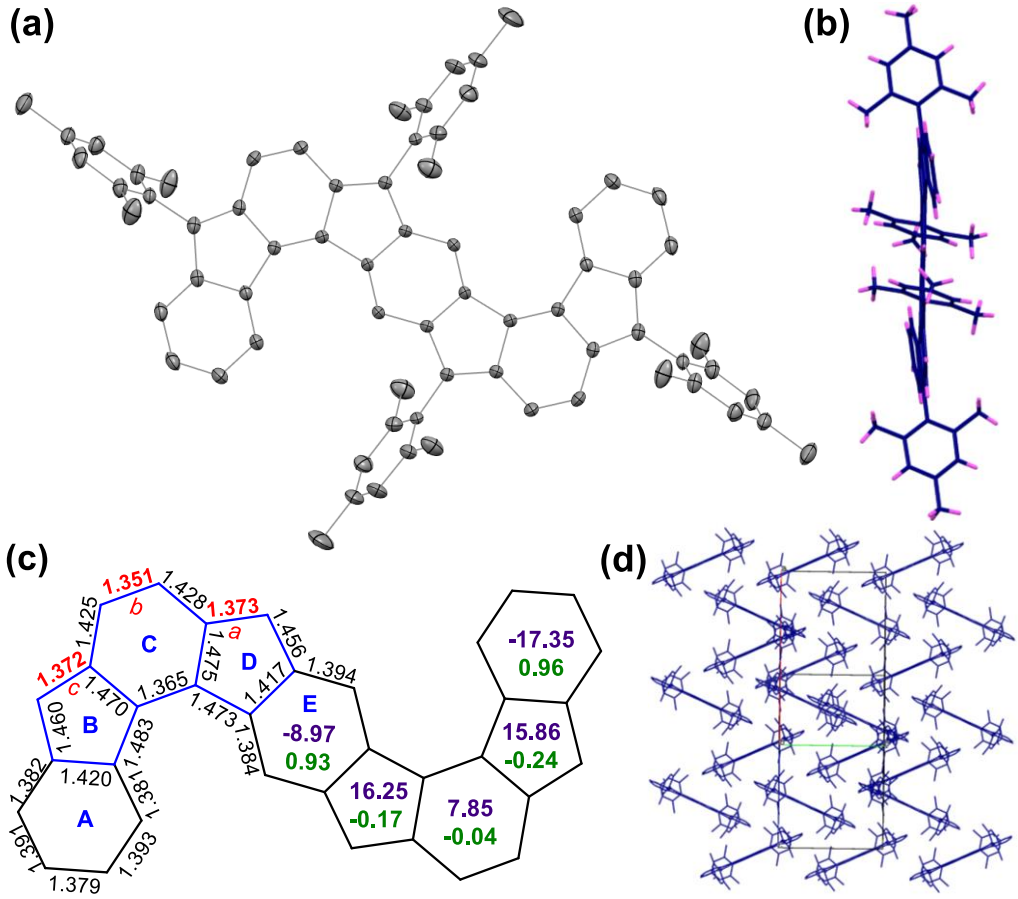

Figure 2C.3 (a) X-ray crystallographic structure of **4** with the ellipsoids drawn at 30% probability level, and the hydrogens are omitted for clarity. (b) Side view of crystal structure **4** with hydrogens shown in pink colour. (c) Experimental bond lengths (Å), calculated $NICS(1)_{zz}$ (purple) and HOMA (green) values for each ring in **4**. (d) Packing diagram for **4**.

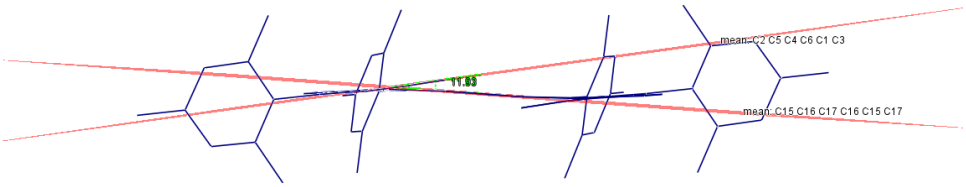

Figure 2C.4 The terminal phenyl ring is deviated from central (core) phenyl ring by 11.93° due to steric congestion in the cove-like region between two hydrogens in close proximity.

The subtle twist, and almost orthogonally deviated mesityl groups from the conjugated backbone prevent dye aggregation; and thus **4** was found to be soluble in common organic solvents like chloroform, DCM, tetrahydrofuran, toluene etc. at ambient temperature. The closest intermolecular C-C contact was found to be 3.454 Å for a symmetric herringbone arrangement in **4**, formed through the intermolecular [C-H$\cdots\pi$] interactions (2.831/2.785 Å) between the methyl hydrogens of one molecule and the π-backbone of another molecule (Figure 2C.5).

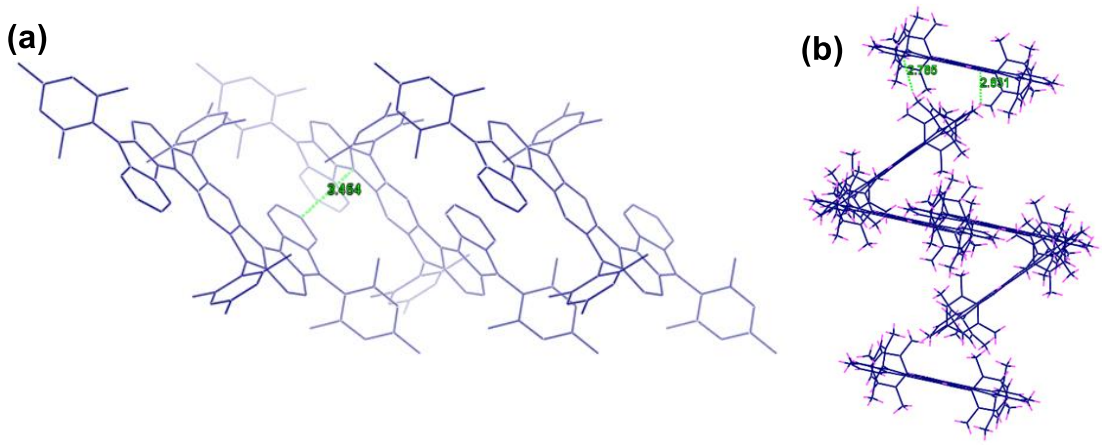

Figure 2C.5 (a) The shortest interplanar C-C contact in **4** was found as 3.454 Å (left image), and (b) the intermolecular [C-H···π] interactions in **4** (2.831/2.785 Å) (right image).

The bond length analysis for the *p*QDM at the *as*-indacene subunit (indicated in blue, Figure 2C.3) revealed the C_{sp}^2=C_{sp}^2 bond *b* as 1.351 Å whereas the *exo*-methylene double bonds *a* and *c* are 1.373 Å and 1.372 Å respectively, which are similar to what was observed for closed-shell [2,1-*c*]IF,[1d] and are shorter than the *p*QDM structure of the *s*-indacene subunit in **1**.[6] The distribution of bond lengths for ring A (avg 1.391 Å) and ring E (avg 1.398 Å) in **4** was found to be homogeneous that additionally suggested localized aromaticity at the terminal and central 6-membered rings. The large bond length alternation indicative of quinoidal resonance in *as*-indacene subunit, in addition to the retention of benzene aromaticity in the central (E, Figure 2C.3) and terminal (A) 6-membered rings were clearly implying a singlet ground state for **4** in the form of canonical structure **4b** (Figure 2C.1e).

DFT calculations, by optimizing the crystal structure, further supported a singlet ground state for **4** with the triplet state being 6.05 kcal/mol higher in energy. An NMR line broadening could consequently be observed at 363-400 K, indicating the population of the triplet state (Figure 2C.6).[15] The nucleus independent chemical shift [$NICS(1)_{zz}$] calculations (at CAM-B3LYP/6-31G(d,p)) revealed strong to moderate quinoidal nature of the rings B (15.86), D (16.25), and C (7.85); whereas a strong to weak aromatic character of the terminal and central 6-membered rings A (−17.35) and E (−8.97) were found, respectively (Figure. 2C.3).[6,12b] The harmonic oscillator model of aromaticity (HOMA) values were also found to be in accordance with the $NICS(1)_{zz}$ values (*vide infra*).

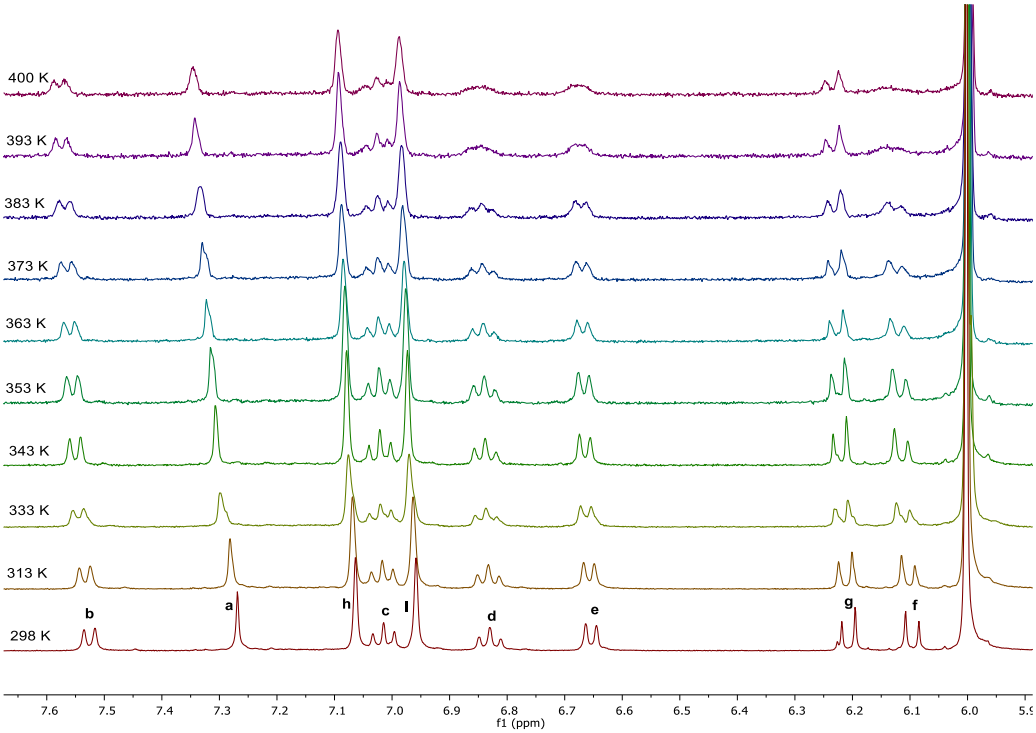

Figure 2C.6 Variable temperature ^{1}H NMR spectrum of **4** (in $C_2D_2Cl_4$, 400 MHz).

All the experimental and theoretical studies were eventually supporting the aromatic/quinoidal alternating resonance form **4b** (among the five canonical structures) as the major contributor to the ground electronic state for **4** (Figure 2C.1e, π-sextets were shown in orange hexagon).

2C.3.3 Optical and electrochemical properties

The electronic absorption spectrum of **4** in chloroform showed two major higher energy absorption bands in the UV-vis region (λ_{max} = 401 nm, ε = 49600 M^{-1} cm^{-1}; λ_{max} = 524 nm, ε = 22850 M^{-1} cm^{-1}), and one broad lower energy absorption band (λ_{max} = 836 nm, ε = 8400 M^{-1} cm^{-1}) reaching 1150 nm in the near-IR region (Figure 2C.7). The time dependent DFT calculations in the gas phase predicted a highest occupied molecular orbital (HOMO) to lowest unoccupied molecular orbital (LUMO) transition at 1043.9 nm for **4** with moderate oscillator strength (f = 0.2171) which was attributable to the lower energy transition at 836 nm (Figure 2C.8 and Table 2C.1).

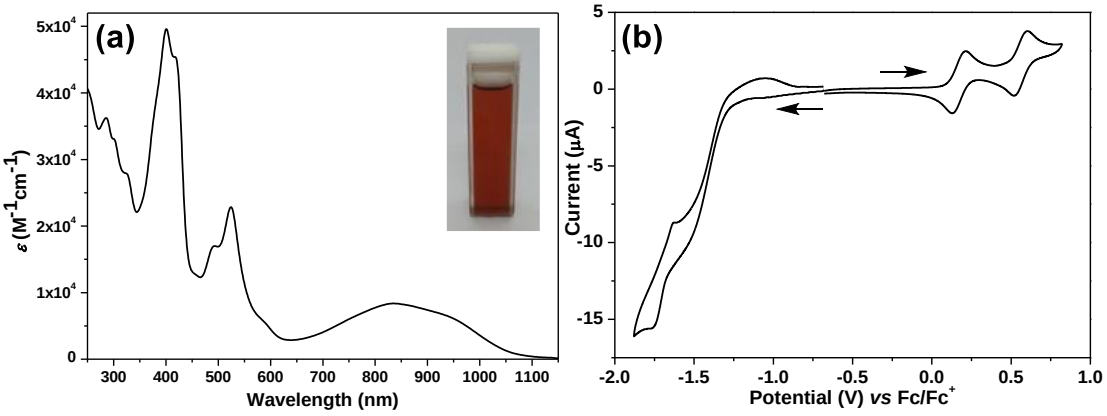

Figure 2C.7 (a) UV-vis-NIR spectrum of **4** in $CHCl_3$ and (b) CV of **4** (0.001 M) taken at 298 K, in dry and degassed dichloromethane with 0.1 M Bu_4NPF_6 under nitrogen atmosphere. All data were collected using Pt-disk electrode as a working electrode, Pt wire as a counter electrode and Ag wire as a pseudo-reference electrode. Scan direction is shown using arrow.

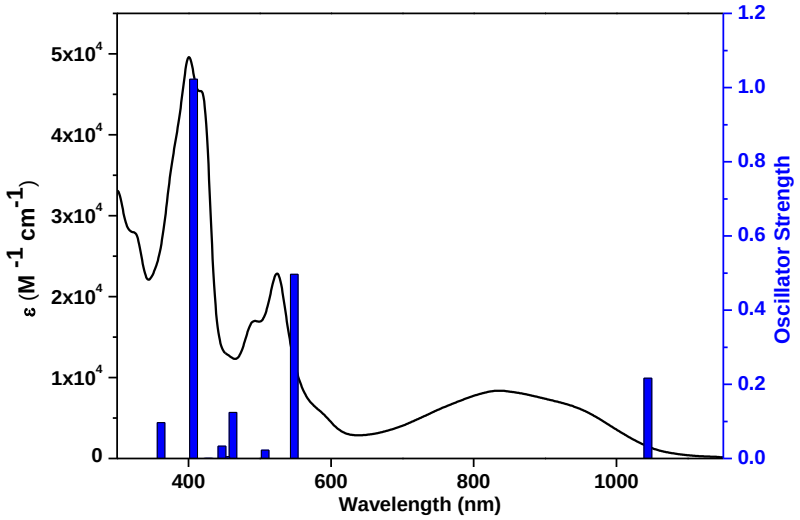

Figure 2C.8 Experimental absorption spectrum of **4**, against the simulated stick diagram showing oscillator strength at B3LYP/6-31G(d,p) level of theory.

Table 2C.1 TD-DFT transitions at B3LYP/6-31G(d,p) level.

Wavelength (nm)	Osc. Strength (*f*)	Major contributions
1043.9	0.2171	HOMO->LUMO (95%)
694.5	0	H-1->LUMO (95%)
663.5	0	HOMO->L+1 (93%)
548.2	0.497	H-2->LUMO (83%)
507.2	0.0231	H-3->LUMO (90%)
464.6	0	H-4->LUMO (92%)
462.3	0.1248	H-1->L+1 (81%)
452.1	0.0051	H-7->LUMO (14%), H-6->LUMO (81%)
451.1	0	H-5->LUMO (93%)
446.7	0.0337	H-7->LUMO (83%), H-6->LUMO (12%)

434.1	0	H-11->LUMO (33%), H-10->LUMO (22%), H-2->L+1 (34%)
429.0	0	H-11->LUMO (41%), H-10->LUMO (58%)
429.0	0.0006	H-12->LUMO (95%)
427.2	0	H-8->LUMO (91%)
426.9	0.0005	H-9->LUMO (92%)
416.6	0	H-11->LUMO (17%), H-10->LUMO (11%), H-2->L+1 (45%)
407.0	1.0226	HOMO->L+2 (84%)
380.8	0	H-13->LUMO (24%), H-3->L+1 (64%)
367.8	0	H-13->LUMO (69%), H-3->L+1 (27%)
361.4	0.0973	H-4->L+1 (88%)

No noticeable change in absorption profile was observed by changing solvent polarity, suggesting negligible intramolecular charge transfer character. The lower energy absorption maximum for **4** was remarkably red shifted (~114 nm) compared to that of isomer **1** with electron-withdrawing group.[6] Notably, the low energy HOMO → LUMO transition for [2,1-*c*]IF is allowed,[16] similar to **4**. The π-extension in **4** clearly shifted the lower energy absorption maximum to the longer wavelength compared to that of 603 nm for **3**,[1d] however, it was 73 nm less than the antiaromatic cyclic congener TCPTP.[15] In comparison to **1**, a lower optical HOMO-LUMO energy gap E_g^{opt}= 1.15 eV was obtained for **4** from the UV-vis-NIR absorption onset, however, the electrochemical energy gap E_g^{ec} = 1.37 eV was found to be the same. This observation is in line with earlier reports that [2,1-*c*]IF-based π-systems may show lower HOMO-LUMO energy gap compared to the analogous [1,2-*b*]IF π-systems.[1d,3e,6] Unlike the [2,1-*c*]IF,[1d,3e] two reversible oxidation waves were found for **4** with the half-wave potentials at $E_{1/2}^{ox}$= 0.17 V and 0.56 V (*vs* ferrocene/ferrocenium (Fc/Fc^+)), while the electron acceptability was greatly reduced as quasi-reversible reduction waves appeared at $E_{1/2}^{red}$= −1.41 V and −1.69 V (*vs* Fc/Fc^+) (Figure 2C.7b) in cyclic voltammogram. The HOMO and LUMO levels were estimated as −4.89 eV and −3.52 eV from the CV, respectively, which were in line with the theoretical values (Figure 2C.9**,** Table 2C.2).

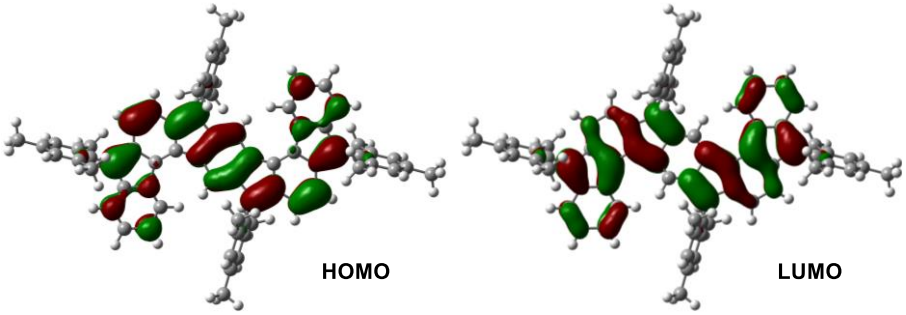

Figure 2C.9 Frontier molecular orbital profiles for **4**.

Table 2C.2 Summary of experimental and theoretical HOMO-LUMO energy levels.[a]

Comp	HOMO (eV)	LUMO (eV)	E_g^{DFT} (eV)	E_g^{ec}(eV)	E_g^{opt}(eV)
4	-4.89^{Exp} -4.54^{B3LYP} $-5.74^{CAM\text{-}B3LYP}$	-3.52^{Exp} -2.97^{B3LYP} $-1.94^{CAM\text{-}B3LYP}$	1.57^{B3LYP} $3.80^{CAM\text{-}B3LYP}$	1.37	1.15

[a]E_g^{DFT} = Theoretical HOMO-LUMO energy gap (from closed-shell geometry), E_g^{ec} = Electrochemical HOMO-LUMO energy gap, E_g^{opt} = Optical HOMO-LUMO energy gap.

2C.4 Conclusions

In conclusion, synthesis and characterization of [2,1-*c*:6,5-*c*′]*s*-IDF **4** as the second structural isomer of the conjugated *s*-IDF series containing 34π-electrons was studied in this chapter. All experimental and theoretical studies corroborate to an aromatic/quinoidal alternating form for **4** determining the singlet ground state with a thermally accessible triplet state owing to the narrow singlet–triplet energy gap. Compound **4** showed low oxidation potential, small HOMO-LUMO energy gap, and a low energy $\pi \rightarrow \pi^*$ transition with the absorption spectrum reaching the NIR region. This synthetic approach may allow the introduction of separate aryl/heteroaryl/ethynyl groups at the *exo*-methylene carbons on *p*QDM subunits in order to make new derivatives of **4** with improved solid-state packing, and optoelectronic properties which are currently underway. Our work will also shed light on the syntheses of higher order fully fused π-extended IF oligomers as the non-alternant alternatives of alternant acenes with tuneable properties and ground state.

2C.5 Experimental Section

2C.5.1 General Information: Chemicals and reagents were purchased from commercial suppliers (Merck, GLR innovations, BLDpharm) and used without further purification. Thin layer chromatography (TLC) was performed using pre-coated plates

purchased from Merck (silica gel 60 PF254, 0.25 mm). Column chromatography was performed using silica gel 100-200 mesh. NMR spectra were recorded in $CDCl_3$ and C_6D_6 (Eurisotop) at 298 K, on JEOL JNM-ECS400 spectrometer at operating frequencies of 400 MHz (^{1}H) or 100 MHz (^{13}C) as indicated in the individual spectrum. Chemical shifts (δ) are given in ppm relative to residual solvent (chloroform δ = 7.26, benzene δ = 7.16, 1,1,2,2-tetrachloroethane δ = 6.00 for ^{1}H, and chloroform δ = 77.16 for proton decoupled ^{13}C NMR) and coupling constants (*J*) in Hz. Multiplicity is tabulated as s for singlet, d for doublet, dd for doublet of doublet, t for triplet, q for quartet and m for multiplet. High resolution mass spectra (HRMS) were recorded using electron spray ionization (ESI) methods on Waters (XEVO G2-XS QTOF) mass spectrometer. UV-vis-NIR spectrum of **4** was recorded in JASCO V-670 spectrophotometer. Cyclic voltammetry of **4** was performed in CH instruments using dry dichloromethane/$TBAPF_6$ solvent/electrolyte couple at a scan rate of 50 mV/s. Melting points were determined using BIBBY-SMP30 melting point analyzer. Single crystal X-ray structural data were collected on a CMOS based Bruker D8 Venture PHOTON 100 diffractometer equipped with a INCOATEC micro-focus source with graphite monochromated Mo Kα radiation (λ = 0.71073 Å) operating at 50 kV and 30 mA.

2C.5.2 Syntheses

2-(9-mesityl-9*H*-fluoren-4-yl)-4,4,5,5-tetramethyl-1,3,2-dioxaborolane (7). An oven-dried glass tube was charged with **5** (400 mg, 1.10 mmol), bis(pinacolatodiboron) **6** (559.19 mg, 2.20 mmol), KOAc (324.17 mg, 3.30 mmol), dry 1,4-dioxane (5 mL). The suspension was purged with N_2 for 30 mins before adding $PdCl_2$(dppf)·DCM (89.83 mg, 10 mol%), and the glass tube was sealed. The reaction mixture was stirred at 85 °C for 3 h. After being cooled to room temperature, volatile organics were removed under reduced pressure and water was added. The mixture was extracted with DCM (5 x 60 mL), dried over anhydrous Na_2SO_4, and filtered. The organic layer was removed under reduced pressure, and the crude obtained was quickly column chromatographed on short silica gel pad (hexanes:DCM, 70:30) to afford the title product **7** as white solid (349 mg, 77% yield). R_f = 0.4 (20% DCM/hexanes); **mp**: 156-157 °C; **^{1}H NMR** (400 MHz, $CDCl_3$): δ 8.79 (d, *J* = 7.8 Hz, 1H), 7.86 (d, *J* = 7.2 Hz, 1H), 7.39 (t, *J* = 7.4 Hz, 1H), 7.28 (t, *J* = 7.3 Hz, 1H), 7.25–7.19 (m, 3H), 7.02 (s, 1H), 6.65 (s, 1H), 5.43 (s, 1H), 2.67 (s, 3H), 2.28 (s, 3H), 1.50 (s, 6H), 1.48 (s, 6H), 1.08 (s, 3H); **^{13}C{^{1}H} NMR** (100 MHz,

$CDCl_3$): δ 147.7, 147.4, 145.4, 142.0, 137.9, 137.8, 136.1, 134.9, 134.2, 130.5, 128.7, 127.0, 126.6, 126.0, 124.0, 123.7, 84.0, 49.5, 21.8, 20.9, 18.8; **HRMS** (ESI) *m/z*: $[M + H]^+$ Calcd for $C_{28}H_{32}O_2B$ 411.2495, found 411.2489.

2,5-bis(9-mesityl-9*H*-fluoren-4-yl)terephthalaldehyde (9). An oven-dried glass tube was charged with compound **7** (298.71 mg, 0.727 mmol), 2,5-dibromophenyl-1,4-dialdehyde **8** (85 mg, 0.291 mmol), K_2CO_3 (201.20 mg, 1.46 mmol), tetrahydrofuran (10 mL) and water (1 mL), and the mixture was purged with nitrogen for 30 mins. Catalyst $Pd(PPh_3)_4$ (33.62 mg, 10 mol%) was subsequently added under nitrogen, and the glass tube was sealed before being warmed to 90 °C. After 12 h, the THF was evaporated under reduced pressure, and water was added. The mixture was extracted with DCM (4 x 50 mL), and the organic layer washed with saturated brine solution, and water. The organic layer was dried over anhydrous Na_2SO_4, filtered, and removed under vacuum. The residue was purified by silica gel column chromatography (hexanes:DCM, 60:40) to afford the title product **9** as yellow solid (151 mg, 76% yield). R_f = 0.48 (35% DCM/hexanes); **mp**: 318-319 °C; **^{1}H NMR** (400 MHz, $CDCl_3$): δ 10.03–9.93 (m, 2H), 8.31– 8.29 (m, 2H), 7.44–7.31 (m, 6H), 7.25–6.93 (m, 10H), 6.73-6.71 (m, 2H), 5.60-5.59 (m, 2H), 2.73 (brs, 6H), 2.31 (brs, 6H), 1.20–1.16 (m, 6H); **^{13}C{^{1}H} NMR:** (100 MHz, $CDCl_3$): δ 191.6, 191.4, 191.2, 148.3, 148.3, 148.3, 148.2, 148.2, 148.1, 148.1, 148.1, 148.0, 144.5, 144.5, 144.4, 144.4, 144.3, 139.9, 139.9, 139.9, 139.8, 139.8, 139.1, 139.1, 139.0, 139.0, 138.9, 137.9, 137.9, 137.8, 137.7, 137.6, 137.6, 137.5, 136.7, 136.7, 136.6, 133.6, 133.5, 133.5, 131.3, 131.2, 131.2, 130.8, 130.7, 130.4, 130.3, 130.2, 130.1, 130.1, 129.7, 129.6, 129.4, 129.2, 129.1, 129.0, 128.4, 128.3, 127.9, 127.7, 127.7, 127.3, 127.2, 127.0, 127.0, 126.9, 124.7, 124.6, 124.5, 122.2, 49.8, 49.8, 49.7, 29.8, 21.9, 21.0, 21.02, 19.1, 19.1, 18.9, 18.8, 18.8; **HRMS** (ESI) *m/z*: $[M + H]^+$ Calcd for $C_{52}H_{43}O_2$ 699.3263, found 699.3244.

5,8,14,17-tetramesityl-5,8,14,17-tetrahydro-*s*-indaceno[2,1-*c*:6,5-*c*′]difluorene (12). 2-Mesitylmagnesium bromide (1.0 M in THF, 0.99 mL, 0.99 mmol) was added to the dry THF (5 mL) solution of **9** (139 mg, 0.198 mmol) under N_2. The mixture was stirred at room temperature for 24 h, and quenched with saturated aq. NH_4Cl solution. The volatile organics were evaporated, and the mixture was extracted with DCM (4 x 50 mL). The organic layer was dried over anhydrous Na_2SO_4, filtered, and removed under reduced pressure to afford crude tetracarbinol **11** (252 mg, **HRMS** (ESI) *m/z*: $[M - H]^+$ Calcd for $C_{70}H_{65}O_2$ 937.4985, found 937.4962). To the solution of crude **9** (249 mg, 0.265 mmol) in anhydrous DCM (20 mL), $BF_3{\cdot}Et_2O$ (0.1 mL) was added dropwise

under nitrogen and the reaction mixture was stirred for 10 min at room temperature. Once starting material **11** is consumed, as monitored by TLC, saturated aqueous NH_4Cl solution was added and the reaction mixture was extracted with DCM (4 x 50 mL). The organic layer was dried over anhydrous Na_2SO_4, filtered, and evaporated under reduced pressure. The residue was subjected to silica gel column chromatography (hexanes:DCM, 84:16), followed by trituration with methanol afforded off-white solid **12** (116 mg, 64% yield in two steps). $\boldsymbol{R_f}$ = 0.32 (10% DCM/hexanes); **mp**: 288-289 °C; **^{1}H NMR** (400 MHz, $CDCl_3$): δ 8.50–8.04 (m, 4H), 7.39–7.28 (m, 2H), 7.24–7.02 (m, 12H), 6.79–6.58 (m, 4H), 5.83–5.73 (m, 2H), 5.59–5.54 (m, 2H), 2.89–2.67 (m, 12H), 2.38–2.21 (m, 12H), 1.18–0.99 (m, 12H); **^{13}C{^{1}H} NMR:** (100 MHz, $CDCl_3$): δ 149.1, 148.5, 148.3, 147.5, 147.2, 141.4, 141.2, 140.1, 137.9, 137.8, 136.3, 134.9, 134.6, 130.8, 130.6, 129.2, 128.9, 126.9, 126.4, 124.3, 123.6, 122.9, 122.6, 122.2, 119.4, 119.2, 50.0, 29.8, 29.5, 21.9, 21.0, 19.2, 19.0, 18.8, 18.7, 15.98; **HRMS** (ESI) *m/z*: $[M + H]^+$ Calcd for $C_{70}H_{63}$ 903.4930, found 903.4926.

5,8,14,17-tetramesityl-*s*-indaceno[2,1-*c*:6,5-*c*′]difluorene (4). DDQ (26.4 mg, 0.116 mmol, 2.1 equiv) was added to the **12** (50 mg, 0.055 mmol) in dry toluene (1 mL) under N_2, and the reaction mixture was warmed to 80 °C for 45 mins. Once the starting material was consumed (monitored by TLC), the toluene was removed *in vacuo* and the crude was purified by silica gel column chromatography (hexanes:DCM, 90:10) to afford the title product **4** as brown solid in quantitative yield. $\boldsymbol{R_f}$ = 0.4 (20% DCM/hexanes); **mp**: > 390 °C; **^{1}H NMR** (400 MHz, C_6D_6): δ 7.85 (d, *J* = 7.6 Hz, 2H), 7.77 (s, 2H), 6.91 (s, 4H), 6.84 (s, 4H), 6.82 (t, *J* = 7.5 Hz, 2H), 6.73 (t, *J* = 7.5 Hz, 2H), 6.60 (d, *J* = 7.3 Hz, 2H), 6.31 (d, *J* = 9.2 Hz, 2H), 6.24 (d, *J* = 9.1 Hz, 2H), 2.25 (s, 12H), 2.23 (s, 6H), 2.19 (s, 6H), 2.14 (s, 12H); **^{1}H NMR** (400 MHz, $C_2D_2Cl_4$): δ 7.52 (d, *J* = 7.6 Hz, 2H), 7.27 (s, 2H), 7.06 (s, 4H), 7.01 (t, *J* = 7.5 Hz, 2H), 6.96 (s, 4H), 6.83 (t, *J* = 7.5 Hz, 2H), 6.65 (d, *J* = 7.4 Hz, 2H), 6.20 (d, *J* = 9.3 Hz, 2H), 6.09 (d, *J* = 9.2 Hz, 2H), 2.42 (s, 6H), 2.35 (s, 6H), 2.27 (s, 12H), 2.13 (s, 12H); Insufficient solubility did not allow ^{13}C NMR study. **HRMS** (ESI) *m/z*: $[M + H]^+$ Calcd for $C_{70}H_{59}$ 899.4617, found 899.4594.

2C.5.3 Single Crystal Data

Suitable single crystals of **4** were selected using paratone oil and mounted on glass fiber with the help of gum. The intensity data and geometric parameters of these crystals were garnered with the help of Bruker D8 Venture X-ray diffractometer having a micro-focus

sealed X-ray tube Mo-Kα (λ = 0.71073 Å) source of X-rays along with a PHOTON 100 detector with inclining Phi and Omega (width of 0.5 for one frame) working at a scan speed of 10 s per frame. The crystal was kept at 298 K during data collection. Data acquisition as well as extraction of data was accomplished by utilizing Bruker Apex-3 and Bruker SAINT software packages using a narrow -frame algorithm.[17] By utilizing OLex2,[18] the crystal structure was solved with the help of olex2.solve[19] structure solution program by employing intrinsic Phasing methods and crystal structure refinement was done with the SHELXL[20] refinement package by putting into use Least Squares minimization. Refinement of all non-hydrogen atoms was completed with the help of anisotropic thermal parameters.

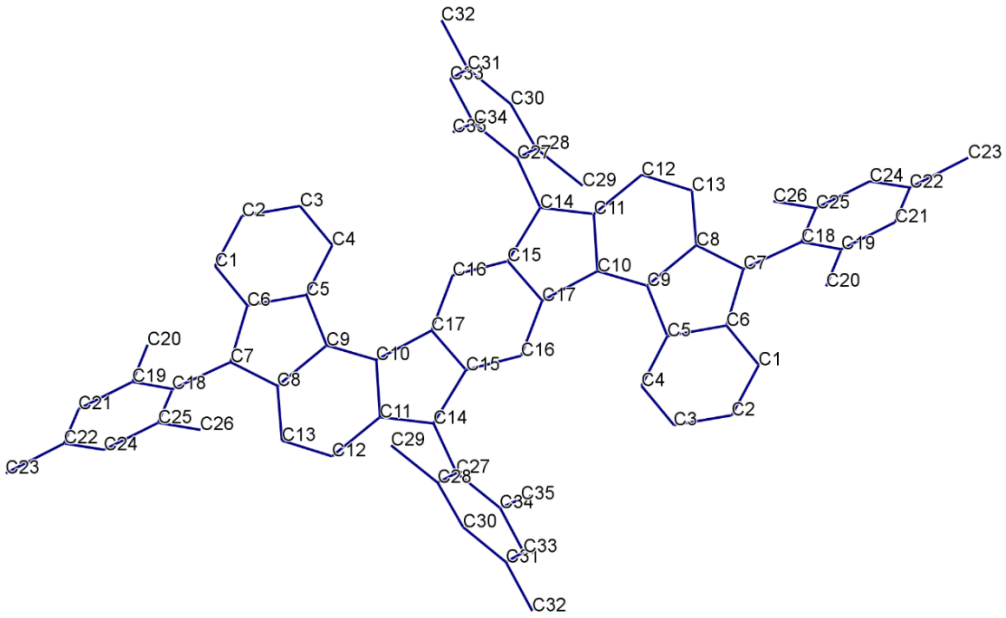

Figure 2C.10 Crystal structure of **4** with labels.

Table 2C.3 Crystal data and structure refinement for **4**.

CCDC No.	2011386
Empirical formula	C70 H58
Formula weight	899.16
Temperature	100(2) K
Wavelength	0.71073 Å
Crystal system	Monoclinic
Space group	C2/c
Unit cell dimensions	a = 28.3914(11) Å b = 12.6728(4) Å c = 15.8260(6) Å α= 90° β= 98.2380(10)° γ = 90°
Volume	5635.4(4) $Å^3$
Z	4
Density (calculated)	1.060 Mg/m^3

Absorption coefficient	0.060 mm^{-1}
F(000)	1912
Crystal size	0.256 x 0.246 x 0.065 mm^3
Theta range for data collection	2.251 to 28.139°.
Index ranges	-36<=h<=37, -16<=k<=16, -20<=l<=20
Reflections collected	36309
Independent reflections	6877 [R(int) = 0.0805]
Completeness to theta = 25.242°	99.8 %
Absorption correction	Semi-empirical from equivalents
Max. and min. transmission	0.996 and 0.985
Refinement method	Full-matrix least-squares on F^2
Data / restraints / parameters	6877 / 0 / 322
Goodness-of-fit on F^2	1.022
Final R indices [I>2sigma(I)]	R1 = 0.0616, wR2 = 0.1574
R indices (all data)	R1 = 0.0930, wR2 = 0.1737
Extinction coefficient	n/a
Largest diff. peak and hole	0.301 and -0.240 e.$Å^{-3}$

2C.5.4 DFT calculations: Density functional theory calculations were performed with Gaussian 09 package using a high performance computing cluster facility of IIT Ropar, utilizing both the B3LYP and CAM-B3LYP (restricted and unrestricted) level of theory with basis set 6-31G(d,p), in the gas phase.[12a] $NICS(1)_{zz}$ values were estimated at the same levels using the standard GIAO procedure. Excitation energy was computed using time-dependent density functional theory (same theory level) for the singlet closed shell optimized geometry. Molecular orbital contributions were determined using GaussSum 3.0 package.[21] Diradical (y_0) and tetraradical (y_1) character indices were determined on the basis of the HOMO/LUMO and HOMO-1/LUMO+1 occupation numbers in natural orbital analysis, for the unrestricted CAM-B3LYP/6-31G(d,p) optimized singlet geometry. The y is formally expressed as $y = 1 - (2T/(1 + T^2))$, where T is represented by using the occupation numbers of UCAM-B3LYP natural orbitals as: $T = (n\text{HOMO} - n\text{LUMO})/2$ for diradical and $T = (n\text{HOMO-1} - n\text{LUMO+1})/2$ for tetraradical. A molecule with $y = 0$ indicates a closed-shell structure, whereas a molecule with $0 < y < 1$ implies diradicaloid (diradical-like) or tetraradicaloid (tetraradical-like) structures.

Table 2C.4 Relative energies of optimized geometries for **4** at B3LYP/6-31G(d,p) level.

State	HF	Kcal/mol
Singlet Closed Shell	-2702.55611363	-1695853.961
Singlet Open Shell	-2702.55611363	-1695853.961
Triplet Open Shell	-2702.54645986	-1695847.904

$\Delta E_{T\text{-}CS}$ = 6.05 kcal/mol

Table 2C.5 Relative energies of optimized geometries, and radical character index for **4** at CAM-B3LYP/6-31G(d,p) level.

State	HF	Kcal/mol	y_0	y_1
Singlet Closed Shell	-2700.94911548	-1694869.879		
Singlet Open Shell	-2700.94911546	-1694869.878	0.0052	0.0008
Triplet Open Shell	-2700.94080361	-1694864.663		

$\Delta E_{T\text{-}CS}$ = 5.21 kcal/mol

Table 2C.6 $NICS(1)_{zz}$ and HOMA[22] values of each ring for the mesityl-substituted **3** and **4**.

Compounds	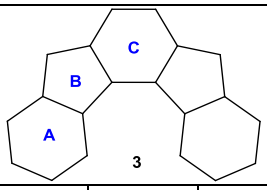			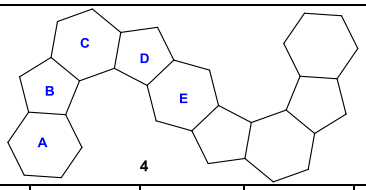				
Rings	A	B	C	A	B	C	D	E
B3LYP/6-31G(d,p)								
NICS(1)zz	-13.30	19.29	8.17	-12.18	20.45	8.09	21.09	-0.33
HOMA	0.92	-0.22	0.05	0.91	-0.21	0.10	-0.12	0.85
CAM-B3LYP/6-31G(d,p)								
NICS(1)zz	-17.99	14.39	7.41	-17.35	15.86	7.85	16.25	-8.97
HOMA	0.96	-0.23	-0.06	0.96	-0.24	-0.04	-0.17	0.93

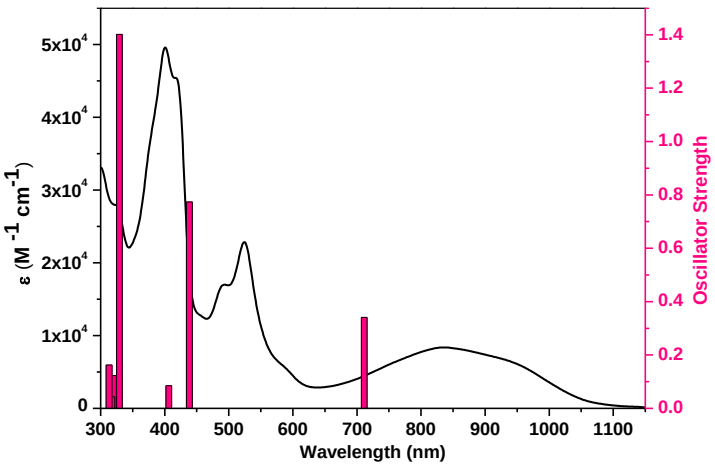

Figure 2C.11 Experimental absorption spectrum of **4**, against the simulated stick diagram showing oscillator strength at CAM-B3LYP/6-31G(d,p) level of theory.

Table 2C.7 TD-DFT transitions at CAM-B3LYP/6-31G(d,p) level.

Wavelength (nm)	Osc. Strength (*f*)	Major contributions
711.4	0.3411	HOMO->LUMO (86%)
544.8	0	H-1->LUMO (51%), HOMO->L+1 (36%)
438.4	0.7732	H-2->LUMO (79%)
418.9	0	H-3->L+1 (10%), H-1->LUMO (35%), HOMO->L+1 (46%)
406.3	0.0851	H-3->LUMO (67%), H-1->L+1 (16%)
361.9	0	H-8->LUMO (10%), H-4->LUMO (44%), H-2->L+1 (21%)
336.9	0	H-13->LUMO (13%), H-4->LUMO (16%), H-3->L+1 (12%), H-2->L+1 (38%), HOMO->L+1 (10%)
329.2	1.4014	HOMO->L+2 (80%)
320.1	0.1232	H-7->LUMO (19%), H-6->LUMO (44%), H-1->L+1 (11%)
318.9	0	H-6->L+1 (20%), H-5->LUMO (74%)
317.6	0.0435	H-7->LUMO (23%), H-6->LUMO (29%), H-5->L+1 (10%), H-1->L+1 (21%)
315.4	0	H-8->LUMO (63%), H-7->L+1 (10%), H-4->LUMO (14%)
313.0	0.1621	H-7->LUMO (41%), H-1->L+1 (38%)
293.7	0.0016	H-12->LUMO (80%)
293.3	0	H-11->LUMO (93%)
291.7	0.0211	H-14->LUMO (12%), H-10->LUMO (54%), H-9->L+1 (13%)
291.5	0	H-10->L+1 (16%), H-9->LUMO (75%)
290.0	0.0144	H-14->LUMO (25%), H-10->LUMO (26%)
289.4	0	H-1->L+2 (39%), HOMO->L+3 (32%)
285.0	0	H-13->LUMO (44%), H-2->L+1 (13%)

It is evident from gas-phase computational calculations that CAM-B3LYP/6-31G(d,p) may overestimate the HOMO-LUMO gap, and hence the HOMO to LUMO electronic absorption maximum is underestimated. Therefore, B3LYP/6-31G(d,p) level was used for optimization of **4** as well as the TD-DFT calculations. However, the three major transitions (Table 2C.1 and Table 2C.7) for **4** are well reproduced by both the level of theories. The deviations from experimental spectrum may originate due to the polarization effects, and the solvent polarity.

2C.6 References

1. (*a*) D.T. Chase, B.D. Rose, S.P. McClintock, L.N. Zakharov and M. M. Haley, *Angew. Chem. Int. Ed.* 2011, **50**, 1127–1130; (*b*) A. Shimizu and Y. Tobe, *Angew. Chem. Int. Ed.* 2011, **50**, 6906–6910; (*c*) A. Shimizu, R. Kishi, M. Nakano, D. Shiomi, K. Sato, T. Takui, I. Hisaki, M. Miyata and Y. Tobe, *Angew. Chem. Int. Ed.* 2013, **52**, 6076–6079; (*d*) A. G. Fix, P. E. Deal, C. L. Vonnegut, B. D. Rose, L. N. Zakharov and M. M. Haley, *Org. Lett.* 2013, **15**, 1362–1365; (*e*) J. J. Dressler, Z. Zhou, J. L. Marshall, R. Kishi, S. Takamuku, Z. Wei, S. N. Spisak, M. Nakano, M. A. Petrukhina and M. M. Haley, *Angew. Chem. Int. Ed.* 2017, ***56***, 15363–15367.

2. (*a*) Y. Tobe, *Chem. Rec.* 2015, **15**, 86–96; (*b*) G. E. Rudebusch and M.M. Haley, *Polycyclic arenes and heteroarenes: synthesis, properties, and applications.* Wiley‐VCH, 2015, 37–68; (*c*) C. K. Frederickson, B. D. Rose and M. M. Haley, *Acc. Chem. Res.* 2017, **50**, 977–987.

3. (*a*) B. D. Rose, C. L. Vonnegut, L. N. Zakharov and M. M. Haley, *Org. Lett.* 2012, **14**, 2426–2429; (*b*) H. Miyoshi, S. Nobusue, A. Shimizu, I. Hisaki, M. Miyata and Y. Tobe, *Chem. Sci.* 2014, **5**, 163–168; (*c*) G. E. Rudebusch, J. L. Zafra, K. Jorner, K. Fukuda, J. L. Marshall, I. Arrechea-Marcos, G. L. Espejo, R. Ponce Ortiz, C. J. Gómez-García, L. N. Zakharov, M. Nakano, H. Ottosson, J. Casado and M. M. Haley, *Nat. Chem.* 2016, **8**, 753–759; (*d*) J. E. Barker, C. K. Frederickson, M. H. Jones, L. N. Zakharov and M. M. Haley, *Org. Lett.* 2017, **19**, 5312–5315; (*e*) T. Jousselin-Oba, P. E. Deal, A. G. Fix, C. K. Frederickson, C. L. Vonnegut, A. Yassar, L. N. Zakharov, M. Frigoli and M. M. Haley, *Chem. Asian J.* 2019, **14**, 1737–1744.

4. (*a*) B. S. Young, D. T. Chase, J. L. Marshall, C. L. Vonnegut, L. N. Zakharov and M. M. Haley, *Chem. Sci.* 2014, **5**, 1008–1014; (*b*) J. L. Marshall, K. Uchida, C. K. Frederickson, C. Schütt, A. M. Zeidell, K. P. Goetz, T. W. Finn, K. Jarolimek, L. N. Zakharov, C. Risko, R. Herges, O. Jurchescu and M. M. Haley, *Chem. Sci.* 2016, **7**, 5547–5558; (*c*) G. E. Rudebusch, A. G. Fix, H. A. Henthorn, C. L. Vonnegut, L. N. Zakharov and M. M. Haley, *Chem. Sci.* 2014, **5**, 3627–3633; (*d*) J. L. Marshall, G. E. Rudebusch, L. N. Zakharov and M. M. Haley, *Tetrahedron Lett.* 2015, **56**, 3235–3239.

5. C. K. Frederickson, L. N. Zakharov and M. M. Haley, *J. Am. Chem. Soc.* 2016, **138**, 16827–16838.

6. P. Hu, S. Lee, T. S. Herng, N. Aratani, T. P. Gonçalves, Q. Qi, X. Shi, H. Yamada, K.-W. Huang, J. Ding, D. Kim and J. Wu, *J. Am. Chem. Soc.* 2016, **138**, 1065–1077.

7. C. Tönshoff and H. F. Bettinger, *Angew. Chem. Int. Ed.* 2010, **49**, 4125–4128.

8. H. Okamoto, R. Eguchi, S. Hamao, H. Goto, K. Gotoh, Y. Sakai, M. Izumi, Y. Takaguchi, S. Gohda and Y. Kubozono, *Sci Rep.* 2015, **4**, 5330.

9. U. Scherf and K. Müllen, *Polymer* 1992, **33**, 2443–2446.

10. M. Kertesz, *Macromolecules* 1995, **28**, 1475–1480.

11. K. Fukuda, J. Fujiyoshi, H. Matsui, T. Nagami, S. Takamuku, Y. Kitagawa, B. Champagne and M. Nakano, *Org. Chem. Front.* 2017, **4**, 779–789.

12. (*a*) Gaussian 09, Revision B.01, M. J. Frisch, G. W. Trucks, H. B. Schlegel, G. E. Scuseria, M. A. Robb, J. R. Cheeseman, G. Scalmani, V. Barone, B. Mennucci, G. A. Petersson, H. Nakatsuji, M. Caricato, X. Li, H. P. Hratchian, A. F. Izmaylov, J. Bloino, G. Zheng, J. L. Sonnenberg, M. Hada, M. Ehara, K. Toyota, R. Fukuda, J. Hasegawa, M. Ishida, T. Nakajima, Y. Honda, O. Kitao, H. Nakai, T. Vreven, J. A. Montgomery, Jr., J. E. Peralta, F. Ogliaro, M. Bearpark, J. J. Heyd, E. Brothers, K. N. Kudin, V. N. Staroverov, T. Keith, R. Kobayashi, J. Normand, K. Raghavachari, A. Rendell, J. C. Burant, S. S. Iyengar, J. Tomasi, M. Cossi, N. Rega, J. M. Millam, M. Klene, J. E. Knox, J. B. Cross, V. Bakken, C. Adamo, J. Jaramillo, R. Gomperts, R. E. Stratmann, O. Yazyev, A. J. Austin, R. Cammi, C. Pomelli, J. W. Ochterski, R. L. Martin, K. Morokuma, V. G. Zakrzewski, G. A. Voth, P. Salvador, J. J. Dannenberg, S. Dapprich, A. D. Daniels, O. Farkas, J. B. Foresman, J. V. Ortiz, J. Cioslowski and D. J. Fox, Gaussian, Inc., Wallingford CT, 2010; (*b*) CAM-B3LYP/6-31G(d,p) calculation was also conducted in order to compare with reported structural isomer **1**.

13. N. Prusinowska, M. Bardziński, A. Janiak, P. Skowronek, and M. Kwit, *Chem. Asian J.* 2018, **13**, 2691–2699.

14. Crystallographic data with CCDC Number 2011386 for **4** was deposited at the Cambridge Crystallographic Data Centre.

15. S. Nobusue, H. Miyoshi, A. Shimizu, I. Hisaki, K. Fukuda, M. Nakano and Y. Tobe, *Angew. Chem. Int. Ed.* 2015, **54**, 2090–2094.

16. B. D. Rose, L. E. Shoer, M. R. Wasielewski and M. M. Haley, *Chem. Phys. Lett.* 2014, **616–617**, 137–141.

17. Bruker, SAINT V8.38A, (Bruker AXS Inc., 2017).

18. O. V. Dolomanov, L. J. Bourhis, R. J. Gildea, J. A. Howard and H. Puschmann, *J. Appl. Crystallogr.* 2009, **42**, 339–341.

19. L. J. Bourhis, O. V. Dolomanov, R. J. Gildea, J. A. Howard and H. Puschmann, *Acta Crystallogr. A.* 2015, **71**, 59–75.

20. G. M. Sheldrick, *Acta Crystallogr. C Struct. Chem*. 2015, **71**, 3–8.

21. N. M. O'Boyle, A. L. Tenderholt and K. M. Langner, *J. Comp. Chem.* 2008, **29**, 839–845.

22. J. Kruszewski and T.M. Krygowski, *Tetrahedron Lett.* 1972, **13,** 3839–3842.

2C.7 Appendix

NMR Spectra

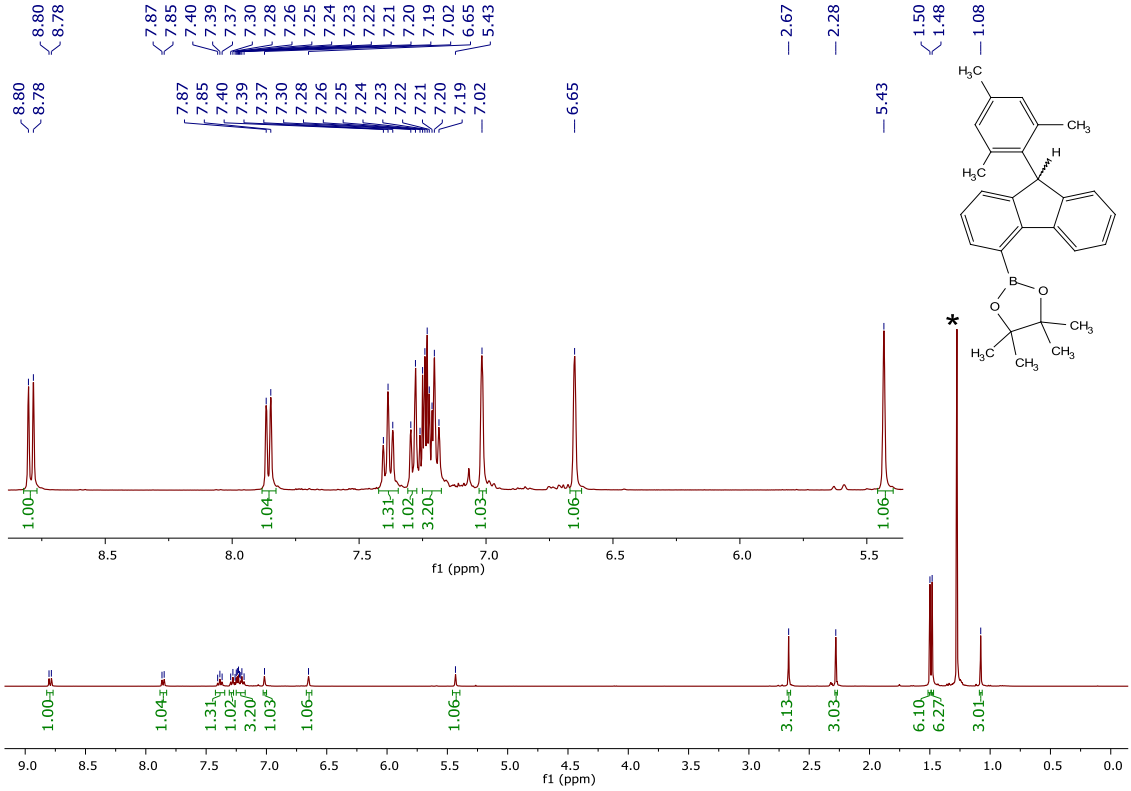

Figure 2C.12 ^{1}H NMR spectrum of **7** (in $CDCl_3$, 400 MHz).*B_2Pin_2 impurity.

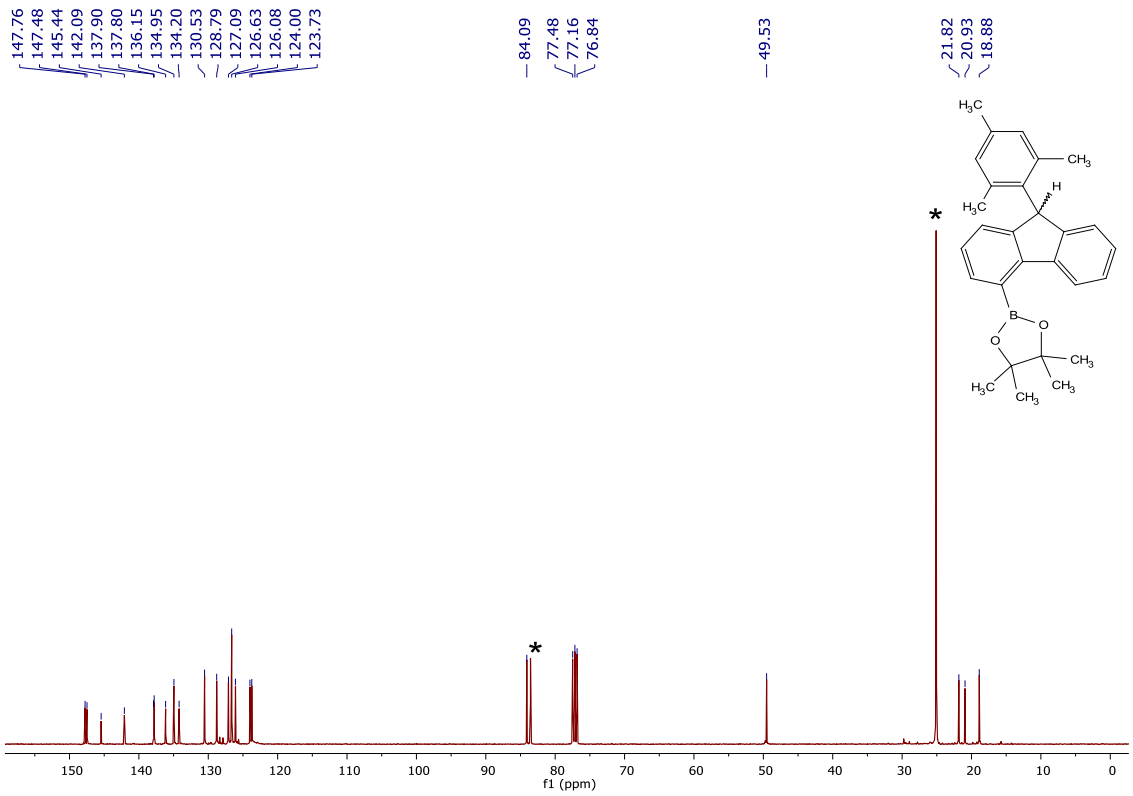

Figure 2C.13 ^{13}C NMR spectrum of **7** (in $CDCl_3$, 100 MHz).*B_2Pin_2 impurity.

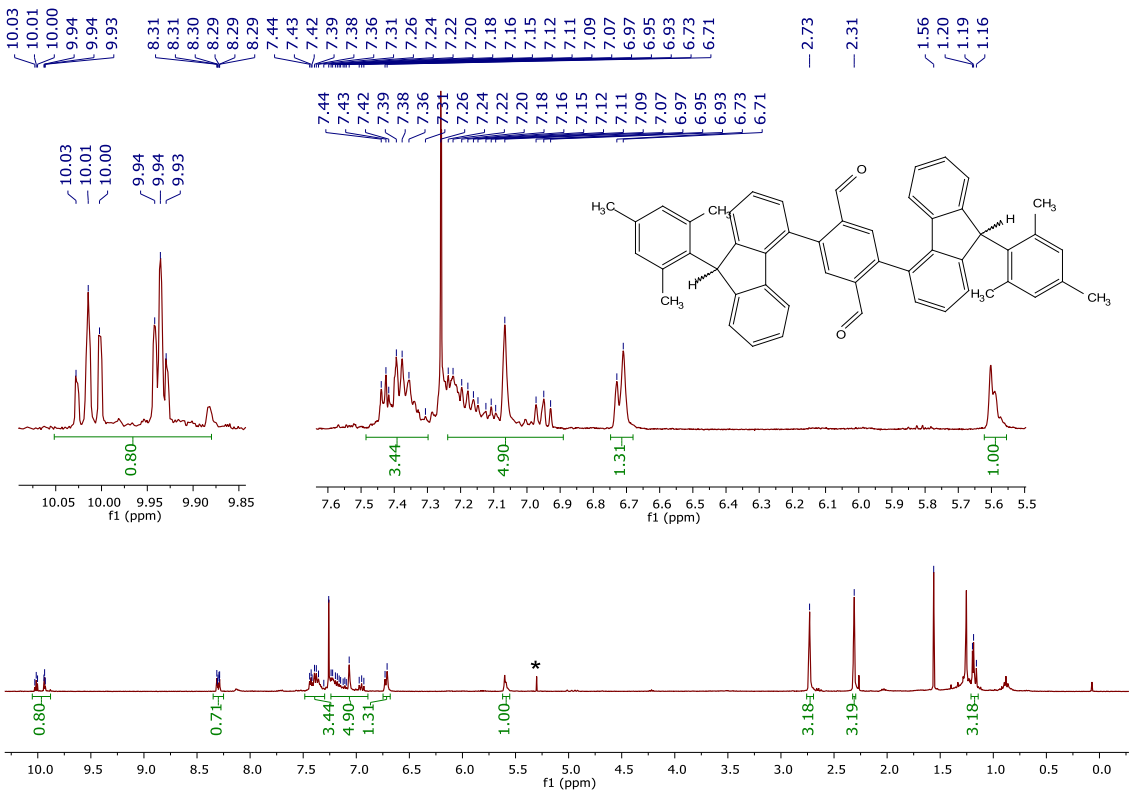

Figure 2C.14 ^{1}H NMR spectrum of **9** (in $CDCl_3$, 400 MHz).*CH_2Cl_2 impurity.

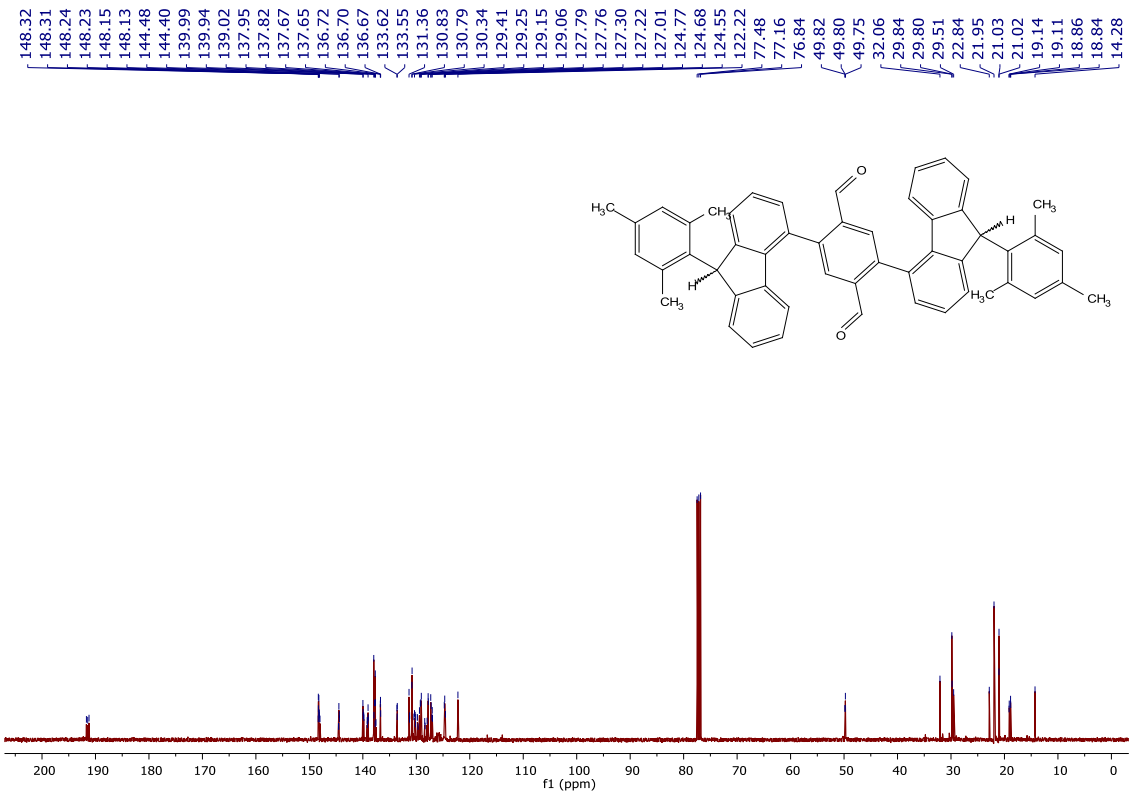

Figure 2C.15 ^{13}C NMR spectrum of **9** (in $CDCl_3$, 100 MHz).

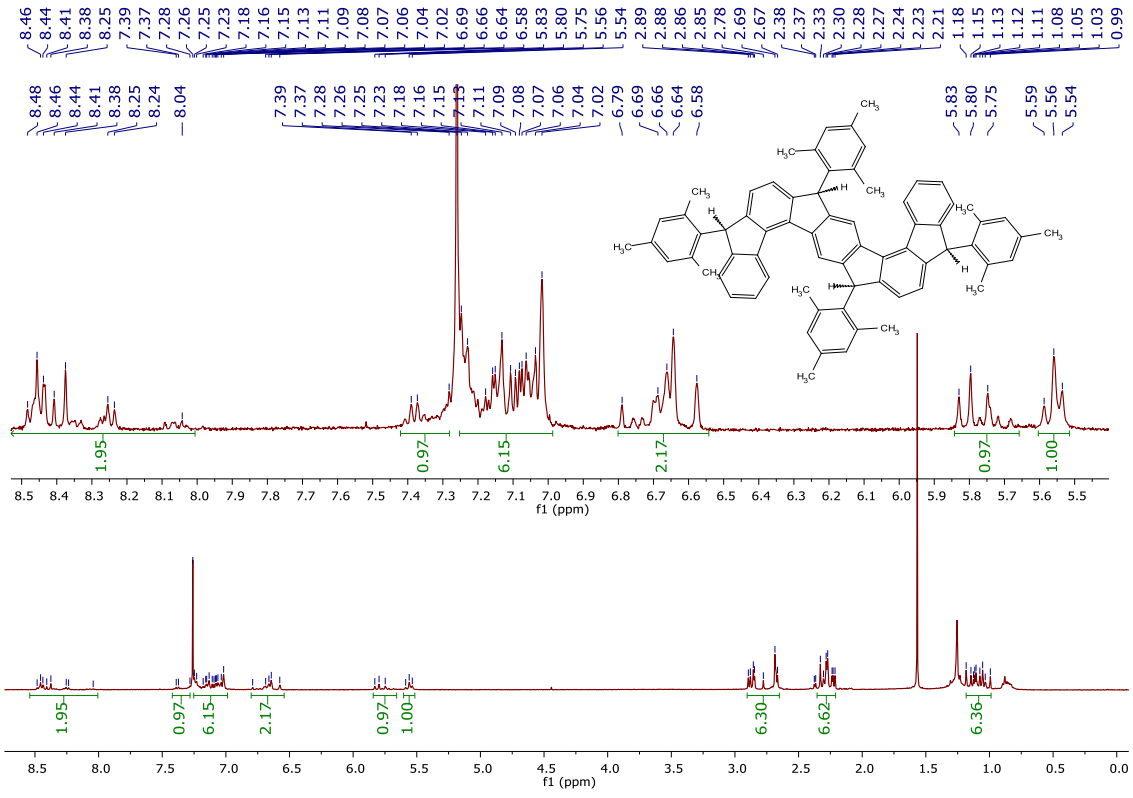

Figure 2C.16 ^{1}H NMR spectrum of **12** (in $CDCl_3$, 400 MHz).

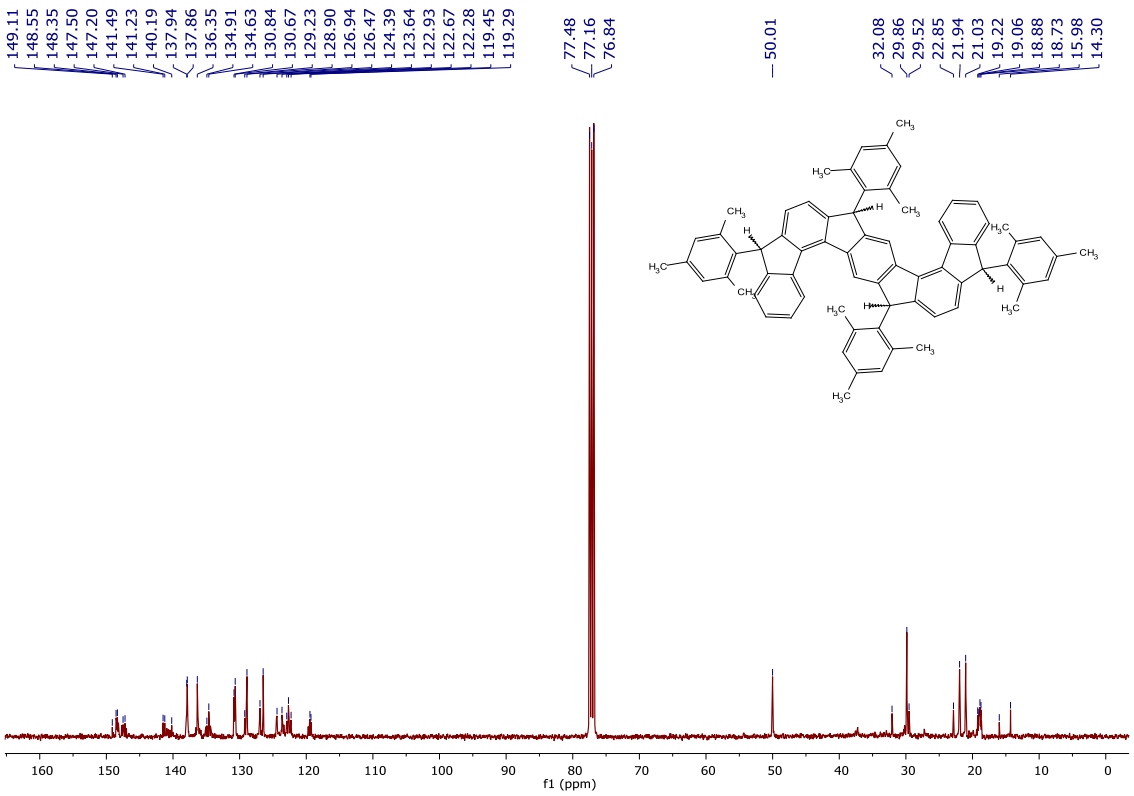

Figure 2C.17 ^{13}C NMR spectrum of **12** (in $CDCl_3$, 100 MHz).

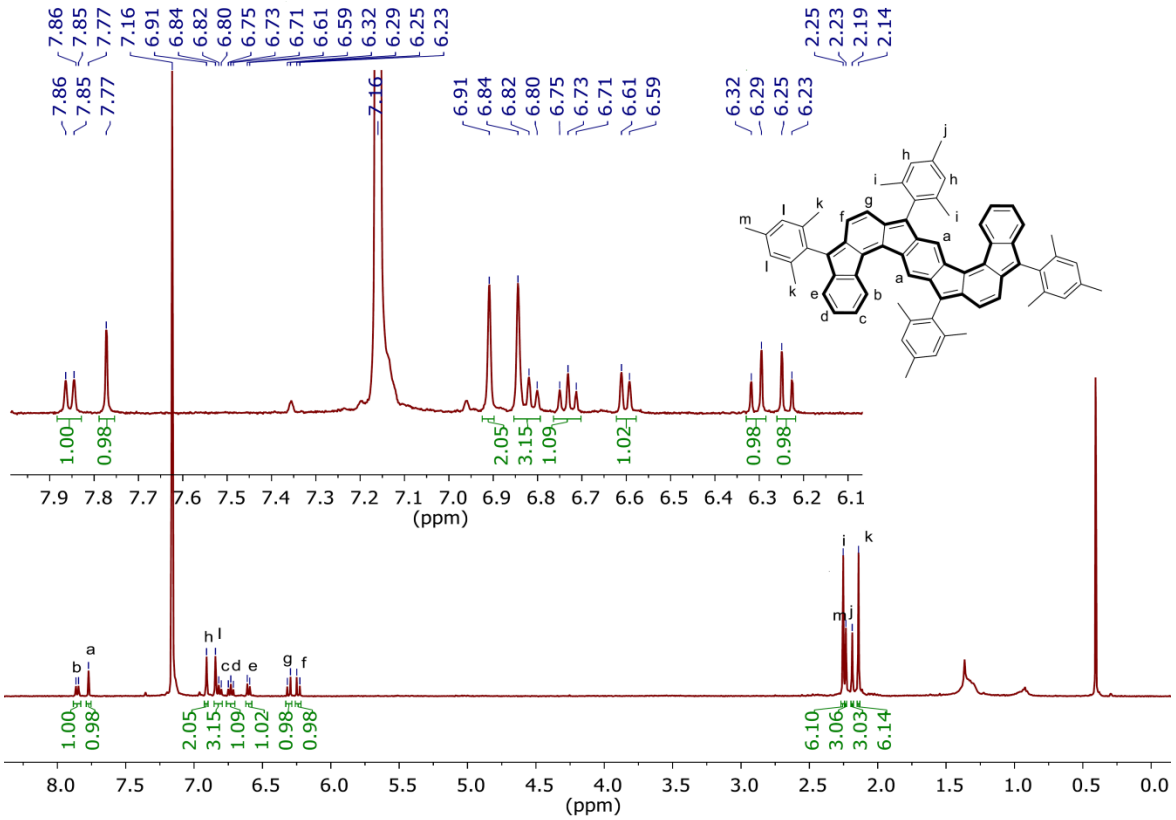

Figure 2C.18 ^{1}H NMR spectrum of **4** (in C_6D_6, 400 MHz). H_2O at δ 0.40 ppm.

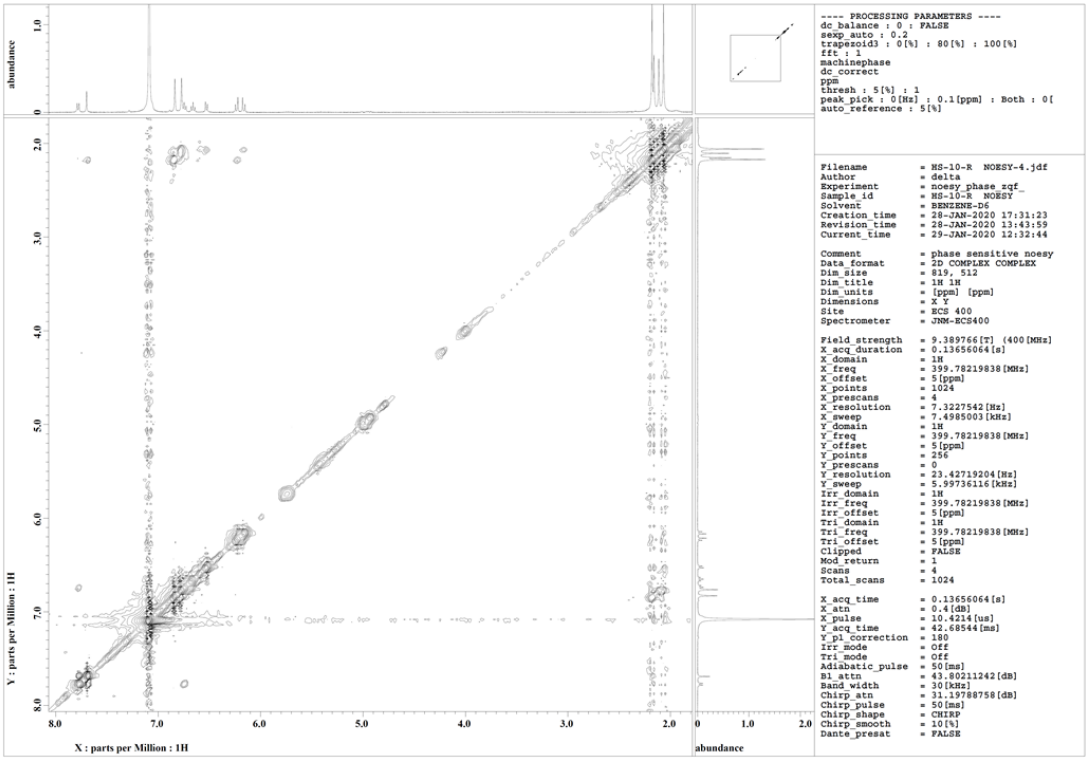

Figure 2C.19 ^{1}H-^{1}H NOESY, full spectrum of **4** in C_6D_6.

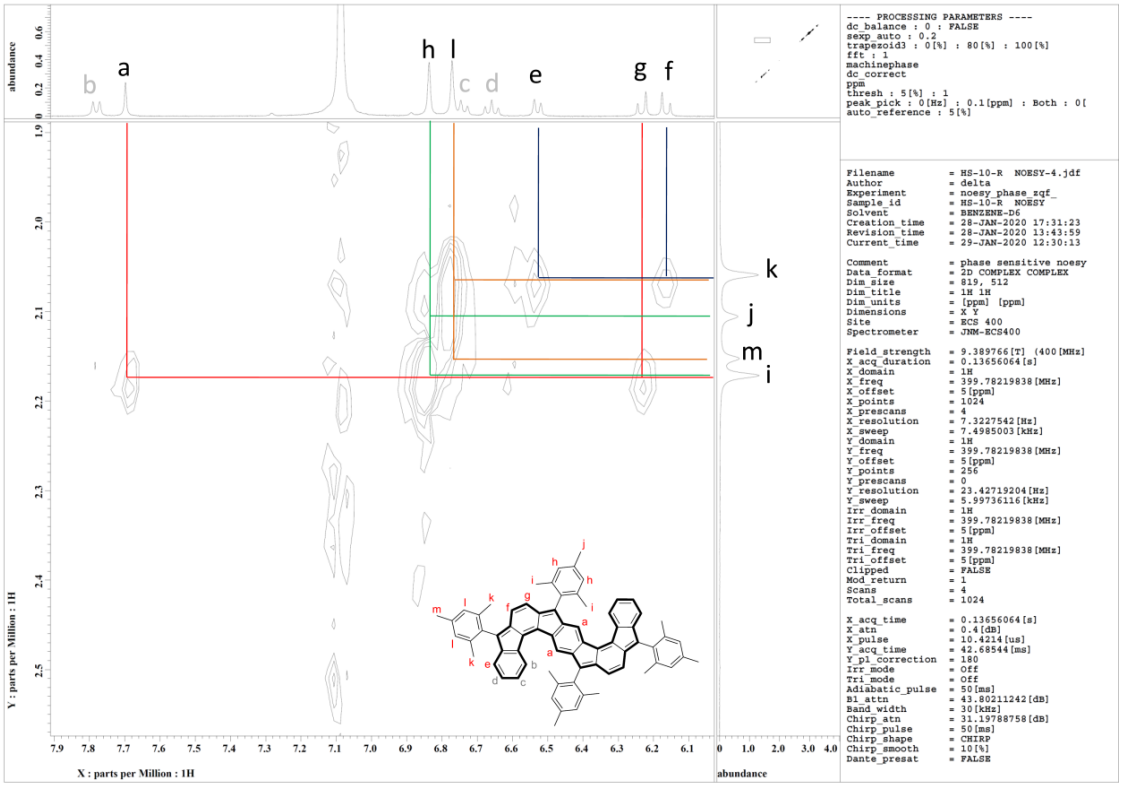

Figure 2C.20 Expanded ^{1}H-^{1}H NOESY (aromatic *vs* aliphatic region) spectrum of **4**.

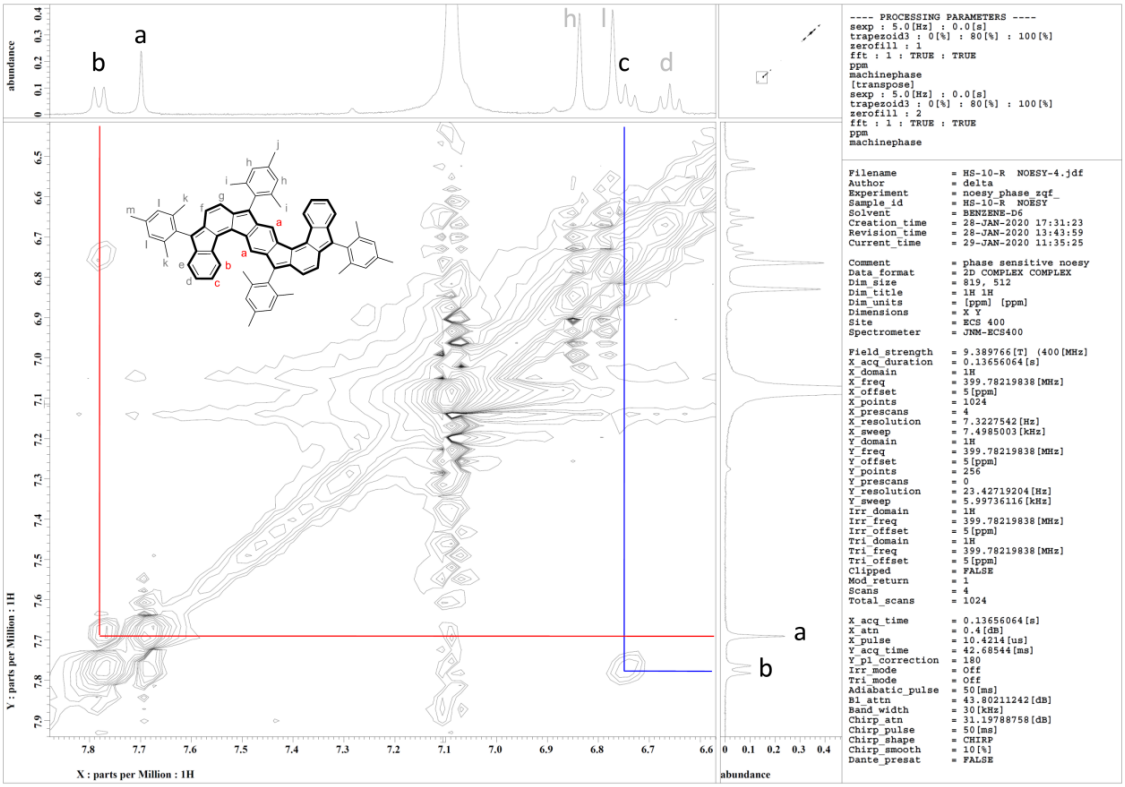

Figure 2C.21 Expanded ^{1}H-^{1}H NOESY (aromatic *vs* aromatic region) spectrum of **4**.

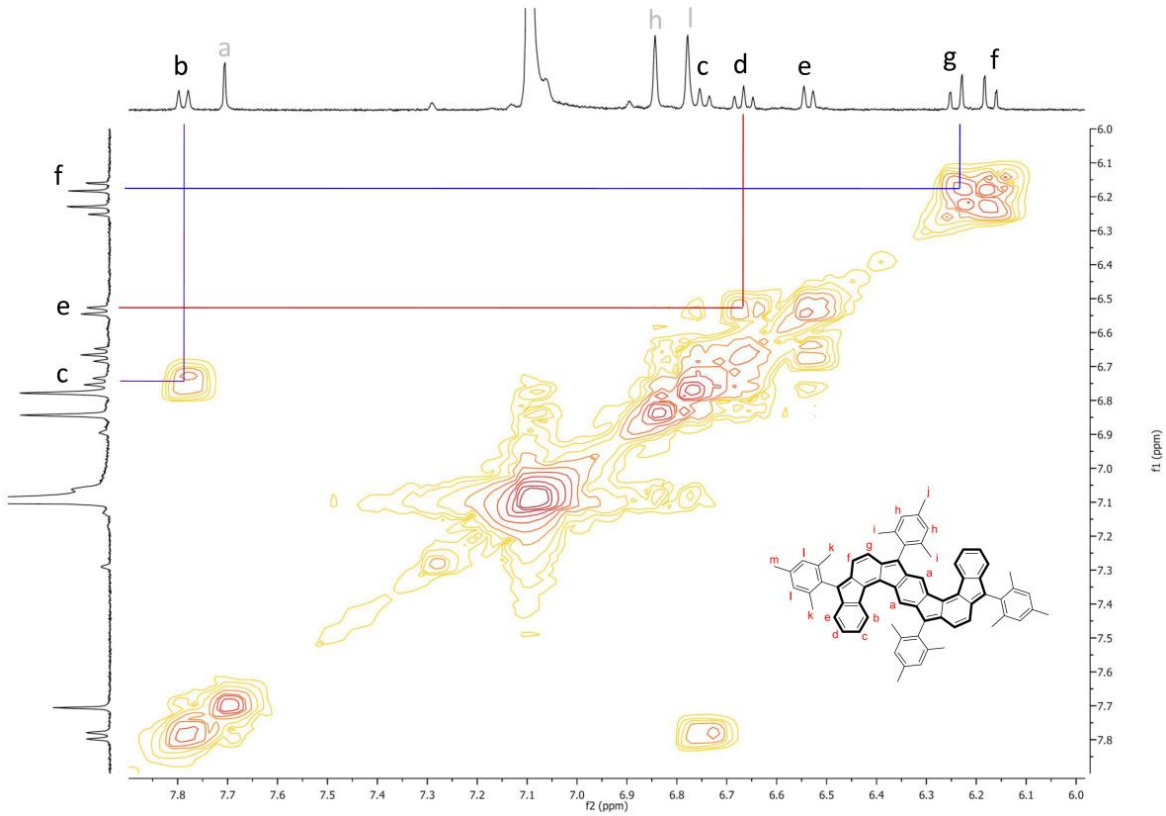

Figure 2C.22 ^{1}H-^{1}H COSY spectrum of **4** in C_6D_6.

Chapter 3

Revisiting indeno[1,2-*b*]fluorene by steric promoted synthesis while isolating the second stable 4nπ indeno[2,1-*a*]fluorene

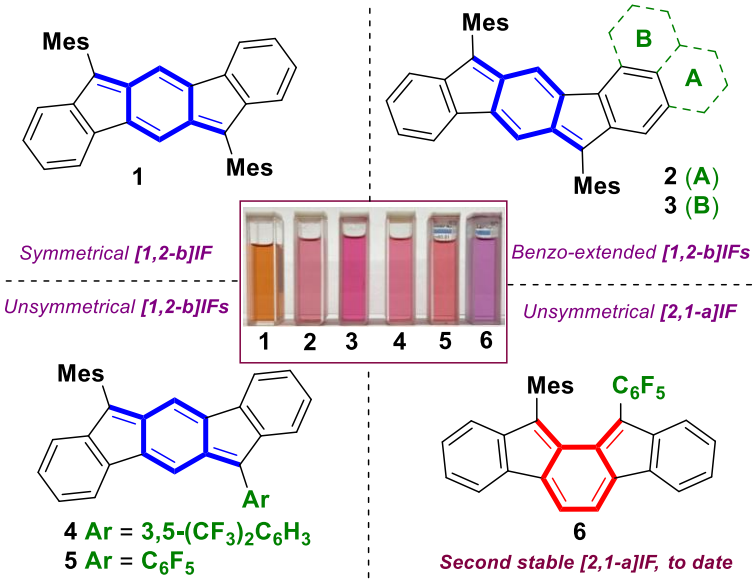

❖ This work was co-authored with Nikhil Bhardwaj, who provided synthetic support, Dr. Soumyajit Das, who provided guidance and editorial assistance. This work was originally published in ***Organic & Biomolecular Chemistry***. (Reference: *Org. Biomol. Chem.*, 2022, **20**, 8071-8077)

3.1 Abstract

Described herein are the steric promoted synthesis and characterization of symmetric, unsymmetric, and benzo-extended indeno[1,2-*b*]fluorenes **1**-**5**, including isolation of a stable 4nπ indeno[2,1-*a*]fluorene **6**. Single-crystal XRD analyses of **5** and **6** gave the unambiguous confirmation of unsymmetrical [1,2-*b*]IF and [2,1-*a*]IF motifs, respectively. The different ground state antiaromaticity of **5** and **6** was explained by Gimarc's approach for topological charge destabilization. The electronic properties of unsymmetrical IFs **2**-**5** mostly lie midway between **1** and the other known symmetrical counterparts.

3.2 Introduction

Fully conjugated indenofluorene (IF)[1] regioisomers, the formally antiaromatic IF motifs of parent aromatic dihydro-IFs,[2] have lately drawn tremendous attention of the scientific community since the first successful syntheses and characterization,[3] likely driven by the wide range of applications of parent aromatic IFs in organic electronic devices[4] comprising the field effect transistors,[4a-c] light emitting diodes,[4d-g] and photovoltaics[4h,4i].

Fully conjugated indeno[1,2-*b*]fluorene is one of the extensively studied IF scaffolds,[5] which was regarded as the formally antiaromatic pentacyclic analogue of pentacene considering the outer 4nπ-conjugation circuit. An improved synthesis of conjugated [1,2-*b*]IF derivatives was achieved by Haley et al. in 2011,[3a] while the earlier reports were only limited to the examples by Swager[6] and Scherf[7]. The [1,2-*b*]IF scaffold was generated by the addition of [(triisopropylsilyl)ethynyl]lithium (TIPSELi) to the corresponding dione precursor to produce dicarbinol derivative, and subsequent reduction of the alcohol by $SnCl_2$,[3a] an approach which was often used to synthesize acenes.[8] The same strategy was utilized to produce symmetrically disubstituted [1,2-*b*]IF derivatives,[5b] including pentafluorophenyl (C_6F_5) disubstituted [1,2-*b*]IF that showed ambipolar transistor behaviour with hole and electron mobilities = 7×10^{-4} cm^2 V^{-1} s^{-1} and 3×10^{-3} cm^2 V^{-1} s^{-1}, respectively. Apart from its promises as active material for bulk-heterojunction device[9] and single-molecule conductance studies,[10] various π-extended [1,2-*b*]IF derivatives were found to be fundamentally important in terms of tunable *s*-indacene paratropicity,[11] open-shell radical character,[12] redox amphotericity,[3a,5,13] and rare[14] photoluminescence[15] properties.

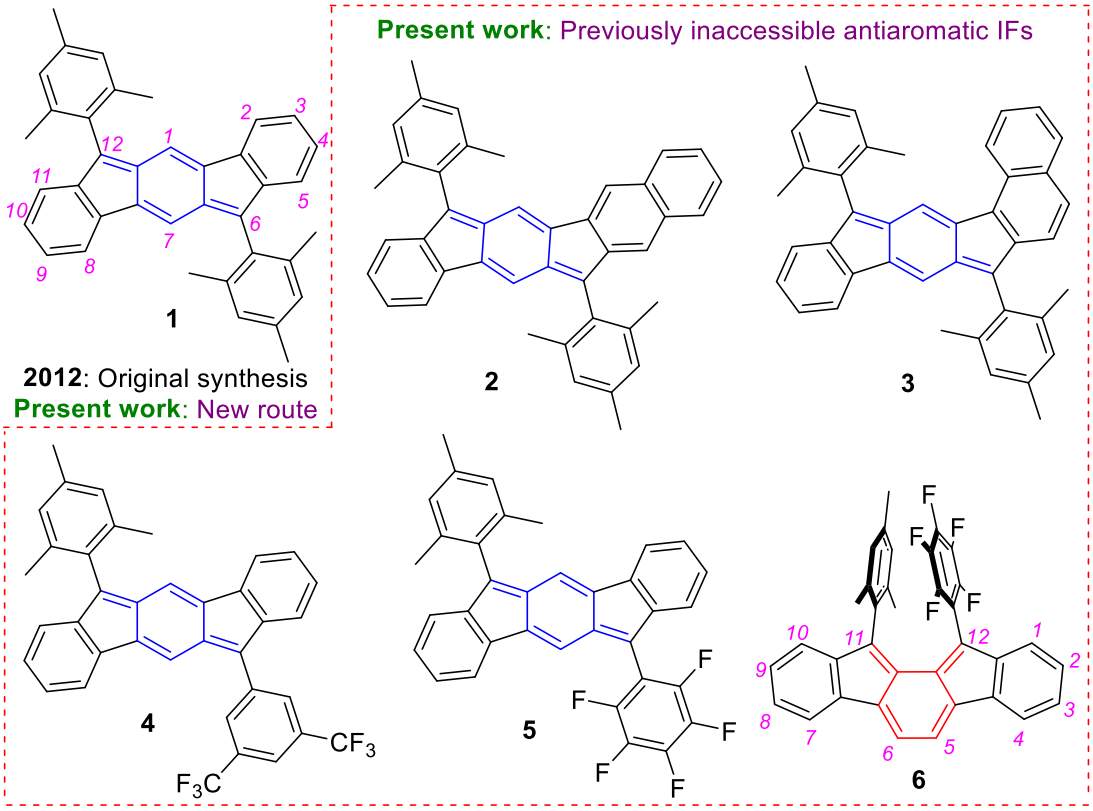

Figure 3.1 Target molecules: *p*-QDM embedded [1,2-*b*]IFs **1**-**5**, and *o*-QDM embedded [2,1-*a*]IF **6**

[1,2-*b*]IF is made of a *para*-quinoidal (*para*-quinodimethane or *p*-QDM unit shown in blue for **1**-**5** in Figure 3.1) core with *s*-indacene skeleton, whereas indeno[2,1-*a*]fluorene backbone possesses an *ortho*-quinoidal (*ortho*-quinodimethane or *o*-QDM unit shown in red for **6** in Figure 3.1) core embedded in *as*-indacene skeleton.[16] The presence of *o*-QDM subunit makes a polycyclic hydrocarbon (PH) quite unstable due to the reactive *s*-*cis* diene substructure.[17] Tobe et al. demonstrated that bulky mesityl (Mes) group protected *s*-*cis* diene containing *o*-QDM embedded 11,12-mesityl disubstituted [2,1-*a*]IF[3b] was isolable, stable and crystallographic characterization was possible, whereas the same [2,1-*a*]IF unit with ethynyl[18] or phenyl[19,3b] substitution at the apical carbons was either difficult to isolate or was unstable. The formally antiaromatic [2,1-*a*]IF was a closed-shell molecule with a large singlet-triplet energy gap (–13.5 kcal/mol or 0.58 eV).[20,3b] Presence of *s*-*cis* diene in isomeric PH may result in a reduced HOMO-LUMO energy gap,[21] and similarly, [2,1-*a*]IF exhibited a smaller electronic gap[3b] than that of isomeric [1,2-*b*]IF[5b] bearing the same mesityl substituents.

The syntheses of these [1,2-*b*]IF and [2,1-*a*]IF isomers are, to date, limited to only one synthetic strategy, i.e., addition of nucleophile to the dione precursor and

followed by the $SnCl_2$-mediated reduction of formed dicarbinols.[22,8,5c] This popular strategy lacks generating the unsymmetrical [1,2-*b*]IF or [2,1-*a*]IF scaffolds, thereby possibly hindering the growth of 4nπ congeners of unsymmetrically disubstituted (4n+2)π pentacenes[23] with potential for organic optoelectronics applications.[24] Another possible weakness of the strategy, as discussed in literature,[5c] could be the harsh reagents and conditions which were employed to synthesize the dione precursors[25] for [1,2-*b*]IF[26] and [2,1-*a*]IF[27] isomers.

Development of alternative synthetic approaches for the 4nπ IF isomers like indeno[2,1-*c*]fluorene has lately gained our[28] and other groups'[29] attention, and as a result, newer arrays of π-extended [2,1-*c*]IFs like tetraradicaloid *s*-indacenodifluorene with near-infrared absorption and stable carbon-centered non-alternant helical monoradical are now accessible. Notably, no alternative method for the syntheses of other IF regioisomers presently exists. Since the 6,12-mesityl disubstituted [1,2-*b*]IF **1** (Figure 3.1) was reported to be stable in comparison to its phenyl counterpart,[5c] we envisaged a mild synthesis approach for **1** by simply utilizing the steric hindrance of bulky mesityl group, inspired by some earlier works[30] where the exclusive formation of single regioisomer were attributed to the steric clash between the bulky substituents.[15] The approach was further extended to synthesize some of the yet inaccessible unsymmetrical [1,2-*b*]IFs **2**, **3**, **4**, **5** with *p*-QDM core, and [2,1-*a*]IF **6** with the elusive *o*-QDM core. Bulky aryl substituents were reported to sterically protect the potential radical sites of IF, thereby stabilizing the [1,2-*b*]IF.[5c] Herein, we showed that choice of aryl substituents may not only afford stable IFs but also govern the formation of desired IF isomer.

3.3 Results and Discussion

3.3.1 Synthesis

Syntheses of the fully conjugated IFs began with commercially available **7** and **8** (Scheme 3.1), which were subjected to a selective Suzuki coupling to generate the aldehyde derivative **9**. Addition of 2-mesitylmagnesium bromide (2-MesMgBr) to **9** afforded alcohol **10**, which on subsequent intramolecular Friedel-Crafts reaction in presence of $BF_3{\cdot}Et_2O$ furnished the important intermediate compound **11** in 73% yield over two steps. Compound **11** was treated with bis(pinacolato)diboron **12** under standard Miyaura-borylation reaction condition to afford **13**.[28] Pd^0-catalyzed Suzuki

reaction between **13** and **14** afforded the aldehyde **15**, which was further treated with Grignard reagent 2-MesMgBr and subsequently with $BF_3{\cdot}Et_2O$ to afford the dihydro-IF **16**. Treatment of **16** with 2,3-dichloro-5,6-dicyano-1,4-benzoquinone (DDQ) in 1,2-dichloroethane (1,2-DCE) for 2 h afforded **1** in 95% yield. The formation of **1** was unambiguously confirmed by the ^{1}H nuclear magnetic resonance (NMR), high resolution mass spectrometry (HRMS) analyses (*vide infra*), and the results are in line with literature.[5b]

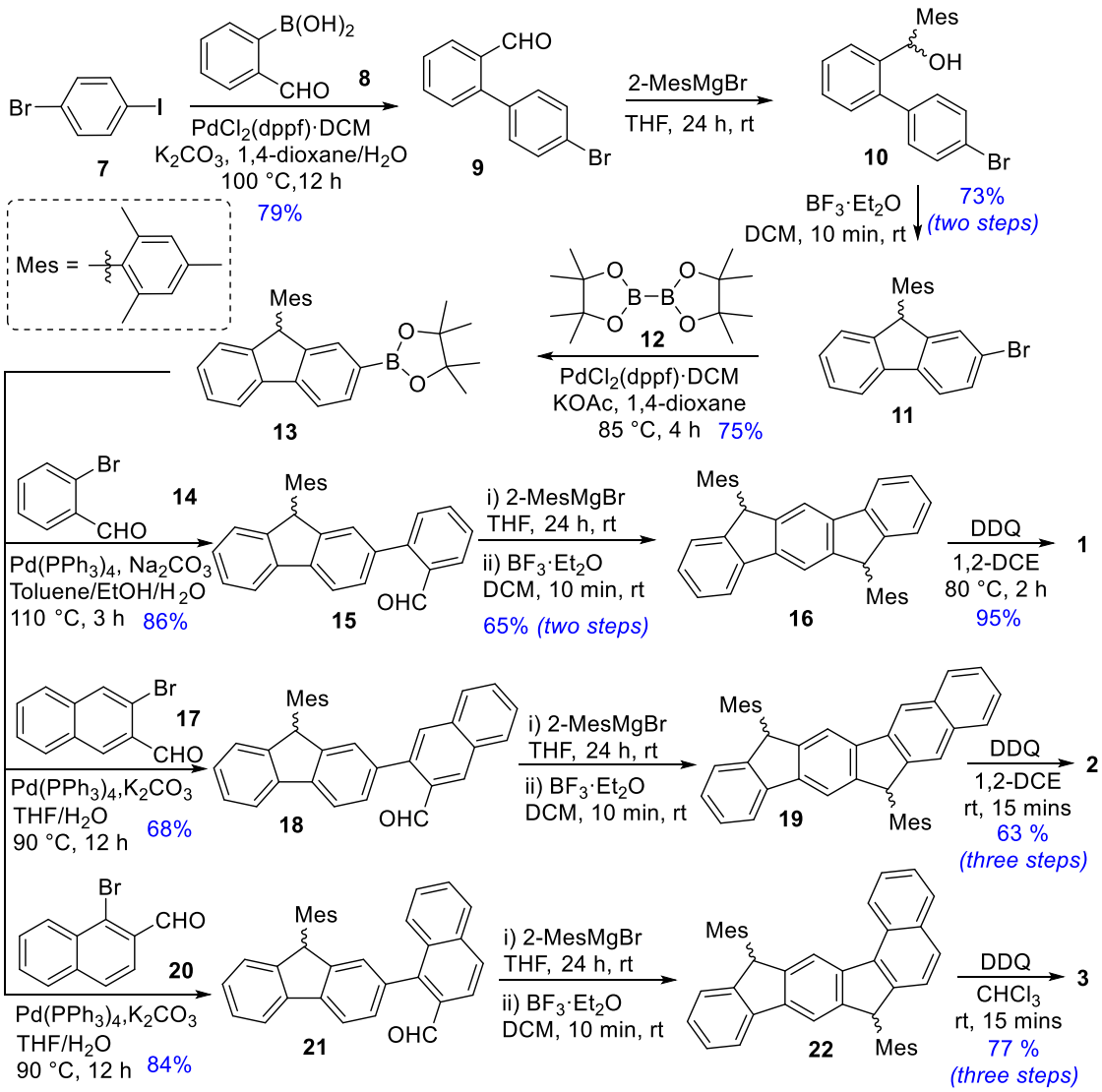

Scheme 3.1 Synthesis route to [1,2-*b*]IF **1** and its benzo-extended derivatives **2** and **3**.

After confirming the exclusive formation of [1,2-*b*]IF **1**, we further utilized the same reaction sequences to construct the previously unknown benzo-[1,2-*b*]IF isomers **2** and **3**, from known bromonaphthaldehyde derivatives **17** and **20**, respectively (Scheme 3.1). Treatment of **13**, separately under identical Suzuki reaction condition, with **17** and

20 afforded the corresponding naphthaldehyde derivatives **18** and **21**, respectively, which on subsequent reactions with 2-MesMgBr and $BF_3{\cdot}Et_2O$ afforded **19** and **22**, respectively, which without any purification were treated with DDQ to afford the desired regioisomers **2** and **3**, in 63% and 77% yield, respectively, over three steps. These fully conjugated IFs **2** and **3** were clearly identified by the characteristic[11a] UV-vis absorption bands (*vide infra*), and were further confirmed by NMR and HRMS analyses (*vide infra*).

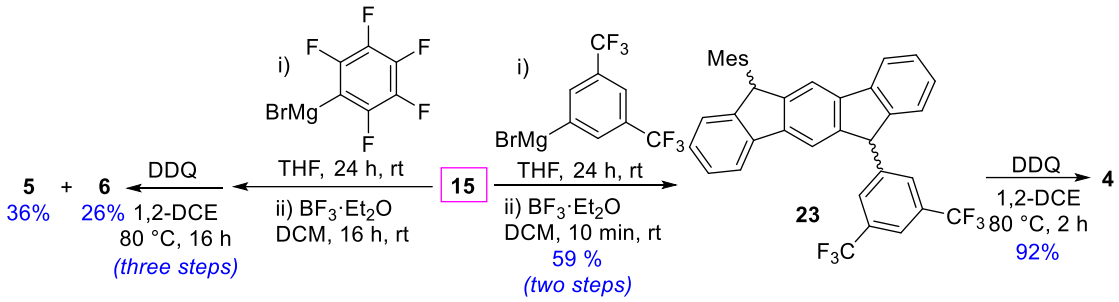

Scheme 3.2 Synthesis route to [1,2-*b*]IF **4**, **5** and [2,1-*a*]IF **6** from aldehyde **15**.

We then turned our attention to synthesize 3,5-bis(trifluoromethyl)phenyl substituted **4**, utilizing the same synthetic sequences. The aldehyde **15** was sequentially treated with Grignard reagent 3,5-$(CF_3)_2C_6H_3MgBr$ and $BF_3{\cdot}Et_2O$ to afford **23**, which on further treatment with DDQ, expectedly, afforded the unsymmetrically disubstituted [1,2-*b*]IF **4** in excellent yield (Scheme 3.2). Following the successful isolation of **4**, we switched to the less bulky pentafluorophenyl (C_6F_5) group, anticipating least hindrance among the three aryl substituents and a loss in regioselectivity was expected. Interestingly, treatment of **15** with C_6F_5MgBr and followed by sequential reactions of the formed carbinol intermediate with $BF_3{\cdot}Et_2O$ and DDQ afforded a mixture of bench-stable and chromatographically (silica gel) separable unsymmetrically disubstituted IF regioisomers **5** and **6** (Scheme 3.2), possessing *p*-QDM and *o*-QDM units, respectively, as confirmed by NMR analyses (*vide infra*). The formation of **5** and **6** were further unambiguously confirmed by the single-crystal X-ray diffraction (SCXRD) analyses.

3.3.2 Single crystal, ground state and (anti)aromaticity analysis

Single crystals of **5** and **6** were obtained by slow evaporation of ethyl acetate/hexane and acetonitrile/hexane mixtures, respectively. The crystallographic analysis revealed planar backbone for **5** and **6** with *s*-indacene and *as*-indacene skeleton (ring B-C-D), respectively, with the typical $C_{sp}{}^2$-$C_{sp}{}^2$ bond length arrangements for *p*-QDM[12a] and *o*-

QDM[3b] moiety (Figure 3.2a and 3.2b), which are in line with the literature reports and indicate a quinoidal contribution in the ground state. The outer six-membered rings (A and E) of **5** and **6** have C_{sp}^2-C_{sp}^2 bond lengths typical of a benzene motif, denoting aromatic character.[12a,3b]

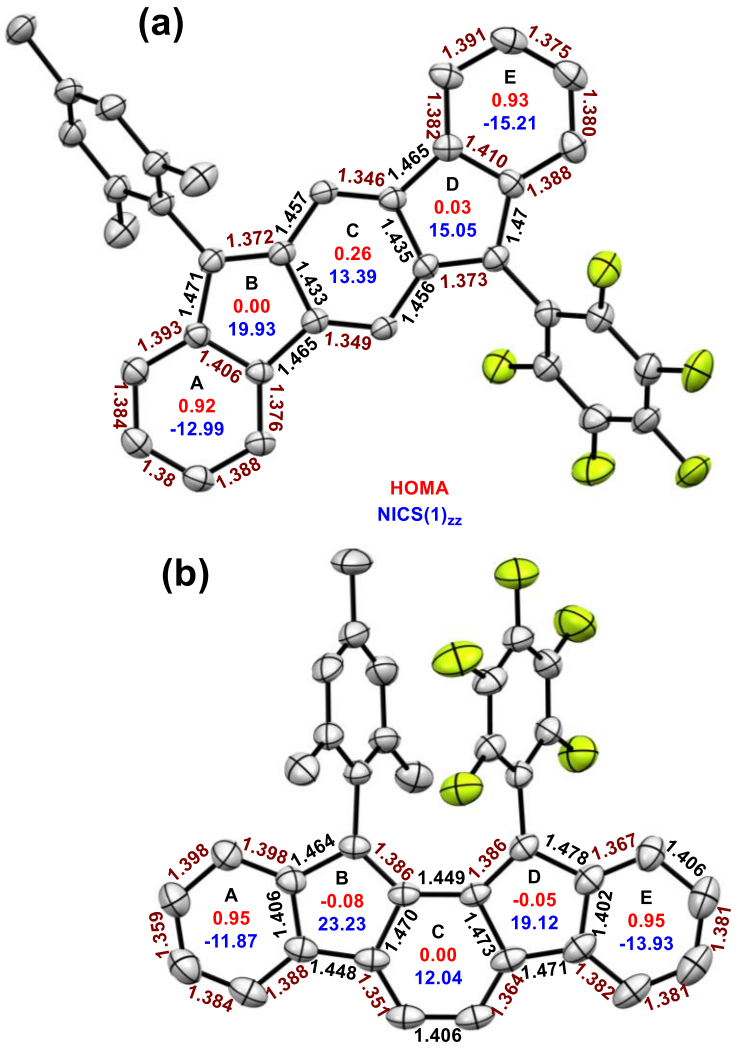

Figure 3.2 X-ray crystallographic structures of (a) **5** and (b) **6** with ellipsoids drawn at 30% probability level, and the C_{sp}^2-C_{sp}^2 bond distances for *p*-QDM unit (in Å) of **5** (mean bond lengths of two crystallographically independent molecules) and *o*-QDM unit of **6** are shown (hydrogens omitted). The HOMA (red) and NICS(1)$_{zz}$ (blue) indices for the rings A-E are shown for the optimized ground state structure.

Density functional theory (DFT) calculations of the crystal structures at the B3LYP/6-31G(d)[3b] level of theory suggested the ground states of **5** and **6** as closed-shell singlet with large singlet-triplet energy gaps ($\Delta E_{S\text{-}T}$) of –16.9 kcal mol^{-1} and –13.9 kcal mol^{-1}, respectively, similar to the literature reports (*vide infra*).[5b,12a,3b] It is known that the bond lengths either do not alternate or their alternation is very weak for strongly aromatic compounds, and such bond length alternation (BLA) could be quantified by

harmonic oscillator model for aromaticity (HOMA) analyses.[31] HOMA value is close to 1 for aromatic rings and close to 0 for nonaromatic rings,[32] however, a negative value doesn't necessarily mean antiaromaticity.[33] HOMA analyses[34] for the optimized structures **5** and **6** showed significant BLA for the rings B (**5**: 0, **6**: –0.08), C (**5**: 0.26, **6**: 0), and D (**5**: 0.03, **6**: –0.05), supporting the quinoidal arrangement; while the non-significant BLA of the outer rings A (**5**: 0.92, **6**: 0.93) and E (**5**: 0.95, **6**: 0.95) support their strong benzene-like aromaticity. The aromaticity of the outer rings A and E are further supported by the large negative nucleus independent chemical shift [NICS(1)$_{zz}$][35] values (Figure 3.2a and 3.2b), while positive NICS(1)$_{zz}$ values for the rings B, C, and D imply antiaromaticity of *s*-indacene[11] and *as*-indacene.[3b]

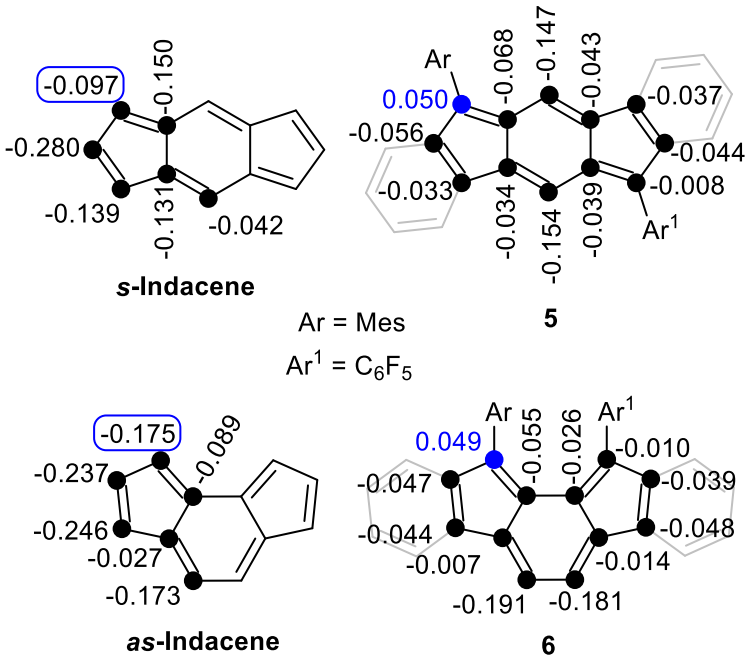

Figure 3.3 NPA charges of parent indacenes and the corresponding IF derivatives **5** and **6**. Ar = mesityl and Ar^1 = pentafluorophenyl.

Natural population analyses (NPA) suggested the charges for the apical carbons for parent *s*-indacene and *as*-indacene as –0.097[36] and –0.175, respectively (Figure 3.3). According to the Haley's extension of Gimarc's principle of topological charge stabilization, π-conjugated systems will be destabilized if a positive charge is imposed at the positions with high negative charges in the parent hydrocarbon skeleton.[36,37] The higher negative charge (–0.175) on the apical carbon of parent *as*- indacene, compared to that of *s*-indacene, suggested that enforcing an equivalent amount of positive charge

(+0.049 for **6**) due to mesityl group would largely destabilize ring B of the *as*-indacene unit in comparison to the *s*-indacene unit (+0.050 for **5**); thereby increasing the antiaromatic character of *as*-indacene.[3b] As a consequence, antiaromaticity of ring B for **6** was enhanced in comparison to **5**, which is reflected by the higher positive $NICS(1)_{zz}$ value for **6** (B = 23.23) than that of **5** (B = 19.93).

The relatively weaker antiaromatic character of ring D for both **5** and **6** can be analogously rationalized by the smaller negative values enforced by the C_6F_5 substituent. However, considering the smaller negative charge of the apical carbon of parent *s*-indacene in comparison to *as*-indacene, a low negative value (–0.008) of the apical carbon connected to C_6F_5 of **5** plausibly reduced the antiaromatic character of ring D when compared to that of **6** with nearly identical amount of negative charge (–0.010). Similarly, the weaker local antiaromaticity of ring D than B, for both **5** and **6**, is also in line with the Gimarc's charge destabilization approach. Overall, **6** showed a greater degree of antiaromaticity than **5**, which is validated by the smaller optical/electrochemical/theoretical HOMO-LUMO energy gaps (Table 3.1, Table 3.10).

3.3.3 Optical and electrochemical properties

The UV-vis absorption spectra of the unsymmetrically disubstituted [1,2-*b*]IFs **4** and **5** were characteristically similar to the symmetrically disubstituted [1,2-*b*]IF **1**[5b,12a] (Figure 3.4), with the lower-energy absorption maxima of 531 nm ($\varepsilon = 18380\ M^{-1}\ cm^{-1}$) and 527 nm ($\varepsilon = 22940\ M^{-1}\ cm^{-1}$), respectively. However, the spectra for **4** and **5** are red shifted by 15 nm and 11 nm, with respect to **1**, suggesting better electronic communication between IF and 3,5-$(CF_3)_2C_6H_3$ or C_6F_5 π-rings. When the benzo-extended [1,2-*b*]IFs were compared, the absorption profiles of **2** and **3** lie halfway between **1** and the corresponding *s*-indacenodinaphthalene (*s*-IDN) isomers.[11a] In line with the literature, relatively greater degree of antiaromatic character for compound **3** than **2** was expected due to enhanced paratropicity of the *s*-indacene unit for **3** owing to the attachment of its *s*-indacene unit to the 1,2-position of naphthalene ring.[11a] As a result, the UV-vis absorption maximum of **3** (545 nm) was 16 nm red-shifted than that of **2** (529 nm), and displayed smaller optical energy gap (Figure 3.4 and Table 3.1).

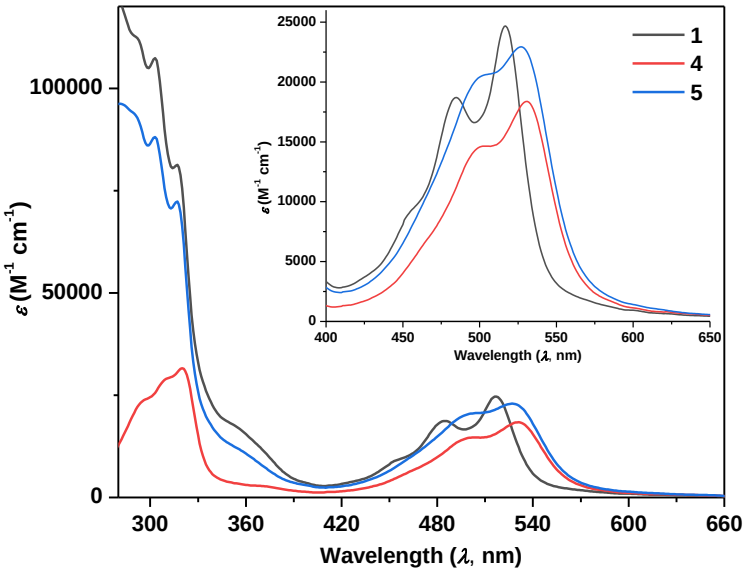

Figure 3.4 UV-vis absorption profiles for [1,2-*b*]IFs **1**, **4**, **5** (expansion in inset), recorded in dichloromethane.

Table 3.1 Photophysical and electrochemical data of **2**–**6**.[a]

IF	$E_{1/2}^{red1}$ [V]	$E_{1/2}^{ox1}$ [V]	HOMO [eV]	LUMO [eV]	E_g^{ec} [eV]	λ_{abs} [nm]	E_g^{opt} [eV]
2	–1.70	0.46	–5.16	–3.22	1.94	529, 493, 334	2.19
3	–1.58	0.54	–5.23	–3.34	1.89	545, 511, 342	2.16
4	–1.49	0.65	–5.34	–3.50	1.84	531, 501	2.17
5	–1.73	0.47	–5.20	–3.22	1.98	527, 502	2.19
6	–1.31	0.75	–5.45	–3.63	1.82	537, 320, 293	1.55

[a] $E_{1/2}^{red1}$ and $E_{1/2}^{ox1}$ are half-wave potentials of the first reduction and oxidation waves, respectively; HOMO = −(4.8+E_{ox}^{onset}) and LUMO = −(4.8+E_{red}^{onset}), where E_{ox}^{onset} and E_{red}^{onset} are the onset potentials of the first oxidative and reductive waves, respectively; E_g^{ec} = electrochemical energy gap; λ_{abs} = absorption maxima; E_g^{opt} = optical energy gap.

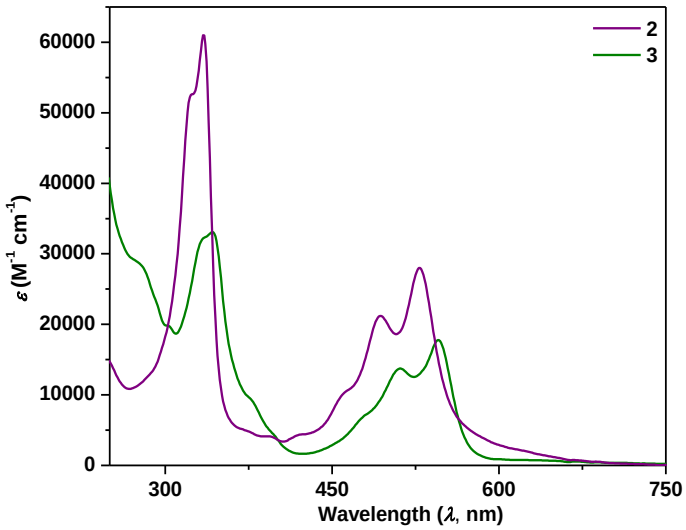

Figure 3.5 UV-vis absorption profiles for [1,2-b]IFs **2** and **3** recorded in dichloromethane.

The UV-vis absorption profile of *o*-QDM embedded **6** (Figure 3.6) exhibited two higher energy bands in the UV region (λ_{max} = 320 nm, ε = 11540 M^{-1} cm^{-1}; λ_{max} = 293 nm, ε = 26990 M^{-1} cm^{-1}) and a lower energy band in the visible region (λ_{max} = 537 nm, ε = 11100 M^{-1} cm^{-1}), along with a broad absorption tail stretched from 600 to 800 nm, which is characteristically similar to the reported [2,1-*a*]IF[3b] and relatively red-shifted, and could be attributed to the admixture of HOMO-1→LUMO and HOMO→LUMO transitions (Table 3.2).

Table 3.2 Summary of TDDFT calculations of compound **6**.

Wavelength (nm)	Osc. Strength (f)	Major contribution
708.9	0.0369	H-1->LUMO (43%), HOMO->LUMO (57%)
558.7	0.2859	H-1->LUMO (56%), HOMO->LUMO (43%)
472.9	0.049	H-2->LUMO (98%)
449.9	0.0043	H-3->LUMO (99%)
413.5	0.0095	H-4->LUMO (97%)
373.4	0.0002	H-6->LUMO (40%), H-5->LUMO (59%)
365.5	0.0007	H-6->LUMO (55%), H-5->LUMO (34%)
356.3	0.0142	H-7->LUMO (90%)
329.2	0.1207	HOMO->L+1 (89%)
313.5	0.1094	HOMO->L+2 (85%)
310.0	0.021	H-8->LUMO (92%)
295.7	0.0055	HOMO->L+3 (96%)
285.1	0.2439	H-1->L+1 (60%), H-1->L+2 (10%), HOMO->L+4 (16%)
284.0	0.037	H-1->L+2 (15%), HOMO->L+4 (72%)

278.1	0.3915	H-1->L+1 (11%), H-1->L+2 (60%), HOMO->L+5 (11%)
268.8	0.1307	H-9->LUMO (12%), HOMO->L+5 (66%)
266.1	0.1391	H-9->LUMO (24%), H-1->L+4 (21%), HOMO->L+5 (14%), HOMO->L+6 (24%)
262.3	0.0206	H-2->L+1 (13%), HOMO->L+6 (28%), HOMO->L+7 (38%)
260.2	0.0402	H-2->L+1 (65%)
259.8	0.0029	H-1->L+3 (89%)

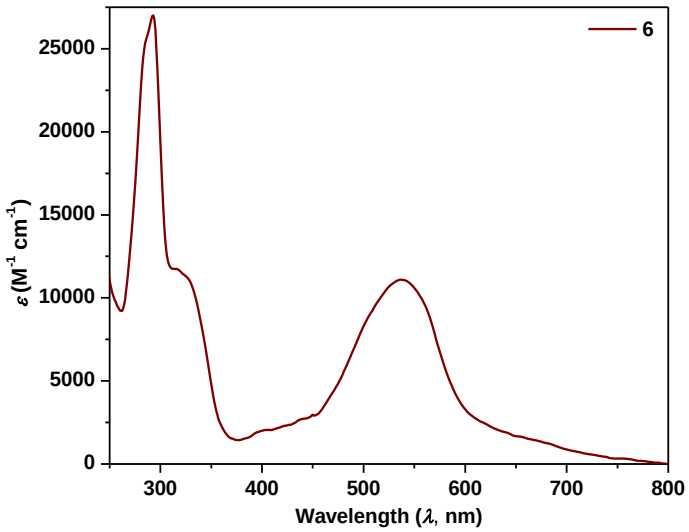

Figure 3.6 UV-vis absorption profile for [2,1-*a*]IF **6**, recorded in dichloromethane.

An obvious smaller optical HOMO-LUMO energy gap for **6** (1.55 eV) was roughly estimated, from the lowest energy absorption onset,[3b] than that of the reported dimesityl analogue. The smaller electronic gap of **6** in comparison to that of [1,2-*b*]IF isomer **5** (2.19 eV), bearing same substituents, was noted; a trend which was observed for mesityl disubstituted analogues too.[5b,3b] Similar to the other formally antiaromatic IFs, these new IF derivatives don't exhibit fluorescence.[14]

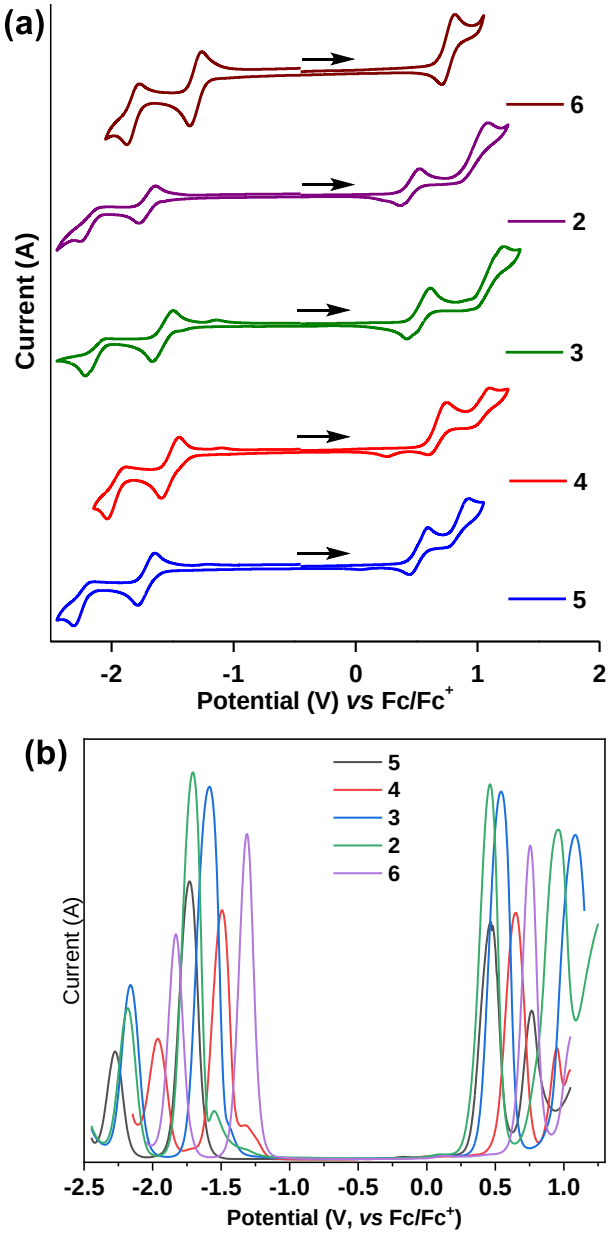

Figure 3.7 (a) Cyclic voltammograms and (b) Differential pulse voltammogram of new IFs **2**-**6** (0.001 M) in dichloromethane. All data were taken at 298 K, in dry and degassed dichloromethane with 0.1 M Bu_4NPF_6 under nitrogen atmosphere. All data were collected using Pt-disk electrode as a working electrode, Pt wire as a counter electrode and Ag wire as a pseudo-reference electrode. Scan direction is shown using arrow.

The cyclic voltamogramms of the new IFs are shown in Figure 3.7a, and the half-wave potentials ($E_{1/2}$, *vs* ferrocene/ferrocenium (Fc/Fc^+)) were extracted from the differential pulse voltammogram peak values (Figure 3.7b). The benzo-extended [1,2-*b*]IF derivatives **2** and **3** were reversibly reduced with first $E_{1/2}^{red1}$ = –1.70 V and $E_{1/2}^{red1}$

= –1.58 V, along with the quasi-reversible second reductions $E_{1/2}^{red2}$ = –2.18 V and $E_{1/2}^{red2}$ = –2.16 V (Figure 3.7 and Table 3.10). The less negative reduction potential of **3** further validated its greater degree of antiaromaticity, resulting in its easier reduction in comparison to isomeric **2**. The first oxidations of **2** and **3** were reversible while second oxidations were quasi-reversible. Compound **3** was found to show higher first and second oxidation potentials than those of **2**, similar to the reversed trend to the reduction potentials which were also observed for *s*-IDN isomers.[11a]

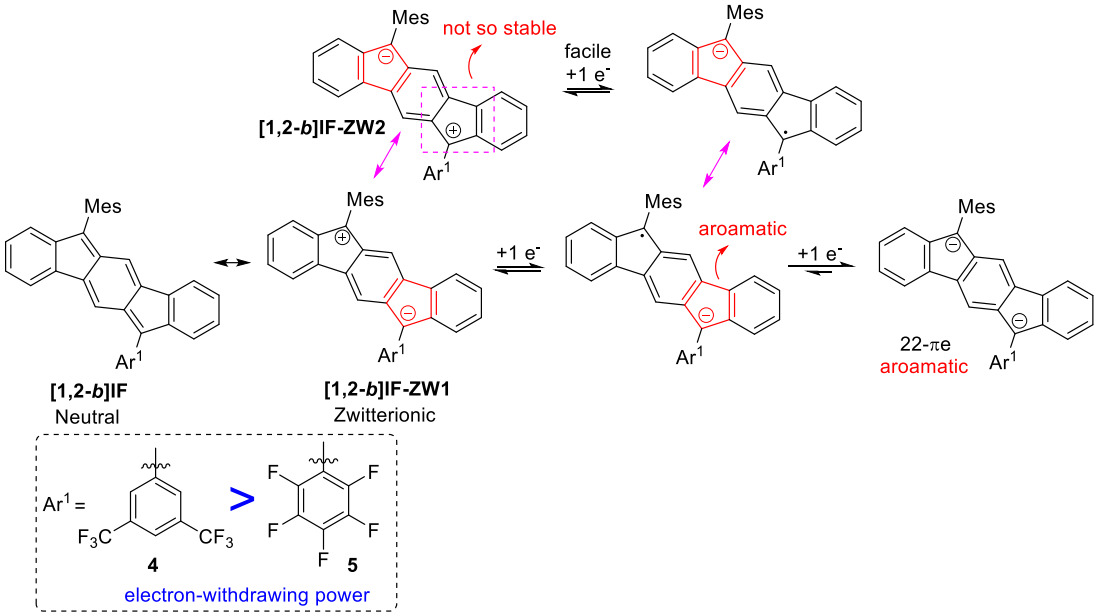

Figure 3.8 Supporting figure that may explain the electron-withdrawing effect on **4** *vs* **5**. Stronger the electron-withdrawing ability of the apical substituent, easier is the one-electron reduction considering **[1,2-*b*]IF-ZW2** substructure (Electron-donating power of mesityl group is not so strong).[38]

Similar redox events were observed for [1,2-*b*]IF derivatives **4** and **5**, with the redox potentials lying midway between **1** and the corresponding symmetrically aryl [3,5-$(CF_3)_2C_6H_3$ and C_6F_5] disubstituted [1,2-*b*]IFs,[5b,12a] like the absorption profiles. Assuming **[1,2-*b*]IF-ZW2** as one of the zwitterionic forms of [1,2-*b*]IF with aromatic cyclopentadienyl anion (Figure 3.8), reduction of [1,2-*b*]IF with electron-withdrawing group grafted at the apical carbocation centre was expected to occur at lower negative potential to relieve antiaromaticity (cyclopentadienyl cation). Moreover, the stronger the electron-withdrawing effect of apical aryl group, the lower should be the reduction potential of [1,2-*b*]IF. According to reports,[39] C_6F_5 group may withdraw electrons (inductively, -I effect) more strongly than a phenyl group, but far less strongly than a trifluoromethyl (CF_3) group. The pronounced -I effect of 3,5-$(CF_3)_2C_6H_3$[39b] group thus

allowed **4** to be reduced relatively easily (low-lying LUMO than **5**) at a lower negative potential than that of **5** or **1**[12a] due to facile injection of electrons (Figure 3.8 and Table 3.10).

The [2,1-*a*]IF derivative **6** displayed a reversible oxidation $E_{1/2}^{ox}$ = 0.75 V and two reversible reduction events: $E_{1/2}^{red1}$ = –1.31 V and $E_{1/2}^{red2}$ = –1.83 V, with a low-lying LUMO of –3.63 eV in comparison to that of dimesityl analog,[3b] suggesting the potential for **6** as a better electron-acceptor for application in optoelectronics.[9,40] Our NICS calculation suggested that **6** should have a stronger antiaromaticity (larger positive NICS value of indacene unit) than **5**, which is reflected by the lower reduction potentials (reversible) for **6** (with a low-lying LUMO) than those of **5** (Table 3.1 and Table 3.10). The higher oxidation potential of antiaromatic **6** than **5**, unlike the aromatic dispirofluorene-[2,1-*a*]IF,[41,27] could be attributed to the lack of its ability to form cofacial π-stacks in the herringbone arrangement due to intermolecular T-shaped interaction between two IF units (Figure 3.9).

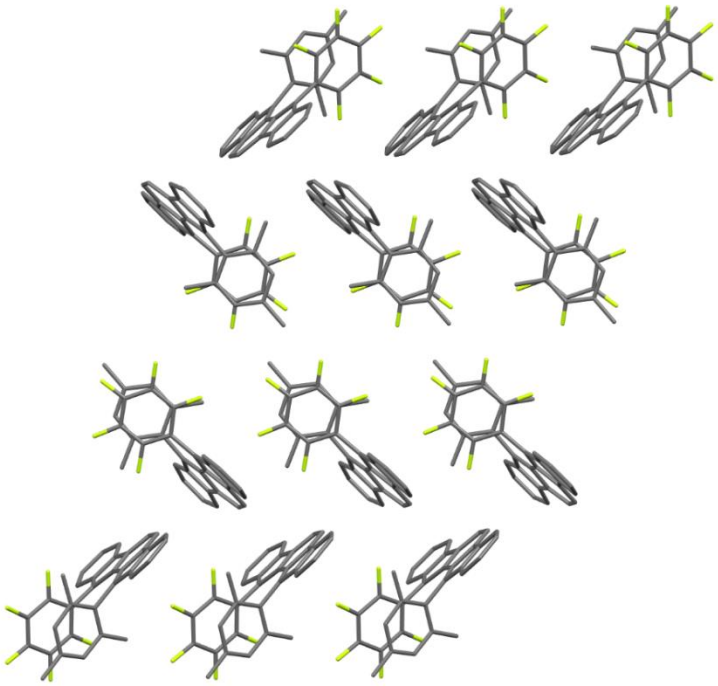

Figure 3.9 Herringbone packing arrangement for **6** with two IF molecules forming T-shaped interaction in one-dimensional stack.

The herringbone packing of **5** showed short interplanar distance of 3.367 Å between two partly cofacially stacked IF units suggesting a better π-π interaction in **5** (Figure 3.10), that could result in its lower oxidation potential (Table 3.1 and Figure 3.7).[41]

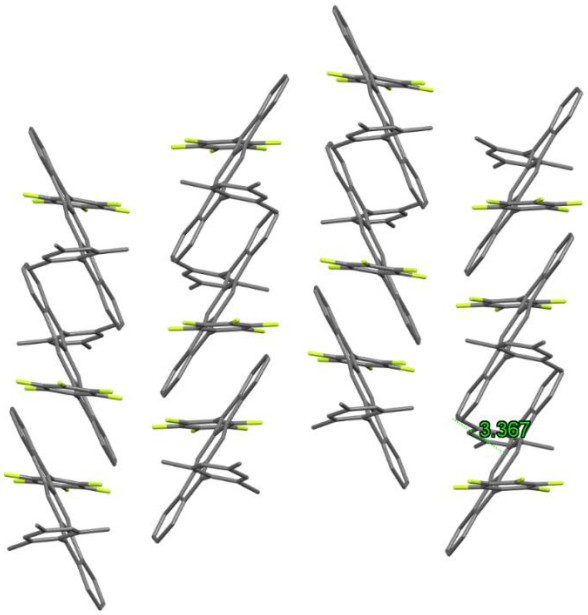

Figure 3.10 Herringbone packing arrangement for **5** with two IF molecules cofacially stacked at an interplanar distance of 3.367 Å, implying strong π- π interaction.

3.4 Conclusions

A new synthetic approach to construct [1,2-*b*]IF motif utilizing the steric crowding of apical substituents was disclosed. It was observed that [1,2-*b*]IF derivatives **1**-**4** were exclusively formed when bulky mesityl or 3,5-$(CF_3)_2C_6H_3$ were used as substituents, while use of C_6F_5 as one of the substituents afforded a mixture of [1,2-*b*]IF **5** and [2,1-*a*]IF **6** which are separable and isolable by silica gel column chromatography in air. The lower reduction potential and higher oxidation potential of **3**, than those of **2**, are in line with the predicted greater degree of antiaromaticity for **3** due to the attachment of its *s*-indacene unit to the 1,2-position of naphthalene.[11a] Compound **6** is the second example in the antiaromatic [2,1-*a*]IF series which is bench-stable and could be characterized by SCXRD analysis. Computational studies suggested **6** to have a smaller HOMO-LUMO energy gap due to greater degree of antiaromaticity than isomeric **5**, which was validated experimentally by small optical/electrochemical energy gaps. Notably, **6** was found to show a low-lying LUMO energy level than that of the dimesityl analogue, including a slightly larger singlet-triplet energy gap. The presented synthesis approach has the potential for constructing heteroatom-embedded isoelectronic IFs,[42] and π-conjugated IF oligomers or polymers by solution-based methods which is currently underway in our lab, considering the studies on IF-based polymers are mostly limited to on-surface synthesis.[43]

3.5 Experimental Section

3.5.1 General Information

All reagents and chemicals were obtained from commercial sources and used as received. Silica gel (100-200 mesh) was used for column chromatography. NMR spectra, in $CDCl_3$ solution, were recorded on JEOL JNM ECS-400 spectrometer at 298 K. Chemical shifts (δ) are given in ppm relative to residual solvent (chloroform δ = 7.26 for ^1H, and δ = 77.16 for proton-decoupled ^{13}C NMR), and coupling constants (*J*) are expressed in hertz (Hz). Multiplicity is tabulated as s for singlet, d for doublet, dd for doublet of doublet, t for triplet, q for quartet and m for multiplet. High resolution mass spectra (HRMS) were recorded using electron spray ionization (ESI) methods on Waters (XEVO G2-XS QTOF) mass spectrometer. UV-Vis absorption spectra were recorded on a JASCO V-770 spectrophotometer in dichloromethane. Cyclic voltammetry (CV) measurements were performed in dry dichloromethane at room temperature under nitrogen atmosphere on CHI-1110C instrument electrochemical analyzer with a three-electrode cell setup (Ag wire as pseudoreference electrode, Pt disk as working electrode, Pt wire as counter electrode), using Bu_4NPF_6 as supporting electrolyte at 50 mV/s scan rate. The potential was externally calibrated against the ferrocene/ferrocenium couple (half-wave potential = 0.45 V). Melting points were determined using BIBBY-SMP30 melting point analyzer.

3.5.2 Synthesis

4'-bromo-[1,1'-biphenyl]-2-carbaldehyde (9). Commercially available **7** (6 g, 21.21 mmol), 2-formylphenylboronic acid **8** (4.14 g, 27.6 mmol), and K_2CO_3 (8.8 g, 63.6 mmol) were added to 1,4-dioxane (25 mL) and water (7 mL) in an oven-dried thick-walled glass tube. The mixture was degassed with nitrogen for 10 mins. Catalyst $PdCl_2$(dppf)·DCM complex (260 mg, 0.42 mmol) was added. After sealing the glass vial, the reaction mixture was heated with stirring at 100 °C for 12 h. After being cooled to room temperature, water was added and the crude mixture was extracted with dichloromethane (DCM) (3 x 100 mL). The organic layer was dried over anhydrous Na_2SO_4, filtered, and evaporated under reduced pressure and crude residue was purified by silica gel column chromatography (hexanes:EtOAc, 96:4) to give compound **9** as yellow solid (4.38 g, 79% yield). $\boldsymbol{R_f}$ = 0.62 (5% EtOAc/hexanes); **mp**: 68-69 °C; **^{1}H NMR** (400 MHz, $CDCl_3$): δ 9.97 (d, *J* = 0.9 Hz, 1H), 8.02 (ddd, *J* = 7.8, 1.5, 0.5 Hz, 1H), 7.66 (dd, *J* = 7.5, 1.5 Hz, 1H), 7.64 – 7.61 (m, 1H), 7.60 (d, *J* = 2.0 Hz, 1H), 7.55

– 7.50 (m, 1H), 7.41 (ddd, *J* = 7.6, 1.3, 0.5 Hz, 1H), 7.27 (d, *J* = 2.0 Hz, 1H), 7.25 (d, *J* = 2.0 Hz, 1H); **$^{13}C\{^{1}H\}$ NMR** (100 MHz, $CDCl_3$): δ 192.1, 192.0, 144.6, 136.8, 133.8, 133.7, 131.7, 131.7, 130.7, 128.3, 128.0, 122.7; **HRMS** (ESI) m/z: $[M + H]^+$ Calcd for $C_{13}H_{10}OBr$ 260.9915, found 260.9911.

2-bromo-9-mesityl-9H-fluorene (11). To compound **9** (4 g, 15.32 mmol) in dry THF (35 mL) was added dropwise 2-mesitylmagnesium bromide (1M solution in THF, 30.64 mL, 30.64 mmol) under N_2 atmosphere. After stirring at room temperature for 24 h, the reaction mixture was quenched with saturated solution of ammonium chloride (50 mL), and extracted with DCM (3 x 100 mL). The combined organic phase was washed with water and brine, dried over Na_2SO_4, and evaporated under reduced pressure to afford crude carbinol **10** as light-yellow solid (6.04 g). To a DCM solution of alcohol **10** (6.04 g), was added $BF_3{\cdot}Et_2O$ (0.4 mL) dropwise under nitrogen. After stirring the reaction mixture for 10 min at room temperature, a saturated aqueous NH_4Cl solution was added to the reaction mixture and it was extracted with DCM (3 x 100 mL). The organic layer was dried over anhydrous Na_2SO_4, filtered, and removed under reduced pressure to afford a residue which was purified by silica gel column chromatography (hexanes) to give **11** as white solid (4.06 g, 73% yield in two steps). $\boldsymbol{R_f}$ = 0.65 (hexanes); **mp**: 130-131 °C; **^{1}H NMR** (400 MHz, $CDCl_3$): δ 7.80 (dt, *J* = 7.6, 0.9 Hz, 1H), 7.68 (d, *J* = 8.1 Hz, 1H), 7.51 (m, 1H), 7.39 (tt, *J* = 7.5, 1.1 Hz, 1H), 7.34 (t, *J* = 1.6 Hz, 1H), 7.28 – 7.25 (m, 1H), 7.23 – 7.18 (m, 1H), 7.02 (s, 1H), 6.67 (s, 1H), 5.46 (s, 1H), 2.66 (s, 3H), 2.29 (s, 3H), 1.10 (s, 3H); **$^{13}C\{^{1}H\}$ NMR** (100 MHz, $CDCl_3$): δ 149.3, 147.0, 140.0, 139.9, 137.9, 137.8, 136.7, 133.1, 130.7, 130.1, 129.0, 127.7, 127.4, 127.1, 124.3, 121.4, 121.2, 120.2, 49.8, 21.8, 20.9, 18.8; **HRMS** (ESI) m/z: $[M + H]^+$ Calcd for $C_{22}H_{20}Br$ 363.0748, found 363.0748.

2-(9-mesityl-9H-fluoren-2-yl)-4,4,5,5-tetramethyl-1,3,2-dioxaborolane (13). To an oven-dried glass tube was added **11** (3.6 g, 9.91 mmol), bis(pinacolatodiboron) **12** (5.03 g, 19.82 mmol), $PdCl_2(dppf){\cdot}DCM$ (809 mg, 10 mol%), KOAc (2.92 g, 29.73 mmol) and dioxane (20 mL). The glass tube was sealed and the reaction mixture was heated at 85 °C for 4 h. After cooling to room temperature, volatile organics were removed under reduced pressure and water was added. The reaction mixture was extracted with DCM (5 x 60 mL), dried over anhydrous Na_2SO_4, and filtered. The organic layer was removed under reduced pressure, and the crude obtained was purified on a silica gel column chromatography (hexanes:EtOAc, 97:3) to give 3.03 g of compound **13** in 75% yield as a white solid. $\boldsymbol{R_f}$ = 0.65 (hexanes:EtOAc = 95:5); **mp**: 170-171 °C; **^{1}H NMR** (400 MHz,

$CDCl_3$): δ 7.88 – 7.83 (m, 3H), 7.68 (s, 1H), 7.39 (t, *J* = 7.4 Hz, 1H), 7.27 – 7.25 (m, 1H), 7.20 (d, *J* = 7.4 Hz, 1H), 7.02 (s, 1H), 6.64 (s, 1H), 5.49 (s, 1H), 2.68 (s, 3H), 2.28 (s, 3H), 1.33 (s, 12H), 1.07 (s, 3H); **$^{13}C\{^1H\}$ NMR** (100 MHz, $CDCl_3$): δ 147.9, 146.5, 143.9, 140.8, 138.0, 137.9, 136.2, 133.9, 133.8, 130.5, 130.3, 128.9, 127.8, 126.9, 124.3, 120.5, 119.5, 83.8, 49.7, 25.1, 24.9, 21.9, 20.9, 18.7; **HRMS** (ESI) m/z: $[M + H]^+$ Calcd for $C_{28}H_{32}O_2B$ 411.2495, found 411.2496.

2-(9-mesityl-9H-fluoren-2-yl)benzaldehyde (15). A solution of **13** (990 mg, 5.35 mmol), 2-bromobenzaldehyde **14** (2.22 g, 5.40 mmol), Na_2CO_3 (3.40 g, 32.10 mmol) and $Pd(PPh_3)_4$ (186 mg, 3 mol%) in toluene:EtOH:H_2O (2:1:1) were added to the solution, and the resulting mixture was refluxed for 3 h. After being cooled to room temperature, the mixture was washed with water and extracted with DCM (3 x 50 mL). The DCM layer was dried over anhydrous Na_2SO_4, filtered, and removed under vacuum. The obtained material was subjected to column chromatography (hexanes:EtOAc, 97:3) to afford aldehyde **15** as yellow solid (1.79 g, 86% yield). R_f = 0.59 (5% EtOAc/hexanes); **mp**: 137-138 °C; **^{1}H NMR** (400 MHz, $CDCl_3$): δ 9.97 (m, 1H), 7.99 (ddd, *J* = 7.9, 1.5, 0.6 Hz, 1H), 7.92 (dd, *J* = 7.8, 0.7 Hz, 1H), 7.89 (dt, *J* = 7.7, 1.0 Hz, 1H), 7.59 (td, *J* = 7.5, 1.5 Hz, 1H), 7.47 (dt, *J* = 7.6, 1.1 Hz, 1H), 7.45 – 7.42 (m, 2H), 7.41 – 7.37 (m, 2H), 7.30 (td, *J* = 7.3, 1.1 Hz, 1H), 7.26 – 7.23 (m, 1H), 7.00 (s, 1H), 6.66 (s, 1H), 5.56 (s, 1H), 2.67 (s, 3H), 2.26 (s, 3H), 1.14 (s, 3H); **$^{13}C\{^1H\}$ NMR** (100 MHz, $CDCl_3$): δ 192.5, 147.8, 147.6, 146.3, 141.0, 140.2, 137.8, 137.7, 136.8, 136.5, 1133.8, 133.5, 133.4, 131.0, 130.7, 129.3, 129.0, 127.8, 127.7, 127.6, 127.1, 125.7, 124.3, 120.4, 119.9, 49.9, 21.9, 20.9, 18.9. **HRMS** (ESI) m/z: $[M + H]^+$ Calcd for $C_{29}H_{25}O$ 389.1905, found 389.1900.

6,12-dimesityl-6,12-dihydroindeno[1,2-*b*]fluorene (16). 2-Mesitylmagnesium bromide (1.0 M in THF, 1.1 mL, 1.1 mmol) was added dropwise to the dry THF solution of **15** (200 mg, 0.51 mmol) under nitrogen atmosphere. The mixture was stirred at room temperature for 24 h, and then quenched by saturated aqueous NH_4Cl solution and extracted with DCM (3 x 50 mL). The organic layer was dried over anhydrous Na_2SO_4 and the solvent was removed under reduced pressure to afford crude product as yellow solid (365 mg, **HRMS** m/z: $[M]^+$ Calcd for $C_{38}H_{34}$ 490.2661, found 490.2661). The crude alcohol (319 mg) was then subjected to Friedel-Crafts cyclization with $BF_3{\cdot}Et_2O$ (0.1 mL) in anhydrous DCM (10 mL) at room temperature. Once the starting material disappeared, a saturated aqueous NH_4Cl solution was added to the reaction mixture and extracted with DCM. The organic layer was dried over anhydrous Na_2SO_4, filtered, and

the solvent was subsequently removed under reduced pressure. The residue was purified by silica gel column chromatography (hexanes) to afford dihydro precursor **16** as pink-white solid (165 mg, 65% yield in two steps). $\boldsymbol{R_f}$ = 0.40 (hexanes); **mp**: 270-271 °C; **^{1}H NMR** (400 MHz, $CDCl_3$): δ 7.72 (d, *J* = 7.3 Hz, 2H), 7.66 (d, *J* = 9.1 Hz, 2H), 7.36 – 7.30 (m, 2H), 7.21 (d, *J* = 4.7 Hz, 4H), 7.09 (s, 2H), 6.68 (d, *J* = 10.2 Hz, 2H), 5.58 (s, 2H), 2.76 (s, 6H), 2.32 – 2.31 (m, 6H), 1.17 – 1.09 (m, 6H). **^{13}C{^{1}H} NMR** (100 MHz, $CDCl_3$): δ 147.6, 146.6, 146.5, 141.0, 140.7, 140.6, 138.1, 138.0, 137.9, 137.9, 136.4, 136.3, 134.4, 134.3, 130.7, 130.6, 128.9, 127.0, 126.9, 126.8, 124.1, 120.1, 120.1, 115.9, 115.9, 49.6, 49.5, 22.0, 21.0, 18.8, 18.6. **HRMS** (ESI) m/z: $[M]^+$ Calcd for $C_{38}H_{34}$ 490.2661, found 490.2661.

6,12-dimesitylindeno[1,2-*b*]fluorene (1): DDQ (41 mg, 0.18 mmol, 1.3 equiv) was added to dihydro precursor **16** (69 mg, 0.14 mmol) in dry 1,2-dichloroethane (3 mL) under N_2, and the reaction mixture was warmed to 80 °C for 2 h. Once the starting material was consumed (monitored by TLC), the 1,2 dichloroethane was removed in vacuo and the crude material was purified by silica gel column chromatography (hexanes) to afford the desired product **1** as red solid (65 mg, 95% yield). $\boldsymbol{R_f}$ = 0.46 (hexanes); **mp**: 212-213 °C; **^{1}H NMR** (400 MHz, $CDCl_3$): δ 7.30 (d, *J* = 7.0 Hz, 2H), 7.02 (s, 4H), 6.99 (td, *J* = 7.4, 1.4 Hz, 2H), 6.94 (td, *J* = 7.3, 1.3 Hz, 2H), 6.84 (s, 2H), 6.67 (d, *J* = 8.1 Hz, 2H), 2.39 (s, 6H), 2.18 (s, 12H); **HRMS** (ESI) m/z: $[M]^+$ Calcd for $C_{38}H_{32}$ 488.2504, found 488.2504.

3-(9-mesityl-9H-fluoren-2-yl)-2-naphthaldehyde (18). An oven-dried thick-walled glass tube was charged with **13** (470 mg, 1.15 mmol), pre-synthesized **17** (401 mg, 1.15 mmol), K_2CO_3 (780 mg, 5.65 mmol). These solids were then placed under N_2 atmosphere and dissolved in THF (5 ml)/water (1 ml), and had been sparged with nitrogen for 25 mins. After sparging, catalyst $Pd(PPh_3)_4$ (40 mg, 0.03 mmol) was added, and the suspension was heated at 90 °C for 12 h under sealed condition. The reaction mixture was cooled to room temperature, water was added and the resultant mixture was extracted with EtOAc (3 x 50 mL). The organic layer was dried over anhydrous Na_2SO_4, filtered, and evaporated under reduced pressure to afford a crude residue which was column chromatographed on silica gel (hexanes:EtOAc, 97:3) to afford the title product **18** as yellow solid (340 mg, 68% yield). $\boldsymbol{R_f}$ = 0.44 (5% EtOAc/hexanes); **mp**: 74-75 °C; **^{1}H NMR** (400 MHz, $CDCl_3$): δ 10.10 (s, 1H), 8.54 (s, 1H), 8.01 (d, *J* = 7.8 Hz, 1H), 7.95 (d, *J* = 7.8 Hz, 1H), 7.91 (s, 1H), 7.89 (d, *J* = 3.7 Hz, 1H), 7.86 (s, 1H), 7.62 (ddd, *J* = 8.3, 6.9, 1.4 Hz, 1H), 7.58 – 7.52 (m, 1H), 7.49 – 7.41 (m, 2H), 7.36 – 7.33 (m, 1H),

7.30 (t, *J* = 7.2 Hz, 1H), 7.27– 7.25 (m, 1H), 7.00 (d, *J* = 1.9 Hz, 1H), 6.68 (d, *J* = 1.9 Hz, 1H), 5.59 (s, 1H), 2.69 (s, 3H), 2.26 (s, 3H), 1.18 (s, 3H); **$^{13}C\{^{1}H\}$ NMR** (100 MHz, $CDCl_3$): δ 192.7, 192.7, 147.8, 147.5, 140.9, 140.7, 140.3, 137.2, 136.5, 135.6, 133.5, 131.9, 131.8, 130.7, 129.9, 129.9, 129.8, 129.4, 129.2, 129.0, 127.9, 127.7, 127.1, 127.0, 125.7, 124.3, 120.4, 120.0, 49.9, 21.9, 20.9, 18.9; **HRMS** (ESI) m/z: $[M + H]^+$ Calcd for $C_{38}H_{34}$ 439.2062, found 439.2060.

6,14-dimesitylbenzo[b]indeno[2,1-*h*]fluorene (2). 2-Mesitylmagnesium bromide (1.0 M in THF, 0.7 mL, 0.7 mmol) was added dropwise to the dry THF solution of **18** (152 mg, 0.34 mmol) under nitrogen atmosphere. The mixture was stirred at room temperature for 24 h. After complete disappearance of carbonyl **18**, the reaction mixture was quenched with saturated aqueous solution of saturated ammonium chloride (20 mL) and diluted with ethyl acetate (30 mL). The layers were separated and the organic layer was washed with brine. The extracts were dried over sodium sulfate, filtered, and was concentrated in vacuo to afford crude alcohol (183 mg, **HRMS** (ESI) m/z: $[M - H]^+$ Calcd for $C_{42}H_{37}O$ 557.2844, found 557.2845). Under nitrogen condition, a DCM solution of alcohol (136 mg, 0.24 mmol) was reacted with 0.1 ml of $BF_3{\cdot}Et_2O$ at room temperature. Completion of Friedel-craft reaction and formation of compound **19** (97 mg, **HRMS** (ESI) m/z: $[M + H]^+$ Calcd for $C_{42}H_{37}$ 541.2895, found 541.2894) was monitored by TLC (a partial conversion of **19** to **2** was also observed in TLC, likely by air oxidation). The obtained reaction mixture was filtered through short silica plug. Afterwards, crude precursor **19** (30 mg, 0.05 mmol) was dissolved in 1,2-dichloroethane (2 mL) and treated with DDQ (16 mg, 0.07 mmol, 1.3 equiv) for 15 mins at room temperature. After removing 1,2-dichloroethane in vacuo, the final compound **2** was obtained as red solid (27 mg, 63% yield over three steps) after purification of the crude reaction residue by silica gel (hexanes) column chromatography. $\boldsymbol{R_f}$ = 0.46 (hexanes); **mp**: >350 °C; **^{1}H NMR** (400 MHz, $CDCl_3$): δ 7.77 (s, 1H), 7.69 – 7.62 (m, 1H), 7.58 – 7.51 (m, 1H), 7.44 – 7.37 (m, 1H), 7.29 (ddd, *J* = 6.7, 4.0, 2.0 Hz, 2H), 7.10 (s, 1H), 7.08 (s, 2H), 7.04 (s, 2H), 7.03 – 6.98 (m, 4H), 6.77 – 6.71 (m, 1H), 2.44-2.41 (m, 6H), 2.19 (m, 12H); **$^{13}C\{^{1}H\}$ NMR** (100 MHz, $CDCl_3$): δ 145.0, 144.6, 142.9, 142.4, 140.8, 138.0, 137.9, 137.8, 137.6, 137.4, 137.4, 136.9, 135.7, 134.7, 134.1, 133.6, 130.2, 130.1, 128.8, 128.4, 128.3, 128.2, 126.5, 126.1, 121.6, 120.7, 120.6, 119.4, 118.3, 116.9, 21.4, 21.3, 20.5; **HRMS** (ESI) m/z: $[M + H]^+$ Calcd for $C_{42}H_{34}$ 538.2661, found 538.2659.

1-(9-mesityl-9H-fluoren-2-yl)-2-naphthaldehyde (21). An oven-dried thick-walled glass tube was charged with **13** (700 mg, 1.71 mmol), commercially available **20** (401

mg, 1.71 mmol), K_2CO_3 (1.16 g, 8.41 mmol), THF (5 ml), water (1 ml), and purged with nitrogen for 25 mins. After purging, catalyst $Pd(PPh_3)_4$ (59 mg, 0.05 mmol) was added. The mixture was heated at 90 °C for 12 h after sealing the glass tube. After being cooled to room temperature, water was added and the resultant mixture was extracted with EtOAc (3 x 50 mL). The organic layer was dried over anhydrous Na_2SO_4, filtered, and evaporated under reduced pressure to afford a crude residue which was column chromatographed on silica gel (hexanes:EtOAc, 97:3) to afford the title product **21** as yellow solid (626 mg, 84% yield). $\boldsymbol{R_f}$ = 0.5 (5% EtOAc/hexanes); **mp**: 168-169 °C; **^{1}H NMR** (400 MHz, $CDCl_3$): δ 10.19 – 9.82 (m, 1H), 8.37 – 7.87 (m, 6H), 7.78 – 7.54 (m, 2H), 7.51 – 7.36 (m, 3H), 7.31 (dd, *J* = 7.3, 1.1 Hz, 1H), 7.28 – 7.25 (m, 1H), 6.94 (t, *J* = 2.7 Hz, 1H), 6.65 (t, *J* = 2.8 Hz, 1H), 5.60 (d, *J* = 10.1 Hz, 1H), 2.64 (d, *J* = 4.9 Hz, 3H), 2.22 (d, *J* = 5.6 Hz, 3H), 1.27 – 1.18 (m, 3H); **^{13}C{^{1}H} NMR** (100 MHz, $CDCl_3$): δ 193.0, 192.6, 192.4, 147.6, 147.6, 147.5, 147.5, 147.0, 146.9, 141.2, 141.2, 140.2, 137.9, 137.6, 136.6, 136.5, 136.1, 134.7, 134.1, 134.0, 133.4, 133.3, 132.7, 132.6, 131.4, 131.2, 130.8, 130.6, 130.0, 129.8, 129.6, 129.2, 129.0, 128.9, 128.8, 128.8, 128.3, 128.3, 128.2, 127.9, 127.8, 127.6, 127.2, 127.0, 126.9, 126.9, 126.6, 124.4, 122.9, 122.2, 120.4, 119.9, 49.94, 21.8, 20.9, 18.9, 18.8; **HRMS** (ESI) m/z: $[M + H]^+$ Calcd for $C_{33}H_{27}O$ 439.2062, found 439.2062.

7,13-dimesitylbenzo[g]indeno[1,2-*b*]fluorene (3). Under nitrogen atmosphere, 2-mesitylmagnesium bromide (1.0 M in THF, 2.25 mL, 2.25 mmol) was added dropwise to the dry THF solution of aldehyde **21** (493 mg, 1.12 mmol). Then the mixture was stirred at room temperature for 24 h. After complete conversion of **21** to intermediate alcohol, the reaction mixture was quenched with saturated aqueous ammonium chloride (30 mL) and diluted with ethyl acetate (50 mL). The layers were separated and the organic layer was washed with brine. The extracts were dried over sodium sulfate, filtered, and was concentrated in vacuo to afford crude product (706 mg, **HRMS** (ESI) m/z: $[M - H]^+$ Calcd for $C_{42}H_{37}O$ 557.2844, found 557.2844). To the solution of crude alcohol (609 mg, 1.09 mmol) in anhydrous DCM (10 mL) at room temperature, $BF_3{\cdot}Et_2O$ (0.1 mL) was added dropwise under nitrogen, and the reaction mixture was stirred for 10 min at room temperature. Completion of the reaction and formation of compound **22** (456 mg, **HRMS** (ESI) m/z: $[M + H]^+$ Calcd for $C_{42}H_{37}$ 541.2895, found 541.2892) was monitored by TLC (a partial conversion of **22** to **3** was also observed in TLC, likely by air oxidation). After filtration through short silica plug, a chloroform (5 mL) solution of crude dihydro intermediate **22** (150 mg, 0.27 mmol) was treated with

DDQ (82 mg, 0.36 mmol, 1.3 equiv) for 15 mins at room temperature. After evaporation of solvent, the obtained material was subjected to silica gel column chromatography (hexanes) to afford pure **3** as red solid (133 mg, 77% yield over three steps). $\boldsymbol{R_f}$ = 0.46 (hexanes); **mp**: 285-286 °C; **^{1}H NMR** (400 MHz, $CDCl_3$): δ 8.00 (d, *J* = 8.4 Hz, 1H), 7.64 (d, *J* = 7.5 Hz, 1H), 7.39 (d, *J* = 8.3 Hz, 1H), 7.34 (ddd, *J* = 8.5, 6.8, 1.4 Hz, 1H), 7.27 (d, *J* = 2.4 Hz, 1H), 7.25 (d, *J* = 0.9 Hz, 1H), 7.22 (d, *J* = 7.6 Hz, 1H), 7.04 (d, *J* = 5.2 Hz, 4H), 6.96 (t, *J* = 7.4 Hz, 1H), 6.88 (t, *J* = 7.3 Hz, 1H), 6.78 (d, *J* = 8.3 Hz, 1H), 6.75 (s, 1H), 6.62 (d, *J* = 7.3 Hz, 1H), 2.43-2.41 (m, 6H), 2.23-2.22 (m, 12H); **^{13}C{^{1}H} NMR** (100 MHz, $CDCl_3$): δ 148.3, 146.0, 144.3, 143.4, 140.5, 138.4, 137.7, 137.5, 137.3, 137.1, 135.4, 134.9, 134.2, 132.1, 130.1, 130.0, 129.8, 129.5, 128.5, 128.5, 128.3, 127.8, 127.7, 127.3, 125.0, 124.4, 123.6, 122.5, 120.5, 120.4, 119.8, 21.3, 20.6, 20.5; **HRMS** (ESI) m/z: $[M]^+$ Calcd for $C_{42}H_{34}$ 538.2661, found 538.2659.

6-(3,5-bis(trifluoromethyl)phenyl)-12-mesityl-6,12-dihydroindeno[1,2-*b*]fluorene (23). A Grignard reagent mixture was prepared from 1-bromo-3,5-bis(trifluoromethyl)benzene (0.76 mL, 4.41 mmol), magnesium (129 mg, 5.30 mmol) and I_2 (one pellet) in freshly distilled dry THF (5 mL). To a THF solution of aldehyde **15** (343 mg, 0.88 mmol) was added the freshly prepared Grignard reagent at room temperature under N_2 atmosphere. The resulting solution was stirred for overnight. After complete consumption of carbonyl, the reaction mixture was quenched with saturated solution of ammonium chloride (50 mL), and the volatile organics were evaporated in vacuo. The residue was extracted with DCM (3 x 50 mL), washed with water, and dried over sodium sulfate. The organic layer was filtered, and the filtrate was removed under reduced pressure to afford intermediate alcohol (657 mg, **HRMS** m/z: $[M - H]^+$ Calcd for $C_{37}H_{25}F_6$ 583.1860 , found 583.1860). To the solution of crude alcohol (608 mg, 1.01 mmol) in anhydrous DCM (5 mL) at room temperature, $BF_3{\cdot}Et_2O$ (0.2 mL) was added dropwise under nitrogen, and the reaction mixture was stirred for 10 min at room temperature to perform an intra-molecular ring-closure reaction. After 10 min, a saturated aqueous NH_4Cl solution was added to the reaction mixture and it was extracted with DCM (3 x 30 mL). The organic layer was dried over anhydrous Na_2SO_4, filtered, and removed under reduced pressure to afford a residue which was purified by silica gel column chromatography (hexanes) to give **23** as white/pink solid (303 mg, 59% yield over two steps. $\boldsymbol{R_f}$ = 0.46 (hexanes); **mp:** 89-90 °C; **^{1}H NMR** (400 MHz, $CDCl_3$): δ 7.78 (s, 1H), 7.74 (t, *J* = 7.5 Hz, 2H), 7.65 (d, *J* = 4.7 Hz, 2H), 7.56 (d, *J* = 1.5 Hz, 2H), 7.43 – 7.27 (m, 3H), 7.26 – 7.21 (m, 3H), 7.08 (d, *J* = 2.1 Hz, 1H), 6.69 (d, *J* = 1.9 Hz,

1H), 5.57 (s, 1H), 5.23 (s, 1H), 2.75 (s, 3H), 2.31 (s, 3H), 1.10 (m, 3H); **^{13}C{^{1}H} NMR** (100 MHz, $CDCl_3$): δ 147.9, 147.6, 146.7, 146.6, 145.7, 145.6, 145.1, 14.2, 141.1, 140.7, 138.1, 138.0, 137.8, 136.6, 136.6, 133.9, 132.3, 132.0, 130.8, 130.7, 129.0, 129.0, 128.6, 128.2, 127.6, 127.4, 127.0, 125.2, 124.3, 124.3, 120.4, 120.1, 120.0, 116.8, 116.8, 116.2, 116.2, 53.7, 53.6, 49.7, 49.7, 22.0, 21.9, 21.0, 21.0, 18.9, 18.71; **HRMS** (ESI) m/z: $[M - H]^+$ Calcd for $C_{37}H_{25}F_6$ 583.1860, found 583.1860.

6-(3,5-bis(trifluoromethyl)phenyl)-12-mesitylindeno[1,2-*b*]fluorene (4). DDQ (25 mg, 0.11 mmol, 1.3 equiv) was added to degassed solution of 1,2- dichloroethane (2 ml) of **23** (50 mg, 0.08 mmol) under N_2, and the reaction mixture was warmed to 80 °C for 2 h in a sealed tube. Once the starting material was consumed (monitored by TLC), the 1,2-dichloroethane was removed in vacuo and the crude was purified by silica gel column chromatography (hexanes) to afford title product **12** (46 mg, 92% yield) as deep red solid. R_f = 0.59 (hexanes); **mp**: 225-226 °C; **^{1}H NMR** (400 MHz, $CDCl_3$): δ 8.03 (s, 2H), 7.96 (s, 1H), 7.36 (d, *J* = 7.6 Hz, 2H), 7.15 (s, 1H), 7.14 – 7.05 (m, 4H), 7.03 (s, 2H), 6.98 (t, *J* = 7.5 Hz, 1H), 6.92 (s, 1H), 6.70 (d, *J* = 7.4 Hz, 1H), 2.40 (s, 3H), 2.18 (s, 6H); **^{13}C{^{1}H} NMR** (100 MHz, $CDCl_3$): 148.5, 144.2, 142.4, 140.9, 139.8, 138.9, 138.0, 137.9, 137.5, 137.0, 136.5, 135.0, 134.8, 132.9, 132.6, 132.2, 131.9, 129.6, 129.0, 128.5, 128.4, 128.2, 128.1, 127.7, 127.4, 124.7, 122.7, 122.0, 121.8, 121.2, 121.0, 120.7, 120.6, 119.3, 117.4, 21.3, 20.4; **HRMS** (ESI) m/z: $[M]^+$ Calcd for $C_{37}H_{24}F_6$ 582.1782, found 582.1782.

6-mesityl-12-(perfluorophenyl)indeno[1,2-*b*]fluorene (5) & **11-mesityl-12-(perfluorophenyl)indeno[2,1-*a*]fluorene (6).** Under nitrogen atmosphere, in 10 mL dry THF solution of **15** (346 mg, 0.89 mmol), (perfluorophenyl)magnesium bromide (0.5 M solution in diethylether, 5.34 mL, 2.67 mmol) was added dropwise. The mixture was stirred at room temperature for 24 h. After removal of the solvent, the crude compound was quenched with NH_4Cl (20 mL) and extracted into DCM (3 x 50 mL), washed with brine, and dried over anhydrous sodium sulfate. The starting material **15** was consumed, so the crude (713 mg, **HRMS** m/z: $[M - H^+]$ Calcd for $C_{35}H_{24}OF_5$ 555.1747, found 555.1745) was used for next step without purification. To the solution of crude solid (668 mg) in anhydrous DCM (10 mL) at room temperature, 0.1 mL of $BF_3{\cdot}Et_2O$ was added dropwise under nitrogen, and the reaction mixture was stirred for 16 h at room temperature. Once the reaction was complete, as monitored by thin layer chromatography (TLC), a saturated aqueous NH_4Cl (10 mL) solution was added to the reaction mixture and extracted with DCM (3 x 30mL). The organic layer was dried over

anhydrous Na_2SO_4, filtered, and concentrated under reduced pressure to give crude precursor (305 mg, **HRMS** (ESI) m/z: $[M - H]^+$ Calcd for $C_{35}H_{22}F_5$ 537.1642, found 537.1642). DDQ (211 mg, 0.93 mmol, 10 equiv) was added to the mixture of crude dihydro precursor (50 mg, 0.09 mmol) in dry 1,2-dichloroethane (5 mL) under N_2, and the reaction mixture was heated at 80 °C for overnight. Once the starting material was consumed (monitored by TLC), the 1,2-dichloroethane was removed in vacuo and the crude was purified by silica gel column chromatography in pure hexanes to afford the product **5** (26 mg, 36% yield over three steps) and **6** (19 mg, 26% in three steps) as red and purple solid, respectively.

Analytical data of compound 5. R_f = 0.68 (hexanes); **mp**: 243-244 °C; **^{1}H NMR** (400 MHz, $CDCl_3$): δ 7.36 – 7.30 (m, 2H), 7.07 – 7.00 (m, 5H), 6.95 (t, *J* = 7.5 Hz, 1H), 6.87 (d, *J* = 4.1 Hz, 3H), 6.67 (d, *J* = 7.4 Hz, 1H), 2.39 (s, 3H), 2.18 (s, 6H); **^{13}C{^{1}H} NMR** (100 MHz, $CDCl_3$): δ 149.9, 144.3, 142.2, 140.8, 138.9, 138.1, 137.3, 136.9, 134.9, 129.5, 128.6, 128.4, 128.3, 128.1, 127.4, 122.8, 121.7, 120.8, 120.8, 120.7, 117.9, 21.3, 20.4; **HRMS** (ESI) m/z: $[M]^+$ Calcd for $C_{35}H_{21}F_5$ 536.1563, found 536.1563.

Analytical data of compound 6. R_f = 0.56 (hexanes); **mp**: 212-213 °C; **^{1}H NMR** (400 MHz, $CDCl_3$): δ 7.40 (d, *J* = 7.1 Hz, 1H), 7.33 (d, *J* = 7.3 Hz, 1H), 7.08 (d, *J* = 6.6 Hz, 1H), 7.06 – 6.95 (m, 4H), 6.90 (t, *J* = 7.4 Hz, 1H), 6.72 (s, 2H), 6.53 (d, *J* = 7.3 Hz, 1H), 6.40 (d, *J* = 7.4 Hz, 1H), 2.27 (s, 3H), 2.01 (s, 6H); **^{13}C{^{1}H} NMR** (100 MHz, $CDCl_3$): δ 148.9, 144.7, 143.6, 143.5, 142.7, 138.0, 136.5, 136.3, 135.4, 132.9, 131.7, 129.1, 128.6, 128.5, 128.0, 127.8, 127.0, 123.0, 122.8, 120.7, 120.6, 120.4, 120.2, 20.8, 19.9; **HRMS** (ESI) m/z: $[M]^+$ Calcd for $C_{35}H_{21}F_5$ 536.1563, found 536.1565.

3.5.3 Single crystal data

Suitable single crystals of **5** and **6** were selected using paratone oil and mounted on glass fiber with the help of gum. The intensity data and geometric parameters of these crystals were garnered with the help of Bruker D8 Venture X-ray diffractometer having a micro-focus sealed X-ray tube Mo-Kα (λ = 0.71073 Å) source of X-rays along with a PHOTON 100 detector with inclining Phi and Omega (width of 0.5 for one frame) working at a scan speed of 10 s per frame. The crystal was kept at 298 K during data collection. Data acquisition as well as extraction of data was accomplished by utilizing Bruker Apex-3 and Bruker SAINT software packages using a narrow-frame algorithm.[44] By utilizing OLex2,[45] the crystal structure was solved with the help of olex2.solve[46] structure solution program by employing intrinsic Phasing methods and crystal structure

refinement was done with the SHELXL[47] refinement package by putting into use Least Squares minimization. Refinement of all non-hydrogen atoms was completed with the help of anisotropic thermal parameters.

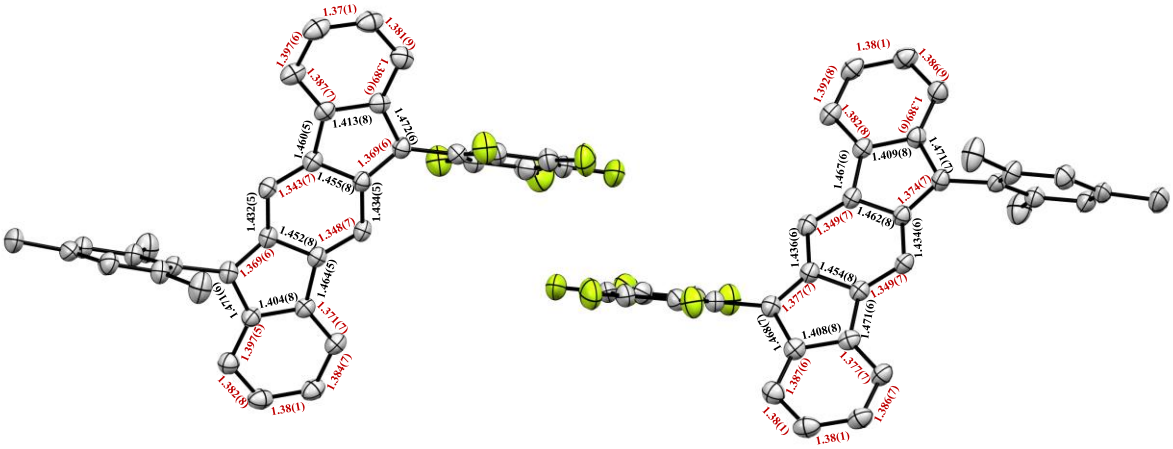

Figure 3.11 ORTEP drawing of **5** with thermal ellipsoids at 30% probability level, showing the bond lengths with e.s.d values for the two crystallographically independent molecules.

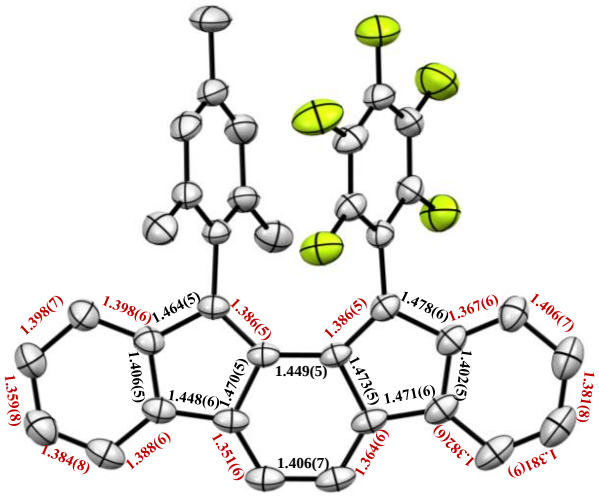

Figure 3.12 ORTEP drawing of **6** showing with thermal ellipsoids at 30% probability level showing the bond lengths with e.s.d values.

Table 3.3 Crystal data and structure refinement for **5** and **6**

Compounds	**5**	**6**
CCDC numbers	2205894	2205895
Solvents, and conditions for recrystallization	Ethyl acetate/hexane, by evaporation at rt in dark	Acetonitrile/hexane, by evaporation at rt in dark
Empirical formula	$C_{35}H_{21}F_5$	$C_{35}H_{21}F_5$
Formula weight	536.52	536.52

Temperature/K	298.00	298
Crystal system	triclinic	Monoclinic
Space group	P-1	C2/c
a/Å	13.8434(14)	26.325(3)
b/Å	14.8766(13)	8.0202(10)
c/Å	16.0001(16)	24.777(3)
α/°	117.393(3)	90
β/°	111.710(3)	97.845(4)
γ/°	93.822(3)	90
Volume/Å^3	2603.7(4)	5182.3(11)
Z	4	8
ρ_{calc}g/cm^3	1.369	1.375
μ/mm^{-1}	0.103	0.104
F(000)	1104.0	2208.0
Crystal size/mm^3	0.256 × 0.236 × 0.198	0.236 × 0.154 × 0.059
Radiation	MoKα (λ = 0.71073)	MoKα (λ = 0.71073)
2Θ range for data collection/°	4.93 to 51.536	4.858 to 54.298
Index ranges	-16 ≤ h ≤ 15, -18 ≤ k ≤ 16, 0 ≤ l ≤ 19	-33 ≤ h ≤ 33, -10 ≤ k ≤ 10, -31 ≤ l ≤ 31
Reflections collected	9906	61587
Data/restraints/parameters	9906/0/729	5586/0/365
Goodness-of-fit on F^2	1.033	1.023
Final R indexes [I>=2σ (I)]	R_1 = 0.0619, wR_2 = 0.1600	R_1 = 0.0827, wR_2 = 0.2053
Final R indexes [all data]	R_1 = 0.1234, wR_2 = 0.2111	R_1 = 0.1696, wR_2 = 0.2682
Largest diff. peak/hole / e Å^{-3}	0.34/-0.24	0.60/-0.25

3.5.4 DFT calculations

Density functional theory (DFT) calculations were performed with Gaussian 09 package using a high-performance computing cluster facility of IIT Ropar in gas phase using the B3LYP (restricted and unrestricted) level of theory with basis set 6-31G(d).[48] NICS (standard GIAO method) and HOMA[49] indices were calculated for the optimized closed-shell structures for **5** and **6**. The NICS indices were averaged by two positions (above and below the plane) for each molecule. Charge analysis was performed for the singlet closed-shell structures using natural population analysis (NPA) as implemented in G09.

Table 3.4 Relative energies for the optimized structure **5** at B3LYP/6-31G(d) level.

State	Hartree	kcal/mol
Singlet Closed-Shell	-1845.548217	-1158081.507
Singlet Open-Shell	-1845.548217	-1158081.507
Triplet Open-Shell	-1845.521241	-1158064.579

$\Delta E_{\text{Triplet-Singlet}}$ = 16.92 kcal/mol.

Table 3.5 Relative energies for the optimized structure **6** at B3LYP/6-31G(d) level.

State	Hartree	kcal/mol
Singlet Closed-Shell	-1845.536124	-1158073.918
Singlet Open-Shell	-1845.536124	-1158073.918
Triplet Open-Shell	-1845.513937	-1158059.996

$\Delta E_{\text{Triplet-Singlet}}$ = 13.92 kcal/mol.

NPA analyses

Compound 5.

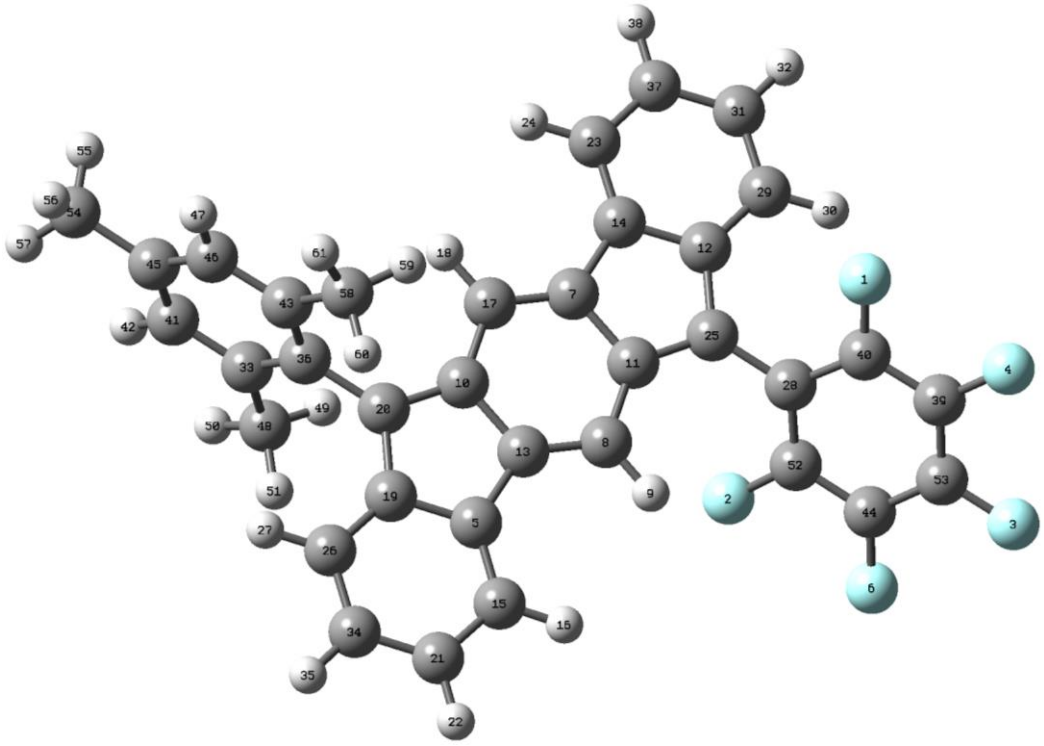

Figure 3.13 Optimized closed-shell structure of **5**.

Table 3.6 Natural Population of **5**.

Atom	No	Natural Charge	Core	Valence	Rydberg	Total
F	1	-0.31041	1.99994	7.30414	0.00633	9.31041
F	2	-0.31175	1.99994	7.30551	0.00631	9.31175
F	3	-0.30274	1.99994	7.29588	0.00692	9.30274
F	4	-0.30653	1.99994	7.29977	0.00681	9.30653
C	5	-0.03283	1.99899	4.01919	0.01465	6.03283
F	6	-0.30687	1.99994	7.30012	0.00681	9.30687
C	7	-0.04327	1.99903	4.02911	0.01513	6.04327
C	8	-0.15425	1.99895	4.14275	0.01255	6.15425
H	9	0.24112	0.00000	0.75756	0.00133	0.75888
C	10	-0.06845	1.99894	4.05473	0.01478	6.06845
C	11	-0.03858	1.99898	4.02465	0.01496	6.03858
C	12	-0.04368	1.99899	4.02978	0.01491	6.04368
C	13	-0.03369	1.99903	4.01947	0.01519	6.03369
C	14	-0.03651	1.99899	4.02296	0.01456	6.03651
C	15	-0.20847	1.99902	4.19697	0.01248	6.20847
H	16	0.23726	0.00000	0.76179	0.00095	0.76274
C	17	-0.14709	1.99895	4.13640	0.01175	6.14709
H	18	0.24629	0.00000	0.75261	0.00110	0.75371
C	19	-0.05615	1.99898	4.04240	0.01478	6.05615
C	20	0.05022	1.99897	3.93319	0.01763	5.94978
C	21	-0.22647	1.99912	4.21360	0.01374	6.22647
H	22	0.23808	0.00000	0.76115	0.00077	0.76192
C	23	-0.20909	1.99902	4.19761	0.01247	6.20909
H	24	0.23627	0.00000	0.76279	0.00094	0.76373
C	25	-0.00760	1.99894	3.98977	0.01890	6.00760
C	26	-0.21022	1.99902	4.19851	0.01269	6.21022
H	27	0.24472	0.00000	0.75425	0.00103	0.75528
C	28	-0.17298	1.99886	4.15932	0.01480	6.17298
C	29	-0.20930	1.99902	4.19696	0.01331	6.20930
H	30	0.23821	0.00000	0.76058	0.00121	0.76179
C	31	-0.23393	1.99912	4.22103	0.01379	6.23393
H	32	0.23802	0.00000	0.76121	0.00077	0.76198
C	33	0.00373	1.99898	3.98351	0.01378	5.99627
C	34	-0.23567	1.99912	4.22271	0.01384	6.23567
H	35	0.23851	0.00000	0.76072	0.00077	0.76149
C	36	-0.08043	1.99889	4.06718	0.01436	6.08043
C	37	-0.23015	1.99912	4.21726	0.01377	6.23015
H	38	0.23727	0.00000	0.76196	0.00077	0.76273
C	39	0.29721	1.99837	3.67672	0.02770	5.70279
C	40	0.38044	1.99840	3.59432	0.02685	5.61956
C	41	-0.23231	1.99896	4.22165	0.01170	6.23231
H	42	0.22994	0.00000	0.76889	0.00117	0.77006
C	43	0.00291	1.99897	3.98432	0.01379	5.99709
C	44	0.29667	1.99837	3.67728	0.02768	5.70333
C	45	-0.01743	1.99902	4.00417	0.01424	6.01743

C	46	-0.23225	1.99896	4.22161	0.01169	6.23225
H	47	0.22989	0.00000	0.76894	0.00117	0.77011
C	48	-0.69126	1.99939	4.68473	0.00714	6.69126
H	49	0.24803	0.00000	0.75102	0.00095	0.75197
H	50	0.23685	0.00000	0.76236	0.00079	0.76315
H	51	0.24802	0.00000	0.75095	0.00103	0.75198
C	52	0.37873	1.99840	3.59601	0.02686	5.62127
C	53	0.31526	1.99841	3.65873	0.02759	5.68474
C	54	-0.68696	1.99939	4.68027	0.00730	6.68696
H	55	0.24447	0.00000	0.75458	0.00095	0.75553
H	56	0.23922	0.00000	0.75991	0.00088	0.76078
H	57	0.23872	0.00000	0.76041	0.00087	0.76128
C	58	-0.69044	1.99939	4.68388	0.00716	6.69044
H	59	0.24718	0.00000	0.75184	0.00097	0.75282
H	60	0.24765	0.00000	0.75139	0.00097	0.75235
H	61	0.23690	0.00000	0.76230	0.00080	0.76310

==========

* Total *	0.00000	79.96274	195.44537	0.59190	276.00000

Compound 6.

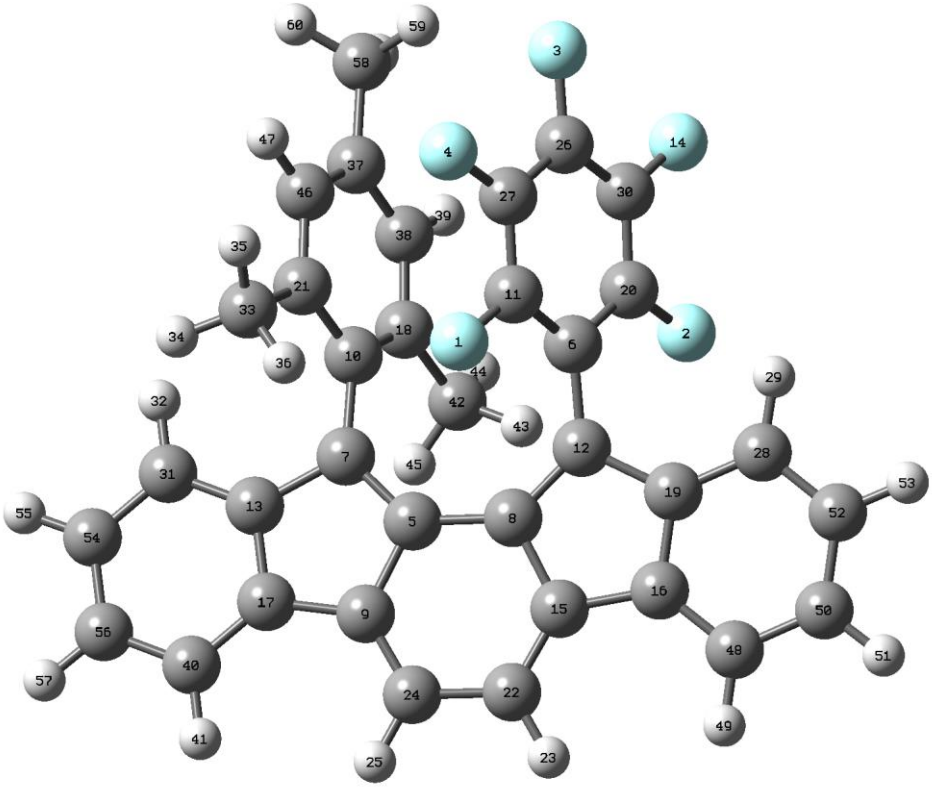

Figure 3.14 Optimized closed-shell structure of **6**.

Table 3.7 Natural Population of **6**.

Atom	No	Natural Charge	Core	Valence	Rydberg	Total
F	1	-0.31228	1.99993	7.30605	0.00630	9.31228
F	2	-0.31343	1.99994	7.30723	0.00626	9.31343
F	3	-0.30764	1.99994	7.30091	0.00679	9.30764
F	4	-0.30823	1.99994	7.30151	0.00678	9.30823
C	5	-0.05530	1.99894	4.04137	0.01499	6.05530
C	6	-0.17014	1.99885	4.15580	0.01549	6.17014
C	7	0.04877	1.99899	3.93578	0.01646	5.95123
C	8	-0.02592	1.99896	4.01200	0.01495	6.02592
C	9	-0.00667	1.99903	3.99290	0.01474	6.00667
C	10	-0.08224	1.99889	4.06835	0.01500	6.08224
C	11	0.39444	1.99836	3.57963	0.02757	5.60556
C	12	-0.01019	1.99896	3.99250	0.01874	6.01019
C	13	-0.04716	1.99897	4.03350	0.01468	6.04716
F	14	-0.30912	1.99994	7.30246	0.00672	9.30912
C	15	-0.01369	1.99903	3.99998	0.01468	6.01369
C	16	-0.04836	1.99898	4.03466	0.01472	6.04836
C	17	-0.04445	1.99897	4.03063	0.01485	6.04445
C	18	0.00717	1.99897	3.97964	0.01422	5.99283
C	19	-0.03865	1.99898	4.02486	0.01481	6.03865
C	20	0.37696	1.99838	3.59744	0.02722	5.62304
C	21	-0.00344	1.99899	3.98948	0.01497	6.00344
C	22	-0.18067	1.99899	4.16882	0.01286	6.18067
H	23	0.24001	0.00000	0.75910	0.00090	0.75999
C	24	-0.19142	1.99899	4.17952	0.01291	6.19142
H	25	0.23976	0.00000	0.75934	0.00090	0.76024
C	26	0.31688	1.99840	3.65712	0.02760	5.68312
C	27	0.30460	1.99834	3.66895	0.02811	5.69540
C	28	-0.21214	1.99902	4.19975	0.01337	6.21214
H	29	0.23779	0.00000	0.76112	0.00109	0.76221
C	30	0.29917	1.99835	3.67466	0.02783	5.70083
C	31	-0.21340	1.99902	4.20136	0.01302	6.21340
H	32	0.24544	0.00000	0.75360	0.00096	0.75456
C	33	-0.69252	1.99938	4.68509	0.00806	6.69252
H	34	0.24453	0.00000	0.75434	0.00113	0.75547
H	35	0.24023	0.00000	0.75877	0.00099	0.75977
H	36	0.25152	0.00000	0.74719	0.00128	0.74848
C	37	-0.01769	1.99902	4.00406	0.01461	6.01769
C	38	-0.23630	1.99895	4.22542	0.01193	6.23630
H	39	0.23235	0.00000	0.76648	0.00117	0.76765
C	40	-0.20530	1.99902	4.19386	0.01242	6.20530
H	41	0.23481	0.00000	0.76423	0.00096	0.76519
C	42	-0.69013	1.99938	4.68325	0.00749	6.69013
H	43	0.24754	0.00000	0.75068	0.00178	0.75246
H	44	0.23779	0.00000	0.76139	0.00082	0.76221
H	45	0.24760	0.00000	0.75150	0.00090	0.75240

C	46	-0.23581	1.99895	4.22436	0.01250	6.23581
H	47	0.23369	0.00000	0.76511	0.00120	0.76631
C	48	-0.20385	1.99902	4.19241	0.01241	6.20385
H	49	0.23424	0.00000	0.76480	0.00096	0.76576
C	50	-0.23511	1.99912	4.22219	0.01380	6.23511
H	51	0.23733	0.00000	0.76190	0.00077	0.76267
C	52	-0.22959	1.99912	4.21668	0.01380	6.22959
H	53	0.23801	0.00000	0.76122	0.00077	0.76199
C	54	-0.23226	1.99911	4.21932	0.01382	6.23226
H	55	0.23822	0.00000	0.76100	0.00077	0.76178
C	56	-0.23080	1.99912	4.21789	0.01379	6.23080
H	57	0.23755	0.00000	0.76168	0.00077	0.76245
C	58	-0.68912	1.99938	4.68222	0.00752	6.68912
H	59	0.24785	0.00000	0.75026	0.00188	0.75215
H	60	0.24003	0.00000	0.75908	0.00088	0.75997
H	61	0.23876	0.00000	0.76038	0.00085	0.76124

==========

* Total *	0.00000	79.96262	195.43682	0.60056	276.00000

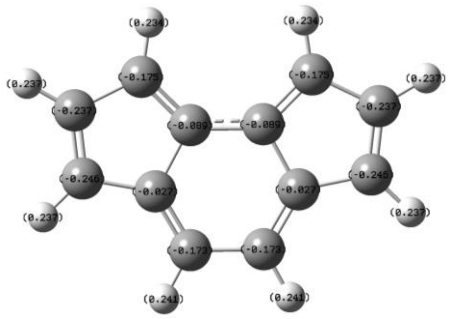

Figure 3.15 NPA charges of parent *as*-Indacene

Table 3.8 Frontier molecular orbital profiles.

Compd.	HOMO (eV)	LUMO (eV)	E_g^{DFT}
5	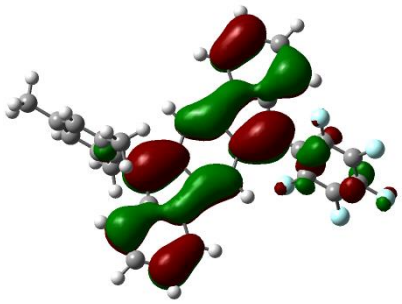 -5.24	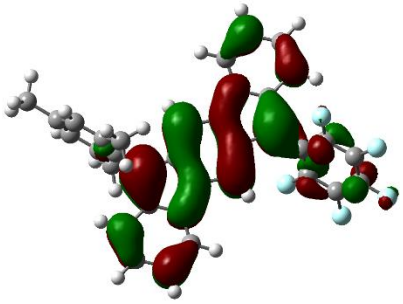 -2.91	2.33 eV

6	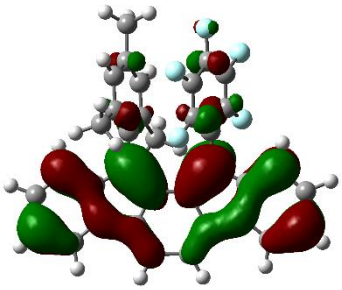 -5.22	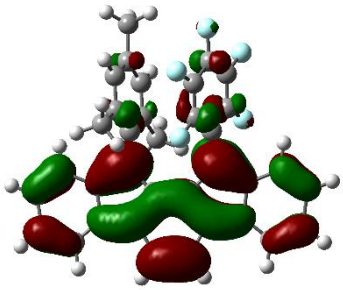 -3.00	2.22 eV

Table 3.9 Summary of TDDFT calculations of compound **5**.

Wavelength (nm)	Osc. Strength (f)	Major contribution
642.8	0.0002	H-1->LUMO (100%)
538.3	0.5377	HOMO->LUMO (95%)
439.6	0.0038	H-2->LUMO (99%)
414.2	0.0008	H-3->LUMO (100%)
368.4	0.0292	H-5->LUMO (22%), H-4->LUMO (74%)
362.9	0.0096	H-5->LUMO (62%), H-4->LUMO (16%), HOMO->L+1 (17%)
356.3	0.0023	H-5->LUMO (10%), HOMO->L+1 (78%)
351.1	0.0019	H-6->LUMO (95%)
338.2	0.0928	H-7->LUMO (89%)
312.8	0.3305	H-1->L+1 (18%), HOMO->L+2 (74%)
294.7	0.3767	H-8->LUMO (53%), H-1->L+1 (29%)
292.4	0.019	HOMO->L+3 (93%)
286.8	0.0097	H-1->L+2 (94%)
284.9	0.9618	H-8->LUMO (32%), H-1->L+1 (40%), HOMO->L+2 (12%)
277.1	0.0291	HOMO->L+4 (95%)
272.5	0.04	H-9->LUMO (92%)
266.3	0.0008	H-1->L+3 (97%)
263.7	0.0004	HOMO->L+5 (35%), HOMO->L+6 (36%)
261.9	0.0076	H-2->L+1 (83%), HOMO->L+5 (14%)
261.6	0.0233	HOMO->L+5 (39%), HOMO->L+6 (44%)

Table 3.10 Summary of photophysical and electrochemical data for **2-6**.

IF	$E_{1/2}^{red1}$ [V]	$E_{1/2}^{red2}$ [V]	$E_{1/2}^{ox1}$ [V]	$E_{1/2}^{ox2}$ [V]	HOMO [eV]	LUMO [eV]	E_g^{ec} [eV]	λ_{abs} [nm]	ε [M^{-1} cm^{-1}]	E_g^{opt} [eV]
1[12a]	–1.56	–2.07	0.71	-	–5.41	–3.32	2.09	515	42640	2.21
2	–1.70	–2.18	0.46	0.95	–5.16	–3.22	1.94	529, 493, 334	27990, 21200, 60980	2.19
3	–1.58	–2.16	0.54	1.08	–5.23	–3.34	1.89	545, 511, 342	17770, 13750, 33080	2.16
4	–1.49	–1.96	0.65	0.95	–5.34	–3.5	1.84	531, 501	18380, 14640	2.17
5	–1.73	–2.27	0.47	0.76	–5.2	–3.22	1.98	527, 502	22940, 20590	2.19
6	–1.31	–1.83	0.75	-	–5.45	–3.63	1.82	537, 320 293	11100, 11540, 26990	1.55

3.6 References

1. A. Can, A. Facchetti and H. Usta, *J. Mater. Chem. C*, 2022, **10**, 8496–8535.

2. C. Poriel and J. Rault-Berthelot, *Acc. Chem. Res.* 2018, **51**, 1818–1830.

3. (*a*) D. T. Chase, B. D. Rose, S. P. McClintock, L. N. Zakharov and M. M. Haley, *Angew. Chem. Int. Ed.,* 2011, **50**, 1127–1130; (*b*) A. Shimizu and Y. Tobe, *Angew. Chem. Int. Ed.*, 2011, **50**, 6906–6910; (*c*) A. Shimizu, R. Kishi, M. Nakano, D. Shiomi, K. Sato, T. Takui, I. Hisaki, M. Miyata and Y. Tobe, *Angew. Chem., Int. Ed.,* 2013, **52**, 6076–6079; (*d*) A. G. Fix, P. E. Deal, C. L. Vonnegut, B. D. Rose, L. N. Zakharov and M. M. Haley, *Org. Lett.*, 2013, **15**, 1362–1365; (*e*) J. J. Dressler, Z. Zhou, J. L. Marshall, R. Kishi, S. Takamuku, Z. Wei, S. N. Spisak, M. Nakano, M. A. Petrukhina and M. M. Haley, *Angew. Chem., Int. Ed.,* 2017, **56**, 15363–15367.

4. (*a*) Z.-P. Fan, X.-Y. Li, X.-E. Luo, X. Fei, B. Sun, L.-C. Chen, Z.-F. Shi, C.-L. Sun, X. Shao and H.-L. Zhang, *Adv. Funct. Mater.* 2017, **27**, 1702318; (*b*) S. Bebiche, P. A. Cisneros-Perez, T. Mohammed-Brahim, M. Harnois, J. Rault-Berthelot, C. Poriel and E. Jacques, *Mater. Chem. Front.*, 2018, **2**, 1631–1641; (*c*) M. Romain, M. Chevrier, S. Bebiche, T. Mohammed-Brahim, J. Rault-Berthelot, E. Jacques and C. Poriel, *J. Mater. Chem. C*, 2015, **3**, 5742–5753. (*d*) M. Romain, C. Quinton, D. Tondelier, B. Geffroy, O. Jeannin, J. Rault-Berthelot and C. Poriel, *J. Mater. Chem. C*, 2016, **4**, 1692–1703; (*e*) M. Romain, D. Tondelier, B. Geffroy, O. Jeannin, E. Jacques, J. Rault-Berthelot and C. Poriel, *Chem. Eur. J.* 2015, **21**, 9426–9439; (*f*) L. -C. Chi, W. -Y. Hung, H. -C. Chiu and K.-T Wong, *Chem. Commun.* 2009, 3892; (*g*) D. Thirion, M. Romain, J. Rault-Berthelot and C. Poriel, *Mater. Adv.*, 2021, **2**, 1271–1283; (*h*) J. Kim, S. H. Kim, I. H. Jung, E. Jeong, Y. Xia, S. Cho, I. -W. Hwang, K. Lee, H. Suh, H. -K. Shim and H. Y. Woo, *J. Mater. Chem.*, 2010, **20**, 1577–1586; (*i*) D. Xia, D. Gehrig, X. Guo, M. Baumgarten, F. Laquai and K. Müllen, *J. Mater. Chem. A*, 2015, **3**, 11086–11092.

5. (*a*) D. T. Chase, A. G. Fix, B. D. Rose, C. D. Weber, S. Nobusue, C. E. Stockwell, L. N. Zakharov, M. C. Lonergan and M. M. Haley, *Angew. Chem. Int. Ed.*, 2011, **50**, 11103–11106; (*b*) D. T. Chase, A. G. Fix, S. J. Kang, B. D. Rose, C. D. Weber, Y. Zhong, L. N. Zakharov, M. C. Lonergan, C. Nuckolls and M. M. Haley, *J. Am. Chem. Soc.*, 2012, **134**, 10349–10352; (*c*) C. K. Frederickson, B. D. Rose and M. M. Haley, *Acc. Chem. Res.*, 2017, **50**, 977–987; (*d*) J.-i. Nishida, S. Tsukaguchi and Y. Yamashita, *Chem. Eur. J.*, 2012, **18**, 8964–8970.

6. Q. Zhou, P. J. Carroll and T. M. Swager, *J. Org. Chem.*, 1994, **59**, 1294–1301.

7. H. Reisch, U. Wiesler, U. Scherf and N. Tuytuylkov, *Macromolecules* 1996, **29**, 8204–8210.

8. J. L. Marshall, D. Lehnherr, B. D. Lindner, R. R. Tykwinski, *ChemPlusChem* 2017, **82**, 967–1001.

9. (*a*) M. J. Kendrick, A. Neunzert, M. M. Payne, B. Purushothaman, B. D. Rose, J. E. Anthony, M. M. Haley, and O. Ostroverkhova, *J. Phys. Chem. C.*, 2012, **116**, 18108–18116; (*b*) Y.-C. Lo, H.-C. Ting, Y.-Z. Li, Y.-H. Li, S.-W. Liu, K.-W. Huang and K.-T. Wong. *Org. Chem. Front.*, 2017, **4**, 675–681.

10. R. Casares, Á. Martínez-Pinel, S. Rodríguez-González, and I. R. Márquez, L. Lezama, M. T. González, E. Leary, V. Blanco, J. G. Fallaque, C. Díaz, F. Martín, J. M. Cuerva, and A. Millán, *J. Mater. Chem. C*, 2022, **10**, 11775–11782.

11. (*a*) C. K. Frederickson, L. N. Zakharov and M. M. Haley, *J. Am. Chem. Soc.* 2016, **138**, 16827–16838; (*b*) H. K. Saha, D. Mallick and S. Das, *Chem. Commun.*, 2022, **58**, 8492–8495.

12. (*a*) P. Hu, S. Lee, T. S. Herng, N. Aratani, T. P. Gonçalves, Q. Qi, X. Shi, H. Yamada, K. Huang, J. Ding, D. Kim and J. Wu, *J. Am. Chem. Soc.*, 2016, **138**, 1065–1077; (*b*) J. Guo, Y. Yang, C. Dou and Y. Wang, *J. Am. Chem. Soc.*, 2021, **143**, 18272–18279.

13. S. Das, S. Lee, M. Son, X. Zhu, W. Zhang, B. Zheng, P. Hu, Z. Zeng, Z. Sun, W. Zeng, R.-W. Li, K.-W. Huang, J. Ding, D. Kim and J. Wu, *Chem. Eur. J.*, 2014, **20**, 11410–11420.

14. B. D. Rose, L. E. Shoer, M. R. Wasielewski and M. M. Haley, *Chem. Phys. Lett.*, 2014, **616-617**, 137–141.

15. C. K. Frederickson, J. E. Barker, J. J. Dressler, Z. Zhou, E. R. Hanks, J. P. Bard, L. N. Zakharov, M. A. Petrukhina and M. M. Haley, *Synlett.*, 2018, **29**, 2562–2566.

16. S. Das and J. Wu, *Phys. Sci. Rev.*, 2017, **2**, 109.

17. (*a*) K. Sahara, M. Abe, H. Zipse and T. Kubo, *J. Am. Chem. Soc.*, 2020, **142**, 5408–5418; (*b*) P. Hu, S. Lee, K. H. Park, S. Das, T. S. Herng, T P. Gonçalves, K. Huang, J. Ding, D. Kim and J. Wu, *J. Org. Chem.*, 2016, **81**, 2911–2919.

18. J. E. Barker, T. Kodama, M. K. Song, C. K. Frederickson, T. Jousselin-Oba, L. N. Zakharov, J. Marrot, M. Frigoli, R. P. Johnson and M. M. Haley, *ChemPlusChem* 2019, **84**, 665–672.

19. A. Le Berre, *Ann. Chim.* 1957, **13**, 371.

20. A. Shimizu, S. Nobusue, H. Miyoshi and Y. Tobe, *Pure Appl. Chem.*, 2014, **86**, 517–528.

21. C. Zong, X. Zhu, Z. Xu, L. Zhang, J. Xu, J. Guo, Q. Xiang, Z. Zeng, W. Hu, J. Wu, R. Li and Z. Sun, *Angew. Chem. Int. Ed.*, 2021, **60**, 16230–16236.

22. (*a*) Y. Tobe, *Chem. Rec.*, 2015, **15**, 86–96; (*b*) Y. Tobe, *Physical Organic Chemistry of Quinodimethanes, Top. Curr. Chem.*, Springer, 2017, **375**, 107.

23. (*a*) D. Lehnherr, J. Gao, F. A. Hegmann and R. R. Tykwinski, *Org. Lett.*, 2008, **10**, 4779–4782; (*b*) S. H. Etschel, A. R. Waterloo, J. T. Margraf, A. Y. Amin, F. Hampel, C. M. Jäger, T. Clark, M. Halik and R. R. Tykwinski, *Chem. Commun.*, 2013, **49**, 6725–6727; (*c*) J. Zirzlmeier, D. Lehnherr, P. B. Coto, E. T. Chernick, R. Casillas, B. S. Basel, M. Thoss, R. R. Tykwinski and D. M. Guldi, *Proc. Natl. Acad. Sci. U. S. A.* 2015, **112**, 5325–5330; (*d*) R. R. Tykwinski, *Acc. Chem. Res.*, 2019, **52**, 2056–2069.

24. (*a*) Y. Wu, Y. Wang, J. Chen, G. Zhang, J. Yao, D. Zhang and H. Fu, *Angew. Chem. Int. Ed.*, 2017, **56**, 9400–9404; (*b*) S. Naskar and M. Das, *Chem. Phy. Lett.* 2020, **749**, 137368; (*c*) T. Ullrich, D. Munz and D. M. Guldi, *Chem. Soc. Rev.*, 2021, **50**, 3485–3518; (*d*) C. Hong, J. Baltazar and J. D. Tovar, *Eur. J. Org. Chem.*, 2022, e202101343.

25. W. Deuschel, *Helv. Chim. Acta* 1951, **34**, 2403–2416.

26. S. Merlet, M. Birau and Z. Y. Wang, *Org. Lett.*, 2002, **4**, 2157–2159.

27. D. Thirion, C. Poriel, J. Rault-Berthelot, F. Barrière, O. Jeannin, *Chem. Eur. J.*, 2010, **16**, 13646–13658.

28. H. Sharma, P. K. Sharma and S. Das, *Chem. Commun.*, 2020, **56**, 11319–11322.

29. (*a*) S. Herzog, A. Hinz, F. Breher, and J. Podlech, *Org. Biomol. Chem.*, 2022, **20**, 2873–2880. (*b*) Q. Jiang, Y. Han, Y. Zou, H. Phan, L. Yuan, T. S. Herng, J. Ding and C. Chi, *Chem. Eur. J.*, 2020, **26**, 15613–15622.

30. (*a*) S. Schneebeli, M. Kamenetska, F. Foss, H. Vazquez, R. Skouta, M. Hybertsen, L. Venkataraman and R. Breslow, *Org. Lett.* 2010, **12**, 4114–4117; (*b*) G. E. Rudebusch, J. L. Zafra, K. Jorner, K. Fukuda, J. L. Marshall, I. Arrechea-Marcos, G. L.

Espejo, R. P. Ortiz, C. J. Gómez-García, L. N. Zakharov, M. Nakano, H. Ottosson, J. Casado and M. M. Haley, *Nat. Chem.* 2016, **8**, 753–759.

31. (*a*) J. Kruszewski, T. M. Krygowski, *Tetrahedron Lett.*, 1972, **13**, 3839–3842; (*b*) T. M. Krygowski, *J. Chem. Inf. Comput. Sci.* 1993, **33**, 70–78; (*c*) Krygowski, T.M., Szatylowicz, H. Aromaticity: what does it mean? *ChemTexts*, 2015, **1**, 12.

32. J. Dominikowska, M. EL. Palusiak, *Struct. Chem.* 2012, **23**, 1173–1183.

33. K. Uehara, P. Mei, T. Murayama, F. Tani, H. Hayashi, M. Suzuki, N. Aratani, H. Yamada, *Eur. J. Org. Chem.* 2019, 860–861.

34. T. Lu and F. Chen, *J. Comput. Chem.*, 2012, **33**, 580–592.

35. H. Fallah-Bagher-Shaidaei, C. S. Wannere, C. Corminboeuf, R. Puchta and P. v. R. Schleyer, *Org. Lett.* 2006, **8**, 863–866.

36. J. E. Barker, T. W. Price, L. J. Karas, R. Kishi, S. N. MacMillan, L. N. Zakharov, C. J. Gómez-García, J. I. Wu, M. Nakano and M. M. Haley, *Angew. Chem. Int. Ed.*, 2021, **60**, 22385–22392.

37. B. M. Gimarc, *J. Am. Chem. Soc.* 1983, **105**, 1979–1984.

38. W. Kueh, X. Shi, T. W. Phua, H. Kueh, Y. C. Liau, C. Chi. *Org. Lett.* 2022, **24**, 5935–5940.

39. (*a*) W. A. Sheppard, *J. Am. Chem. Soc.* 1970, **92**, 5419–5422; (*b*) P. K. Sharma and S. Das, *J. Org. Chem.* 2022, **87**, 5430–5436.

40. K. Paudel, B. Johnson, M. Thieme, M. M. Haley, M. M. Payne, J. E. Anthony and O. Ostroverkhova, *Appl. Phys. Lett.*, 2014, **105**, 043301.

41. D. Thirion, C. Poriel, F. Barrière, R. Métivier, O. Jeannin and J. Rault-Berthelot, *Org. Lett.* 2009, **11**, 4794–4797.

42. J. L. Marshall, N. J. O'Neal, L. N. Zakharov, and M. M. Haley, *J. Org. Chem.*, 2016, **81**, 3674–3680.

43. (*a*) M. Di Giovannantonio, J. Urgel, U. Beser, A. V. Yakutovich, J. Wilhelm, C. A. Pignedoli, P. Ruffieux, A. Narita, K. Müllen, and R. Fasel, *J. Am. Chem. Soc.*, 2018, **140**, 3532–3536 (*b*) M. Di Giovannantonio and R. Fasel, *J. Polym. Sci.*, 2022, **60**, 1814–1826.

44. Bruker, SAINT V8.38A, (Bruker AXS Inc., 2017).

45. O. V. Dolomanov, L. J. Bourhis, R. J. Gildea, J. A. Howard and H. Puschmann, *J. Appl. Crystallogr.* 2009, **42**, 339–341.

46. L. J. Bourhis, O. V. Dolomanov, R. J. Gildea, J. A. Howard and H. Puschmann, *Acta Crystallogr. A.* 2015, **71**, 59–75.
47. G. M. Sheldrick, *Acta Crystallogr. C Struct. Chem*. 2015, **71**, 3–8.
48. Gaussian 09, *Revision B.01*, M. J. Frisch, G. W. Trucks, H. B. Schlegel, G. E. Scuseria, M. A. Robb, J. R. Cheeseman, G. Scalmani, V. Barone, B. Mennucci, G. A. Petersson, H. Nakatsuji, M. Caricato, X. Li, H. P. Hratchian, A. F. Izmaylov, J. Bloino, G. Zheng, J. L. Sonnenberg, M. Hada, M. Ehara, K. Toyota, R. Fukuda, J. Hasegawa, M. Ishida, T. Nakajima, Y. Honda, O. Kitao, H. Nakai, T. Vreven, J. A. Montgomery, Jr., J. E. Peralta, F. Ogliaro, M. Bearpark, J. J. Heyd, E. Brothers, K. N. Kudin, V. N. Staroverov, T. Keith, R. Kobayashi, J. Normand, K. Raghavachari, A. Rendell, J. C. Burant, S. S. Iyengar, J. Tomasi, M. Cossi, N. Rega, J. M. Millam, M. Klene, J. E. Knox, J. B. Cross, V. Bakken, C. Adamo, J. Jaramillo, R. Gomperts, R. E. Stratmann, O. Yazyev, A. J. Austin, R. Cammi, C. Pomelli, J. W. Ochterski, R. L. Martin, K. Morokuma, V. G. Zakrzewski, G. A. Voth, P. Salvador, J. J. Dannenberg, S. Dapprich, A. D. Daniels, O. Farkas, J. B. Foresman, J. V. Ortiz, J. Cioslowski and D. J. Fox, Gaussian, Inc., Wallingford CT, 2010.
49. J. Kruszewski and T. M. Krygowski, *Tetrahedron Lett.* 1972, **13**, 3839–3842.

3.7 Appendix

NMR Spectra

Figure 3.16 ^{1}H NMR spectrum of **9** (in $CDCl_3$, 400 MHz).

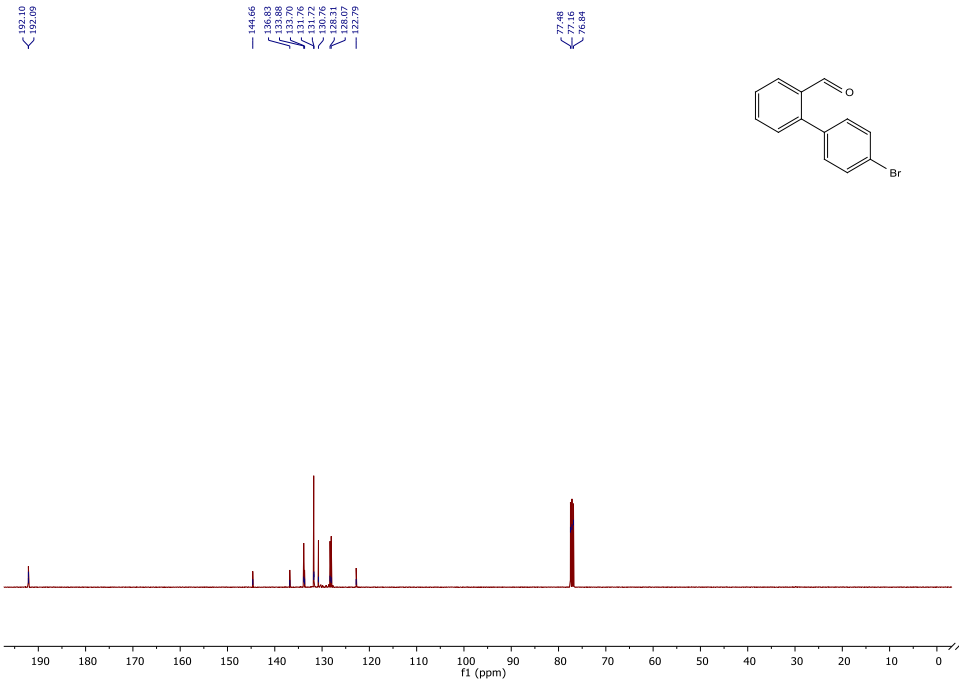

Figure 3.17 ^{13}C NMR spectrum of **9** (in $CDCl_3$, 100 MHz).

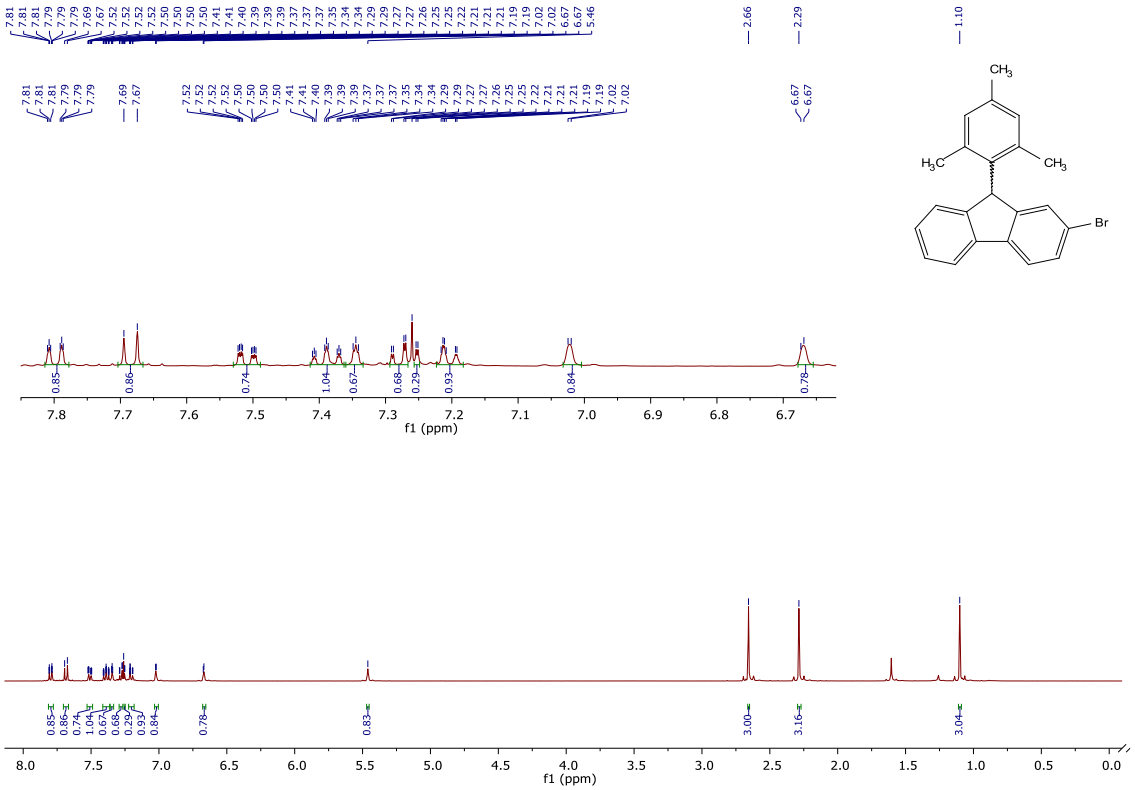

Figure 3.18 ^{1}H NMR spectrum of **11** (in $CDCl_3$, 400 MHz).

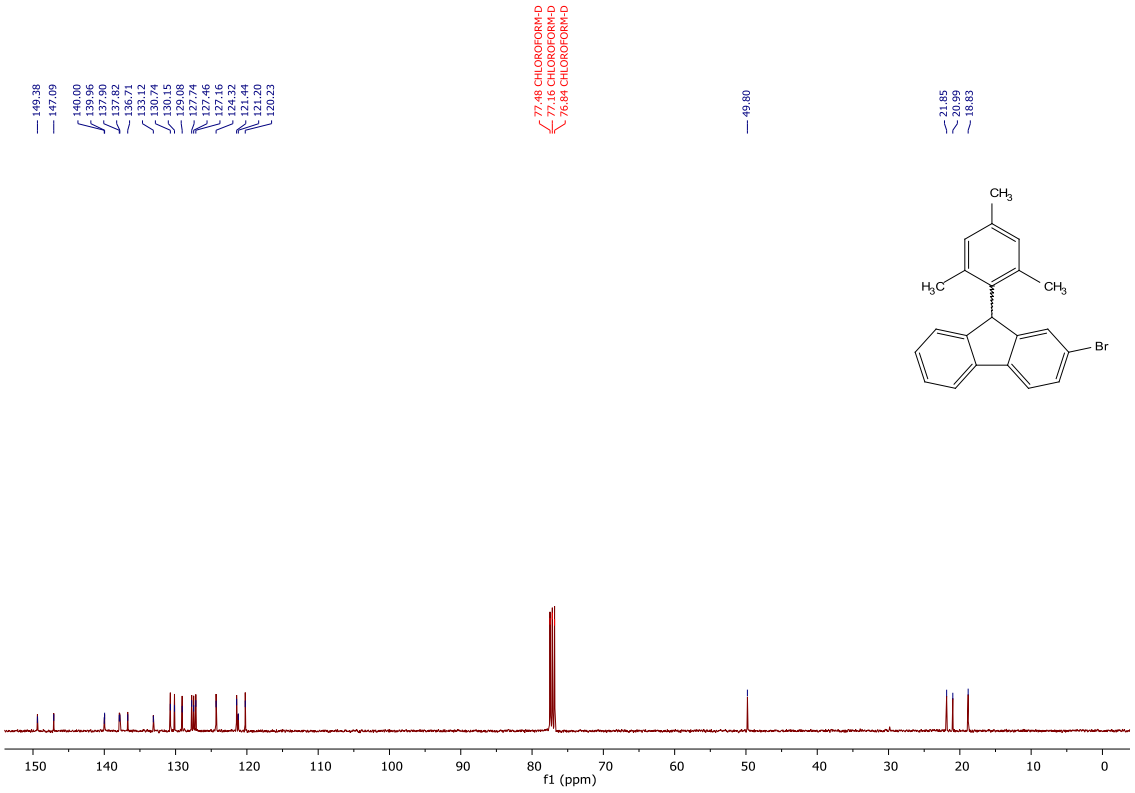

Figure 3.19 ^{13}C NMR spectrum of **11** (in $CDCl_3$, 100 MHz).

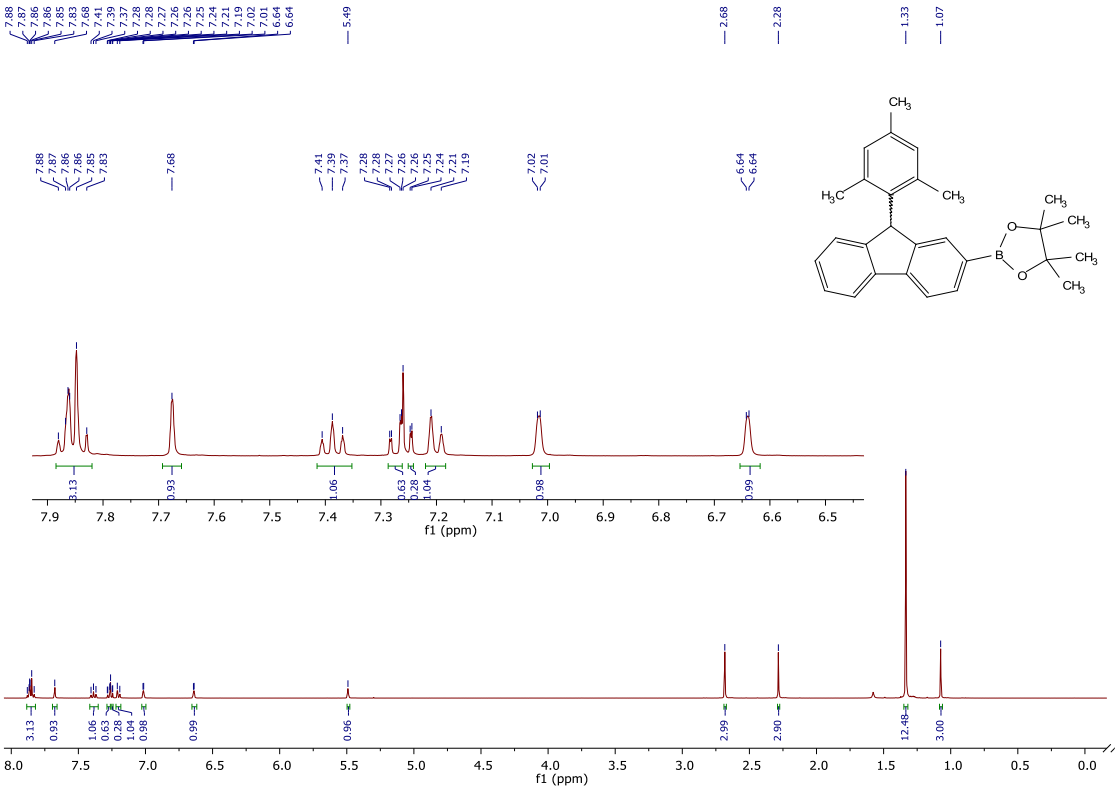

Figure 3.20 ^{1}H NMR spectrum of **13** (in $CDCl_3$, 400 MHz).

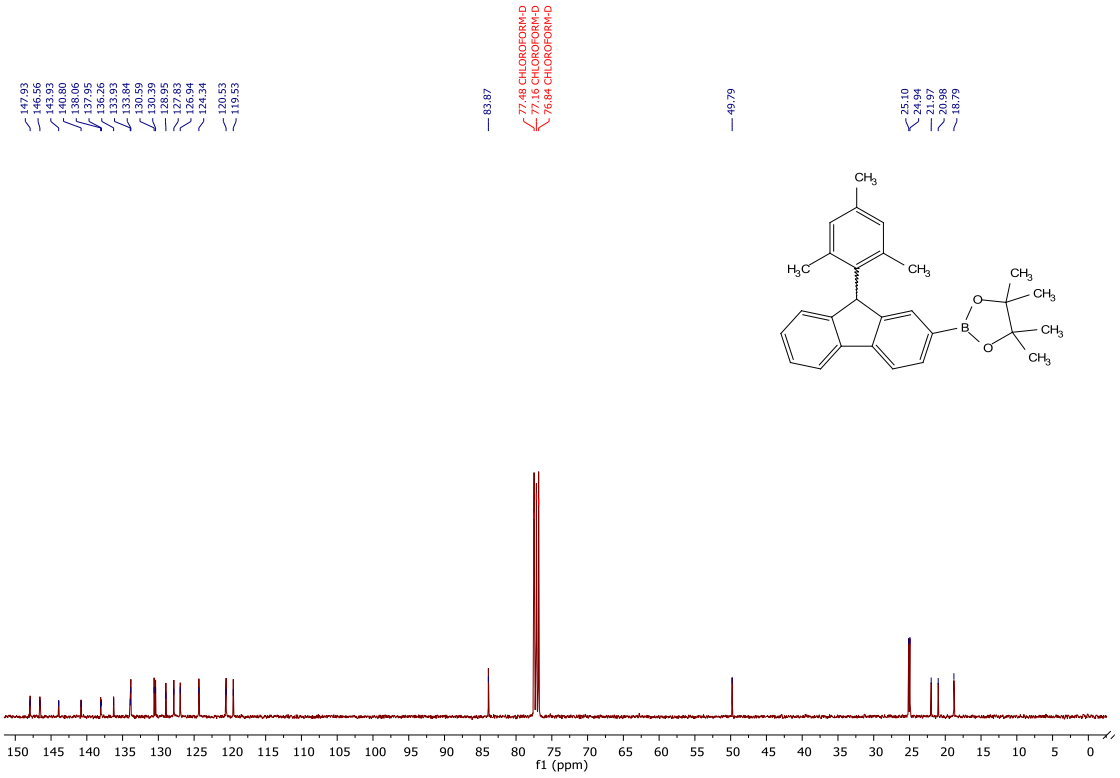

Figure 3.21 ^{13}C NMR spectrum of **13** (in $CDCl_3$, 100 MHz).

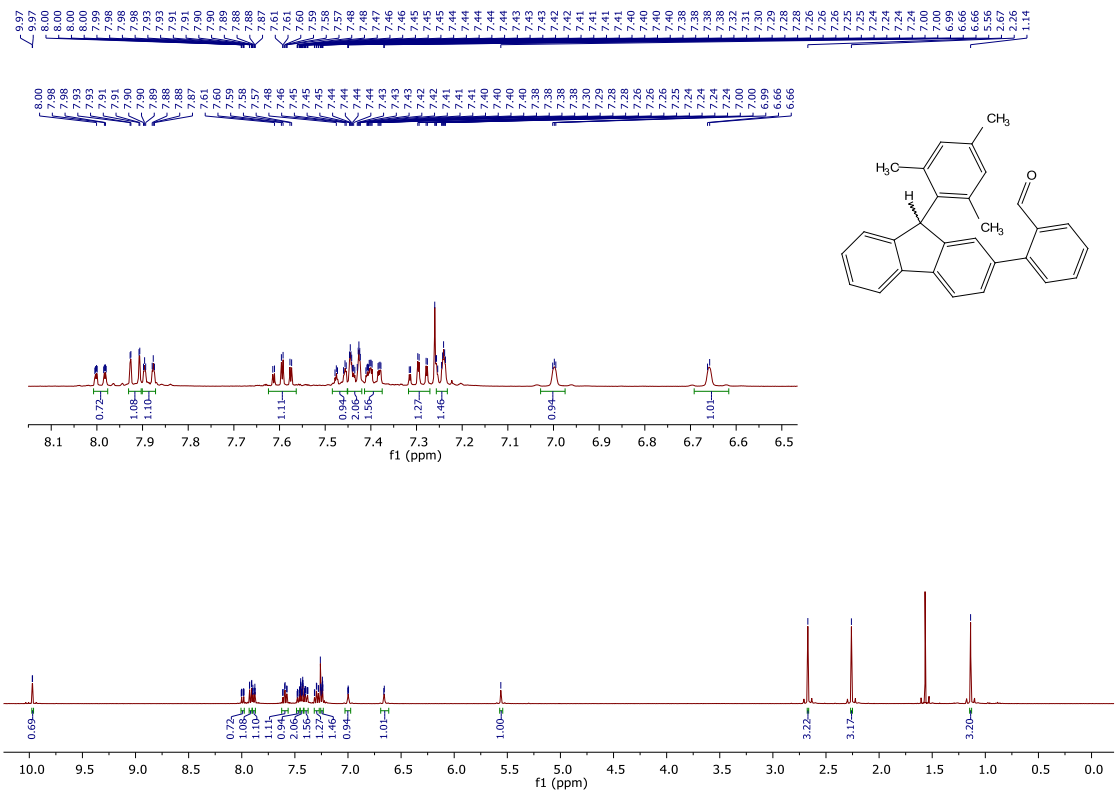

Figure 3.22 ^{1}H NMR spectrum of **15** (in $CDCl_3$, 400 MHz).

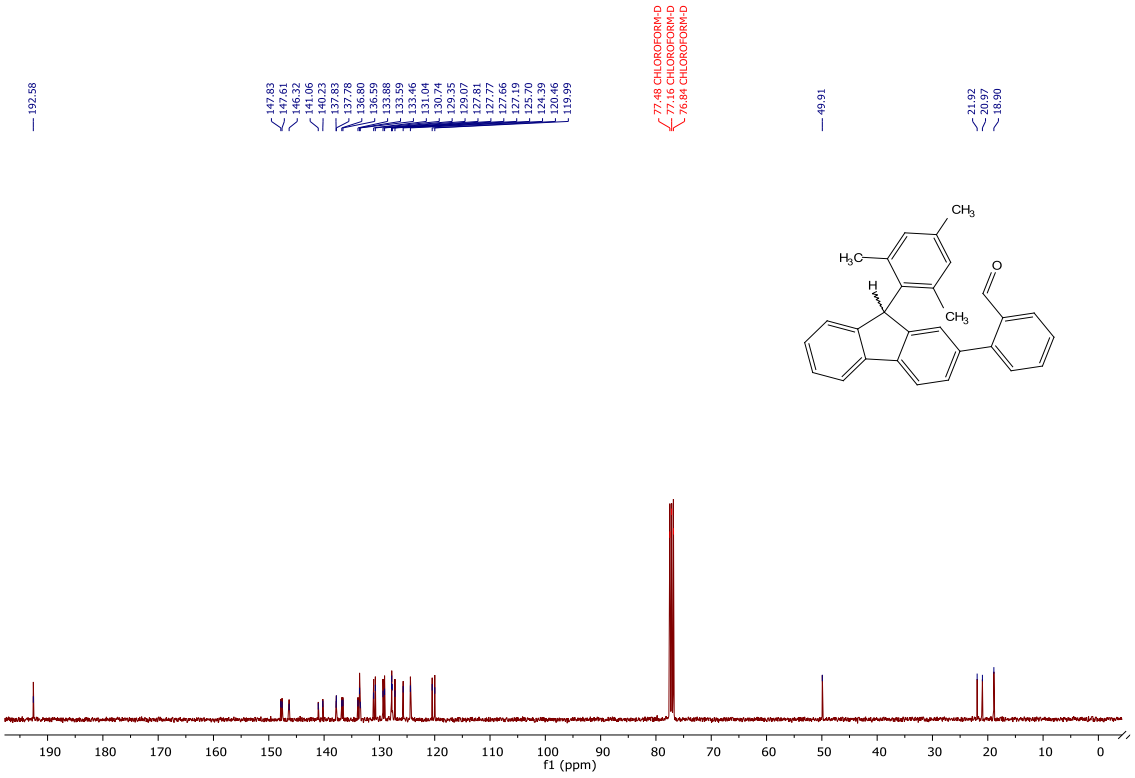

Figure 3.23 ^{13}C NMR spectrum of **15** (in $CDCl_3$, 100 MHz).

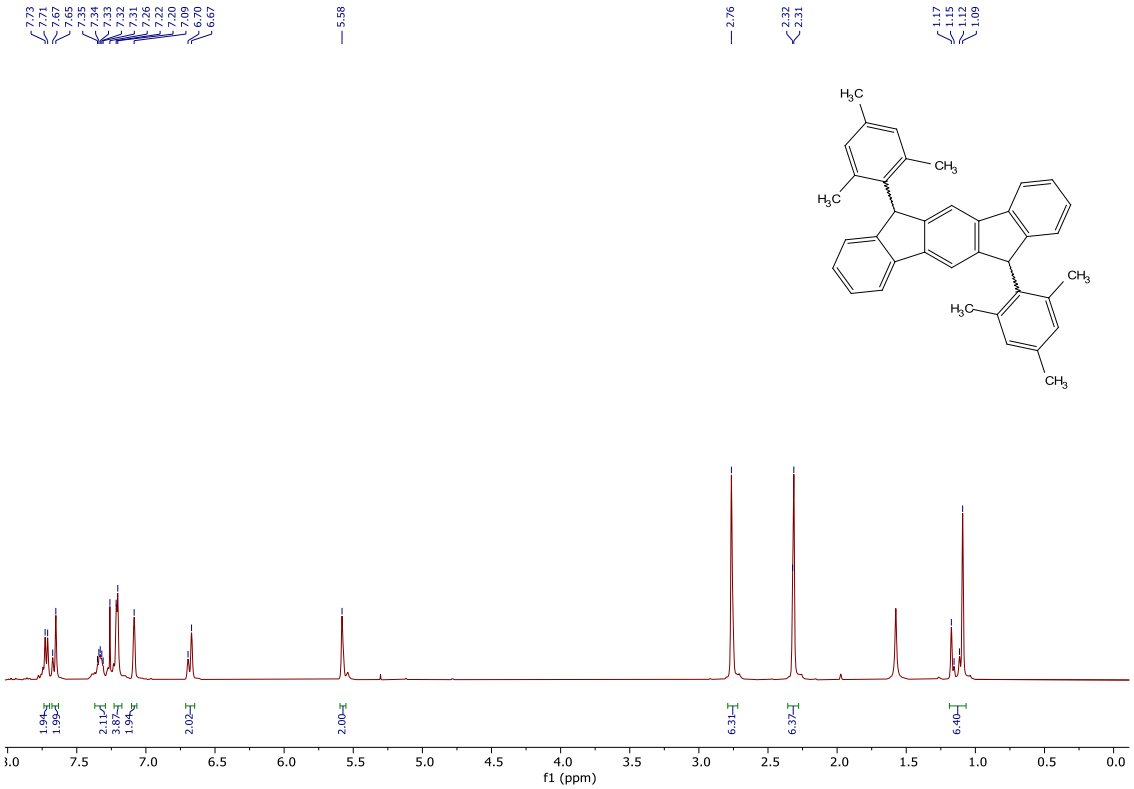

Figure 3.24 ^{1}H NMR spectrum of **16** (in $CDCl_3$, 400 MHz).

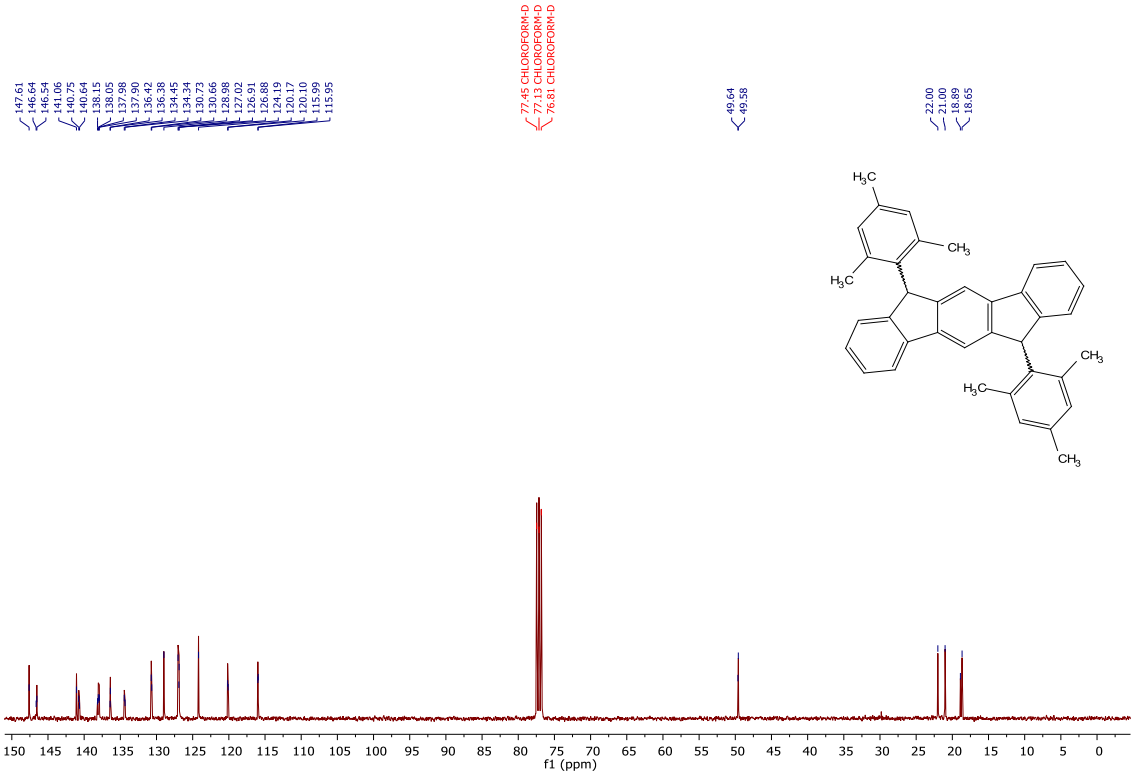

Figure 3.25 ^{13}C NMR spectrum of **16** (in $CDCl_3$, 100 MHz).

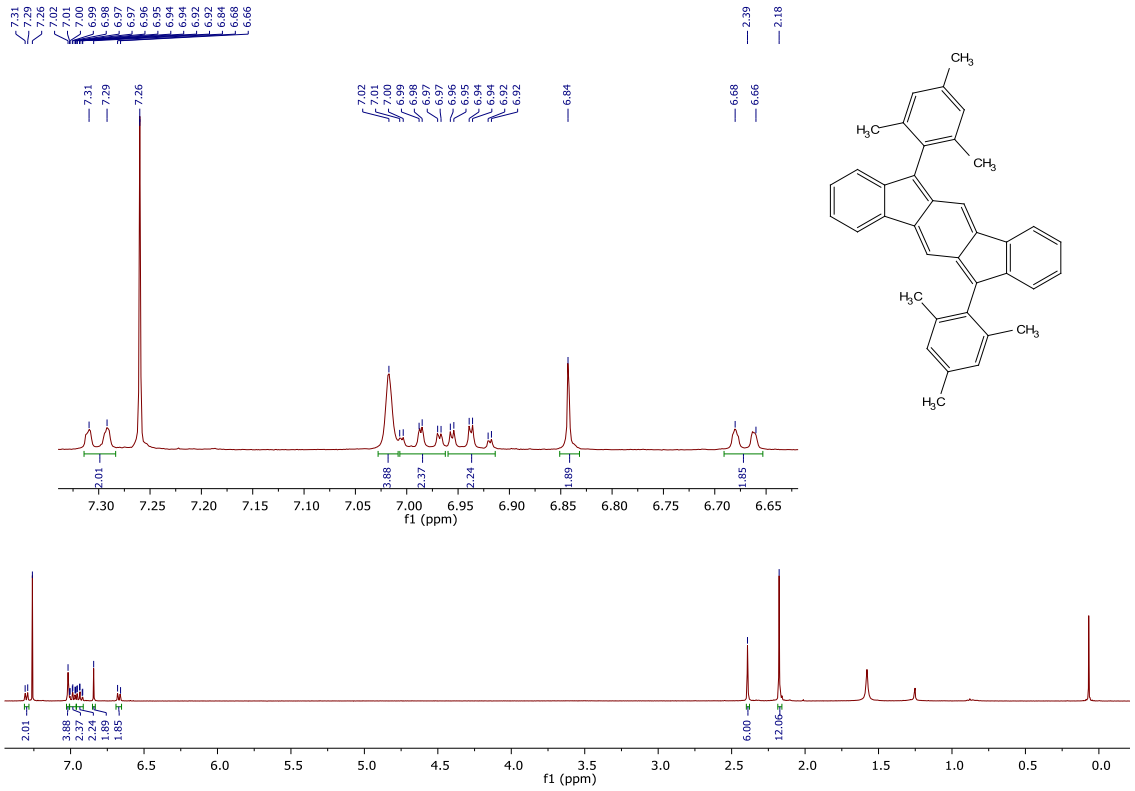

Figure 3.26 ^{1}H NMR spectrum of **1** (in $CDCl_3$, 400 MHz).

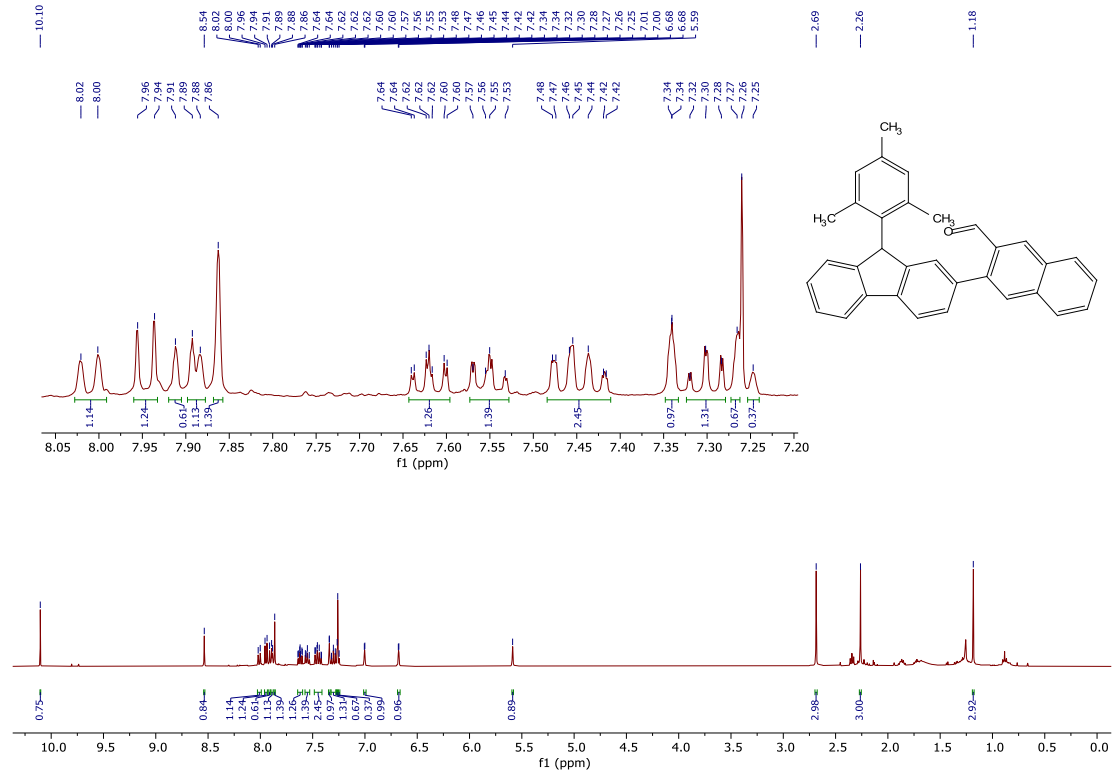

Figure 3.27 ^{1}H NMR spectrum of **18** (in $CDCl_3$, 400 MHz).

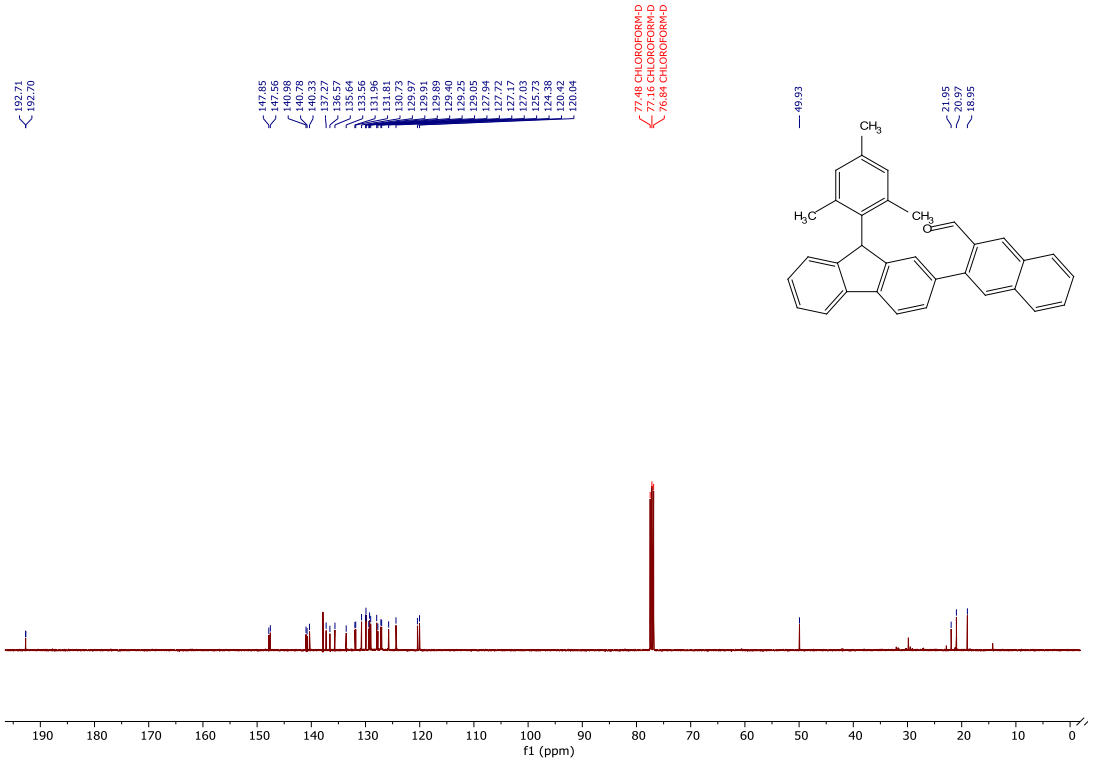

Figure 3.28 ^{13}C NMR spectrum of **18** (in $CDCl_3$, 100 MHz).

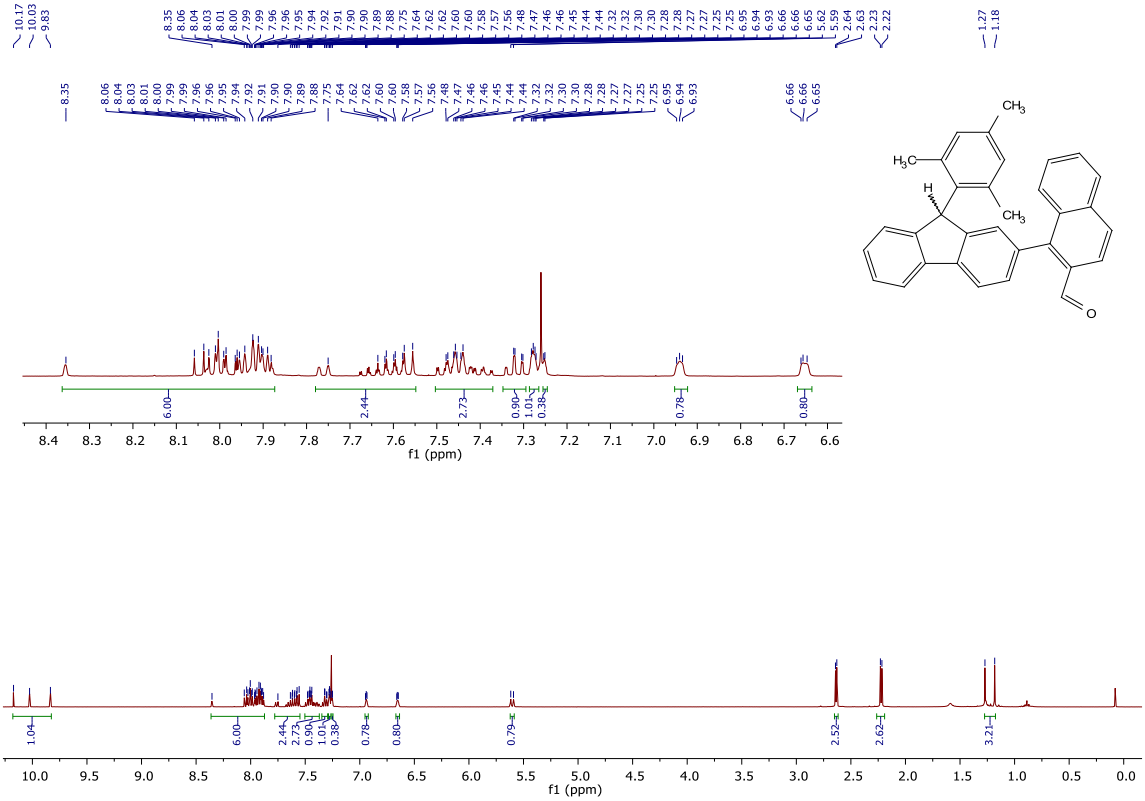

Figure 3.29 ^{1}H NMR spectrum of **21** (in $CDCl_3$, 400 MHz).

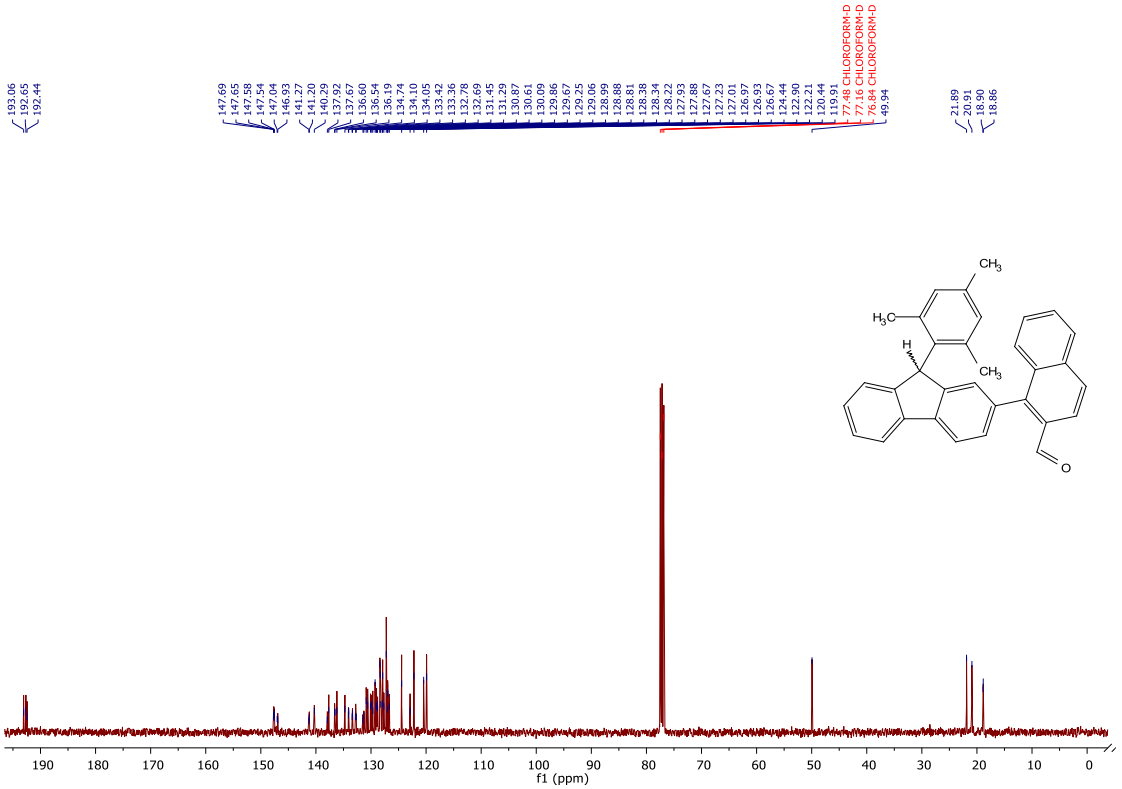

Figure 3.30 ^{13}C NMR spectrum of **21** (in $CDCl_3$, 100 MHz).

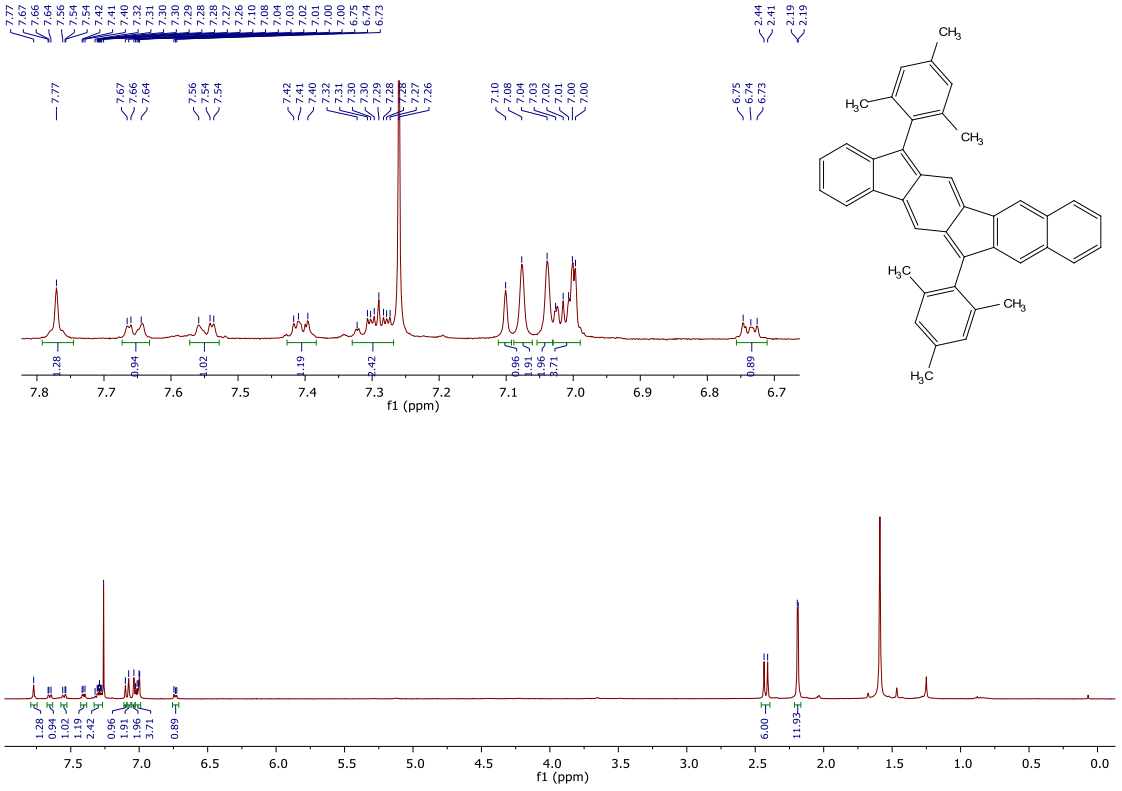

Figure 3.31 ^{1}H NMR spectrum of **2** (in $CDCl_3$, 400 MHz).

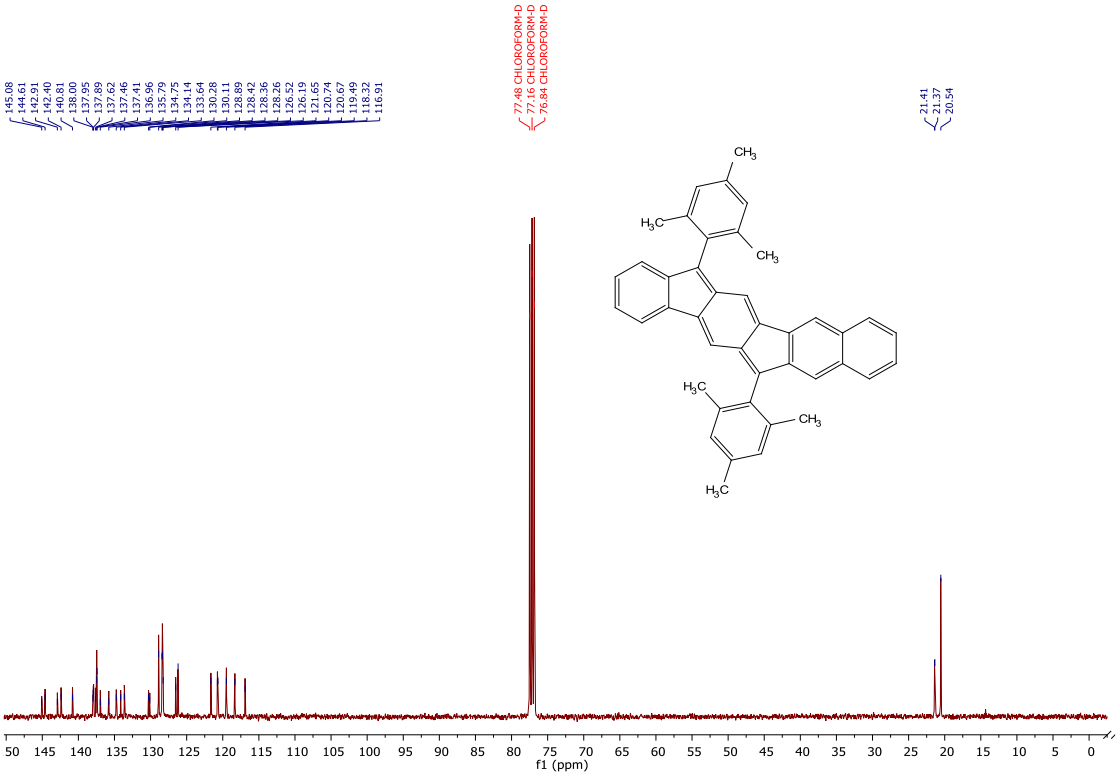

Figure 3.32 ^{13}C NMR spectrum of **2** (in $CDCl_3$, 100 MHz).

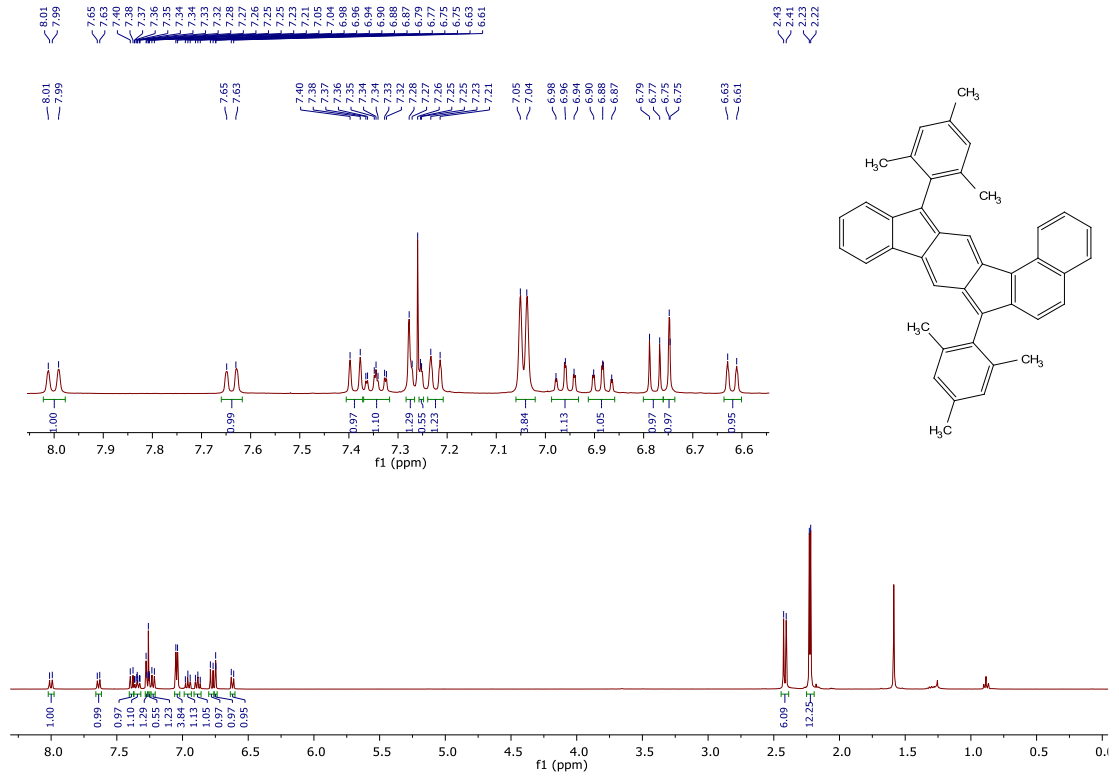

Figure 3.33 ^{1}H NMR spectrum of **3** (in $CDCl_3$, 400 MHz).

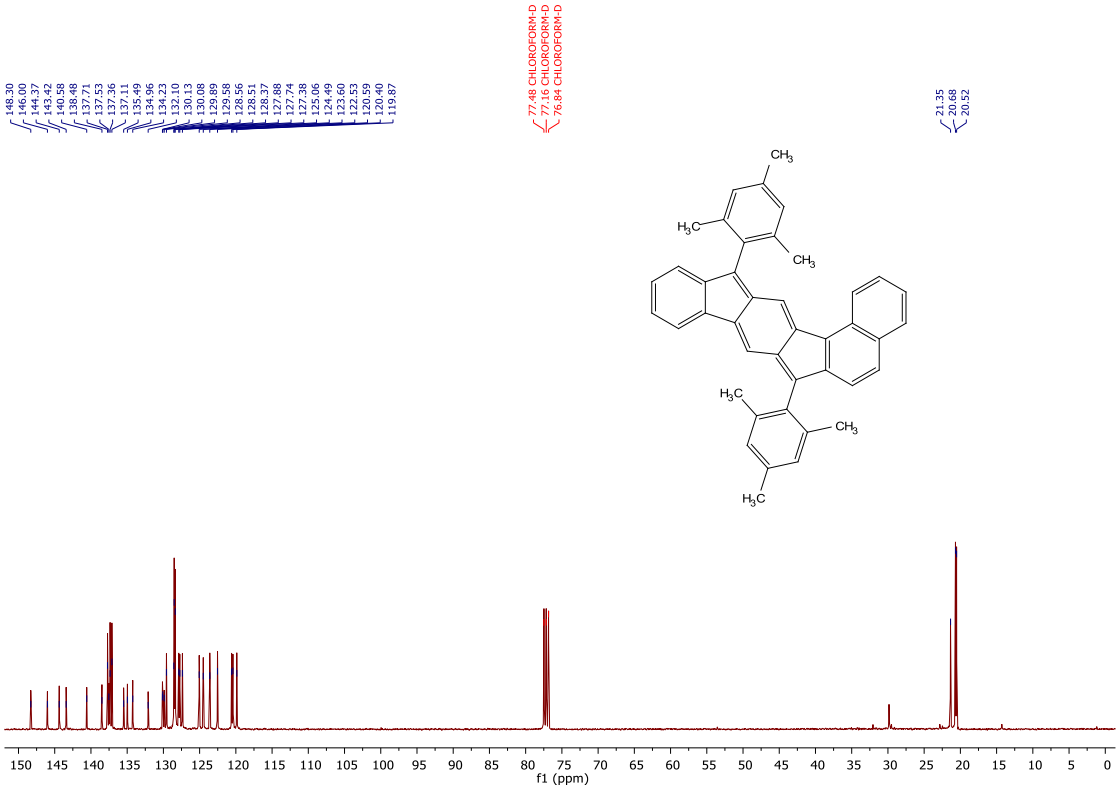

Figure 3.34 ^{13}C NMR spectrum of **3** (in $CDCl_3$, 100 MHz).

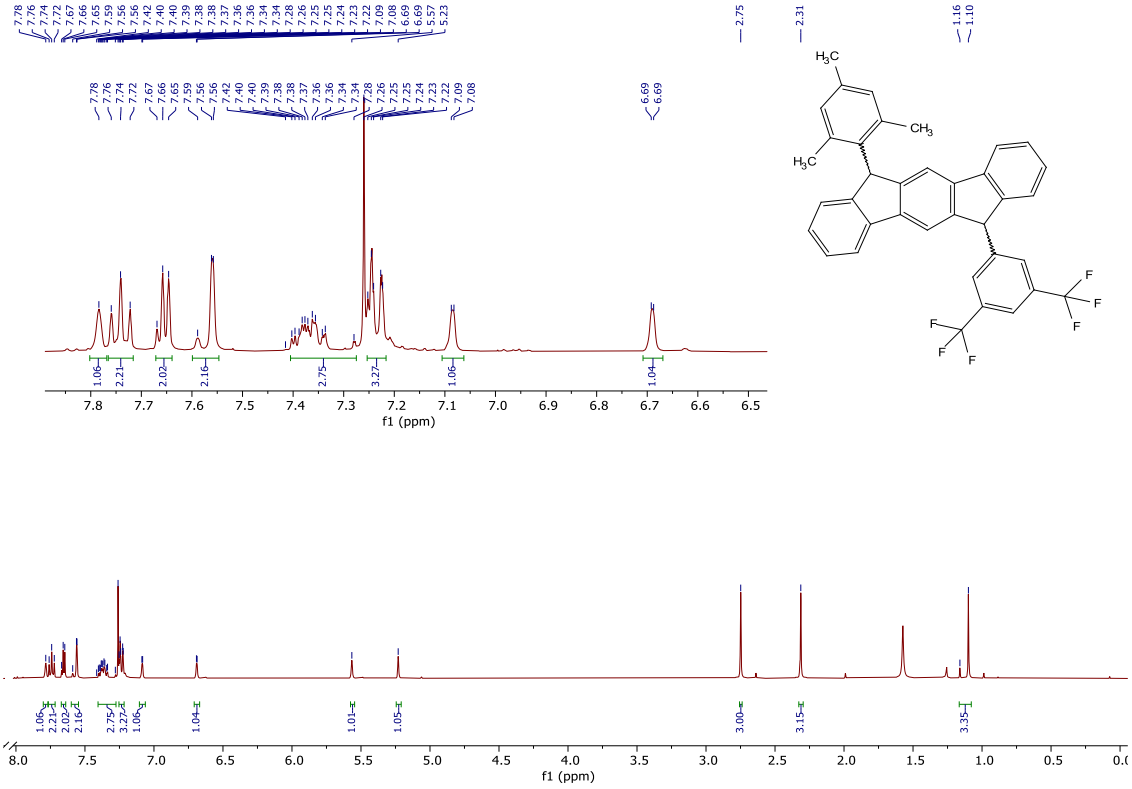

Figure 3.35 ^{1}H NMR spectrum of **23** (in $CDCl_3$, 400 MHz).

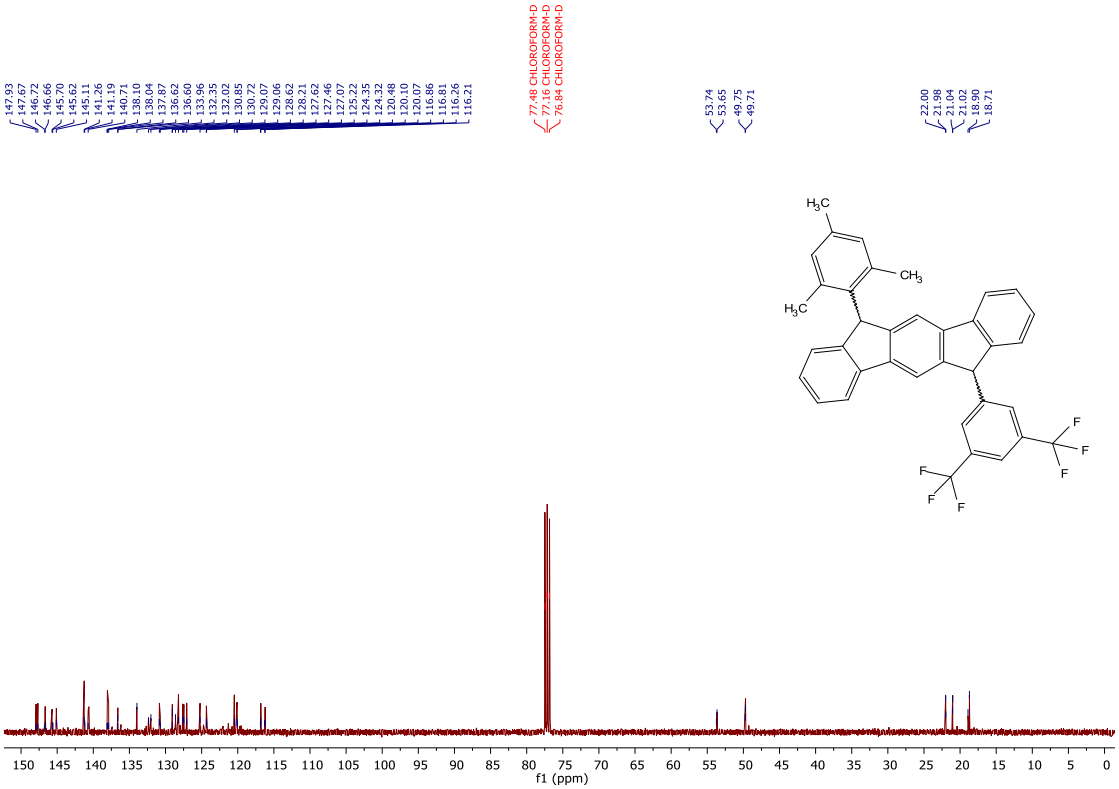

Figure 3.36 ^{13}C NMR spectrum of **23** (in $CDCl_3$, 100 MHz).

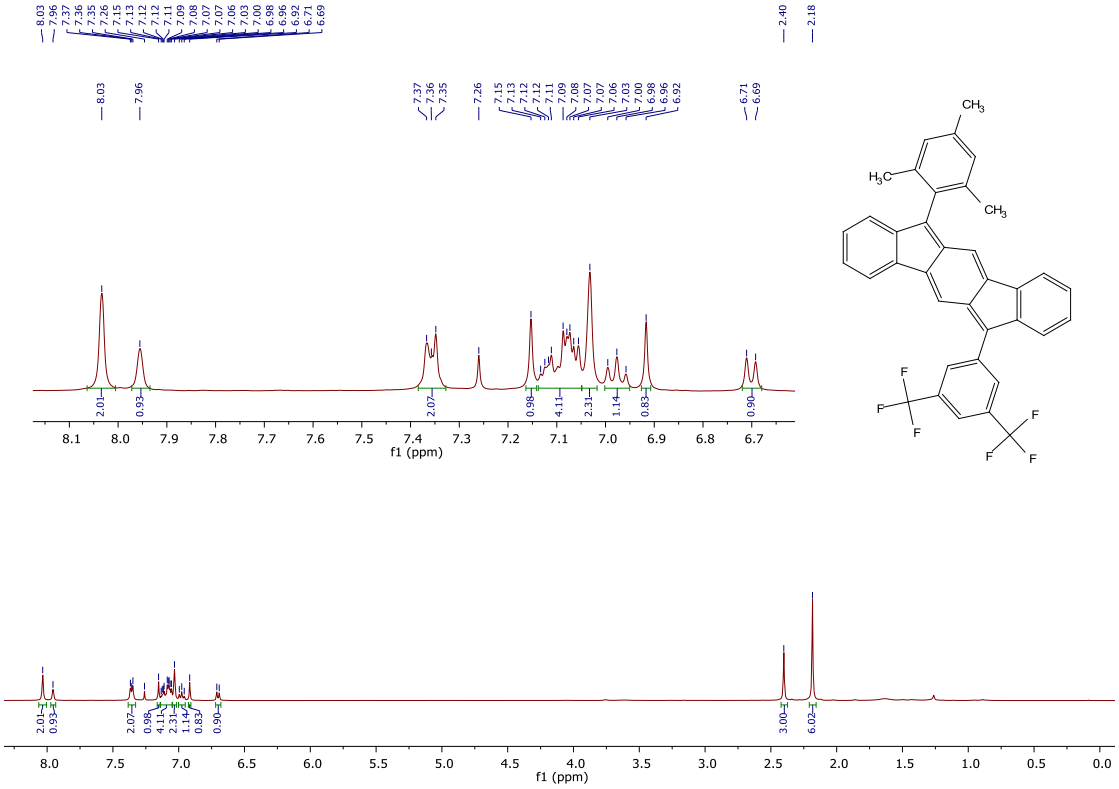

Figure 3.37 ^{1}H NMR spectrum of **4** (in $CDCl_3$, 400 MHz).

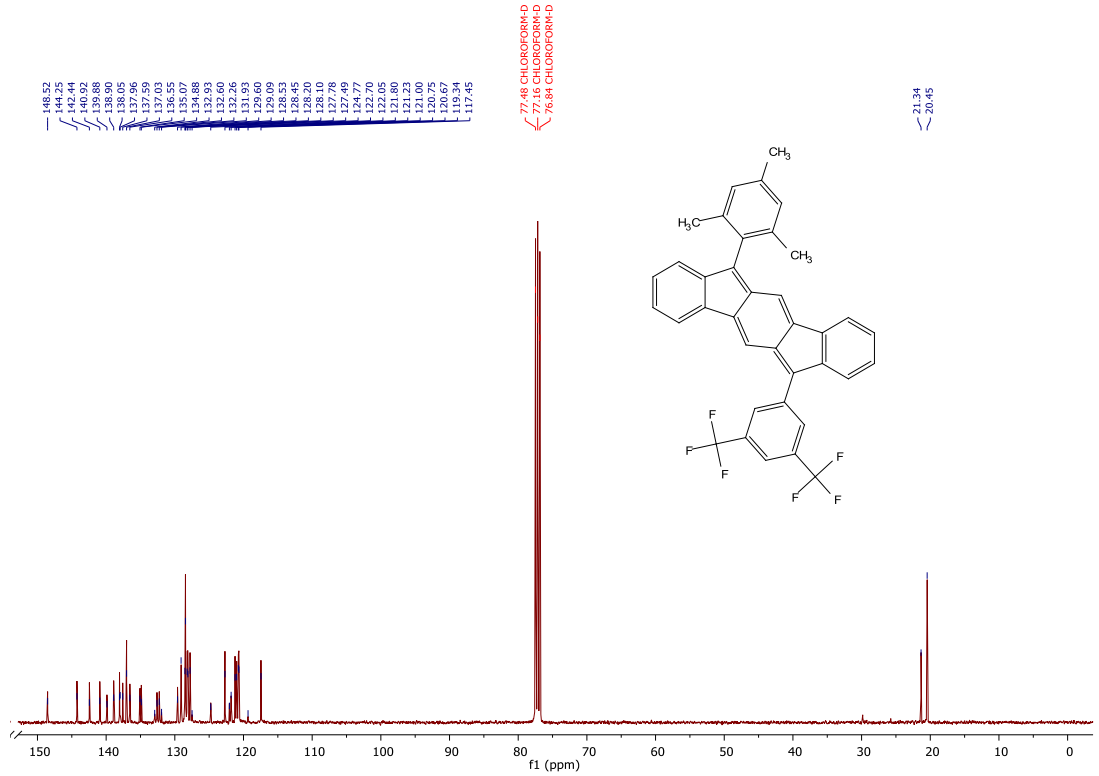

Figure 3.38 ^{1}H NMR spectrum of **4** (in $CDCl_3$, 100 MHz).

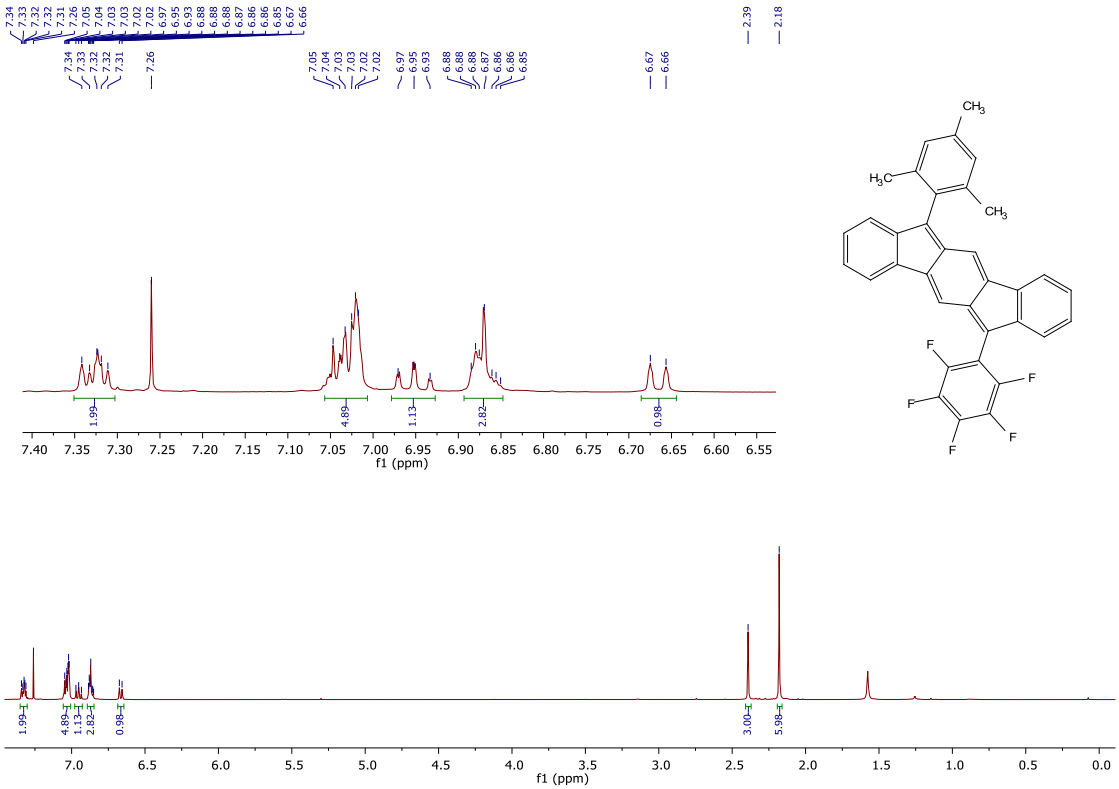

Figure 3.39 ^{1}H NMR spectrum of **5** (in $CDCl_3$, 400 MHz).

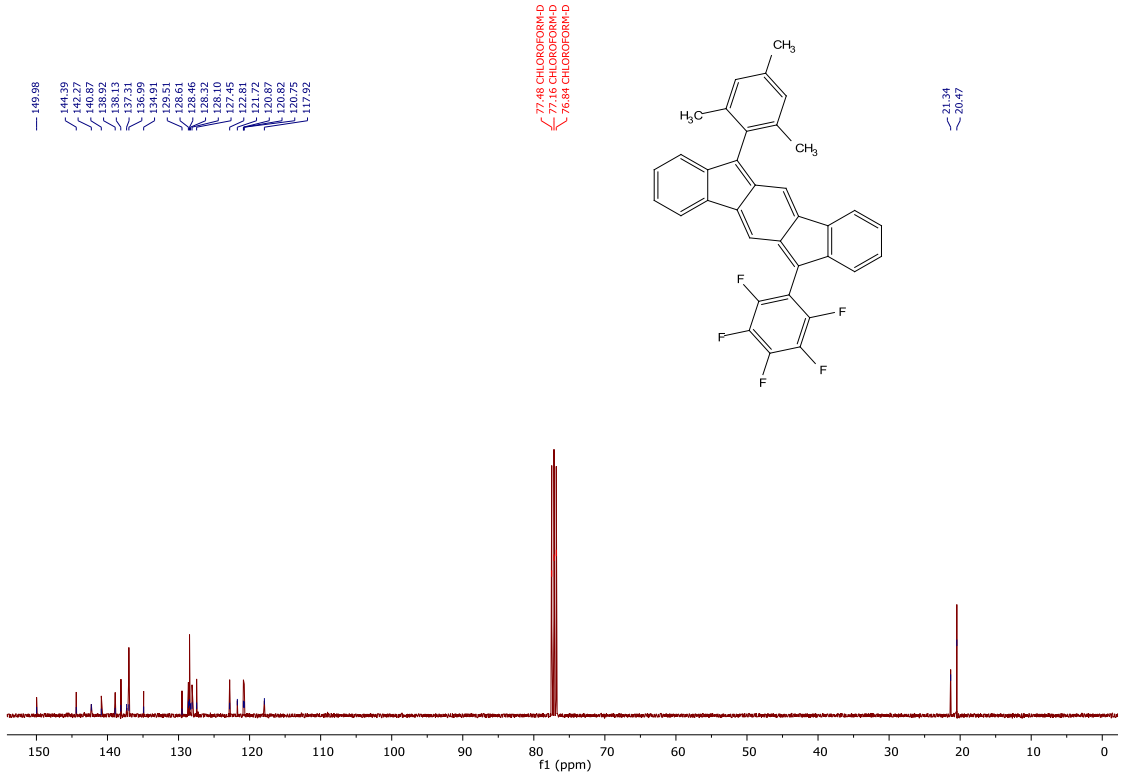

Figure 3.40 ^{13}C NMR spectrum of **5** (in $CDCl_3$, 100 MHz).

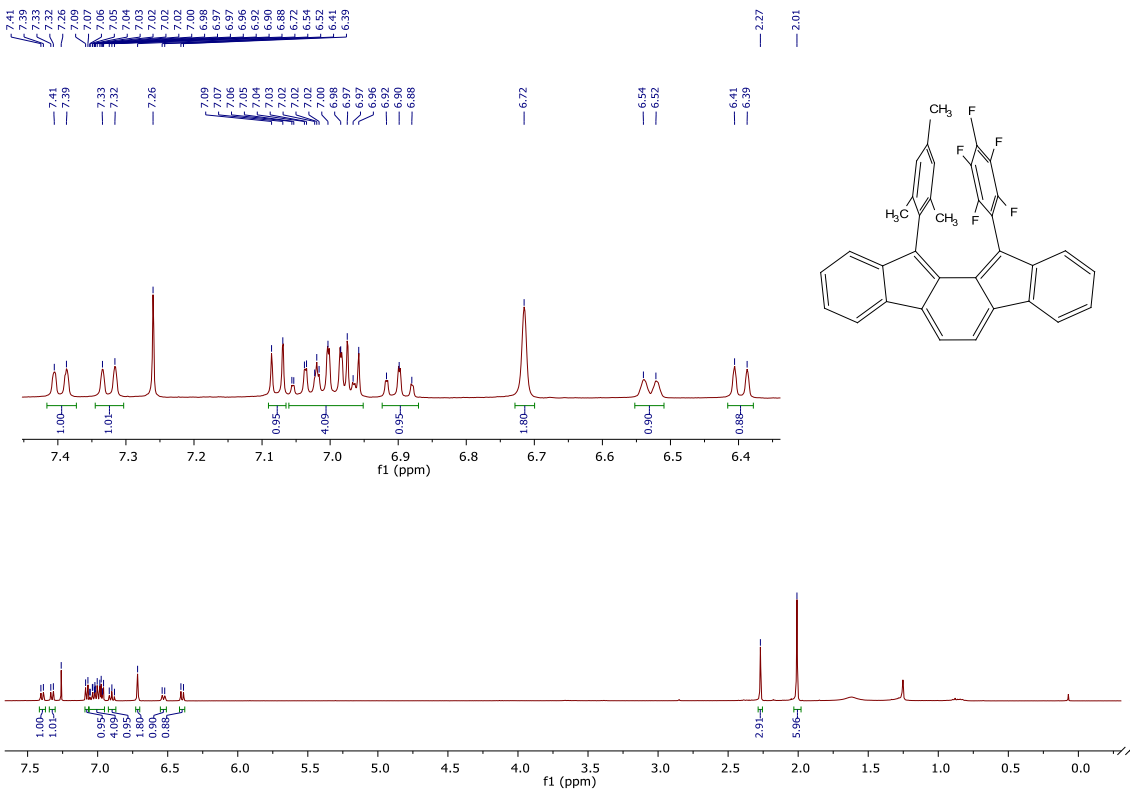

Figure 3.41 ^{1}H NMR spectrum of **6** (in $CDCl_3$, 400 MHz).

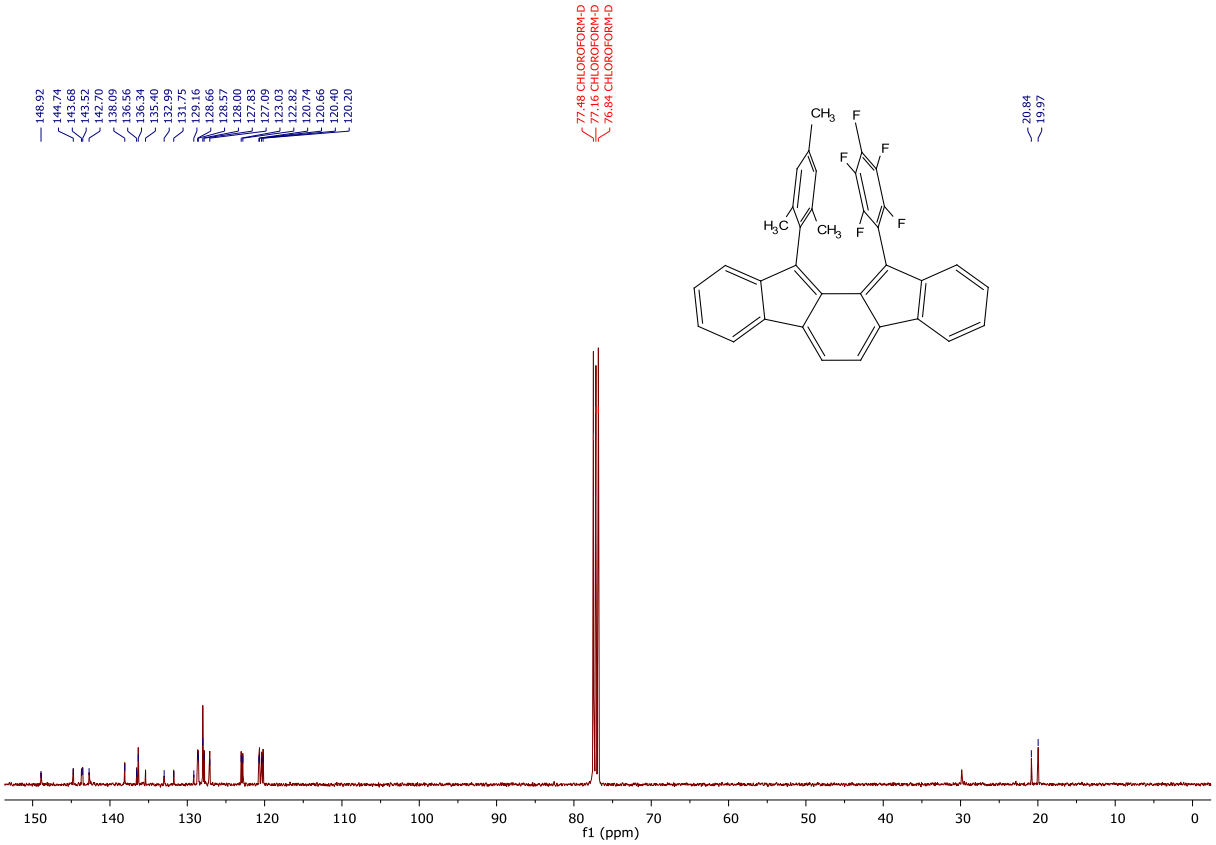

Figure 3.42 ^{13}C NMR spectrum of **6** (in $CDCl_3$, 100 MHz).

Chapter 4

Syntheses and Properties of Hole-Transporting Biindenofluorenes

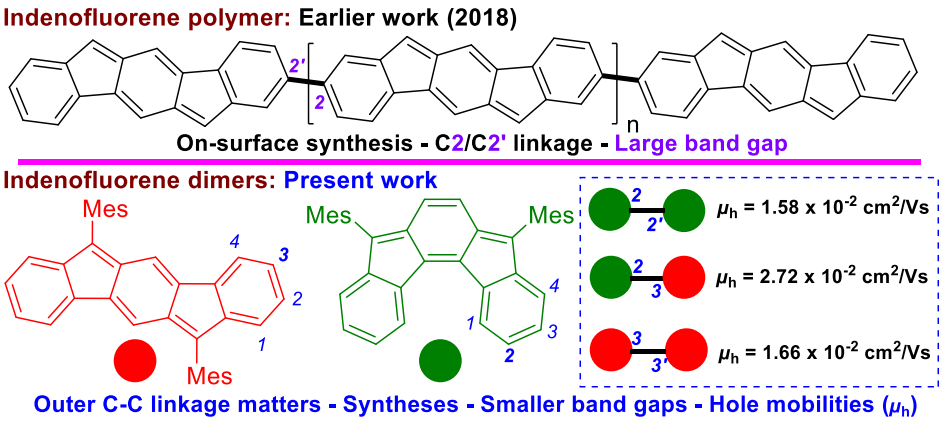

❖ This work was co-authored with Vishal Mittal, who provided synthetic support, Ankita and Dr. Upendra Kumar Pandey, who performed SCLC measurements, Dr. Soumyajit Das, who provided guidance and editorial assistance. This work was originally published in ***Organic Letters***. (Reference: *Org. Lett.* 2024, **26**, 2617–2622)

4.1 Abstract

Described herein is a straightforward approach to synthesizing three biindenofluorene (BIF) derivatives, composed of antiaromatic indenofluorene units, which are the first non-alternant congeners of known bipentacene. Dimerization of indeno[1,2-*b*]fluorene and indeno[2,1-*c*]fluorene units by connecting carbons 3 and 3′ and carbons 2 and 2′, respectively, is shown to influence the highest occupied and lowest unoccupied molecular orbital energy levels of the resulting BIFs, affording band gaps (1.5−1.6 eV) that are smaller than that of a known indenofluorene polymer (2.3 eV). The hole mobilities of BIFs were determined to be $\sim 10^{-2}$ cm^2 V^{-1} s^{-1}

4.2 Introduction

Indeno[1,2-*b*]fluorene ([1,2-*b*]IF) bearing sp^2-hybridized methine bridges at the five-membered rings displays formal 20π antiaromaticity (Figure 4.1a).[1] The antiaromatic character resulted in unique optoelectronic properties,[2] including a smaller highest occupied molecular orbital (HOMO)−lowest unoccupied molecular orbital (LUMO) energy gap compared to that of dihydro[1,2-*b*]IF bearing an sp^3-hybridized methylene bridge.[3] The vulnerability of pentacene to photo and air oxidation[4] has driven the search for a stable pentacene-like topology, offering [1,2-*b*]IF as the first non-alternant analogue of linear acene,[5,6] while four additional constitutional isomers were subsequently synthesized.[7] The π-extended [1,2-*b*]IF-based derivatives have attracted attention in charge-transport[8] and single-molecule conductance[9] studies, in addition to the understanding of antiaromaticity, diradical, and emissive properties.[10]

From the HOMO and LUMO profiles of [1,2-*b*]IF (Figure 4.1a), it is obvious that substituents of different electronic character may modulate its electronic properties when they are attached to the apical carbons.[10a] Thus, the HOMO−LUMO gap of Mes-[1,2-*b*]IF was larger than that of triisopropylethynyl disubstituted TIPS-[1,2-*b*]IF (R = H). Similarly, electronically different substituents at carbons 2 and 8 of the IF backbone (Figure 4.1a) for TIPS-[1,2-*b*]IF exerted a negligible effect on the optoelectronic properties because these positions bear negligible distributions of HOMO and LUMO densities.[8a] This is evident from the reported phenyl versus 3,5-$(CF_3)_2C_6H_3$ disubstituted TIPS-[1,2-*b*]IFs absorbing in identical wavelength regions (570 nm) when compared to that of TIPS-[1,2-*b*]IF (568 nm).[11] Recently, Poly-[1,2-*b*]IF, an IF polymer comprising the [1,2-*b*]IF repeating unit, was synthesized on surface (Figure 4.1b).[12] Despite being a π-conjugated polymer, Poly-[1,2-*b*]IF surprisingly displayed a large band gap (2.3 eV),

and the value is comparable to the monomer's HOMO−LUMO gap.[8a] This indicates that π-extension through carbons 2 and 2′(8) had a negligible effect on its optoelectronic properties likely due to poor electronic communication. Therefore, connecting π-rings by carbons 2 and 8 of [1,2-*b*]IF may not be an ideal design for constructing small band gap IF-based organic semiconductors.

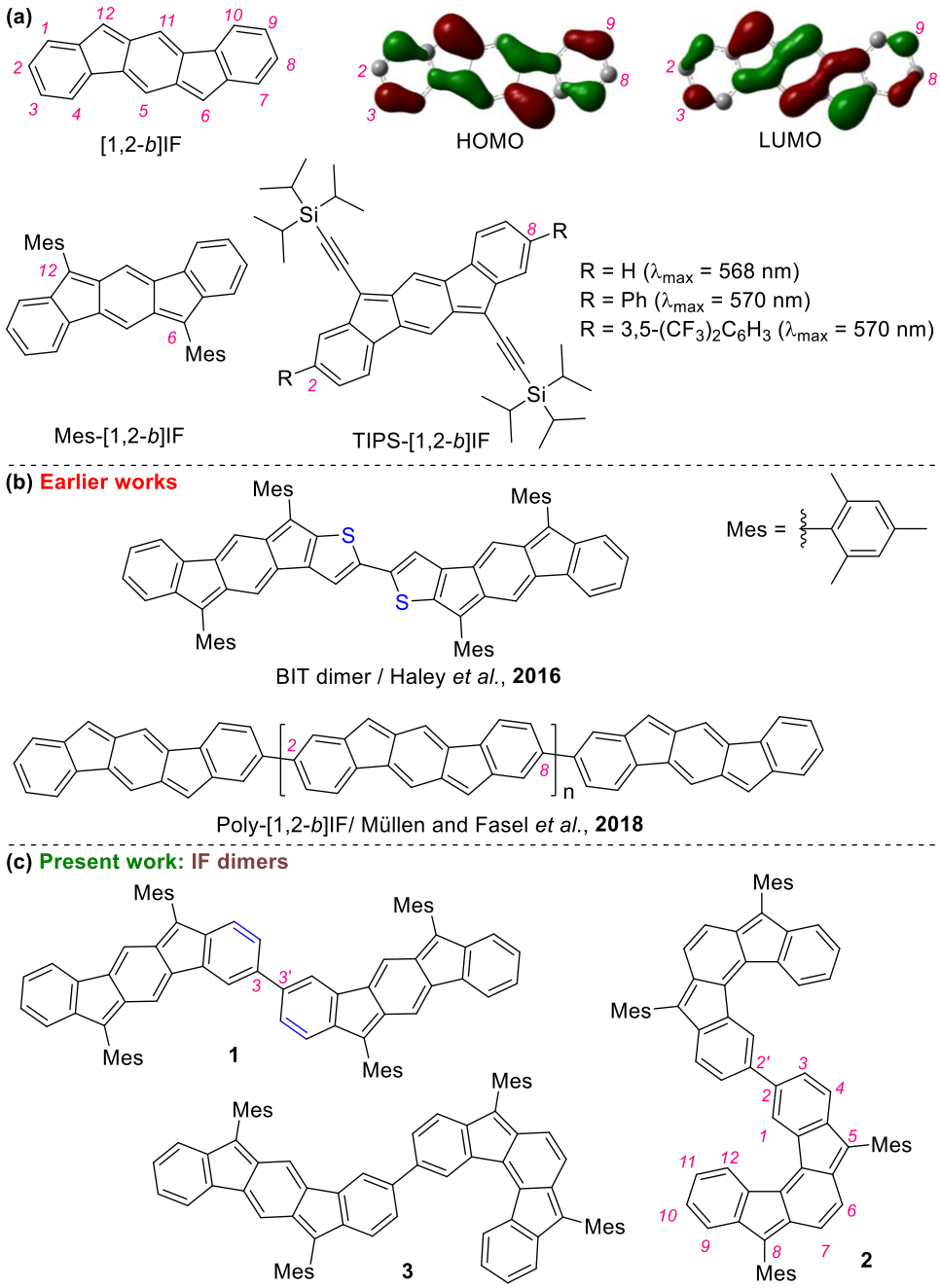

Figure 4.1 (a) Parent indeno[1,2-*b*]fluorene and its HOMO & LUMO profiles, including some substituted indeno[1,2-*b*]fluorenes. (b) Benzo-indaceno-thiophene (BIT) dimer and the on-surface synthesized indenofluorene polymer. (c) Targeted biindenofluorene derivatives **1-3**.

Intrigued by this observation, we revisited the HOMO and LUMO profiles of the parent [1,2-*b*]IF and noticed that positions C3 and C9 of [1,2-*b*]IF contain appreciable HOMO and LUMO coefficients, with the HOMO density being greater at these positions than the LUMO density (Figure 4.1a). Because the syntheses and properties of IF dimers are unknown, while the pentacene dimer (or bipentacene) has been well investigated in singlet-fission studies,[13] we designed of biindenofluorene (BIF) **1** with the monomer units connected through carbons 3 and 3′(9) of [1,2-*b*]IF (Figure 4.1c) to modulate the optoelectronic properties. Notably, an unexpected low-yield synthesis of a benzo-indaceno-thiophene dimer (BIT dimer) was reported by Haley et al. that represents a heterocyclic BIF (Figure 4.1b).[14] BIF **1** may be seen as an isoelectronic carbocyclic analogue of the BIT dimer with a C=C bond (sp^2 carbon unit colored blue) replacing the sulfur atom. 2,2′-Biindeno[2,1-*c*]fluorene **2** was also designed, which is composed of a curved [2,1-*c*]IF unit[7c] in which the IF dimer is connected through carbons 2 and 2′(11) bearing larger HOMO and LUMO coefficients.[15] We further synthesized BIF **3**, a hybrid IF dimer comprising [1,2-*b*]IF and [2,1-*c*]IF units (Scheme 4.1). Because both HOMO and LUMO energy levels were envisaged to be electronically influenced in this design,[16] with the HOMO likely being more destabilized, BIFs **1**−**3** were hypothesized to show a band gap smaller than those of Poly-[1,2-*b*]IF and the corresponding monomers. Herein, we report the first syntheses and characterizations of BIFs **1**−**3**, including their hole-transport properties measured by the space charge limited current (SCLC) method.

4.3 Results and Discussion

4.3.1 Synthesis

Suzuki coupling between commercially available **4** and the requisite fluoreno-pinacolboronates FL^1-Bpin[17] and FL^2-Bpin[18] afforded aldehydes **5** and **6**, respectively. Miyaura borylation of **5** and **6** using bis(pinacolato)diboron, B_2Pin_2, gave **7** and **8** in 95% and 86% yields, respectively. Suzuki reactions between **7** and **5**, **8** and **6**, and **5** and **8** afforded the desired dialdehydes **9** (both R = FL^1), **10** (both R = FL^2), and **11** (R = FL^1 and FL^2 blend), respectively, in moderate to good yields. Subsequent reactions[17] of **9**−**11** with 2-mesitylmagnesium bromide, $BF_3{\cdot}Et_2O$, and DDQ in 1,2-dichloroethane (1,2-DCE) gave BIFs **1**−**3**, respectively, in good yields. The formation of new BIFs **1**−**3** was confirmed by high-resolution mass spectrometry (HRMS) and one- and two-dimensional nuclear magnetic resonance (NMR) spectral analyses (*vide infra*). While

we failed to grow single crystals for **2** and **3**, single crystals of **1** were successfully grown and analyzed by single-crystal X-ray diffraction (SCXRD).

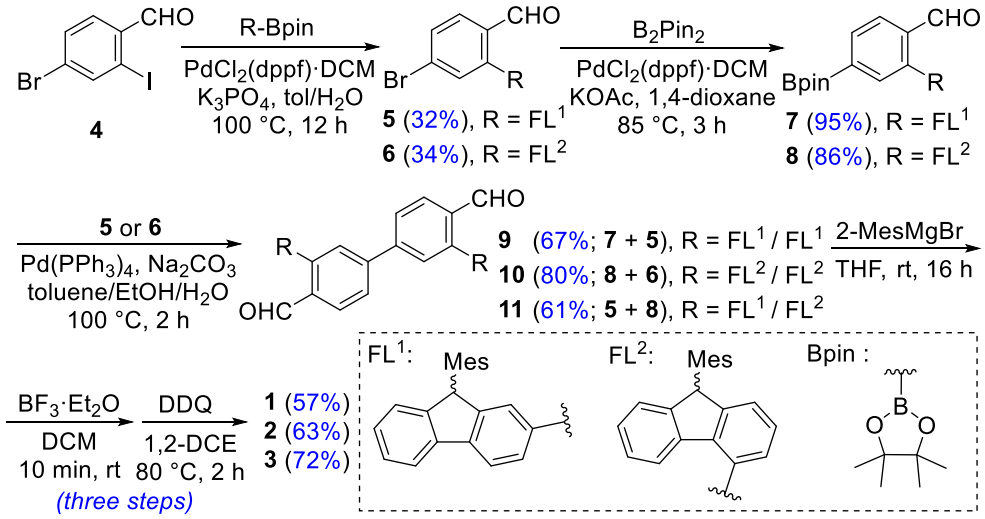

Scheme 4.1 A general synthetic route to BIFs **1**, **2** and **3**.

4.3.2 Single crystal and ground state analysis

SCXRD analysis provided unambiguous confirmation of the formation of **1** (Figure 4.2), strengthening the applicability of our sterically promoted approach to making the [1,2-*b*]IF scaffold.[17] Expectedly, the SCXRD analysis suggested a dibenzo-*s*-indacene dimer with a *para*-quinoidal backbone, and a typical C−C bond length arrangement of a quinoidal[17] fully conjugated [1,2-*b*]IF motif was noted for **1** (*vide infra)*.

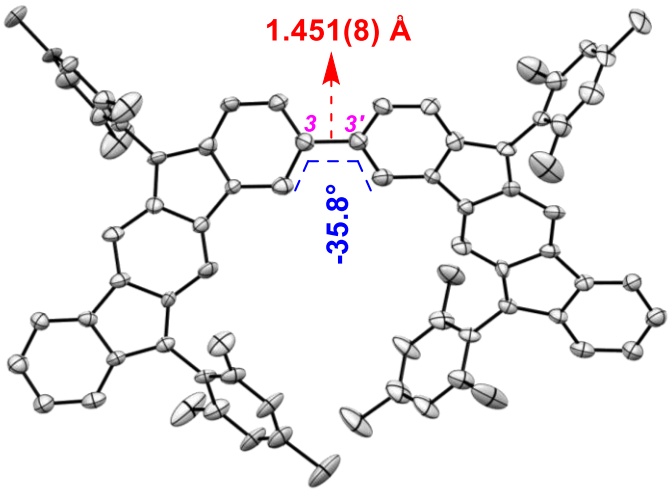

Figure 4.2 ORTEP drawing of **1** with ellipsoids at the 30% probability level (hydrogens omitted).

The C_{sp}^2–C_{sp}^2 single-bond length connecting two [1,2-*b*]IF rings at carbons 3 and 3′(9) is found to be 1.451(8) Å, which is strikingly smaller than the typical C_{sp}^2–C_{sp}^2 single-bond distance connecting two phenyl units of a biphenyl [1.496(3)Å][19] and

matches that of the BIT dimer. Additionally, the torsional angle is 35.8°, which is larger than that of the co-planar BIT dimer (≈0.6°)[14] but apparently smaller than the typical biphenyl torsional angle (≈45°).[20] Such observations clearly suggested greater π-delocalization and electronic communication between two IF units for **1**. Similarly, **2** and **3** would also show greater electronic communication between the two IF units as they are connected through the carbons of the outer benzene rings with appreciable HOMO and LUMO coefficients, as revealed by theoretical bond length analyses (Table 4.11). Density functional theory (DFT) calculations at the B3LYP/6-31G(d,p) level suggested closed-shell ground states for **1**−**3** (Table 4.7-4.9).

4.3.3 Optical and electrochemical properties

Ultraviolet−visible−near-infrared (UV−vis−NIR) analyses (Figure 4.3) suggested that BIF **1** absorbed in the low-energy region at a λ_{max} of 563 nm [ε = 37340 M^{-1} cm^{-1}; TDDFT, $\lambda_{max(TD)}$ = 531nm; oscillator strength (*f*) = 0.4608] that originated from the HOMO−2 → LUMO+1, HOMO−1 → LUMO, and HOMO → LUMO+1 transitions and is 47 nm red-shifted compared to Mes-[1,2-*b*]IF;[8a] however, it is 24 nm blue-shifted compared to the co-planar BIT dimer.[14] The absorption tail extending from 645 to 800 nm may be attributed to several electronic transitions, including the HOMO → LUMO transition [$\lambda_{max(TD)}$ = 686.3 nm; *f* = 0.3856] (Figure 4.3, Table 4.1). The absorption profile of BIF **2** is identical to that of [2,1-*c*]IF, with broad absorption in the low-energy region at a λ_{max} of 632 nm [ε = 7400 M^{-1} cm^{-1}; $\lambda_{max(TD)}$ = 605 nm; *f* = 0.0745] that extends to 850 nm with shoulders around 686 and 765 nm due to the HOMO → LUMO transition [$\lambda_{max(TD)}$ = 802.9 nm; *f* = 0.1074] (Figure 4.3, Table 4.2). The lower-energy absorption of BIF **3** is a blend of [1,2-*b*]IF and [2,1-*c*]IF, absorbing at a λ_{max} of 545 nm [$\lambda_{max(TD)}$ = 517 nm; *f* = 0.3633] with **2**-like shoulders extending in the NIR region (Figure 4.3, Table 4.3).

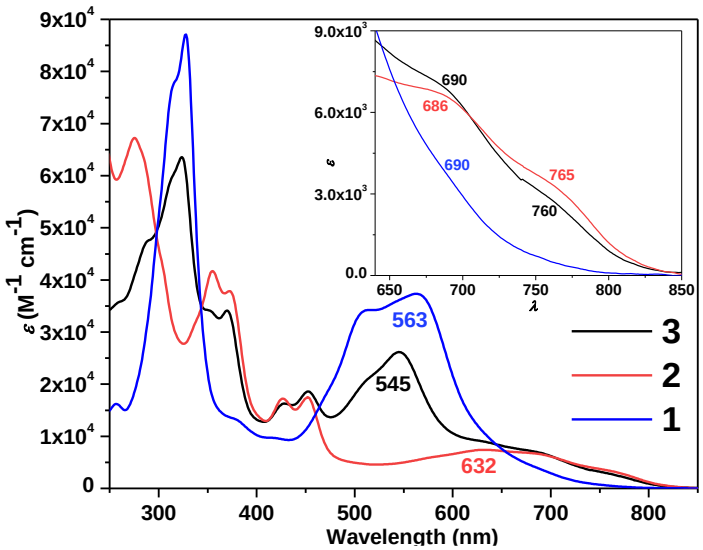

Figure 4.3 UV-vis-NIR spectra of **1-3** in chloroform, with inset showing expansion from 640 to 850 nm region

Table 4.1 Summary of TDDFT calculations of compound **1**.

Wavelength (nm)	Osc. Strength (*f*)	Major contributions
686.3	0.3856	H-2->LUMO (11%), HOMO->LUMO (84%)
643.0	0.0025	H-3->LUMO (16%), H-2->L+1 (17%), H-1->LUMO (26%), HOMO->L+1 (41%)
606.6	0.1054	H-3->L+1 (16%), H-2->LUMO (68%), HOMO->LUMO (14%)
576.4	0.0137	H-3->LUMO (46%), H-2->L+1 (20%), HOMO->L+1 (27%)
531.8	0.4608	H-2->L+1 (11%), H-1->LUMO (60%), HOMO->L+1 (23%)
515.4	0.0747	H-1->L+1 (84%)
486.7	0.2347	H-3->LUMO (35%), H-2->L+1 (52%)
468.6	0.0271	H-3->L+1 (73%), H-2->LUMO (14%), H-1->L+1 (10%)
423.3	0.0307	H-5->L+1 (20%), H-4->LUMO (73%)
422.2	0.0002	H-5->LUMO (71%), H-4->L+1 (16%)
419.7	0.0046	H-7->L+1 (23%), H-6->LUMO (71%)
419.0	0	H-7->LUMO (69%), H-6->L+1 (18%)
399.9	0.0013	H-9->L+1 (16%), H-8->LUMO (83%)
399.9	0.0002	H-9->LUMO (81%), H-8->L+1 (16%)
397.3	0.0001	H-11->L+1 (20%), H-10->LUMO (77%)
397.2	0.0011	H-11->LUMO (79%), H-10->L+1 (19%)
381.4	0.011	H-1->L+3 (12%), HOMO->L+2 (76%)
376.1	0.0062	H-1->L+2 (19%), HOMO->L+3 (75%)
374.1	0.0497	H-12->LUMO (69%)
369.8	0.0053	H-6->L+1 (12%), H-5->LUMO (21%), H-4->L+1 (66%)

Table 4.2. Summary of TDDFT calculations of compound **2**.

Wavelength (nm)	Osc. Strength (*f*)	Major contributions
802.9	0.1074	HOMO->LUMO (93%)
724.8	0.0983	HOMO->L+1 (89%)
665.8	0.0515	H-1->LUMO (89%)
605.1	0.0745	H-1->L+1 (90%)
475.5	0.0567	H-4->LUMO (55%), H-3->LUMO (29%)
458.3	0.068	H-2->LUMO (76%)
454.4	0.0357	H-4->LUMO (13%), H-4->L+1 (17%), H-3->LUMO (24%), H-3->L+1 (16%)
446.6	0.1669	H-4->LUMO (13%), H-3->LUMO (29%), H-3->L+1 (23%)
434.2	0.0808	H-2->L+1 (63%)
428.8	0.0188	H-7->LUMO (14%), H-6->LUMO (32%), H-5->LUMO (24%)
424.6	0.0046	H-8->LUMO (63%), H-8->L+1 (11%)
422.0	0.0237	H-6->LUMO (22%), H-6->L+1 (14%), H-5->LUMO (23%), H-5->L+1 (15%), H-3->L+1 (13%)
421.1	0.0122	H-7->LUMO (44%), H-7->L+1 (24%)
418.6	0.0267	H-4->L+1 (49%)
403.9	0.0009	H-11->LUMO (57%), H-11->L+1 (12%), H-9->LUMO (15%)
402.8	0.0003	H-12->LUMO (72%), H-12->L+1 (15%)
401.9	0.0013	H-11->LUMO (15%), H-9->LUMO (41%), H-9->L+1 (23%)
399.9	0.0016	H-13->LUMO (21%), H-10->LUMO (41%), H-10->L+1 (19%)
399.1	0.0028	H-13->LUMO (43%), H-10->LUMO (19%), H-10->L+1 (11%)
388.1	0.0713	H-13->L+1 (20%), H-5->L+1 (25%), HOMO->L+2 (26%)

Table 4.3. Summary of TDDFT calculations of compound **3**.

Wavelength (nm)	Osc. Strength (*f*)	Major contributions
765.1	0.3268	HOMO->LUMO (84%)
663.1	0.0786	HOMO->L+1 (70%)
601.2	0.0509	H-2->LUMO (24%), H-1->LUMO (54%)
597.3	0.1729	H-2->LUMO (34%), H-2->L+1 (19%), H-1->LUMO (21%), HOMO->L+1 (12%)
517.4	0.3633	H-1->L+1 (79%)
505.2	0.0284	H-2->LUMO (29%), H-2->L+1 (60%)
452.6	0.1076	H-4->LUMO (24%), H-3->LUMO (50%)

445.2	0.0914	H-4->LUMO (50%), H-4->L+1 (14%), H-3->LUMO (23%)
427.7	0.014	H-5->LUMO (76%), H-5->L+1 (18%)
423.6	0.001	H-6->LUMO (67%), H-6->L+1 (32%)
421.5	0.0203	H-8->L+1 (11%), H-7->LUMO (74%)
418.7	0.0046	H-8->LUMO (64%), H-8->L+1 (15%), H-7->L+1 (10%)
411.7	0.0191	H-3->LUMO (10%), H-3->L+1 (79%)
403.1	0.0004	H-9->LUMO (82%), H-9->L+1 (18%)
401.4	0.0005	H-10->LUMO (83%), H-10->L+1 (16%)
399.2	0.0005	H-11->LUMO (71%), H-11->L+1 (27%)
397.3	0.0016	H-12->LUMO (72%), H-12->L+1 (26%)
391.0	0.0404	H-4->LUMO (15%), H-4->L+1 (67%)
380.4	0.0137	H-1->L+2 (23%), HOMO->L+2 (72%)
373.9	0.0003	H-8->L+1 (11%), H-6->LUMO (26%), H-6->L+1 (54%)

Table 4.4 Photophysical and electrochemical data of BIFs **1–3**.

Compound	$E_{1/2}^{\mathrm{ox}}$ [V]	$E_{1/2}^{\mathrm{red}}$ [V]	HOMO [eV]	LUMO [eV]	$\lambda_{\max}$ [nm]	$E_{\mathrm{g}}^{\mathrm{opt}}$ [eV]	$E_{\mathrm{g}}^{\mathrm{DFT}}$ [eV]
1	0.41 0.62	–1.60 –1.65	–5.11	–3.37	563	1.60	2.06
2	0.34 0.53	–1.55 –1.62	–5.06	–3.44	632	1.50	1.96
3	0.38 0.60	–1.55 –1.66	–5.10	–3.43	545	1.52	2.00

The observations clearly suggest an improved electronic communication between two IF units for the new BIFs. The optical HOMO−LUMO energy gaps, roughly estimated from the absorption onset, of BIFs **1**−**3** were 1.60, 1.50, and 1.52 eV, respectively (Table 4.4). As hypothesized, the HOMO−LUMO energy gaps are remarkably smaller for IF dimers than for the reported IF polymer (band gap of 2.3 eV),[12] demonstrating greater π-delocalization in BIFs. This further suggests that oligomerization/polymerization by linking the appropriate carbon atoms of the outer benzene rings for an IF unit is essential for achieving small band gap IF-based organic semiconductors. The BIFs were non-emissive to the naked eye, like the monomers.[2]

Unlike the monomer counterparts, BIFs **1**−**3** were reversibly oxidized to the radical cation ($E_{1/2}^{\mathrm{ox1}}$; 0.41 V for **1**, 0.34 V for **2**, and 0.38 V for **3**, *vs* Fc/Fc^{+} in dichloromethane) and dication ($E_{1/2}^{\mathrm{ox2}}$; 0.62 V for **1**, 0.53 V for **2**, and 0.60 V for **3**) states

in a cyclic voltammetry (CV) experiment (Figure 4.4), implying the stability of the charged species presumably due to extended delocalization (Figure 4.5).

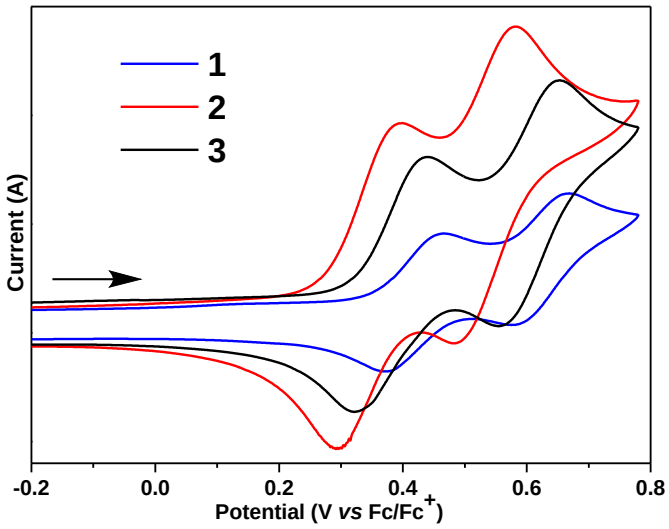

Figure 4.4 CVs of **1**-**3** showing the reversible two-electron oxidations.

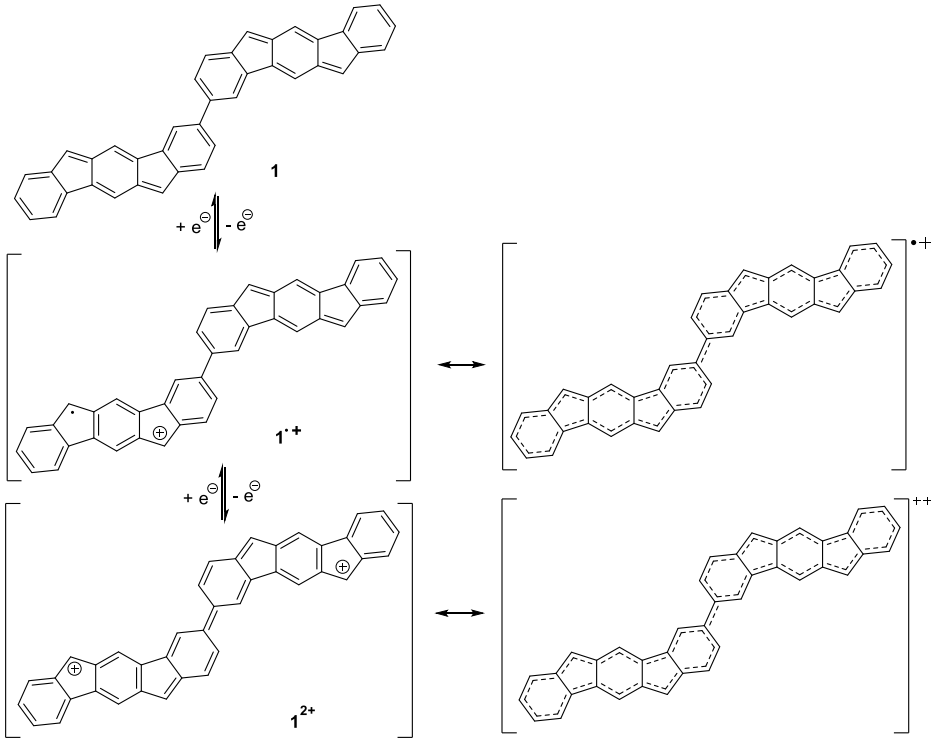

Figure 4.5 Highly delocalized radical cation and dication structures explaining the excellent reversibility of first and second oxidation waves. Parent **1** is drawn as representative example, and the same logic applies for **2** and **3**.

However, all of the BIFs are sufficiently stable for months as solids. Similar to the monomer counterparts, the BIFs can be reversibly reduced to the radical anion ($E_{1/2}^{red1}$; −1.60 V for **1**, −1.55 V for **2**, and −1.55 V for **3**) and dianionic ($E_{1/2}^{red2}$; −1.65 V for **1**, −1.62 V for **2**, and −1.66V for **3**) states (Table 4.4, Figure 4.16). The HOMO and

LUMO energy levels of **1**−**3** were −5.11 and −3.37 eV, − 5.06 and −3.44 eV, and −5.10 and −3.43 eV, respectively, as estimated from the onset potentials of the oxidation/reduction waves, affording electrochemical energy gaps of 1.74, 1.62, and 1.67 eV for **1**−**3**, respectively, that agree with the trend observed for optical and theoretical energy gaps (Table 4.4). Notably, BIF counterparts **1a**−**3a** (Figures 4.13−4.15) of **1**−**3**, respectively, that are linked through carbons 2 and 2′, carbons 3 and 3′, and carbons 2 and 3 of the[1,2-*b*]IF, [2,1-*c*]IF, and [1,2-*b*]IF/[2,1-*c*]IF units with low HOMO and LUMO orbital distributions displayed 0.33, 0.20, and 0.21 eV larger HOMO−LUMO energy gaps, respectively, as determined by DFT calculations.

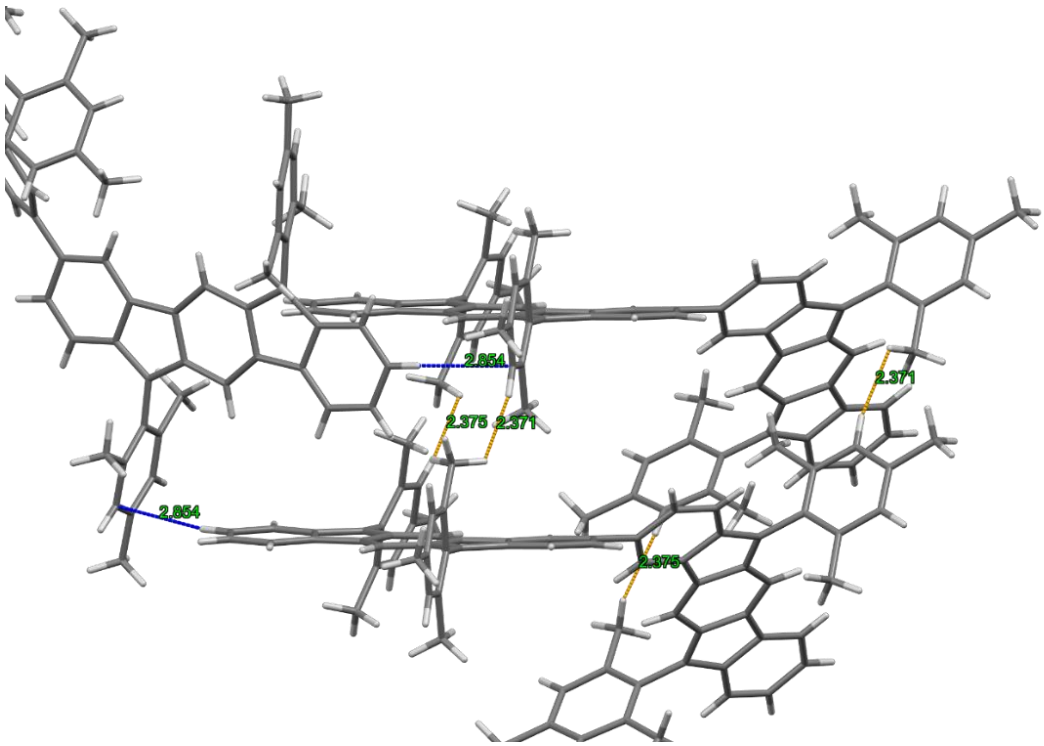

Figure 4.6 The non-covalent [C–H···π] (2.854 Å) and [C–H···H] (2.375/2.371 Å) interactions observed for **1** in the herringbone-type packing motif.

4.3.4 SCLC studies

The presence of C−H···π short contacts in a herringbone-type solid-state packing of **1** (Figure 4.6), suitably positioned HOMO energy levels[21] of dimers **1**−**3** compared to those of the corresponding IF monomers, and the excellent reversibility during two-stage oxidation processes of the BIFs prompted us to investigate their potential as hole transporters. The hole mobility values of BIFs **1**−**3** were extracted from the SCLC technique in the hole only device configuration. Hole only devices were fabricated in

the ITO/Ag/MoO3/BIFs **1**−**3**/MoO3/Ag configuration. For detailed fabrication and characterization steps, *see section 4.6.5.*

The HOMO energy level of BIFs **1**−**3** when they were used with the ITO/Ag/MoO3 injecting electrode provides an ohmic contact for hole only devices, one of the prerequisites for the SCLC technique in which it serves as an infinite reservoir of charge.[22] The SCLC mobility of the thin film was determined by fitting the characteristic *J*−*V* data using the modified Mott−Gurney equation given by (eq 1)[23]

$$J = \frac{9}{8}\mu\varepsilon_r\varepsilon_o\frac{(V-V_{bi})^2}{d^3}\exp\left(0.891\gamma\sqrt{\frac{(V-V_{bi})}{d}}\right) \qquad (1)$$

where J is the measured current density (device area of 6.6 mm^2), ε_o is the permittivity of free space, ε_r is the relative dielectric constant of the material, V is the applied voltage, V_{bi} is the built-in potential, d is the thickness of the compound, μ is the mobility, and γ is the fitting parameter representing the strength of the field dependence on mobility. The measured hole mobilities for BIFs **1**−**3** are summarized in Table 4.5 [an average of at least the five best devices (Table 4.12)].

Table 4.5 Measured SCLC mobility ($cm^2 \cdot V^{-1} \cdot s^{-1}$) of BIFs **1**–**3**.

BIFs	1	2	3
Hole mobility ($\times 10^{-2}$)	1.66 ± 0.41	1.58 ± 0.20	2.72 ± 1.17

Semilog fitted *J*−*V* characteristics for **1**−**3** are shown in Figure 4.7, where the hole mobility was extracted from the linear part of the fitted curve. We observed that all of the BIFs reported in this work have similar hole mobilities, which is obvious because their HOMO levels are identical for the hole only devices.

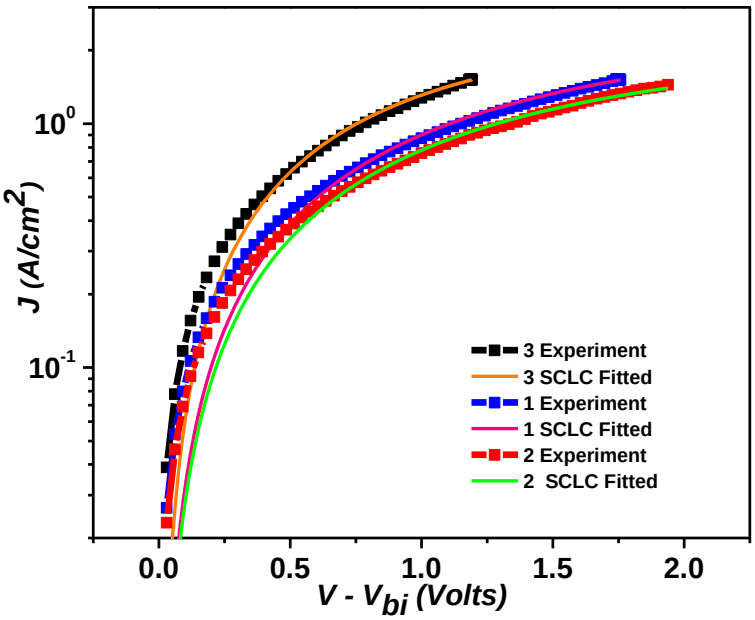

Figure 4.7 *J–V* characteristics in the semi-log plot used for extracting hole mobility using modified the Mott–Gurney SCLC equation for BIFs **1**, **2** and **3**. V_{bi} = 0 V, as both injecting electrode as well as counter electrodes are same (ITO/Ag/MoO_3).

4.4 Conclusions

In conclusion, we report the syntheses and characterizations of IF dimers **1**−**3** with improved optoelectronic properties and HOMO−LUMO energy gaps smaller than the band gaps of related IF oligomers or polymers.[12,24] Compared to that of 2,2′-bipentacene,[13a] the HOMO levels of BIFs **1**−**3** are stabilized while the HOMO−LUMO energy gaps remain nearly identical. Charge-carrier mobility data revealed hole mobilities on the order of 10^{-2} cm^2 V^{-1} s^{-1} for thin films of BIFs **1**−**3**, which are the first of their kind reported in this work and are 1−2 orders of magnitude higher than those of the corresponding monomers.[8a,15] SCXRD analysis of **1** revealed a shortened C−C single-bond length connecting two [1,2-*b*]IFs, which suggested greater electronic communication between two IF units when they are linked through carbons 3 and 3′ of[1,2-*b*]IF. Our study further suggested that carbons 2 and 2′ of[2,1-*c*]IF should be the preferred choice for oligomerization/polymerization. With the presented synthetic approach, it is possible to synthesize newer arrays of IF dimers and oligomers, including ethynyl/aryl/heteroaryl π-spacers with tuneable bandgaps, thus unlocking the gateway to antiaromatic IF dimers as nonbenzenoid congeners of pentacene dimers for potential application in organic optoelectronics.

4.5 Experimental section

4.5.1 General information

Chemicals and reagents were purchased from commercial suppliers (Merck, GLR innovations, BLDpharm, Spectrochem) and used without further purification. Thin layer chromatography (TLC) was performed using pre-coated silica-plates purchased from Merck (silica gel 60 PF254, 0.25 mm). Column chromatography was performed using silica gel 100-200 mesh. NMR spectra were recorded in $CDCl_3$ at room temperature, on JEOL JNM-ECS400 spectrometer at operating frequencies of 400 MHz (^1H) or 100 MHz (^{13}C) as indicated in the individual spectrum. Chemical shifts (δ) are given in ppm relative to residual solvent (chloroform δ = 7.26 for ^1H, and δ = 77.16 for proton-decoupled ^{13}C NMR), and coupling constants (*J*) are expressed in hertz (Hz). Multiplicity is tabulated as s for singlet, d for doublet, dd for doublet of doublet, t for triplet, q for quartet and m for multiplet. Structural assignments were made with additional information from gCOSY, and gNOESY experiments. High-resolution mass spectra (HRMS) were recorded using electron spray ionization (ESI) methods on Waters (XEVO G2-XS QTOF) mass spectrometer. UV-vis-NIR spectra were recorded in JASCO V-770 spectrophotometer. Cyclic voltammetry measurements of **1-3** (0.001 M) were performed using an electrochemical analyzer potentiostat model CHI-1115C from CH Instruments with a conventional three-electrode cell at 298 K under a nitrogen atmosphere at a scan rate of 50 mV/s. This electrochemical cell contains a platinum (Pt) disk (disk shaped with 2-mm diameter) as a working electrode, Pt wire as a counter electrode, and silver (Ag) wire as a pseudo-reference electrode. The Pt working electrode was polished with 1.0 micron α-alumina polishing powder in a figure-eight motion. Electrolyte solution (0.1 M) was prepared by dissolving tetrabutylammonium hexafluorophosphate (Bu_4NPF_6) in 5 mL dry dichloromethane (DCM). The DCM solution was degassed by bubbling nitrogen gas for 10 minutes prior to measurements. The direction of initial scan was chosen as reductive, with the initial potential values set at zero for all and switching between negative potential (**1**: –2.0 V, **2**: –1.8 V, **3**: –1.8 V) first, and then going to positive potential (1.2 V for all), and finally returning to zero (*vs* Ag wire). The potential was externally calibrated against the ferrocene/ferrocenium (Fc/Fc^+) couple (0.42 V) and reported herein. Melting points were determined using Cole-Parmer MP 250D-P melting point analyzer. Compound **4** (CAS No.: 1261470-87-4) was purchased from BLDpharm.

4.5.2 Synthesis

General procedure A for synthesis of compounds 5 and 6. An oven-dried thick-walled glass tube was charged with **4**, requisite boronic acid ester FL-Bpin (FL^1-Bpin for **5**, and FL^2-Bpin for **6**), K_3PO_4, and toluene/H_2O (9:1). The solution was purged with N_2 for 30 min. After adding $PdCl_2$(dppf)·DCM to the solution under N_2 atmosphere, the vial was sealed and the resulting mixture was heated at 100 °C using an oil bath for 12 h. After being cooled to room temperature, water was added and the resultant mixture was extracted with DCM (3 x 50 mL). The organic phase was dried over Na_2SO_4, and evaporated under reduced pressure. The residue was purified by column chromatography to give the desired product.

4-bromo-2-(9-mesityl-9H-fluoren-2-yl)benzaldehyde (5). Compound **4** (1 g, 3.22 mmol) and 2-(9-mesityl-9H-fluoren-2-yl)-4,4,5,5-tetramethyl-1,3,2-dioxaborolane (1.32 g, 3.22 mmol) were reacted in the presence of $PdCl_2$(dppf)·DCM (131 mg, 5 mol%) and K_3PO_4 (3.41 g, 16.08 mmol) in toluene/H_2O (9 mL/1 mL) according to general procedure A. The obtained material was subjected to column chromatography (SiO_2, CH_2Cl_2/hexane 45:100) to give aldehyde **5** as a white solid. (486 mg, 32% yield): R_f = 0.55 (10% EtOAc/hexanes); **mp**: 171-172°C; **^{1}H NMR** (400 MHz, $CDCl_3$) δ 9.90 (s, 1H), 7.93 (d, *J* = 7.8 Hz, 1H), 7.89 (d, *J* = 7.5 Hz, 1H), 7.85 (d, *J* = 8.0 Hz, 1H), 7.61 (d, *J* = 1.9 Hz, 1H), 7.59 (dd, *J* = 8.3, 2.1 Hz, 1H), 7.47 – 7.40 (m, 1H), 7.37 (dd, *J* = 8.1, 1.7 Hz, 1H), 7.34 – 7.28 (m, 1H), 7.27 (s, 1H), 7.24 (d, *J* = 7.1 Hz, 1H), 7.02 (d, *J* = 2.0 Hz, 1H), 6.67 (d, *J* = 1.9 Hz, 1H), 5.56 (s, 1H), 2.68 (s, 3H), 2.27 (s, 3H), 1.14 (s, 3H); **^{13}C{^{1}H} NMR** (100 MHz, $CDCl_3$) δ 191.5, 147.9, 147.7, 147.6, 141.5, 139.9, 137.8, 137.7, 136.7, 135.1, 133.7, 133.2, 132.5, 131.1, 131.0, 130.7, 129.2, 129.1, 128.6, 128.0, 127.2, 125.4, 124.4, 120.5, 120.1, 49.8, 21.9, 20.9, 18.9; **HRMS** (ESI) *m/z*: [M + H]$^+$ calcd for $C_{29}H_{24}OBr$ 467.1011, found 467.1001 (error: -2.1 ppm).

4-bromo-2-(9-mesityl-9H-fluoren-4-yl)benzaldehyde (6). Compound **4** (1.5 g, 4.82 mmol) and 2-(9-mesityl-9H-fluoren-4-yl)-4,4,5,5-tetramethyl-1,3,2-dioxaborolane (1.98 g, 4.82 mmol) were reacted in the presence of $PdCl_2$(dppf)·DCM (197 mg, 5 mol%) and K_3PO_4 (5.12 g, 24.12 mmol) in toluene/H_2O (9 mL/1 mL) according to general procedure A. The obtained material was subjected to column chromatography (SiO_2, CH_2Cl_2/hexane 45:100) to give aldehyde **6** as a white solid. (757 mg, 34% yield): R_f = 0.55 (10% EtOAc/hexanes); **mp**: 92-93 °C; **^{1}H NMR** (400 MHz, $CDCl_3$) δ 9.79-9.71 (m, 1H), 8.01 (dd, *J* = 8.3, 1.9 Hz, 1H), 7.79 (dd, *J* = 8.3, 2.0 Hz, 1H), 7.70 (dd, *J* = 10.9, 1.9 Hz, 1H), 7.34 – 7.29 (m, 2H), 7.24 – 7.14 (m, 3H), 7.10 – 7.02 (m, 2H), 6.68

(d, J = 2.4 Hz, 1H), 6.62 (dd, J = 7.7, 3.3 Hz, 1H), 5.53 (s, 1H), 2.70 (s, 3H), 2.30 – 2.29 (m, 3H), 1.13-1.11 (m, 3H); **^{13}C{^{1}H} NMR** (100 MHz, $CDCl_3$) δ 191.2, 190.9, 148.1, 147.9, 146.4, 139.7, 139.0, 138.9, 137.9, 137.8, 137.7, 137.6, 136.6, 134.0, 133.8, 133.6, 133.5, 133.0, 132.9, 132.0, 131.0, 130.8, 130.7, 129.5, 129.2, 129.0, 128.9, 127.6, 127.0, 124.6, 124.4, 122.3, 49.7, 49.6, 21.9, 21.0, 18.9, 18.7; **HRMS** (ESI) *m/z*: $[M + H]^+$ calcd for $C_{29}H_{24}OBr$ 467.1011, found 467.1008 (error: -0.6 ppm).

General procedure B for synthesis of compounds 7-8. In a sealed glass vial, compound **5**/**6**, B_2Pin_2 (4,4,4',4',5,5,5',5'-octamethyl-2,2'-bi(1,3,2-dioxaborolane)), and KOAc, dry 1,4-dioxane, were added and the solution was purged with N_2 for 30 min. $PdCl_2$(dppf)·DCM was then added to the solution, the vial was sealed and the resulting mixture was warmed at 85 °C using an oil bath for 3 h. After completion of reaction, water was added and the resultant mixture was extracted with DCM (3 x 50 mL). The organic phase was dried over Na_2SO_4, and evaporated under reduced pressure. The residue was purified by column chromatography to give the desired product.

2-(9-mesityl-9H-fluoren-2-yl)-4-(4,4,5,5-tetramethyl-1,3,2-dioxaborolan-2-yl)benzaldehyde (7). Compound **5** (277 mg, 0.592 mmol) and B_2Pin_2 (301 mg, 1.19 mmol) were reacted in the presence of $PdCl_2$(dppf)·DCM (48 mg, 10 mol%) and KOAc (174 mg, 1.78 mmol) in dry 1,4-dioxane (5 mL) according to general procedure B. The obtained material was subjected to column chromatography (SiO_2, EtOAc/hexane 10:100) to give aldehyde **7** as a white solid. (289 mg, 95% yield): $\boldsymbol{R_f}$ = 0.24 (10% EtOAc/hexanes); **mp**: 80-81 °C; **^{1}H NMR** (400 MHz, $CDCl_3$): δ 9.96 (s, 1H), 7.97 (d, J = 7.8 Hz, 1H), 7.91 (d, J = 7.9 Hz, 2H), 7.88 (d, J = 3.4 Hz, 2H), 7.42 (dt, J = 8.0, 6.7 Hz, 2H), 7.29 (d, J = 7.2 Hz, 1H), 7.25 (d, J = 7.2 Hz, 1H), 7.00 (d, J = 1.9 Hz, 1H), 6.66 (d, J = 1.9 Hz, 1H), 5.55 (s, 1H), 2.68 (s, 3H), 2.26 (s, 3H), 1.36 (s, 12H), 1.14 (s, 3H); **^{13}C{^{1}H} NMR** (100 MHz, $CDCl_3$): δ 192.8, 147.6, 147.6, 145.3, 140.9, 140.3, 137.8, 137.1, 136.8, 136.5, 135.6, 133.8, 133.5, 130.7, 129.3, 129.0, 127.7, 127.1, 126.5, 125.8, 124.3, 120.4, 119.9, 84.4, 49.9, 25.0, 21.9, 20.9, 18.9; **HRMS** (ESI) *m/z*: $[M + H]^+$ calcd for $C_{35}H_{36}BO_3$ 515.2758, found 515.2762 (error: 0.8 ppm).

2-(9-mesityl-9H-fluoren-4-yl)-4-(4,4,5,5-tetramethyl-1,3,2-dioxaborolan-2-yl)benzaldehyde (8). Compound **6** (300 mg, 0.641 mmol) and B_2Pin_2 (326 mg, 1.28 mmol) were reacted in the presence of $PdCl_2$(dppf)·DCM (52 mg, 10 mol%) and KOAc (189 mg, 1.93 mmol) in dry 1,4-dioxane (5 mL) according to general procedure B. The obtained material was subjected to column chromatography (SiO_2, EtOAc/hexane 10:100) to give aldehyde **8** as a white solid. (283 mg, 86% yield): $\boldsymbol{R_f}$ = 0.24 (10%

EtOAc/hexanes); **mp**: 191-192 °C; **^{1}H NMR** (400 MHz, $CDCl_3$): δ 9.87 – 9.82 (m, 1H), 8.13 (dd, *J* = 7.8, 4.8 Hz, 1H), 8.07 (dd, *J* = 7.8, 3.5 Hz, 1H), 7.96 (d, *J* = 11.1 Hz, 1H), 7.35 – 7.27 (m, 2H), 7.24 (dd, *J* = 6.9, 2.0 Hz, 1H), 7.21 – 7.16 (m, 1H), 7.14 (dt, *J* = 7.5, 3.7 Hz, 1H), 7.05 (s, 1H), 7.03 – 6.97 (m, 1H), 6.69 (s, 1H), 6.55 (dd, *J* = 7.5, 2.0 Hz, 1H), 5.55-5.53 (m, 1H), 2.71 (s, 3H), 2.30 (s, 3H), 1.42 – 1.34 (m, 12H), 1.15 – 1.14 (m, 3H); **^{13}C{^{1}H} NMR** (100 MHz, $CDCl_3$): δ 192.6, 192.3, 147.9, 147.8, 147.7, 143.9, 140.2, 140.1, 139.1, 137.9, 137.8, 137.7, 137.4, 136.9, 136.5, 136.0, 135.8, 134.7, 134.5, 133.8, 132.8, 130.8, 130.6, 129.4, 129.3, 129.0, 127.3, 126.9, 126.8, 126.3, 126.1, 124.2, 124.0, 123.9, 122.6, 122.5, 84.5, 49.6, 25.1, 24.9, 21.9, 21.0, 19.0, 18.7; **HRMS** (ESI) *m/z*: $[M + H]^+$ calcd for $C_{35}H_{36}BO_3$ 515.2758, found 515.2766 (error: 1.6 ppm).

General procedure C for synthesis of compounds 9-11. A solution of **5**/**6**, boronic acid ester **7**/**8**, and Na_2CO_3 in toluene/EtOH/H_2O (95:5:5) was purged with N_2 for 30 min. $Pd(PPh_3)_4$ was then added to the solution, and the resulting mixture was heated at 100 °C using an oil bath for 2 h in a sealed glass vial. After being cooled to room temperature, water was added and the resultant mixture was extracted with DCM (3 x 50 mL). The organic phase was dried over Na_2SO_4, and evaporated under reduced pressure. The residue was purified by column chromatography to give the desired product.

3,3'-bis(9-mesityl-9H-fluoren-2-yl)-[1,1'-biphenyl]-4,4'-dicarbaldehyde (9). Compound **5** (180 mg, 0.384 mmol) and **7** (198 mg, 0.384 mmol) were reacted in the presence of $Pd(PPh_3)_4$ (13 mg, 0.03 equiv.) and Na_2CO_3 (245 mg, 2.31 mmol) in toluene/EtOH/H_2O (4.5 mL/0.5 mL/0.5 mL) according to general procedure C. The obtained material was subjected to column chromatography (SiO_2, CH_2Cl_2/hexane 70:100) to give dialdehyde **9** as a yellow solid. (201 mg, 67% yield): $\boldsymbol{R_f}$ = 0.35 (10% EtOAc/hexanes); **mp**: 160-161°C; **^{1}H NMR** (400 MHz, $CDCl_3$): δ 9.98 (s, 2H), 8.09 (d, *J* = 7.9 Hz, 2H), 7.95 (d, *J* = 7.7 Hz, 2H), 7.90 (d, *J* = 7.6 Hz, 2H), 7.73 (dd, *J* = 8.0, 1.8 Hz, 2H), 7.69 (d, *J* = 1.8 Hz, 2H), 7.44 (t, *J* = 7.8 Hz, 4H), 7.31 (t, *J* = 7.4 Hz, 2H), 7.27 (d, *J* = 2.6 Hz, 3H), 7.25 (s, 1H), 6.99 (d, *J* = 2.0 Hz, 2H), 6.65 (d, *J* = 1.8 Hz, 2H), 5.57 (s, 2H), 2.67 (s, 6H), 2.25 (s, 6H), 1.14 (s, 6H); **^{13}C{^{1}H} NMR** (100 MHz, $CDCl_3$): δ 192.0, 147.9, 147.6, 146.9, 144.7, 141.3, 140.1, 137.8, 137.7, 136.6, 136.4, 133.4, 133.3, 130.7, 129.9, 129.1, 129.0, 128.4, 127.9, 127.2, 126.8, 125.7, 124.4, 120.5, 120.1, 49.9, 29.8, 21.9, 20.9, 18.9; **HRMS** (ESI) *m/z*: $[M + H]^+$ calcd for $C_{58}H_{47}O_2$ 775.3576, found 775.3586 (error: 1.3 ppm).

3,3'-bis(9-mesityl-9H-fluoren-4-yl)-[1,1'-biphenyl]-4,4'-dicarbaldehyde (10). Compound **6** (184 mg, 0.394 mmol) and **8** (203 mg, 0.394 mmol) were reacted in the presence of $Pd(PPh_3)_4$ (14 mg, 0.03 equiv.) and Na_2CO_3 (251 mg, 2.37 mmol) in toluene/EtOH/H_2O (4.5 mL/0.5 mL/0.5 mL) according to general procedure C. The obtained material was subjected to column chromatography (SiO_2, CH_2Cl_2/hexane 70:100) to give dialdehyde **10** as a yellow solid. (246 mg, 80% yield): $\boldsymbol{R_f}$ = 0.35 (10% EtOAc/hexanes); **mp**: 54-55°C; **^{1}H NMR** (400 MHz, $CDCl_3$): δ 9.94 – 9.79 (m, 2H), 8.31 – 8.21 (m, 2H), 8.06 – 7.93 (m, 2H), 7.94 – 7.78 (m, 2H), 7.42 – 7.27 (m, 6H), 7.17 (m, 4H), 7.07 – 6.93 (m, 4H), 6.69 (tt, *J* = 8.0, 4.7 Hz, 4H), 5.57 – 5.53 (m, 2H), 2.77 – 2.62 (m, 6H), 2.30 (s, 6H), 1.20 – 1.05 (m, 6H); **^{13}C{^{1}H} NMR** (100 MHz, $CDCl_3$): δ 191.7, 191.4, 148.0, 148.0, 147.9, 145.6, 145.6, 145.2, 145.1, 145.0, 145.0, 144.9, 140.0, 140.0, 139.9, 139.1, 139.1, 139.0, 139.0, 138.0, 137.8, 137.7, 137.7, 136.6, 136.6, 134.2, 133.9, 133.8, 133.6, 132.2, 132.2, 130.8, 130.6, 130.0, 129.9, 129.8, 129.7, 129.7, 129.4, 129.4, 129.2, 129.2, 129.0, 128.3, 128.2, 127.5, 127.0, 126.9, 124.4, 122.3, 49.7, 49.7, 21.9, 21.0, 19.0, 19.0, 18.7; **HRMS** (ESI) *m/z*: $[M + H]^+$ calcd for $C_{58}H_{47}O_2$ 775.3555, found 775.3578 (error: 3.0 ppm).

3-(9-mesityl-9H-fluoren-2-yl)-3'-(9-mesityl-9H-fluoren-4-yl)-[1,1'-biphenyl]-4,4'-dicarbaldehyde (11). Compound **5** (229 mg, 0.489 mmol) and **8** (252 mg, 0.489 mmol) were reacted in the presence of $Pd(PPh_3)_4$ (17 mg, 0.03 equiv.) and Na_2CO_3 (311 mg, 2.94 mmol) in toluene/EtOH/H_2O (4.5 mL/0.5 mL/0.5 mL) according to general procedure C. The obtained material was subjected to column chromatography (SiO_2, CH_2Cl_2/hexane 70:100) to give dialdehyde **11** as a yellow solid. (230 mg, 61% yield): $\boldsymbol{R_f}$ = 0.35 (10% EtOAc/hexanes); **mp**: 178-179°C; **^{1}H NMR** (400 MHz, $CDCl_3$): δ 10.06 – 9.95 (m, 1H), 9.86 (m, 1H), 8.26 (dd, *J* = 8.2, 4.9 Hz, 1H), 8.11 (t, *J* = 7.5 Hz, 1H), 8.00 – 7.88 (m, 3H), 7.86 – 7.73 (m, 3H), 7.45 (q, *J* = 8.4 Hz, 2H), 7.39 – 7.24 (m, 6H), 7.24 – 7.12 (m, 2H), 7.08 – 6.97 (m, 3H), 6.72 – 6.63 (m, 3H), 5.57–5.55 (m, 2H), 2.72-2.67 (m, 6H), 2.33 – 2.23 (m, 6H), 1.16 – 1.14 (m, 6H); **^{13}C{^{1}H} NMR** (100 MHz, $CDCl_3$): δ 191.9, 191.7, 191.4, 148.1, 148.0, 147.9, 147.9, 147.5, 147.0, 145.6, 145.2, 144.3, 141.3, 140.1, 140.0, 139.9, 139.0, 138.0, 137.8, 137.7, 137.7, 136.6, 136.3, 133.8, 133.7, 133.6, 133.5, 133.3, 132.2, 130.8, 130.7, 130.6, 130.2, 129.9, 129.9, 129.4, 129.2, 129.1, 129.0, 128.7, 128.5, 128.3, 128.1, 127.9, 127.5, 127.2, 127.0, 126.9, 126.7, 125.7, 124.4, 122.3, 120.5, 120.1, 49.9, 21.9, 21.9, 21.0, 20.9, 18.9, 18.8; **HRMS** (ESI) *m/z*: $[M + H]^+$ calcd for $C_{58}H_{47}O_2$ 775.3576, found 775.3580 (error: 0.5 ppm).

General procedure D for synthesis of BIFs 1-3. To a THF solution of dialdehyde was added 2-mesitylmagnesium bromide (1M solution in diethylether) at room temperature under N_2 atmosphere, and the resulting solution was stirred for 16 h. After addition of saturated ammonium chloride, the organic phase was separated, and the aqueous phase was extracted with CH_2Cl_2. The combined organic phase was washed with brine, dried over Na_2SO_4, and concentrated under reduced pressure. The residue was subjected to column chromatography to give crude alcohol, which was used without further purification. To a CH_2Cl_2 solution of crude alcohol was added $BF_3{\cdot}OEt_2$ (0.1 ml) at room temperature under N_2 atmosphere. After stirring the mixture at room temperature for 10 min, saturated ammonium chloride was added. The organic phase was separated, and the aqueous phase was extracted with CH_2Cl_2. The combined organic phase was dried over Na_2SO_4 and evaporated under reduced pressure to give the crude dihydro intermediate which was used without further purification. The dihydro intermediate was dissolved in 1,2-dichloroethane and then Dichloro-5,6-dicyano-1,4-benzoquinone (DDQ) was added at room temperature under N_2 atmosphere. After heating the mixture at 80 °C using an oil bath for 2 h, the mixture was cooled and then evaporated under reduced pressure. The residue was subjected to column chromatography (10% CH_2Cl_2/Hexane) to give the desired product.

6,6',12,12'-tetramesityl-3,3'-biindeno[1,2-*b*]fluorene (1). According to general procedure D, dialdehyde **9** (166 mg, 0.214 mmol) in THF (15 mL) was reacted with 2-mesitylmagnesiumbromide (1.07 ml, 1.07 mmol, 5 equiv.). The obtained material was filtered through a short silica plug to give crude alcohol, which was subjected to Friedel–Crafts cyclization with $BF_3{\cdot}OEt_2$ (0.1 ml). The crude dihydro intermediate (120 mg) was oxidized with DDQ (111 mg, 0.49 mmol). The obtained material was purified according to the general procedure D to give **1** (93 mg, 57% in 3 steps) as a pink solid. $\boldsymbol{R_f}$ = 0.56 (5% EtOAc/hexanes); **mp**: 326-327 °C; **^{1}H NMR** (400 MHz, $CDCl_3$): δ 7.53 (s, 2H), 7.31 (d, *J* = 7.2 Hz, 2H), 7.16 (d, *J* = 7.7 Hz, 2H), 7.02 (d, *J* = 6.9 Hz, 8H), 7.00 – 6.91 (m, 4H), 6.87 (d, *J* = 16.1 Hz, 4H), 6.69 (dd, *J* = 7.6, 3.7 Hz, 4H), 2.41 – 2.40 (m, 12H), 2.20 – 2.18 (m, 24H); **^{13}C{^{1}H} NMR** (100 MHz, $CDCl_3$): δ 145.5, 145.5, 144.2, 143.3, 140.2, 139.0, 139.0, 138.5, 137.8, 137.7, 137.6, 137.3, 137.2, 135.4, 134.9, 130.1, 128.3, 127.8, 127.1, 126.3, 122.2, 122.1, 120.5, 119.2, 119.1, 119.0, 21.4, 21.3, 20.5; **HRMS** (ESI) *m/z*: $[M + H]^+$ calcd for $C_{76}H_{63}$ 975.4930, found 975.4918 (error: -1.2 ppm).

5,5',8,8'-tetramesityl-2,2'-biindeno[2,1-*c*]fluorene (2). According to general procedure D, dialdehyde **10** (93 mg, 0.12 mmol) in THF (15 mL) was reacted with 2-

mesitylmagnesiumbromide (0.6 ml, 0.6 mmol, 5 equiv.). The obtained material was filtered through a short silica plug to give crude alcohol, which was subjected to Friedel–Crafts cyclization with $BF_3{\cdot}OEt_2$ (0.1 ml). The crude dihydro intermediate (51 mg) was oxidized with DDQ (26 mg, 0.114 mmol). The obtained material was purified according to the general procedure D to give **2** (45 mg, 63% in 3 steps) as a green solid. $\boldsymbol{R}_\mathbf{f}$ = 0.59 (5% EtOAc/hexanes); **mp**: 232-233 °C; **^{1}H NMR** (400 MHz, $CDCl_3$): δ 8.40 (d, *J* = 1.5 Hz, 2H), 8.15 (d, *J* = 7.5 Hz, 2H), 7.40 (dd, *J* = 7.9, 1.5 Hz, 2H), 7.04 (d, *J* = 7.4 Hz, 2H), 7.00 (d, *J* = 7.9 Hz, 8H), 6.92 (t, *J* = 7.5 Hz, 2H), 6.83 (d, *J* = 7.8 Hz, 2H), 6.72 (d, *J* = 7.4 Hz, 2H), 6.19 (s, 4H), 2.38 – 2.37 (m, 12H), 2.22 – 2.18 (m, 24H); **^{13}C{^{1}H} NMR** (100 MHz, $CDCl_3$): δ 145.1, 143.3, 140.0, 139.4, 138.6, 137.6, 137.5, 137.3, 137.2, 136.4, 130.0, 129.2, 128.3, 128.2, 127.7, 127.4, 125.3, 124.3, 122.1, 121.9, 121.0, 21.3, 20.5, 20.4; **HRMS** (ESI) *m/z*: $[M + H]^+$ calcd for $C_{76}H_{63}$ 975.4930, found 975.4904 (error: -2.7 ppm).

2-(6,12-dimesitylindeno[1,2-*b*]fluoren-3-yl)-5,8-dimesitylindeno[2,1-*c*]fluorene (3). According to general procedure D, dialdehyde **11** (195 mg, 0.251 mmol) in THF (15 mL) was reacted with 2-mesitylmagnesiumbromide (1.26 mL, 1.26 mmol, 5 equiv.). The obtained material was filtered through a short silica plug to give crude alcohol, which was subjected to Friedel–Crafts cyclization with $BF_3{\cdot}OEt_2$ (0.1 ml). The crude dihydro intermediate (90 mg) was oxidized with DDQ (67 mg, 0.294 mmol). The obtained material was purified according to the general procedure D to give **3** (69 mg, 72% in 3 steps) as a red solid. $\boldsymbol{R}_\mathbf{f}$ = 0.53 (5% EtOAc/hexanes); **mp**: 260−261 °C; **^{1}H NMR** (400 MHz, $CDCl_3$): δ 8.33 (d, *J* = 1.5 Hz, 1H), 8.11 (d, *J* = 7.5 Hz, 1H), 7.65 (d, *J* = 1.7 Hz, 1H), 7.33 (d, *J* = 7.2 Hz, 1H), 7.31 – 7.26 (m, 2H), 7.09 – 7.00 (m, 6H), 6.97 (tt, *J* = 7.3, 3.4 Hz, 7H), 6.90 (s, 1H), 6.80 (d, *J* = 7.8 Hz, 1H), 6.75 – 6.67 (m, 3H), 6.13 (s, 2H), 2.42 (s, 3H), 2.37-2.36 (m, 9H), 2.25 (s, 6H), 2.21 (s, 6H), 2.17 – 2.15 (m, 12H); **^{13}C{^{1}H} NMR** (100 MHz, $CDCl_3$): δ 146.2, 145.8, 145.3, 145.1, 144.2, 143.4, 143.3, 140.2, 139.5, 139.1, 139.0, 138.9, 138.6, 137.8, 137.7, 137.7, 137.5, 137.3, 137.2, 137.1, 136.9, 136.5, 136.3, 135.5, 134.9, 130.0, 130.0, 129.2, 128.4, 128.2, 127.9, 127.3, 127.2, 126.6, 126.1, 125.4, 124.1, 122.4, 122.1, 121.9, 121.8, 121.0, 120.5, 119.2, 119.1, 118.9, 21.3, 21.3, 20.6, 20.5, 20.4, 20.4; **HRMS** (ESI) *m/z*: $[M + H]^+$ calcd for $C_{76}H_{63}$ 975.4930, found 975.4906 (error: -2.5 ppm).

4.5.3 Single crystal data

Single crystals of **1** were selected using paratone oil and mounted on glass fiber with the help of gum. The intensity data and geometric parameters of these crystals were garnered with the help of Bruker D8 Venture X-ray diffractometer having a micro-focus sealed X-ray tube Mo-Kα (λ = 0.71073 Å) source of X-rays along with a PHOTON 100 detector with inclining Phi and Omega (width of 0.5 for one frame) working at a scan speed of 10 s per frame. The crystal was kept at 298 K during data collection. Data acquisition as well as extraction of data was accomplished by utilizing Bruker Apex-3 and Bruker SAINT software packages using a narrow -frame algorithm.[25] By utilizing OLex2,[26] the crystal structure was solved with the help of olex2.solve[27] structure solution program by employing intrinsic Phasing methods and crystal structure refinement was done with the SHELXL[28] refinement package by putting into use Least Squares minimization. Refinement of all non-hydrogen atoms was completed with the help of anisotropic thermal parameters.

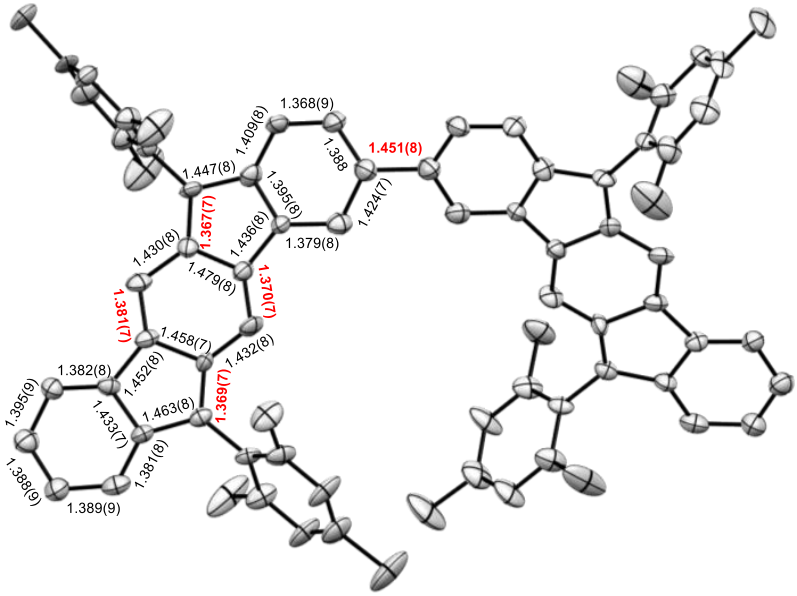

Figure 4.8 ORTEP drawing of **1** with thermal ellipsoids at 30% probability level, showing the bond lengths with e.s.d values.

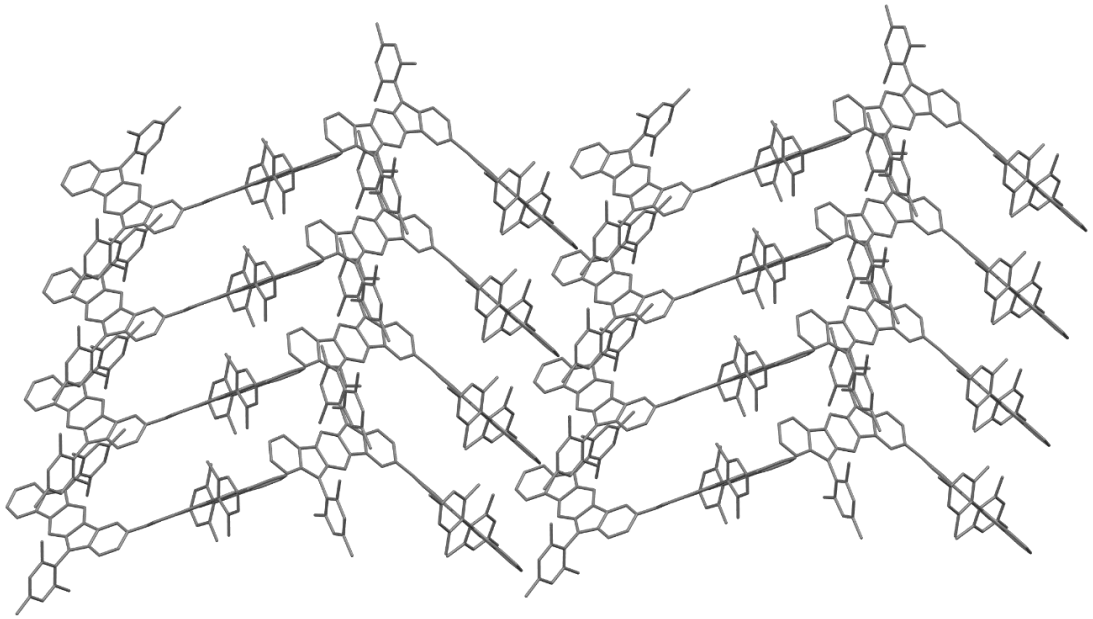

Figure 4.9 2D Herringbone-type packing in **1**

Table 4.6 Crystal data and structure refinement for **1**

CCDC Number	2331509
Solvents, and conditions for recrystallization	Recrystallization from chloroform at rt in dark
Empirical formula	$C_{76}H_{62}$
Formula weight	975.25
Temperature/K	298.00
Crystal system	Orthorhombic
Space group	$P2_12_12$
a/Å	32.806(6)
b/Å	7.9143(15)
c/Å	12.549(2)
α/°	90
β/°	90
γ/°	90
Volume/Å^3	3258.0(11)
Z	2
ρ_{calc}g/cm^3	0.994
μ/mm^{-1}	0.056
F(000)	1036.0
Crystal size/mm^3	0.235 × 0.123 × 0.023
Radiation	MoKα (λ = 0.71073)
2Θ range for data collection/°	4.942 to 51.496
Index ranges	$-40 \leq h \leq 40$, $-9 \leq k \leq 9$, $-15 \leq l \leq 15$
Reflections collected	55491

Independent reflections	6222 [R_{int} = 0.1630, R_{sigma} = 0.1038]
Data/restraints/parameters	6222/1/350
Goodness-of-fit on F^2	1.005
Final R indexes [I>=2σ (I)]	R_1 = 0.0862, wR_2 = 0.1726
Final R indexes [all data]	R_1 = 0.1448, wR_2 = 0.1978
Largest diff. peak/hole / e $Å^{-3}$	0.20/-0.18
Flack parameter	10.0(10)

4.5.4 DFT calculations

Density functional theory (DFT) calculations were performed in gas phase, with Gaussian 09 package using a high-performance computing cluster facility of IIT Ropar, at the B3LYP (restricted and unrestricted) level of theory with basis set 6-31G(d,p).[29]

Table 4.7 Relative energies for the optimized structure **1** at B3LYP/6-31G(d,p) level.

State	Hartree	kcal/mol
Singlet Closed-Shell	−2933.635073	−1840882.411
Singlet Open-Shell	−2933.635073	−1840882.411
Triplet Open-Shell	−2933.608606	−1840865.803

$\Delta E_{\text{Triplet-Singlet}}$ = 16.60 kcal/mol.

Table 4.8 Relative energies for the optimized structure **2** at B3LYP/6-31G(d,p) level.

State	Hartree	kcal/mol
Singlet Closed-Shell	−2933.618527	−1840872.028
Singlet Open-Shell	−2933.618526	−1840872.028
Triplet Open-Shell	−2933.597405	−1840858.774

$\Delta E_{\text{Triplet-Singlet}}$ = 13.25 kcal/mol.

Table 4.9 Relative energies for the optimized structure **3** at B3LYP/6-31G(d,p) level.

State	Hartree	kcal/mol
Singlet Closed-Shell	−2933.626441	−1840876.994
Singlet Open-Shell	−2933.626378	−1840876.955
Triplet Open-Shell	−2933.605485	−1840863.844

$\Delta E_{\text{Triplet-Singlet}}$ = 13.11 kcal/mol.

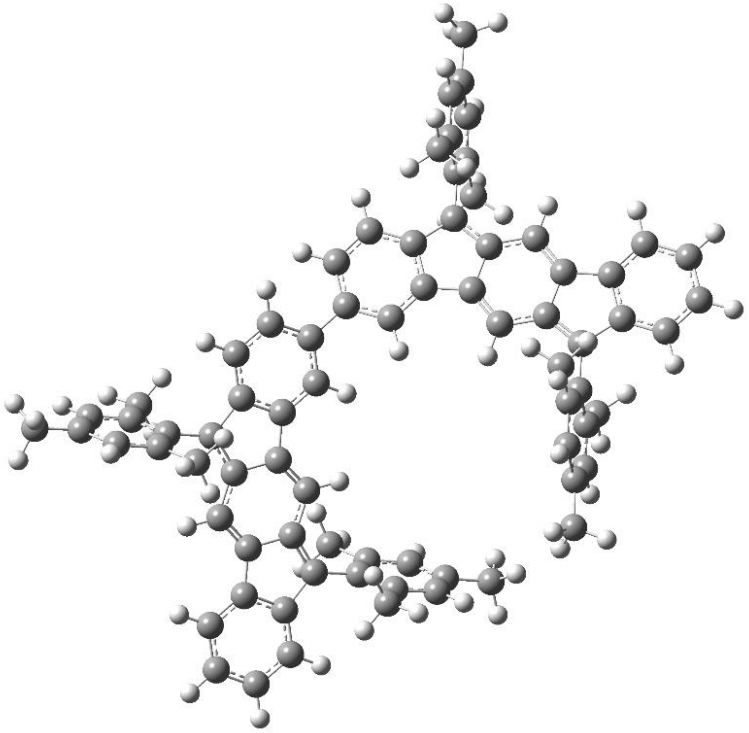

Figure 4.10 Optimized closed shell structure for **1**.

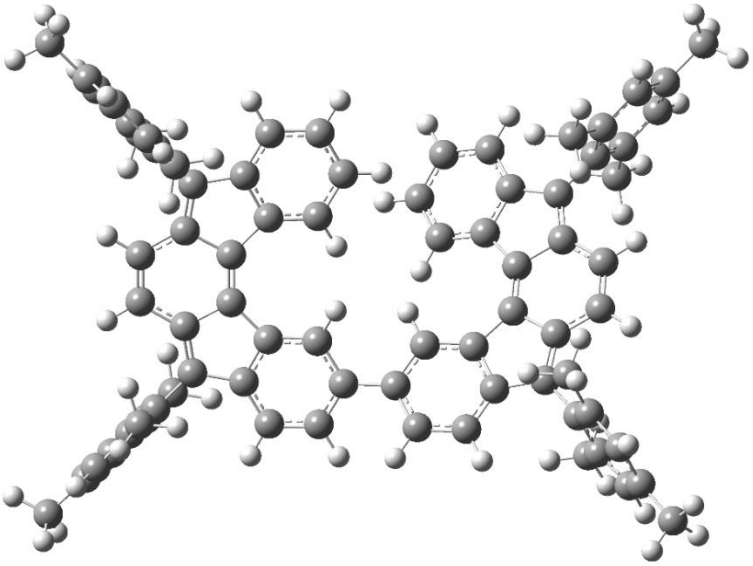

Figure 4.11 Optimized closed shell structure for **2**.

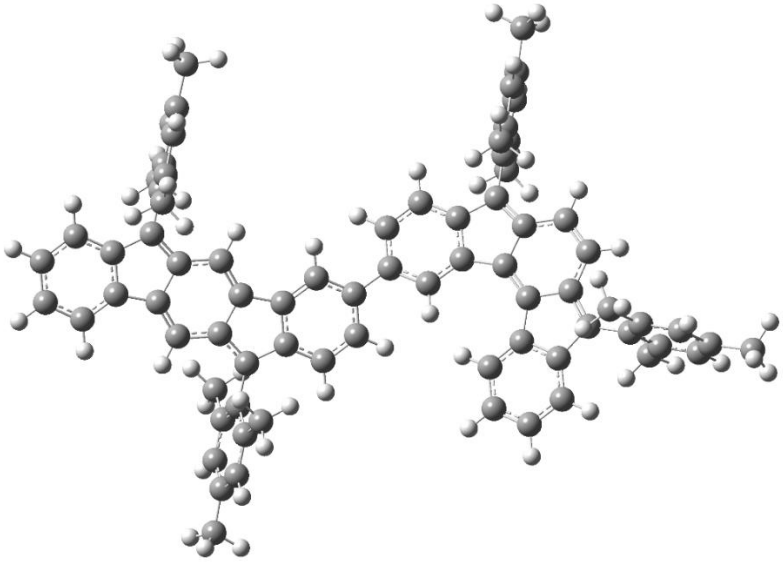

Figure 4.12 Optimized closed shell structure for **3**.

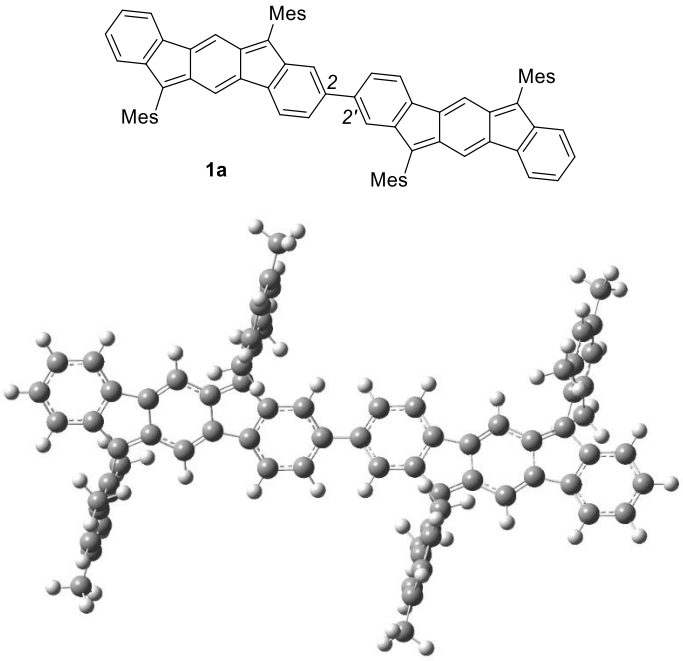

Figure 4.13 Optimized closed shell structure for **1a** (E_g^{DFT} = 2.40 eV).

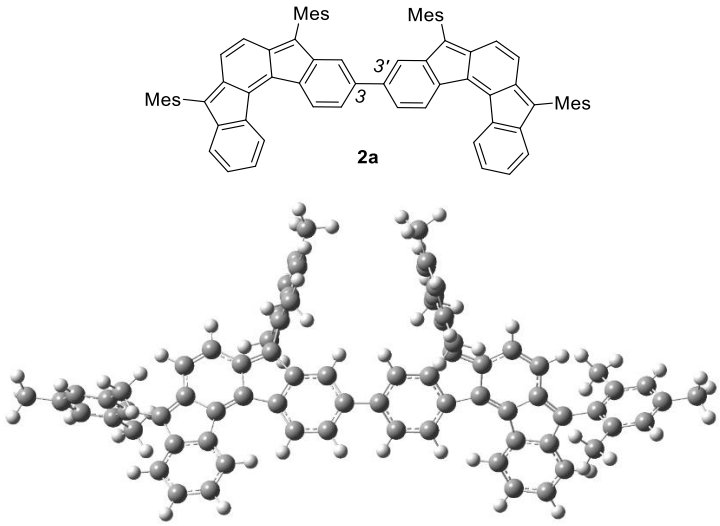

Figure 4.14 Optimized closed shell structure for **2a** (E_g^{DFT} = 2.16 eV).

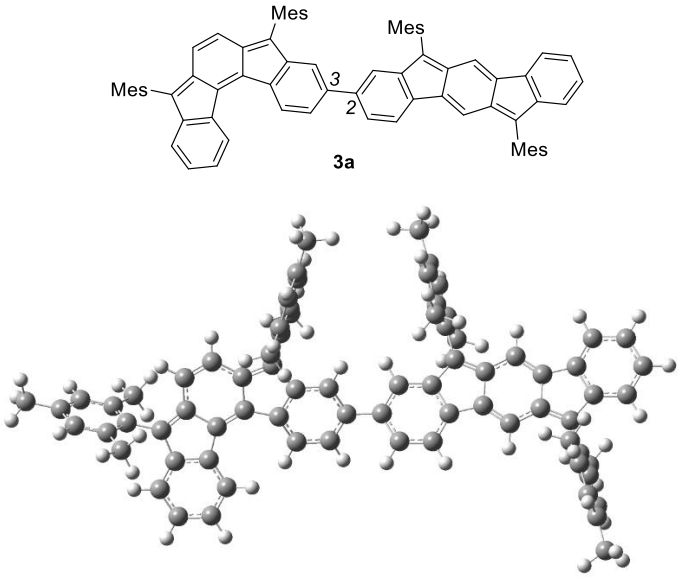

Figure 4.15 Optimized closed shell structure for **3a** (E_g^{DFT} = 2.20 eV).

Table 4.10 Frontier molecular orbital profiles of **1**-**3**

Compd.	HOMO (eV)	LUMO (eV)	E_g^{DFT}
1	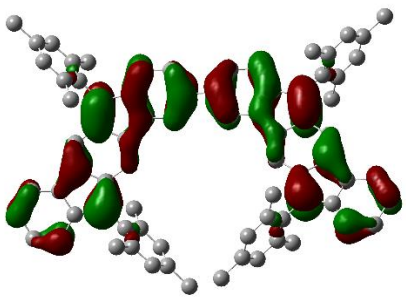 –4.80	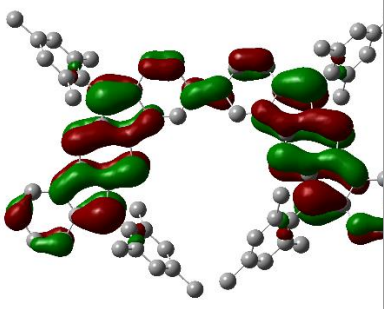 –2.73	2.07 eV

2	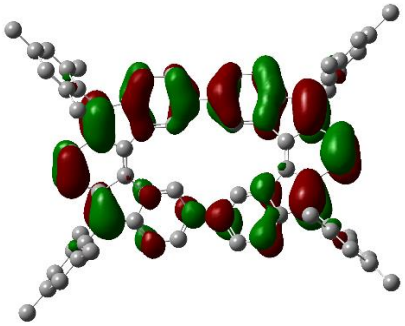 –4.71	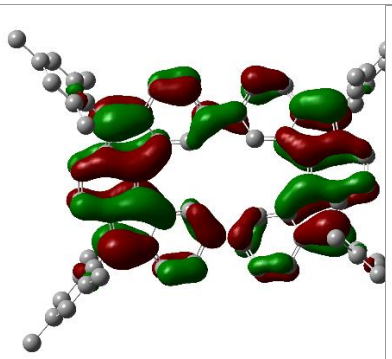 –2.75	1.96 eV
3	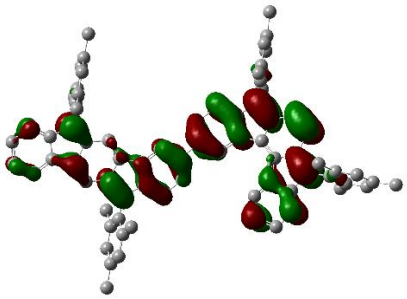 –4.74	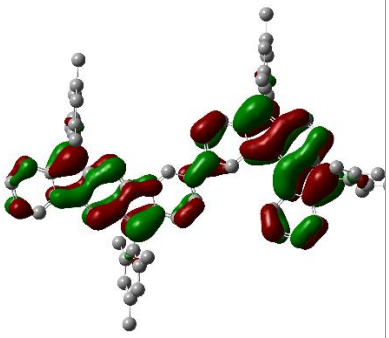 –2.75	1.99 eV

Table 4.11 Comparison of theoretical C_{sp}^2-C_{sp}^2 bond-length connecting the IF monomer units, as estimated by DFT calculations.

BIFs	C-C bond-length (Å) connecting IF monomers
1	1.48047
2	1.48114
3	1.48054

Crystal structure of **1**, with improved optoelectronic properties and smaller HOMO-LUMO gap, suggested that the C-C bond-length for **1** connecting two [1,2-*b*]IF units to be shorter (1.451(8) Å) than that of a biphenyl (1.496(3) Å) molecule. Crystal structure optimization by DFT approach further suggested that the same C-C bond of BIF **1** to have a bond-length of 1.480 Å (Table 4.11, Figure 4.10), which is clearly shorter than biphenyl molecule. Structure optimization of BIFs **2** and **3** (Figure 4.11 and 4.12), which are formed by connecting 2,2'(11)-carbons and 2/3-carbons of [2,1-*c*]IF units for **2** and [2,1-*c*]IF/[1,2-*b*]IF units for **3**, respectively, with larger HOMO/LUMO coefficients, suggested shorter C-C bond-length of ~1.480 Å (Table 4.11) that connected the IF monomer units, and the bond distance is identical to **1**; implying improved electronic communication between the IF monomer units for **2** and **3**, like **1**.

4.5.5 Electrochemistry

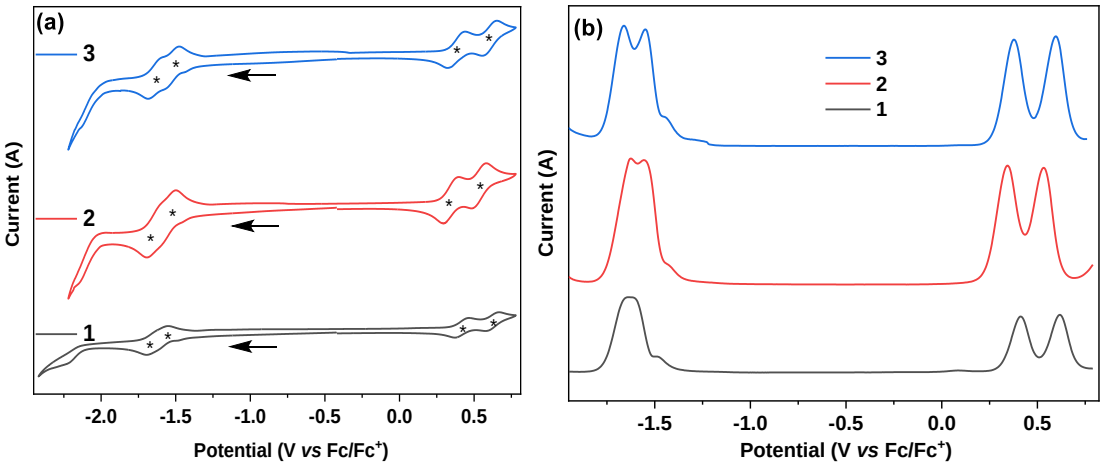

Figure 4.16 IUPAC representation of (a) cyclic voltammograms (asterisk (*) denotes half-wave redox potentials) and (b) differential pulse voltammograms of BIFs **1-3** (0.001 M) taken at 298 K, in dry and degassed dichloromethane with 0.1 M Bu_4NPF_6 under nitrogen atmosphere. All data were collected using Pt-disk electrode as a working electrode, Pt wire as a counter electrode and Ag wire as a pseudo-reference electrode. Starting point was 0 V (*vs* Ag wire), which is now plotted as –0.42 V (*vs* Fc/Fc^+) after referencing against ferrocene/ferrocenium. Scan direction (toward negative potential first, and then going to positive potential) is shown using arrow.

4.5.6 SCLC Mobility Data for compounds 1, 2, and 3.

Table 4.12 Statistics of 5 best hole mobilities in $cm^2 V^{-1} s^{-1}$ for best 5 devices for BIFs **1**, **2** and **3**.

Device	**1**	**2**	**3**
1	1.05×10^{-02}	1.50×10^{-02}	2.36×10^{-02}
2	2.07×10^{-02}	1.60×10^{-02}	1.17×10^{-02}
3	1.47×10^{-02}	1.81×10^{-02}	2.33×10^{-02}
4	1.97×10^{-02}	1.72×10^{-02}	4.09×10^{-02}
5	1.72×10^{-02}	1.29×10^{-02}	3.67×10^{-02}
Average	1.66×10^{-02}	1.58×10^{-02}	2.72×10^{-02}
STD	0.41×10^{-02}	0.20×10^{-02}	1.17×10^{-02}

Fabrication of device

The hole only devices were fabricated with configuration ITO/Ag /MoO_3/BIFs **1-3**/MoO_3/Ag to extract the mobility. Initially, prepatterned ITO glass substrates were cleaned sequentially using 5% soap solution, deionized water, acetone, and isopropyl alcohol in an ultra-sonicator (BioBee, India) for 20 minutes respectively at temperature 40 °C. Further, the cleaned substrate was dried using gentle blow of nitrogen. Cleaned

substrates were then UV ozone treated for 30 min at 50 ºC. The substrates were then loaded into a thermal evaporator for Ag (100 nm) connected with glove box (H_2O < 50 ppm, O_2<1 PPM) for MoO_3 (10 nm) electrode (anode) deposition under a base pressure of 2 × 10^{-6} mbar. BIFs **1-3** were then spin coated on the above substrates at 1500 rpm for 45 sec from 10 mg/ml solution in chloroform to obtain a thickness of 100 nm, duly verified with Dektak surface profilometer. The substrates were then again loaded in thermal evaporator for cathode electrode deposition of MoO_3 (10 nm) /Ag (100 nm) to complete the device. The active are of each device was 6.6 mm^2, calculated from the overlap of both cathode and anode electrodes. *J-V* characteristics of the fabricated samples were performed using Keithley 2450 source measure unit in dark. Relative dielectric constant of BIFs **1-3** (ε_r∼3.4) were measured using high-frequency LCR meter ZM2376 with an applied oscillation level voltage of 1V over the frequency range 20Hz-1MHz.

4.6 References

1**.** Y. Tobe, *Physical Organic Chemistry of Quinodimethanes*, Springer, 2017, **375**, 107.

2. B. D. Rose, L. E. Shoer, M. R. Wasielewski and M. M. Haley, *Chem. Phys. Lett.*, 2014, **616–617**, 137.

3**.** A. Can, A. Facchetti and H. Usta, *J. Mater. Chem. C*, 2022, **10**, 8496–8535.

4. S. S. Zade and M. Bendikov, *J. Phys. Org. Chem.*, 2012, **25**, 452–461.

5. D. T. Chase, B. D. Rose, S. P. McClintock, L. N. Zakharov and M. M. Haley, *Angew. Chem. Int. Ed.*, 2011, **50**, 1127–1130.

6. M. M. Haley, *Chem. Rec.*, 2015, **15**, 1140–1143.

7. (*a*) A. Shimizu and Y. Tobe, *Angew. Chem., Int. Ed.*, 2011, **50**, 6906–6910; (*b*) A. Shimizu, R. Kishi, M. Nakano, D. Shiomi, K. Sato, T. Takui, I. Hisaki, M. Miyata, and Y. Tobe, *Angew. Chem., Int. Ed.*, 2013, **52**, 6076–6079; (*c*) A. G. Fix, P. E. Deal, C. L. Vonnegut, B. D. Rose, L. N. Zakharov, and M. M. Haley, *Org. Lett.*, 2013, **15**, 1362–1365; (*d*) J. J. Dressler, Z. Zhou, J. L. Marshall, R. Kishi, S. Takamuku, Z. Wei, S. N. Spisak, M. Nakano, M. A. Petrukhina, and M. M. Haley, *Angew. Chem., Int. Ed.*, 2017, **56**, 15363–15367.

8. (*a*) D. T. Chase, A. G. Fix, S. J. Kang, B. D. Rose, C. D. Weber, Y. Zhong, L. N. Zakharov, M. C. Lonergan, C. Nuckolls and M. M. Haley, *J. Am. Chem. Soc.*, 2012, **134**, 10349–10352; (*b*) Y.-C. Lo, H.-C. Ting, Y.-Z. Li, Y.-H. Li, S.-W. Liu, K.-W. Huang and

K.-T. Wong, *Org. Chem. Front.*, 2017, **4**, 675–681; (*c*) A. M. Zeidell, L. Jennings, C. K. Frederickson, Q. Ai, J. J. Dressler, L. N. Zakharov, C. Risko, M. M. Haley and O. D. Jurchescu, *Chem. Mater.*, 2019, **31**, 6962–6970.

9. R. Casares, Á. Martínez-Pinel, S. Rodríguez-González, I. R. Márquez, L. Lezama, M. T. González, E. Leary, V. Blanco, J. G. Fallaque, C. Díaz, F. Martín, J. M. Cuerva and A. Millán, *J. Mater. Chem. C*, 2022, **10**, 11775–11782.

10. (*a*) C. K. Frederickson, B. D. Rose and M. M. Haley, *Acc. Chem. Res.*, 2017, **50**, 977–987;

(*b*) P. Hu, S. Lee, T. S. Herng, N. Aratani, T. P. Gonçalves, Q. Qi, X. Shi, H. Yamada, K. Huang, J. Ding, D. Kim and J. Wu, *J. Am. Chem. Soc.*, 2016, **138**, 1065–1077.

11. D. T. Chase, A. G. Fix, B. D. Rose, C. D. Weber, S. Nobusue, C. E. Stockwell, L. N. Zakharov, M. C. Lonergan and M. M. Haley, *Angew. Chem., Int. Ed.*, 2011, **50**, 11103–11106.

12. M. D. Giovannantonio, J. I. Urgel, U. Beser, A. V. Yakutovich, J. Wilhelm, C. A. Pignedoli, P. Ruffieux, A. Narita, K. Müllen, and R. Fasel, *J. Am. Chem. Soc.*, 2018, **140**, 3532–3536.

13. (*a*) E. Kumarasamy, S. N. Sanders, A. B. Pun, S. A. Vaselabadi, J. Z. Low, M. Y. Sfeir, M. L. Steigerwald, G. E. Stein and L. M. Campos, *Macromolecules*, 2016, **49**, 1279−1285; (*b*) S. N. Sanders, E. Kumarasamy, A. B. Pun, M. T. Trinh, B. Choi, J. Xia, E. J. Taffet, J. Z. Low, J. R. Miller, X. Roy, X.-Y. Zhu, M. L. Steigerwald, M. Y. Sfeir and L. M. Campos, *J. Am. Chem. Soc.*, 2015, **137**, 8965−8972.

14. J. L. Marshall, N. J. O'Neal, L. N. Zakharov and M. M. Haley, *J. Org. Chem.*, 2016, **81**, 3674−3680.

15. H. Sharma, Ankita, P. Bhardwaj, U. K. Pandey and S. Das, *Organic Materials*, 2023, **5**, 72−83.

16. (*a*) D. C. Grenz, M. Schmidt, D. Kratzert and B. Esser, *J. Org. Chem.*, 2018, **83**, 656–663; (*b*) J. Wilbuer, D. C. Grenz, G. Schnakenburg and B. Esser, *Org. Chem. Front.*, 2017, **4**, 658–663.

17. H. Sharma, N. Bhardwaj and S. Das, *Org. Biomol. Chem.*, 2022, **20**, 8071–8077.

18. H. Sharma, P. K. Sharma and S. Das, *Chem. Commun.*, 2020, **56**, 11319–11322.

19. G. -P. Charbonneau, Y. Delugeard, *Acta Cryst.*, 1976, **B32**, 1420–1423.

20. P. L. A. Popelier, P. I. Maxwell, J. C. R. Thacker and I. Alkorta, *Theor. Chem. Acc.*, 2019, **138**, 12.

21. T. P. Nguyen, J. H. Shim and J. Y. Lee, *J. Phys. Chem. C*, 2015, **119**, 11301–11310.

22. G. A. H. Wetzelaer and P. W. M. Blom, *Phys. Rev. B: Condens. Matter Mater. Phys.*, 2014, **89**, 241201.

23. (*a*) P. N. Murgatroyd, *J. Phys. D: Appl. Phys.*, 1970, **3**, 151; (*b*) A. J. Campbell, D. D. C. Bradley and D. G. Lidzey, *J. Appl. Phys.*, 1997, **82**, 6326−6342.

24. B. Du, L. Wang, S.-C. Yuan, T. Lei, J. Pei and Y. Cao, *Polymer*, 2013, **54**, 2935−2944.

25. Bruker, SAINT V8.38A, (Bruker AXS Inc., 2017).

26. O. V. Dolomanov, L. J. Bourhis, R. J. Gildea, J. A. Howard and H. Puschmann, *J. Appl. Crystallogr.* 2009, **42**, 339–341.

27. J. Bourhis, O. V. Dolomanov, R. J. Gildea, J. A. Howard and H. Puschmann, *Acta Crystallogr. A.* 2015, **71**, 59–75.

28. G. M. Sheldrick, *Acta Crystallogr. C Struct. Chem.* 2015, **71**, 3–8.

29. Gaussian 09, *Revision B.01*, M. J. Frisch, G. W. Trucks, H. B. Schlegel, G. E. Scuseria, M. A. Robb, J. R. Cheeseman, G. Scalmani, V. Barone, B. Mennucci, G. A. Petersson, H. Nakatsuji, M. Caricato, X. Li, H. P. Hratchian, A. F. Izmaylov, J. Bloino, G. Zheng, J. L. Sonnenberg, M. Hada, M. Ehara, K. Toyota, R. Fukuda, J. Hasegawa, M. Ishida, T. Nakajima, Y. Honda, O. Kitao, H. Nakai, T. Vreven, J. A. Montgomery, Jr., J. E. Peralta, F. Ogliaro, M. Bearpark, J. J. Heyd, E. Brothers, K. N. Kudin, V. N. Staroverov, T. Keith, R. Kobayashi, J. Normand, K. Raghavachari, A. Rendell, J. C. Burant, S. S. Iyengar, J. Tomasi, M. Cossi, N. Rega, J. M. Millam, M. Klene, J. E. Knox, J. B. Cross, V. Bakken, C. Adamo, J. Jaramillo, R. Gomperts, R. E. Stratmann, O. Yazyev, A. J. Austin, R. Cammi, C. Pomelli, J. W. Ochterski, R. L. Martin, K. Morokuma, V. G. Zakrzewski, G. A. Voth, P. Salvador, J. J. Dannenberg, S. Dapprich, A. D. Daniels, O. Farkas, J. B. Foresman, J. V. Ortiz, J. Cioslowski and D. J. Fox, Gaussian, Inc., Wallingford CT, 2010.

4.7 Appendix

NMR Spectra

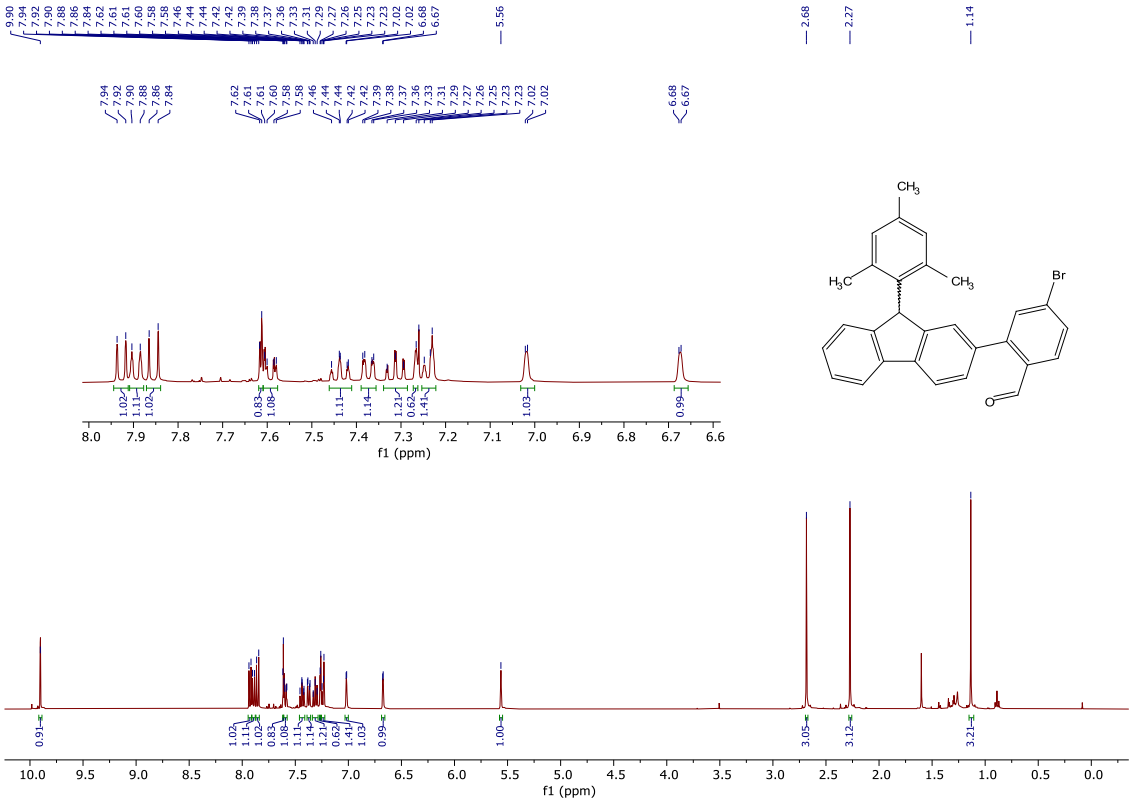

Figure 4.17 ^{1}H NMR spectrum of **5** (in $CDCl_3$, 400 MHz, 298 K).

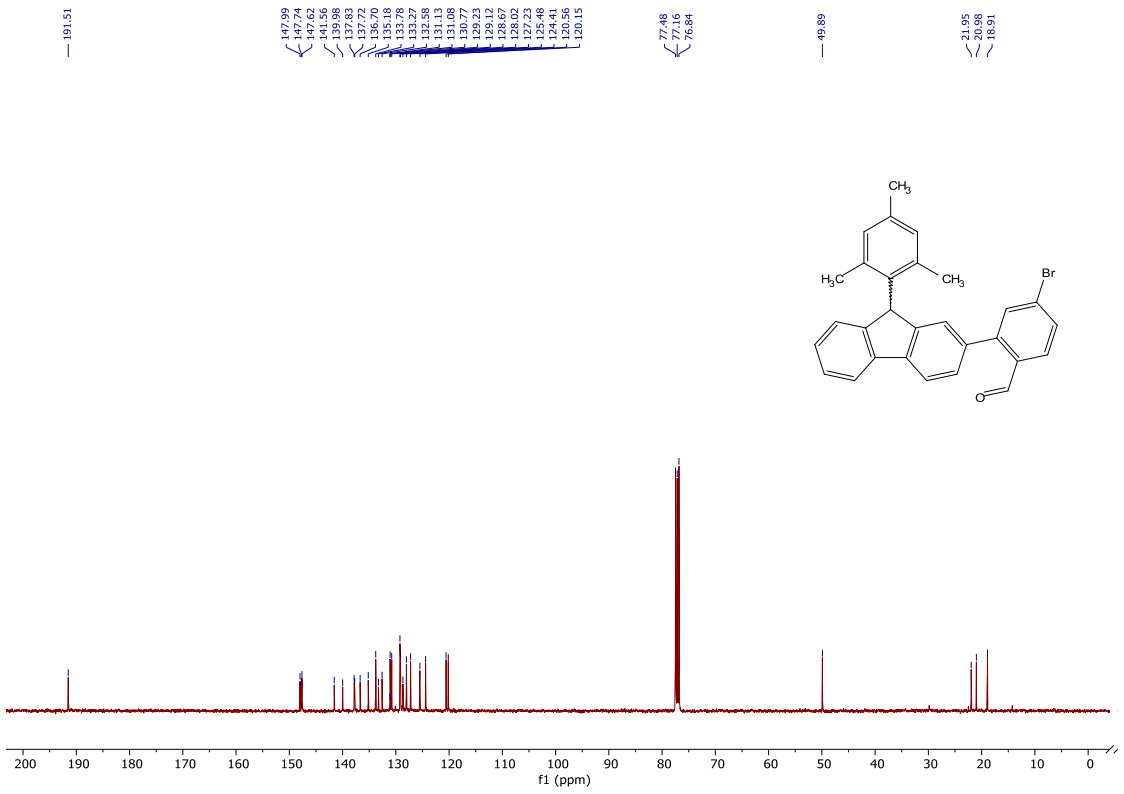

Figure 4.18 $^{13}C\{^{1}H\}$ NMR spectrum of **5** (in $CDCl_3$, 100 MHz, 298 K).

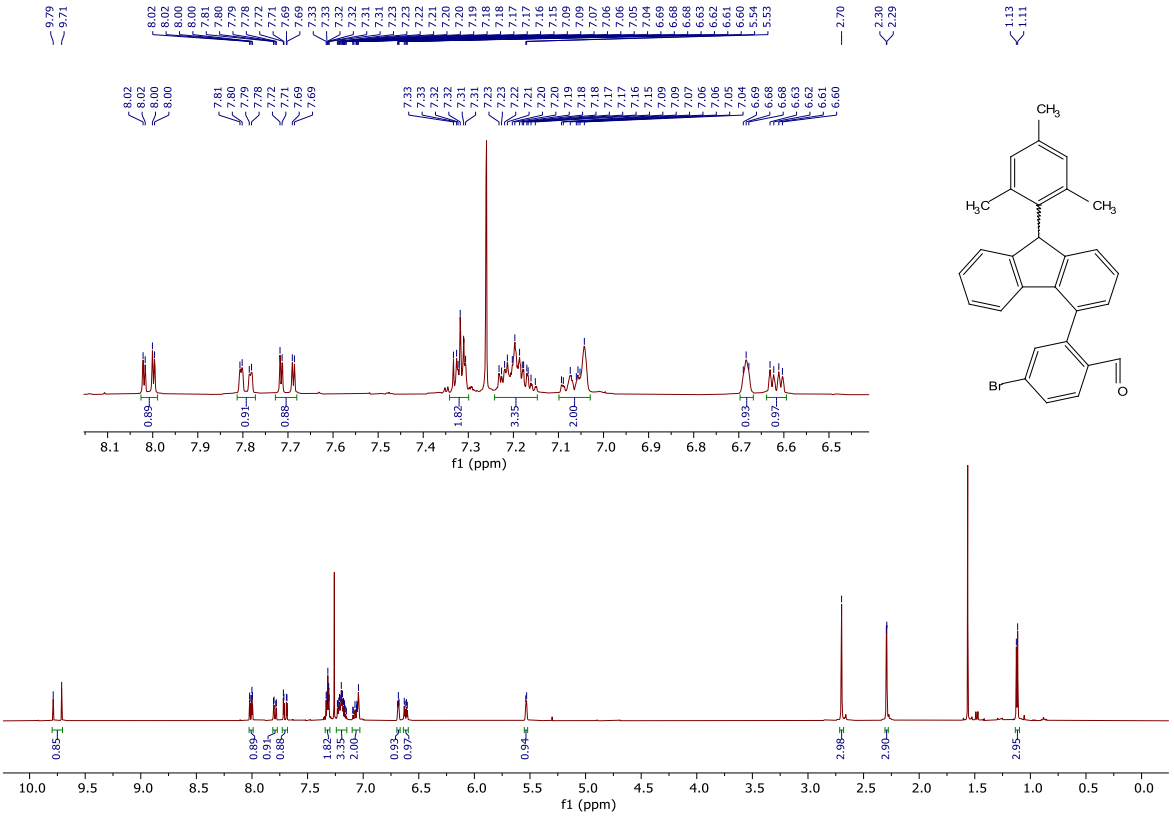

Figure 4.19 ^{1}H NMR spectrum of **6** (in $CDCl_3$, 400 MHz, 298 K).

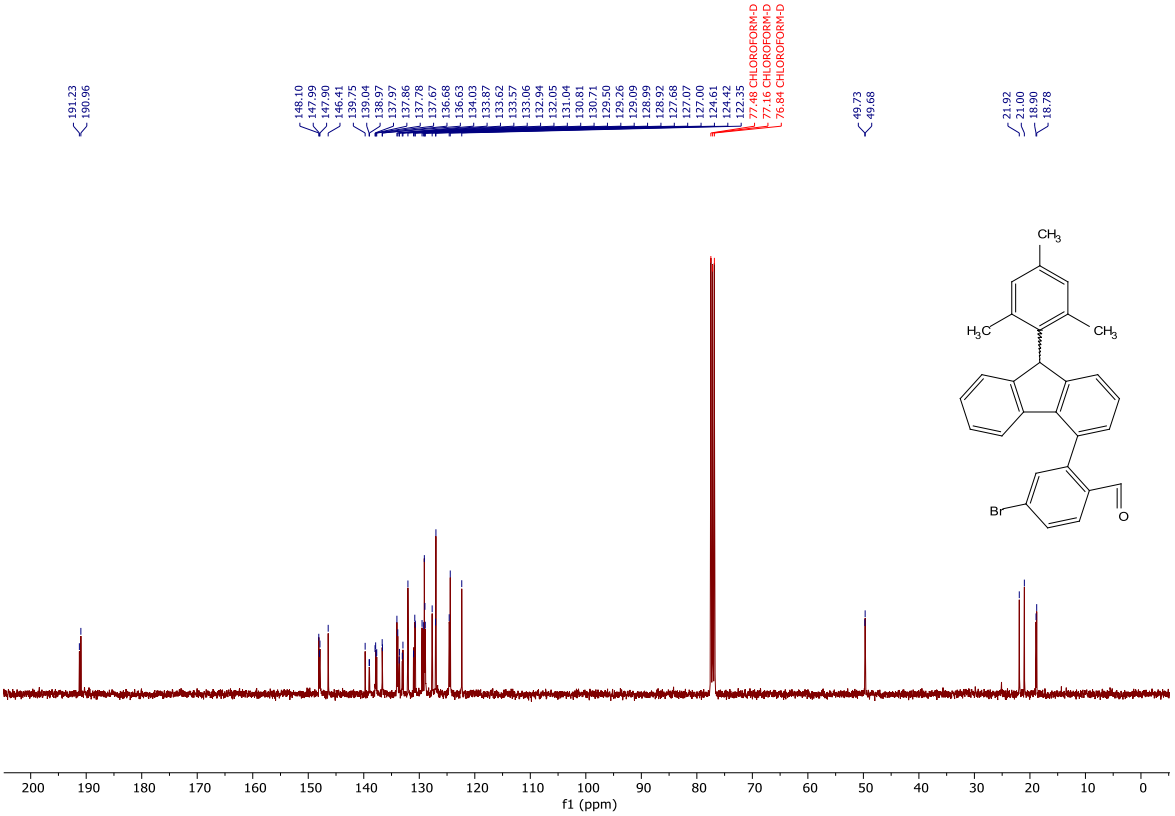

Figure 4.20 $^{13}C\{^{1}H\}$ NMR spectrum of **6** (in $CDCl_3$, 100 MHz, 298 K).

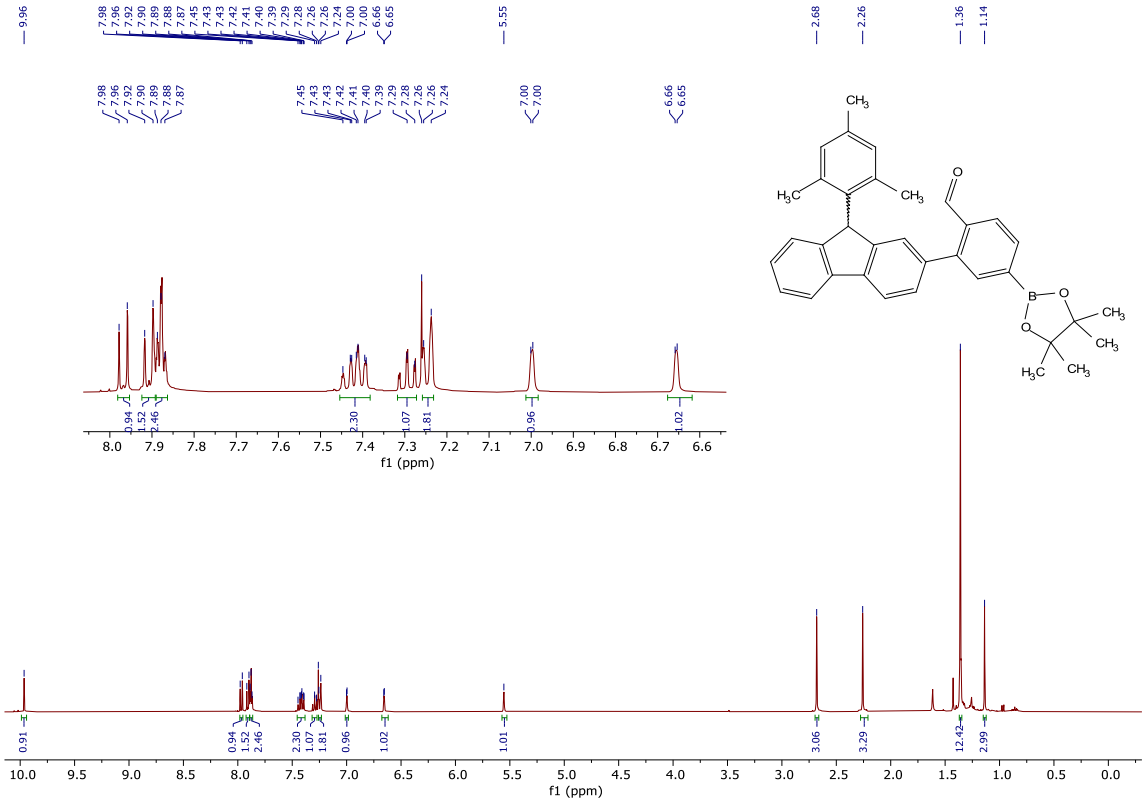

Figure 4.21 ^{1}H NMR spectrum of **7** (in $CDCl_3$, 400 MHz, 298 K).

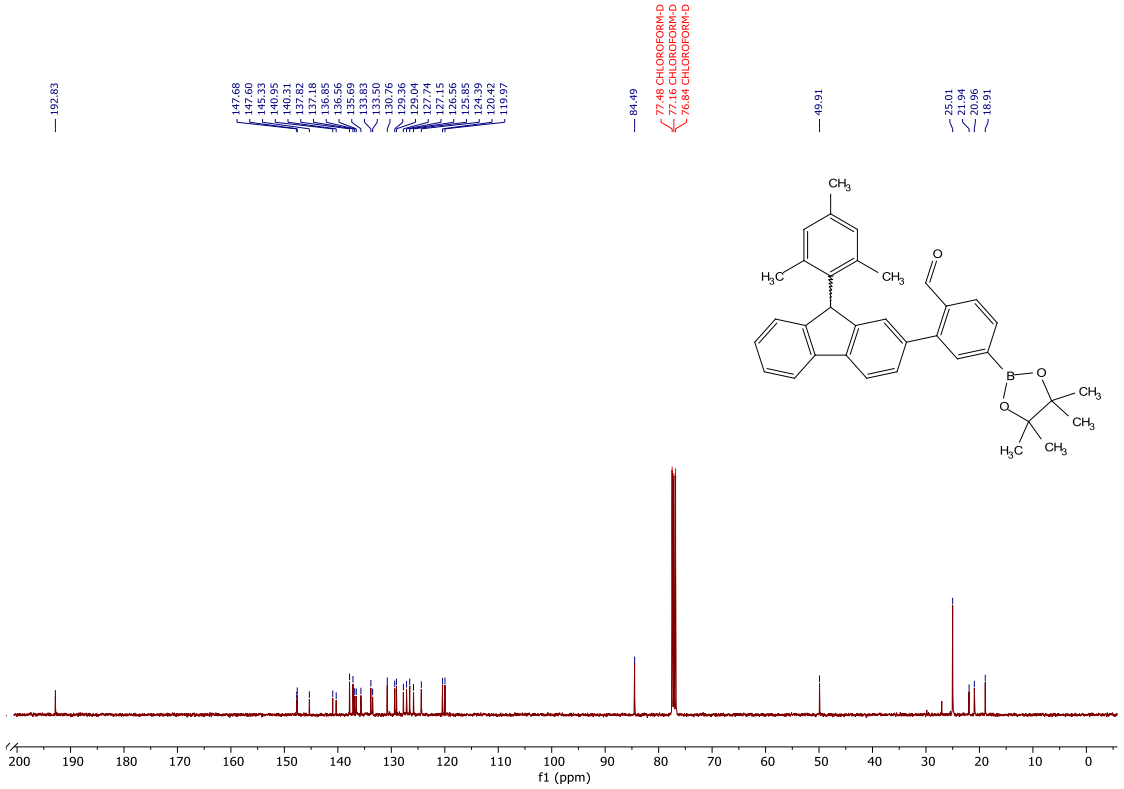

Figure 4.22 $^{13}C\{^{1}H\}$ NMR spectrum of **7** (in $CDCl_3$, 100 MHz, 298 K).

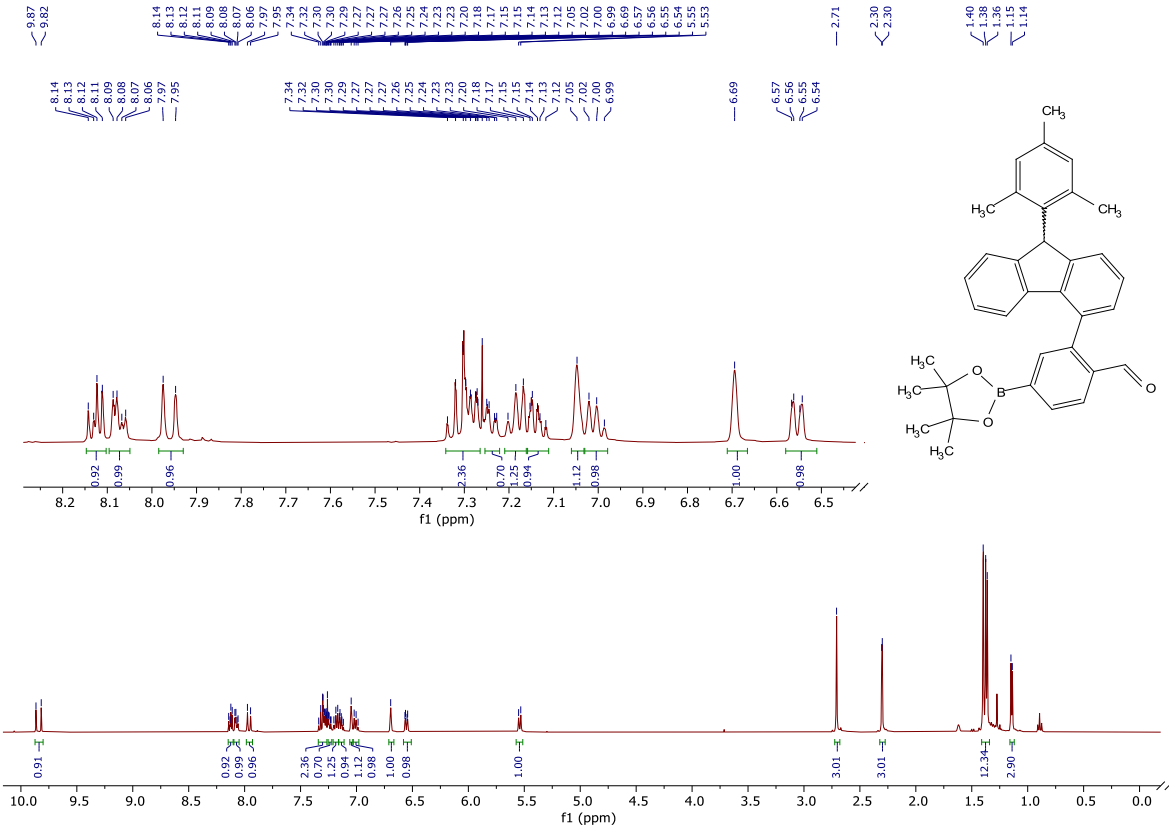

Figure 4.23 ^{1}H NMR spectrum of **8** (in $CDCl_3$, 400 MHz, 298 K).

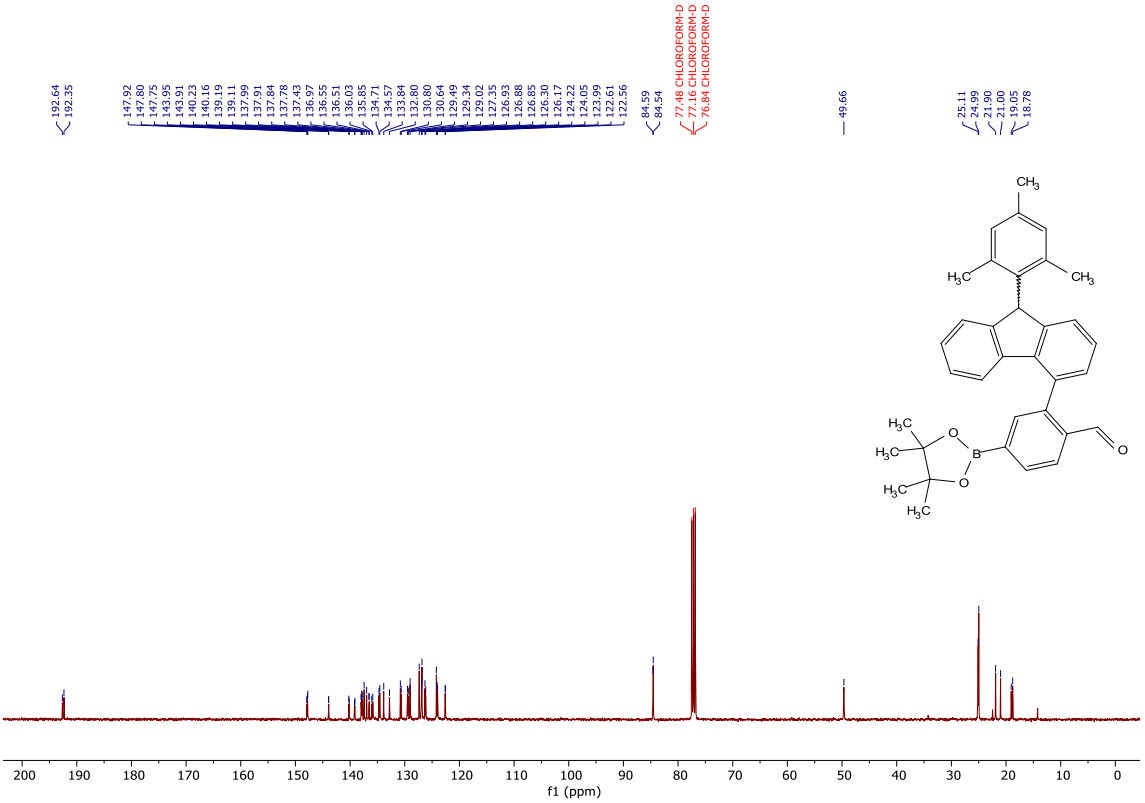

Figure 4.24 $^{13}C\{^{1}H\}$ NMR spectrum of **8** (in $CDCl_3$, 100 MHz, 298 K).

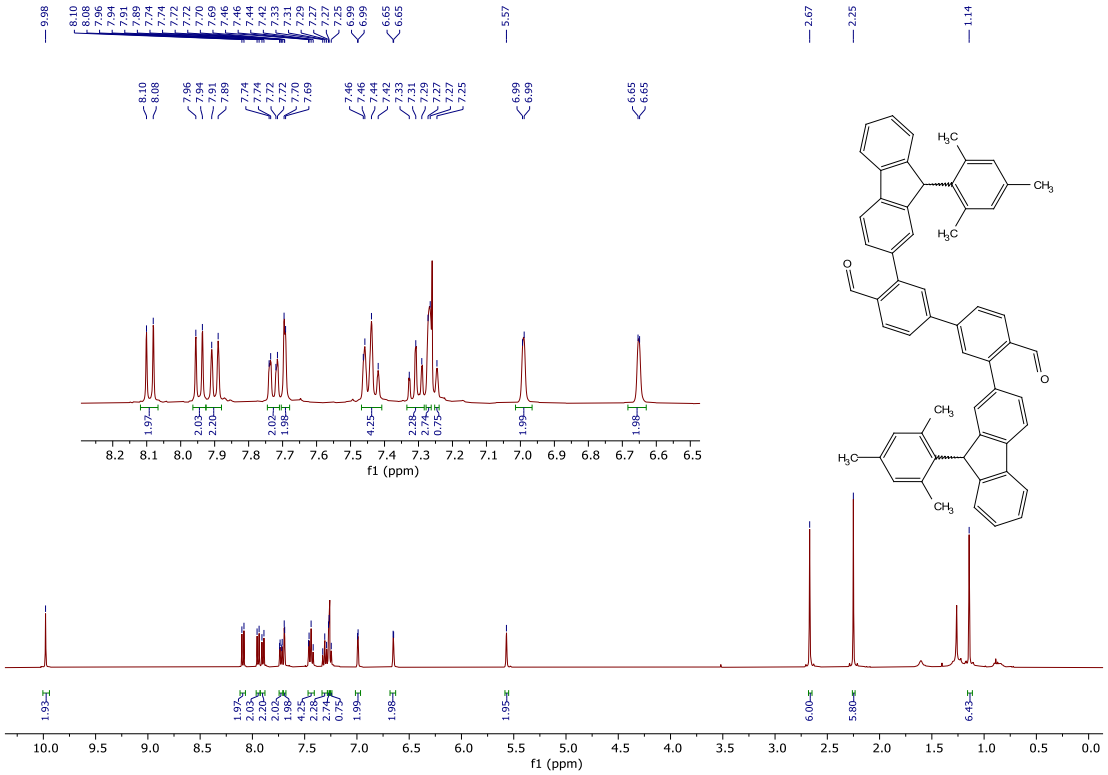

Figure 4.25 ^{1}H NMR spectrum of **9** (in $CDCl_3$, 400 MHz, 298 K).

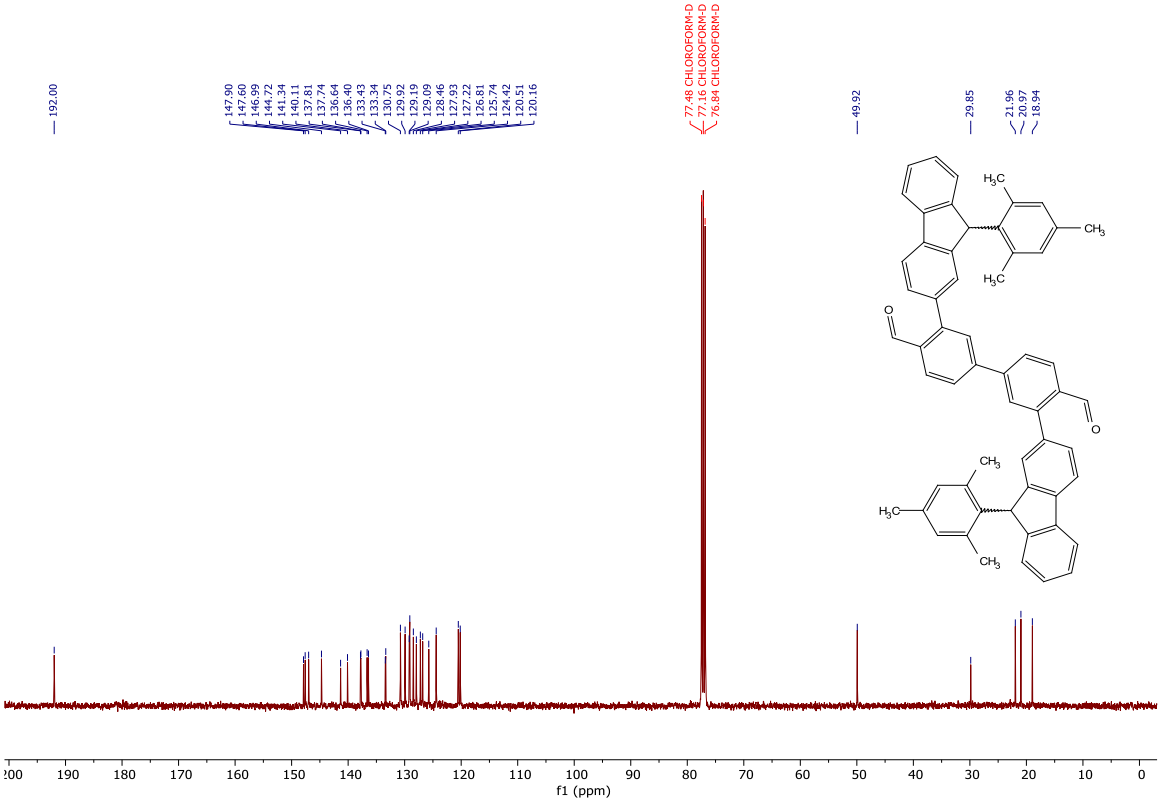

Figure 4.26 $^{13}C\{^{1}H\}$ NMR spectrum of **9** (in $CDCl_3$, 100 MHz, 298 K).

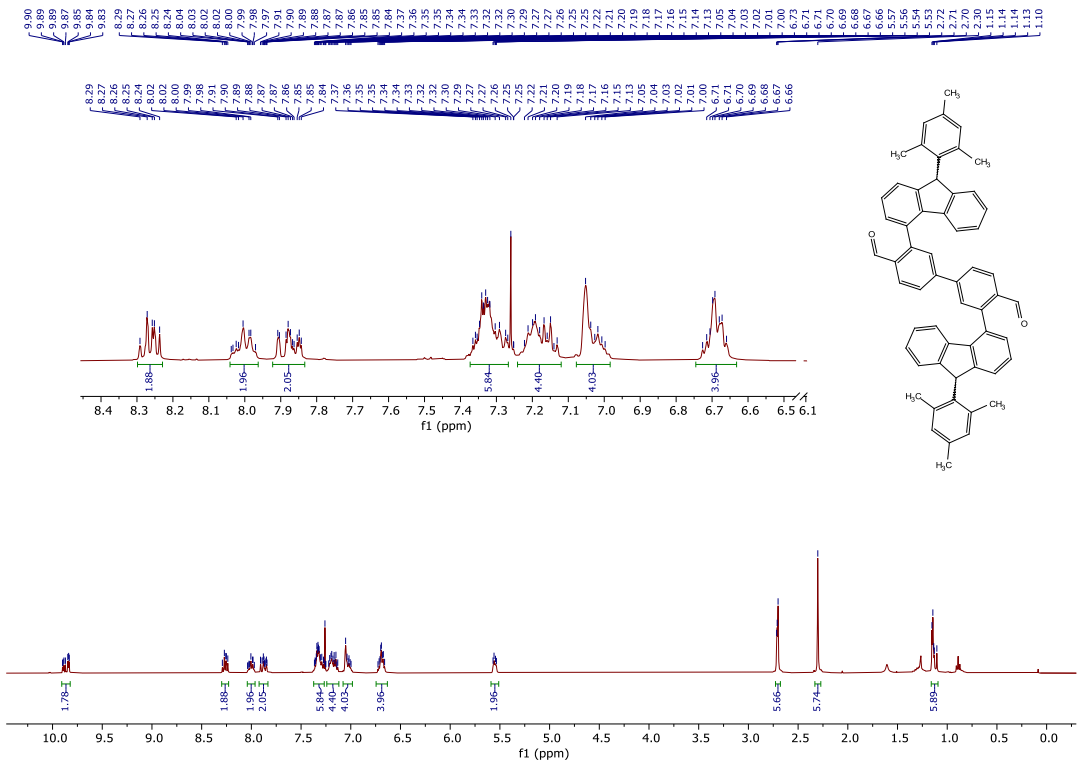

Figure 4.27 ^{1}H NMR spectrum of **10** (in $CDCl_3$, 400 MHz, 298 K).

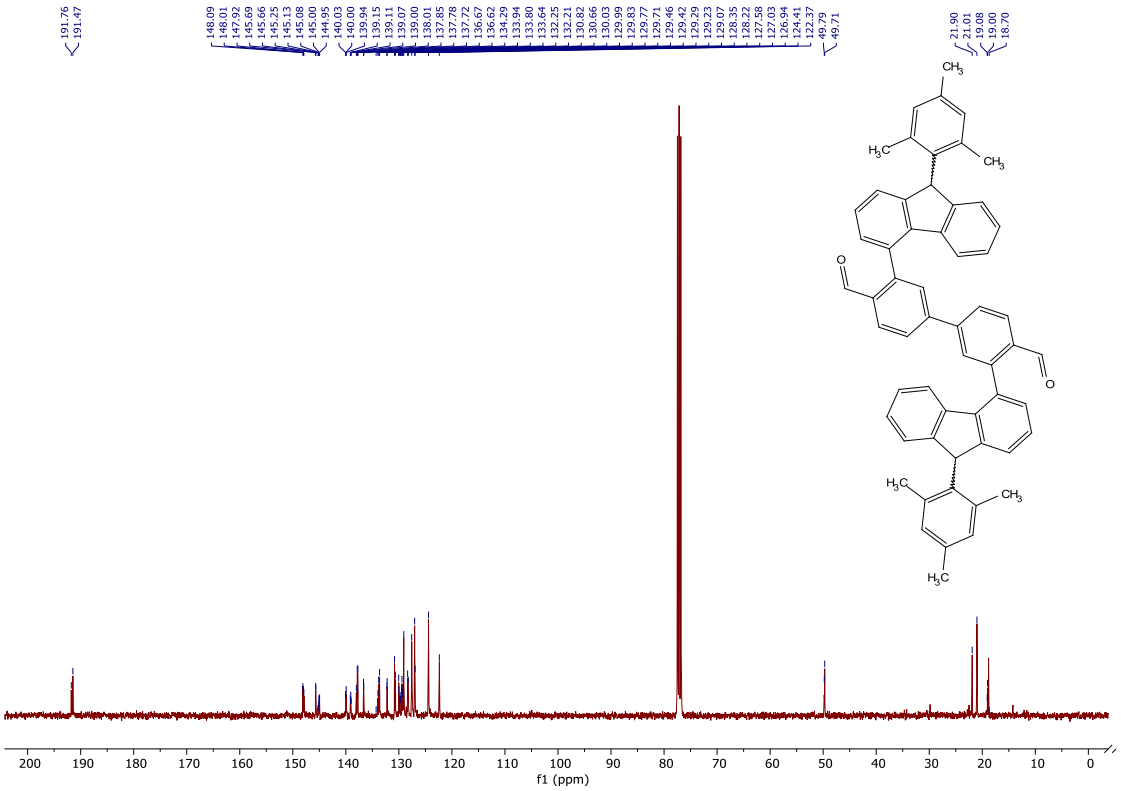

Figure 4.28 $^{13}C\{^{1}H\}$ NMR spectrum of **10** (in $CDCl_3$, 100 MHz, 298 K).

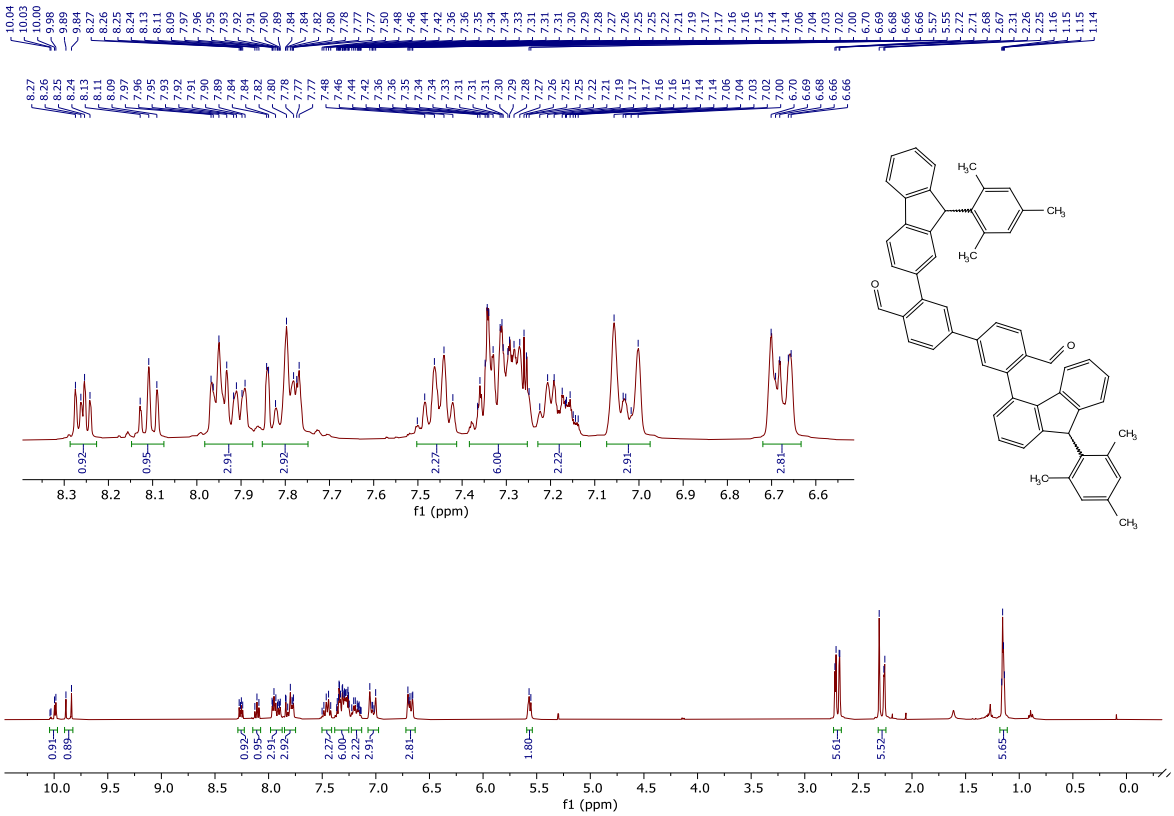

Figure 4.29 ^{1}H NMR spectrum of **11** (in $CDCl_3$, 400 MHz, 298 K).

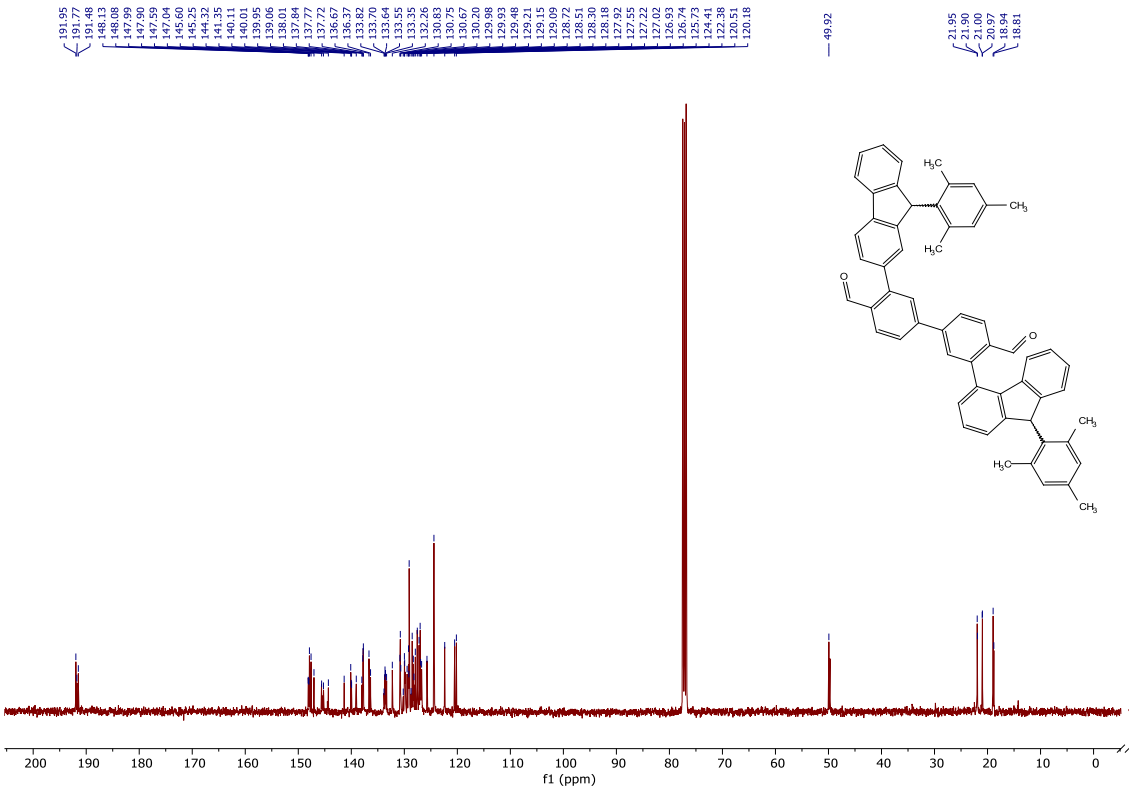

Figure 4.30 $^{13}C\{^{1}H\}$ NMR spectrum of **11** (in $CDCl_3$, 100 MHz, 298 K).

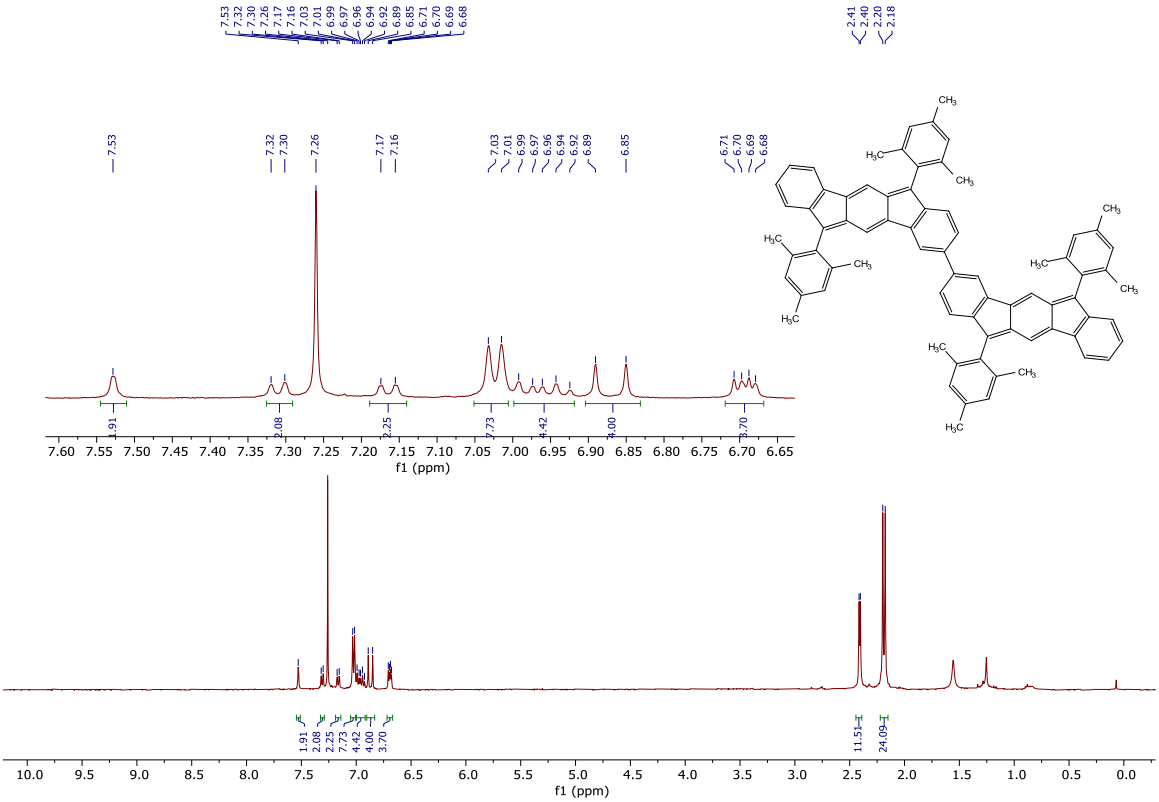

Figure 4.31 ^{1}H NMR spectrum of **1** (in $CDCl_3$, 400 MHz, 298 K).

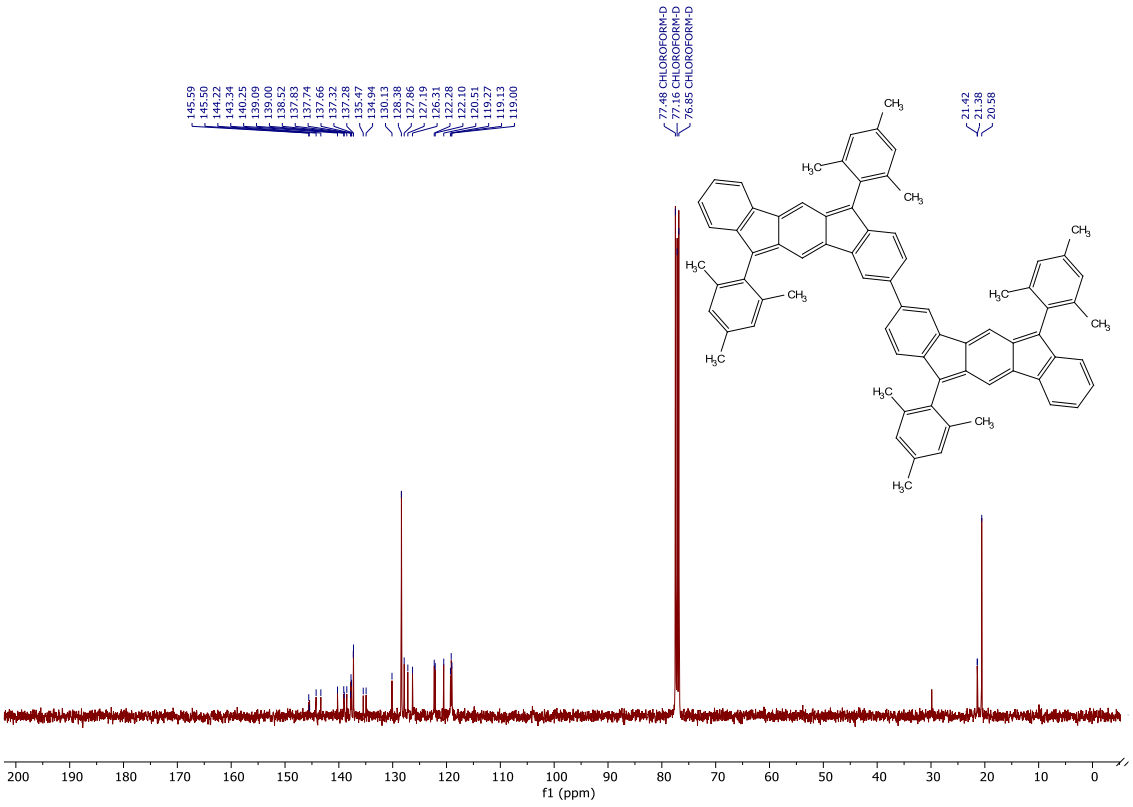

Figure 4.32 ^{13}C{^{1}H} NMR spectrum of **1** (in $CDCl_3$, 100 MHz, 298 K).

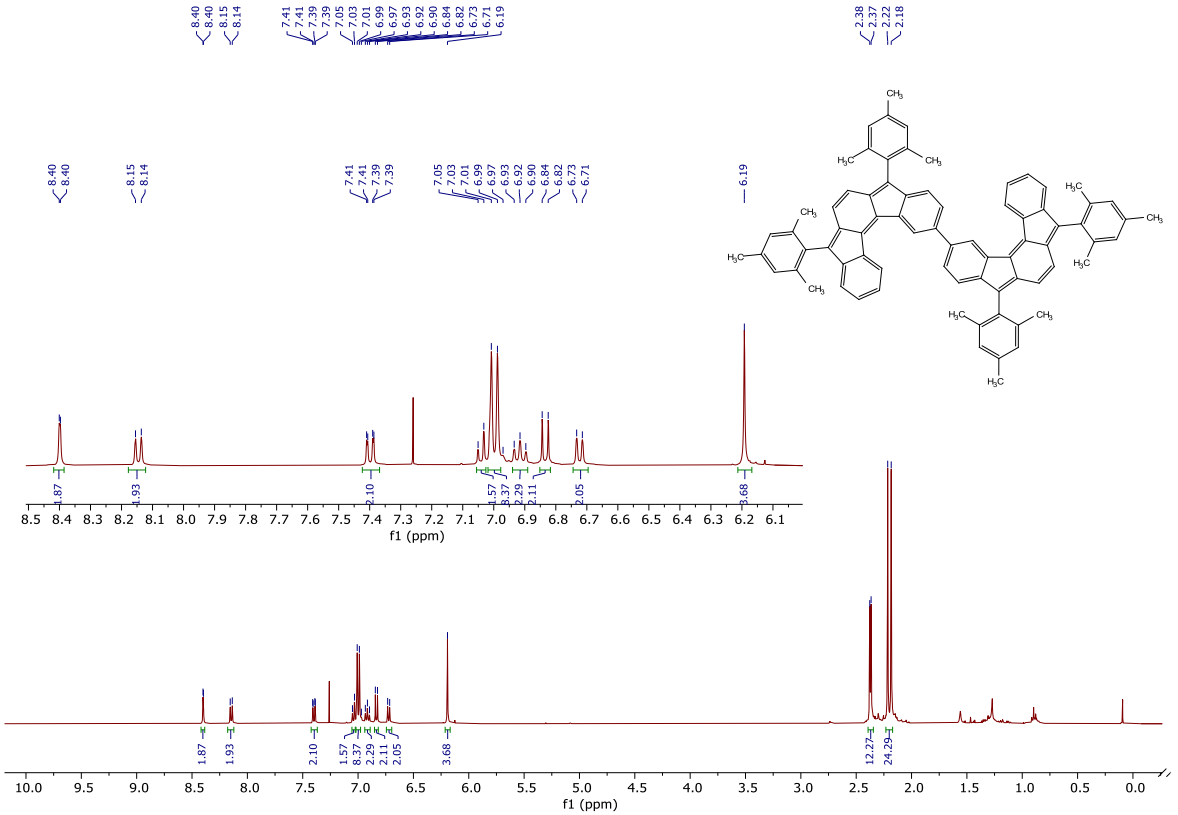

Figure 4.33 ^{1}H NMR spectrum of **2** (in $CDCl_3$, 400 MHz, 298 K).

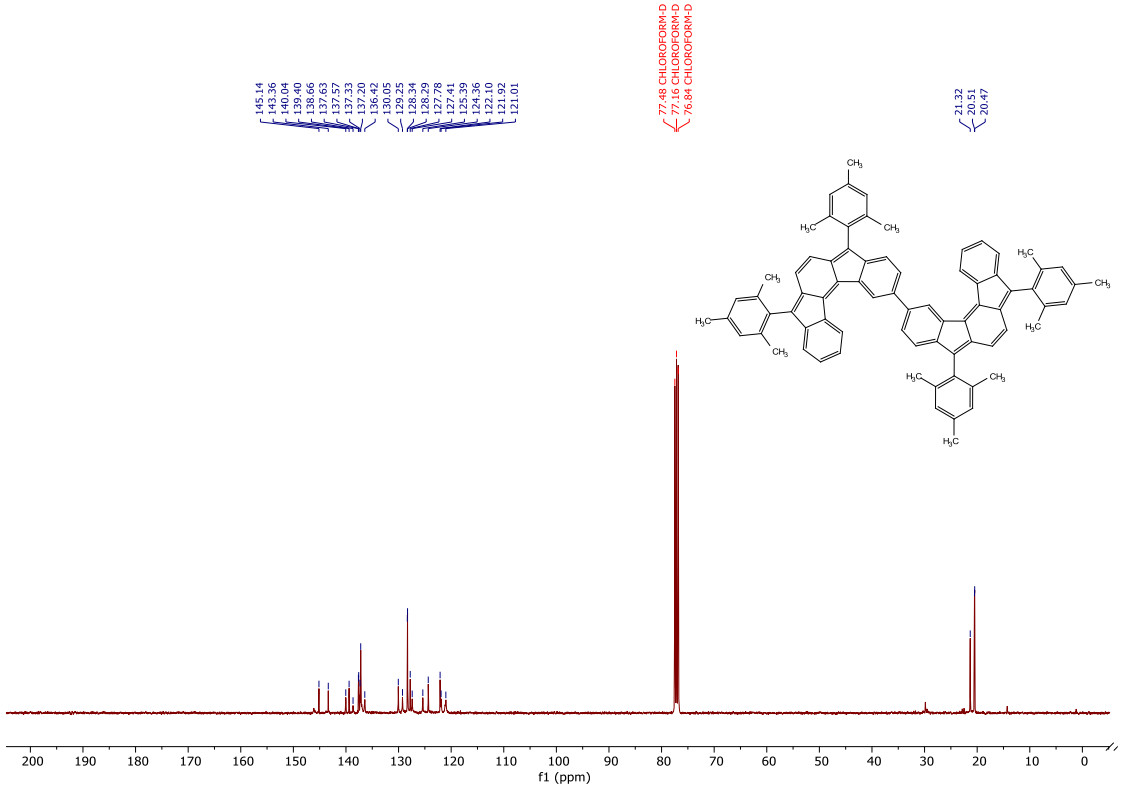

Figure 4.34 $^{13}C\{^{1}H\}$ NMR spectrum of **2** (in $CDCl_3$, 100 MHz, 298 K).

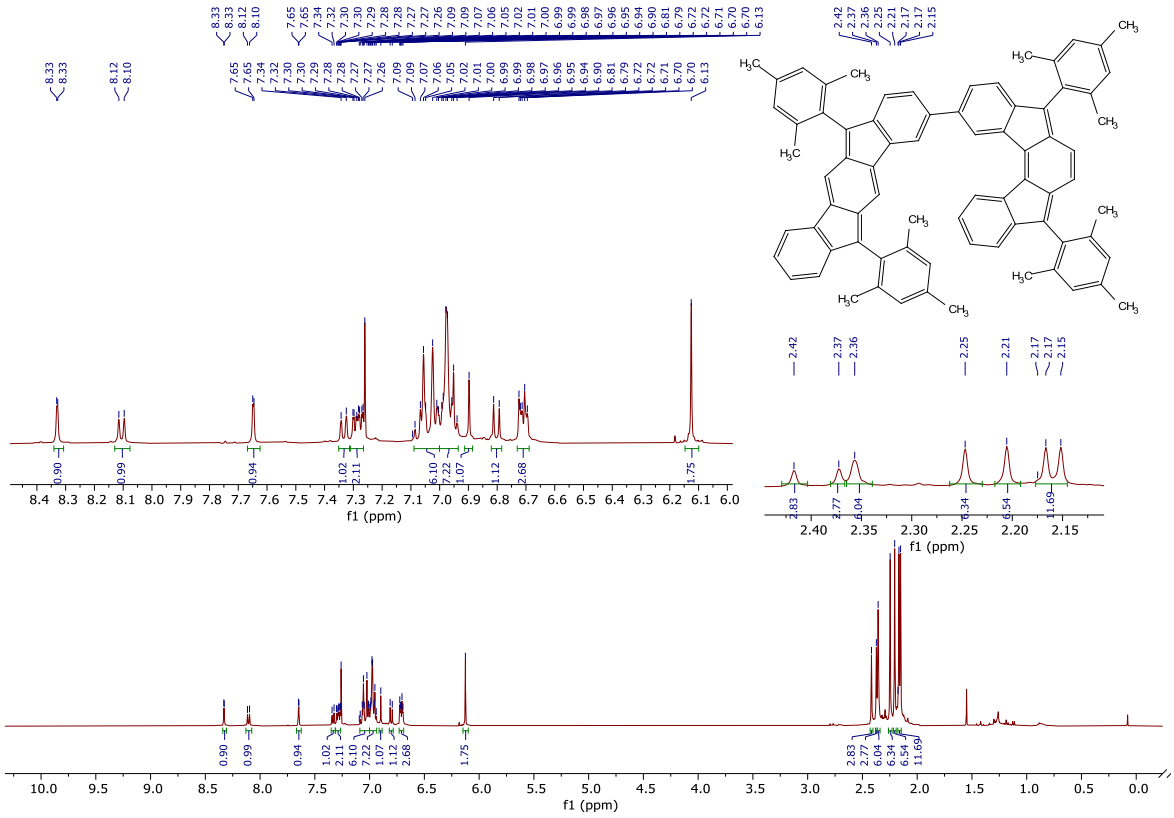

Figure 4.35 ^{1}H NMR spectrum of **3** (in $CDCl_3$, 400 MHz, 298 K).

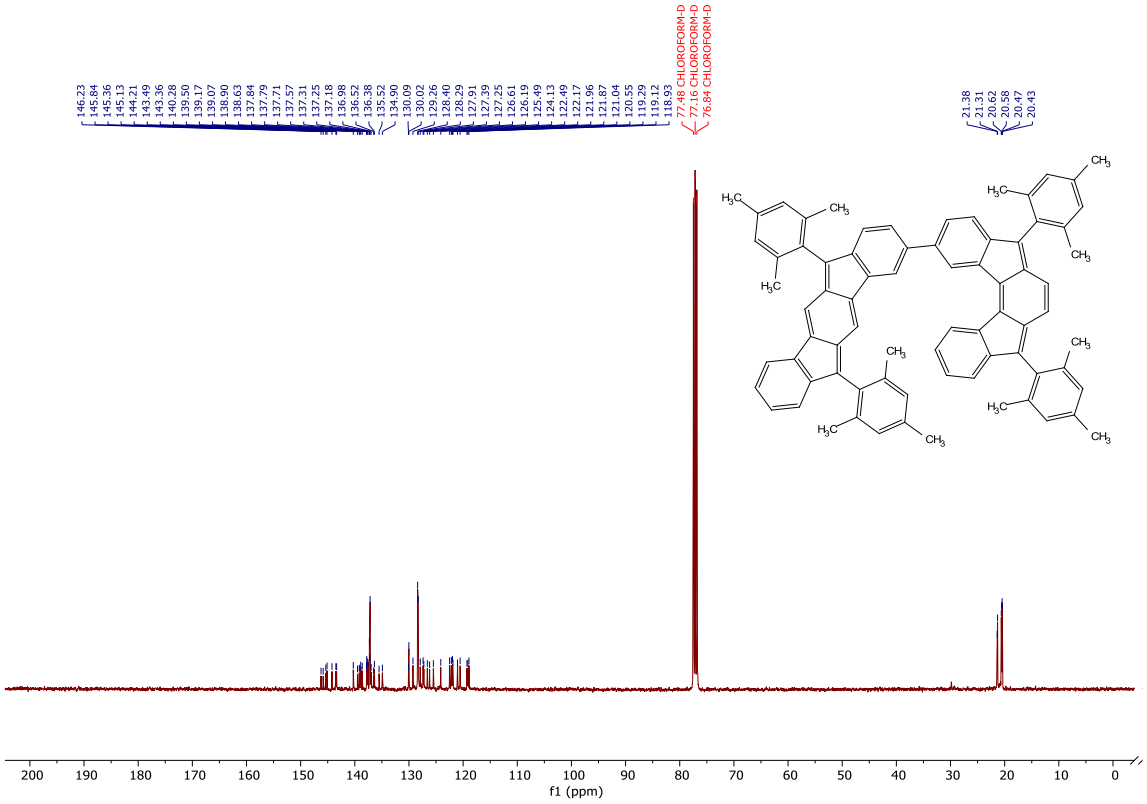

Figure 4.36 $^{13}C\{^{1}H\}$ NMR spectrum of **3** (in $CDCl_3$, 100 MHz, 298 K).

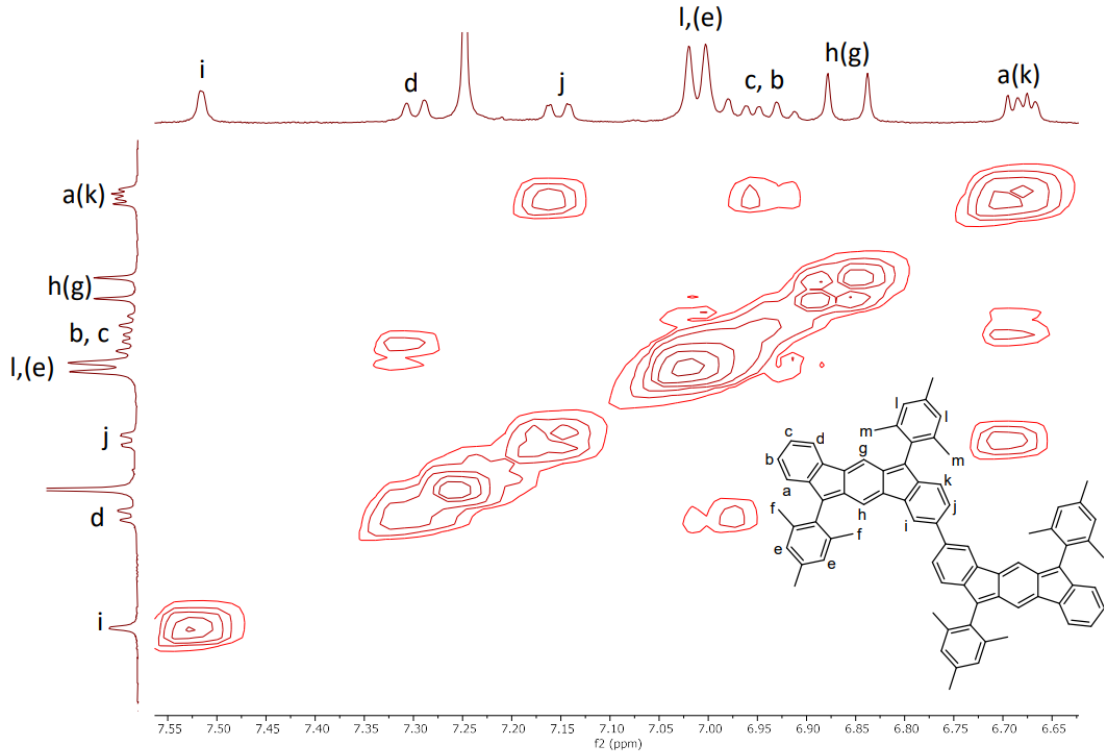

Figure 4.37 ^{1}H-^{1}H COSY spectrum of **1** (in $CDCl_3$, 100 MHz, 298 K)**.**

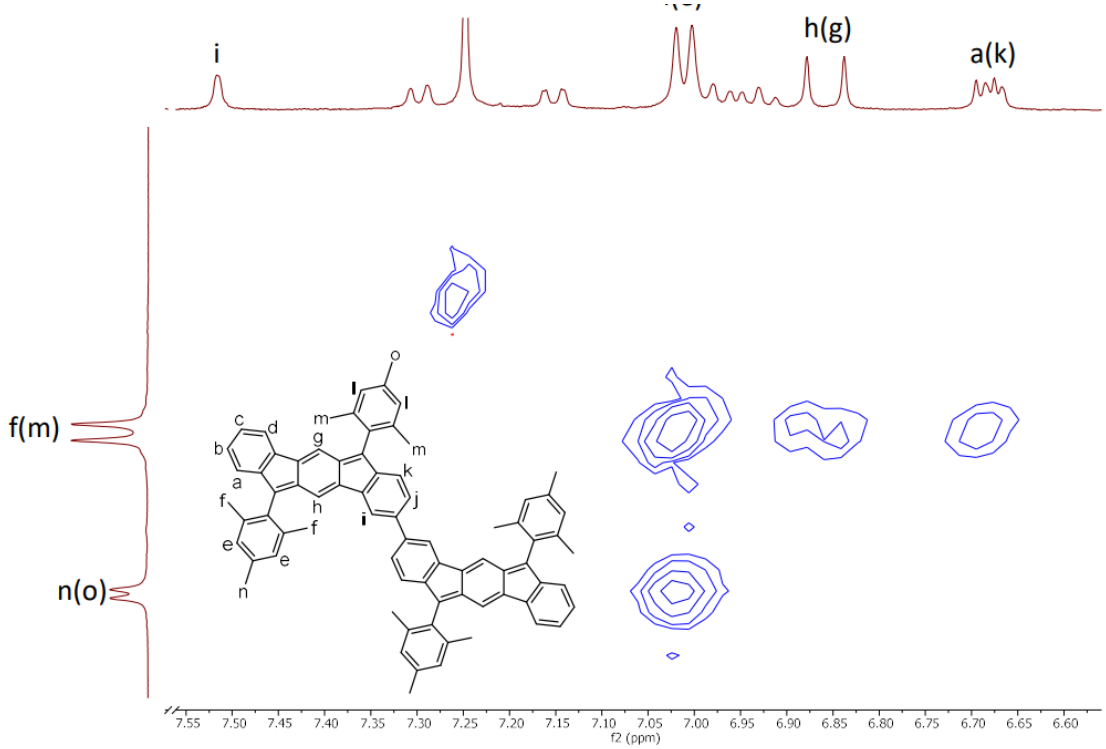

Figure 4.38 Expanded ^{1}H-^{1}H NOESY (aromatic *vs* aliphatic region) spectrum of **1**.

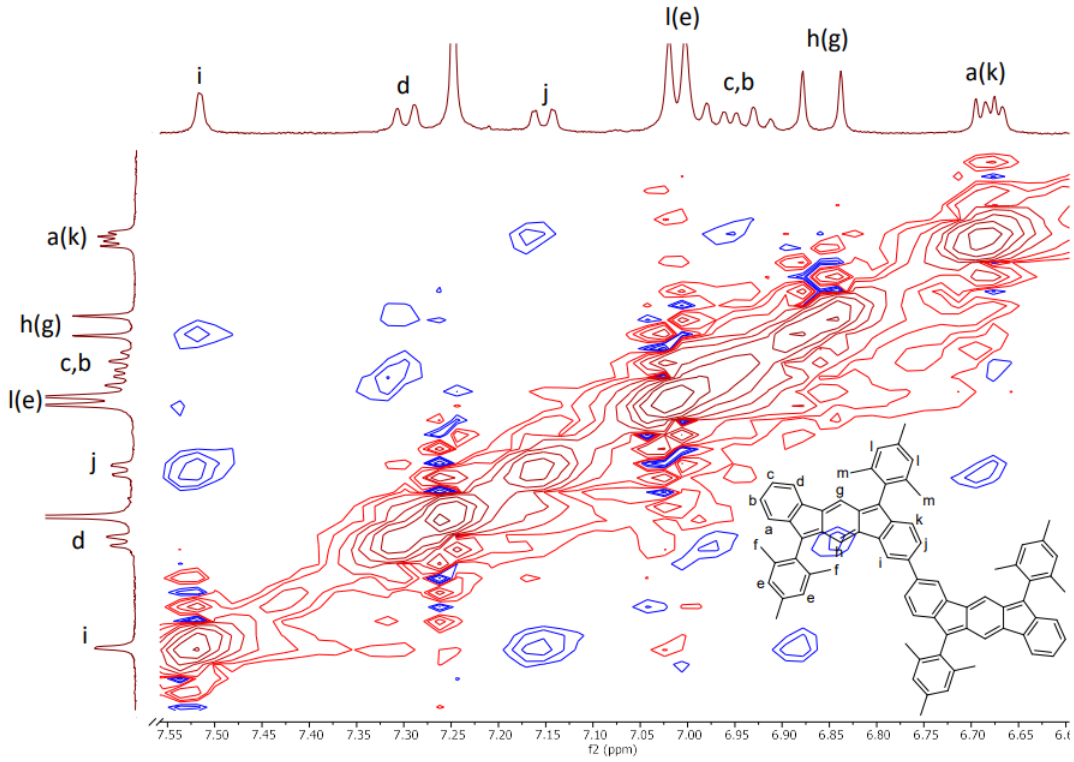

Figure 4.39 Expanded ^{1}H-^{1}H NOESY (aromatic *vs* aromatic region) spectrum of **1**.

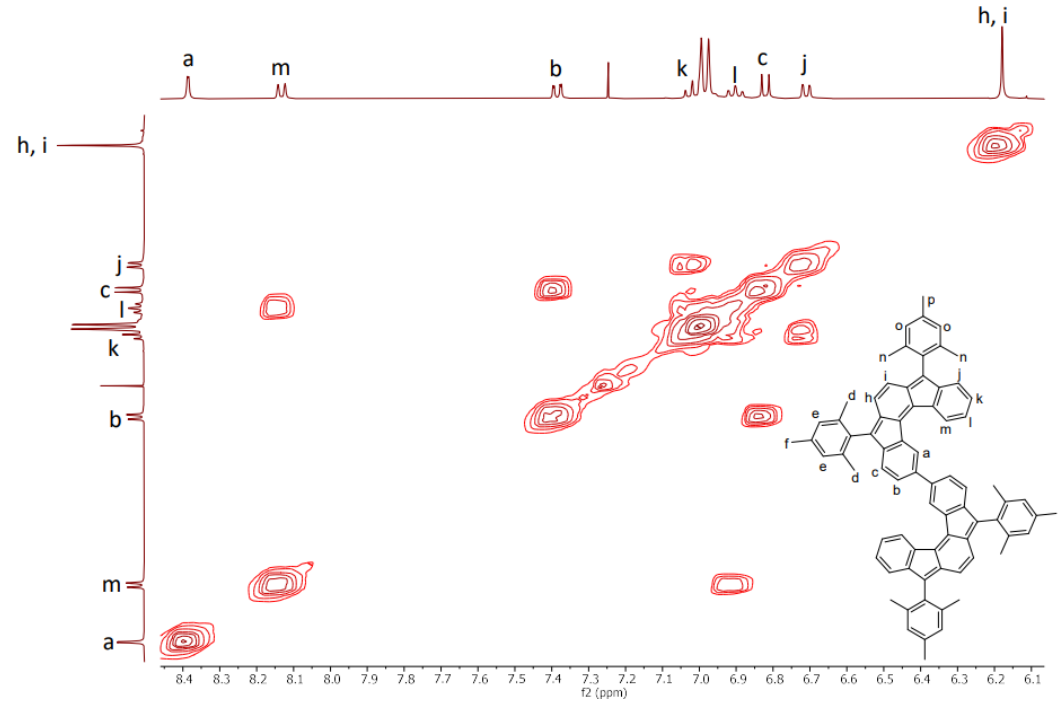

Figure 4.40 ^{1}H-^{1}H COSY spectrum of **2** (in $CDCl_3$, 100 MHz, 298 K).

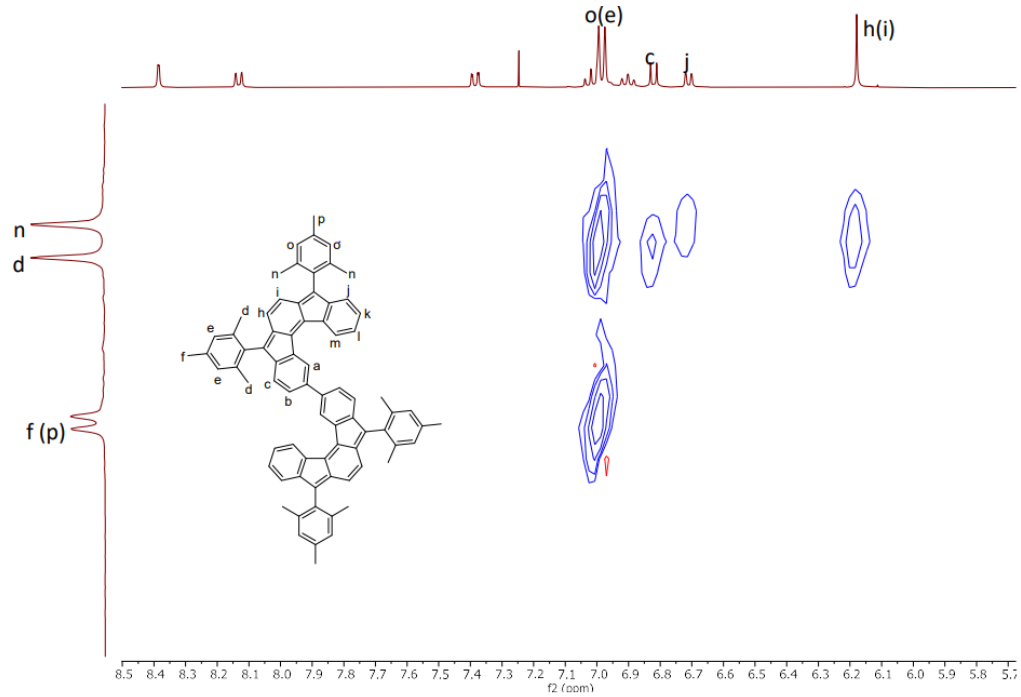

Figure 4.41 Expanded ^{1}H-^{1}H NOESY (aromatic *vs* aliphatic region) spectrum of **2**.

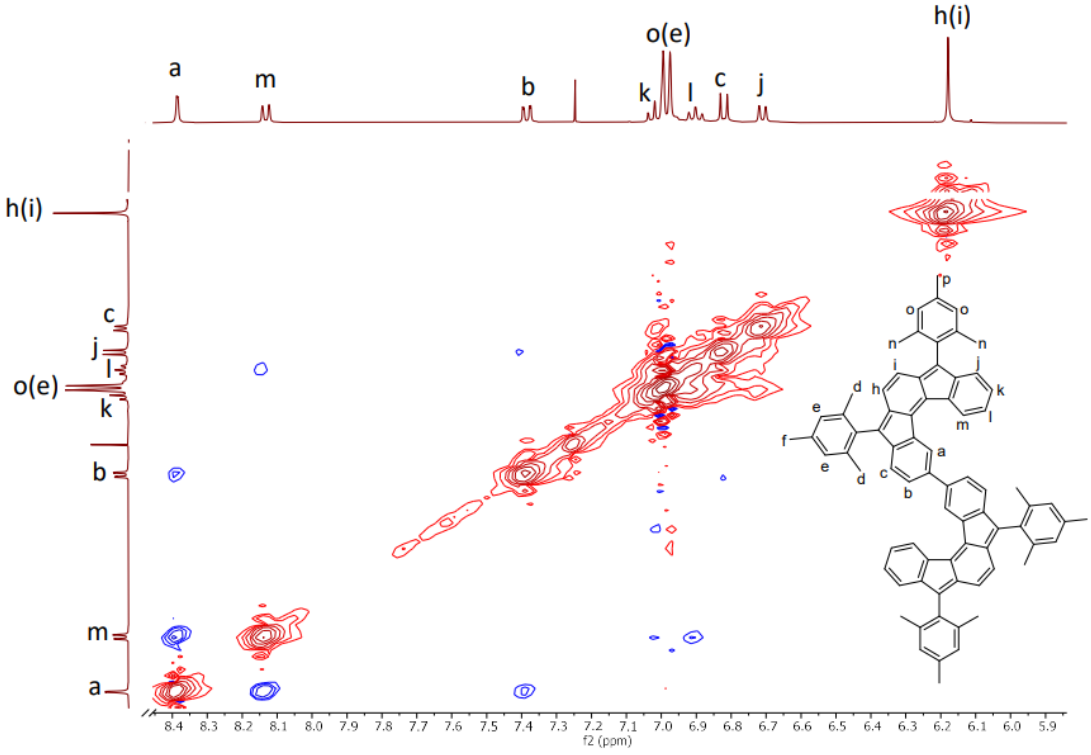

Figure 4.42 Expanded ^{1}H-^{1}H NOESY (aromatic *vs* aromatic region) spectrum of **2**.

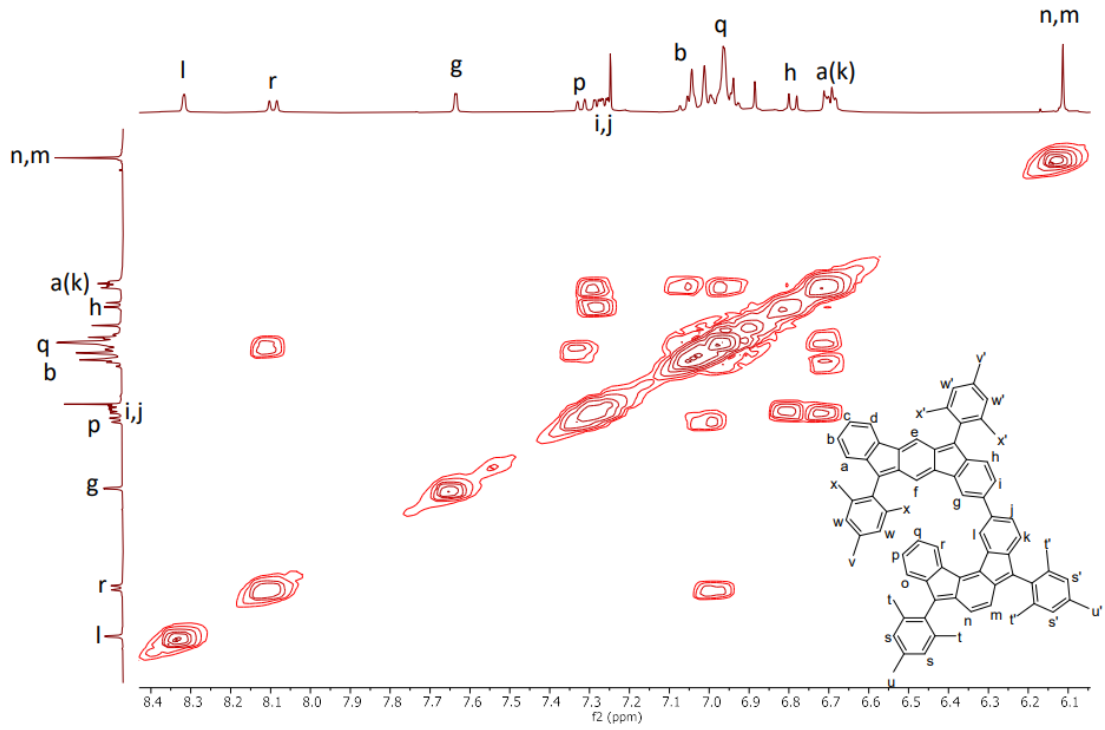

Figure 4.43 ^{1}H-^{1}H COSY spectrum of **3** (in $CDCl_3$, 100 MHz, 298 K).

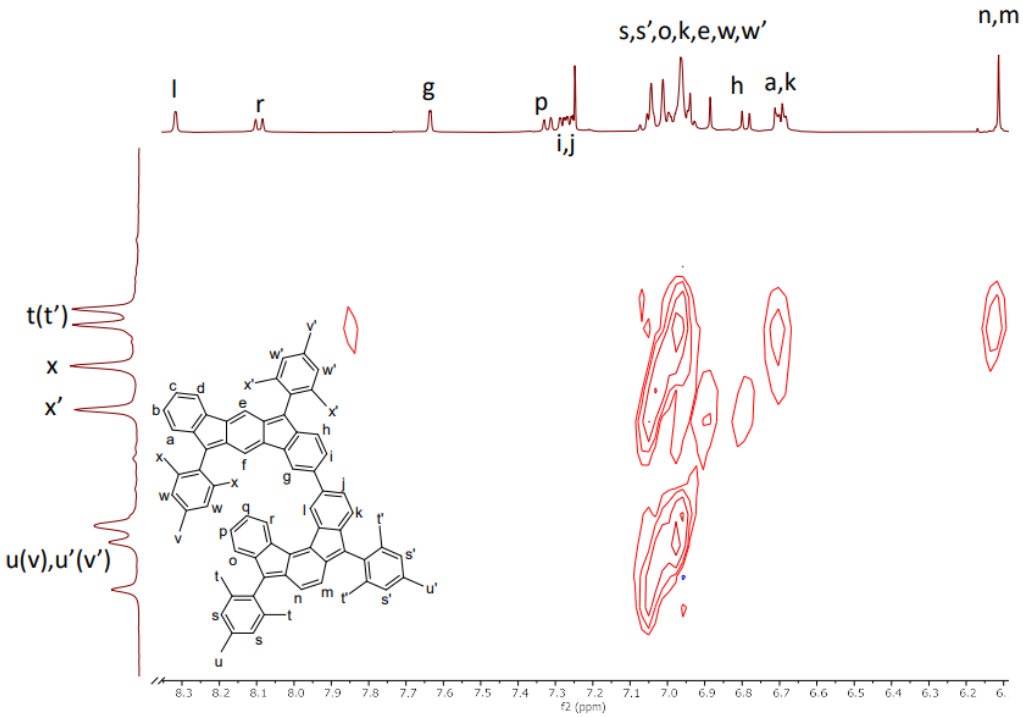

Figure 4.44 Expanded ^{1}H-^{1}H NOESY (aromatic *vs* aliphatic region) spectrum of **3**.

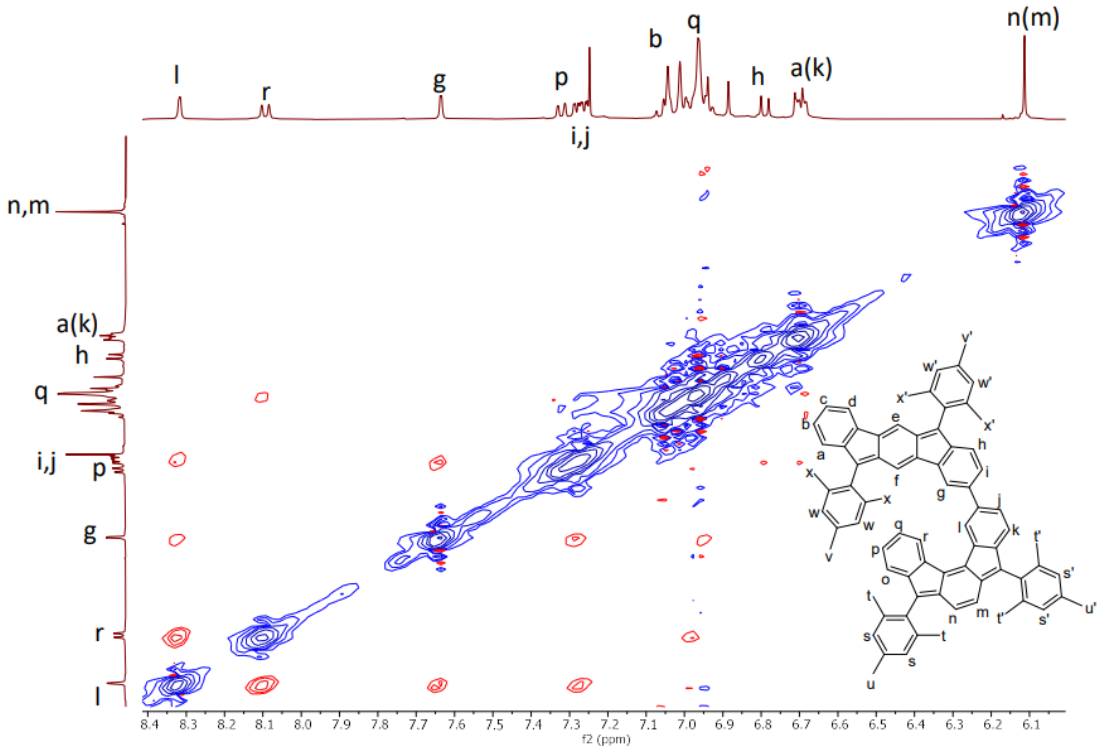

Figure 4.45 Expanded ^{1}H-^{1}H NOESY (aromatic *vs* aromatic region) spectrum of **3**.

Chapter 5

6,6′-Biindeno[1,2-*b*]fluorene: an open-shell indenofluorene dimer

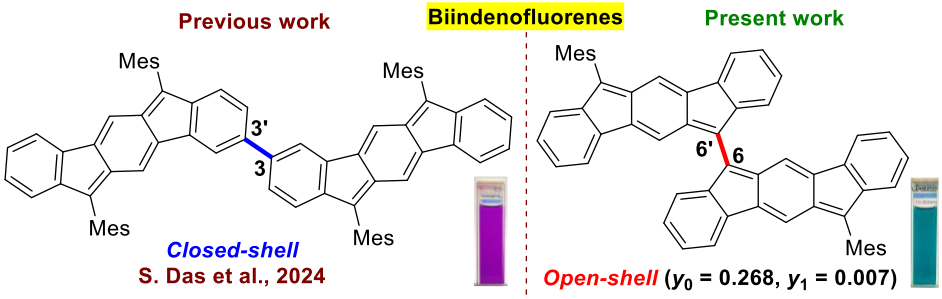

❖ This work was co-authored with Palash Jana, Dr. Subhajit Bandyopadhyay who performed ESR measurements, Dr. Dibyendu Mallick who carried out ACID calculations, and Dr. Soumyajit Das, who provided guidance and editorial assistance. This work was originally published in ***Chemical Science*** as an Edge article. (Reference*: Chem. Sci.*, 2024, **15**, 20215–20222)

5.1 Abstract

Nakano et al. reported that the antiaromatic indenofluorene (IF) isomers are diradicaloid molecules having varying degrees of open-shell character, with indeno[1,2-*b*]fluorene displaying a weaker diradical character index (y_0 = 0.072). Unlike 6,12-trimethylsilylethynyl disubstituted [1,2-*b*]IF, the 6,12-aryl disubstituted [1,2-*b*]IF derivatives did not show any experimental evidence of diradical properties. This raised the question of whether a [1,2-*b*]IF dimer would prefer a closed-shell or an open-shell ground state. To address this, herein we report the synthesis of a 6,6′-biindeno[1,2-*b*]fluorene derivative, which is a [1,2-*b*]IF dimer, constructed by linking two [1,2-*b*]IF units with a C–C single bond at carbons 6 and 6' bearing the largest orbital coefficients for the highest occupied and lowest unoccupied molecular orbitals (HOMO and LUMO). The C6–C6′ linkage effectively narrowed the HOMO–LUMO gap while the strong desire to avoid *s*-indacene antiaromaticity restored two Clar sextets in two proaromatic *para*-quinodimethane subunits, resulting in an open-shell bifluorenylidene-type diradicaloid (y_0 = 0.268) ground state with minor tetraradical character index (y_1 = 0.007). The open-shell nature was confirmed by single crystal X-ray and electron spin resonance analyses, and supported by theoretical calculations.

5.2 Introduction

Open-shell (OS) singlet diradicaloid[1] polycyclic hydrocarbons (PHs) have received widespread attention in the fields of organic synthesis,[2] physical organic,[3] structural organic,[4] and organic materials[5] chemistry. The recovery of aromaticity in proaromatic quinoidal PHs[6] is a major driving force toward the OS ground state for higher order zethrenes,[7] π-extended quinodimethanes (QDMs),[8] anthenes,[9] benzenoid[10] and non-benzenoid acenes,[11] *peri*-acenoacenes,[12] and formally antiaromatic indenofluorene (IF) isomers.[13] The five IF isomers are predicted to be OS diradicaloids,[13c,f] but the degree of diradical character (y_0) for indeno[1,2-*a*]fluorene and indeno[2,1-*b*]fluorene is larger than that of the other three isomers including indeno[1,2-*b*]fluorene (y_0 = 0.072). Indeed, 6,12-aryl and 6,12-triisopropylsilylethynyl (TIPSE) disubstituted [1,2-*b*]IFs[14] didn't show any experimental evidence of OS diradicaloid features despite carrying a proaromatic *para*-QDM (*p*-QDM shown in red, Figure 5.1a) subunit in the π-backbone. Antiaromatic molecules are regarded as delocalized diradicals.[15] Zhao reported that replacing bulkier TIPSE with a trimethylsilylethynyl group in [1,2-*b*]IF resulted in

cyclo-oligomeric products due to diradical contribution of the [1,2-*b*]IF,[16] clearly indicating its OS character.[17,13c]

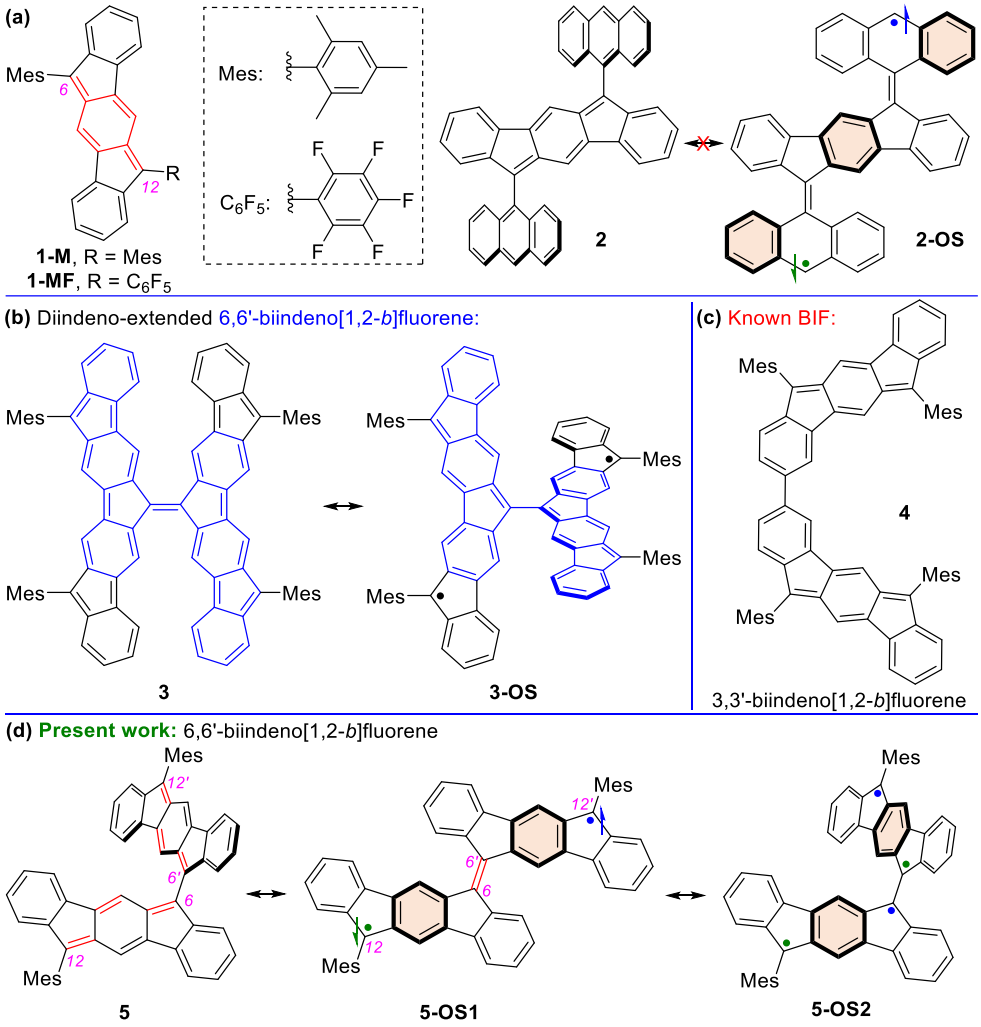

Figure 5.1 (a) Antiaromatic indeno[1,2-*b*]fluorene derivatives **1-M**, **1-MF** and **2**. (b) Zimmerman and Stępień's tetrafluorenofulvalene (TFF) **3**. (c) our reported 3,3′ -biindeno[1,2-*b*]fluorene derivative **4**. (d) closed-shell structure of targeted mesityl disubstituted 6,6′ -biindeno[1,2-*b*]fluorene **5** and its representative open-shell (OS) diradicaloid bifluorenylidene-type structure **5-OS1** and tetraradicaloid biindenofluorene-type structure **5-OS2**.

Aryl substitutions on the apical carbons (C6 and C12, Figure 5.1a) of [1,2-*b*]IF for either symmetrical[14b] **1-M** or unsymmetrical[18] **1-MF** didn't allow any diradical properties to be observed experimentally, despite lowering of the highest occupied molecular orbital (HOMO)-lowest unoccupied molecular orbital (LUMO) energy gap (hereafter denoted as HLG) in **1-MF** than **1-M** due to a smaller dihedral angle between the C_6F_5 unit and IF backbone enabling a greater π-delocalization. Quinoidal π-extension of the *s*-indacene core in the form of 2,6-anthraquinodimethane (2,6-AQDM)

may result in an OS π-extended [1,2-*b*]IF,[19] similar to non-benzenoid bis(phenalenyl)[20] and benzenoid nonazethrene[7b] bearing a 2,6-AQDM core. While the 2,6-naphthaquinodimethane (2,6-NQDM)-embedded π-extended [1,2-*b*]IF was originally reported to be closed-shell (CS), its OS properties were accessed subsequently only above 200 °C.[21] Notably, benzenoid octazethrene containing a 2,6-NQDM subunit is an OS molecule.[22]

Alongside aromaticity recovery, a small HLG is crucial[23] for PHs displaying OS ground state. Extension of the π-delocalization path is the key to decrease the HLG. In this regard, Yamashita's work on anthryl disubstituted [1,2-*b*]IF **2** is noteworthy (Figure 5.1a).[24] Molecule **2** displayed a CS ground state, though one can draw structure **2-OS** with three additional aromatic benzene rings (Clar sextets[7d]). Presumably, the large dihedral angle (~76°) between the anthryl groups and IF backbone for **2** inhibits efficient π-delocalization, and thus recovery of the three Clar sextets in **2-OS** has negligible contribution to the ground state structure. Sterically overcrowded alkene bridged PHs have lately gained attention as novel OS diradicaloids as they release steric strain and recover Clar sextets when switching from the Kekulé-type CS quinoidal form to OS diradical form.[25] Tetrafluorenofulvalene (TFF)[26] **3** is the latest example among them bearing two π-extended [1,2-*b*]IF units connected through an apical olefinic C–C linkage (Figure 5.1b). TFF **3** was viewed[26] as a diradicaloid **3-OS** bearing diindeno-fused 6,6′-biindeno[1,2-*b*]fluorene (6,6′-[1,2-*b*]BIF unit shown in blue for **3**). While **3** clearly exhibited an OS singlet ground state with a small singlet(S)–triplet(T) energy gap (ΔE_{S-T}) due to the release of steric strain and recovery of Clar sextets as it switches from its non-aromatic olefinic form to polyradical forms, what remained unknown is whether the 6,6′-[1,2-*b*]BIF motif without diindeno-radical (shown in black for **3-OS**) fusion exhibits OS properties.

We envisaged the design of 12,12′-dimesityl-6,6′-biindeno[1,2-*b*]fluorene **5** that can recover two additional Clar sextets in its OS diradical **5-OS1** and tetraradical **5-OS2** forms (Figure 5.1d). The **5-OS2** and **5** forms are viewed as biindenofluorene (BIF) motifs while **5-OS1** is a diindeno-fused bifluorenylidene (BF) diradical. BF usually prefers a twisted form over the folded form,[25a] and BF-based materials are promising hole and electron transporters in organic photovoltaics.[27] Interestingly, an extended quinoidal form of 6,6′-[1,2-*b*]BIF was theoretically shown to contribute to a poly-IF which is a π-elongated BF-type structure.[28] However, synthesis of a hypothetical smaller

quinoidal fragment like **5**, which majorly contributes to the ground state properties of Scherf's poly-IF,[28] remained unknown thus far. Our recently reported BIF **4** (Figure 5.1c) displayed a CS ground state, which was formed by dimerizing two [1,2-*b*]IF units through carbons 3 and 3′ with appreciable HOMO and LUMO coefficients.[29] Because the apical carbons 6/6′(12) contain larger HOMO and LUMO distributions than those of carbons 3/3′(9),[29] we hypothesized that dimerizing two [1,2-*b*]IF units by apical carbons 6 and 6′ may significantly influence both HOMO and LUMO energy levels in **5**.

Moreover, the large alternation of C=C/C–C bonds of the *p*-QDM subunit of *s*-indacene makes **5** a polyene-like system considering the apical π-conjugation path resembling a dodecahexaene subunit (shown in red for **5**, Figure 5.1d). This polyene subunit may act as a plausible π-delocalization path due to a smaller inter-IF torsional angle. It is known that the C–C double bond for ethylene is quite short, while in longer polyene chain, an increase of the C–C double bond and shortening of the adjacent C–C single bond may occur, leading to an extension of π-conjugation and a decrease of HLG.[30] A small torsional angle may lead to a greater electronic communication between the IF units for **5**, resulting in a smaller HLG. The hypotheses of a smaller HLG for the BIF **5** than that of **4** and recovery of two Clar sextets in OS forms for **5** enthused us to explore the ground state properties of **5** by computational and experimental approaches.

5.3 Results and Discussion

5.3.1 DFT studies

Since a *para*-quinoidal 6,6′-[1,2-*b*]BIF-type π-extended structure is reported to dominate the ground state of BF-type poly-IF to favor mutual distortion,[28] we first conducted density functional theory (DFT) calculations to examine if **5** is OS in the ground state. The DFT calculations of **5,** using the same level of theory ((U)CAM-B3LYP/6-31G(d,p)) as that used for **3**,[26] suggested that the energy of the OS singlet state is 4.85 kcal mol^{-1} lower than that of the triplet state (i.e. ΔE_{S-T} = –4.85 kcal mol^{-1}, Table 5.1).

Table 5.1 Relative energies for the optimized structure **5** at CAM-B3LYP/6-31G(d,p) level of theory

State	Hartree	kcal/mol
Singlet Closed-Shell	-2234.270543	-1402024.874
Singlet Open-Shell	-2234.274569	-1402027.401
Triplet biradical	-2234.266828	-1402022.543

Compound 5 : $\Delta E_{Singlet(OS)-Triplet}$ = −4.85 kcal/mol. ΔE_{OS-CS} = −2.52 kcal/mol. ΔE_{CS-T} = −2.33 kcal/mol. Occupation numbers of HOMO-1 = 1.889, HOMO = 1.435, LUMO = 0.564, LUMO+1 = 0.111, affording a 26.8% diradical character (singlet diradical character index (y_0) = 0.268) and 0.7% tetraradical character (singlet tetraradical character index (y_1) = 0.007).

The frontier molecular orbital (FMO) profiles of singly occupied molecular orbitals (SOMO) display a characteristic disjointed nature of the alpha (SOMO-α) and beta (SOMO-β) spins for the ground state singlet diradical (Figure 5.2b and 5.2c), while the spin densities are found to be delocalized over the π-conjugated IF backbone with four apical carbons bearing the larger spin densities (Figure 5.2a). The large spin densities on the four apical carbons imply singlet diradical and tetraradical characters, which were found to be 26.8% and 0.7%, respectively, based on the natural orbital occupancy number (NOON) calculations.

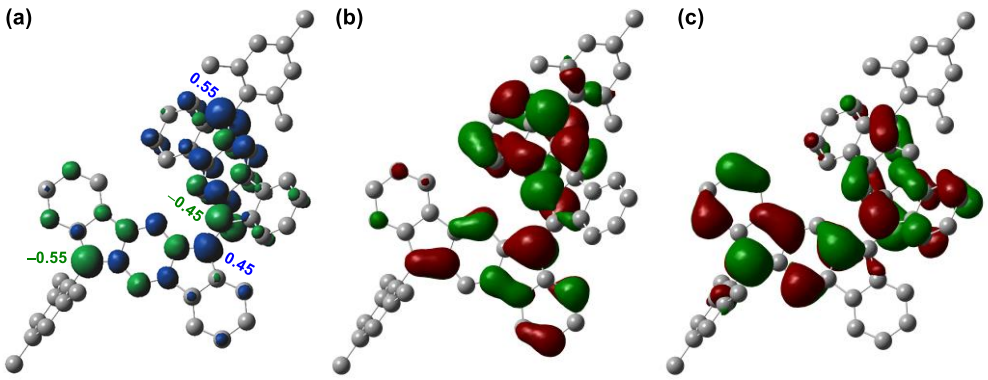

Figure 5.2 (a) Spin density map of **5**. Isovalue for surfaces: MO = 0.02, density = 0.005. frontier molecular orbital profiles for the (b) α-spin and (c) β-spin of **5**.

The negligible tetraradical character of **5** may be attributed to the minor driving force (no additional Clar sextet recovery; only a minor inter-IF steric clash) toward **5-OS2** from **5-OS1** (Figure 5.1d). However, the strong desire[6a] to avoid *s*-indacene antiaromaticity through recovery of two Clar sextets may drive quinoidal **5** to become diradicaloid **5-OS1** in the singlet ground state by enhancing the C6–C6′ π-bond

character while locating radicals at apical carbons 12 and 12′ bearing largest spin densities (Mulliken spin density of 0.55). As molecules with intermediate diradical character are important for non-linear optics, singlet fission and molecular electronics,[3,5] we designed a sterically promoted synthetic approach to construct **5** and study its ground state characteristics experimentally.

5.3.2 Synthesis

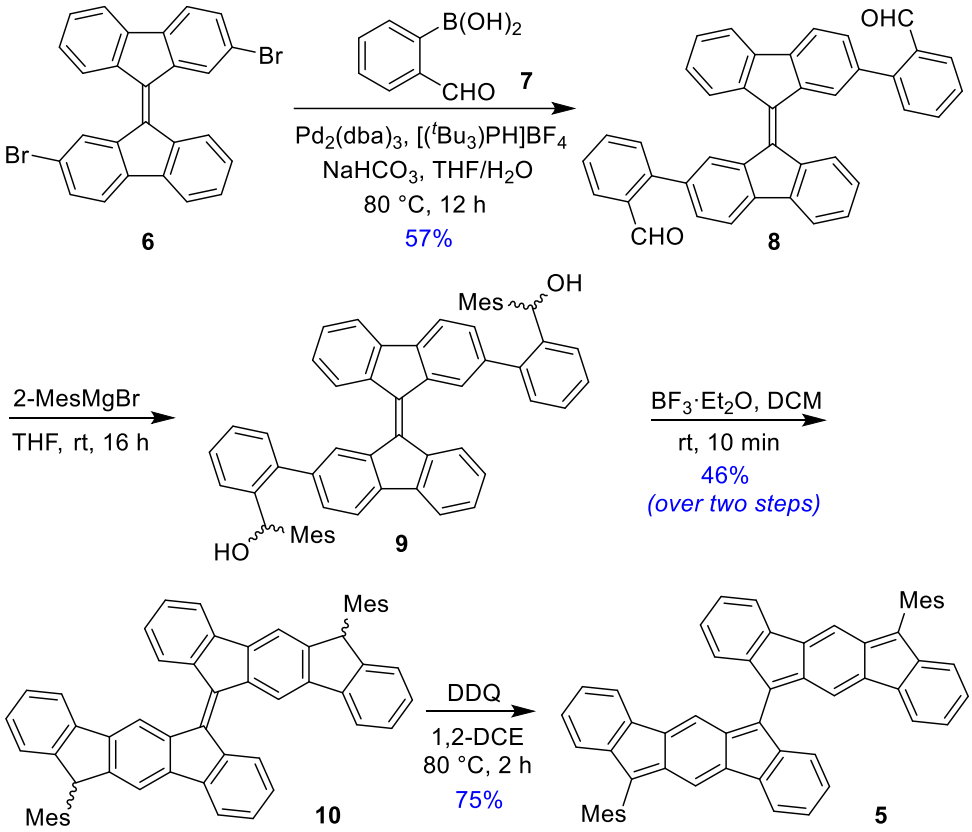

Scheme 5.1 Synthesis of BIF **5**.

BIF **5** was synthesized in multiple steps as illustrated in Scheme 5.1. 2,2′-Dibromo-9,9′-bifluorenylidene **6** was synthesized as a diastereomeric mixture following a literature method[31], and then it was subjected to a two-fold Suzuki coupling with (2-formylphenyl)boronic acid to afford dialdehyde **8** in 57% yield. Treatment of **8** with an excess of 2-mesitylmagnesium bromide at room temperature gave dicarbinol **9**, which, without purification, was treated with $BF_3{\cdot}Et_2O$ in dichloromethane (DCM) to afford dihydro derivative **10** (46% yield over two steps) by utilizing the steric crowding of bulky mesityl (Mes) groups.[18] Treatment of dihydro precursor **10** with 2,3-dichloro-5,6-dicyano-1,4-benzoquinone (DDQ) in 1,2-dichloroethane (1,2-DCE) for 2 h at 80 °C produced **5** as a blue solid in 75% yield after silica gel column chromatographic

purification. While nuclear magnetic resonance (NMR, *vide infra*) and high-resolution mass spectrometry (HRMS) analyses indicated the formation of desired product **5**, unambiguous structural confirmation was obtained from single crystal X-ray diffractometry (SCXRD) analysis (Figure 5.3a).

5.3.3 Single crystal, ESR, ground state and (anti)aromaticity analysis

Single crystals[32] of **5** were obtained by slow solvent diffusion of methanol into DCM/carbon disulfide (1 : 1) solution. As depicted in Figure 5.3a and 5.3b, the two [1,2-*b*]IF units of twisted BIF **5** form a torsional angle of ~56.5° which is much smaller than that of anthryl disubstituted [1,2-*b*]IF **2**,[24] suggesting a greater π-delocalization/electronic communication between two IF units. The bond lengths (bonds *a* to *j* are labelled in Figure 5.3a) of **5** from SCXRD analyses are in line with those from DFT analyses, and are summarized in Table 5.2. The π-delocalization is evident from the C–C bond length analyses (Table 5.2, see the Figure 5.8 for full bond length analyses including e.s.d values), as an increase of the C–C double bond lengths (C_{sp^2}=C_{sp^2} bonds *a*, *b*, *c*, *d*) for the *p*-QDM subunit of **5** was clearly observed when compared to those of symmetrical **1-M** (*a*/*c* and *b*/*d*) and unsymmetrical **1-MF**. At the same time, the C–C single bond lengths (C_{sp^2}–C_{sp^2} bonds *e*, *f*, *g*, *h*) of the *p*-QDM subunit of **5** were also found to be shorter than those of the **1-M** (*e*/*g* and *f*/*h*). Moreover, the bond length for central C–C single bond *i* connecting the IF units for **5** was found to be 1.452 Å (DFT: 1.414 Å), which corresponds to a formal single bond in the CS configuration. However, it is shorter than the C-C single bond *j* (crystal: 1.501 Å; DFT: 1.480 Å) connecting mesityl group and [1,2-*b*]IF core, and clearly shorter than the C-C single bond connecting the anthryl and [1,2-*b*]IF rings in **2** (1.492 Å).[24] The distance is comparable to BIF **4** (1.451 Å),[29] suggesting some π-bond character for the central C–C bond *i* in **5** which is strengthened due to π-electron delocalization.

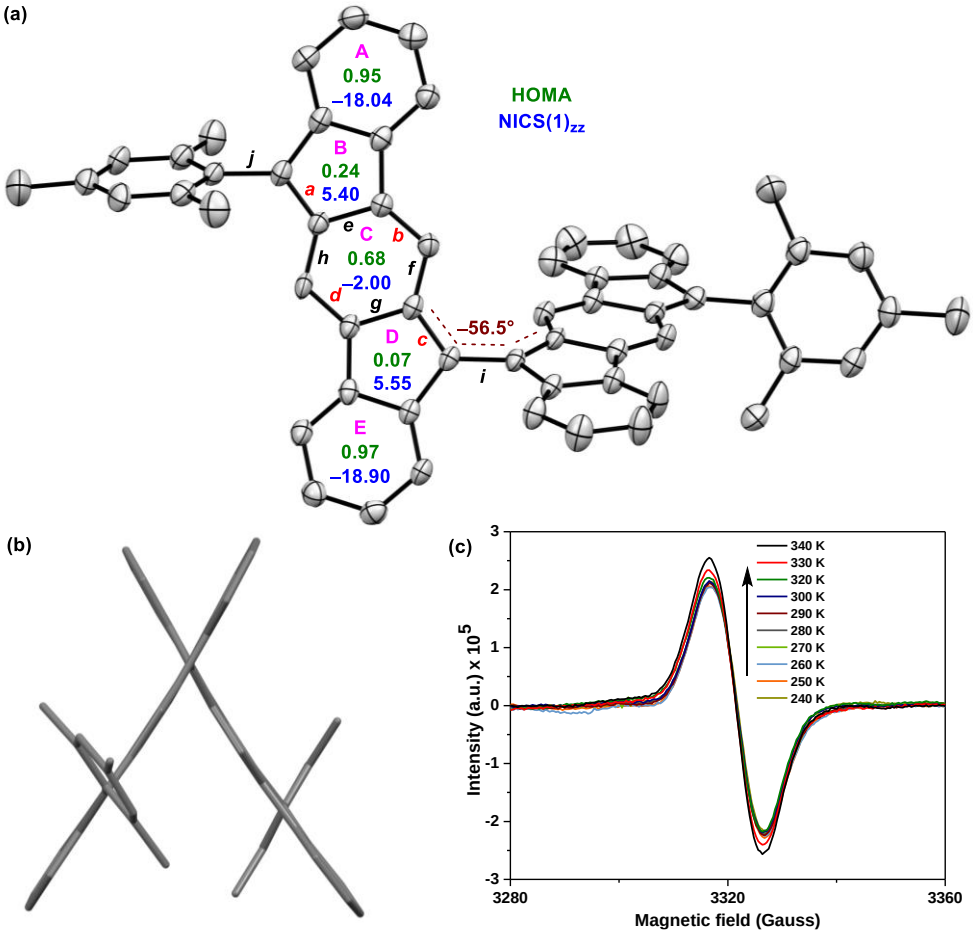

Figure 5.3 (a) X-ray crystallographic structure of **5** with the ellipsoids drawn at 30% probability level (hydrogens omitted), including NICS(1)$_{zz}$ (blue) and HOMA (green) indices. (b) side-view of **5**. (c) ESR spectra of **5** recorded at variable temperatures for the powder form.

Table 5.2 Comparison of mean C–C bond lengths (Å) for **5**, **1-MF**, and **1-M**

Bonds[a]	**5**[b]	**5**[c]	**1-MF**[d]	**1-M**[e]
a	1.392	1.403	1.372	1.380
b	1.364	1.368	1.349	1.356
c	1.392	1.429	1.373	1.380
d	1.367	1.371	1.346	1.356
e	1.456	1.441	1.433	1.467
f	1.415	1.416	1.456	1.433
g	1.459	1.436	1.435	1.467
h	1.416	1.414	1.457	1.433
i	1.452	1.414	–	–
j	1.501	1.480	1.482	1.484

[a]*a-j* bonds are labelled in Figure 5.3a. [b]SCXRD data. [c]DFT data. [d]SCXRD data from reference 18. [e]SCXRD data from reference 14b.

The above findings clearly indicate the major contribution of a diradicaloid structure **5-OS1** in the electronic ground state of **5**, which is in line with the computational analyses and the broad NMR signals observed for core protons due to thermally populated triplet species (Figure 5.4).

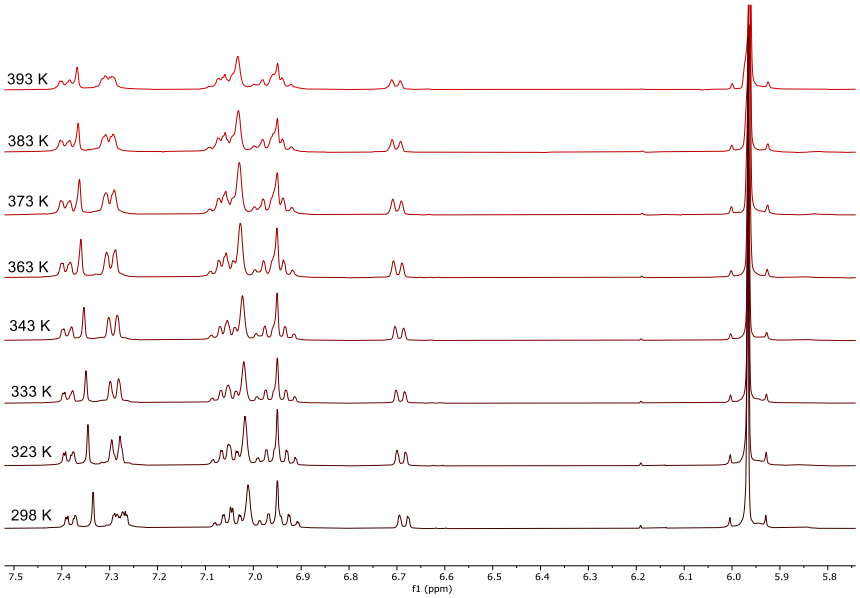

Figure 5.4 Variable temperature ^{1}H NMR spectrum of **5** (in $C_2D_2Cl_4$, 400 MHz).

Electron Spin Resonance (ESR) studies of solid **5** displayed a featureless broad ESR signal (Figure 5.3c), and when the temperature dropped, the signal intensity dropped as well. This can be explained by the fact that triplet biradical species have smaller populations at lower temperatures, thus further confirming the OS singlet ground state for **5** with $\Delta E_{S-T} = -4.35 \pm 0.6$ kcal mol^{-1}, as obtained by fitting of the ESR data using the Bleaney–Bowers equation (Figure 5.15).[33,23b]

The harmonic oscillator model of aromaticity (HOMA, Figure 5.3a)[34] for the ground state structure of **5** suggested insignificant bond length alternation (BLA) for rings A (0.95) and E (0.97) and large BLA for rings B (0.24) and D (0.07), similar to **1-MF**.[18] However, a not so large BLA was found for the benzenoid ring C (0.68), implying its moderate aromatic character according to the geometrical criterion of aromaticity. Nucleus independent chemical shift [NICS(1)$_{zz}$, Figure 5.3a][35] calculations for the ground state structure of **5** using the BHandHLYP functional[36] suggested aromaticity for rings A (−18.04) and E (−18.90) and moderate antiaromaticity for rings B (5.40) and D (5.55). A weak aromatic character for the central benzenoid ring C (−2.0) for **5**, which is in line with the HOMA analysis, further indicated a major contribution of the OS

diradical form to the electronic ground state. To support the NICS analysis, we conducted anisotropy of the induced current density[37] (ACID) calculation for **5** and current density vectors were plotted onto the ACID isosurfaces (Figure 5.5). The ACID plot clearly exhibited strong diatropicity (clockwise ring current) for rings A and E, and a diatropic ring current with low intensity over ring C, signifying strong to weak aromaticity for six-membered rings A/E to C. The five-membered rings B and D were found to be atropic (nonaromatic), implying the diatropic ring currents of fused benzene rings could induce some paratropic effect.[38] The aromaticity indices overall suggested that the contribution of the diradical structure **5-OS1** is much more important for **5** in the singlet ground state.

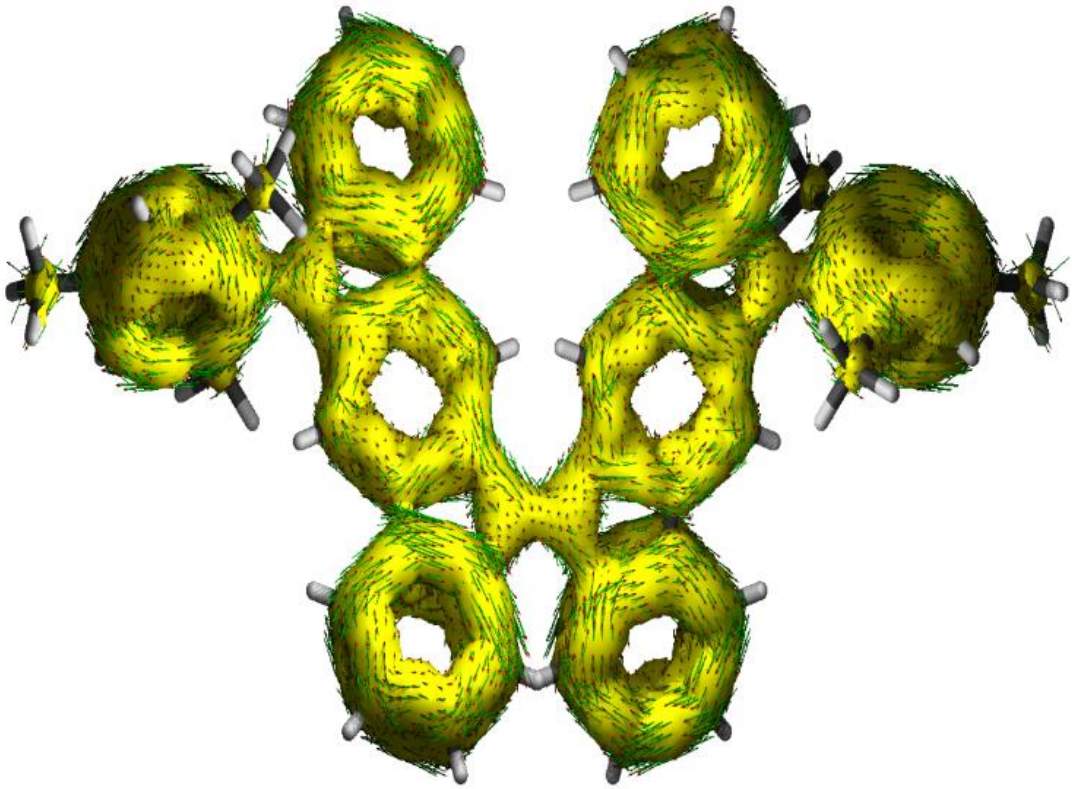

Figure 5.5 Current–density vectors plotted onto the ACID isosurface of 0.02 for the π system of **5**.

5.3.4 Optical and electrochemical properties

The ultraviolet-visible-near infrared (UV-vis-NIR) spectrum (Figure 5.6a) of teal colored **5** in chloroform displayed a broad absorption band in the low energy region at λ_{max} = 661 nm (ε = 48 000 M^{-1} cm^{-1}), which may be attributed to the HOMO→LUMO transition according to time dependent-DFT (TD-DFT: $\lambda_{max(TD)}$ = 582 nm, oscillator

strength (f) = 0.7125) calculations (Table 5.3), with the absorption tail extended to ~ 825 nm in the NIR region.

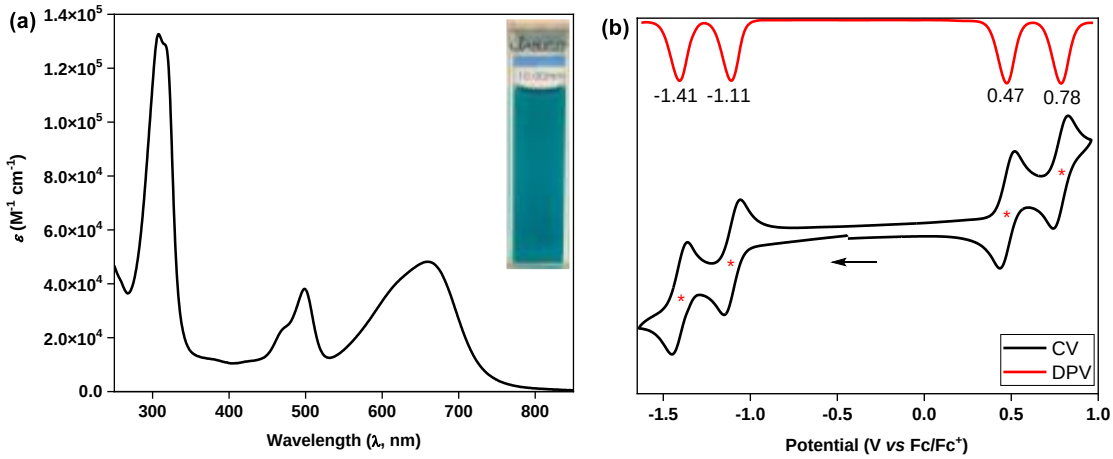

Figure 5.6 (a) UV-vis-NIR spectrum of **5** in chloroform. (b) CV (asterisk (*) denotes half-wave redox potentials) and DPV of **5** (0.001 M) taken at 298 K, in dry and degassed dichloromethane with 0.1 M Bu_4NPF_6 under nitrogen atmosphere. All data were collected using Pt-disk electrode as a working electrode, Pt wire as a counter electrode and Ag wire as a pseudo-reference electrode. Scan direction (toward negative potential first, and then going to positive potential) is shown using arrow.

Table 5.3 Summary of TDDFT calculation for **5**

Wavelength (nm)	Osc. Strength (f)	Major contributions
582.1	0.7125	HOMO->LUMO (95%)
516.5	0.0027	H-3->LUMO (55%), H-2->L+1 (23%), H-1->LUMO (19%)
513.7	0.015	H-3->L+1 (17%), H-2->LUMO (74%)
435.5	0.4826	HOMO->L+1 (87%)
433.4	0.1697	H-3->LUMO (27%), H-1->LUMO (64%)
358.0	0.043	H-3->L+1 (27%), H-1->L+1 (63%)
330.0	0.0003	H-3->L+1 (52%), H-2->LUMO (23%), H-1->L+1 (22%)
329.4	0.0005	H-3->LUMO (15%), H-2->L+1 (70%)
324.9	0.0001	H-5->L+1 (19%), H-4->LUMO (73%)
324.7	0.0214	H-5->LUMO (75%), H-4->L+1 (20%)
323.9	0.0009	H-1->L+3 (12%), HOMO->L+2 (66%)
317.5	0.0019	H-1->L+2 (18%), HOMO->L+3 (60%)
300.4	0.1872	H-10->LUMO (61%), H-9->L+1 (16%)
300.3	0.0058	H-8->LUMO (50%), H-7->LUMO (22%)
300.1	0.0507	H-10->L+1 (10%), H-9->LUMO (72%)
297.7	0.0036	H-11->LUMO (17%), H-7->L+1 (12%), H-6->LUMO (56%)

295.7	0.0007	H-8->LUMO (19%), H-7->LUMO (57%), H-6->L+1 (13%)
293.4	0.0049	H-11->LUMO (39%), H-10->LUMO (12%), H-8->L+1 (12%), H-6->LUMO (18%)
269.5	0.7444	H-12->LUMO (17%), H-3->L+2 (29%), H-2->L+3 (27%)
258.8	1.9368	H-3->L+3 (18%), H-2->L+2 (41%), H-1->L+3 (13%)
256.3	0.2009	H-12->LUMO (55%), H-2->L+3 (10%)
252.7	0.1483	H-13->LUMO (51%)
247.3	0.0048	H-11->LUMO (11%), H-8->L+1 (26%), H-1->L+2 (19%), HOMO->L+3 (12%)
244.3	0	H-11->L+1 (17%), H-1->L+3 (14%)
242.6	0.0349	H-9->L+1 (10%), H-8->L+1 (28%), H-1->L+2 (15%)
239.6	0.0242	H-14->LUMO (46%), H-9->L+1 (16%)
238.5	0.0071	H-15->LUMO (33%), HOMO->L+6 (24%)
237.8	0.0948	H-14->LUMO (11%), H-9->L+1 (32%)
236.9	0.0393	H-11->L+1 (30%), H-10->L+1 (16%)
236.3	0.0972	H-10->L+1 (32%), H-5->L+1 (14%)

The lowest energy band for **5** was found to be 98 nm red-shifted than that of **4**, implying a greater electronic communication in **5**, which is also reflected by an enhancement of the molar extinction coefficient (ε). The optical HLG of **5** is 1.50 eV, as roughly estimated from the absorption onset, which is 0.10 eV and 0.52 eV smaller than its BIF **4** and bipentacene (BP)[39] counterparts, respectively. BIF **5** was found to be non-emissive by the naked eye, similar to the monomer,[40] and quite stable under ambient conditions with a half-life of 19 days in toluene (Figure 5.7).

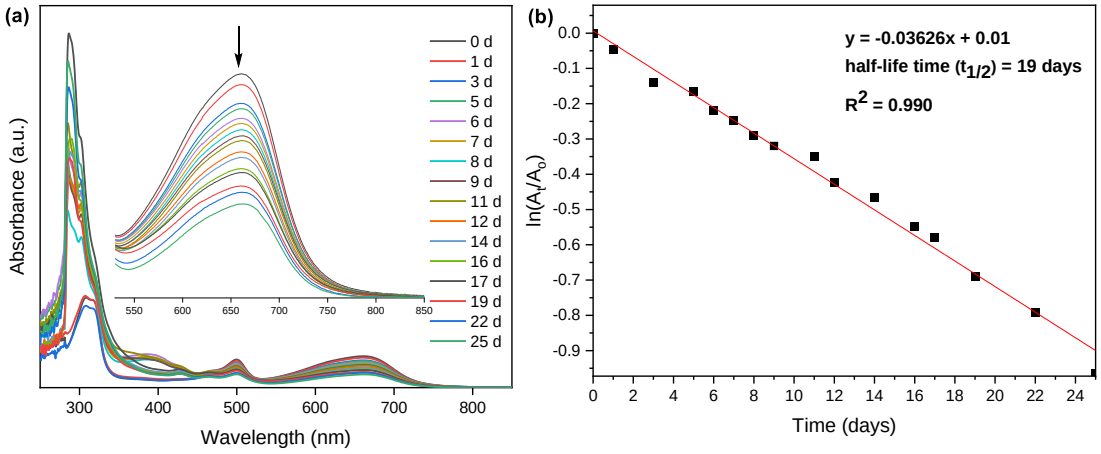

Figure 5.7 (a) Absorption spectral changes under ambient light conditions for compound **5** in toluene (0 days to 25 days). (b) Fitting with first-order kinetics.

Cyclic voltammetry (CV) and differential pulse voltammetry (DPV) analyses of **5** in the DCM/Bu_4NPF_6 solvent/electrolyte couple exhibited four-stage redox amphotericity (Figure 5.6b), displaying two reversible reduction waves with half-wave potentials $E_{1/2}^{red1}$= −1.11 V and $E_{1/2}^{red2}$= −1.41 V and two reversible oxidation waves at $E_{1/2}^{ox1}$ = 0.47 V and $E_{1/2}^{ox2}$ = 0.78 V (*vs* ferrocene/ferrocenium (Fc/Fc^+)). The excellent reversibility of the redox waves for **5** may be attributed to the dominance of an OS ground state, suggesting promise for application in organic electronics.[5c,41] The HOMO and LUMO energy levels of **5** were found to be −5.18 and −3.80 eV, respectively, based on the onset redox potentials, affording an electrochemical HLG of 1.38 eV, which is 0.36 eV smaller than that of **4**. Notably, the low-lying LUMO of BIF **5** is remarkably stabilized by 0.82 eV when compared to that of its aromatic BP counterpart with the same solubilizing group.[39]

5.4 Conclusions

In summary, we have designed and synthesized a stable diradicaloid BIF **5**, as demonstrated by computational and experimental analyses, that exhibits four-stage redox amphotericity and improved optoelectronic properties compared to the known BIF and BP counterparts.[29,39] Our BIF gains a sterically hindered BF-type OS diradicaloid ground state through gaining of partial double bond character for the inter-IF C–C single bond, which, by design, is opposite to the conventionally designed sterically overcrowded alkene-type switchable di/tetra-radicaloids.[25,26] A shorter C_{sp^2}–C_{sp^2} single bond length linking the two [1,2-*b*]IF units was found in the SCXRD analysis of **5**, which is attributed to the better π-electron delocalization between two IF cores owing to a reduced inter-IF torsional angle as they are π-extended through carbons 6 and 6′ of [1,2-*b*]IF units bearing large HOMO and LUMO distributions. Our study showed that the oligomerization of antiaromatic IF units through appropriate carbon positions may significantly influence the optoelectronic properties, as the electronic ground state was effectively tuned. Syntheses of other regioisomeric BIF diradicaloids for organic electronics and photonics studies are presently underway.

5.5 Experimental Section

5.5.1 General Information

Chemicals and reagents were purchased from commercial suppliers (Merck, GLR innovations, BLD pharm, Spectrochem) and used without further purification. Thin layer chromatography (TLC) was performed using pre-coated silica-plates purchased from Merck (silica gel 60 PF254, 0.25 mm). Column chromatography was performed using silica gel 100-200 mesh. NMR spectra were recorded in $CDCl_3$ at room temperature, on JEOL JNM-ECS400 spectrometer at operating frequencies of 400 MHz (^1H) or 100 MHz (^{13}C) as indicated in the individual spectrum. Chemical shifts (δ) are given in ppm relative to residual solvent (chloroform δ = 7.26, 1,1,2,2-tetrachloroethane δ = 6.00 ^1H, and δ = 77.16 for proton-decoupled ^{13}C NMR), and coupling constants (*J*) are expressed in hertz (Hz). Multiplicity is tabulated as s for singlet, d for doublet, dd for doublet of doublet, t for triplet, q for quartet and m for multiplet. Structural assignments were made with additional information from gCOSY, and gNOESY experiments. High-resolution mass spectra (HRMS) were recorded using electron spray ionization (ESI) methods on Waters (XEVO G2-XS QTOF) mass spectrometer. UV-vis-NIR spectra were recorded in JASCO V-770 spectrophotometer. Cyclic voltammetry measurements of **5** (0.001 M) was performed using an electrochemical analyzer potentiostat model CHI-1115C from CH Instruments with a conventional three-electrode cell at 298 K under a nitrogen atmosphere at a scan rate of 50 mV/s. This electrochemical cell contains a platinum (Pt) disk (disk shaped with 2-mm diameter) as a working electrode, Pt wire as a counter electrode, and silver (Ag) wire as a pseudo-reference electrode. The Pt working electrode was polished with 1.0 micron α-alumina polishing powder in a figure-eight motion. Electrolyte solution (0.1 M) was prepared by dissolving tetrabutylammonium hexafluorophosphate (Bu_4NPF_6) in 5 mL dry dichloromethane (DCM). The DCM solution was degassed by bubbling nitrogen gas for 10 minutes prior to measurements. The direction of initial scan was chosen as reductive, with the initial potential values set at zero for **5** and switching between negative potential (− 1.2 V) first, and then going to positive potential (1.4 V), and finally returning to zero (*vs* Ag wire). The potential was externally calibrated against the ferrocene/ferrocenium (Fc/Fc^+) couple (0.43 V). Melting points were determined using Cole-Parmer MP 250D-

P melting point analyzer. ESR spectra were recorded using an EMX MICRO X Bruker ESR instrument.

5.5.2 Synthesis

2,2'-([9,9'-bifluorenylidene]-2,2'-diyl)dibenzaldehyde (8): An oven-dried thick-walled glass tube was charged with pre-synthesized **6** (800 mg, 1.65 mmol), (2-formylphenyl)boronic acid (987 mg, 6.58 mmol) **7**, $NaHCO_3$ (2.76 g, 32.91 mmol), tetrahydrofuran (8 mL), distilled water (0.6 mL) and purged with N_2 for 30 mins. $Pd_2(dba)_3$ (151 mg, 0.164 mmol), and $[(t\text{-}Bu)_3PH]BF_4$ (191 mg, 0.658 mmol) were added subsequently and the resulting mixture was heated at 80 °C using an oil bath for 12 h. After cooling to room temperature, the THF was evaporated, water was added and the resultant mixture was extracted with DCM (3 x 50 mL). The organic phase was dried over Na_2SO_4, and evaporated under reduced pressure. The residue was subjected to column chromatography (SiO_2, DCM/hexane 70:100) to give dialdehyde **8** as orange solid. (507 mg, 57% yield): R_f = 0.46 (20% EtOAc/hexanes); **mp**: 165-166°C; **^{1}H NMR** (400 MHz, $CDCl_3$): δ 10.06 (m, 2H), 8.50 – 8.45 (m, 1H), 8.38 – 8.35 (m, 2H), 8.01 (td, J = 7.9, 1.6 Hz, 2H), 7.80 – 7.73 (m, 4H), 7.62 (td, J = 7.4, 1.4 Hz, 1H), 7.50 – 7.44 (m, 4H), 7.43 – 7.34 (m, 4H), 7.30 – 7.24 (m, 3H), 7.12 (d, J = 7.4 Hz, 1H); **^{13}C{^{1}H} NMR** (100 MHz, $CDCl_3$): δ 192.2, 192.1, 146.0, 145.8, 141.2, 140.8, 138.4, 138.4, 136.6, 136.4, 133.9, 133.8, 133.7, 131.6, 131.2, 130.8, 130.5, 129.8, 128.1, 128.0, 127.9, 127.7, 127.6, 126.9, 126.8, 120.4, 120.1, 119.7; **HRMS** (ESI) *m/z*: $[M + H]^+$ calcd for $C_{40}H_{25}O_2$ 537.1855, found 537.1854 (error: -0.2 ppm).

12,12'-dimesityl-12H,12'H-6,6'-biindeno[1,2-*b*]fluorenylidene (10): To a dry THF solution (10 ml) of dialdehyde **8** (285 mg, 0.531 mmol)**,** was added 2-mesitylmagnesiumbromide (2.66 ml, 2.66 mmol, 5 equiv) at room temperature under N_2 atmosphere, and the resulting solution was stirred for 16 h. After consumption of starting material (monitored by TLC), saturated ammonium chloride was added, the organic phase was separated, and the aqueous phase was extracted with DCM. The combined organic phase was washed with brine, dried over Na_2SO_4, and concentrated under reduced pressure to give crude alcohol **9**. Without further purification, the crude dicarbinol **9** was subjected to Friedel-Craft cyclization reaction with $BF_3{\cdot}OEt_2$ (0.1 ml) in a DCM solution. After stirring the reaction mixture for 10 min at room temperature, a saturated aqueous NH_4Cl solution was added to the reaction mixture and it was

extracted with DCM (3 x 100 mL). The organic layer was dried over anhydrous Na_2SO_4, filtered, and removed under reduced pressure to afford a residue which was purified by silica gel column chromatography (EtOAc/hexane 2:100) to give **10** as orange-reddish solid. (180 mg, 46% yield in two steps): $\boldsymbol{R_f}$ = 0.42 (5% EtOAc/hexanes); **mp**: 251-252°C; **^{1}H NMR** (400 MHz, $CDCl_3$): δ 9.05 (d, *J* = 4.1 Hz, 1H), 8.87 (s, 1H), 8.53 (d, *J* = 7.8 Hz, 1H), 8.40 (d, *J* = 7.8 Hz, 1H), 7.72 (d, *J* = 7.5 Hz, 1H), 7.65 – 7.55 (m, 5H), 7.36 – 7.28 (m, 4H), 7.24 – 7.16 (m, 7H), 7.10 (t, *J* = 2.7 Hz, 2H), 6.74 – 6.72 (m, 2H), 5.65 – 5.60 (m, 2H), 2.77 – 2.76 (m, 6H), 2.34 – 2.33 (m, 6H), 1.31 – 1.23 (m, 6H); **^{13}C{^{1}H} NMR** (100 MHz, $CDCl_3$): δ 149.3, 149.2, 147.3, 141.6, 141.4, 141.2, 141.1, 140.9, 140.8, 140.3, 140.2, 139.0, 138.9, 138.2, 138.2, 137.9, 137.8, 137.7, 136.6, 134.0, 133.9, 133.9, 130.7, 130.7, 129.3, 129.2, 129.0, 127.3, 127.2, 127.2, 127.0, 126.8, 126.7, 126.7, 124.2, 124.2, 120.2, 120.1, 119.9, 119.6, 119.4, 118.3, 118.2, 115.9, 115.8, 50.0, 50.0, 22.0, 21.0, 19.1, 19.0, 18.9; **HRMS** (ESI) *m/z*: $[M + H]^+$ calcd for $C_{58}H_{45}$ 741.3521, found 741.3492 (error: -3.9 ppm).

12,12'-dimesityl-6,6'-biindeno[1,2-*b*]fluorene (5): DDQ (55 mg, 0.242 mmol, 2 equiv) was added to degassed solution of 1,2- dichloroethane (4 ml) of **10** (90 mg, 0.121 mmol) under N_2, and the reaction mixture was warmed to 80 °C using an oil bath for 2 h in a sealed tube. Once the starting material was consumed (monitored by TLC), the 1,2 dichloroethane was removed in vacuo and the crude was purified by silica gel column chromatography (EtOAc/hexane 2:100) to afford title product **5** as blue solid. (67 mg, 75% yield): $\boldsymbol{R_f}$ = 0.46 (5% EtOAc/hexanes); **mp**: 365-366°C; **^{1}H NMR** (400 MHz, $CDCl_3$): δ 7.38 (d, *J* = 1.6 Hz, 1H), 7.36 (s, 3H), 7.32 – 7.28 (m, 3H), 7.27 (d, *J* = 1.3 Hz, 1H), 7.07 (d, *J* = 6.9 Hz, 2H), 7.04 (t, *J* = 1.8 Hz, 5H), 7.03 – 6.98 (m, 3H), 6.96 (dd, *J* = 3.6, 1.4 Hz, 1H), 6.94 – 6.92 (m, 3H), 6.70 (d, *J* = 7.2 Hz, 2H), 2.41 (s, 6H), 2.23 – 2.20 (m, 12H); **^{13}C{^{1}H} NMR** (100 MHz, $CDCl_3$): δ 147.5, 144.0, 143.2, 139.4, 139.3, 138.4, 138.2, 138.2, 137.8, 137.2, 137.1, 136.2, 135.2, 129.9, 128.4, 128.0, 127.8, 127.7, 127.5, 123.7, 122.5, 120.8, 120.4, 119.8, 119.7, 21.3, 20.5, 20.5; **HRMS** (ESI) *m/z*: $[M]^+$ calcd for $C_{58}H_{42}$ 738.3287, found 738.3287 (error: 0 ppm).

5.5.3 Single crystal data

Single crystals of **5** were selected using paratone oil and mounted on glass fiber with the help of gum. The intensity data and geometric parameters of these crystals were garnered with the help of Bruker D8 Venture X-ray diffractometer having a micro-focus

sealed X-ray tube Mo-Kα (λ = 0.71073 Å) source of X-rays along with a PHOTON 100 detector with inclining Phi and Omega (width of 0.5 for one frame) working at a scan speed of 10 s per frame. The crystal was kept at 298 K during data collection. Data acquisition as well as extraction of data was accomplished by utilizing Bruker Apex-3 and Bruker SAINT software packages using a narrow -frame algorithm.[42] By utilizing OLex2,[43] the crystal structure was solved with the help of olex2.solve[44] structure solution program by employing intrinsic Phasing methods and crystal structure refinement was done with the SHELXL[45] refinement package by putting into use Least Squares minimization. Refinement of all non-hydrogen atoms was completed with the help of anisotropic thermal parameters.

Table 5.4 Crystal data and structure refinement for **5**.

CCDC No.	2362686
Empirical formula	$C_{58}H_{42}$
Formula weight	738.91
Temperature/K	298.00
Crystal system	Monoclinic
Space group	$P2_1$
a/Å	14.265(3)
b/Å	8.009(2)
c/Å	19.200(4)
α/°	90
β/°	106.474(6)
γ/°	90
Volume/Å^3	2103.5(8)
Z	2
ρ_{calc}g/cm^3	1.167
μ/mm^{-1}	0.066
F(000)	780.0
Crystal size/mm^3	0.315 × 0.045 × 0.023
Radiation	MoKα (λ = 0.71073)
2Θ range for data collection/°	4.424 to 51.362
Index ranges	$-17 \leq h \leq 17$, $-9 \leq k \leq 9$, $-23 \leq l \leq 23$
Reflections collected	35050
Independent reflections	7972 [R_{int} = 0.0901, R_{sigma} = 0.0841]
Data/restraints/parameters	7972/1/529
Goodness-of-fit on F^2	1.023
Final R indexes [I>=2σ (I)]	R_1 = 0.0657, wR_2 = 0.1376
Final R indexes [all data]	R_1 = 0.1116, wR_2 = 0.1557

Largest diff. peak/hole / e Å^{-3}	0.35/-0.16
Flack parameter	5.3(10)

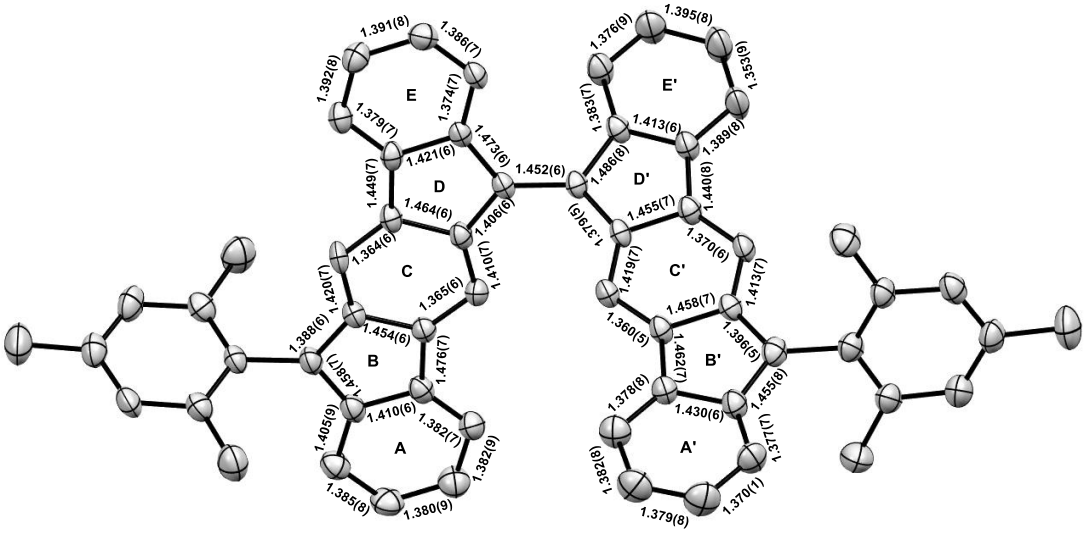

Figure 5.8 Full crystallographic bond length analyses of **5** with e.s.d values.

Compound 4:

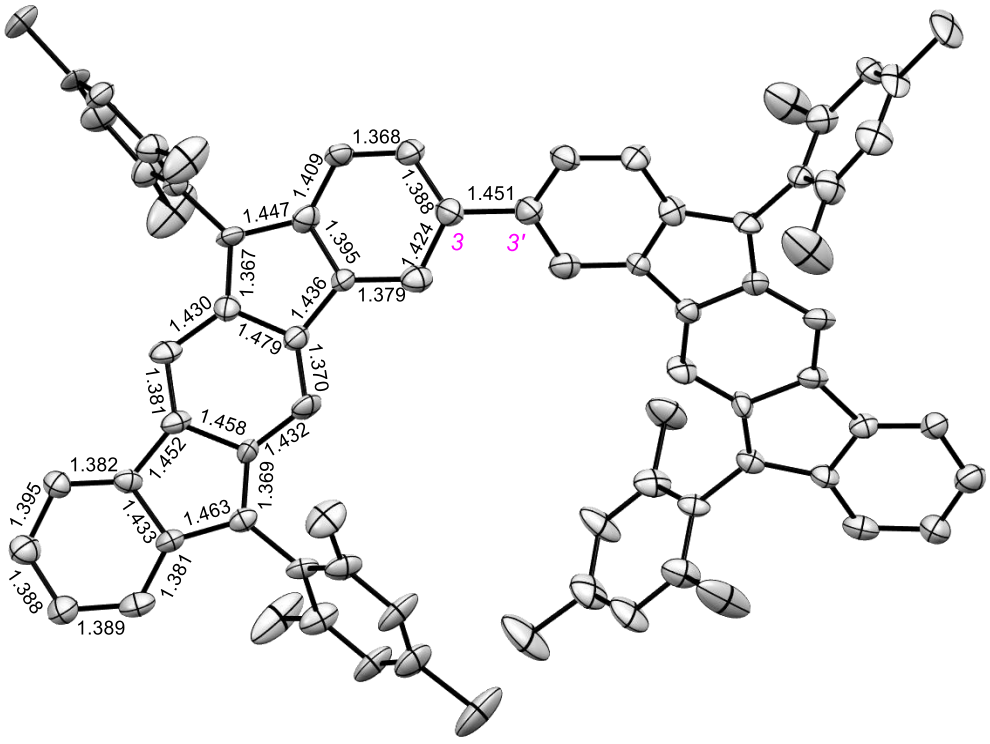

Figure 5.9 X-ray crystallographic C-C bond lengths of **4** (for comparison with **5**).

Compound 5:

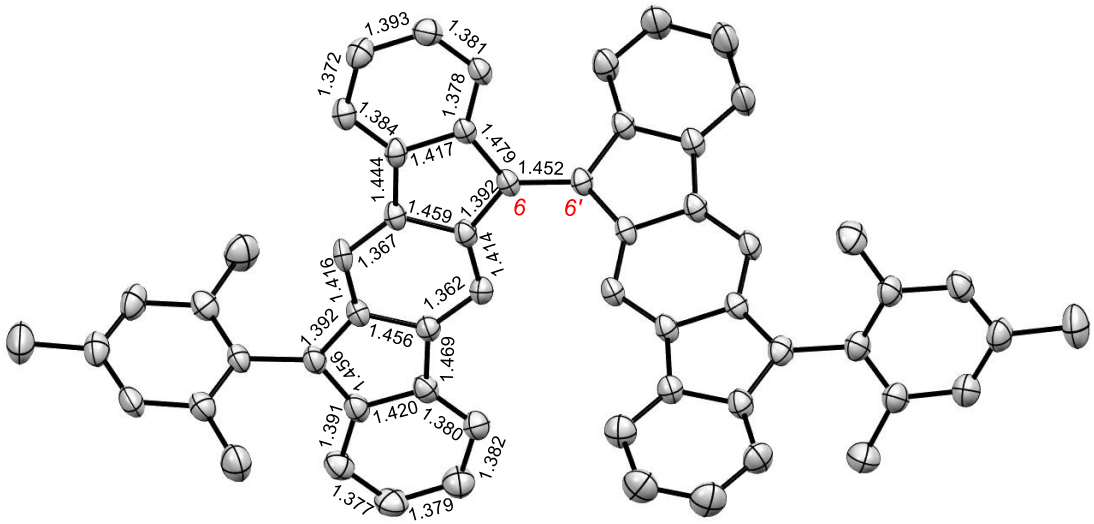

Figure 5.10 X-ray crystallographic C-C bond lengths of **5**.

5.5.4 DFT calculations

Gas-phase density functional theory (DFT) calculations were performed with Gaussian 09 package using a high-performance computing cluster facility of IIT Ropar at the CAM-B3LYP level of theory with basis set 6-31G(d,p).[46] Optimization of the molecular geometries for **5**, was done by restricted CAM-B3LYP, and unrestricted CAM-B3LYP wave-functions using broken symmetry formalism.[47] The calculated NOON (natural orbital occupation number) value was based on the broken symmetry CAM-B3LYP method for ground state structure.[48] NICS (standard GIAO method)[49] values were calculated for the optimized structure at (U)BHandHLYP/6-31G(d,p) level, and the reported NICS(1)$_{zz}$ values are the average of two positions (1Å above and below the plane). Molecular orbital contributions for TDDFT calculation were determined using the GaussSum 3.0 package.[50]

Table 5.5 NICS(1)$_{zz}$ values of each ring for **5**

Rings	Closed shell 5	Open shell singlet 5	Open shell triplet 5	Closed shell 1[51]
A	-18.18	-18.04	-16.63	-19.5
B	6.35	5.40	5.40	13.6
C	7.31	-2.0	-9.27	11.3
D	6.07	5.55	5.30	-
E	-18.34	-18.90	-19.48	-

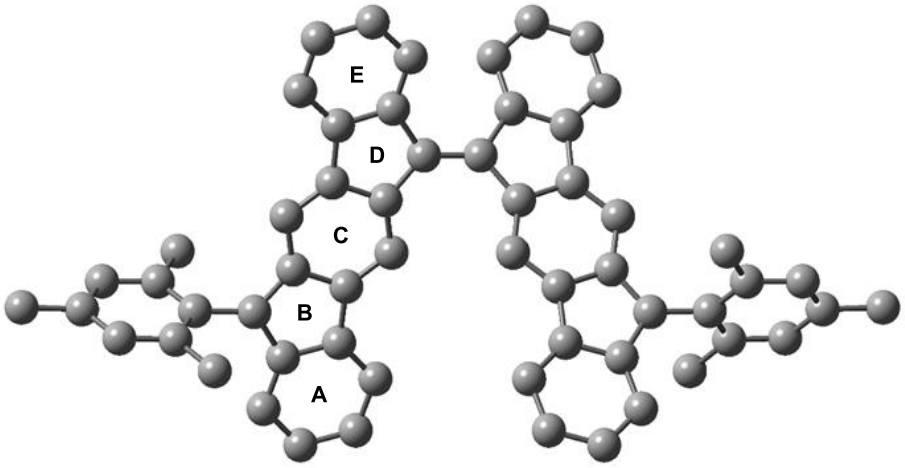

Figure 5.11 Optimized structure of **5** in the open-shell ground state.

TDDFT computation of compound 5

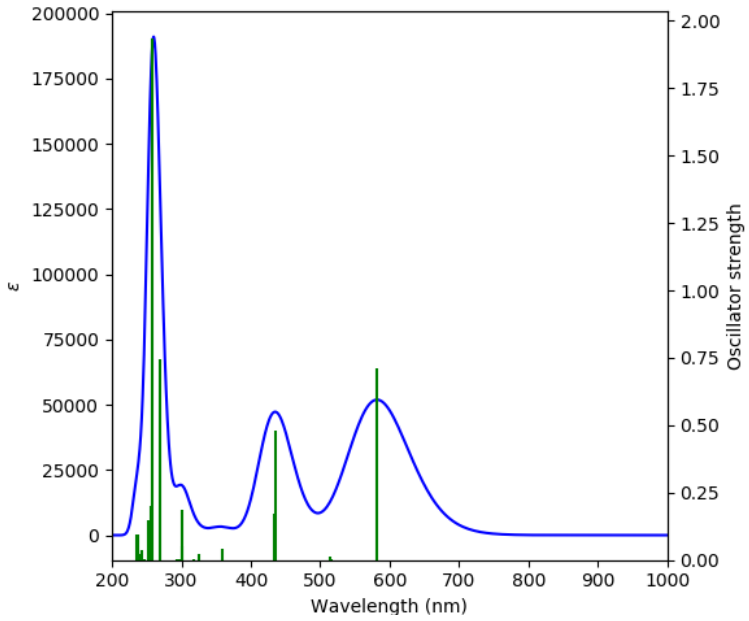

Figure 5.12 Theoretical absorption of **5** at CAM-B3LYP/6-31G(d,p) level of theory.

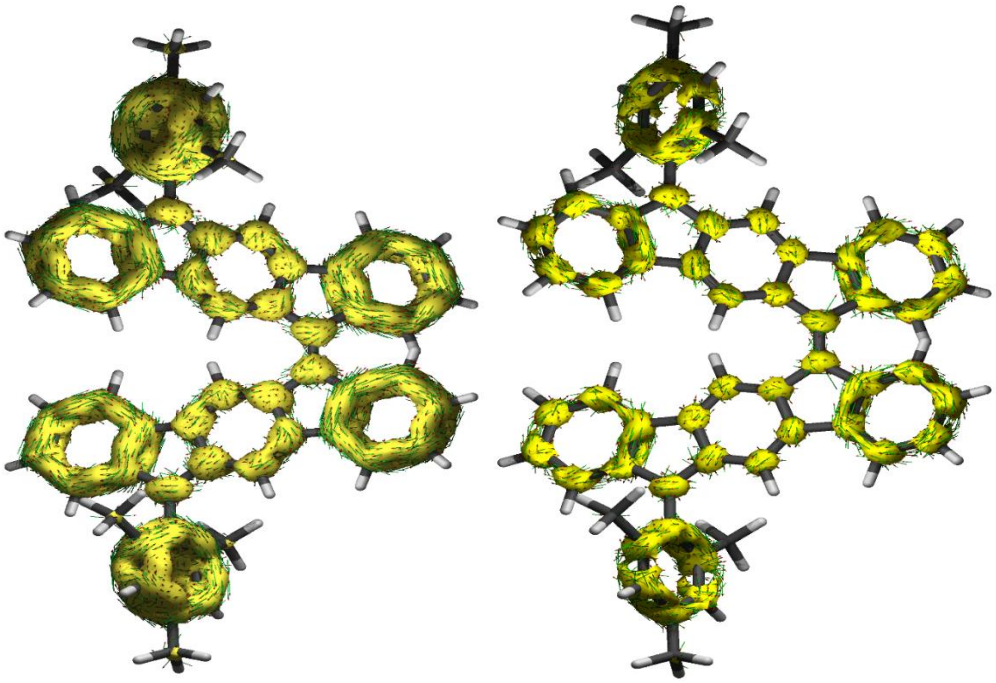

Figure 5.13 ACID plots of **5** at isosurface values of 0.0353 (left) and 0.055 (right). The critical isosurface value (CIV) for central benzenoid ring C is found to be 0.0353. The CIV for outer benzene rings A as well as E is 0.055.

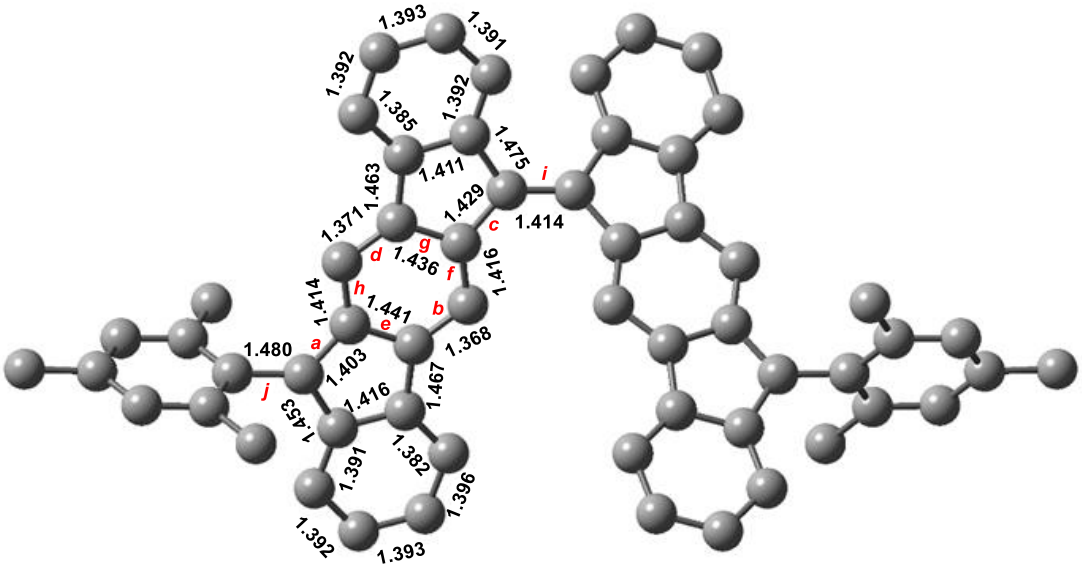

Figure 5.14 DFT-optimized C-C bond lengths of ground state open-shell structure **5**.

5.5.5 ESR measurement and Bleaney-Bowers plot

To get the ground state spin multiplicity and the energy separation between the singlet and triplet state, VT-ESR experiments were carried out using the solid sample of **5** displaying $g_e = 2.0043$. The modified Bleaney-Bowers equation was used to fit the *IT*

against the *T* data points to get the energy separation between the singlet and triplet spin state of the diradicaloid species.

$$IT = \frac{2\rho N_A g^2 \beta^2}{k_b} * \frac{1}{3 + \exp\left(-\frac{2J}{k_b T}\right)} + \frac{(1-\rho) N_A g^2 \beta^2}{2k_b}$$

Here, *2J* is the energy separation between singlet and triplet state ($\Delta E_{S\text{-}T}$), '*I* 'is the ESR intensity, 'T' is the temperature in Kelvin scale, *g* is the g factor, N_A is the Avogadro constant, β is the Bohr magneton, k_b is the Boltzmann constant, and ρ is the paramagnetic purity.

The *IT* vs. *T* data set was fitted according to the below equation using Origin 2021 software package.

$$IT = \frac{a}{3 + \exp\left(-\frac{b}{T}\right)} + c$$

$$a = \frac{2\rho N_A g^2 \beta^2}{k_b}\ ;\ b = \frac{2J}{k_b}\ ;\ c = \frac{(1-\rho) N_A g^2 \beta^2}{2k_b}$$

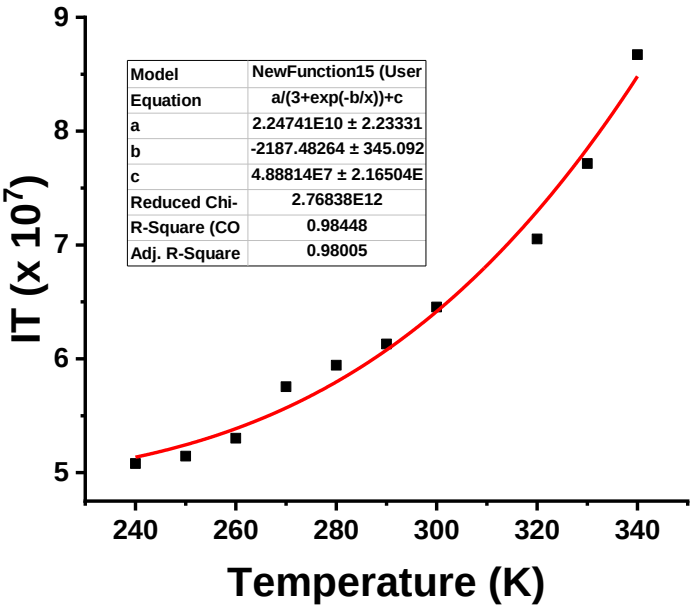

Figure 5.15 Bleaney-Bowers plot for **5**.

b = –2187.48 ± 345.09; $2J = k_B * b$ = –4.35 ± 0.6 kcal/mol

5.5.6 Explanation of four-stage redox amphotericity

The diradicaloid ground state ($y_0 = 0.268$) of **5** is clearly evident from the cyclic voltammetry and differential pulse voltammetry (Figure 5.6b). The excellent reversibility during oxidation (facile electron ejection) and reduction (facile electron injection) events showing sequential one-electron transfer processes can be explained

through the diradical-like structure **5-OS1**, as shown below. During reduction, electrons can be injected easily at lower reduction potential (low-lying LUMO = –3.80 eV) as formation of locally aromatic cyclopentadienyl anions (shown below) in the five membered rings can be favored. During oxidation, the double bond arrangement in benzene rings became such that it avoids formation of locally antiaromatic cyclopentadienyl cation (shown below) in the five membered rings.

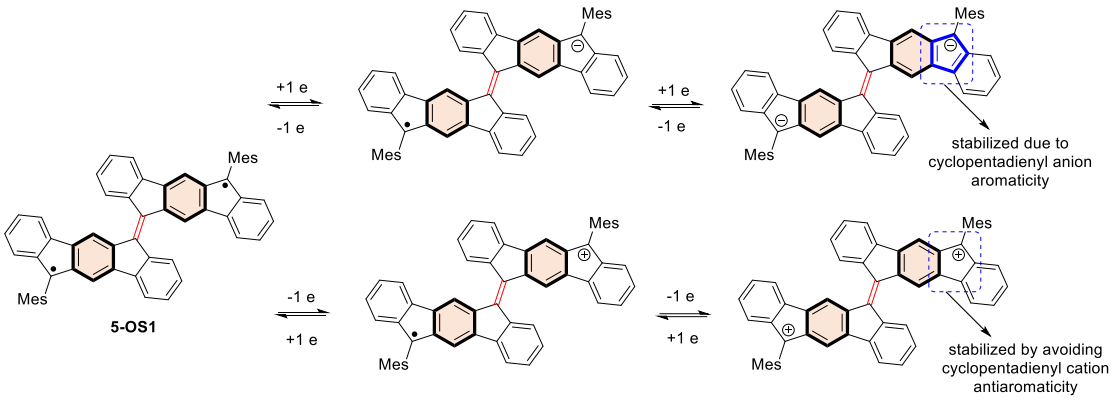

Figure 5.16 Plausible reason for four-stage redox amphotericity of **5**.

5.6 References

1. J. Wu, *Diradicaloids*, Jenny Stanford Publishing, New York, 2022.

2. (*a*) J. Hu, Q. Xiang, X. Tian, L. Ye, Y. Wang, Y. Ni, X. Chen, Y. Liu, G. Chen and Z. Sun, *J. Am. Chem. Soc.*, 2024, **146**, 10321–10330; (*b*) F. Kuriakose, M. Commodore, C. Hu, C. J. Fabiano, D. Sen, R. R. Li, S. Bisht, Ö. Üngör, X. Lin, G. F. Strouse, A. E. DePrince III, R. A. Lazenby, F. Mentink-Vigier, M. Shatruk and I. V. Alabugin, *J. Am. Chem. Soc.*, 2022, **144**, 23448–23464; (*c*) A. Borissov, P. J. Chmielewski, C. J. Gómez García, T. Lis and M. Stępień, *Angew. Chem. Int. Ed.*, 2023, **62**, e202309238; (*d*) P. Ravat, T. Šolomek, M. Rickhaus, D. Häussinger, M. Neuburger, M. Baumgarten and M. Juríček, *Angew. Chem. Int. Ed.*, 2016, **55**, 1183–1186; (*e*) M. Feofanov, V. Akhmetov, D. I. Sharapa and K. Amsharov, *Org. Lett.*, 2020, **22**, 5741–5745.

3. (*a*) S. Muhammad, M. Nakano, A. G. Al-Sehemi, Y. Kitagawa, A. Irfan, A. R. Chaudhry, R. Kishi, S. Ito, K. Yoneda and K. Fukuda, *Nanoscale*, 2016, **8**, 17998–18020; (*b*) M. Nakano, *Chem. Rec.*, 2017, **17**, 27–62; (*c*) Z. Zhou, K. Yang, L. He, W. Wang, W. Lai, Y. Yang, Y. Dong, S. Xie, L. Yuan, Z. Zeng, *J. Am. Chem. Soc.*, 2024, **146**, 6763–6772; (*d*) M. Nakano, R. Kishi, T. Nitta, T. Kubo, K. Nakasuji, K. Kamada,

K. Ohta, B. Champagne, E. Botek and K. Yamaguchi, *J. Phys. Chem. A*, 2005, **109**, 885–891; (*e*) T. Minami and M. Nakano, *J. Phys. Chem. Lett.*, 2012, **3**, 145–150.

4. (*a*) C. Liu, M. E. Sandoval-Salinas, Y. Hong, T. Y. Gopalakrishna, H. Phan, N. Aratani, T. S. Herng, J. Ding, H. Yamada, D. Kim, D. Casanova and J. Wu, *Chem*, 2018, **4**, 1586–1595; (*b*) S. Das, T. S. Herng, J. L. Zafra, P. M. Burrezo, M. Kitano, M. Ishida, T. Y. Gopalakrishna, P. Hu, A. Osuka, J. Casado, J. Ding, D. Casanova and J. Wu, *J. Am. Chem. Soc.*, 2016, **138**, 7782-7790; (*c*) K. Horii, R. Kishi, M. Nakano, D. Shiomi, K. Sato, T. Takui, A. Konishi and M. Yasuda, *J. Am. Chem. Soc.*, 2022, **144**, 3370–3375.

5. (*a*) T. Jousselin-Oba, M. Mamada, J. Marrot, A. Maignan, C. Adachi, A. Yassar and M. Frigoli, *J. Am. Chem. Soc.*, 2019, **141**, 9373–9381; (*b*) C. Zong, X. Zhu, Z. Xu, L. Zhang, J. Xu, J. Guo, Q. Xiang, Z. Zeng, W. Hu, J. Wu, R. Li and Z. Sun, *Angew. Chem. Int. Ed.*, 2021, **60**, 16230–16236; (*c*) X. Hu, W. Wang, D. Wang and Y. Zheng, *J. Mater. Chem. C*, 2018, **6**, 11232–11242.

6. (*a*) Z. Zeng, X. Shi, C. Chi, J. T. L. Navarrete, J. Casado and J. Wu, *Chem. Soc. Rev.*, 2015, **44**, 6578– 6596; (*b*) S. Das and J. Wu, *Phys. Sci. Rev.*, 2017, **2**, 20160109.

7. (*a*) Z. Sun, Z. Zeng and J. Wu, *Acc. Chem. Res.*, 2014, **47**, 2582–2591; (*b*) R. Huang, H. Phan, T. S. Herng, P. Hu, W. Zeng, S. Dong, S. Das, Y. Shen, J. Ding, D. Casanova and J. Wu, *J. Am. Chem. Soc.*, 2016, **138**, 10323–10330; (*c*) S. Das, S. Lee, M. Son, X. Zhu, W. Zhang, B. Zheng, P. Hu, Z. Zeng, Z. Sun, W. Zeng, R. Li, K. Huang, J. Ding, D. Kim and J. Wu, *Chem. Eur. J.*, 2014, **20**, 11410-11420; (*d*) Z. Sun, S. Lee, K. H. Park, X. Zhu, W. Zhang, B. Zheng, P. Hu, Z. Zeng, S. Das, Y. Li, C. Chi, R. Li, K. Huang, J. Ding, D. Kim and J. Wu, *J. Am. Chem. Soc.*, 2013, **135**, 18229–18236.

8. (*a*) Z. Zeng, Y. M. Sung, N. Bao, D. Tan, R. Lee, J. L. Zafra, B. S. Lee, M. Ishida, J. Ding, J. T. L. Navarrete, Y. Li, W. Zeng, D. Kim, K. Huang, R. D. Webster, J. Casado and J. Wu, *J. Am. Chem. Soc.*, 2012, **134**, 14513–14525; (*b*) Z. Zeng, M. Ishida, J. L. Zafra, X. Zhu, Y. M. Sung, N. Bao, R. D. Webster, B. S. Lee, R. Li, W. Zeng, Y. Li, C. Chi, J. T. L. Navarrete, J. Ding, J. Casado, D. Kim and J. Wu, *J. Am. Chem. Soc.*, 2013, **135**, 6363–6371.

9. (*a*) A. Konishi, Y. Hirao, M. Nakano, A. Shimizu, E. Botek, B. Champagne, D. Shiomi, K. Sato, T. Takui, K. Matsumoto, H. Kurata and T. Kubo, *J. Am. Chem. Soc.*, 2010, **132**, 11021–11023; (*b*) A. Konishi, Y. Hirao, K. Matsumoto, H. Kurata, R. Kishi,

Y. Shigeta, M. Nakano, K. Tokunaga, K. Kamada and T. Kubo, *J. Am. Chem. Soc.*, 2013, **135**, 1430–1437.

10. (*a*) M. Bendikov, H. M. Duong, K. Starkey, K. N. Houk, E. A. Carter and F. Wudl, *J. Am. Chem. Soc.*, 2004, **126**, 7416–7417; (*b*) B. Purushothaman, M. Bruzek, S. R. Parkin, A. Miller and J. E. Anthony, *Angew. Chem. Int. Ed.*, 2011, **50**, 7013–7017.

11. (*a*) T. Maekawa, H. Ueno, Y. Segawa, M. M. Haley and K. Itami, *Chem. Sci.*, 2016, **7**, 650-654; (*b*) H. Sharma, P. K. Sharma and S. Das, *Chem Commun.*, 2020, **56**, 11319-11322; (*c*) T. Xu, X. Hou, Y. Han, H. Wei, Z. Li and C. Chi, *Angew. Chem. Int. Ed.*, 2023, **62**, e202304937.

12. (*a*) T. Jousselin-Oba, M. Mamada, K. Wright, J. Marrot, C. Adachi, A. Yassar and M. Frigoli, *Angew. Chem. Int. Ed.*, 2022, **61**, e202112794; (*b*) M. Desroches and J.-F. Morin, *Chem. Eur. J.*, 2018, **24**, 2858–2862.

13. (*a*) A. Shimizu, R. Kishi, M. Nakano, D. Shiomi, K. Sato, T. Takui, I. Hisaki, M. Miyata and Y. Tobe, *Angew. Chem., Int. Ed.*, 2013, **52**, 6076–6079; (*b*) J. J. Dressler, Z. Zhou, J. L. Marshall, R. Kishi, S. Takamuku, Z. Wei, S. N. Spisak, M. Nakano, M. A. Petrukhina and M. M. Haley, *Angew. Chem., Int. Ed.*, 2017, **56**, 15363–15367. (*c*) K. Fukuda, T. Nagami, J. Fujiyoshi and M. Nakano, *J. Phys. Chem. A*, 2015, **119**, 10620–10627; (*d*) C. K. Frederickson, B. D. Rose and M. M. Haley, *Acc. Chem. Res.*, 2017, **50**, 977–987; (*e*) Tobe, Y. *Top. Curr. Chem.*, 2018, **375**, 107–168; (*f*) M. D. Giovannantonio, K. Eimre, A. V. Yakutovich, Q. Chen, S. Mishra, J. I. Urgel, C. A. Pignedoli, P. Ruffieux, K. Müllen, A. Narita and R. Fasel, *J. Am. Chem. Soc.*, 2019, **141**, 12346-12354.

14. (*a*) D. T. Chase, B. D. Rose, S. P. McClintock, L. N. Zakharov and M. M. Haley, *Angew. Chem. Int. Ed.*, 2011, **50**, 1127–1130; (*b*) D. T. Chase, A. G. Fix, S. J. Kang, B. D. Rose, C. D. Weber, Y. Zhong, L. N. Zakharov, M. C. Lonergan, C. Nuckolls and M. M. Haley, *J. Am. Chem. Soc.*, 2012, **134**, 10349–10352.

15. M. Abe, *Chem. Rev.*, 2013, **113**, 7011– 7088.

16. X. Fu and D. Zhao, *Org. Lett.*, 2015, **17**, 5694–5697.

17. S. Moles Quintero, M. M. Haley, M. Kertesz and J. Casado, *Angew. Chem. Int. Ed.*, 2022, **61**, e202209138.

18. H. Sharma, N. Bhardwaj and S. Das, *Org. Biomol. Chem.*, 2022, **20**, 8071−8077.

19. G. E. Rudebusch, J. L. Zafra, K. Jorner, K. Fukuda, J. L. Marshall, I. Arrechea-Marcos, G. L. Espejo, R. P. Ortiz, C. J. Gómez-García, L. N. Zakharov, M. Nakano, H. Ottosson, J. Casado and M. M. Haley, *Nat. Chem.*, 2016, **8**, 753–759.

20. A. Shimizu, Y. Hirao, K. Matsumoto, H. Kurata, T. Kubo, M. Uruichib and K. Yakushib, *Chem. Commun.*, 2012, **48**, 5629-5631.

21. (*a*) J. E. Barker, C. K. Frederickson, M. H. Jones, L. N. Zakharov and M. M. Haley, *Org. Lett.*, 2017, **19**, 5312–5315; (*b*) H. Hayashi, J. E. Barker, A. C. Valdivia, R. Kishi, S. N. MacMillan, C. J. Gómez-García, H. Miyauchi, Y. Nakamura, M. Nakano, S. Kato, M. M. Haley and J. Casado, *J. Am. Chem. Soc.*, 2020, **142**, 20444–20455.

22. Y. Li, W. Heng, B. S. Lee, N. Aratani, J. L. Zafra, N. Bao, R. Lee, Y. M. Sung, Z. Sun, K. Huang, R. D. Webster, J. T. L. Navarrete, D. Kim, A. Osuka, J. Casado, J. Ding and J. Wu, *J. Am. Chem. Soc.*, 2012, **134**, 14913–14922.

23. (*a*) W. Zeng, Q. Qi and J. Wu, *Eur. J. Org. Chem.*, 2018, **2018**, 7–17; (*b*) P. K. Sharma, P. Jana, S. Bandyopadhyay and S. Das, *Chem. Commun.*, 2024, **60**, 7319-7322.

24. J.-i Nishida, S. Tsukaguchi and Y. Yamashita, *Chem. Eur. J.*, 2012, **18**, 8964–8970.

25. (*a*) Y. Ishigaki, T. Harimoto, T. Shimajiri and T. Suzuki, *Chem. Rev.*, 2023, **123**, 13952–13965; (*b*) X. Xu, S. Takebayashi, H. Hanayama, S. Vasylevskyi, T. Onishi, T. Ohto, H. Tada and A. Narita, *J. Am. Chem. Soc.*, 2023, **145**, 3891–3896; (*c*) C. Wentrup, M. J. Regimbald-Krnel, D. Müller and P. Comba, *Angew. Chem. Int. Ed.*, 2016, **55**, 14600–14605.

26. B. Prajapati, M. D. Ambhore, D. Dang, P. J. Chmielewski, T. Lis, C. J. Gómez-García, P. M. Zimmerman and M. Stępień. *Nat. Chem.*, 2023, **15**, 1541–1548.

27. K. Rakstys, M. Saliba, P. Gao, P. Gratia, E. Kamarauskas, S. Paek, V. Jankauskas and M. K. Nazeeruddin, *Angew. Chem. Int. Ed.*, 2016, **55**, 7464-7468; (*b*) H. U. Kim, J.-H. Kim, H. Suh, J. Kwak, D. Kim, A. Grimsdale, S. C. Yoon and D.-H. Hwang, *Chem. Commun.*, 2013, **49**, 10950-10952.

28. H. Reisch, U. Wiesler, U. Scherf and N. Tuytuylkov, *Macromolecules*, 1996, **29**, 8204–8210.

29. H. Sharma, Ankita, V. Mittal, U. K. Pandey and S. Das, *Org. Lett.*, 2024, **26**, 2617–2622.

30. (*a*) N. Suaud, N. B. Amor, N. Guihéry and J. Malrieu, *Theor. Chem. Acc.*, 2021, **140**, 117; (*b*) T. Kupka, A. Buczek, M. A. Broda, M. Stachów and P. Tarnowski, *J. Mol. Model.*, 2016, **22**, 101.

31. J. Xu, A. Takai, A. Bannaron, T. Nakagawa, Y. Matsuo, M. Sugimoto, Y. Matsushita and M. Takeuchi, *Mater. Chem. Front.*, 2018, **2**, 780-784.
32. CCDC 2362686 for **5**.
33. (*a*) P. Jana, S. Koppayithodi, S. Mahato, S. Molla and S. Bandyopadhyay, *J. Phys. Chem. Lett.*, 2023, **14**, 7433–7439; (*b*) B. Bleaney and K. D. Bowers, *Proc. R. Soc. London, Ser. A*, 1952, **214**, 451–465.
34. T. Lu and F. Chen, *J. Comput. Chem.*, 2012, **33**, 580-592.
35. H. Fallah-Bagher-Shaidaei, C. S. Wannere, C. Corminboeuf, R. Puchta and P. v. R. Schleyer, *Org. Lett.*, 2006, **8**, 863–866.
36. (*a*) S. Lehtola, M. Dimitrova, H. Fliegl and D. Sundholm, *J. Chem. Theory Comput.*, 2021, **17**, 1457-1468; (*b*) H. K. Saha, D. Mallick and S. Das, *Chem. Commun.*, 2022, **58**, 8492-8495.
37. D. Geuenich, K. Hess, F. Köhler and R. Herges, *Chem. Rev.*, 2005, **105**, 3758–3772.
38. P. K. Sharma, A. Babbar, D. Mallick and S. Das, *J. Org. Chem.*, 2023, **88**, 5473–5482.
39. S. Lukman, A. J. Musser, K. Chen, S. Athanasopoulos, C. K. Yong, Z. Zeng, Q. Ye, C. Chi, J. M. Hodgkiss and J. Wu, *Adv. Funct. Mater.*, 2015, **25**, 5452-5461.
40. B. D. Rose, L. E. Shoer, M. R. Wasielewski and M. M. Haley, *Chem. Phys. Lett.*, 2014, **616–617**, 137.
41. T. Y. Gopalakrishna, W. Zeng, X. Lua and J. Wu, *Chem. Commun.*, 2018, **54**, 2186-2199.
42. Bruker, SAINT V8.38A, (Bruker AXS Inc., 2017)
43. O. V. Dolomanov, L. J. Bourhis, R. J. Gildea, J. A. Howard, H. Puschmann, *J. Appl. Crystallogr.* 2009, **42**, 339–341.
44. L. J. Bourhis, O. V. Dolomanov, R. J. Gildea, J. A. Howard, H. Puschmann, *Acta Crystallogr. A.* 2015, **71**, 59–75.
45. G. M. Sheldrick, *Acta Crystallogr. C Struct. Chem*. 2015, **71**, 3–8.
46. Gaussian 09, *Revision B.01*, M. J. Frisch, G. W. Trucks, H. B. Schlegel, G. E. Scuseria, M. A. Robb, J. R. Cheeseman, G. Scalmani, V. Barone, B. Mennucci, G. A. Petersson, H. Nakatsuji, M. Caricato, X. Li, H. P. Hratchian, A. F. Izmaylov, J. Bloino, G. Zheng, J. L. Sonnenberg, M. Hada, M. Ehara, K. Toyota, R. Fukuda, J. Hasegawa, M. Ishida, T. Nakajima, Y. Honda, O. Kitao, H. Nakai, T. Vreven, J. A. Montgomery,

Jr., J. E. Peralta, F. Ogliaro, M. Bearpark, J. J. Heyd, E. Brothers, K. N. Kudin, V. N. Staroverov, T. Keith, R. Kobayashi, J. Normand, K. Raghavachari, A. Rendell, J. C. Burant, S. S. Iyengar, J. Tomasi, M. Cossi, N. Rega, J. M. Millam, M. Klene, J. E. Knox, J. B. Cross, V. Bakken, C. Adamo, J. Jaramillo, R. Gomperts, R. E. Stratmann, O. Yazyev, A. J. Austin, R. Cammi, C. Pomelli, J. W. Ochterski, R. L. Martin, K. Morokuma, V. G. Zakrzewski, G. A. Voth, P. Salvador, J. J. Dannenberg, S. Dapprich, A. D. Daniels, O. Farkas, J. B. Foresman, J. V. Ortiz, J. Cioslowski, D. J. Fox, Gaussian, Inc., Wallingford CT, 2010.

47. (a) T. Kubo, *Chem. Lett.* 2015, **44**, 111–122; b) S. Das, J. Wu, in *Polycyclic arenes and heteroarenes: synthesis, properties, and applications*, (Ed.: Q. Miao), John Wiley & Sons Inc., 2015, 3.

48. K. Yamaguchi, *Chem. Phys. Lett.* 1975, **33**, 330–335.

49. Z. Chen, C. S. Wannere, C. Corminboeuf, R. Puchta, P. v. R. Schleyer, *Chem. Rev*. 2005, **105**, 3842–3888.

50. N. M. O'boyle, A. L. Tenderholt, K. M. Langner, *J. Comput. Chem*. 2008, **29**, 839–845.

51. P. Hu, S. Lee, T. S. Herng, N. Aratani, T. P. Gonçalves, Q. Qi, X. Shi, H. Yamada, K. Huang, J. Ding, D. Kim, J. Wu, *J. Am. Chem. Soc.* 2016, **138**, 1065–1077.

5.7 Appendix

NMR Spectra

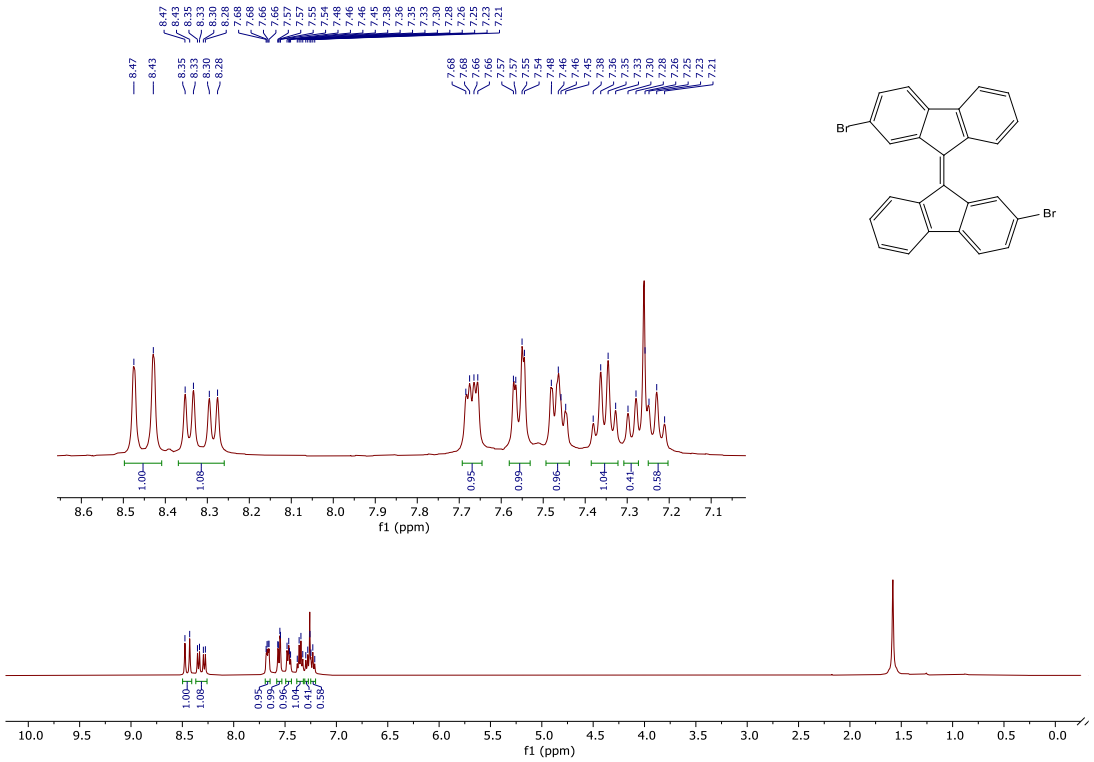

Figure 5.17 ^{1}H NMR spectrum of **6** (in $CDCl_3$, 400 MHz, 298 K).

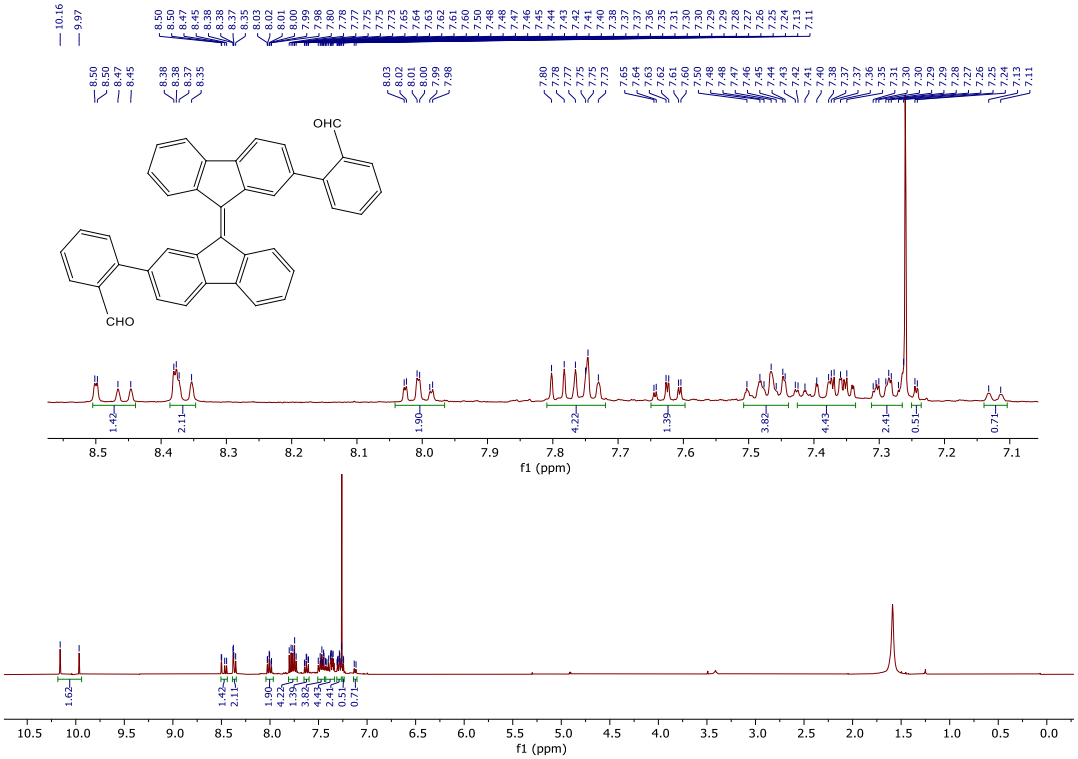

Figure 5.18 ^{1}H NMR spectrum of **8** (in $CDCl_3$, 400 MHz, 298 K).

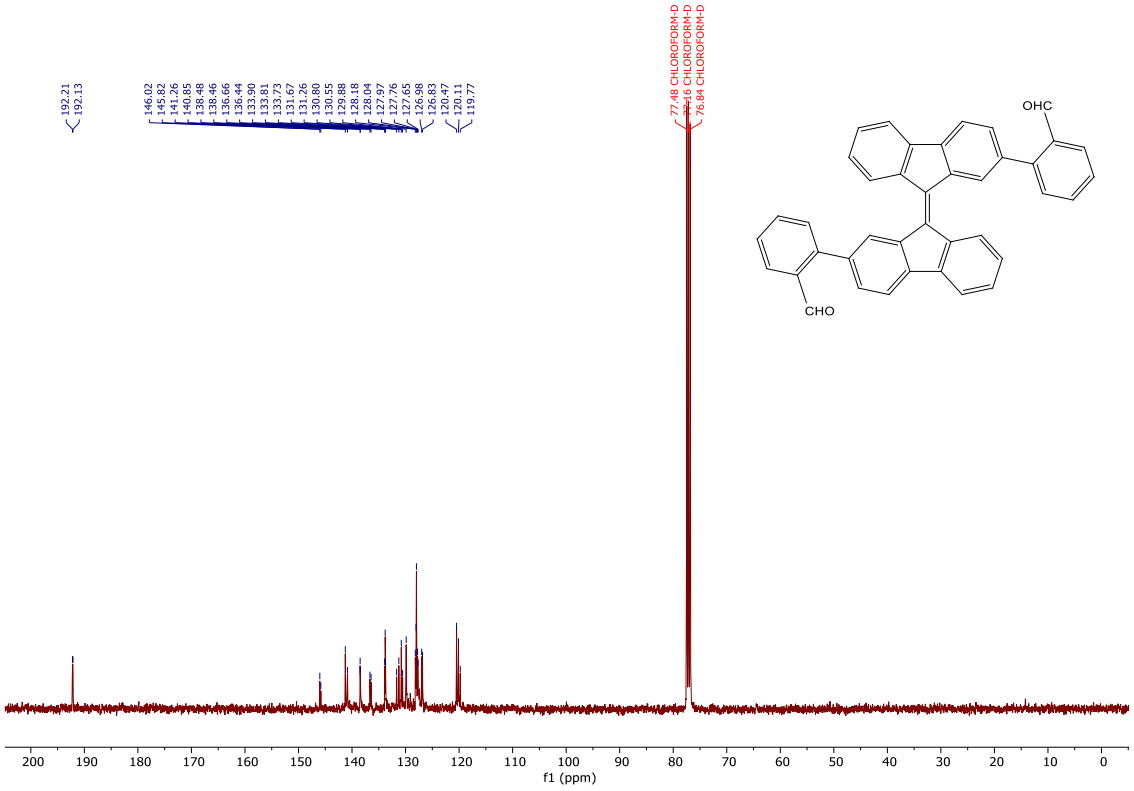

Figure 5.19 $^{13}C\{^{1}H\}$ NMR spectrum of **8** (in $CDCl_3$, 100 MHz, 298 K).

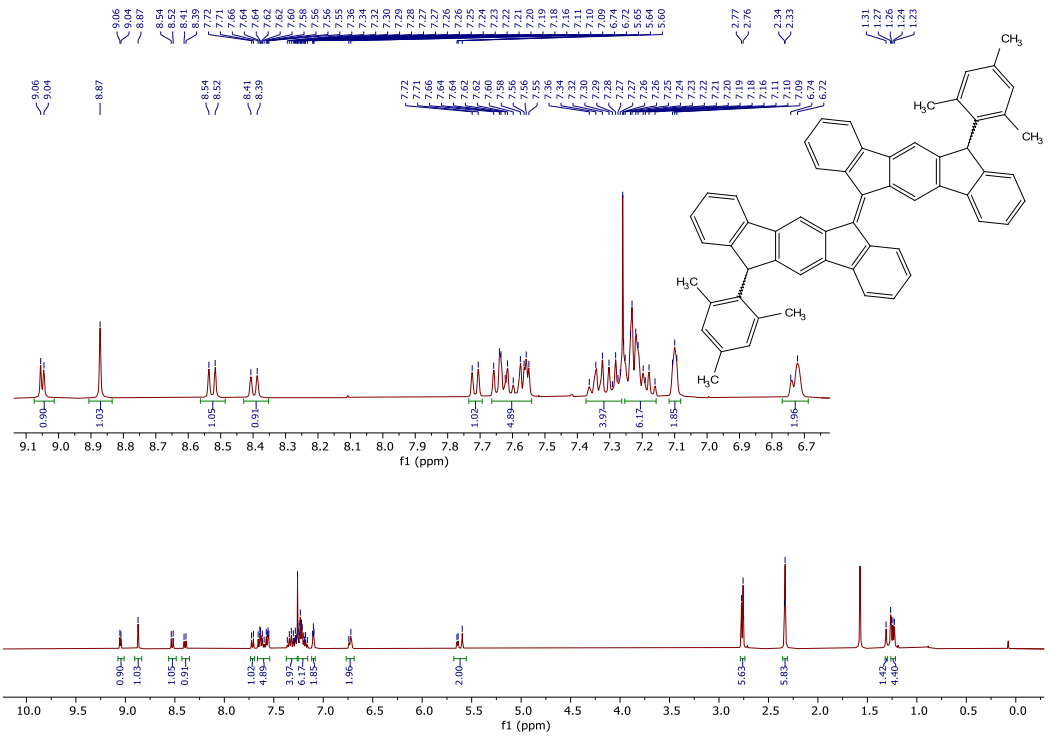

Figure 5.20 ^{1}H NMR spectrum of **10** (in $CDCl_3$, 400 MHz, 298 K).

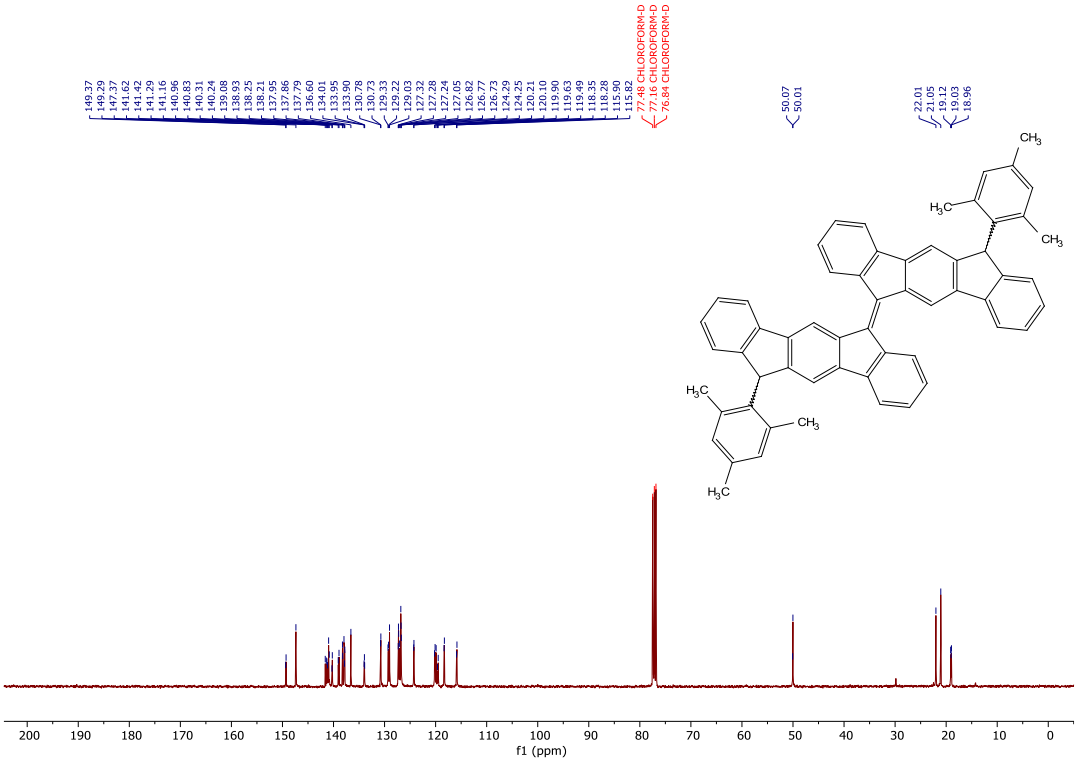

Figure 5.21 $^{13}C\{^{1}H\}$ NMR spectrum of **10** (in $CDCl_3$, 100 MHz, 298 K).

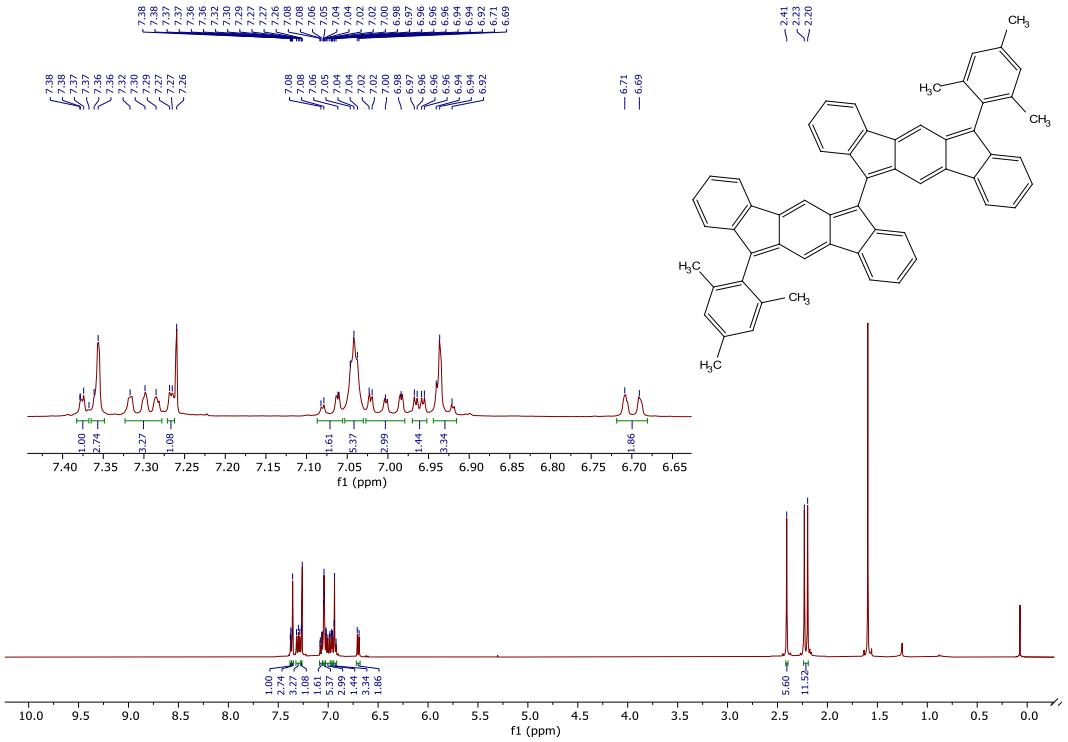

Figure 5.22 ^{1}H NMR spectrum of **5** (in $CDCl_3$, 400 MHz, 298 K).

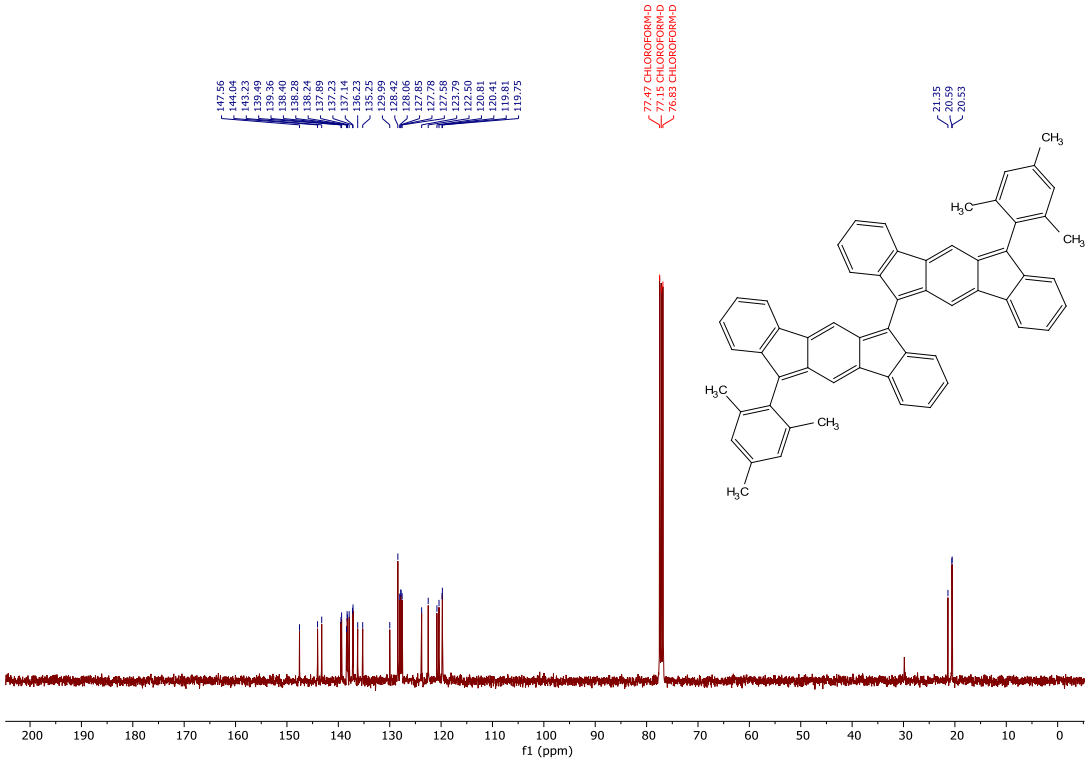

Figure 5.23 $^{13}C\{^{1}H\}$ NMR spectrum of **5** (in $CDCl_3$, 100 MHz, 298 K).

Chapter 6

Conclusion

6.1 Conclusion

My thesis, titled "**Syntheses and Properties of *π*-Extended Indenofluorene Derivatives**" comprises five chapters.

In conclusion, **Chapter 1** provides a comprehensive literature survey of the synthesis, properties and applications of five antiaromatic IFs and their *π*-extended derivatives. In **Chapter 2**, I have shown a new synthetic approach to symmetrical and unsymmetrical [2,1-*c*]IFs, and further extended this approach to synthesize a curved *s*-IDF system that caught attention of *Synfacts* editorial board.[1] These IFs exhibit balanced ambipolar charge-transport properties, in the order of $cm^2\ V^{-1}\ s^{-1}$. In **Chapter 3**, I report a steric-promoted synthetic approach to construct [1,2-*b*]IF and benzo-extended [1,2-*b*]IF isomers, including the first synthesis of an unsymmetrical antiaromatic [2,1-*a*]IF. Computationally, the [2,1-*a*]IF isomer showed a smaller HOMO-LUMO energy gap due to greater degree of antiaromaticity than isomeric [1,2-*b*]IF, which is experimentally validated by UV-vis and cyclic voltammetry studies. In **Chapter 4**, I report the syntheses and characterizations of three IF dimers (in the form of biindenofluorenes (BIFs)) with improved optoelectronic properties and HOMO−LUMO energy gaps (1.5 to 1.6 eV) smaller than the band gaps of related IF oligomers or polymers (2.3 eV). The analysis of charge-carrier mobility data of BIFs revealed hole mobilities on the order of $10^{-2}\ cm^2\ V^{-1}\ s^{-1}$ for thin films, which are 1−2 orders of magnitude higher than those of the corresponding monomers. In **Chapter 5**, I report the design and synthesis of a stable open-shell diradicaloid 6,6'-biindeno[1,2-*b*]fluorene, that exhibits four-stage redox amphotericity and improved optoelectronic properties. This work demonstrates a greater electronic communication between two [1,2-*b*]IF units when they are linked through carbons 6 and 6′, In comparison to 3 and 3′ of [1,2-*b*]IF in Chapter 4. The greater π-delocalization is evident from a shorter C_{sp^2}–C_{sp^2} single bond length linking the two [1,2-*b*]IF units, as found in SCXRD and DFT analyses. In all, my work demonstrates that the oligomerization of antiaromatic IF units through appropriate carbon positions may significantly influence the optoelectronic properties, as the electronic ground state can be effectively tuned.

6.2 References

1. T. M. Swager, H. Feng, *Synfacts* 2021, **17**, 32.